NATIONAL AERONAUTICS AND SPACE ADMINISTRATION

Space Programs Summary 37-54, Vol. III

Supporting Research and Advanced Development

For the Period October 1 to November 30, 1968

1+9

FACILITY FORM 602

N 69-19427 (ACCESSION NUMBER)	N69 19436 (THRU)
250 (PAGES)	1 (CODE)
CR-98695 (NASA CR OR TMX OR AD NUMBER)	34 (CATEGORY)

JET PROPULSION LABORATORY
CALIFORNIA INSTITUTE OF TECHNOLOGY
PASADENA, CALIFORNIA

December 31, 1968

NATIONAL AERONAUTICS AND SPACE ADMINISTRATION

Space Programs Summary 37-54, Vol. III

Supporting Research and Advanced Development

For the Period October 1 to November 30, 1968

JET PROPULSION LABORATORY
CALIFORNIA INSTITUTE OF TECHNOLOGY
PASADENA, CALIFORNIA

December 31, 1968

JPL SPACE PROGRAMS SUMMARY 37-54, VOL. III

Prepared Under Contract No. NAS 7-100
National Aeronautics and Space Administration

Preface

The Space Programs Summary is a multivolume, bimonthly publication that presents a review of technical information resulting from current engineering and scientific work performed, or managed, by the Jet Propulsion Laboratory for the National Aeronautics and Space Administration. The Space Programs Summary is currently composed of four volumes:

Vol. I.	*Flight Projects* (Unclassified)
Vol. II.	*The Deep Space Network* (Unclassified)
Vol. III.	*Supporting Research and Advanced Development* (Unclassified)
Vol. IV.	*Flight Projects and Supporting Research and Advanced Development* (Confidential)

Contents

SYSTEMS DIVISION

I. Systems Analysis Research 1

A. A Solar Electric Propulsion Spacecraft Asteroid Probe
C. G. Sauer, NASA Code 120-26-07-03 1

B. Progress Toward a Numerically Integrated Lunar Ephemeris
D. B. Holdridge and J D. Mulholland, NASA Code 129-04-06-02 4

C. Effect of Precession and Nutation Errors on Radar Observations
J. H. Lieske, NASA Code 129-04-04-02 7

D. Behavior of a Clock Moving Radially in a Centrally Symmetric Gravitational Field
H. Lass and P Gottlieb, NASA Code 129-04-01-01 12

E. A Simulated Leasts Square Solution for Parameters of the *Mariner* Mars 1969 Encounter Orbit
J. D. Anderson, NASA Code 129-04-01-02 14

F. Computational Accuracy of Square-Root Filtering
P. Dyer and S. R. McReynolds, NASA Code 125-17-05-02 15

II. Systems Analysis 20

A. ASTRAL: Optimized Low-Thrust Trajectories Using Approximate Closed-Form Solutions to the Equations of Motion
W. Stavro and D. J. Alderson, NASA Code 120-26-07-03 20

B. An Earth–Venus–Mercury Mission Opportunity in 1978
F. M. Sturms, Jr., NASA Code 684-30-01-10 26

C. Trajectory Analysis of a 1975 Mission to Mercury via an Impulsive Flyby of Venus
R. A. Wallace, NASA Code 684-90-01-07 30

D. Missions to the Outer Planets
R. A. Wallace, NASA Code 684-30-01-10 35

PROJECT ENGINEERING DIVISION

III. Environmental Requirements 37

A. The Effect of Low Numbers of Microorganisms on Samples Assayed by the NASA Standard Procedure
E. J. Sherry, NASA Code 189-58-23-02 37

GUIDANCE AND CONTROL DIVISION

IV. Flight Computers and Sequencers 40

A. Automatic Roving Vehicle Computer Development
L. Y. Lim, NASA Code 125-17-04-06 40

Contents (contd)

V. Spacecraft Power 43

A. Effect of Electrolyte Concentration on the Electrical Characteristics of AgO–Zn
R. S. Bogner and R. Patterson, NASA Code 120-34-01-15 43

B. Testing of Thermoelectric Generators
P. Rouklove, NASA Code 120-27-06-08 44

C. Power Conditioner for a Thermionic Diode Array
G. I. Cardwell, NASA Code 120 27-05-01 49

D. Development of the Heat-Sterilizable Battery
R. Lutwack, NASA Codes 120-34-01-03, -10, -20 50

E. Integrated Heat Pipe/Tubular Thermoelectric Module
S. Bain, NASA Code 120-27-06-08 51

VI. Guidance and Control Analysis and Integration 57

A. Support Equipment for a Strapdown Navigator
R. E. Williamson, NASA Code 125-17-01-04 57

VII. Spacecraft Control 60

A. Actuator Development for a Clustered Ion Engine Array
J. D. Ferrera and G. S. Perkins, NASA Code 120-26-04-10 60

B. Sterilizable Inertial Sensors: Gas Bearing Gyros
P. J. Hand, NASA Code 186-58-02-03 63

C. Ion Engine Thrust-Phase Attitude Control With Flexible Solar Arrays
G. E. Fleischer, NASA Code 125-19-04-01 65

VIII. Guidance and Control Research 70

A. Preignition Characteristics of Cesium Thermionic Diodes
K. Shimada, NASA Code 129-02-01-07 70

B. Barrier Heights of Blocking Contacts to Vacuum-Cleaved Photoconducting CdS in the Conducting State
R. J. Stirn, NASA Code 129-02-05-01 73

ENGINEERING MECHANICS DIVISION

IX. Electronic Parts Engineering 83

A. MOSFET Screening Methodology
R. A. Summers, NASA Code 186-70-01-04 83

B. Power Pulse Method of Screening Resistors
K. C. Evans, NASA Code 186-70-01-04 84

C. High-Impact Survival of Electronic Parts
K. R. Bilodeau and K. C. Evans, NASA Code 186-68-13-05 85

X. Advanced Projects Development 89

A. Parachute and Deployment Mortar Jettison Mechanisms
T. H. Mack, NASA Code 186-68-12-05 89

Contents (contd)

PROPULSION DIVISION

XI. Solid Propellant Engineering 91

A. Interior Ballistic Design and Experimental Development of a Self-Obturating, Propellant-Actuated Device
O. K Heiney, NASA Code 128-32-52-01 91

B. T-Burner Studies
E. H. Perry, NASA Code 128-32-50-01 93

XII. Polymer Research 97

A. A Model for the Effect of Dewetting on Mechanical Behavior of Composites Based on a Parabola-Shaped Void Cavity
R. F. Fedors and R F. Landel, NASA Code 128-32-43-01 97

B. Investigation on Sterilizable Polymer Battery Separators
E. F. Cuddihy and J. Moacanin, NASA Code 120-34-01-03 100

C. Creep of Elastomer Undergoing Aging
J. Moacanin, H. Y. Tom, R. F. Fedors, and R. F. Landel, NASA Code 129-03-11-04 105

D. Stress Relaxation in Compression of SBR—Glass Bead Composites
J. Moacanin and H. Y. Tom, NASA Code 186-68-13-03 107

XIII. Research and Advanced Concepts 114

A. Further Heat-Transfer Results With an Applied, Transverse Magnetic Field in a Square Channel
E. J. Roschke, NASA Code 129-01-05 11 114

B. Thermionic Diode Kinetics Experiment
H. Gronroos, NASA Code 120-27-05-01 119

C. Liquid-Metal MHD Power Conversion
D. G. Elliott, D. J. Cerini, and L. G. Hays, NASA Code 120-27-06-03 125

XIV. Liquid Propulsion 128

A. Combustion Effects in Sprays
J. Houseman, NASA Code 128-31-50-01 128

SPACE SCIENCES DIVISION

XV. Lunar and Planetary Instruments 133

A. A Mars Meteorology Wind Tunnel
J. M. Conley, NASA Code 185-47-01-02 133

XVI. Space Instruments 137

A. A Low-Noise Charge-Sensitive Video Preamplifier for Use With the SEC Camera Tube
D. F. Stout, NASA Code 186-68-06-09 137

B. Alignment of the Flight-Model Infrared Interferometer
F. L. Murphy, NASA Code 185-37-01-02 144

Contents (contd)

XVII. Lunar and Planetary Sciences 148

A. Meteoritic Sampling of the Solar Wind

H. C. Lord, III, NASA Code 195-42-12-01 148

XVII. Bioscience 150

A. Organic Analysis of Soil by Pyrolysis—Gas Chromatography—Mass Spectrometry—A Candidate Experiment for a Mars Lander

P. G. Simmonds, G. P. Shulman, and C. H. Stembridge, NASA Code 189-55 02-09 150

XIX. Physics 156

A. Jupiter's Red Spot and the Solar Wind

M. Eikrem and M. Neugebauer, NASA Code 385-48-01-01 156

B. An ICR Study of the Ion-Molecule Thermal Reaction Rates of H_2, D_2, and HD

D. D. Elleman, J. King, Jr., and M. T. Bowers, NASA Code 129-02-05-04 158

C. Compressional Waves in the Solar Wind

T. W. J. Unti, NASA Code 385-48 01-01 161

D. Debever Vectors in Dyadic Notation

B. K. Harrison, NASA Code 129-02-07-02 162

E. Dielectric Function of a Low-Density Electron Gas

J. S. Zmuidzinas, NASA Code 129-02-07-02 164

F. The Microwave Spectrum of the OD Free Radical

R. L. Poynter, NASA Code 129-02-06-11 166

TELECOMMUNICATIONS DIVISION

XX. Communications Systems Research 171

A. Sequential Decoding: Short Constraint Length Convolutional Codes

J. A. Heller, NASA Code 125-21-01-02 171

B. Coding and Synchronization Studies: Dynamics of Second-Order Phase-Locked Loops

W. C. Lindsey, NASA Code 125-21-02-03 177

C. Coding and Synchronization Studies: On Solution to the Second-Order Phase-Locked Loop

J. K. Holmes, NASA Code 125-21-02-03 182

D. Coding and Synchronization Studies: Power Allocation Length Into Rapidly Varying Phase Error

W. C. Lindsey and J. F. Hayes, NASA Code 125-21-02-03 187

E. Propagation Studies: Absolute Time by Pulsar

G. A. Morris, Jr., NASA Code 125-21-02-04 190

F. Communications Systems Development: Effects of Phase-Locked Loop Dynamics on Phase-Coherent Communications

I. F. Blake and W. C. Lindsey, NASA Code 150-22-11-08 192

Contents (contd)

G. Communications Systems Development: Efficiency of Noisy Reference Detection
R. C. Tausworthe, NASA Code 150-22-11-08 195

H. Information Processing: Limiters in Phase-Locked Loops: A Correction to Previous Theory
R. C. Tausworthe, NASA Code 150-22-11-09 201

XXI. Communications Elements Research 205

A. System Studies for 90-GHz Space Communications Systems: Atmospheric Effects on Millimeter Wave Propagation
T. Sato, NASA Code 125-21-03-04 205

B. Spacecraft Antenna Research: RF Breakdown Characteristics of S-Band Sterilizable High-Impact Antennas
K. Woo, NASA Code 186-68-04-06 205

C. Radiation From a Horizontal Electric Dipole Antenna Located in a Cylindrically Stratified Plasma
R. Woo, NASA Code 125-22-01-02 207

XXII. Spacecraft Telemetry and Command 211

A. Approximate Analysis of Channel Imbalance Effects in Non-Coherent FSK Receivers With Large BT Products
C. Carl, NASA Code 186-68-04-19 211

XXIII. Spacecraft Radio 221

A. Low-Data-Rate Telemetry RF Systems Development
R. Postal, NASA Code 150-22-17-06 221

XXIV. Mariner Telecommunications 224

A. Photon-Actuated Solid-State Switch Development
D. Bergens, NASA Code 125-25-02-05 224

✓ ADVANCED STUDIES

XXV. Future Projects Office 230

A. Lunar Mission Planning
R. G. Brereton, NASA Code 195-06-10-01 230

✓ FACILITIES OFFICE

XXVI. Technical Facilities 239

A. Variable Optical Techniques Applied to Solar Simulation
M. N. Wilson and R. R. Beal 239

I. Systems Analysis Research

SYSTEMS DIVISION

A. A Solar Electric Propulsion Spacecraft Asteroid Probe, *C. G. Sauer*

1. Introduction

In the past several years a number of studies have been made in determining the applicability of solar-electric-propulsion (SEP) spacecraft to the unmanned scientific investigation of the solar system.

This article presents several trajectory and spacecraft parameters for a solar-electric-propulsion spacecraft that could be used as a deep-space asteroid probe. The purposes of this mission would be to make: (1) an engineering test flight of a spacecraft using electric-propulsion thrustors and lightweight rollout solar panels as a power source, and (2) a scientific investigation of the region of the solar system encompassing 2 to 3 AU, including the asteroid belt. A minimum thrustor operating time of 400 days at an initial power level of approximately 4.6 kW at 1 AU is desired.

2. Spacecraft Description

The launch vehicle proposed for this mission is an *Atlas SLV3C/ Centaur* with an injected weight capability at escape of 2500 lb. The SEP spacecraft would have a mass of 750 lb, not including the solar panels, thrustors, and power-conditioning subsystems. The "installed" power capability of the solar panels proposed for this spacecraft is 6 kW at 1 AU; however, an assumed 18% degradation due to solar flares and environmental uncertainties results in a net power capability of 4.92 kW. Of this amount, 320 W is reserved for spacecraft auxilliary purposes, leaving a net thrustor input power at 1 AU of 4.6 kW. In the data to be presented, a total spacecraft mass of 480 kg was used, not including the low-thrust propellant mass.

The mission profile consists of a spacecraft injection at a *vis viva* energy of C_3 equal to 10 to 16 km^2/s^2. The spacecraft is injected so that the hyperbolic velocity is aligned in the direction of the motion of the earth and in the ecliptic plane. Shortly after injection, the spacecraft would be aligned so that the SEP engines will be thrusting in a direction normal to the sun line and in the ecliptic plane. Since a specific target has not been identified, the selection of a launch date at this time is somewhat arbitrary; consequently, the trajectories shown in this analysis were initiated with an initial heliocentric longitude of zero corresponding to a launch date late in September.

The required propellant mass, exclusive of residuals, is shown in Fig. 1 as a function of departure C_3 for propulsion times of 400, 500, and 600 days. Since the propellant mass flow rate is directly proportional to thrustor input power, the mass flow rate will decrease with increasing probe distance from the sun because of the drop in power

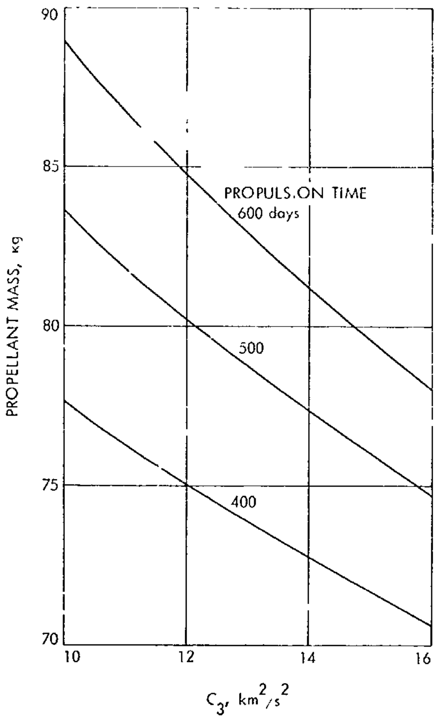

Fig. 1. SEP spacecraft asteroid probe, propellant mass versus C_3

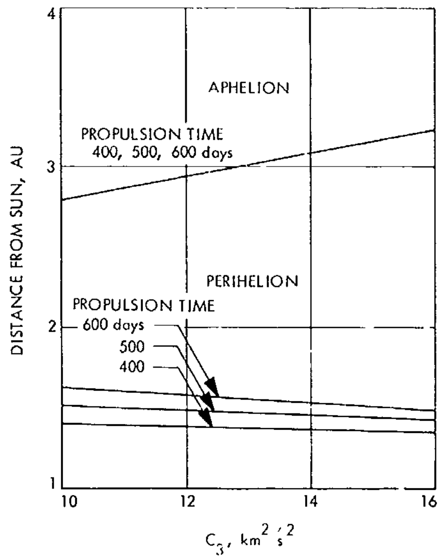

Fig. 2. SEP spacecraft asteroid probe, aphelion and perihelion distance versus C_3

from the solar panels. The additional propellant required for thrusting an additional 100 to 200 days is relatively small, since the available power to the thrustors and also the propellant flow rate has dropped to about one sixth of the initial value after 400 to 500 days. An additional 100 days of propulsion requires, at most, 5 kg additional propellant (Fig. 1).

3. Trajectory Characteristics

The aphelion and perihelion of the heliocentric trajectory after thrust cutoff is shown in Fig. 2 as a function of departure C_3. The effect of increasing the propulsion time does not materially affect the aphelion distance since thrust cutoff occurs near this point, and additional thrusting has the effect of raising the perihelion but does not affect the aphelion distance. The aphelion distance does increase with increasing C_3, however, and an aphelion range of 2¾ to 3¼ AU can be covered with a departure C_3 in the range of 10 to 16 km^2/s^2. The perihelion distance decreases slightly with increasing C_3 and increases with an increase in propulsion time.

The path of the spacecraft in the ecliptic plane is shown in Figs. 3 and 4 for a propulsion time of 400 days and for departure *vis viva* energies of 10 and 16 km^2/s^2. Figure 3 shows the path of the vehicle for a departure C_3 of 10 km^2/s^2. The probe spends 250 days to 950 days beyond 2 AU with aphelion occurring at 600 days. In Fig. 4 the path of the spacecraft for a departure C_3 of 16 km^2/s^2 remains beyond 2 AU for 210 days to 1110 days or for a total of 900 days as compared with the 700 days for the trajectory shown in Fig. 3.

The power available to the thrustors is shown in Fig. 5 as a function of time along the trajectory. Because of thrustor design considerations, it would seem inadvisable to operate the low-thrust engines at a power level less than around ½ kW. For a trajectory with a departure C_3 of 16 km^2/s^2 this point occurs at about 400 days, and in order to provide additional operating time, the motors could be restarted at about 900 days. The second trajectory, corresponding to a C_3 of 10 km^2/s^2, has a minimum power of ½ kW at aphelion.

4. Communication Parameters

Figure 6 presents the communication distance as a function of time for the same trajectories used previously. A communication distance of 530 to 560 million km is required to observe the thrust cutoff point at 400 days. Delaying thrust cutoff until 600 days will reduce the communication distance by about a factor of 2. An interesting feature of the trajectory shown in Fig. 3 for a C_3 of 10 km^2/s^2 is that it is close to being synchronous with the period of the earth—quite close to 3 yr. Opposition with the earth occurs close to aphelion and perihelion of the spacecraft trajectory.

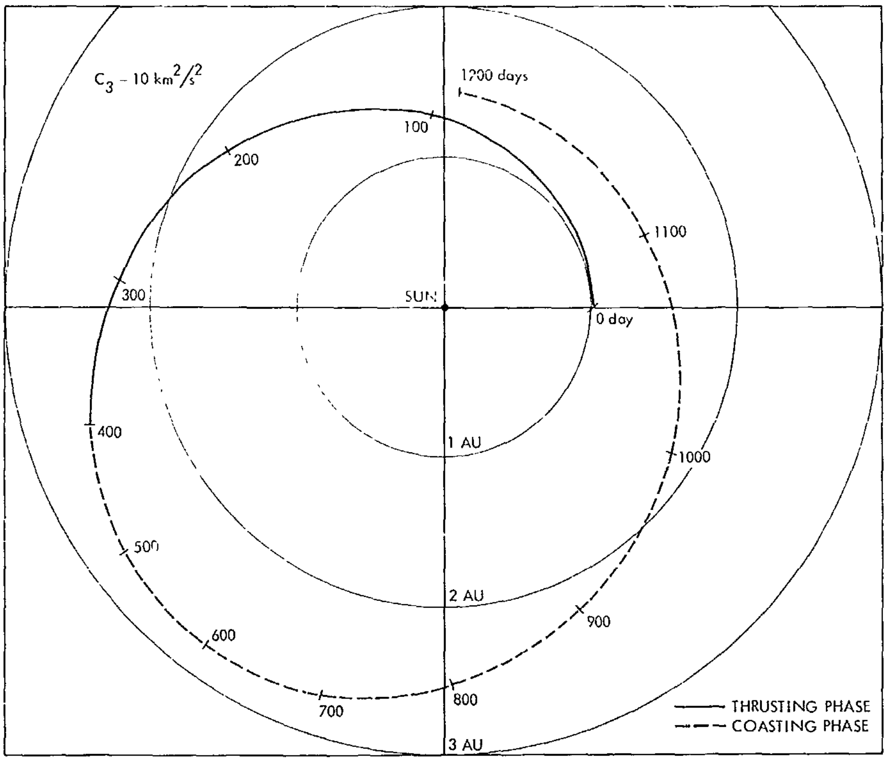

Fig. 3. SEP spacecraft asteroid probe, $C_3 = 10\ km^2/s^2$

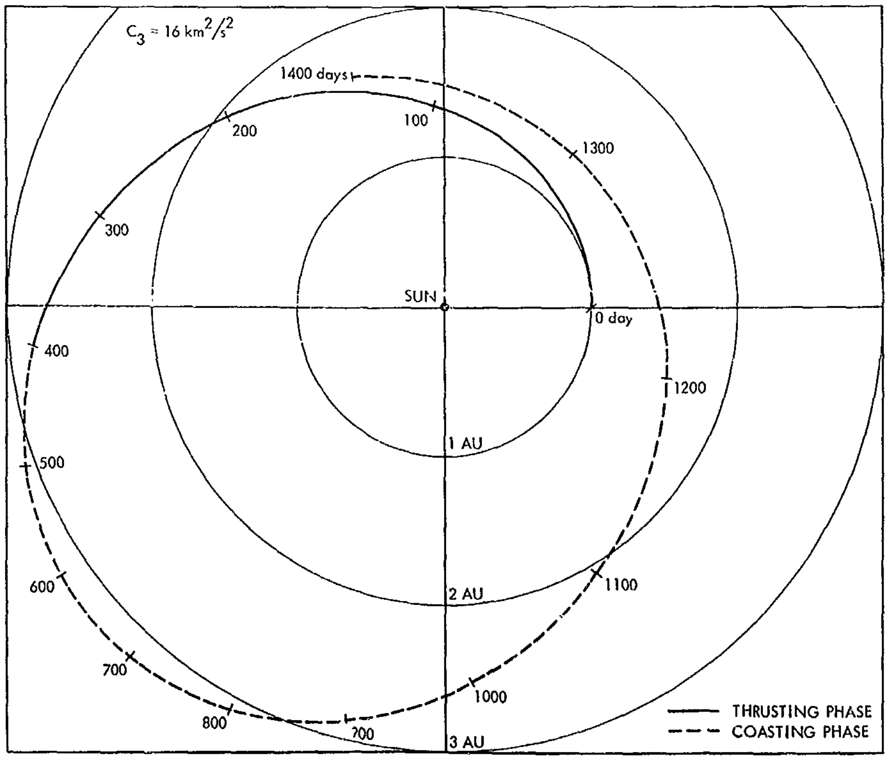

Fig. 4. SEP spacecraft asteroid probe, $C_3 = 16\ km^2/s^2$

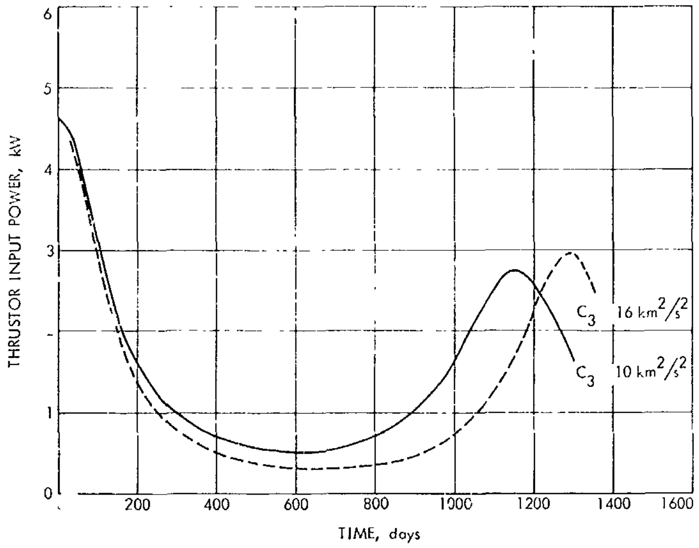

Fig. 5. SEP spacecraft asteroid probe thrustor input power

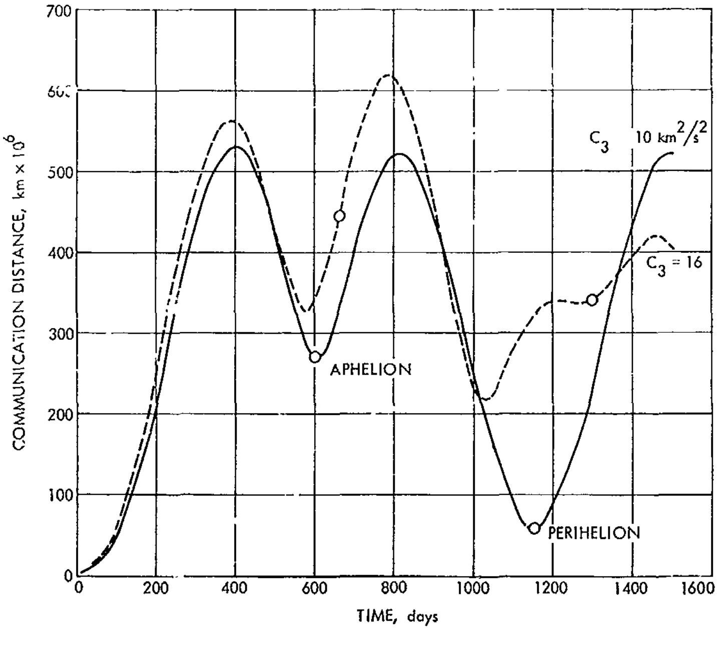

Fig. 6. SEP spacecraft asteroid probe communication distance versus time

The antenna direction, given by the earth-probe-sun angle, is shown in Fig. 7 as a function of time. Excluding the initial 60 to 70 days, a maximum antenna direction from the sun line of not more than 35 deg is required for the duration of the mission. Initially this angle is around 90 deg as the probe recedes from the earth in the direction of the motion of the earth. At the point where the earth-probe-sun angle has decreased to 35 deg, the communication distance is around 15 million km.

B. Progress Toward a Numerically Integrated Lunar Ephemeris, *D. B. Holdridge and J. D. Mulholland*

For the past year it has been evident that the high accuracy required of the lunar ephemeris, if it is to achieve maximum utility in the analysis of spacecraft data, can be obtained at the present time only by numerical integration of the equations of motion (Ref. 1). The imple-

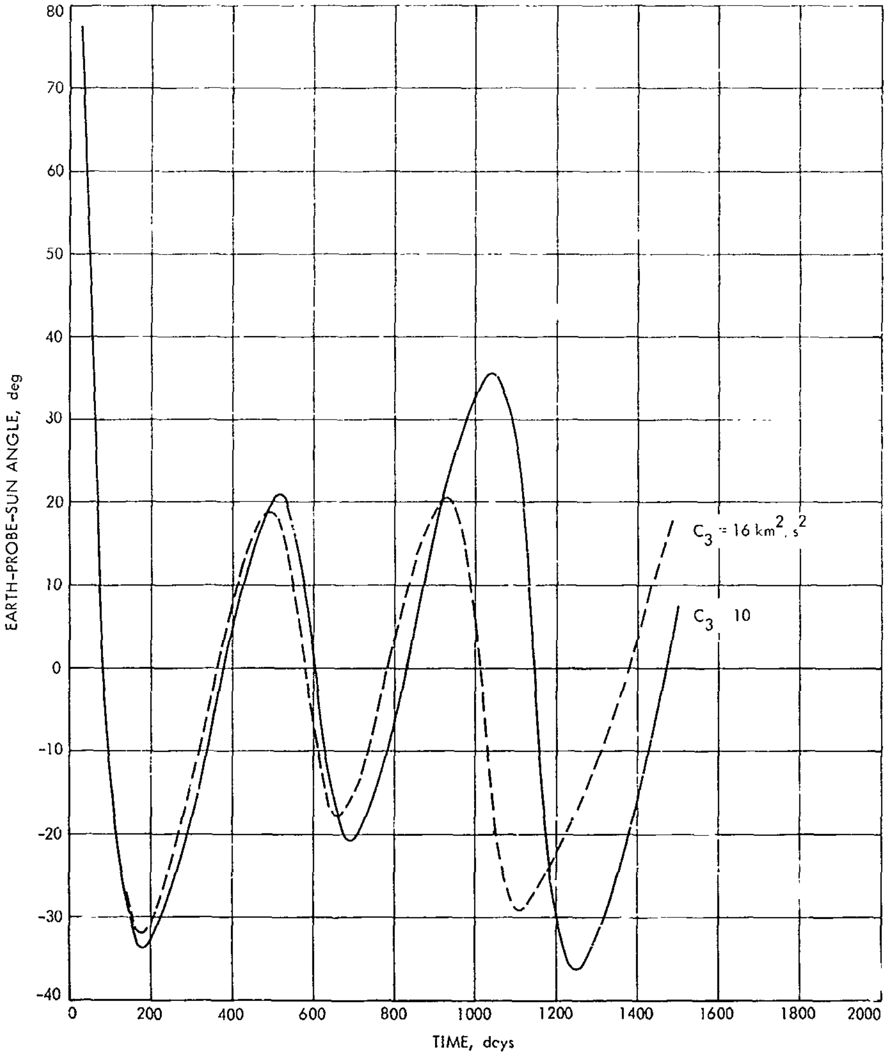

Fig. 7. SEP spacecraft asteroid probe earth–probe–sun angle

mentation of such an ephemeris has been pursued in two conceptually distinct, but complementary, phases.

1. Numerical Fit to Theory

The work that was reported in Ref. 1 and in SPS 37-49, Vol. III, pp. 13–15, consisted of a single-body integration of the lunar orbit over a 2-yr interval, differentially corrected to fit the theory-based ephemeris designated LE 4 (Ref. 2) by means of a modified version of the planetary orbit determination program (PLOD; Ref. 3). After it was established that serious defects existed in the theoretical ephemeris, an effort was mounted for the extension of this work to a meaningful time span. To properly treat the long-term characteristics of the motion, the nodal period (18.6 yr) may be regarded as a practical minimum interval over which to extend the differential correction procedure. The interval actually adopted was from JED 243 3280.5 to 244 0800.5, slightly more than 20 yr, beginning at the epoch of the JPL ephemeris tape system.

There are several arguments in favor of producing acceptable fits to the theoretical ephemeris as a prior step to dealing with the observations. The most cogent one in the early stages of the work was the ease and rapidity with which the PLOD program could be modified to perform this task. At present, it is far more important that this process can be regarded as a controlled experiment that will permit the development of techniques for solving the real problems of fitting the lunar motion without introducing the uncertainties and biases that always accompany observational data. Despite its flaws, the Lunar Theory does conform rather well to the real motion of the moon, particularly in those features that are a hindrance to the production of an accurate ephemeris by numerical integration. These features primarily affect two aspects: (1) the differential correction and, (2) the modeling of effects that arise from other than point-mass gravitational considerations.

The moon is a highly perturbed object, and the standard differential correction procedures used in PLOD, as in other planetary ephemeris development programs, are based on formulas that assume Keplerian motion. This is acceptable in the planetary case, because the planets are remarkably well behaved. In the attempts to extend the correction span beyond 2 yr, the suspicion was amply confirmed that the unperturbed partial derivatives are not adequate in the lunar case. Successive corrections for a series of 5-yr integrations failed to converge to a final set of initial conditions.

The possible ways in which one could produce perturbed partial derivatives were discussed in an earlier article (SPS 37-51, Vol. III, pp. 13–15), and a detailed discussion was given of the implementation of one of the alternatives, that of analytic series expressions. Subsequent to the writing of that article, discussions[1] revealed that the expressions for $a\partial\hat{s}/\partial a$ referred only to the scale factor effect and did not include the dynamical effect (Ref. 4, p. 235) involving the angular motion. It would become necessary to introduce this effect into the computation of $[\partial\kappa_0/\partial\kappa_1]$, and much of the estimated saving in computer running time would have disappeared, in addition to the programming effort that this approach would have entailed. As a consequence, the relatively simple method of finite difference quotients was eventually used for the partial derivative computations.

The availability of reasonably accurate partial derivatives resolved the differential correction problem, and within a relatively short time a converged series of integrated fits over the 20-yr span was obtained, the source theory being LE 6 (Ref. 5). Although the correction series did converge to a final solution, the residuals of that solution were not really satisfactory, and the reason for this situation is believed to lie in the modeling problem.

The major flaw in using a theory as the comparison base for a numerical integration is the possibility that empirical adjustments to the theory may destroy the faithfulness with which it reflects the nominal model on which it was constructed. In the case of the Lunar Theory and our integrations, the tides, the figure of the moon, and perhaps some yet unknown cause have led to such adjustments. In each case, analysis of the observational data showed one or more of the orbital parameters to be inadequately represented by the theory, and in each case the theoretical expressions were replaced by the observational values. The numerical integrations are based on gravitational models not greatly different from that on which the theory is founded, so one would not expect these empirical aspects of the theory to be properly modeled in the integration. It is necessary either to learn how to model them or how to handle such empirical fixes in conjunction with a numerical integration.

Such a component in the lunar motion is attributed to the frictional losses in the tidal deformations of earth. These losses reduce the rotational angular momentum of earth, with subsequent gain in the orbital angular momentum of moon. This gain is reflected in a secular increase in the mean distance and decrease in the sidereal mean motion. This is represented as a secular acceleration of the mean longitude

$$\Delta L = -11''\!.22\,T^2$$

where T is measured in Julian centuries. There is less than complete agreement on the detailed mechanism of this angular momentum transfer, but it is widely assumed (e.g., Ref. 6) that it involves the gravitational couple generated by the tidal bulge. Whatever the mechanism, it is not modeled in the differential equations of motion, and a means must be found of treating the real phenomenon.

Both the perigee and the node have motions that arise from unmodeled causes. The current ephemeris programs treat the moon as a point of mass, whereas the Brown theory embodies a triaxial moon not greatly different from the one currently recommended. The solar system data-processing system is to be modified to include this feature, but in the interim, it is necessary to find an empirical way of treating the motions. Such an empirical treatment is necessary from another aspect, too. Eckert (Ref. 7) has shown that the present observational values of $d\tilde{\omega}/dT$ and $d\Omega/dT$ cannot be satisfied with the present model without assuming an unbelievable lunar density distribution. That is, the perigee and node have motions that *cannot* be modeled in the light of present knowledge. These last two effects combined amount to

$$\Delta\tilde{\omega} = -3''\!.1\,T, \qquad \Delta\Omega = -27''\!.9\,T$$

---

[1] With T. C. Van Flandern, U.S. Naval Observatory, who developed the analytic partial derivatives.

There seems to be no simple resolution of this within the structure of PLOD.

As a means of discovering if these various effects are the cause of the remaining large-scale residuals in the PLOD integrations of the lunar motion, a theoretical ephemeris (LE 12) has been constructed by removing the gravitationally unmodeled effects from LE 6. Numerical integrations fit to this ephemeris are now under way.

2. Use of Lunar Observations

In the long run the fitting of theories must be abandoned, and one must return to the source of all empirical knowledge—the observations. The modifications necessary to convert the solar system data-processing system (SPS 37-51, Vol. III, pp. 4-1[illegible]) to lunar application are now being programmed. Many gains are expected from this. The figure of the moon can be modeled; perhaps the tidal effect can be modeled. It may even be that the unexplained defect of the theory noted above is not due to the figure of the moon at all, but to the currently accepted observational values. A recent analysis of the occultation observations[2] seems to suggest that this is a possibility. If so, this discrepancy should disappear with the use of observational data.

---

[2] Martin, C. F., "ET-UT Time Corrections for the Period 1627–1860," in *Observation, Analysis and Space Research Applications of the Lunar Motion*. Edited by J. D. Mulholland (in preparation).

References

1. Mulholland, J. D., and Devine, C. J., "Gravitational Inconsistency in the Lunar Theory: Numerical Determination," *Science*, Vol. 160, pp. 874–875, May 24, 1968.
2. Mulholland, J. D., and Block, N., *JPL Lunar Ephemeris Number 4* Technical Memorandum 33-346. Jet Propulsion Laboratory, Pasadena, Calif., August 1, 1967.
3. Devine, C. J., *PLOD II: Planetary Orbit Determination Program for the IBM 7094 Computer* Technical Memorandum 33-188. Jet Propulsion Laboratory, Pasadena, Calif., April 15, 1965.
4. Brouwer, D., and Clemence, G. M., *Methods of Celestial Mechanics*. Academic Press, New York, 1961.
5. Mulholland, J. D., *JPL Lunar Ephemeris Number 6* Technical Memorandum 33-408. Jet Propulsion Laboratory, Pasadena, Calif., October 15, 1968.
6. Gerstenkorn, H., "The Model of the So-Called 'Weak' Tidal Friction and the Limits of Its Applicability" in *Mantles of the Earth and Terrestrial Planets*. Edited by S. K. [illegible]corn. Interscience Publishers, Inc., London, 1967.
7. Eckert, W. J., "On the Motions of Perigee and Node and the Distribution of Mass in the Moon," *Astron. J.*, Vol. 70, pp. 787–792, 1965.

C. Effect of Precession and Nutation Errors on Radar Observations, *J. H. Lieske*

The partial derivatives relating errors in the constant of general precession in longitude and the constant of nutation to changes in range and range rate are developed in this article. It will be shown that an error on the order of 1 arc sec/century in the general precession in longitude will introduce drifts on the order of 30 m/century in range and 2 mm/s/century in range rate. The effect probably will be absorbed by station longitude and would amount to a drift on the order of 1/3 m/yr. Errors in the constant of nutation, on the other hand, introduce effects on the order of 600 mm and 0.04 mm/s on the range and range rate, respectively, for an error in the coefficient of nutation of 0.01 arc sec. The partial derivatives will be developed in an equatorial 1950.0 frame, and simplified expressions adequate for most purposes will be given.

In the present investigation it is assumed that the vector $\boldsymbol{\rho}$ from the observer to the object being tracked is given by the expression

$$\boldsymbol{\rho} = \mathbf{r} - \mathbf{R}_e - \mathbf{A}_P^T \mathbf{A}_N^T \mathbf{R}_S \qquad (1)$$

where $\mathbf{r}$ and $\mathbf{R}_e$ are the heliocentric vectors to the object and to the center of the earth referred to the equator and equinox of 1950.0, respectively, and $\mathbf{A}_P^T \mathbf{A}_N^T \mathbf{R}_S$ is the vector from the geocenter to the observer in a 1950.0 frame. The transpose of a matrix $\mathbf{A}$ is denoted by $\mathbf{A}^T$. The precession matrix $\mathbf{A}_P$ and nutation matrix $\mathbf{A}_N$ are given by the usual expressions (Ref. 1)

$$\mathbf{A}_P = \begin{bmatrix} \cos\zeta_0\cos\theta\cos z - \sin\zeta_0\sin z & -\sin\zeta_0\cos\theta\cos z - \cos\zeta_0\sin z & -\sin\theta\cos z \\ \cos\zeta_0\cos\theta\sin z + \sin\zeta_0\cos z & -\sin\zeta_0\cos\theta\sin z + \cos\zeta_0\cos z & -\sin\theta\sin z \\ \cos\zeta_0\sin\theta & -\sin\zeta_0\sin\theta & \cos\theta \end{bmatrix} \qquad (2)$$

$$\mathbf{A}_N = \begin{bmatrix} \cos\Delta\psi & -\cos\bar{\epsilon}\sin\Delta\psi & -\sin\Delta\psi\sin\bar{\epsilon} \\ \sin\Delta\psi\cos\epsilon & \cos\Delta\psi\cos\bar{\epsilon}\cos\epsilon + \sin\bar{\epsilon}\sin\epsilon & \cos\Delta\psi\sin\bar{\epsilon}\cos\epsilon - \cos\bar{\epsilon}\sin\epsilon \\ \sin\Delta\psi\sin\epsilon & \cos\Delta\psi\cos\bar{\epsilon}\sin\epsilon - \sin\bar{\epsilon}\cos\epsilon & \cos\Delta\psi\sin\bar{\epsilon}\sin\epsilon + \cos\bar{\epsilon}\cos\epsilon \end{bmatrix} \tag{3}$$

where ζ_0, z, and θ are the precession parameters employed in reducing positions referred to the mean equator and equinox of 1950.0 to the mean equator and equinox of date, where $\Delta\psi$ is the nutation in longitude, and ϵ and $\bar{\epsilon}$ refer to the true and mean obliquity of the ecliptic of date, respectively. The geocentric position of the observer referred to the true equator and equinox of date is assumed to be in the form

$$\mathbf{R}_S = \begin{bmatrix} \cos\theta_G & -\sin\theta_G & 0 \\ \sin\theta_G & \cos\theta_G & 0 \\ 0 & 0 & 1 \end{bmatrix} \mathbf{S} \tag{4}$$

where θ_G is the true Greenwich sidereal time, and

$$\mathbf{S} = \begin{bmatrix} R_0\cos\phi'\cos\lambda_E \\ R_0\cos\phi'\sin\lambda_E \\ R_0\sin\phi' \end{bmatrix} \tag{5}$$

with R_0 representing the geocentric distance of the observer; ϕ', his geocentric latitude, and λ_E, the observer's longitude measured east from Greenwich.

An important and useful property of these orthogonal rotation matrices is that if **A** is a rotation matrix, or the matrix product of several orthogonal matrices, and if q is a parameter upon which one or several of the matrices depend, then the matrix

$$\mathbf{C} = \frac{\partial \mathbf{A}^T}{\partial q}\mathbf{A}$$

is skew-symmetric, or the sum of several skew-symmetric matrices, and hence the quadratic form

$$B = \mathbf{x}^T\mathbf{C}\mathbf{x} \tag{6}$$

is zero for any vector **x**. This property is useful in obtaining the partial derivative of the scalar slant range $\partial\rho/\partial q$ from the vectors $\boldsymbol{\rho}$ and $\partial\boldsymbol{\rho}/\partial q$. As an example, consider the contribution of $\partial\boldsymbol{\rho}/\partial q$ to the desired quantity $\partial\rho/\partial q$.

If $\mathbf{A}_N$ and $\mathbf{A}_P$ depend upon the parameter q, then

$$\frac{\partial\boldsymbol{\rho}}{\partial q} = -\left(\frac{\partial\mathbf{A}_P^T}{\partial q}\mathbf{A}_N^T + \mathbf{A}_P^T\frac{\partial\mathbf{A}_N^T}{\partial q}\right)\mathbf{R}_S$$

$$\begin{aligned} \rho\frac{\partial\rho}{\partial q} &= (\mathbf{r} - \mathbf{R}_e - \mathbf{A}_P^T\mathbf{A}_N^T\mathbf{R}_S)^T \\ &\quad \times \left(-\frac{\partial\mathbf{A}_P^T}{\partial q}\mathbf{A}_N^T - \mathbf{A}_P^T\frac{\partial\mathbf{A}_N^T}{\partial q}\right)\mathbf{R}_S \\ &= -(\mathbf{r} - \mathbf{R}_e)^T\left(\frac{\partial\mathbf{A}_P^T}{\partial q}\mathbf{A}_N^T + \mathbf{A}_P^T\frac{\partial\mathbf{A}_N^T}{\partial q}\right)\mathbf{R}_S \\ &\quad + \mathbf{R}_S^T\mathbf{A}_N\mathbf{A}_P\frac{\partial\mathbf{A}_P^T}{\partial q}\mathbf{A}_N^T\mathbf{R}_S + \mathbf{R}_S^T\mathbf{A}_N\frac{\partial\mathbf{A}_N^T}{\partial q}\mathbf{R}_S\,. \end{aligned}$$

The skew-symmetric property may be used to show that the last two terms in the above equation are zero because

$$\mathbf{A}_P\frac{\partial\mathbf{A}_P^T}{\partial q}$$

is skew-symmetric, as is

$$\mathbf{A}_N\left(\mathbf{A}_P\frac{\partial\mathbf{A}_P^T}{\partial q}\right)\mathbf{A}_N^T$$

Hence, the quadratic form

$$\mathbf{R}_S^T\left(\mathbf{A}_N\mathbf{A}_P\frac{\partial\mathbf{A}_P^T}{\partial q}\mathbf{A}_N^T\right)\mathbf{R}_S$$

is zero. The same comments apply for

$$\mathbf{R}_S^T\mathbf{A}_N\frac{\partial\mathbf{A}_N^T}{\partial q}\mathbf{R}_S$$

Since there are several forms one may wish to employ for the computed range or doppler, the skew-symmetric property will be extremely useful in computing the various forms. In the remainder of this paper only the vector partial derivatives $\partial\boldsymbol{\rho}/\partial q$ and $\partial\dot{\boldsymbol{\rho}}/\partial q$ will be computed, so that a person may combine them in whatever type of range or doppler equation he desires.

It is clear that the heliocentric positions $\mathbf{r}$ of the planet and $\mathbf{R}_e$ of the earth referred to the 1950.0 equator and equinox will not depend upon the values of precession and nutation (although their estimated values certainly are affected to some extent). We thus need only be concerned with the effect of precession and nutation on $\mathbf{A}_P$, $\mathbf{A}_N$ and $\mathbf{R}_S$ of the observer. The observer's geocentric position $\mathbf{R}_S$ is affected by precession and nutation only through the sidereal time, as indicated by Eq. (4). The true Greenwich sidereal time θ_G is of the form

$$\theta_G = \bar{\theta}_G + \Delta\psi \cos \epsilon + \delta \tag{7}$$

where $\bar{\theta}_G$ is the mean Greenwich sidereal time and δ includes the effects of polar motion, annual periodic variations, etc. While it is true that the origin of the definition of mean Greenwich sidereal time $\bar{\theta}_G$ involved introducing a specific value of the general precession in right ascension, the expression for $\bar{\theta}_G$ is now to be taken *as a definition* of the universal time; hence $\bar{\theta}_G$ will not be affected by any error in precession, since it is *defined* as the Greenwich hour angle of the mean equinox of date. We then see that the true sidereal time is affected by nutation but not precession.

The partial derivatives of ζ_0, z, and θ appearing in Eq. (2) with respect to the general precession in longitude p are taken from Lieske (Ref. 2):

$$\left.\begin{aligned} \frac{\partial \zeta_0}{\partial p} = \frac{\partial z}{\partial p} &= 0.45891T = \frac{T}{2}\cos\epsilon_0 \\ \frac{\partial \theta}{\partial p} &= 0.39780T = T\sin\epsilon_0 \end{aligned}\right\} \tag{8}$$

where T is measured in tropical centuries from 1950.0, and ϵ_0 is the mean obliquity of the ecliptic at 1950.0. The nutation in obliquity is assumed to be of the form

$$\Delta\epsilon = \epsilon - \bar{\epsilon} = N \cos \Omega_{☾} \tag{9}$$

while the nutation in longitude is taken as

$$\Delta\psi = -\gamma N \sin \Omega_{☾} \tag{10}$$

where $N = 9''.210$, $\gamma = 1.8712$ (so that $-\gamma N = -17''.234$) and where $\Omega_{☾}$ is the node of the orbit of the moon on the mean ecliptic of date.

The partial derivatives required for general precession in longitude are

$$\frac{\partial \boldsymbol{\rho}}{\partial p} = -\frac{\partial \mathbf{A}_P^T}{\partial p}\mathbf{A}_N^T\mathbf{R}_S \tag{11}$$

$$\frac{\partial \dot{\boldsymbol{\rho}}}{\partial p} = -\frac{\partial \mathbf{A}_P^T}{\partial p}\mathbf{A}_N^T\dot{\mathbf{R}}_S - \left(\frac{\partial \dot{\mathbf{A}}^T}{\partial p}\mathbf{A}_N^T + \frac{\partial \mathbf{A}_P^T}{\partial p}\dot{\mathbf{A}}_N^T\right)\mathbf{R}_S \tag{12}$$

while those for nutation are

$$\frac{\partial \boldsymbol{\rho}}{\partial N} = -\mathbf{A}_P^T\frac{\partial \mathbf{A}_N^T}{\partial N}\mathbf{R}_S - \mathbf{A}_P^T\mathbf{A}_N^T\frac{\partial \mathbf{R}_S}{\partial N} \tag{13}$$

$$\begin{aligned} \frac{\partial \dot{\boldsymbol{\rho}}}{\partial N} = &-\mathbf{A}_P^T\frac{\partial \mathbf{A}_N^T}{\partial N}\dot{\mathbf{R}}_S - \mathbf{A}_P^T\mathbf{A}_N^T\frac{\partial \dot{\mathbf{R}}_S}{\partial N} \\ &-\left(\dot{\mathbf{A}}_P^T\frac{\partial \mathbf{A}_N^T}{\partial N} + \mathbf{A}_P^T\frac{\partial \dot{\mathbf{A}}^T}{\partial N}\right)\mathbf{R}_S \\ &-\left(\dot{\mathbf{A}}_P^T\mathbf{A}_N^T + \mathbf{A}_P^T\dot{\mathbf{A}}_N^T\right)\frac{\partial \mathbf{R}_S}{\partial N} \end{aligned} \tag{14}$$

The matrices $\mathbf{A}_P$, $\mathbf{A}_N$, and $\mathbf{R}_S$ are already defined in Eqs. (2), (3), (4) and (5), and their partial derivatives may be readily computed. Simplified forms, adequate for most purposes, will be given later. The complete forms will be given in order that one may employ the more exact relations if he so desires.

The matrix $\partial\mathbf{A}_P/\partial p$ is determined from

$$\frac{\partial \mathbf{A}_P}{\partial p} = \frac{\partial \mathbf{A}_P}{\partial \zeta_0}\frac{\partial \zeta_0}{\partial p} + \frac{\partial \mathbf{A}_P}{\partial z}\frac{\partial z}{\partial p} + \frac{\partial \mathbf{A}_P}{\partial \theta}\frac{\partial \theta}{\partial p} \tag{15}$$

where

$$\frac{\partial \zeta_0}{\partial p}, \frac{\partial z}{\partial p}, \frac{\partial \theta}{\partial p}$$

are given by Eq. (8).

The partial derivative of the nutation matrix $\mathbf{A}_N$ with respect to the constant of nutation N is given by

$$\frac{\partial \mathbf{A}_N}{\partial N} = -\gamma \sin \Omega_{☾}\frac{\partial \mathbf{A}_N}{\partial(\Delta\psi)} + \cos \Omega_{☾}\frac{\partial \mathbf{A}_N}{\partial \epsilon} \tag{16}$$

where $\gamma = 1.8712$.

Before computing the partial derivatives of $\boldsymbol{\rho}$ and $\dot{\boldsymbol{\rho}}$ with respect to p and N we still need $\partial \mathbf{R}_S/\partial N$. The required relation is found by combining Eqs. (4), (7), and (10). The result is

$$\frac{\partial \mathbf{R}_S}{\partial N} = -\gamma \sin \Omega_{☾} \cos \epsilon \frac{\partial \mathbf{R}_S}{\partial \theta_a} \tag{17}$$

From Eqs. (11) to (14) combined with Eqs. (8) and (15) to (17) one can then obtain $\partial\boldsymbol{\rho}/\partial p$, $\partial\dot{\boldsymbol{\rho}}/\partial p$, $\partial\boldsymbol{\rho}/\partial N$, and $\partial\dot{\boldsymbol{\rho}}/\partial N$. However, an examination of the maximum effect of each of the terms in Eqs. (11) through (14) upon $\boldsymbol{\rho}$ and $\dot{\boldsymbol{\rho}}$ shows that several of the matrices may be neglected, and others may be simplified. In estimating the effects of the terms upon $\Delta\boldsymbol{\rho}$ and $\Delta\dot{\boldsymbol{\rho}}$, it is assumed that the error in general precession in longitude is approximately 1 arc sec per century (Refs. 3, 4) while that in the nutation coefficient is 0.01 arc sec (Ref. 5).

The effects of $\Delta p = 1$ arc sec per century on $\boldsymbol{\rho}$ and $\dot{\boldsymbol{\rho}}$ are approximately:

For $\Delta\boldsymbol{\rho}$

$$\frac{\partial \mathbf{A}_P^T}{\partial p} \mathbf{A}_N^T \mathbf{R}_S \Delta p \sim 30 \text{ m/century}$$

and for $\Delta\dot{\boldsymbol{\rho}}$

$$\frac{\partial \mathbf{A}_P^T}{\partial p} \mathbf{A}_N^T \dot{\mathbf{R}}_S \Delta p \sim 2 \text{ mm/s/century}$$

$$\frac{\partial \dot{\mathbf{A}}^T}{\partial p} \mathbf{A}_N^T \mathbf{R}_S \Delta p \sim 5 \times 10^{-7} \text{ mm/s/century}$$

$$\frac{\partial \mathbf{A}_P^T}{\partial p} \dot{\mathbf{A}}_N^T \mathbf{R}_S \Delta p \sim 1 \times 10^{-7} \text{ mm/s/century}$$

while the effects of $\Delta N = 0''.01$ upon $\boldsymbol{\rho}$ and $\dot{\boldsymbol{\rho}}$ are approximately:

For $\Delta\boldsymbol{\rho}$

$$\mathbf{A}_P^T \frac{\partial \mathbf{A}_N^T}{\partial N} \mathbf{R}_S \Delta N \sim 600 \text{ mm}$$

$$\mathbf{A}_P^T \mathbf{A}_N^T \frac{\partial \mathbf{R}_S}{\partial N} \Delta N \sim 600 \text{ mm}$$

and for $\Delta\dot{\boldsymbol{\rho}}$

$$\mathbf{A}_P^T \frac{\partial \mathbf{A}_N^T}{\partial N} \dot{\mathbf{R}}_S \Delta N \sim 4 \times 10^{-2} \text{ mm/s}$$

$$\mathbf{A}_P^T \mathbf{A}_N^T \frac{\partial \dot{\mathbf{R}}_S}{\partial N} \Delta N \sim 4 \times 10^{-2} \text{ mm/s}$$

$$\dot{\mathbf{A}}_P^T \frac{\partial \mathbf{A}_N^T}{\partial N} \mathbf{R}_S \Delta N \sim 5 \times 10^{-9} \text{ mm/s}$$

$$\mathbf{A}_P^T \frac{\partial \dot{\mathbf{A}}_N^T}{\partial N} \mathbf{R}_S \Delta N \sim 1 \times 10^{-9} \text{ mm/s}$$

$$\dot{\mathbf{A}}_P^T \mathbf{A}_N^T \frac{\partial \mathbf{R}_S}{\partial N} \Delta N \sim 5 \times 10^{-9} \text{ mm/s}$$

$$\mathbf{A}_P^T \dot{\mathbf{A}}_N^T \frac{\partial \mathbf{R}_S}{\partial N} \Delta N \sim 1 \times 10^{-9} \text{ mm/s}$$

In light of the preceding estimates, we may neglect the terms in parentheses in Eqs. (11) through (14) and may use only the largest terms in the remaining matrices. With these simplifications the partial derivatives for precession reduce to

$$\left.\begin{aligned} \frac{\partial \boldsymbol{\rho}}{\partial p} &= \mathbf{C}_P \mathbf{R}_S \\ \frac{\partial \dot{\boldsymbol{\rho}}}{\partial p} &= \mathbf{C}_P \dot{\mathbf{R}}_S \end{aligned}\right\} \tag{18}$$

where

$$\mathbf{C}_P = \begin{bmatrix} 0 & -T\cos\epsilon_0 & -T\sin\epsilon_0 \\ T\cos\epsilon_0 & 0 & 0 \\ T\sin\epsilon_0 & 0 & 0 \end{bmatrix}$$

and where T is the time in centuries from 1950.0, and ϵ_0 is the obliquity of the ecliptic at 1950.0.

The simplified expressions for the partial derivatives with respect to the constant of nutation are

$$\frac{\partial \boldsymbol{\rho}}{\partial N} = \mathbf{C}_N \mathbf{S}$$

$$\frac{\partial \dot{\boldsymbol{\rho}}}{\partial N} = \dot{\theta}_a \frac{\partial \mathbf{C}_N}{\partial \theta_a} \mathbf{S} \tag{19}$$

where

$$\mathbf{C}_N = \begin{bmatrix} 0 & 0 & \gamma\sin\epsilon\sin\Omega_{☾} \\ 0 & 0 & -\cos\Omega_{☾} \\ -\gamma\sin\epsilon\sin\Omega_{☾}\cos\theta_G + \sin\theta_G\cos\Omega_{☾} & \gamma\sin\epsilon\sin\Omega_{☾}\sin\theta_G + \cos\theta_G\cos\Omega_{☾} & 0 \end{bmatrix}$$

and where $\dot{\theta}_G$ may be taken as 2π rad/86,400 s with sufficient accuracy.

For most applications, Eqs. (18) and (19) will be adequate for representation of the effects of errors in precession and nutation upon ρ and $\dot{\rho}$. If higher precision is desired, one may use the actual matrices such as $\partial\mathbf{A}/\partial p$ and $\partial\mathbf{A}/\partial N$.

With the above approximations, it is seen that the expression for $\partial\rho/\partial p$ is of the form

$$\rho\frac{\partial\rho}{\partial p} = \boldsymbol{\rho}^T \begin{bmatrix} 0 & -T\cos\epsilon_0 & -T\sin\epsilon_0 \\ T\cos\epsilon_0 & 0 & 0 \\ T\sin\epsilon_0 & 0 & 0 \end{bmatrix} \mathbf{R}_S \tag{20}$$

while the partial derivative of the slant range with respect to the observer's longitude is of the form

$$\rho\frac{\partial\rho}{\partial\lambda_E} = \boldsymbol{\rho}^T \begin{bmatrix} 0 & +1 & 0 \\ -1 & 0 & 0 \\ 0 & 0 & 0 \end{bmatrix} \mathbf{R}_S \tag{21}$$

and the partial derivative with respect to the observer's latitude is of the form

$$\rho\frac{\partial\rho}{\partial\phi'} = \boldsymbol{\rho}^T \begin{bmatrix} 0 & 0 & \cos(\theta_G + \lambda_E) \\ 0 & 0 & \sin(\theta_G + \lambda_E) \\ -\cos(\theta_G + \lambda_E) & -\sin(\theta_G + \lambda_E) & 0 \end{bmatrix} \mathbf{R}_S \tag{22}$$

Comparing Eq. (20) with Eqs. (21) and (22) it appears that the observing station's longitude and latitude will both be affected by errors in precession. If a drift on the order of 1/3 m/yr is significant, then the effect of precession should be considered in estimating station coordinates.

References

1. *Explanatory Supplement to the Astronomical Ephemeris and the American Ephemeris and Nautical Almanac.* Her Majesty's Nautical Almanac Office, Her Majesty's Stationery Office, London, 1961.
2. Lieske, J., *Expressions for the Precession Quantities and Their Partial Derivatives*, Technical Report No. 32-1044. Jet Propulsion Laboratory, Pasadena, Calif., 1967.
3. Fricke, W., "Precession and Galactic Rotation from McCormick and Cape Proper Motions in the Systems FK3, N30, FK4," *Astron. J.*, Vol. 72, pp. 642–649, 1967.
4. Fricke, W., "Precession and Galactic Rotation Derived From Fundamental Proper Motions of Distant Stars," *Astron. J.*, Vol. 72, pp. 1368–1379, 1967.
5. Clemence, G., "The System of Astronomical Constants," *Ann. Rev. Astron. Astrophys.*, Vol. 3, pp. 93–111, 1965.

D. Behavior of a Clock Moving Radially in a Centrally Symmetric Gravitational Field,

H. Lass and P. Gottlieb

In a similarly titled paper by R. F. Polishchuk (Ref. 1) the proper time for a test particle moving in a Schwarzchild field under the action of external fields is determined. It is shown that, under certain circumstances, the proper time for the moving object when it returns to its point of departure will exceed the proper time for the object remaining at rest at the point of departure. However, as we will subsequently show, there is a fundamental error in Polishchuk's paper. We will determine, with the proper analysis, that the readings of a moving clock may be less than or may exceed the readings of a stationary clock remaining at the point of departure.

We begin with an analysis of the geodesics (motion of a test particle) associated with the Riemannian metric given by

$$ds^2 = g_{\alpha\beta}\, dx^\alpha\, dx^\beta \tag{1}$$

The geodesics are given by

$$\frac{\delta u^i}{\delta s} = \frac{d^2x^i}{ds^2} + \Gamma^i_{jk}\frac{dx^j}{ds}\frac{dx^k}{ds} = 0 \tag{2}$$

with $u^i = dx^i/ds$, and $\delta u^i/\delta s$ the intrinsic derivative.

If external forces are applied, the equations of motion are given by

$$\frac{\delta u^i}{\delta s} = F^i \tag{3}$$

with F^i a 4-vector, the external force.

Defining $u_i = g_{ij}u^j$ yields

$$u_i u^i = g_{ij}\frac{dx^i}{ds}\frac{dx^j}{ds} \equiv 1$$

along any path, by virtue of Eq. (1). From Eq. (3) we have

$$u_i\frac{\delta u^i}{\delta s} = \frac{1}{2}\frac{\delta}{\delta s}(u_i u^i) = u_i F^i = 0 \tag{4}$$

so that the components $F^i, i = 1,2,3,4$, are not independent, as assumed by Polishchuk.

Let us now turn to the Schwarzchild line element

$$ds^2 = c^2\left(1 - \frac{2GM}{c^2r}\right)dt^2 - \left(1 - \frac{2GM}{c^2r}\right)^{-1}dr^2 - r^2\left(d\theta^2 + \sin^2\theta\, d\phi^2\right) \tag{5}$$

For pure radial motion, $d\theta = d\phi = 0$, and

$$ds^2 = c^2\left(1 - \frac{2GM}{c^2r}\right)dt^2 - \left(1 - \frac{2GM}{c^2r}\right)^{-1}dr^2 \tag{6}$$

From Eq. (4) it follows that

$$\left(1 - \frac{2GM}{c^2r}\right)c\frac{dt}{ds}F_t - \left(1 - \frac{2GM}{c^2r}\right)^{-1}\frac{dr}{ds}F_r = 0 \tag{7}$$

with $F^1 = F_r, F^4 = F_t$.

Eq. (3), with

$$i = 4, \frac{dx^4}{ds} = c\frac{dt}{ds},$$

becomes

$$c\frac{d^2t}{ds^2} + \frac{\dfrac{2GM}{c^2r^2}}{1 - \dfrac{2GM}{c^2r}}\frac{dr}{ds}c\frac{dt}{ds} = F_t = \frac{\dfrac{dr}{ds}F_r}{\left(1 - \dfrac{2GM}{c^2r}\right)^2 c\dfrac{dt}{ds}} \tag{8}$$

Now suppose that the test particle is located at $r = r_0$ with $dr/ds = 0$. We apply an external radial force

$$F_r = \frac{F_0}{c^2} + \frac{GM}{c^2r^2}$$

which is sufficient to overcome gravity, so that the particle begins to accelerate outward ($F_0 > 0, F_0$ a constant).

With this value of F_r, Eq. (8) yields a first integral

$$c^2\left(\frac{dt}{ds}\right)^2 = \frac{2\left(\dfrac{F_0r}{c^2} - \dfrac{GM}{c^2r} + A\right)}{\left(1 - \dfrac{2GM}{c^2r}\right)^2} \tag{9}$$

To find the radial motion one eliminates dt between Eqs. (6) and (9) to obtain

$$\left(\frac{dr}{ds}\right)^2 = \frac{2F_0}{c^2}(r - r_0) \tag{10}$$

with

$$\frac{dr}{ds} = 0 \text{ for } r = r_0.$$

The proper time for the particle to move from r_0 to $r_1 > r_0$ is

$$\tau_{01} = \int \frac{ds}{c} = \frac{1}{(2F_0)^{1/2}} \int_{r_0}^{r_1} \frac{dr}{(r - r_0)^{1/2}} = \left[\frac{2(r_1 - r_0)}{F_0}\right]^{1/2} \tag{11}$$

which is equivalent to the Newtonian time.

Let us now choose r_1 such that if the thrust F_r were removed, the particle would have escape velocity at this point. We note that for a free particle

$$c\left(1 - \frac{2GM}{c^2 r}\right)\frac{dt}{ds} = k = \text{constant} \tag{12}$$

is a first integral. From Eq. (6) we obtain

$$1 = \frac{k^2}{1 - \dfrac{2GM}{c^2 r}} - \frac{1}{1 - \dfrac{2GM}{c^2 r}}\left(\frac{dr}{ds}\right)^2 \tag{13}$$

With $dr/ds = 0$ at $r = \infty$ we obtain $k = 1$, so that

$$\left(\frac{dr}{ds}\right)^2 = \frac{2GM}{c^2 r}$$

At $r = r_1$, Eq. (10) yields

$$F_0 = \frac{GM}{r_1(r_1 - r_0)} \tag{14}$$

which yields the value of F_0 for a given r_1 in order that the test particle reach r_1 with escape velocity.

The proper time for the particle to coast from r_1 to $r_2 > r_1$ is

$$\tau_{12} = \int \frac{ds}{c} = \frac{1}{(2GM)^{1/2}} \int_{r_1}^{r_2} (r)^{1/2} dr = \frac{2}{3(2GM)^{1/2}}(r_2^{3/2} - r_1^{3/2}) \tag{15}$$

At r_2 we apply a radial thrust given by

$$F_r = -\frac{F_1}{c^2} + \frac{GM}{c^2 r^2}$$

until the particle comes to rest at $r_3 > r_2$. As in the previous analysis it is quite simple to show that the proper time for the particle to travel from r_2 to r_3 is

$$\tau_{23} = \left[\frac{2(r_3 - r_2)}{F_1}\right]^{1/2} \tag{16}$$

with

$$F_1 = \frac{GM}{r_2(r_3 - r_2)}$$

The return journey of the test particle is accomplished in the same fashion as its outward journey. The reading of the moving clock for the entire journey is given by

$$\tau = 2\left[\left(\frac{2r_1}{GM}\right)^{1/2}(r_1 - r_0) + \frac{1}{3}\left(\frac{2}{GM}\right)^{1/2}(r_2^{3/2} - r_1^{3/2}) + \left(\frac{2r_2}{GM}\right)^{1/2}(r_3 - r_2)\right] \tag{17}$$

In order to compute the proper time for the journey as viewed by the stationary observer, we must compute the coordinate time T for the journey. The proper time will be given by

$$T' = \left(1 - \frac{2GM}{c^2 r_0}\right)^{1/2} T \tag{18}$$

To compute the coordinate time for the journey from r_0 to r_1 we eliminate ds between Eqs. (6) and (10). This yields

$$dt = \frac{\left(1 + \dfrac{1}{c^2}\left[2F_0(r - r_0) - \dfrac{2GM}{r}\right]\right)^{1/2}}{\left[2F_0(r - r_0)\left(1 - \dfrac{2GM}{c^2 r}\right)\right]^{1/2}} dr \tag{19}$$

Neglecting terms of the order $1/c^4$ and higher yields

$$dt = \frac{1}{(2F_0)^{1/2}}\left\{(r - r_0)^{-1/2} + \frac{1}{c^2} \times \left[F_0(r - r_0)^{1/2} + \frac{GM}{r}(r - r_0)^{-1/2}\right]\right\} dr \tag{20}$$

An integration from r_0 to r_1 yields the coordinate time

$$T_{01} = \left(\frac{2r_1}{GM}\right)^{1/2}(r_1 - r_0) + \frac{1}{c^2} \times \left[\frac{1}{3}\left(\frac{2GM}{r_1}\right)^{1/2}(r_1 - r_0) + \left(\frac{2GM\,r_1(r_1 - r_0)}{r_0}\right)^{1/2}\tan^{-1}\left(\frac{r_1 - r_0}{r_0}\right)^{1/2}\right] \tag{21}$$

We note for $c = \infty$, that $T_{01} = \tau_{01}$, as expected.

During the coast period from r_1 to r_2 we have

$$\left(\frac{dr}{ds}\right)^2 = \frac{2GM}{c^2 r}$$

Eliminating ds^2 from Eq. (6) yields

$$dt = \frac{1}{(2GM)^{1/2}}\frac{(r)^{1/2}\,dr}{1 - \dfrac{2GM}{c^2 r}} \approx \frac{1}{(2GM)^{1/2}}(r)^{1/2}\left(1 + \frac{2GM}{c^2 r}\right)dr \tag{22}$$

A simple integration yields the coordinate time for this part of the journey, given by

$$T_{12} = \frac{1}{3}\left(\frac{2}{GM}\right)^{1/2}(r_2^{3/2} - r_1^{3/2}) + \frac{2}{c^2}(2GM)^{1/2}((r_2)^{1/2} - (r_1)^{1/2}) \tag{23}$$

Neglecting $1/c^4$ terms, etc., the coordinate time during the deceleration period from r_2 to r_3, can be shown to be

$$T_{23} = \left(\frac{2r_2}{GM}\right)^{1/2}(r_3 - r_2) + \frac{1}{3c^2}\left(\frac{2GM}{r_2}\right)^{1/2}(r_3 - r_2) + \frac{1}{c^2}\left[\frac{GMr_2(r_3 - r_2)}{2r_3}\right]^{1/2}\ln\frac{(r_3)^{1/2} + (r_3 - r_2)^{1/2}}{(r_3)^{1/2} - (r_3 - r_2)^{1/2}} \tag{24}$$

The total coordinate time for the trip is

$$T = 2(T_{01} + T_{12} + T_{23}) \tag{25}$$

and the proper time for the trip as noted by the stationary observer is

$$T' = T\left(1 - \frac{2GM}{c^2 r_0}\right)^{1/2} \approx T\left(1 - \frac{GM}{c^2 r_0}\right) \tag{26}$$

It is then a simple matter to show within the order of $1/c^2$ terms that

$$T' - \tau = \frac{2}{c^2}\left\{(2GM)^{1/2}(r_1 - r_0)\left(\frac{r_0 - 3r_1}{3r_0(r_1)^{1/2}}\right) + (2GM)^{1/2}(r_3 - r_2)\left(\frac{r_0 - 3r_2}{3r_0(r_2)^{1/2}}\right) + (2GM)^{1/2}[(r_2)^{1/2} - (r_1)^{1/2}] \times \left[2 - \frac{1}{3r_0}(r_1 + r_2 + (r_1 r_2)^{1/2}\right] + \left[\frac{2GMr_1(r_1 - r_0)}{r_0}\right]^{1/2}\tan^{-1}\left(\frac{r_1 - r_0}{r_0}\right)^{1/2} + \left[\frac{GMr_2(r_3 - r_2)}{2r_3}\right]^{1/2}\ln\frac{(r_3)^{1/2} + (r_3 - r_2)^{1/2}}{(r_3)^{1/2} - (r_3 - r_2)^{1/2}}\right\} \tag{27}$$

The last expression in Eq. (27) shows that for $r_3 >> r_2$ one has $T' > \tau$, and the reading of the moving clock will be less than the reading of the stationary clock.

On the other hand, if $r_3 \approx r_2$ and $r_1 \approx r_0$, the middle term of Eq. (27) shows that $T' < \tau$ for $r_2 >> r_1 > r_0$. Thus, if the coasting period is of long duration compared to the acceleration periods, the reading of the moving clock will be greater than the reading of the stationary clock. In order that one can coast for a considerable distance one must reach r_1 at escape velocity. The long coasting period as well as the red shift for the stationary observer yields $T' < \tau$, a result opposite to that of the special relativity effect wherein $T' > \tau$.

Reference

1. Polishchuk, R. F., "Behavior of a Clock Moving in a Centrally Symmetric Gravitational Field," *Sov. Astron.—AJ*, Vol. II, No. 5, Mar.–Apr. 1968.

E. A Simulated Least Squares Solution for Parameters of the *Mariner* Mars 1969 Encounter Orbit, *J. D. Anderson*

The purpose of this article is to establish the need for range data from the viewpoint of the *Mariner* Mars 1969 celestial mechanics experiment. This has been done before (SPS 37-44, Vol. IV, pp. 4–8 and SPS 37-47, Vol. III, pp. 1–7) for data in both the cruise and encounter phases of the mission. The basic conclusion of these earlier studies is that range data aid in the improvement of the mass and geocentric position of Mars, particularly when the cooling gas venting from the infrared spectrometer is taken into account.

Recently a shorter interval of data during the encounter phase of the mission has been simulated (from $E - 3.5$ days to $E + 3.5$ days), and the effect of adding or deleting Mars DSS range data from a least squares encounter solution has been studied. Doppler data have been simulated at a 15-min sample interval with an accuracy of ± 0.395 mm/s and have been assumed available on a continuous basis except for a period of about 32½ min during earth occultation. Results of this recent study are given in Table 1.

Table 1. Comparison of standard errors for simulated *Mariner* Mars 1969 encounter solutions with and without range data

Parameter	*A priori* error	Range and doppler	Doppler only
X, km	10^6	3.49	4.21
Y, km	10^6	8.31	17.00
Z, km	10^6	19.32	24.29
DX, mm/s	10^6	11.1	13.5
DY, mm/s	10^6	26.2	33.5
DZ, mm/s	10^6	26.2	33.5
$r_{\oplus♂}$, m	10^7	27.6	8014
$\dot{r}_{\oplus♂}$, mm/s	10^3	68.2	92.6
$m_{♂}$, ppm	1960	27.1	37.3
R_{51}, m	1.0	0.46	0.49
λ_{51}, deg	30×10^{-6}	5.6×10^{-6}	8.4×10^{-6}
R_{12}, m	1.0	0.67	0.68
λ_{12}, deg	30×10^{-6}	6.3×10^{-6}	9.1×10^{-6}

The parameters of the solution are given in column 1 in terms of the geocentric position and velocity (X, Y, Z, DX, DY, DZ) of the spacecraft at $E - 3½$ days, the geocentric range $r_{\oplus♂}$ and range rate $\dot{r}_{\oplus♂}$ of the center of mass of Mars, the mass of Mars m (error units are in parts per million), and the geocentric radii and longitudes of Johannesburg and Echo DSSs which were used in the simulation of the doppler data. The assumed *a priori* errors on these parameters are given in column 2, and the standard errors from a doppler-only solution are given in column 4. In column 3 the effect on the standard errors from the addition of Mars DSS range data is given. As with the doppler data, range data were sampled once every 15 min and were assumed to have a standard error of 100 m in one-way range.

Results obtained from Table 1 are qualitatively similar to the earlier studies. Perhaps the most important conclusion is that range data are absolutely necessary to determine the geocentric distance to Mars at planetary encounter. Studies by Curkendall and McReynolds (Ref. 1) are consistent with this conclusion. By looking at Fig. 8 in their paper, it can be concluded that at the *Mariner* Mars 1969 encounter the geometry is not favorable for determining range to the spacecraft from doppler data alone. A major objective of the celestial mechanics experiment is to obtain a good range measurement at encounter and then to compare it with anticipated radar bounce measurements from Mars to determine the physical size of the planet.

Reference

1. Curkendall, D. W., and McReynolds, S. R., *A Simplified Approach for Determining the Information Content and Critical Error Sources of Earth-Based Radio Tracking Data*, AAS Paper 68-112, Sept. 3–5, 1968.

F. Computational Accuracy of Square-Root Filtering, *P. Dyer and S. R. McReynolds*

1. Introduction

Two approaches to square root filtering have emerged recently. One, an approach formulated by Potter (Ref. 1), is based on the computation of the square root of *the covariance matrix*. The other approach, suggested by Businger and Golub (Ref. 2), relies on the computation of the square root of *the information matrix*, and involves the application of Householder transformations (Ref. 3).

Both algorithms were described for systems with uncorrelated measurements and without process noise, although Bellantoni and Dodge (Ref. 4) and Andrew (Ref. 5) have extended Potter's algorithm to incorporate correlated measurements. Recently the authors extended both algorithms to include the effects of process noise.

The classical approach to sequential filtering for systems with process noise is due to Kalman (Ref. 6). Unfortunately, the computation of the Kalman filter is vulnerable to numerical errors, which often results in a computed covariance matrix which is nonpositive. The main advantage of the square root algorithms is that a greater precision is retained. Thus the range of effective observability is extended; that is, more poorly observed variables may be estimated. This property will be illustrated in an example, the estimation of the position of a space probe from doppler measurements. It is also possible to reformulate the basic Kalman filter algorithm to reduce numerical errors (Ref. 7); however, the square-root filters are superior.

2. The Problem

Consider a system described by the transition equations

$$\mathrm{x}(k+1) = F(\mathrm{x})\,\mathrm{x}(k) + G(k)\,\mathrm{w}(k) \qquad k = 1, 2, \cdots, N \tag{1}$$

where

$$\mathrm{x}(k) = [x_1(k), x_2(k), \cdots, x_n(k)]$$

is the state of the system, and

$$\mathrm{w}(k) = [w_1(k), w_2(k), \cdots, w_n(k)]$$

is the process noise at the kth epoch. The matrices F and G are $n \times n$. The measurements at the kth epoch are denoted by

$$\mathrm{z}(k) = [z_1(k), z_2(k), \cdots, z_r(k)]$$

where

$$\mathrm{z}(k) = H(k)\,\mathrm{x}(k) + Q(k)\,\mathrm{v}(k) \qquad k = 1, 2, \cdots, N \tag{2}$$

The measurement noise is denoted by

$$\mathrm{v}(k) = [v_1(k), v_2(k), \cdots, v_r(k)]$$

The matrix H is $r \times n$ and Q is $r \times r$. It is assumed that *all* the measurements are noisy, i.e., the matrix Q has full rank.

The components of w and v are assumed to be statistically independent and gaussian, with zero means and unit variances. This assumption is not restrictive, because any set of correlated gaussian random variables may be linearly transformed to a new set of independent gaussian random variables. One technique which effects this transformation is as follows. Let $\mathrm{w}(k)$ denote correlated process noise with covariance $C(k)$. Now employing the Cholesky square root algorithm (Ref. 8) a matrix $D(k)$ is found such that

$$C(k) = D(k)\,D(k)^T$$

Equation (1) may now be written

$$\mathrm{x}(k+1) = F(k)\,\mathrm{x}(k) + G(k)\,D(k)\,w(k)$$

where the components of $\mathrm{w}(k)$ are independent random parameters with zero mean and unit covariance.

The problem of estimating $\mathrm{x}(k)$ is equivalent to minimizing $J(k)$, where,

$$J(k) = \sum_{i=1}^{k} \{\|\mathrm{v}(i)\|^2 + \|\mathrm{w}(i)\|^2\} + \|\mathrm{x}(1) - \bar{\mathrm{x}}(1)\|^2 \Lambda^{-1}(1) \tag{3}$$

subject to the constraints of Eqs. (1) and (2). In Eq. (3)

$\bar{\mathrm{x}}(1) =$ *a priori* mean of $\mathrm{x}(1)$

$\Lambda(1) =$ *a priori* covariance of $\mathrm{x}(1)$.

3. Square-Root Filters

Let $J_{opt}(k)$ denote the minimum return function[3] for this problem expressed in terms of $\mathrm{x}(k)$. Then

$$J_{opt}(k) = \|\mathrm{x}(k) - \bar{\mathrm{x}}(k)\|^2 \Lambda^{-1}(k) + r^2(k) \tag{4}$$

Here

$\bar{\mathrm{x}}(k) =$ the conditional mean of $\mathrm{x}(k)$

and

$\Lambda(k) =$ the conditional covariance

$r^2(k) =$ sum of the squares of the residuals

The solution to the filtering problem is provided once $J_{opt}(k)$ is computed.

The Kalman filter computes $J_{opt}(k)$ by computing $\Lambda(k)$ and $\bar{\mathrm{x}}(k)$. However, the square root filter based on the Householder transformation computes $R(k)$ and $\mathrm{d}(k)$ where

$$\begin{aligned} R(k) &= \Lambda^{-1/2}(k) \\ \mathrm{d}(k) &= \Lambda^{-1/2}(k)\,\bar{\mathrm{x}}(k) \end{aligned} \tag{5}$$

In terms of $R(k)$ and $\mathrm{d}(k)$, the return $J_{opt}(k)$ is given by

$$J_{opt}(k) = \|R(k)\,\mathrm{x}(k) - \mathrm{d}(k)\|^2 + r^2(k) \tag{6}$$

Clearly $\bar{\mathrm{x}}(k)$ and $\Lambda(k)$ are given by

$$\begin{aligned} \bar{\mathrm{x}}(k) &= R^{-1}(k)\,\mathrm{d}(k) \\ \Lambda(k) &= R^{-1}(k)\,R^{-1}(k)^T \end{aligned} \tag{7}$$

The Potter square root filter computes $\bar{\mathrm{x}}(k)$ and $S(k)$, where

$$S(k) = \Lambda(k)^{1/2}$$

---

[3] See Ref. 9 for the formulation of sequential estimation in terms of dynamic programming.

i.e., $\Lambda(k) = S(k)\,S(k)^T$. Thus

$$S(k) = (R^T(k))^{-1}$$

a. Application of the algorithm. While it is very easy to illustrate the numerical advantages of the procedure with a simple example, it is not so straightforward with a practical example. This is because in such a case, the true solution is generally unknown. We will, therefore, first consider a simple example which may be solved with a least-squares approach.

Example 1[4]

Consider a system of two unknowns $X(1)$ and $X(2)$ and three measurements $Z(1)$, $Z(2)$, and $Z(3)$. The relevant measurement matrix H, is chosen to be

$$H = \begin{bmatrix} 1 & 1 \\ 1 & 1 \\ 1 & 1+e \end{bmatrix} \tag{8}$$

and the noise matrix Q equals the unit matrix. By varying the parameter e the conditioning of the matrix H^TH may be controlled. Now if the measurements are chosen to be $[1, 1, 1]$, the solution is,

$$\begin{aligned} X(1) &= 1 \\ X(2) &= 0 \end{aligned} \tag{9}$$

The solutions obtained via a double-precision least squares program are compared with that given by the Householder square root algorithm in Table 2,[5] which vividly demonstrates the inaccuracies of the least squares approach. With the new algorithm, a correct solution is obtained until $e = 10^{-11}$. One of the features of the program is that a solution of minimum euclidean length is generated when the system has less than full rank. This property is illustrated by the last rows of the table.

Example 2

The second example is concerned with the orbit determination of a space probe using range-rate measurements. It is characterized by a great disparity in the observability of different components of the state and hence is an ideal problem with which to illustrate the properties of the various estimation algorithms.

The coordinate system used is shown in Fig. 8 where X_p, Y_p, Z_p, $\dot{X}_p$, $\dot{Y}_p$, and $\dot{Z}_p$ represent the position and

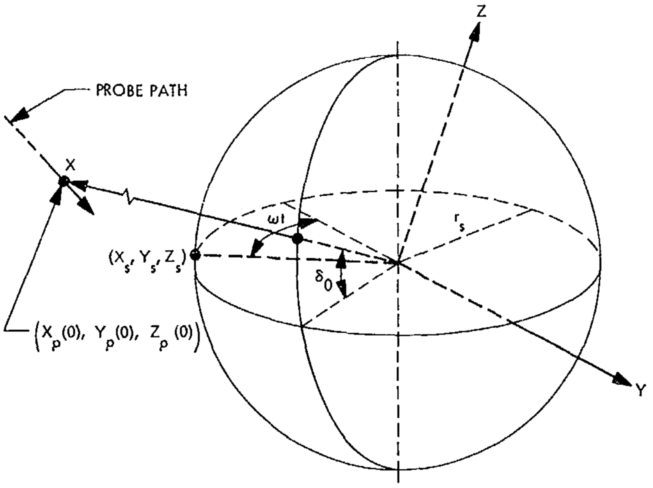

$X_s = r_s \sin \omega t \cos \delta_0$ $\qquad$ $\dot{X}_s = \omega r_s \cos \omega t \cos \delta_0$

$Y_s = -r_s \cos \omega t$ $\qquad$ $\dot{Y}_s = \omega r_s \sin \omega t$

$Z_s = -r_s \sin \omega t \sin \delta_0$ $\qquad$ $\dot{Z}_s = \omega r_s \cos \omega t \sin \delta_0$

WHERE $\delta_0 = 0.34$, AND $r_s = 5212$

Fig. 8. Coordinate system

Table 2. Relative accuracy, Example 1

Value	Least squares		Orthogonal	Transformation
e	X (1)	X (2)	X (1)	X (2)
10^{-1}	1.000000000000000	−0.0000000000000568	0.9999999999999995	0.0000000000000004
10^{-3}	1.000000000010914	−0.0000000000109139	1.000000000000000	0.0000000000000000
10^{-4}	1.000000000465661	−0.0000000009313226	1.000000000000000	0.0000000000000000
10^{-5}	1.000007629394531	−0.0000038146972656	0.9999999999999997	0.0000000000000002
10^{-7}	1.062500000000000	−0.0625000000000000	0.9999999999999996	0.0000000000000003
10^{-9}	1.000000000000000	−1.000000000000000	0.9999999999999996	0.0000000000000004
10^{-11}	1.0	−1.0	0.9999999999999997	0.0000000000000002
10^{-15}	1.0	−0.5	0.4999999999999995	0.4999999999999995

---

[4] This example was shown to the authors by R. Hanson.

[5] The Potter algorithm could not be used here as there was no *a priori* information.

velocity of the probe, and X_s, Y_s, Z_s, $\dot{X}_s$, $\dot{Y}_s$, and $\dot{Z}_s$ denote the position and velocity of the tracking station. The doppler, or range-rate measurement, ρ is a measure of the velocity along the line from the tracking station to the space probe, i.e.,

$$\dot{\rho} = \frac{\mathbf{X}}{|\mathbf{X}|} \cdot \mathbf{V}$$

where X and V are the vectors.

$$\mathbf{X} = \begin{bmatrix} X_p - X_s \\ Y_p - Y_s \\ Z_p - Z_s \end{bmatrix} \qquad \mathbf{V} = \begin{bmatrix} \dot{X}_p - \dot{X}_s \\ \dot{Y}_p - \dot{Y}_s \\ \dot{Z}_p - \dot{Z}_s \end{bmatrix}$$

Thus the required partial derivatives relating to the state of the probe and the data are given by

$$\frac{\partial \dot{\rho}}{\partial V(i)} = \frac{X(i)}{r} \qquad i = 1, 2, 3$$

$$\frac{\partial \dot{\rho}}{X(i)} = \frac{V(i)}{r} - \frac{u\,X(i)}{r^2} \qquad i = 1, 2, 3$$

where the radius

$$r = [X(1)^2 + X(2)^2 + X(3)^2]^{1/2}$$

and the velocity along the radius

$$u = [X(1)\,V(1) + X(2)\,V(2) + X(3)\,V(3)]/r$$

Simple straight-line motion relative to the earth's center was assumed for the probe, i.e.,

$$\ddot{X}_p = 0$$

$$\ddot{Y}_p = 0$$

$$\ddot{Z}_p = 0$$

where the initial state was assumed to be

$$X_p(1) = 10^8\,\mathrm{km}$$

$$X_p(2) = X_p(3) = 0$$

$$V_p(1) = V_p(3) = 0$$

$$V_p(2) = 10\,\mathrm{km/s}$$

It was also assumed that the probe was tracked for two 12-h passes with a 12-h break in the middle while the tracking station was hidden from the probe. Measurements were taken once a minute. The numerical conditioning of the system was adjusted by the choice of the *a priori* covariance; increasing the covariance worsened the conditioning. The measurement noise was assumed to have a variance of $10^{-12}\,(\mathrm{km/s})^2$.

First several cases were chosen to compare the accuracy of the various filters *without* process noise. Kalman, Angstron-Koepcke-Tung, Potter, and Householder filters were tried with various *a priori* matrices. The *a priori* matrices were unit matrices multiplied by 10^8, 10^{12}, and 10^{16}. One final run was made, with no *a priori* information, with the orthogonal filter. The diagonal elements of the final covariance matrices are shown in Table 3.

As can be seen, the two square root filters give essentially the same results. The normal Kalman filter is not nearly as accurate as the Angstrom-Koepcke-Tung filter in the first case, although both fail as *a priori* information decreases.

Next process noise was added to the system. The *a priori* covariance was taken as 10^{12} times the unit matrix, and the covariance of the process noise was taken as

$$10^{-8} \times I \quad (\mathrm{km/sec^2})^2$$

and

$$10^{-10} \times I \quad (\mathrm{km/sec^2})^2$$

Diagonal elements of the final covariance matrices are shown in Table 4 for the square root filters. The filters give essentially equivalent results. The same cases were tried with the other filters and, although positive diagonals were obtained in the first case, the numbers were not accurate to even one significant figure.

Clearly, if the system is badly conditioned, the square root filters give superior results. No marked difference was found between the two square root filters. The orthogonal filter was somewhat more complex to program but could handle problems with *no a priori* information. Furthermore, rank-deficient solutions could easily be obtained. There was little difference in computer time between the various filters.

References

1. Battin, R., *Astronautical Guidance*, p. 339, McGraw Hill Book Co., Inc., New York, 1964.
2. Businger, P., and Golub, G., "Linear Least Squares Solution by Householder Transformation," *Numer. Math.*, Vol. 7, pp. 269–275, 1968.
3. Householder, A. S., *The Theory of Matrices in Numerical Analysis*, Chap. 5, Blaisdell Pub. Co., New York, 1964.
4. Bellatoni, J. F., and Dodge, K. W., "A Square Root Formulation of the Kalman-Schmidt Filter," *AIAA Journal*, Vol. 5, No. 7, pp. 1309–1314, July 1967.
5. Andrews, A., "A Square Root Formulation of the Kalman Covariance Equations," *AIAA Journal*, Vol. 6, No. 6, pp. 1165–1166, June 1968.
6. Kalman, R. E., "A New Approach to Linear Filtering and Prediction Problems," J. Basic Engineering 82 D, pp. 35–45, 1960.
7. Astrom, K. J., Koepcke, R. W., and Tung, F., "On the Control of Linear Discrete Dynamic Systems With Quadratic Loss," Report RJ 222, IBM Research Laboratory, San Jose, Calif., 1962.
8. Faddeeva, V. N., "Computational Methods of Linear Algebra," pp. 81–85, Dover Publications, 1959.
9. Cox, H. C., "Estimation of State Variables via Dynamic Programming," Proceedings of 1964 Joint Automatic Control Conference, pp. 376–381, 1964.

Table 3. Comparison of sequential filters

A priori covariances	Filter	$P(1,1) \times 10^{8}$	$P(2,2) \times 10^{4}$	$P(3,3) \times 10^{4}$	$P(4,4) \times 10^{-11}$	$P(5,5) \times 10^{-7}$	$P(6,6) \times 10^{-6}$
10^{8}	a	0.4048820	0.4166330	0.2008347	0.7749189	0.9823329	0.3004011
	b	0.4033534	0.4156932	0.1907584	0.7751610	0.9786459	0.2941951
	c	0.4033529	0.4156927	0.1907590	0.7751611	0.9786449	0.2941994
	d	0.4033529	0.4156928	0.1907590	0.7751611	0.9786449	0.2941994
10^{12}	a			Negative diagonals			
	b			Negative diagonals			
	c	0.6760298	0.6705581	0.1967947	1.052819	1.640169	0.2942901
	d	0.6760305	0.6705590	0.1967947	1.052820	1.640170	0.2942902
10^{16}	a			Negative diagonals			
	b			Negative diagonals			
	c	0.6760214	0.6705354	0.1967956	1.052758	1.640149	0.2942843
	d	0.6760762	0.6706017	0.1967957	1.052867	1.640281	0.2942902
∞	d	0.6760762	0.6706017	0.1967957	1.052867	1.640281	0.2942902

[a] Kalman.
[b] Angstrom–Koepcke–Tung.
[c] Potter.
[d] Householder.

Table 4. Estimation with process noise

Noise, $(km/s^2)^2$	Filter	$P(1,1) \times 10^{10}$	$P(2,2) \times 10^{6}$	$P(3,3) \times 10^{6}$	$P(4,4) \times 10^{-9}$	$P(5,5) \times 10^{-4}$	$P(6,6) \times 10^{-4}$
10^{-8}	Potter	0.4281827	0.4341234	0.2948340	0.7594377	0.1066931	0.7257993
	Householder	0.4281825	0.4341231	0.2948340	0.7594372	0.1066931	0.7257993
10^{-10}		$\times 10^{8}$	$\times 10^{4}$	$\times 10^{4}$	$\times 10^{-10}$	$\times 10^{-6}$	$\times 10^{-6}$
	Potter	0.6811936	0.6758202	0.2016849	0.1061979	0.1652994	0.3035435
	Householder	0.6811929	0.6758192	0.2016848	0.1061977	0.1652992	0.3035434

II. Systems Analysis

SYSTEMS DIVISION

A. ASTRAL: Optimized Low-Thrust Trajectories Using Approximate Closed-Form Solutions to the Equations of Motion, *W. Stavro and D. J. Alderson*

1. Introduction

Investigators performing analysis of low-thrust trajectories have generally used two approaches to the problem. These approaches are not alternatives to one another, but are independent and justifiable pursuits. The first approach, which is also historically the first, was to attempt to solve the equations of motion of the spacecraft analytically and thus determine its path. This involved the solution of nonlinear differential equations using generally some kind of perturbation scheme. The second approach was to solve the boundary-value optimization problem (where the boundary values are the initial and final position and velocity of the spacecraft for a specified mission) and determine the optimal thrust programs to maximize certain mission parameters. This generally involved the use of the calculus of variations and quite extensive numerical techniques.

Basically, the engineering purpose of studying low-thrust trajectories is to develop a tool to be used in the design and planning of space exploration missions. From this point of view, researchers who followed the second approach (optimization) may be considered to be those who concerned themselves more intimately with the real problem of mission design. However, it must be realized that analysis using the first approach has two great advantages. In the first place, an analytic investigation into the basic equations of motion gives great insight into the general behavior of such trajectories, as for example, the determination of the behavior of the osculating orbital elements. Secondly, the computing time needed to obtain numerical results from the approximate closed-form solutions is appreciably less than the time needed to perform numerical integrations of the equations of motion, thus a computer program which gives approximate results but is simple and fast would be an extremely useful tool for the design of low-thrust trajectories if the approximate results are accurate enough.

A survey of the literature on low-thrust investigations shows that as these approaches were further developed and expanded they became almost completely independent fields of study. For example, intensive work in low-thrust mission optimization made no use of closed-form approximate solutions of the equations of motion, and similarly investigators who developed approximate solutions made no attempt to use these in mission analysis studies.

ASTRAL is the first attempt to combine both these fields of endeavor in order to obtain a useful tool to be utilized in low-thrust mission studies. More specifically, ASTRAL will use an approximate closed-form solution to the differential equations of motion, together with an optimization scheme, to obtain a program that optimizes various mission parameters to maximize a low-thrust payload.

The purpose of this article is to broadly present a description of ASTRAL and to explain the overall structure of the program and its content. An attempt was made to stay away from program specifics, such as input and output format and actual form of the program. These will be published after the program is checked out and is in a working condition.

2. Trajectory Analysis

Numerous attempts have been made to solve the differential equations of motion of a spacecraft under the influence of low thrust. These studies ranged in complexity from very simple approximations to very sophisticated perturbation schemes. The most recent method used to solve these nonlinear equations, which also gave the best results, is the two-variable asymptotic expansion method. This method was especially suitable because of the appearance of two time scales (slow time associated with the changing orbital elements, and fast time associated with the motion of the spacecraft) as well as the small parameter ϵ, which is the ratio of thrust acceleration to gravitational acceleration. Shi and Eckstein (Ref. 1) used this method to solve the equations of motion of a spacecraft under the influence of constant-thrust acceleration, i.e., approximately a nuclear–electric propulsion system. All other investigators before them had also limited their analysis to constant thrust or constant-thrust acceleration. However, the mission studies presently under serious consideration for outer planet exploration in the 1970s have solar–electric propulsion systems. For this system, the magnitude of the thrust is a function of the distance to the sun since the solar power decreases as the distance to the sun increases.

Wesseling (Ref. 2) considers the case where the thrust acceleration varies as the inverse of the square of the distance to the sun in a heliocentric trajectory. He uses the two-variable asymptotic expansion procedure and obtains the first three terms of the asymptotic series. One of the very interesting results he obtained for such a thrust behavior is that the eccentricity of the osculating conic increases, whereas it had been found that for constant-thrust acceleration it decreases. This exhibits the fact that the general behavior of the trajectory (such as the variation of the elements) seemed to depend on the behavior of the thrust acceleration. Recent studies on a solar–electric power plant show a variation of thrust acceleration proportional to the inverse of the distance to the sun raised to a power of approximately 1.4. Possible improvements to Wesseling's solution to incorporate this effect are discussed in Subsection 6 of this article.

ASTRAL was initiated here with the purpose of being a level-1 computer program to be used for solar–electric mission studies. A level-1 program is one which is used in generating the bulk of the ideal performance information, and as such must be capable of optimization of trajectory and spacecraft parameters. The approach used is the coupling of Wesseling's solutions with an optimization scheme.

3. PATH Subroutine

The subroutine in the ASTRAL program which calculates the trajectory (i.e., where Wesseling's solutions are programmed) is called PATH.

Wesseling's analysis makes two important assumptions. First, since the method uses a perturbation scheme on ϵ, it is valid only for small values of that parameter, i.e., low thrust. Of course, the smaller the value of ϵ the closer his solution approximates a numerical integration, if everything else is held constant. Secondly, in order to obtain higher-order terms, the assumption of small eccentricity (same order of magnitude as ϵ) had to be made. Other conditions are that thrust acceleration varied as $1/r^2$ (where r is the distance to the sun) and that its direction is arbitrary but fixed. In checking PATH out, an attempt was made to determine how sensitive the solutions are to various values of eccentricity and ϵ.

Wesseling had [illegible] two programs on the 1620 computer: (1) AS[illegible], which contained his approximate solutions, and [illegible]NUTRAL, which was a numerical integration of the equations of motion to which he compared some of his results. The same process was repeated for the 7094 computer; both Wesseling's results and a numerical integration were programmed. The first step in checking PATH out was to compare it to the 1620 computer version. Once this was done, the main effort became to determine how well the asymptotic solution approximated the numerical integration of the equations for different values of eccentricity and ϵ.

Figures 1a, 1b, and 1c show two-dimensional trajectories for an ϵ of 0.1: Fig. 1a for an initially circular orbit, Figs. 1b and 1c for initial eccentricities e_0 of 0.1 and 0.5. These and other test cases shown here were run for a thrust pointing at an angle of attack of 45 deg [the angle $\eta = 1/(2)^{1/2}$]. Two plots are shown on each of the graphs: one showing Wesseling's solution, the other showing the numerical integration. Figures 1a and 1b give excellent approximations to the numerical integration, whereas Fig. 1c gives intolerable errors. Figure 1d is the same as

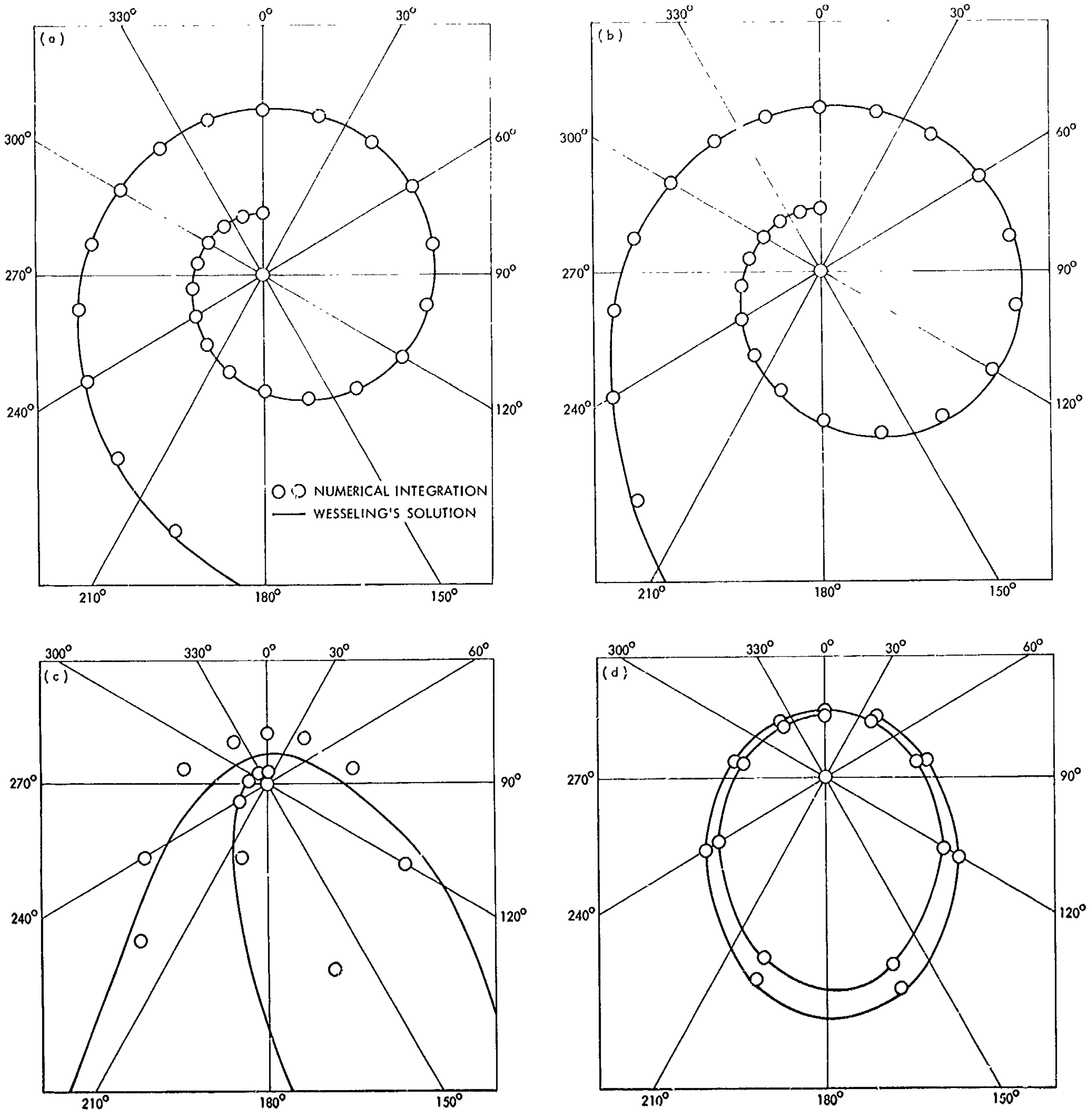

Fig. 1. Two-dimensional trajectories: (a) $e_0 = 0$, $\epsilon = 0.1$; (b) $e_0 = 0.1$, $\epsilon = 0.1$; (c) $e_0 = 0.5$, $\epsilon = 0.1$; (d) $e_0 = 0.5$, $\epsilon = 0.01$

Fig. 1c, except for an ϵ of 0.01, and yields a very good approximation. By studying Figs. 1a and 1d, the following conclusions may be reached:

(1) Excellent approximations are obtained when the initial eccentricity and ϵ are of the order of 0.1 or smaller.

(2) For cases of high eccentricity (about 0.5), the ϵ must be decreased to about 0.01 to obtain good results. This seems to contradict Wesseling's assumption that initial eccentricity has to be of the same order of magnitude as ϵ.

Figure 2 shows time plots for $\epsilon = 0.1$ and initial eccentricities of 0 and 0.1. From these plots, we note that excellent approximations are obtained for about the first half revolution, after which the error increases tremendously, especially for the 0.1 initial eccentricity case. An attempt will be made to investigate these results in order to improve the latter approximations.

Many other runs were made and checked, and, in general, it is concluded that PATH now gives very good approximations to the trajectory of a low-thrust spacecraft whose thrust varies as $1/r^2$, when the initial eccentricity and ϵ are small; and for higher eccentricities, results are still good if ϵ is small enough.

4. Optimization Method

In general, a function-maximizing or optimization method involves the use of a set of one or more points in a parameter space. These points may be restricted to lie within a certain portion of the parameter space, or such constraints may be absent. In either case, the positions and function values, and possibly also function derivative values, of the point or points in the set are used to produce a new point set for further investigation. The resulting sequence of point sets hopefully converges upon the desired optimal location in the parameter space, thus maximizing the given function, subject to the specified constraints if there are any.

In the case under consideration, the partial derivatives of the spacecraft payload with respect to the trajectory parameters cannot be generated in a more efficient manner than by numerical differences, so methods directly using function derivative values are unlikely to be useful. Further, the problem is extensively involved with constraints of all kinds, including some that produce considerable difficulties for methods that make even indirect use of function derivatives. As opposed to these gradient methods, there are the direct search methods.

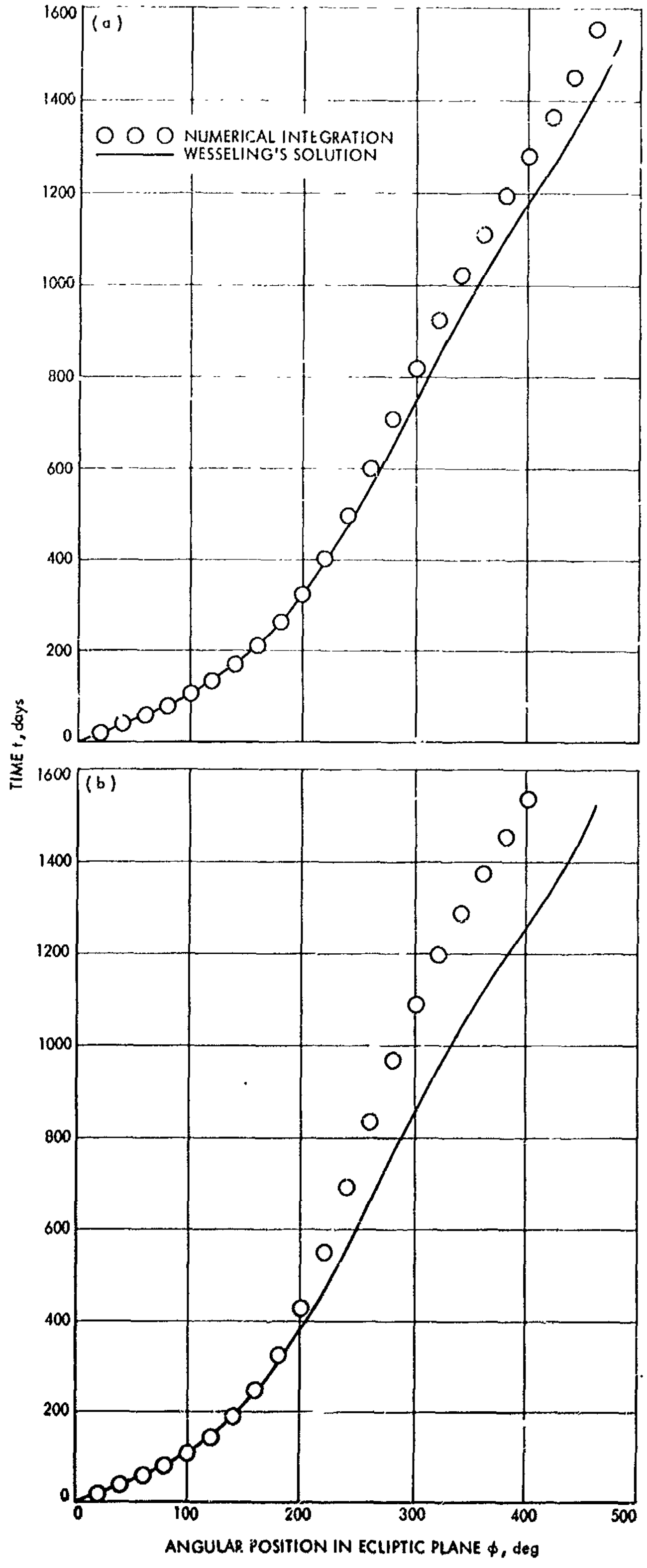

Fig. 2. Time plots: (a) $e_0 = 0$, $\epsilon = 0.1$; (b) $e_0 = 0.1$, $\epsilon = 0.1$

The most effective of these is Box's "complex" method (Ref. 3), and this has been adopted as the basic optimization method in the ASTRAL program.

Maximizing a function of a single variable is qualitatively as well as quantitatively easier than performing the same task with two or more variables. As a result, many multidimensional optimizing methods act by selecting an appropriate one-dimensional subspace of the parameter space and applying a suboptimization process to it. Thus, gradient methods often investigate the line through the point under consideration along which the function is changing most rapidly at the point—the line defined by the gradient vector of the function at the point. The complex method also uses this dimensional reduction technique, though without reference to derivatives. If the parameter space to be dealt with has n dimensions, $n + 1$ or more points in the space are placed in a set. These points form the vertices of a polytope or complex, the n-dimensional equivalent of a polygon or polyhedron.

The one-dimensional subspace chosen for further inspection is that connecting one of the points in the set with the centroid of the other points. This line is analyzed either by a simple bounded exponential search as suggested by Box or by a method involving successive quadratic approximations. If a point is found with a higher function value than the original defining point, it replaces the original point in the complex set. The first choice of defining point is the one with the lowest function value, but if it is not replaced by a point with higher function value than at least one point in the complex set, then all the other points are tried in order of increasing function value. If none of the points can produce an increase in function value, the sequence terminates, ideally with all of the points coinciding at the optimum.

The initial complex set is formed from any guesses or estimates of the optimum that may be available, filled in by randomly chosen points.

Constraints come in two forms: equality and inequality, and in a wide range of degrees of complexity that can be lumped into two levels: explicit and implicit, the distinction as far as the present case is concerned being that it is much easier to determine whether a given point satisfies an explicit constraint than it is to evaluate the function to be maximized, while the same is not true of an implicit constraint. The low-thrust trajectory optimization problem involves all four combinations of constraint types.

Explicit inequality constraints arise, for example, from the fact that a negative value for the length of any of the arcs into which the trajectory is divided would be physically meaningless. They are met by checking each point considered before evaluating the function, and rejecting the point unless all such constraints are met. These constraints turn out to provide upper and lower bounds for all of the variables that constitute the parameter space.

There is exactly one explicit equality constraint, expressing the fact that the lengths of the trajectory arcs must add up to the specified full length of the trajectory. It is eliminated by removing the length of the last trajectory arc from the parameter space and automatically giving it the value required to satisfy the equality constraint. As a result, the condition that the length of the last trajectory arc be non-negative becomes more complicated but remains an explicit inequality constraint.

Implicit inequality constraints arise because the path-generating process can fail in any of the arcs of the trajectory. For example, the trajectory can proceed along a hyperbolic asymptote and thus never reach the ecliptic longitude specified for the end of an arc. These constraints are satisfied by checking at each point considered during evaluation of the function, and rejecting the point (by assigning a very large negative value to the function) unless all such constraints are met.

The implicit equality constraints are the most troublesome. They are produced by the requirement that position and time at the end of the trajectory possess specified values. They are dealt with by modifying the function to be maximized, subtracting "penalty" functions of the errors in final position and time from the payload. By proper choice of parameters in the penalty functions, the optimizing process can be presented with a problem that amounts to first finding a solution to the constraint equations and then maximizing the payload subject to the constraints.

5. The Payload Formulas

The payload of the spacecraft is given by the following formulas:

$$M_{pl} = M_f \left[A_2 \exp\left(-dV_2/C_2\right) - B_2 \right], \qquad A_2 - B_2 = 1$$

$$M_f = M_0 - M_{pp} - M_p$$

$$M_p = M_0 \left[1 - \exp\left(\frac{-1}{I_{sp} g_s} \int_{\Phi_0}^{\Phi_f} \frac{\epsilon g_e a^2}{r^2} \frac{r \cos \Psi}{V_\Phi} \, d\Phi \right) \right]$$

$$M_{pp} = \frac{\alpha}{2\lambda} \epsilon_0 g_c I_{sp} g_s$$

$$M_0 = A_1 \exp(-dV_1/C_1) - B_1, \qquad A_1 - B_1 = M_i$$

Refer to Table 1 for definition of symbols.

6. Present Status and Future Plans

The complete ASTRAL program is presently in a checkout phase. As mentioned in Subsection 3, the PATH subroutine has already been checked out and its limitations identified. The next step is to check out the complete program with the exclusion of the optimizer. This is presently being done by simulating an ASTRAL trajectory on Carl Sauer's integrating low-thrust program[1] and making an initial check on the basic parameters. It will also determine the effect of assuming an inverse-square thrust acceleration and constant mass of the spacecraft.

The next step in the checkout schedule will be to take a Sauer optimum trajectory and attempt to duplicate it. Once this is done, numerous ASTRAL runs will be generated in the vicinity to hand-pick an optimum; then a check will be made to see if ASTRAL will get the same optimum using the optimizer. This procedure will be followed to check out the optimizing scheme. Once past the checkout phase, ASTRAL will be ready to be used as a level-1 program.

A major extension to ASTRAL will be done later to implement it with William Stavro's solutions for arbitrary thrust-power laws. This is a study which investigates the general case where the thrust acceleration can vary as the inverse of the distance to the sun raised to some arbitrary power α. Thus, the value $\alpha = 0$ will signify constant-thrust acceleration (an approximation to the

Table 1. Nomenclature

A_1, B_1, C_1	constants describing initial high-thrust maneuvers
A_2, B_2, C_2	constants describing final high-thrust maneuvers
a	1 AU (149,597,892 km)
dV_1	velocity change in initial high-thrust maneuvers
dV_2	velocity change in final high-thrust maneuvers
g_c	acceleration of solar gravity at 1 AU (0.593 cm s^{-2})
g_s	standard acceleration of earth gravity (980.665 cm s^{-2})
I_{sp}	specific impulse of low-thrust propulsion system
$I_{sp}g_s$	effective exhaust velocity of low-thrust propulsion system
M_f	spacecraft mass just before final high-thrust maneuver (if any), e.g., insertion into orbit about target planet
M_i	spacecraft mass at parabolic orbital status relative to launch planet during initial high-thrust maneuver
M_p	propellant mass
M_{pl}	payload mass
M_{pp}	powerplant mass
M_0	spacecraft mass just after initial high-thrust maneuver, e.g., chemical boost from earth orbit
r	distance of spacecraft from sun
$r\cos\Psi/V_\Phi$	$(d\Phi/dt)^{-1}$, reciprocal of time derivative of Φ
V_Φ	ecliptic longitude component of spacecraft velocity
α	powerplant specific mass at 1 AU
ϵ	ratio of spacecraft thrust acceleration to acceleration of local solar gravity
$\epsilon g_c a^2/r^2$	thrust acceleration of spacecraft
ϵ_0	ratio of spacecraft thrust acceleration to acceleration of local solar gravity at 1 AU
λ	low-thrust propulsion system efficiency
Φ	ecliptic longitude of spacecraft
Φ_f	final value of Φ
Φ_0	initial value of Φ
Ψ	ecliptic latitude of spacecraft

---

[1] This program was used in recent Jupiter mission studies at JPL.

nuclear-electric case), $\alpha = 2$ will parallel Wesseling's analysis, and $\alpha = 1.4$ will reflect recently proposed solar-electric propulsion systems to be used for missions to Jupiter.

References

1. Shi, Y., and Eckstein, M., "Ascent or Descent from Satellite Orbit by Low Thrust," *AIAA J.*, Vol. 4, pp. 2203–2209, 1966.
2. Wesseling, P., "A Two-Variable Asymptotic Solution for Three-Dimensional Solar Powered Low-Thrust Trajectories in the Vicinity of the Ecliptic Plane," *Astronaut. Acta*, Vol. 13, pp. 431–440, 1967.
3. Box, M. J., "A New Method of Constrained Optimization and a Comparison with Other Methods," *Comput. J.*, Vol. 8, pp. 42–52, 1965.

B. An Earth–Venus–Mercury Mission Opportunity in 1978, *F. M. Sturms, Jr.*

In a previous article (SPS 37-39, Vol. IV, pp. 1–5), it was reported that no favorable Earth–Venus–Mercury opportunity existed in 1978, and in particular that no energy match at Venus for the Earth–Venus and Venus–Mercury trajectory legs was possible for launch energies C_3 of less than 21 km^2/s^2. At the time these results were reported, the *Atlas-Centaur* vehicle was unable to inject significant payloads (greater than 1000 lb) to energies higher than about 21 km^2/s^2, and was the rationale for using this constraint. Larger boost vehicles then contemplated could easily deliver large payloads on direct Mercury missions, which require launch energies of about 50 km^2/s^2 (Ref. 1).

More recently, uprating of the *Atlas-Centaur* vehicle, and the entry of a number of intermediate-size launch vehicles into the mission planning picture, require the consideration of higher launch energies. This fact has been reported by A. A. VanderVeen of Bellcomm, Inc., who has determined some preliminary trajectory characteristics.[2]

High-energy Earth–Venus–Mercury trajectories have been generated using JPL's multiple-planet conic program SPARC.[3,4] Figures 3–8 show some of the more important trajectory parameters. Figure 3 shows the region of possible trajectories on a Venus arrival date versus Earth launch date grid. Figures 4–8 show the

---

[2] *Preliminary Results of an Attractive Earth–Venus–Mercury Mission in 1978*, Bellcomm, Inc., Washington, D.C., Oct. 9, 1968 (internal memorandum).

[3] Joseph, A. E., and Richard, R. J., *Space Research Conic Program*, July 1966 (JPL internal document).

[4] Derderian, M., *Space Research Conic Program, Phase III*, Apr. 1968 (JPL internal document).

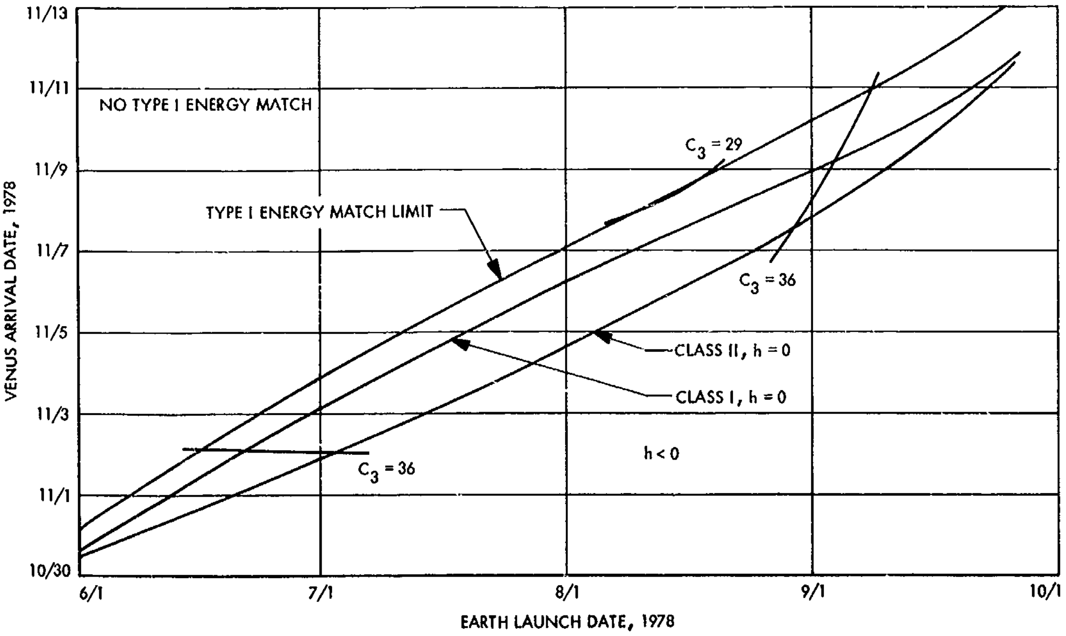

Fig. 3. Region of possible trajectories on a Venus arrival date vs Earth launch date grid

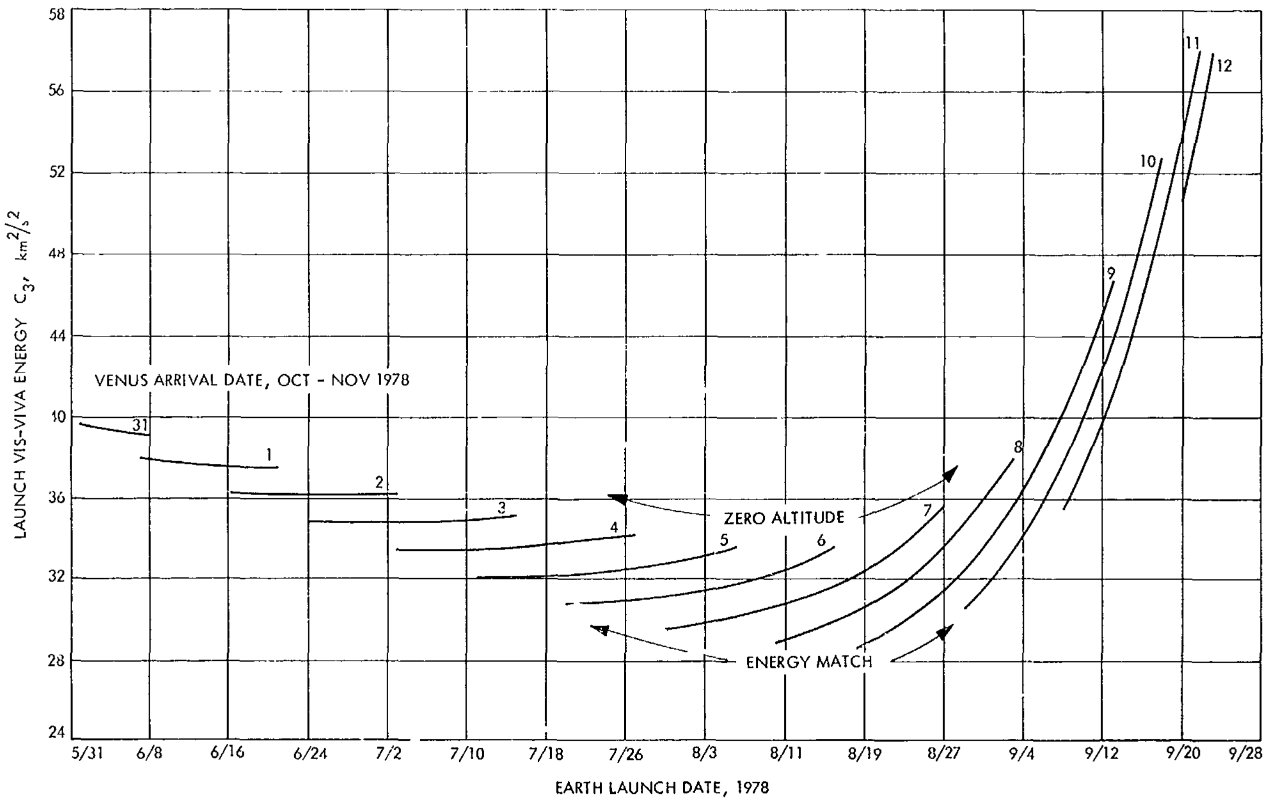

Fig. 4. Launch energy vs Earth launch date

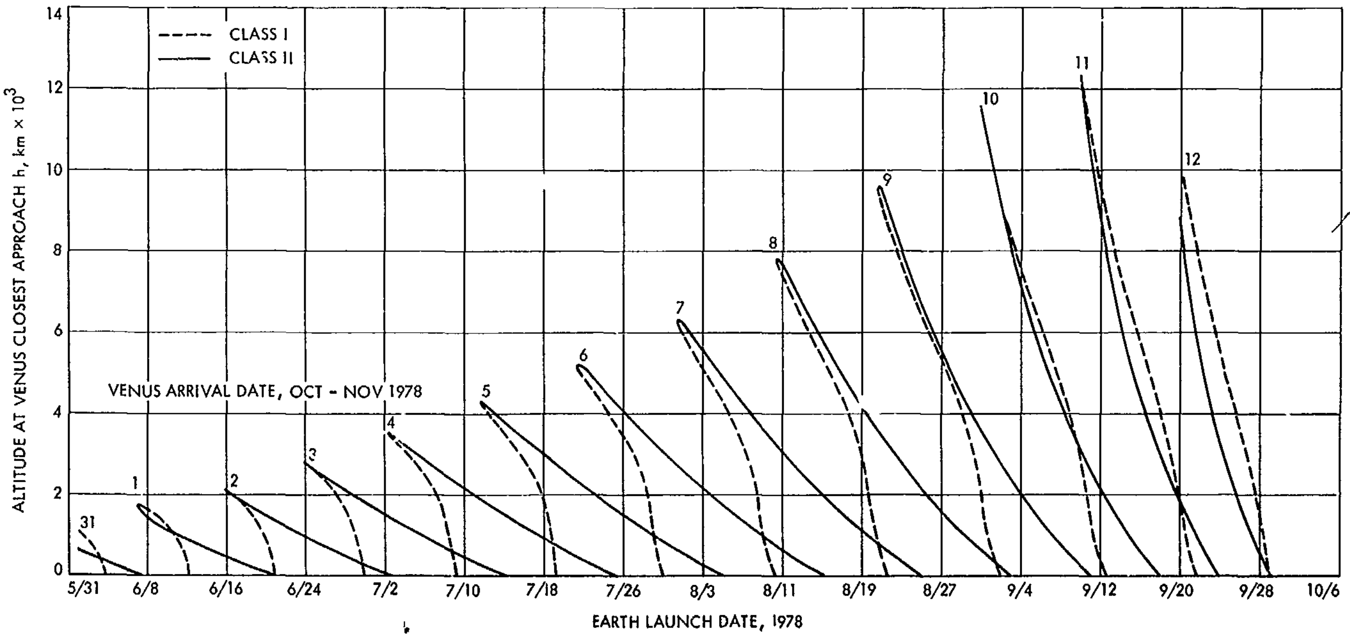

Fig. 5. Altitude of Venus closest approach vs Earth launch date

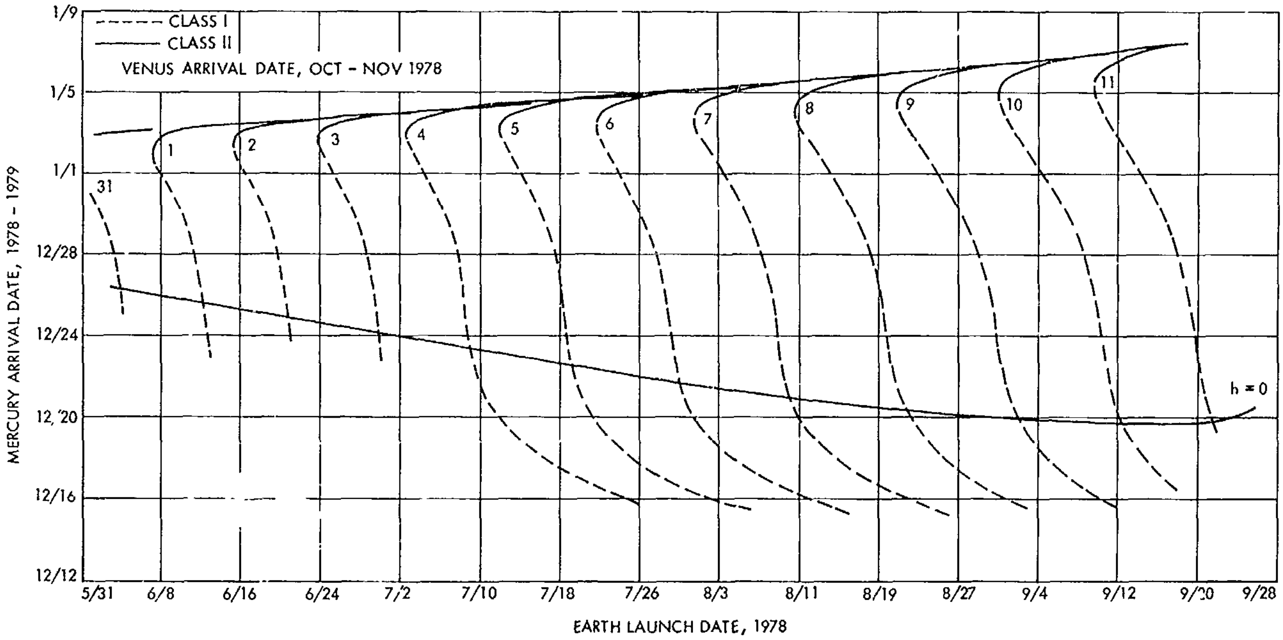

Fig. 6. Mercury arrival date vs Earth launch date

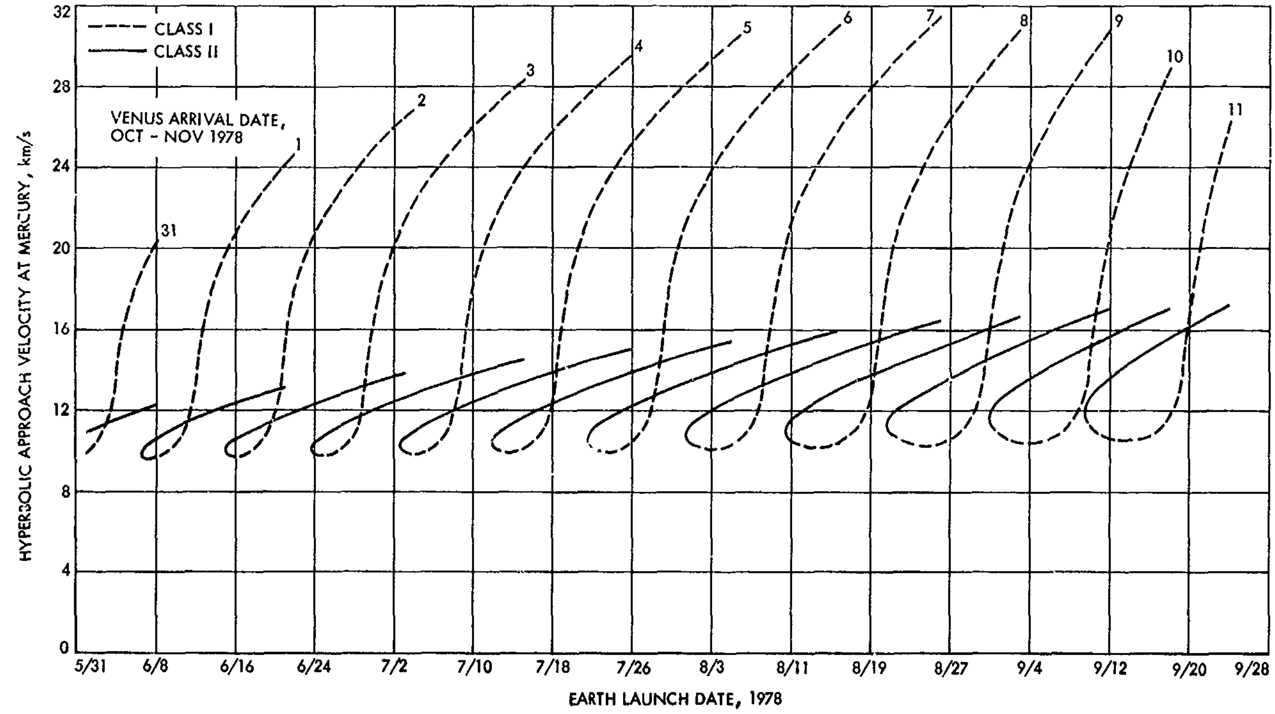

Fig. 7. Hyperbolic approach velocity at Mercury vs Earth launch date

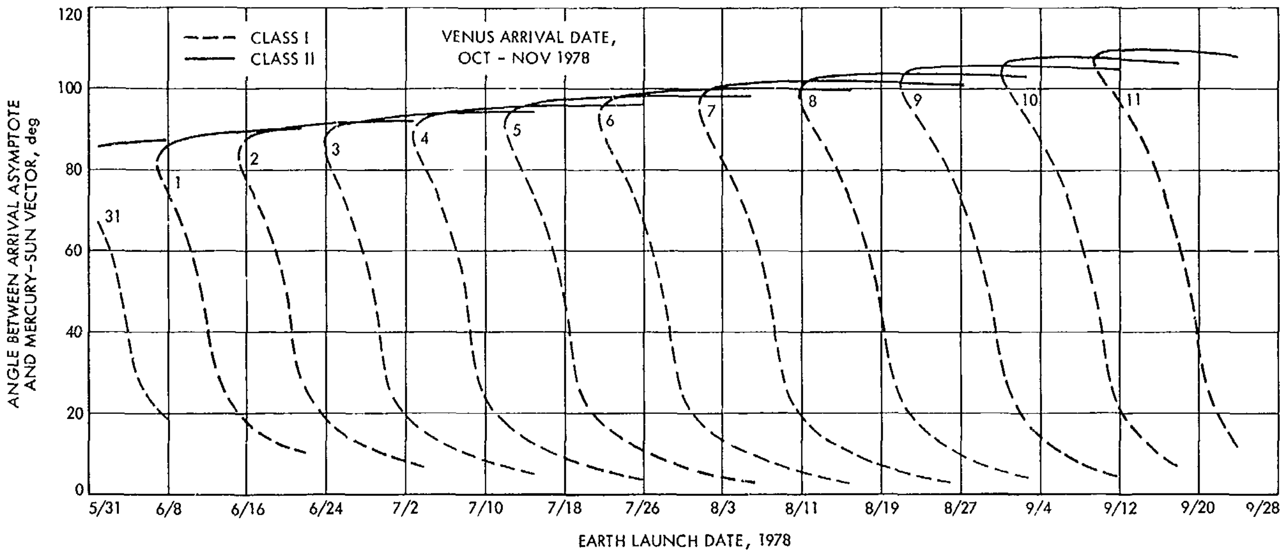

Fig. 8. Angle between arrival asymptote and Mercury–Sun vector vs Earth launch date

following quantities plotted versus Earth launch date, using a constant Venus arrival date as a parameter:

1. Launch energy C_3.
2. Altitude of closest approach h at Venus (Venus radius taken as 6080 km).
3. Mercury arrival date.
4. Hyperbolic approach velocity at Mercury.
5. Angle between arrival asymptote and Mercury–Sun vector (determines lighting for Mercury photography).

A launch energy of 35 km^2/s^2 will produce an adequate launch period. Table 2 shows current payload estimates for several launch vehicles for energies of 35 and 50 km^2/s^2. These performance values were obtained from Ref. 2, except for the SLV-3X/*Centaur* value.

Using the values in Table 2, the SLV-3C/*Centaur* and *Titan* 3C vehicles appear marginal for the 1978 Venus–Mercury mission. The addition of a *Burner II* stage to these vehicles increases the payload to where both the indirect 1978 Venus–Mercury and direct Mercury missions are attractive. The SLV-3X/*Centaur* vehicle is a possible choice for the Venus–Mercury mission in 1978.

Predicted launch-vehicle performance values change frequently, thus affecting the attractiveness of given missions. The values given above indicate that serious consideration should now be given to the 1978 Earth–Venus–Mercury mission opportunity in comparison to more favorable but earlier Venus–Mercury opportunities, and in comparison to direct Mercury missions.

References

1. Clarke, V. C. Jr., et al., *Design Parameters for Ballistic Interplanetary Trajectories, Part II. One-Way Transfers to Mercury and Jupiter*, Technical Report 32-77. Jet Propulsion Laboratory, Pasadena, Calif., Jan. 15, 1966.
2. *Mission Planners Guide to the Burner II*, Report D2 82601-5, The Boeing Co., Seattle, Wash., Apr. 1968.

Table 2. Launch vehicle payloads for two launch energies

Launch vehicle	Payload for $C_3 = 35$ km^2/s^2 (1978 Venus–Mercury), lb	Payload for $C_3 = 50$ km^2/s^2 (direct Mercury), lb
SLV-3C/*Centaur*	750	50
SLV-3C/*Centaur*/*Burner II*	1400	1000
Titan 3C	800	0
Titan 3C/*Burner II*	2250	1500
SLV-3X/*Centaur*[a]	1100	200

[a] Williams, A. N., *Launch Vehicle Data Book*, Aug. 30, 1968 (JPL internal memorandum).

C. Trajectory Analysis of a 1975 Mission to Mercury via an Impulsive Flyby of Venus,[5]

R A. Wallace

1. Introduction

The concept of using gravitational fields to significantly alter the energy and direction of interplanetary trajectories is not a new one. In 1963, M. A. Minovitch proposed several interesting interplanetary missions using this multiple-planet flyby concept (Ref. 1). The advantages of this form of mission are the savings in launch energy and the increase of data return associated with the "two planets for the price of one" idea. It is not surprising, therefore, that a great deal of interest has been generated in multiple-planet flyby missions and, in particular, missions to Mercury via Venus in the 1970's. Direct ballistic trajectories to Mercury generally require launch energies of 45 km^2/s^2 or more, while multiple-planet trajectories to Mercury are available which require less than 30 km^2/s^2.

There are six attractive opportunities for Earth–Venus–Mercury missions during the remainder of the century; these are listed in Table 3. An attractive opportunity is one for which either an *Atlas/Centaur* or *Titan III* launch vehicle can be used to launch a payload of more than 800 lb (i.e., corresponding to an upper limit of launch energy of 33 km^2/s^2). Although the 1970 and 1973 opportunities are excellent, they may not be available because of program considerations. The next opportunity is in 1975, but is plagued with very low Venus closest-approach altitudes. The study summarized here investigates the feasibility of using a small propulsive assist at Venus to allow reasonable Venus flyby altitudes and thereby increase the attractiveness of the 1975 opportunity.

Results of the study are presented in three parts. First, a very brief discussion is given on the general single-impulse flyby analysis which permits the analyst to investigate in detail the impulse requirements of multiple-planet trajectories utilizing propulsive assist. Secondly, an efficient procedure is outlined for the application of the above analysis to the 1975 Earth–Venus–Mercury mission. The final subsection is devoted to the mission design and analysis for the 1975 Earth–Venus–Mercury opportunity.

2. Single-Impulse Flyby Analysis

The analysis used is simple and can be applied to any multiple-planet trajectories where propulsive assist may help in raising closest approach altitudes or taking advantage of particular interplanetary trajectory characteristics, such as reduced flight time. The analysis uses three input control parameters:

(1) Launch and arrival dates (fixes the approach and departure asymptotic velocity vectors).

(2) Closest approach altitude.

(3) Maneuver radius.

These parameters are thought to be the most practical choice of control variables for operating a multiple-planet mission requiring propulsive assist. They also make up a minimum set required to uniquely determine the trajectories at encounter (Fig. 9). The analysis could be carried out two-dimensionally because of the principal constraint of requiring the trajectories to contain the two determining asymptotic velocities. Details of the solution are given in Ref. 2.

Table 3. Earth–Venus–Mercury mission opportunities (ballistic flyby)

Launch year	Launch energy, km^2/s^2	Venus closest-approach altitudes, km
1970	14	3000
1973	19	5000
1975	21	Less than 700
1982	24	2000
1994	24	1400
1998	16	3600

3. Application of Single-Impulse Flyby Analysis

The single-impulse flyby analysis was applied to the region of the 1975 Earth–Venus–Mercury opportunity which exhibited relatively low launch energies and maximum Venus closest-approach altitudes. In a perliminary study, certain factors became evident:

(1) The Venus arrival time is very important in obtaining low impulse maneuvers (sensitivity: 20 m/s/h).

(2) The ΔV is relatively invariant with maneuver radius *for* optimum choice of Venus arrival time. (For non-optimal times, ΔV could vary as much as ⅓ of its minimum value.)

The ΔV sensitivity with Venus arrival time is explained by the fact that the Venus closest-approach altitude was kept constant. It was found, however, that the ΔV sensitivity to closest-approach altitude is also quite high,

---

[5] This article is a summary of Ref. 2.

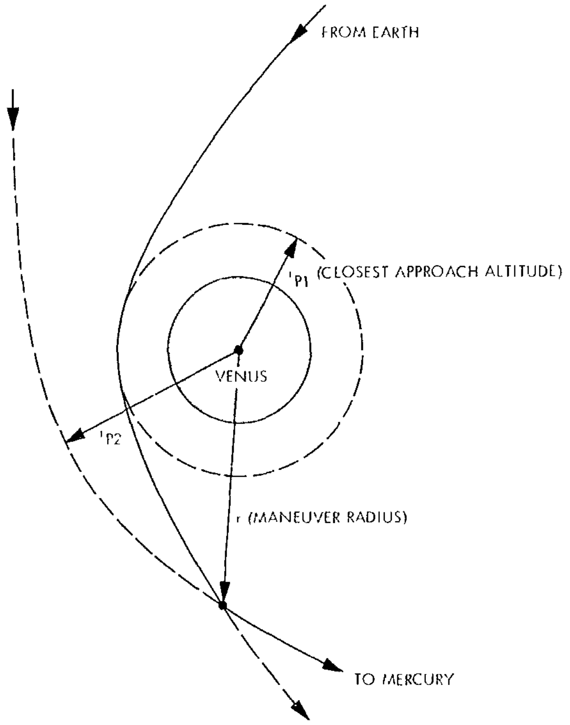

Fig. 9. Encounter trajectories in orbit planet

about 60 m/s for every 100-km change in altitude. Thus, the ΔV sensitivity to Venus arrival time could be softened by changing the Venus flyby altitude with Venus arrival time. It was decided, however, that a minimum acceptable altitude of 1000 km should be used throughout the study. If further decreases were allowable, the savings of 60 m/s for every 100-km decrease could be realized up to a point where too much trajectory bending results and ΔV increases.

In the preliminary study, ΔV was found to be very insensitive to maneuver radius for the optimum choice of Venus arrival times. This is because the two encounter orbits, approach and departure, are almost identical and the velocity differences are almost constant with maneuver radius. One orbit can be thought of as a perturbation of the other because the impulse required is small compared to the orbital velocities (9 to 13 km/s). For non-optimum choice of Venus arrival time, the angle between the two orbits is larger than for the optimum arrival time, although the orbits are almost identical in other respects. The above observations are not applicable at periapsis where the velocity differences are most pronounced.

Since ΔV is almost constant with change in maneuver radius for optimum Venus arrival times, attention during the rest of this study will be restricted to maneuvers performed on the asymptotes (i.e., at about encounter plus or minus several days). There are four major advantages that result from such a policy:

(1) The required impulse can be combined with one of the error-correction maneuvers, resulting in smaller execution errors and greater reliability for fewer maneuvers.

(2) The Venus encounter experiments could be given full operational consideration and not complicated by a maneuver.

(3) A continuous tracking data fit could be acquired throughout encounter, reducing orbit determination errors for the post-encounter error-correction maneuver.

(4) The impulse was found to be smallest at large distances from Venus for the final design trajectories.

Considering these points, the remainder of the discussion is confined to results concerning asymptotic maneuvers.

To define a mission, design charts are required which will clearly show the tradeoffs in the important parameters involved. In the construction of design charts, the first step is to optimize Venus arrival time. Figure 10 is an example of the many plots required in the optimization procedure.

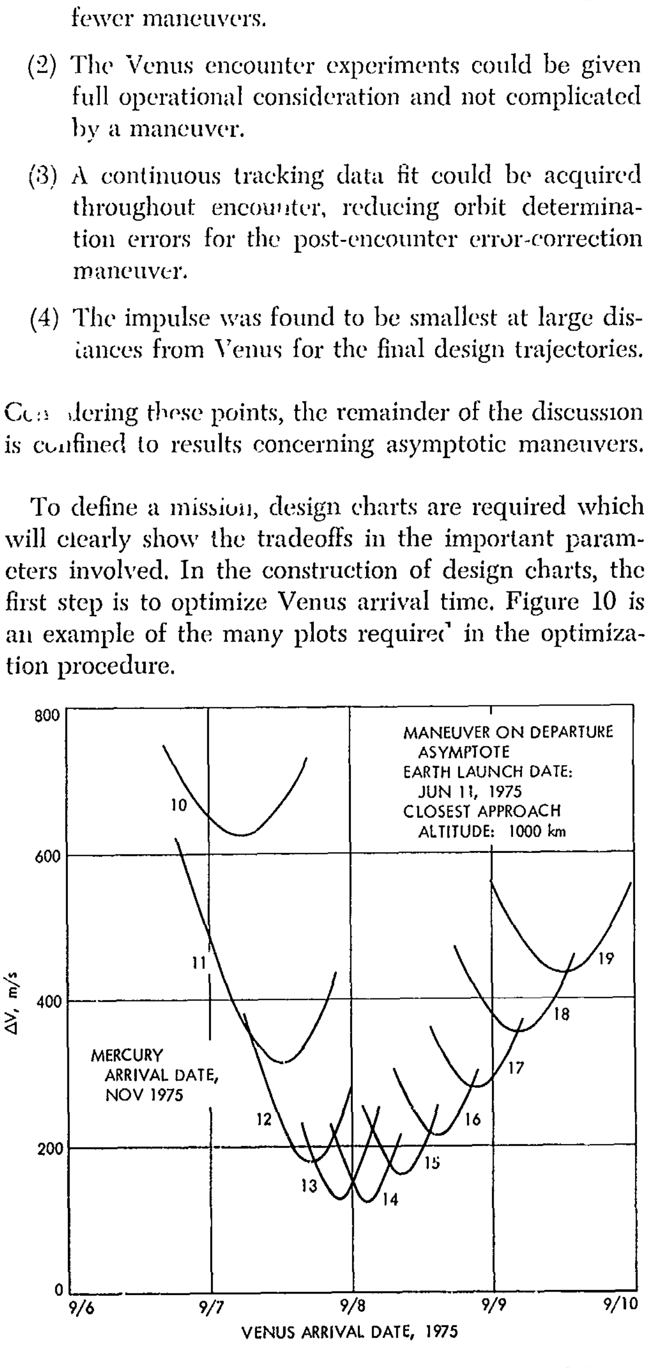

Fig. 10. Maneuver impulse ΔV vs Venus arrival date (Mercury arrival date varied)

Design charts were constructed for maneuvers performed on both the approach and departure asymptotes with Venus arrival time and launch energy as parameters overlayed on the basic ΔV contour chart. Note that all points used in the design charts are for the optimum Venus arrival time. Figure 11 is the design chart for maneuvers performed on the departure asymptote with launch energy as an overlay. It was found that maneuvers performed on the departure asymptote resulted in generally lower ΔV's than those on the approach asymptotes.

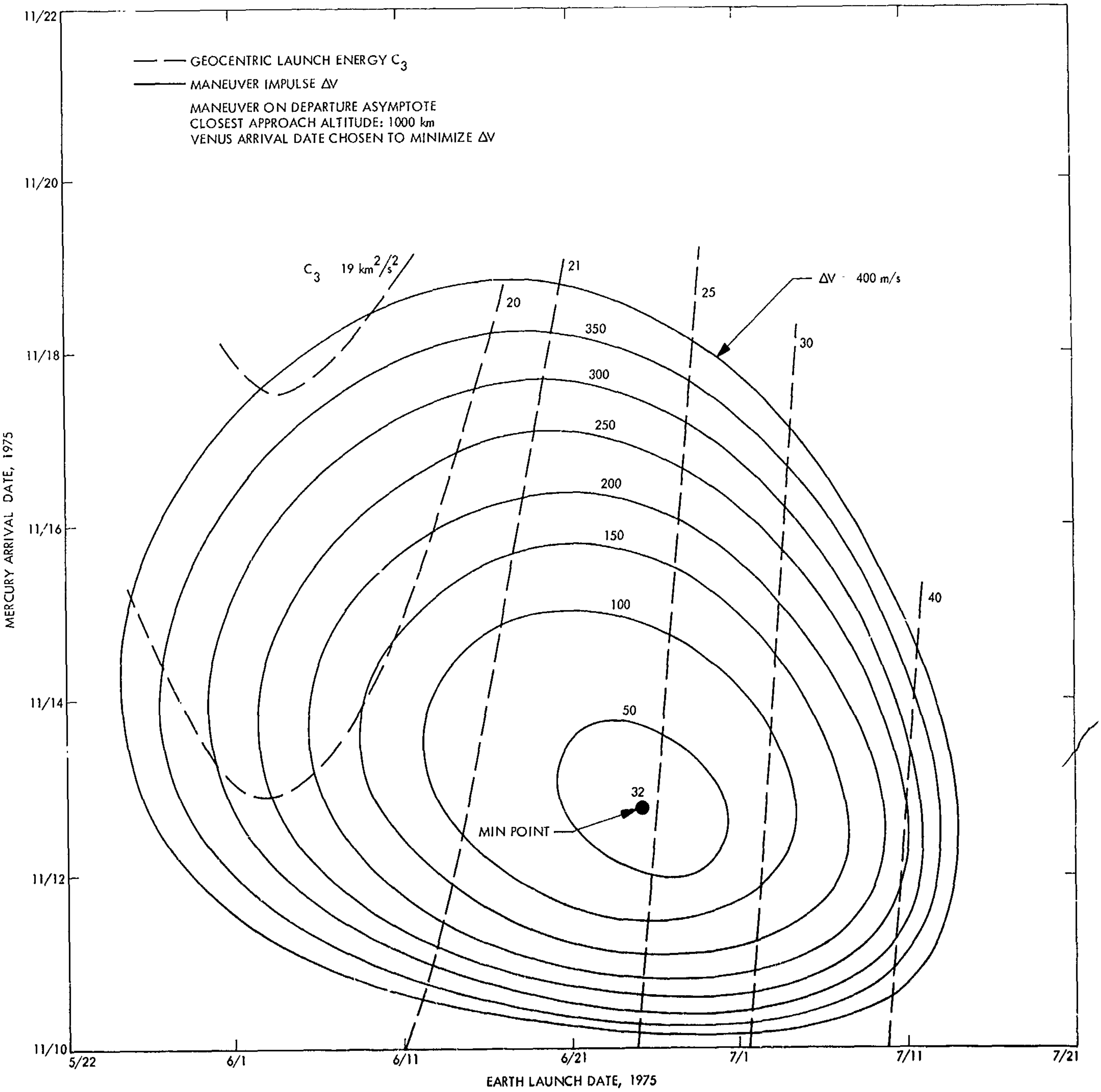

Fig. 11. Earth–Venus–Mercury mission design chart: launch energy C_3 and maneuver impulse ΔV

This is due to the departure speeds being generally higher than the approach speeds (a slower speed at encounter results in greater bending of the trajectory).

4. 1975 Earth–Venus–Mercury Mission Design

Using Fig. 11, the basic design chart, two missions were designed: one requiring low launch energies, the other, low propulsive assist at Venus. There is a definite launch vehicle and ΔV tradeoff available. The low launch-energy mission design is characterized by:

(1) Launch energy ≤ 21 km^2/s^2 (*Atlas/Centaur*).

(2) $\Delta V \leq 350$ m/s.

(3) 20-day launch period (May 27 to June 16, 1975).

(4) Mercury arrival time: Nov. 14, 1975.

The low propulsive-assist mission is characterized by:

(1) Launch energy ≤ 30 km^2/s (*Titan III*).

(2) $\Delta V \leq 100$ m/s.

(3) 20-day launch period (June 12 to July 2, 1975).

(4) Mercury arrival time: Nov. 13, 1975, 12 h.

Note the existence of two attractive mission designs, one requiring more onboard propulsion, but a smaller launch vehicle. Both missions require relatively small impulses when measured against the total ΔV usually required on ballistic multiple-planet missions.

As observed in the preliminary study, ΔV, as shown in Fig. 12 for the low propulsive-assist mission design, is almost constant with maneuver radius, being slightly higher near encounter. The characteristic of ΔV being higher at encounter is due to the dominating angular momentum or orientation requirements.

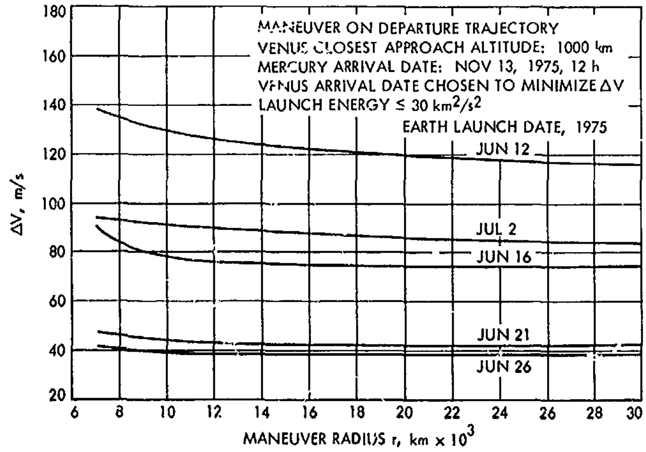

Fig. 12. Low propulsive-assist mission design: maneuver impulse ΔV vs maneuver radius r

Encounter conditions at Venus result in Earth occultation for all launch days in both mission designs. Figure 13 is a plot of the Venus occultation regions for a representative launch day. Note the 3σ error ellipse resulting from a 0.1-m/s spherically distributed midcourse execution error at launch + 5 days. The crossing of this ellipse into the impact zone indicates that a pre-encounter error-correction maneuver is required (a common requirement for multiple-planet missions), and that reducing the Venus closest-approach altitude much below 1000 km may be impractical.

Launch conditions for both mission designs are very good. The characteristics are:

(1) Launch azimuth corridors of 90 to 114 deg.

(2) Launch windows $\geq 2\frac{1}{4}$ h.

(3) Parking orbit coast times: 12 to 16 min (compatible with both the *Atlas/Centaur* and *Titan III* launch vehicles).

(4) Injection over mid-Atlantic to South Africa (reasonable near-earth tracking requirements for the Air Force Eastern Test Range).

For any study which is dependent on conic analysis, it is important that an accurate check be made on the final results. A comparison of the conic results with the precision integrated data is given in Table 4. The integrated data was supplied by the SPACE trajectory program (Ref. 3), a program used with a high degree of accuracy on actual missions to Mars, the moon, and Venus. Errors of between 8 and 13 m/s in ΔV are shown and point to the accuracy which may be realized with conic analyses if relative values (e.g., velocity differences) are required rather than absolute values.

References

1. Minovitch, M. A., *The Determination and Characteristics of Ballistic Interplanetary Trajectories Under the Influence of Multiple Planetary Attractions*, Technical Report 32-464, Jet Propulsion Laboratory, Pasadena, Calif., Oct. 31, 1963.

2. Wallace, R. A., "Trajectory Analysis of a 1975 Mission to Mercury via an Impulsive Flyby of Venus," Paper 68-113, presented at the AAS/AIAA Astrodynamics Specialists Conference, Jackson, Wyoming, Sept. 3–5, 1968.

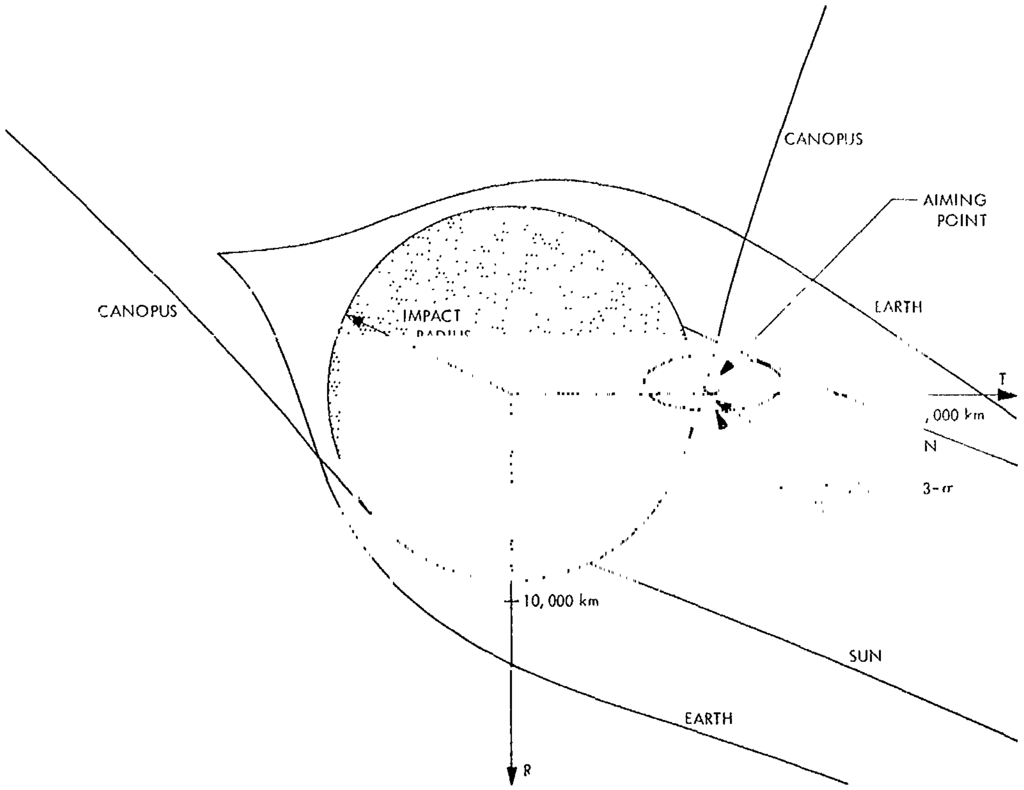

Fig. 13. Venus occultation zones (earth launch: Jun. 11, 1975; Venus arrival: Sept. 8, 1975, 3 h)

Table 4. Conic results vs integrated trajectory program data for various launch dates

Parameter	May 27, 1975		June 11, 1975		July 2, 1975	
	Conic	Integrated	Conic	Integrated	Conic	Integrated
b, km	10,333.96	10,333.14	10,079.9	10,081.89	9766.6	9767.3
θ, deg	353.91	353.91	357.00	357.01	0.42	0.43
VHP, km/s	9.0100	9.1102	9.4529	9.5586	10.0815	10.2069
VHL, km/s	9.2155	9.3370	9.5282	9.6373	10.1075	10.2289
r_p, km	7080.0	7079.7	7080.0	7081.4	7080.0	7080.4
i, deg[a]	8.62	13.10	4.05	1.43	1.48	94.44
I, deg[a]	3.420	3.410	3.406	3.403	3.436	3.436
Ω, deg[a]	31.92	30.72	35.60	36.21	246.83	209.15
ΔV, m/s	368.8	360.5	131.0	122.9	79.8	66.9

[a] Post-maneuver.

[b] b = impact parameter, hyperbolic semiminor axis; θ = targeting angle in B-plane; *VHP* = approach asymptotic speed on uncorrected trajectory; *VHL* = departure asymptotic speed required on departure trajectory; r_p = closest approach distance; i = orbital inclination to the ecliptic, Venus-centered; I = heliocentric inclination to the ecliptic of Venus–Mercury trajectory; Ω = longitude of the ascending node; ΔV = required impulse.

3. White, R. J., et al., *Space Single Precision Cowell Trajectory Program*, Technical Memorandum 33-198. Jet Propulsion Laboratory, Pasadena, Calif., Apr. 15, 1965.

D. Missions to the Outer Planets, *R. A. Wallace*

The 1975 to 1980 time period will afford an unusually favorable opportunity to launch missions to explore all of the outer planets. During this time period, the planetary geometries are such that rare multiple-planet missions involving all the major planets are possible. Such opportunities will not occur again for almost two centuries. This article expands on opportunities previously identified (SPS 37-35, Vol. IV, pp. 12–23) to show energy requirements and other characteristics for realistic launch periods.

Table 5 is a summary chart of eleven missions to the outer planets with launch opportunities from 1976 through 1979.[a] A comprehensive plan to explore all of the outer planets of the solar system could be constructed from this chart. There are four types of missions included:

(1) Single-planet missions: direct missions to Saturn, Uranus, Neptune, and Pluto (four missions).

(2) Two-planet mission: Earth–Jupiter–Pluto (one mission).

(3) Three-planet missions (grand tour minus Saturn): Earth–Jupiter–Uranus–Neptune (two missions).

(4) Four-planet missions (grand tour): Earth–Jupiter–Saturn–Uranus–Neptune (four missions).

Each of the eleven missions shown in Table 5 have been designed with consideration given to launch energy, time of flight, launch period, planetary flyby altitudes, and launch conditions.

The Rings of Saturn may present a formidable obstacle to spacecraft flying by that planet at altitudes less than 150,000 km. The present physical model of the Rings is much in doubt, however, and trajectories passing between the top of the atmosphere and the interior Ring or passing at altitudes greater than 70,000 km may be possible. The 1977 interior Ring passage grand tour mission (1977 Jupiter–Saturn interior Ring–Uranus–Neptune) would be most desirable. If a Saturn flyby altitude of 150,000 km were required, then a flight duration of 13 yr would result. If two spacecraft were available and the risks of catastrophic impact with the Rings of Saturn were found to be high for desirable grand tour missions, then one of the three-planet missions might be used in addition to a grand tour.

There is no question that a mission to Saturn, Uranus, Neptune, or Pluto should be flown with the aid of the gravitational field of Jupiter and/or Saturn. The 1977 Earth–Jupiter–Pluto opportunity is the best of five possible beginning in 1975 and ending in 1979 (Ref. 5). There are Earth–Saturn–Pluto missions available, but the launch energy is 140 km^2/s^2 or more. Launch energies for direct missions to Saturn begin to decrease in 1980 until in 198[illegible] a launch energy of 130 km^2/s^2 is sufficient for a 15-day launch period.

A sample plan to explore the outer planets by launching missions before 1980 might be the following:

(1) 1977 grand tour (interior Saturn Ring passage).

(2) 1978 grand tour minus Saturn.

Alternate missions in case of launch failure might be:

(1) 1978 grand tour (exterior Saturn Ring passage).

(2) 1979 grand tour minus Saturn.

References

1. Wallace, R. A., *Trajectory Considerations for a Mission to Jupiter in 1972*, Technical Memorandum 33-375. Jet Propulsion Laboratory, Pasadena, Calif., Mar. 15, 1968.

2. Clarke, V. C., et al., *Design Parameters for Ballistic Interplanetary Trajectories, Part II. One-Way Transfers to Mercury and Jupiter*, Technical Report 32-77. Jet Propulsion Laboratory, Pasadena, Calif., Jan. 15, 1966.

3. Kingsland, L., "Trajectory Analysis of a Grand Tour Mission to the Outer Planets," AIAA 5th Annual Meeting and Technical Display, pp. 68–1055, Philadelphia, Pa., Oct. 21–24, 1968.

4. White, R. J., et al., *SPACE Single Precision Cowell Trajectory Program*, Technical Memorandum 33-198. Jet Propulsion Laboratory, Pasadena, Calif., Apr. 15, 1965.

5. Flandro, G. A., "Fast Reconnaissance Missions to the Outer Solar System Utilizing Energy Derived from the Gravitational Field of Jupiter," *Astronaut. Acta*, Vol. 12, No. 4, Princeton, N.J., 1966.

---

[a] Earth–Jupiter missions are discussed in Refs. 1 and 2 and in JPL Engineering Planning Document 358, which provides data on launch opportunities from 1974 to 1981. The grand tour (four-planet) missions were designed by L. Kingsland (Ref. 3). The other missions in Table 5 are from unpublished material by the author. All missions but two were designed with the aid of a patched conic computer program SPARC [Derderian, M., *Space Research Conic Program, Phase III*, April 1968 (JPL Internal Document)]. The data for the two 1977 grand tour (four-planet) missions were computed with the aid of a precision integrating program SPACE (Ref. 4).

Table 5. Missions to the outer planets

Characteristics	1976 Jupiter–Saturn interior Ring–Uranus–Neptune	1977 Jupiter–Saturn interior Ring–Uranus–Neptune	1977 Jupiter–Saturn exterior Ring–Uranus–Neptune	1978 Jupiter–Saturn exterior Ring–Uranus–Neptune	1978 Jupiter–Uranus–Neptune	1979 Jupiter–Uranus–Neptune	1977 Jupiter–Pluto	1979 Saturn (direct)	1977–1978 Uranus (direct)	1977 Neptune (direct)	1976 Pluto (direct)
Launch period, days	15	15	15	15	15	15	15	15	15	15	15
Maximum launch energy required, km^2/s^2	104	120	100	108	110	110	110	140	139	150	180
Capability for *Titan III/Centaur* (spacecraft weight; 114-deg azimuth), lb[a]	1400	780	1530	1250	1190	1190	1190	140	150	0	–
Capability for *Titan III/Centaur Burner II* 1440 (spacecraft weight; 114-deg azimuth, lb[1]		1380	1800	1620	1580	1580	1580	900	930	700	–
Maximum declination at launch (absolute value), deg	14	27	33	33	32	27	28	37	7	4	26
Jupiter encounter											
Flight time from launch, days	561	511	652	593	564	579	551	–	–	–	–
Flyby altitude, km (Jupiter surface radius)	16,000 (0.2)	212,000 (3.0)	622,000 (8.8)	1,600,000 (22.5)	62,000 (0.9)	560,000 (7.8)	236,000 (3.3)				
Communication distance, km $\times 10^6$	675	638	900	767	719	749	673				
Saturn encounter											
Flight time from launch, days (yr)	1363 (3.7)	1095 (3.0)	1394 (3.8)	1240 (3.4)	–	–	–	1255 (3.4)	–	–	–
Flyby altitude, km (Saturn surface radius)	8,000 (0.1)	6,000 (0.1)	75,000 (1.2)	80,000 (1.3)				Open			
Communication distance, km $\times 10^6$	1277	1562	1453	1321				1310			
Uranus encounter											
Flight time from launch, days (yr)	2798 (7.7)	2342 (6.4)	2945 (8.1)	2764 (7.6)	2293 (6.6)	2286 (6.3)	–	–	3092 (8.5)	–	–
Flyby altitude, km (Uranus surface radius)	32,000 (1.3)	16,000 (0.7)	86,000 (3.8)	121,000 (5.1)	22,000 (0.9)	41,000 (1.7)			Open		
Communication distance, km $\times 10^6$	2781	2910	2900	2717	2972	2833			2709		
Neptune encounter											
Flight time from launch, days (yr)	3894 (10.7)	3372 (9.2)	4100 (11.2)	4030 (11.0)	3503 (9.6)	3599 (9.9)	–	–	–	6209 (17.0)	–
Flyby altitude, km	Open	Open	Open	Open	Open	Open				Open	
Communication distance, km $\times 10^6$	4519	4613	4587	4642	4440	4457				4659	
Pluto encounter											
Flight time from launch, days (yr)	–	–	–	–	–	–	3500 (9.6)	–	–	–	15,231 (41.7)
Flyby altitude, km							Open				Open
Communication distance, km $\times 10^6$							3919				4934

[a] J. Long, private communication.

III. Environmental Requirements

PROJECT ENGINEERING DIVISION

A. The Effect of Low Numbers of Microorganisms on Samples Assayed by the NASA Standard Procedure, *E. J. Sherry*

1. Introduction

The NASA standard procedure (NSP) (Ref. 1) used to assay a sample for viable bacteria makes two related assumptions. The first is that there is a large number of bacteria (100 or more) present in a sample so that extrapolated counts from serial dilutions are statistically meaningful. This is related to the second assumption, namely, that microorganisms are uniformly distributed in the recovery medium (i.e., each bacteria has an equal probability of being in any position of the medium). These assumptions allow one to interpret an assay procedure as an "occupancy problem[1]" and to extrapolate from the plate counts to the actual number of organisms present on the object sampled. Given large numbers of bacteria, the samples can even be broken into parts, assayed for different types of microorganisms, and the results stated with a certain confidence. However, when the number of organisms is low, a question arises as to the accuracy of the extrapolation procedure.

This condition, i.e., low numbers of microorganisms present per sample, was found in the samples taken during the *Mariner* Venus 67 sampling program (SPS 37-46, Vol. IV, pp. 48–55) and when samples were taken in a class 100 clean room.[2] If one then considers the assembly of a spacecraft in a class 100 clean tent (as is the case with the *Mariner* Mars 1969 spacecraft), one should expect low numbers of organisms per sample. This article discusses the accuracy of the extrapolation with two different assay and recovery techniques when the assumption of the presence of large numbers of organisms is negated.

2. Techniques

Data from the capsule mechanical training model (CMTM) assemblies (SPS 37-52, Vol. I, pp. 31–34) directed by the sterilization assembly development laboratory (SADL) team were used to form a data base for the statistical analysis (SPS 37-50, Vol. III, pp. 71–74). In

---

[1] That is, the plates are rooms and the microorganisms are guests, each with an equal probability of choosing any room. A guest finding his room means that a microorganism is plated out and incubated in an environment that will be suitable for it to grow. A guest not finding his room will mean that either a microorganism is plated out and incubated in an unsuitable environment, or not plated out at all.

[2] Paik, W. W., *et al*, The Effects of Disrupted Laminar Air Flow on the Microbial Burden of Assembled Hardware, JPL Technical Report (in preparation).

particular, the results form the first five assemblies in the CMTM Program (more than 2,800 assays were used).[3] Of the five assemblies, three were in a high-bay area and two were in a laminar down-flow tent[4] (designated as 201, 202, 203, and T01, T02, respectively, in Tables 1 and 2).

Table 1. Percentage of CMTM assays showing no viable microorganisms

Assembly	Total number of assays		Assays showing zero count, %	
	NSP	SP	NSP	SP
Coupon assay technique				
201	83	342	65	59
202	83	334	83	72
203	95	365	79	79
T01	89	357	73	63
T02	91	362	79	81
Average	88	352	76	71
Swab assay technique				
201	—	—	—	—
202	42	152	71	61
203	29	120	69	66
T01	21	102	57	50
T02	34	133	61	66
Average	32	127	64	60

Table 2. Percentage of assays showing no aerobic heat-shocked spores

Assembly	Total number of assays		Assays showing zero count, %	
	NSP	SP	NSP	SP
Coupon assay technique				
201	83	342	95	92
202	83	332	99	97
203	95	364	98	97
T01	89	357	98	93
T02	91	355	99	99
Average	88	350	98	96
Swab assay technique				
201	—	—	—	—
202	42	151	95	87
203	29	120	97	92
T01	21	103	76	83
T02	34	134	91	92
Average	32	127	90	88

The samples, coupons (polished stainless steel, 1×2 in.) and swabs (cross stroking a 2×2-in. area), were taken at random, according to a predetermined sampling plan (Ref. 2), and assayed according to either the NSP or SADL procedure (SP) (Ref. 3). The basic difference between the two procedures is that the SP incubates the plates for only aerobic bacteria while the NSP incubates for both aerobic and anaerobic bacteria. Counts were obtained and recorded after 72 hr. Generally, 450 coupons and 150 swabs were used per assembly with 80% of all samples assayed according to the SP and 20% according to the NSP.

3. Analysis

The large percentage of zero counts found in the assays from each of the five assemblies made it necessary to use a nonparametric test (the Kolmogorov–Smirnov test) to attempt to compare data. Initially, all the samples of a particular type (swab or coupon) were compared by type and day taken. The test of the null hypothesis showed that each assay type was indistinguishable in a day-to-day comparison. Each assembly was tested in this way and yielded the same conclusion. With this information, all samples of the same type from one assembly were grouped and then tested assembly by assembly. Again, it was impossible to distinguish one assembly from another. These tests then allowed the grouping of data by types from all five assemblies to form an "average" assembly.

Table 1 presents the percentage of samples that showed absolutely no viable microorganisms[5] according to type of assay (coupons and swabs), procedure used (NSP or SP), assembly number, and average assembly. Analysis of the data presented in this table by the Kolmogorov–Smirnov test proved that there was a statistically significant difference ($\alpha = 0.1$) between the average number of zeros found by the NSP on coupons and the SP on swabs. Further, there was the same statistically significant difference between the average number of zeros found on coupons and swabs by either procedure.

Table 2 presents the percentage of samples that showed no heat-shocked aerobic spore growth.[6] These data were subjected to the same analysis as that presented in

---

[3] The author wishes to thank G. H. Redmann and D. M. Taylor for permission to use the CMTM data prior to its publication.

[4] The high bay area was a class 100 K room, and the tent a class 100 room, as defined by Federal Standard 209a.

[5] That is, after a 72-hr incubation period, there was no growth recorded on any of the plates for a given sample.

[6] That is, the plates incubated for aerobic heat-shocked spores show no growth after 72 hr. In approximately 20% of these cases, the other plates associated with the sample had vegative or anaerobic heat-shocked spore growth.

Table 1 and showed the same statistically significant differences.

Table 3 is typical of the data from all of the assemblies. It shows that the SP consistently exhibited a higher recovery percentage than the NSP. In addition, Table 1 shows that the SP gave, on the average, a 5% higher recovery percentage than the NSP; Table 2 shows that the SP is, on the average, 2% better. Unfortunately, the Kolmogorov–Smirnov test was unable to prove that the differences between NSP and SP were statistically significant.

Table 3. Cumulative distributions for assembly 203 swab assays listed by assay procedure

No. organisms/assay	NSP (29 assays)	SP (120 assays)
0	68.97	66.67
1	89.66	77.50
2	93.10	82.50
3	96.55	84.17
4	100.00	85.83
5	100.00	88.33
6	100.00	89.17
7	100.00	90.83
8	100.00	92.50
9	100.00	92.50
10	100.00	93.33
11	100.00	93.33
12	100.00	93.33
13	100.00	93.33
14	100.00	93.33
15	100.00	94.17
16	100.00	94.17
18	100.00	94.17
19	100.00	95.00
20–100	100.00	98.33
101–200	100.00	99.17
201–300	100.00	100.00
>300	100.00	100.00

4. Conclusions

The first conclusion that appears from the analysis of the data in Tables 1 and 2 is that, using either procedure, the swabs give a statistically significant higher recovery percentage than coupons. This is contrary to expectation, since one expects swabbing to be a less efficient sampling procedure than the use of coupons. One possible explanation is that swab data were taken directly from the CMTM, while the coupons may have been given preferential treatment by the assembly personnel.

The second conclusion (although not statistically significant) is that the SP gives a higher recovery percentage than the NSP in the case of all microorganisms (Table 1) as well as in the case of only aerobic heat-shocked spores (Table 2). This is clearly shown in Table 3 where the SP consistently exhibits a higher recovery percentage. It is unfortunate that this observation cannot be stated with statistical significance at this time, but it must be noted that the Kolmogorov–Smirnov test would have been capable of rejecting the null hypothesis if the same percentage held for a larger sample population.

The last conclusion leads one to question the two assumptions that allow the NSP to be interpreted as an occupancy problem since the first assumption (large numbers of microorganisms per sample) is obviously violated (Table 3), and the analysis shows the second assumption (microorganisms uniformly distributed in the recovery medium) to be invalid. Thus, the use of the NSP would give a lower estimate of the total burden than the SP. That is, an extrapolation from the samples assayed by the SP would more accurately approximate the actual microbiol burden, because the second assumption is not as sensitive to a two-fold sample partition as it is to a four-fold partition. Carrying this logic one step further, it appears that one should use an assay procedure that plates out the entire sample and incubates for only one type of organism. In this way, since the relationship between types of organisms is fairly well established, if one obtained an accurate count of one type of microorganism (e.g., aerobic spores) one could, perhaps, more accurately extrapolate to the total actual burden. Finally, it must be stated that this is a problem relevant to not only spacecraft but to any sampling program where the number of organisms per sample is low.

References

1. *NASA Standard Procedure for the Microbiological Examination of Space Hardware,* NASA Handbook 4340.1. National Aeronautics and Space Administration, Washington, Aug. 1967.
2. *Microbiological Sampling of Spacecraft Hardware,* SADL Operations Plan 3-120. Jet Propulsion Laboratory, Pasadena, Calif., Oct. 1968.
3. *Microbiological Laboratory Assay Methods,* SADL Procedure 3-211. Jet Propulsion Laboratory, Pasadena, Calif., Oct. 1968.

IV. Flight Computers and Sequencers

GUIDANCE AND CONTROL DIVISION

A. Automatic Roving Vehicle Computer Development, *L. Y. Lim*

1. Introduction

The overall objective of this effort is the design and development of an on-board computer for an automatic roving vehicle. The development of an on-board computer requires a detailed knowledge of the various computational tasks that the computer must perform. One of these computational requirements is the navigation of the vehicle.

This report deals with the development of a computational algorithm for the navigation of the vehicle, i.e., a pathfinding algorithm. The detailed presentation on this subject has been published as a technical report (Ref. 1).

2. The Pathfinding Algorithm

The pathfinding algorithm derived in Ref. 1 assumes that: (1) there exists at least one path between the starting position and the target position; (2) each obstacle has contour lines and finite dimensions, and (3) the vehicle has terrain sensors which can detect its immediate surrounding.

Definition 1. An acceptable point is defined as a point (X,Y) such that $|F(X,Y)| \leq E$, where $F(X,Y)$ is a continuous function that describes the terrain, and E is the elevation limit.

Definition 2. A path is defined as a route that connects two points (X_i, Y_i) and (X_j, Y_j) such that the elevation of each point on the route is $|F(X,Y)| \leq E$.

Definition 3. An obstacle is defined as a finite bounded region of a function whose amplitude or values are greater than E, i.e.,

$$|F(X,Y)| \geq E$$

Let $P_0 = (X_0,Y_0)$ and $P_n = (X_n,Y_n)$ be the starting position and the target position on an unknown terrain. Let there exist at least one path connecting P_0 and P_n. The procedures for finding a path which connects P_0 and P_n are:

Step 0. Define

$$d_m = [(X_n - X_0)^2 + (Y_n - Y_0)^2]^{1/2}$$

Step 1. From P_0 go directly to P_n if there are no obstacles between the starting point and the target point. Every point generated in this case is an acceptable point, and every d_i generated is such that $d_j < d_i$ where $j > i$ and

$$d_i = [(X_n - X_{i-1})^2 + (Y_n - Y_{i-1})^2]^{1/2}$$

However, if there is an obstacle encountered at $P_k = (X_k, Y_k)$, replace d_m by d_k, then go to step 2.

Step 2. At point P_k, scan alternately right then left at appropriate increments until an acceptable point is found. Let P_{k+1} be the acceptable point. If $d_{k+1} < d_k$, replace d_m by d_k and P_0 by P_{k+1} go back to step 1. If $d_{k-1} \geqslant d_k$, go to step 3.

Step 3. Determine whether the point P_{k+1} was the result of scanning right or scanning left. If P_{k+1} was the result of the right scanning process, stay on the right contour of the obstacle. Similarly, if P_{k+1} was determined from the left scanning process, stay on the left contour of the obstacle. In either case the right or left contour is followed until an acceptable point $P_q = (X_q, Y_q)$ satisfies the relationship $d_m > d_q$. Once this relationship has been satisfied, replace d_m by d_q and P_0 by P_q, then return to step 1. The process is repeated until P_n is reached.

3. Application

A computer program was coded in Fortran IV language as implemented in the IBM 7090/94 IBJOB system. Examples and results are contained in Ref. 1. The terrain used in all simulations consisted of gaussian density functions. Figure 1 shows a perspective drawing of a gaussian terrain. Figure 2 shows a sample of the results contained in Ref. 1. The algorithm developed under this task does not require *a priori* information about the map in order to find a navigating route; it requires only local terrain information. However, the determined navigational route is not necessarily the optimum one (minimum distance, etc.).

4. Future Plans

Future tasks will include the following:

(1) Determination of the minimum distance navigational route by using terrain information obtained from orbital reconnaissances.

(2) Development of a computational algorithm for the preprocessing of terrain sensor data.

(3) Incorporation into the present algorithm of the ability to "learn" from its experiences as it navigates on the unknown terrain. This might include such factors as statistical classification of the terrain.

Reference

1. Lim, L. Y., *A Pathfinding Algorithm for a Myopic Robot*, Technical Report 32-1288, Jet Propulsion Laboratory, Pasadena, Calif., Aug. 1, 1968.

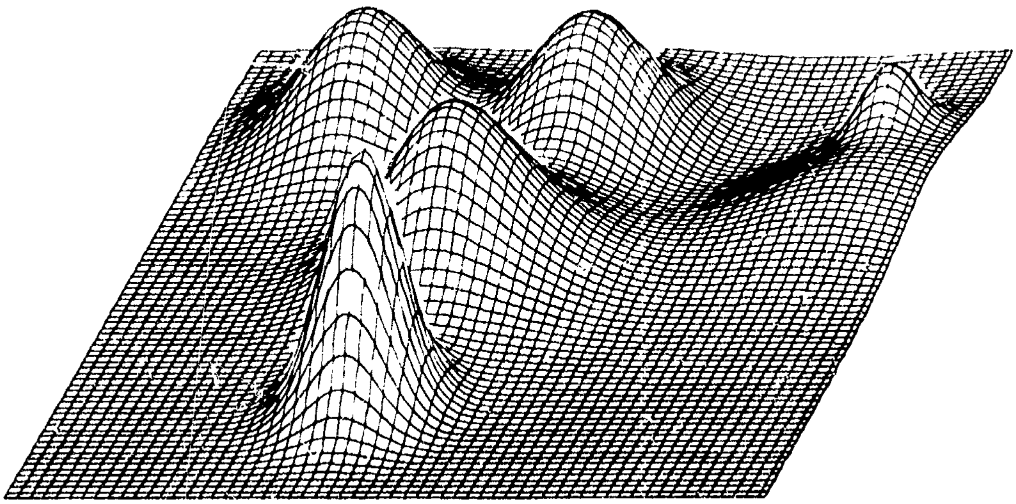

Fig. 1. Perspective drawing of contour configuration

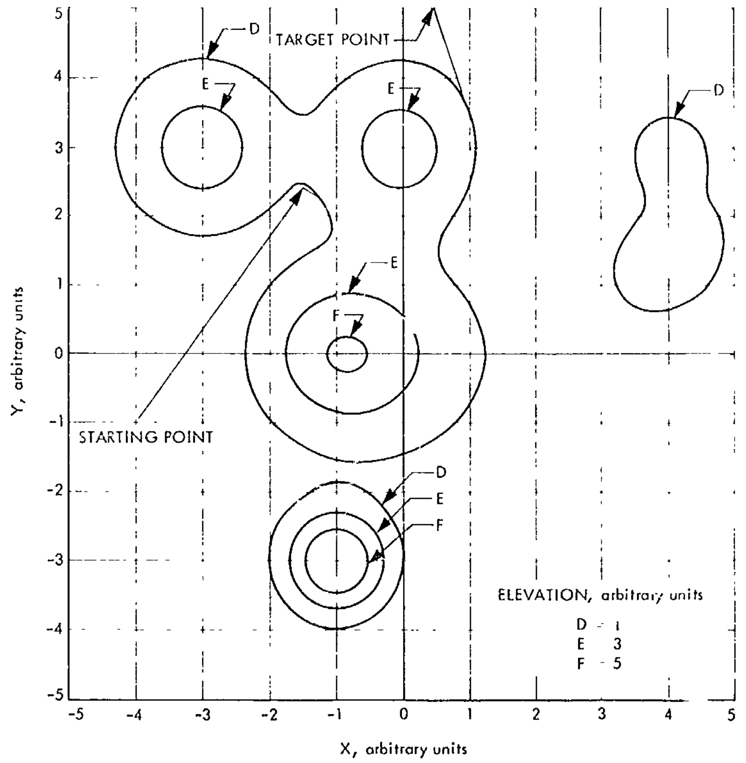

Fig. 2. A simple box canyon configuration

V. Spacecraft Power

GUIDANCE AND CONTROL DIVISION

A. Effect of Electrolyte Concentration on the Electrical Characteristics of AgO–Zn,

R. S. Bogner and R. Patterson

1. Introduction

As part of the JPL advanced battery systems development program, AgO–Zn cells were obtained from Delco-Remy Div. of General Motors Corp. with 40, 45, and 50% concentrations of KOH electrolyte in order to study the effects of concentration on cycle life and electrical performance. The cells were rated by the manufacturer at 25 A-h nominal and were identical in construction except for the electrolyte concentration. The tests were conducted on three 5-cell groups.

2. Experimental Procedure

The cells were charged at 1.5 A for the first seven cycles, and the remaining charge cycles were accomplished at 2.0 A to a minimum cutoff of 1.98 V. All charging was done at room ambient temperature, 75°F, after a minimum 16-h stand period to equilibrate cell temperature.

For the 12 discharge cycles measured, the discharges were made in the order of 2, 10, 30, and 50 A at ambient temperatures of 75, 30, and 100°F. Cell temperature was monitored during the discharge by a transducer mounted on the terminal of one cell in each group. In all instances, the cells were allowed to equilibrate at the ambient discharge temperature for a minimum of 16 h. At the low discharge currents (2 and 10 A), the cells were discharged in series and were removed from the string when their terminal voltage reached 1.30 V, which corresponded to the "knee" of the discharge curves. At the high discharge currents (30 and 50 A), the cells were removed when their terminal voltage reached about 1.00 V, which corresponded to the knee of those discharge curves.

3. Results and Discussion

The average cell capacities and plateau voltages of each five-cell group at the various discharge currents and temperatures are given in Table 1. It is seen that plateau voltage generally varies directly with the ambient temperature as expected. However, the electrolyte concentration at the various discharge currents appears to have little effect on the plateau voltage. At 30°F and at discharge currents of 2 to 30 A, the plateau voltages are decreased by 0.01 to 0.05 V at the 50% concentration. On the other hand, at the 50-A discharge current, the plateau voltage is increased by 0.05 V at the 50%

Table 1. Average plateau voltages and cell capacities in each 5-cell group

Discharge current, A	KOH concentration, wt %	Plateau voltage, V, at indicated temperature			Cell capacity, A-h, at indicated temperature		
		30°F	75°F	100°F	30°F	75°F	100°F
2	50	1.47	1.53	1.55	32.5	47.0	47.5
	45	1.51	1.54	1.55	29.5	47.5	49.0
	40	1.51	1.54	1.55	36.0	50.0	47.5
10	50	1.41	1.50	1.51	20.0	42.0	48.0
	45	1.45	1.50	1.51	21.5	40.0	45.0
	40	1.45	1.50	1.51	24.0	44.0	47.0
30	50	1.30	1.43	1.42	21.0	26.0	25.0
	45	1.32	1.43	1.44	12.0	25.0	25.5
	40	1.34	1.43	1.44	11.0	26.0	24.5
50	50	1.20	1.35	1.38	14.5	26.0	29.0
	45	1.15	1.35	1.37	7.0	16.0	19.5
	40	1.15	1.35	1.38	7.5	17.0	19.0

concentration. During the development of the *Surveyor* battery (Ref. 1), electrolyte concentrations of 33 to 43% KOH were investigated. Those data showed that cell voltage and capacity were maximized at 40% KOH; however, discharge currents were relatively low, so the *Surveyor* data is not in conflict with the present data.

At low discharge currents and within the temperature range evaluated, it is seen in Table 1 that the electrolyte concentration has little effect on the cell capacity. However, at the high discharge currents, it is seen that cell capacity is increased at increased KOH concentration at all test temperatures. As might be expected, cell capacity tends to increase with temperature; however, the cell capacity for the 40% electrolyte tended to decrease slightly or stay relatively constant at temperatures between 75 and 100°F.

The results of this investigation indicate that the effect of electrolyte concentration on cell performance is a complex phenomenon. Cell design parameters such as the type of separator system, plate density, plate thickness, and quantity of electrolyte also play an important role in cell performance.

The results could, in part, be due to an internal heating effect. Since the conductivity varies inversely with the KOH concentrations, it is entirely possible that the internal heating of the cells produced the effects discussed here. Cell temperature was measured at the terminals during the discharge; however, the temperatures recorded are of little value because of the heat generated by current-resistance of the terminals and intercell connections. A study now in progress at Whittaker Corporation for Delco-Remy (Ref. 2) should help differentiate between the interaction of the heating and electrolyte concentration effects. In this study, individual plate or electrode performance is being evaluated as a function of electrolyte concentration and temperature.

In addition to the data presented here, cell shelf life is being investigated as a function of electrolyte concentration at temperatures from −60 to 120°F. Charge characteristics will be obtained on a second set of cells.

4. Conclusions

The data show that electrolyte concentration is an important consideration in the design of AgO–Zn cells and that the optimum electrolyte concentration is dependent on battery application. For example, if the requirement is one of high discharge current at low temperatures, a high electrolyte concentration should be used if the charging can be accomplished at room temperature.

References

1. Moses, A. J., *Summary Report—Surveyor Main and Auxiliary Batteries*. Prepared under JPL Contract 952226. Hughes Aircraft Co., El Segundo, Calif., Oct. 1968.

2. Keralla, J. A., *Silver-Zinc Electrodes and Separator Research*, Technical Report AFAPL-TR-68715. Prepared under Air Force Contract AF 33(615)3487. Delco Remy Div., General Motors Corp., Anderson, Ind., Sept. 3, 1968.

B. Testing of Thermoelectric Generators,

P. Rouklove

1. Introduction

Thermoelectric generators and multi-element thermoelectric modules are being tested at JPL to: (1) provide a set of accurate performance data to allow thorough evaluation of the units, and (2) obtain the experience required for use of thermoelectric generators as power sources for future spacecraft. Seven thermoelectric generators have been, or are presently, under test. Figure 1 shows the JPL thermoelectric laboratory where four of the units are currently under test. Three units are being tested in an ambient condition, while the fourth is undergoing thermal-vacuum environmental tests in the special vacuum chamber.

Fig. 1. Thermoelectric generator test facilities

One series of tests consists of extensive parametric evaluations of the generators at various predetermined values of power input and/or hot junction temperature. The power output and other values are recorded at each value of power input for selected values of voltage output. Another test consists of long-life term evaluation, generally at maximum power input and maximum power output, or a matched load condition. These tests are usually performed in ambient condition using the normal air convection cooling. Another series of tests is performed in a vacuum condition to simulate the environmental conditions that would be imposed on a thermoelectric generator during a space mission. During all tests, the generators are heated by radiant heat from a block being heated electrically, but simulating the mass and center of gravity of a radioisotope capsule.

2. Tests of the First SNAP 11 Generator, SN-2

a. Generator design. The SNAP 11 generator was designed as a possible power source for the *Surveyor* spacecraft. When technical difficulties precluded this usage, the program was redirected to further improve the performance of thermoelectric generators heated by radioisotope decay. Due to the short expected mission duration, the generator was to be fueled with curium-242, whose half life was judged sufficient for the 90 days of a lunar mission.

The design of the generator (shown in Fig. 2) includes provisions for excess isotope inventory, and a thermal mechanism to relieve the excessive thermal energy at the beginning of the mission. This mechanism consists of a thermal shutter that is activated by expansion of a column of NaK, the movement being transmitted through a bellows-and-lever arrangement to the hinged shutter mechanism. This arrangement can be regulated to release any amount of energy above the 550 W (thermal) that is calculated to be necessary for operation of the generator.

The heat source for the generator consists of a fuel capsule that, for purposes of testing, was replaced by an electrically heated block simulating the isotope capsule in size, mass, and center of gravity. The block contained eight sheathed electrical heaters equally distributed along the periphery. The capsule is located inside a metallic cavity, the outer periphery of which is covered with lead-tellaride (2P-2N) thermoelectric elements. These elements are pressed against the cavity wall by spring-loaded push rods and are insulated from the cavity by a thin insulating material with good thermal transmission properties.

The generator is surrounded by a second metallic container, in close thermal contact with the cold junction of the thermoelements, and is provided with fins to radiate the excess heat. The top of the cavity containing

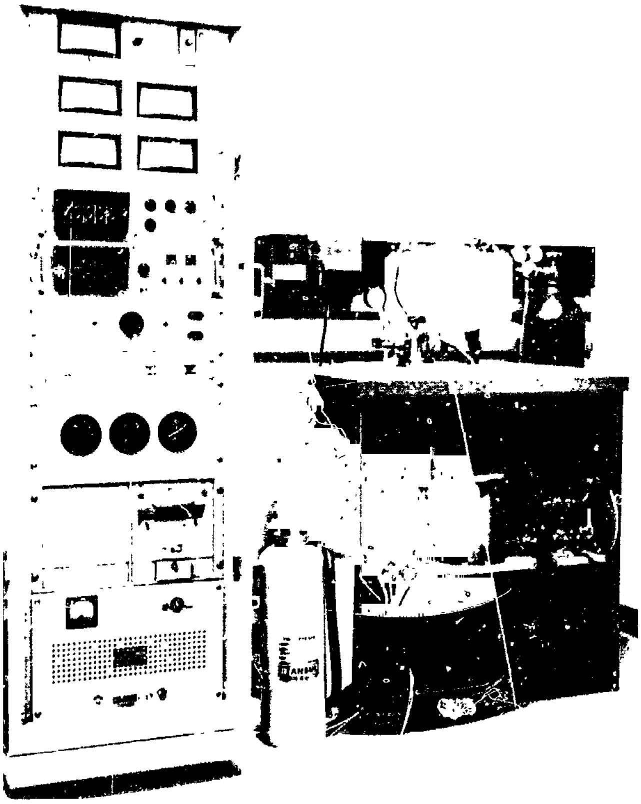

Fig. 2. SNAP 11 generator SN-2 in test

the heater block for the tests was covered by the thermal shutter. The intercavity spacing, hermetically enclosed, is packed with insulating material placed between the thermoelements and was filled with an inert gas to reduce the possible sublimation of the thermoelectric material at the operating temperatures. The SN-2 was provided with a valve to enable addition of the gas. During the tests, this valve was connected to a cylinder of the inert gas through a purifying system. (This arrangement proved to be very useful, since the generator was found to be leaking and gas had to be added to maintain proper pressure.) The nominal power output of the SN-2 generator is 30 W at 3.0 V, and the total generator weight is 30 lb.

b. Test equipment. The equipment used in the SN-2 tests (Fig. 2) was manually operated and consisted of a hot junction over-temperature control and the instrumentation used to read out the power input (volts and amperes) and the power output. A digital voltmeter and scanner were used to record the different instruments and thermocouple readouts. The generator load consisted of a variable resistor.

Power input was controlled by three Variacs preset for three modes of operation: (1) the initial period (lunar day), (2) the midterm operation (lunar night), and (3) the standby mode. Testing was performed in an ambient environment. The power input was adjusted to produce the hot junction temperatures and thermal conditions calculated to represent the various mission conditions. The thermal conditions were naturally heavily dependent upon the expected lunar environment (lunar day, +235°F; lunar night, −235°F).

A standby Variac was used in conjunction with the hot junction over-temperature protection circuit to reduce the power input by 30% in case of excessive heat. This arrangement avoided possible thermal shocks in case the guard circuit tripped the operating input level. To further avoid the possibility of a thermal shock due to loss of line voltage, a relay circuit was included to automatically select any of the three phases still operating. The line voltage was supplied through a voltage stabilizing circuit. All data were recorded on a digital printout on command.

c. Test results. The SN-2 generator was operated at JPL for approximately 3100 h, during which time some degradation in performance was observed. This was traced to an increase in the internal resistance of the generator, related primarily to a deficiency of the bonding of the thermoelectric elements to the "hot shoes." In spite of the fact that approximately 50% of the bonds were found to be deficient, the SN-2 generator was still operating well past the design time (90 days). By 3000 h, it had experienced a 20% decrease in its operating output.

During the tests, dc/dc power conversion system was tested in conjunction with the generator. The converter delivered a nominal voltage output of 28 V with an input of 3.0 V. Although the efficiency of the device was 87%, heavy losses were observed in the primary transmission line of 6 ft of 4/0 cable. Heavy current and voltage transients, resulting from magnetic effects in the power transmission lines, had to be eliminated by extra large capacitors. These losses drastically reduced the efficiency of the combination of the generator and the dc/dc converter.

3. Tests of the Second SNAP 11 Generator, QN-3

a. Generator design. Certain deficiencies observed in the SN-2 generator were corrected in the newer version of the SNAP 11 generator designated QN-3 (Fig. 3). This generator is hermetically sealed with the proper amount of gas. An improved control mechanism of the thermal

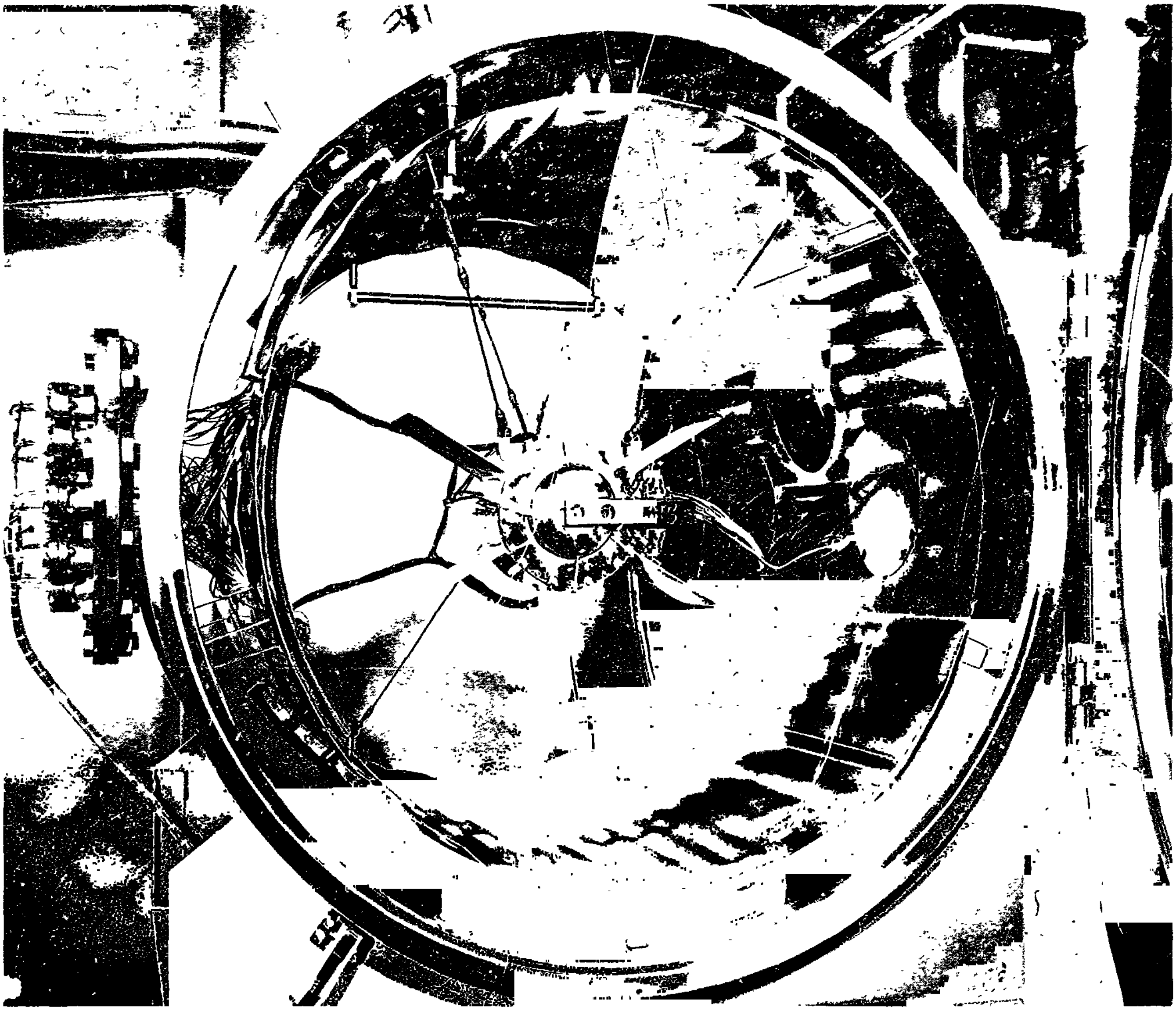

Fig. 3. SNAP 11 generator QN-3 during thermal-vacuum tests in vacuum chamber

shutter is included. The lead telluride thermoelements used are 2N-3P, which, although less efficient than the 2N–2P, are more stable, less fragile, and less prone to contamination. Also, the bond between the elements and the hot shoes is improved. The new 32-lb generator delivers slightly less than its nominal 30-W output.

b. Test equipment. The SN-2 generator tests indicated the need for accelerated testing and more reliable information; thus, the following improvements were made in the test equipment:

The manually operated Variacs were replaced by an automatic power input control built around a "data track" silicon-controlled rectifier. This arrangement allowed automatic control of the power input to within ±1 W, or control of the power input to maintain the hot junction temperature at a selected value to ±1°C. Parallel to that arrangement, a programming device provided the capability to vary the power input according to a pre-traced power/time curve with an accuracy of ±10°C or ±10 W. The resistive load was replaced with an automatically controlled solid-state load developed at JPL that provided the capability to maintain a selected voltage or current output to ±1 mV or ±1 mA.

The over-temperature circuit was further refined, and the open-circuit voltage and current reading circuits were modified to record the data after a defined and constant period of time. The latter modifications were made since the previous readings, taken during an unstable operational period and estimated by the operator, did not provide the desired accuracy.

Data were recorded automatically on an hourly basis, 24 h/day, on data acquisition equipment with a capability for 300 programmed channels. All data were printed out automatically. This arrangement reduced the data-taking interval from 12 to 3 h, resulted in much more accurate data, and freed the technician, previously occupied full time with the operation of the generator, for other activities. The modified test equipment and the automatic data recording equipment are shown in Fig. 1. At present, the automatic data recording equipment is utilized to record the data from all the generators tested, as shown in Fig. 1.

The equipment was capable of fully automatic 24-h unattended operation. Visible and audible alarm systems were included to warn in case of operational deficiencies. To further reduce risks of thermal shocks due to power line failures, a battery bank was connected through a diode to cut-in automatically and instantaneously in case of reduction of the line voltage below a preset limit.

c. *Test results*

Ambient and thermal-vacuum testing. The generator was tested at JPL in air for 5600 h over a wide range of power input and power output. At the initial examination, it was observed that the generator was subjected to shock during transportation of above 10 *g* in the vertical direction. This may have resulted in the slight increase of the internal resistance with the corresponding decrease in power output that was observed but that was not indicated in the test data provided by the manufacturer. No power output degradation was observed during the tests.

Additional testing for approximately 4900 h was performed on the generator in a vacuum environment (Fig. 3). During this period, the generator was tested over a wide range of power input and output at shroud thermal conditions of 235°C and −235°F for three complete thermal cycles.

At the end of the third thermal cycle at a high shroud temperature, it was observed that the pressure of the inert gas within the generator was decreasing. This condition was attributed to high gas diffusion or leakage through the Viton "O" rings used in the hermetic seal of the generator. The thermal-vacuum tests were terminated when the inner generator pressure dropped from 14.8 to 10.8 psi.

Prior to delivery to JPL, the QN-3 generator had been operated by the contractor for approximately 2500 h. Comparison of the SN-2 and QN-3 test results indicated that the QN-3 generator did not present the power output degradation pattern observed with the SN-2. The SN-2 was observed to degrade along an exponential-type curve during the first 1000 h of operation, the curve slowly becoming asymptotic to a stable operational line. From initiation of the testing at JPL, the QN-3 generator operated in a straight-line pattern.

After the opening of the vacuum chamber, a heavy deposit (shown in Fig. 3) was observed on the walls of the chamber and in the vacuum system. The deposit, characterized as Au, Cd, Al, and Mg, was probably the result of the following processes: The Au evolved from the gold plating of the thermal shutter and the generator's top end; the Cd resulted from some of the braze materials used; and the Al and Mg evolved from some of the high-temperature cements used to affix the thermocouples and form the insulation layers separating the heating block from the inner can walls.

The deposit found in the vacuum system was of an organic nature (paraffin and other compounds) and could have evolved from the cover of some of the cables provided by the contractor that were used in the electrical interconnection between the generator and the test equipment. The results of the tests indicated that a thermoelectric generator could successfully operate for long periods of time in severe thermal environments.

Vibration and acceleration testing. The QN-3 was also subjected to vibration and acceleration tests in the *Z* (thrust) and *Y* spacecraft axes. During the tests, the generator was mounted 30 deg to the vertical to duplicate the possible position on the spacecraft.

The tests were performed with the generator heated with 570 W and electrically loaded to deliver approximately 15 W at 2.0 V. The tests consisted of acceleration up to 10 *g* static and vibration up to 18 *g* (peak), using both sinusoidal and complex wave forms. No high-intensity shock tests were performed. Some heater–shutter flapping was observed at excitation between 13 and 24 Hz, and the radiator fins vibrated.

Both tests were terminated as a result of heater block failures, once due to an internal short circuit of the sheathed heaters and once as a result of breakage of interconnecting wires within the heater block. Except for the heater block failures, the generator successfully passed the tests and appeared to operate properly, the power output being similar to that observed during some of the initial tests of the generator.

Future testing of the QN-3 generator will include long-term life testing at maximum power input and output compatible with the operating conditions of the generator.

4. Tests of SNAP 19 Generators

Two SNAP 19 generators, similar to those to be flown on the *Nimbus* spacecraft, were delivered to JPL for testing. One has 3P-2N lead telluride thermoelements, while the other has 2P–2N elements, but with improved bonding of the elements to the "hot shoes." Both generators, similar in outward appearance, were designed to deliver 30-W nominal power output.

The general internal construction of the SNAP 19 generators is similar to that of the SNAP 11 generators, although in detail they differ greatly. The major difference is that no thermal shutter is provided, since the generators are designed to operate with a long-half-life isotope. Both generators supplied to JPL were to be operated with electrical heaters for the tests.

One SNAP 19 generator (3P–2N) was first parametrically tested in ambient conditions at several values of power input and output for 2672 h. This generator has now completed 552 h of testing in the thermal-vacuum test chamber. The other SNAP 19 generator (2P–2N) was parametrically tested and is now being used in long-term life tests in ambient conditions to evaluate the new bonding technique. Its total operating time at JPL is 603 h. The test performance of the SNAP 19 generators will be discussed in a future issue of the SPS, Vol. III, as well as in JPL technical reports.

C. Power Conditioner for a Thermionic Diode Array, *G. I. Cardwell*

1. Introduction

A reactor thermionic power system requires a power conditioner to operate in conjunction with an array of thermionic diodes. Such a power conditioner has been developed to operate in an experimental test setup. Called the "kinetic experiment," a computer simulation of a reactor controls the heat energy to the array of real thermionic diodes functioning in a closed-loop test of the reactor thermionic power system. The power conditioner must be capable of switching the low-voltage high-current power generated by the diodes and must boost the voltage to a useful level. Ideally, the power conditioner should appear to be a dc transformer with a constant voltage setup ratio and predictable losses. The power conditioner should generate minimum voltage and/or current perturbations.

2. General Requirements

The general requirements for the power conditioner were specified as follows:

(1) *Input.* The input voltage shall vary from 5 to 1 Vdc as the input current varies from 0 to 600 A. Voltage and current spikes or ripple produced on the input bus by the power conditioner shall be minimal.

(2) *Output.* The output voltage of the power conditioner shall be unregulated and shall vary from 100 to 500 Vdc with the variations of input voltage.

(3) *Efficiency.* Though not the prime factor with the power conditioner, the efficiency shall be as high as possible within practical limits.

(4) *Reliability.* The breadboard shall have an expected life of 1000 h.

(5) *Protection.* Should the load impedance be lowered to a point where the input current exceeds 600 A, the power conditioner will shut off and will produce a signal to operate a mechanical switch to load the source.

3. System Design

Several types of "flyback" systems, bridge inverter systems, and center-tapped inverter systems were considered. The high amplitude of current necessitated the paralleling of power switches with any type of system used. These switches would have to be operated in a multiphase manner to reduce ripple and spikes, the number of phases depending upon the number of switches used.

The very low input voltage eliminated the bridge inverter systems, and the high setup ratios combined with low breakdown voltage switches eliminated the "flyback" systems. Thus, the only suitable system was the center-tapped inverter system. It appeared that five center-tapped inverter systems switching in a five-phase sequence would handle the current. Each inverter should have a stepup ratio of 20:1. The rectified outputs of each inverter were placed in series to force current sharing and to present a total stepup ratio of 100:1. A clock-and-counter approach was chosen for the phase sequencing, because it appeared to be more accurate and more straightforward than the alternate method using a group of matched magnetic timers. Figure 4 shows the functional block diagram of the power conditioner.

4. Status of Development

At the present time, the total running logic, including the over-current and start/stop circuits, has been built and tested. One center-tapped inverter has been operated at 60% load, but specific performance data are not yet available.

D. Development of the Heat-Sterilizable Battery, *R. Lutwack*

1. JPL Contract 951296 With ESB, Inc.

This is a program for the development of AgO–Zn batteries that provide satisfactory performance after sterilization. Although the problems of (1) fabricating uniform cells, (2) decreasing capacity loss as a result of sterilization, (3) developing secondary cells, and (4) developing impact-resistant cells remain to be solved, considerable progress has been made.

Two batteries of six cells each (sealed after sterilization) were cycled at a depth of discharge of 60% nominal capacity. Failures occurred as early as 33 cycles, but the usual cycle life was 120 to 130; one cell reached 200 cycles. The failure mode was by Ag penetration through

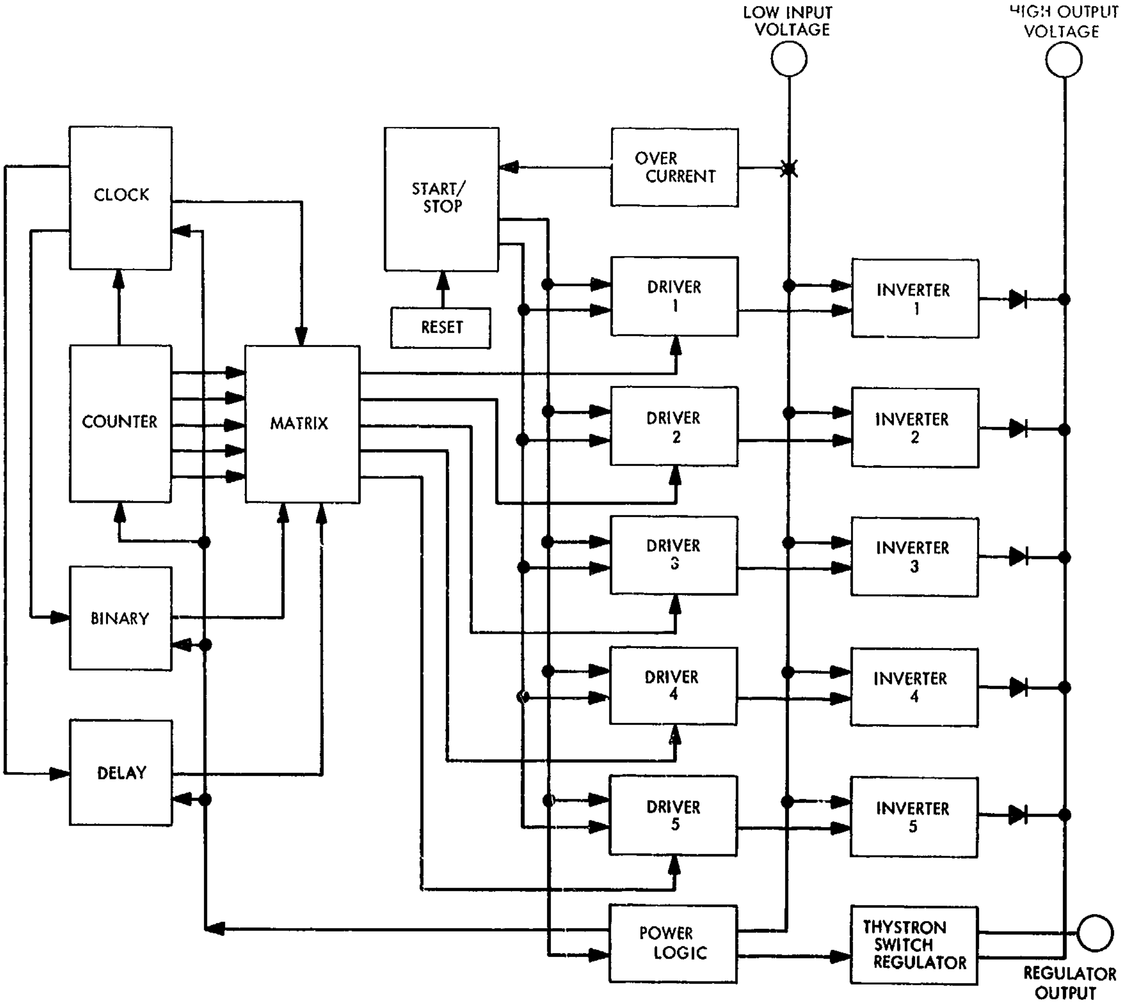

Fig. 4. Power conditioner block diagram

all of the separator layers, although there were indications of Zn shorting over the top of the separator to the lead wires of the Ag plates. It was concluded that additional layers of separator and a different Zn plate design are needed if the cycle life is to be extended. It was shown that the performance of a cell that is sterilized after being electrically cycled depends greatly on the state of charge. Prior to sterilization, the cell should be discharged so that no Zn metal remains and no HgO is formed. A procedure in which the discharges are made through successively larger resistances until an open-circuit voltage between 0.75 to 0.81 V is reached has been successful in reducing the capacity losses.

One of the causes of the non-uniformity of cells seems to be an attack on one of the plates by a component of the epoxy formulation used to seal the case. Modifications of the sealing technique are being explored in an effort to eliminate this problem. Electrochemical and design investigations continue in an effort to improve cell performance.

2. JPL Contract 951972 With Texas Instruments, Inc.

This is a research and development program for heat-sterilizable and impact-resistant Ni–Cd cells. From factorial design experiments in which the parameters were the separator, KOH concentration, percentage of pore fill, and heat sterilization, the following results were obtained from data for 35 cycles before sterilization and 30 cycles after sterilization:

(1) Capacities increased after sterilization an average of 33% for seven cells over 5 cycles.

(2) End-of-charge voltage increased after sterilization an average of 52 mV for seven cells over 5 cycles.

(3) Cell resistances were not significantly changed by sterilization.

(4) Capacity and the end-of-charge voltage after sterilization decreased with cycling.

(5) Pack tightness was shown to be an important design factor.

(6) Only one of the separator materials tested gave satisfactory performance.

This investigation of the effects of heat sterilization and the efforts to improve the cell design continue.

3. JPL Contract 952109 With the University of California at Berkeley

This is a research program to study the permeability characteristics of membranes as functions of different forces and includes a detailed theoretical application of the thermodynamics of the steady state to the transport across membranes and experimental determinations of the derived relationships. A practical method of transport-parameter evaluation from the basic flux equations of linear non-equilibrium thermodynamics has been outlined. A cell has been constructed for measuring osmosis, electro-osmosis, dialysis, transport number, membrane potential, streaming potential, and conductivity under uniform hydrodynamic conditions, using feedback mechanisms to keep solution concentrations constant despite the mass transfer that occurs. The cell is being tested to assure that it will conform to the design requirements.

E. Integrated Heat Pipe/Tubular Thermoelectric Module, *S. Bain*

1. Introduction

The use of an integrated heat pipe/tubular thermoelectric module as an energy conversion system for space application is currently under investigation at JPL. The heat pipe is used as a thermal coupling from the heat source to the hot junction surface of the thermoelectric module. Such a design makes the system flexible since the heat source can then be remote from the generator. The JPL test unit described herein employs an electrically heated source that simulates the isotope fuel that would normally be used in the final design. The satisfactory performance of the system thus far demonstrates that a heat pipe can be effectively used to thermally couple a heat source to a thermoelectric module. The information obtained in the tests described here will be useful in evaluating future devices employing heat pipe configurations.

2. Design

The integrated heat pipe/tubular thermoelectric module (Fig. 5), designed and fabricated by Westinghouse Astronuclear Laboratory (WANL), consists of a heat pipe and heater block, a tubular module, and a unidirectional radiator. The thermoelectric module and the aluminum unidirectional radiator are mounted on the condenser end of the heat pipe, while cartridge heaters fitted in nickel blocks are used on the evaporator end. All electrical instrumentation wires terminate in junction boxes on the test stand.

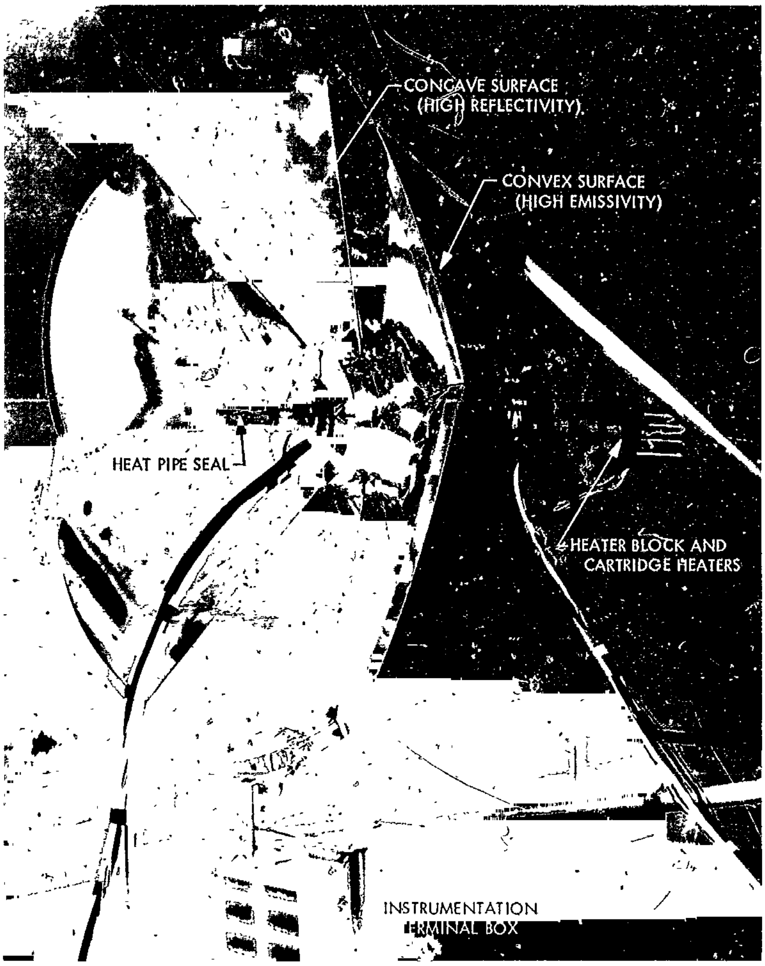

Fig. 5. Integrated heat pipe/tubular thermoelectric module

a. Tubular module. The heart of the generator is the tubular thermoelectric module developed for the Atomic Energy Commission by WANL. As shown in Fig. 6, the module has a 1.1-in. inner diameter, a 2.6-in. outer diameter, and a 7.2-in. active thermoelectric length.

b. Heat pipe and heater block. The total length of the 304 stainless-steel heat pipe is 18 in., with a 1-in. outer diameter. Approximately 37 cm^3 of sodium metal is used as the working fluid in the evaporator section. Heat is added to the sodium by conduction through the wall from nickel heater blocks. To assure good heat transfer between the evaporator and the nickel heater blocks, a layer of flame-sprayed copper is deposited on the evaporator end. Five layers of 60-mesh 304 stainless-steel screen are used as a wick and are held in place against the inner wall by a perforated stainless-steel sleeve.

The liquid sodium is transported in the vapor state throughout the condenser section and is returned to the evaporator by the stainless-steel wick. The heat is dissipated by the radiator attached to the outer wall of the thermoelectric module. Movement of the vapor arises from the natural pressure difference which results from the heat addition and removal. The cycle continues as the condensate is carried from the condenser end to the evaporator by the capillary action of the wick. Heat pipes are capable of a thermal conductance greater than that for any known homogeneous piece of metal. The heat pipe employed was capable of operating at a temperature of 1200°F with a heat transfer of 2800 W.

c. Unidirectional radiator. The radiator was fabricated from 6061 aluminum. Six finned sections are clamped on the outer periphery of the thermoelectric module. The hub of the assembled sections cover the condenser section

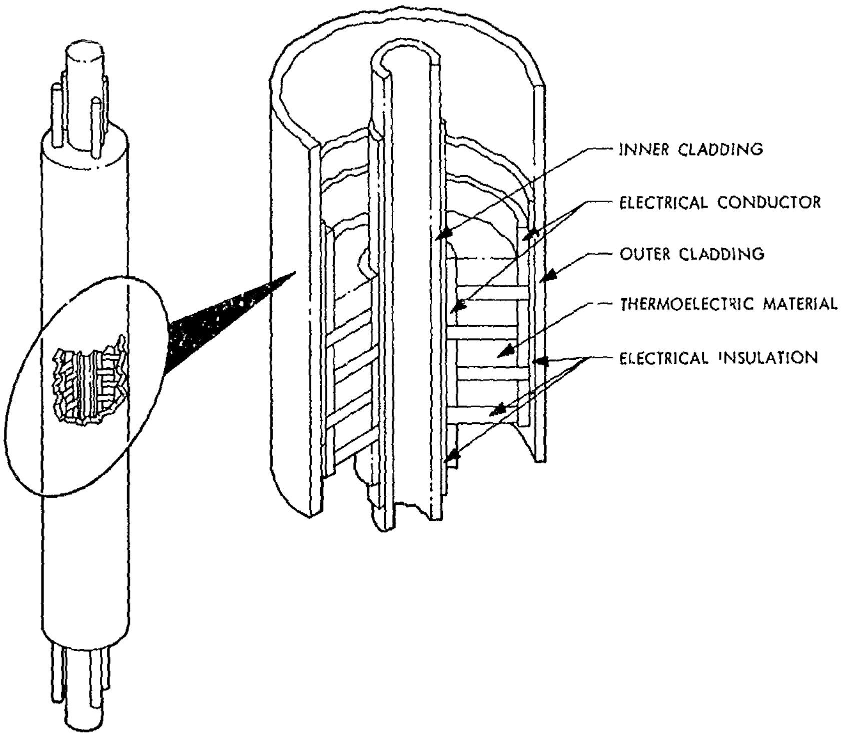

Fig. 6. Tubular module internal construction

of the system. To achieve a unidirectional radiator, the concave surface is highly polished for low emissivity, whereas the convex side is coated with a high-emissivity material. The nickel heater blocks clamped in place are shown in Fig. 5. The cartridge heaters are also exposed. In Fig. 5, the low-emissivity polished aluminum concave surface can be seen.

The radiator was designed to maintain the average outer clad temperature of the generator at approximately 200°C, with the average inner clad temperature of the generator at 535°C. The planar unidirectional radiator was not fully optimized for a particular space system, but serves merely to display a space concept in the employment of such a device.

3. Thermal Characteristics

To assure good heat transfer between the system interfaces, special consideration was given to specific areas, such as those between the heater blocks and the evaporator section of the heat pipe, the condenser section of the heat pipe and the module, and the module outer diameter and the radiator. The thermal impedance between the evaporator and the heater blocks was minimized by flame-spraying copper on the heat pipe and by machining the evaporator section to a precision fit with the heater block inner diameter. A boron nitride sleeve was inserted between the condenser section of the heat pipe and the module to accommodate the instrumentation needed to monitor the inner clad module temperatures. A high-temperature heat-transfer cement was placed between the interface of the radiator hub and the module outer surface to decrease the thermal impedance.

Verification tests were performed by WANL to determine the heat-transfer capabilities of the complete system and to assess the heat pipe performance under a module load. The temperature difference between the heat pipe and the module interface was less than 18°F. From the test data, the isothermal temperature distribution over the active length of the module was apparent.

4. WANL System Performance Testing

Prior to delivery of the completed system to JPL, the system was operated at WANL for 600 h at design conditions. Two thermal cycles were experienced, one after the first 433 h of operation at design temperatures, and the other after an additional 147 h. Figure 7 shows the data taken during the tests. The data taken before final shutdown prior to shipment are given in Table 2.

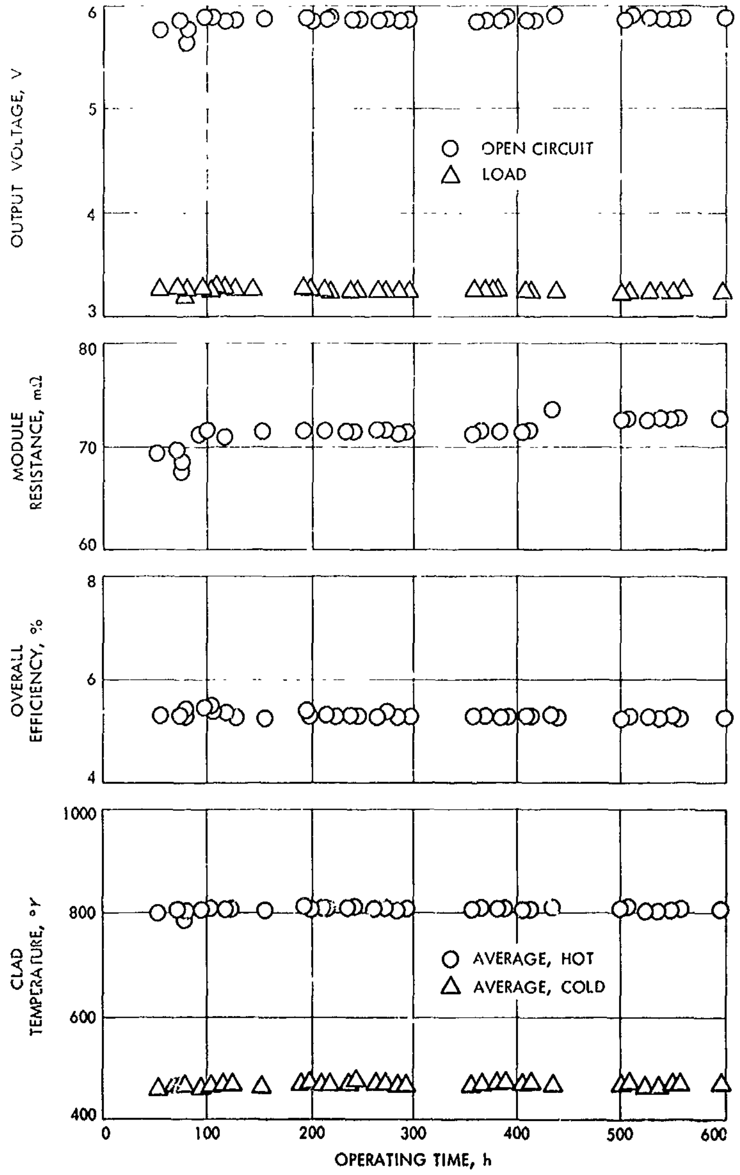

Fig. 7. WANL system performance data

Table 2. WANL and JPL initial system performance data

Characteristic	WANL initial data	JPL initial data
Average module inner clad temperature, °C	534	544
Average module outer clad temperature, °C	191	220
Open-circuit voltage, V	5.80	5.66
Load voltage, V	3.25	3.153
Load current, A	36.5	34.51
Power output, W	118.6	108.83
Power input, W	2140	2255
Overall efficiency, %	5.54	4.82

5. JPL System Performance Testing

a. Test instrumentation and techniques. In the continuation of the system performance testing at JPL, efforts were made to duplicate the test instrumentation and techniques used at WANL. The test apparatus was set up in the JPL environmental test facility. A matched-load condition was maintained at all times, except when open-circuit voltage data were taken. A maximum power input to the system was established at 2400 W, with the designed maximum inner clad temperature of 565°C (1050°F). Operation with 1050°F on the inner clad necessitated a limitation of 1100°F on the condenser section of the heat pipe. After the 1100°F temperature was reached, power input was kept constant until temperatures stabilized along the heat pipe.

An adjustable load consisting of a group of fixed resistors was fabricated at WANL and used during the initial tests. A 0.162-Ω fixed resistor with taps at 0.027-Ω intervals and a 0.5- to 1.0-Ω trim was paralleled to the fixed section. This made the load adjustable from approximately 0.026 to 0.150 Ω. The total load consisted of the lead length from the output of the generator terminals to the fixed load. The measured resistance of 0.070 Ω was within 0.005 Ω of a matched-load condition when the module was operating at an average hot junction temperature of 535°C and an average cold junction temperature of 195°C.

The cartridge heaters were wired in a series–parallel configuration and operated from a 0- to 230-V supply dc source. An ac source was used at WANL. The primary circuit was controlled by an adjustable variable transformer (Variac). The electrical power input and increments as functions of time to attain the correct operating level are shown in Fig. 8.

Chromel-alumel thermocouples were used throughout the unit. Thermocouples of the sheathed type were attached along the module's inner and outer clad surfaces. All thermocouple readouts were per the National Bureau of Standards' millivolt temperature curves utilizing the correct cold junction compensation. An automatic data scanning system was used during the data acquisition. The outer clad of the tubular module was monitored with ten thermocouples; the inner clad, with four thermocouples; the radiator, with seven thermocouples; and the copper on the heat pipe, with three thermocouples. As many as possible of the original thermocouples were used to achieve a good comparison with WANL data.

Power input and output were measured with the data acquisition system. Precision shunts were used throughout to obtain direct readouts in millivolts. The open-circuit voltage was measured by reading across the voltage probes of the module when the load circuit was momentarily opened. An extremely fast readout instrument, a Hewlett-Packard Model 2401C integrating digital voltmeter, was used to obtain accurate measurements of the open-circuit voltage. The sampling period was kept small (approximately 0.1 s).

b. Test results. Operation was continuous for approximately 1367 h at a fixed power input of 2250 W. Plotted in Fig. 9 as functions of time are the efficiency, open- and closed-circuit voltages, power output, and module resistance. After the uninterrupted steady-state operation, a planned shutdown took place for a modification to the instrumentation. This shutdown constituted the third thermal cycle.

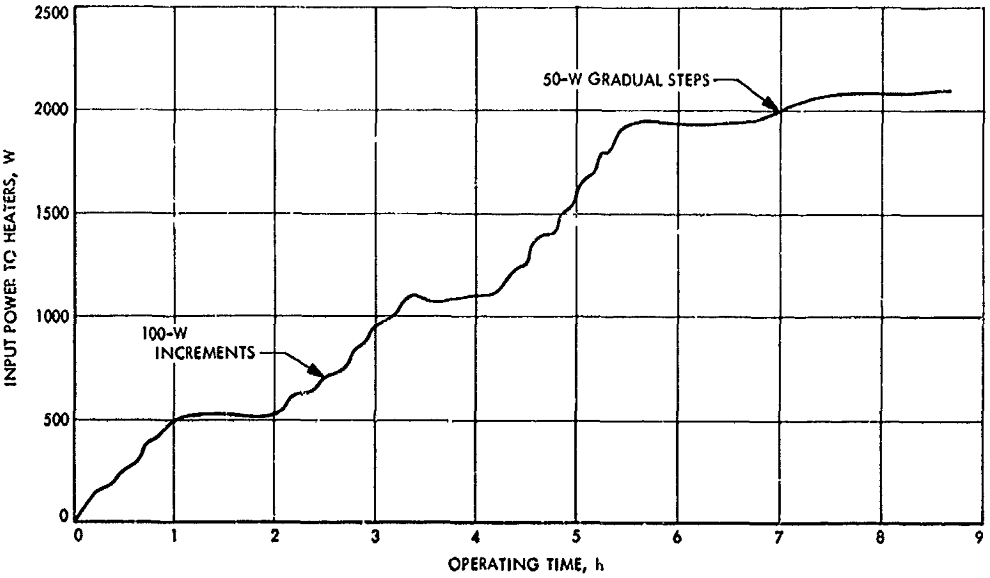

Fig. 8. Input power to heaters as a function of operating time: initial JPL data

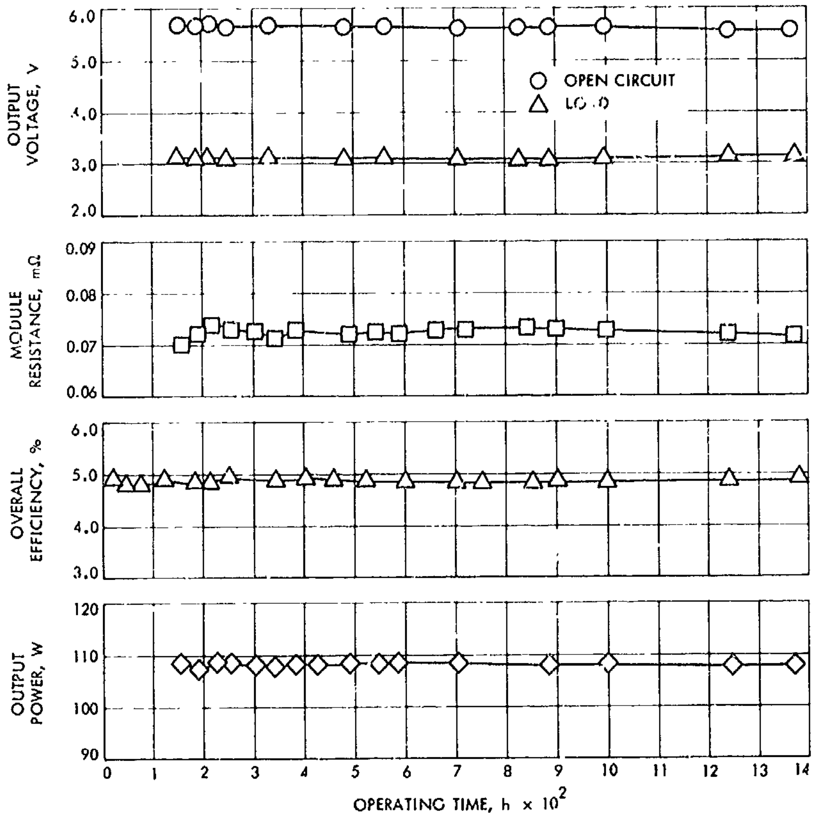

Fig. 9. JPL system performance data

System shutdown was initiated by cutting the electrical power to the heaters, thus permitting the system to cool down to ambient conditions. The data taken prior to shutdown are given in Table 2. These data represent the average data shown in the plotted points and are characteristic of the data produced on the first startup at JPL. The differences between the WANL anl JPL data were not explainable at the time of the JPL readings. The integrity of all instrumentation was verified. Resistance shunts between the module and the readout mechanism were eliminated as possible causes.

The second startup was interrupted with a power outage; at the time, the generator was producing 86.9 W for 2050-W input. A similar situation occurred during the third startup with a further reduction in performance; a power output of 82.0 W was noted for a power input of 2223 W. These shutdowns were the fourth and fifth thermal cycles on the generator. The power and instrumentation difficulties were solved and the testing was resumed.

A noticeable decrease in output was apparent on each restart. A decrease in module resistance was also detected. The temperature profile of the system remained essentially unchanged. The data were discussed in detail with WANL personnel in an attempt to determine the cause of the decrease in the observed performance.

The final shutdown of the generator took place with WANL personnel present. Prior to shutdown, the generator accumulated an additional 310 h under the following conditions:

Open-circuit voltage, V	4.04
Load voltage, V	2.39
Load current, A	26.7
Maximum power output, W	63.2
Power input, W	2360
Resistance, Ω	0.062

Diagnostic analysis is presently being conducted at WANL to determine the exact mechanism of failure.

VI. Guidance and Control Analysis and Integration

GUIDANCE AND CONTROL DIVISION

A. Support Equipment for a Strapdown Navigator, *R. E. Williamson*

The objectives of this effort are to provide a test van, data acquisition equipment, prime power, and system engineering for a strapdown electrostatic aerospace navigator (SEAN).

a. Van system. The test van has been procured and road tested with a mockup system installation that was comprised of consoles and lumped masses equivalent to a normal installation. These vibration and shock tests provided the information required for optimum location of the inertial measurement unit (IMU) in the van layout.

The vibration isolators for each of the cabinets have been procured and the design of the mounting cradles and baseplates established. The location of the SEAN system and its instrumentation is shown in Fig. 1.

b. Power subsystem. The uninterruptible power conversion unit has been procured and has been operated with dummy loads while being powered from the various optional power sources. Sources used included the 400- and 60-Hz laboratory powers, the 120-Vdc battery power, and the 400-Hz mobile engine-generator set power.

Design and fabrication of the power cabinet containing the power conversion unit and the three groups of nickel–cadmium batteries have been completed.

c. Data acquisition. The data acquisition system will provide the capabilities required to evaluate and troubleshoot the SEAN system. To meet these requirements, three means of data acquisition are to be used.

Digital recording system. A magnetic tape digital recording system will be provided to record computed system outputs (position, velocity, navigation time), total IMU data (gyro and velocity meter counts), and other required parameters. The system outputs recorded during flight tests will be used in conjunction with a recording of the range radar tracking of the aircraft to obtain system error plots. The total IMU data may be used for postflight analysis, such as separation of error sources, development of additional computer programs, improvement of gyro drift compensation schemes, and evaluation of the IMU and computer performance.

A complete recording system is being procured. The system manufacturer was provided with two flight-qualified digital magnetic tape recorders that were procured (Fig. 2). The design and fabrication of the recording system control unit, and the integration of the control

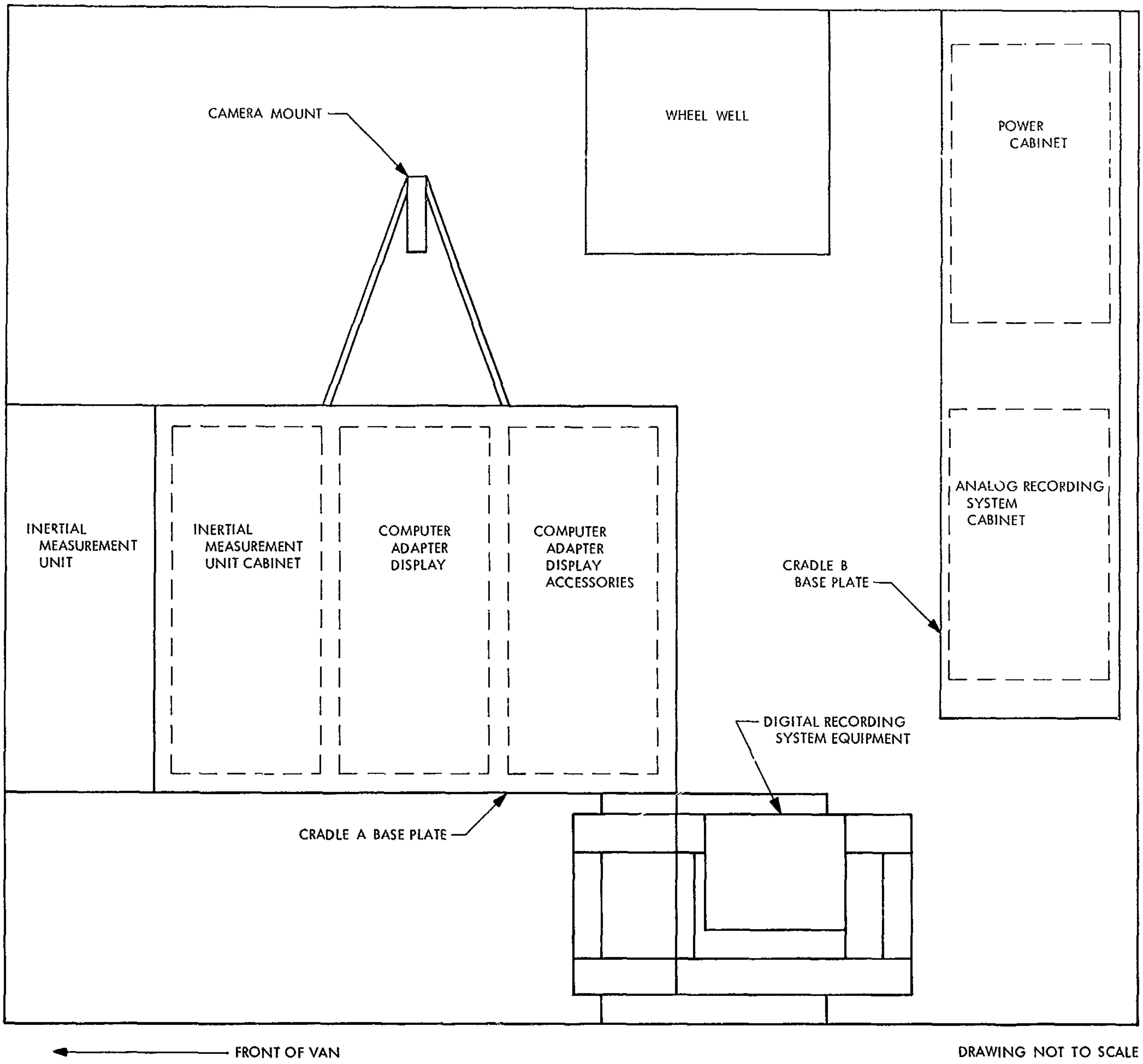

Fig. 1. SEAN van installation arrangement

Fig. 2. Digital magnetic tape recorder

unit with the Alert computer and the tape transports will be performed by the system manufacturer. Delivery of the complete system is expected in early December 1968.

Oscillographic recording system. An oscillographic recording system will be provided to monitor analog functions, such as gyro suspension G loading, IMU temperatures, gyro status, and power supply voltages. A Brush, Model Mark 848, 8-channel, thermal-writing recorder has been purchased as a versatile instrument to be used in monitoring the various IMU analog signals during laboratory tests, and for monitoring the gyro suspension circuits during flight tests. A second recorder, a Mid-Western, Model 603, 36-channel, optical-writing recorder, has been obtained from the JPL loan pool to monitor the additional IMU analog functions and the battery and power supply voltages.

Photo recorder. An instrumentation camera will be used to photographically record the computer-adapter display (CAD) output information (latitude, longitude, speed, azimuth, time). The camera is a 35-mm remotely controlled photorecorder designed for use in aircraft. It will be controlled by the SEAN Alert computer to photograph the display panel every 2 to 10 s to provide a continuous record of the flight test for at least 4 h. A lens has been procured, and the camera has been checked out optically and electrically.

d. Altimeter. A CPU-46/A altitude computer, Bendix Type 31101, has been procured to provide digitized altitude information. Integration of the altimeter with the SEAN computer-adapter display is planned for the first part of December 1968.

e. System integration support. System cables required for integration of the SEAN equipment into the van and flight test configuration are being procured. Approximately two-thirds of the required cables have been received with the balance due by the end of November. The SEAN system block and cabling diagrams have been updated and released. Detail schematics and signal descriptions have been prepared for those interfaces where equipments have not yet been integrated. Special interface tests are being run where necessary to define the interface characteristics.

VII. Spacecraft Control

GUIDANCE AND CONTROL DIVISION

A. Actuator Development for a Clustered Ion Engine Array, *J. D. Ferrera and G. S. Perkins*

1. Introduction

At the present time, there is a great deal of interest in solar-powered electric-propulsion systems suitable for interplanetary spacecraft applications. One such electric-propulsion application is a Jupiter flyby mission in 1975.[1] Another mission under study is an asteroid shot in 1974 using mercury electron-bombardment ion thrusters as an engineering experiment.

To prepare for these candidate flights, a breadboard system was designed and built in calendar year 1968 that incorporates the minimal features considered necessary for a deep space probe. All major components necessary for any solar-electric system are present. The portion of the system that will be enclosed in a vacuum chamber for system testing is shown in Fig. 1. The vacuum chamber end dome is 36 in. in diameter; the ion engines are 10 in. in diameter, 14 in. in length, and weigh 10 lb each. Each engine is gimballed to provide roll attitude control. The engine array is translated in the X and Y directions (in the test described, only one axis of translation is considered) to align the resultant thrust vector with the center of gravity of the spacecraft for pitch and yaw control.

2. Translation Actuator

The characteristics of the translation actuator (Fig. 2) are listed in Table 1. Two features are particularly noteworthy. One is the application of a harmonic drive gear train to obtain a very low value of backlash (<5 arc sec) and high output torsional stiffness. The other is the space compatibility of the flat-strap type of drive. Fatigue cracks that might develop in the strap are self-healing in space vacuum.

In this test the balls used in the roller bearings that support the moving platform on two 1-in.-diam rails are made of stainless steel. In a space vacuum application these balls could be made of a ceramic to eliminate the possibility of cold-welding. A rotary infinite-resolution potentiometer is used for position feedback. Where possible, similar metals are used to minimize thermal expansion problems. Thermistors are mounted inside the actuator to provide temperature information since the ion engines themselves are expected to reach temperatures as high as 500°F. Individual electrical lines are shielded to prevent electrical interference.

---

[1] Barber, T. A., et al., *1975 Jupiter Flyby Mission Using a Solar Electric Propulsion Spacecraft,* Mar. 1, 1968 (JPL internal document).

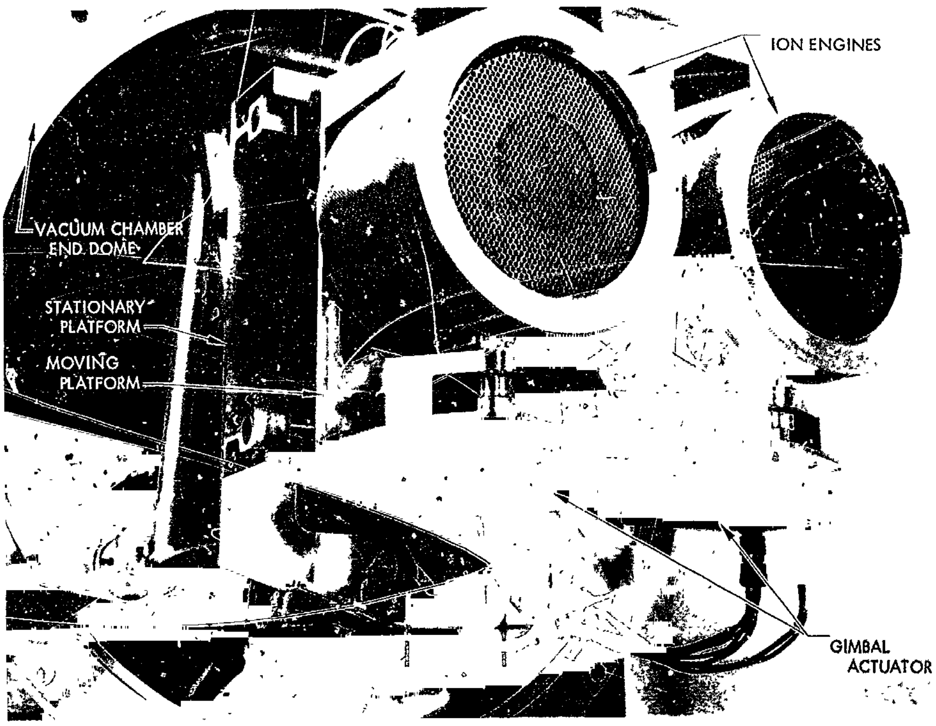

Fig. 1. Ion engine system

3. Gimbal Actuator

The characteristics of the gimbal actuator (Fig. 3) are also listed in Table 1. A unique feature of this actuator is the drive arrangement utilized to minimize backlash in order to obtain 20 arc sec per stepper motor step of output rotation. The linear motion of the saddle nut is transformed to rotary motion of the sector through two beryllium copper straps. The saddle nut is also pinched slightly prior to the machining of screw threads such that, in its assembled state, the screw threads are forced into contact with the lead screw threads. A solid rod connects the saddle nut to the pickoff arm. The pickoff for position feedback is a linear-variable differential transformer (LVDT). Thus, there is zero backlash between the actuator output shaft and the position pickoff.

The lead screw itself is a hollow aluminum shaft, hard-anodized after machining. Aluminum is used for the lead screw to maintain similar metals throughout to minimize thermal expansion problems.

The drive motors in both actuators are size 11, 90-deg permanent-magnet stepper motors. The actuator case is painted black and the intermediate shaft connecting the actuator to the ion engine is made of stainless steel to minimize heat transfer into the actuator.

Table 1. Actuator characteristics

Parameter	Translation actuator	Gimbal actuator
Output travel, in.	±3	–
Output travel, deg	–	±10
Nominal stepping rate, steps/s	100	50
Actuator slewing rate, in./s	0.25	–
Actuator slewing rate, mrad/s	–	5
Temperature range, °F	−50 to +275	−50 to +275
Test duration, h	1000	1000
Resolution, in./step	0.0025	–
Resolution, arc sec/step	–	20
Backlash, arc sec	< 5	0
Gear train ratio	2830:1	15708:1
Power required, W	7	7
Output torque at nominal rate, in.-lb	50	55
Weight, lb	7.25	4.3
Leak rate (90% nitrogen–10% helium), cm^3/h	< 0.005	< 0.005
Pickoff scale factor, V/deg	0.14	–
Pickoff scale factor, V/in.	–	12.55
Pickoff linearity, %	0.5	0.14 (full scale)
Excitation, Vdc	±24	24

4. Development Status and Projected Plans

The actuators for the breadboard system have been functionally tested and then assembled into the system

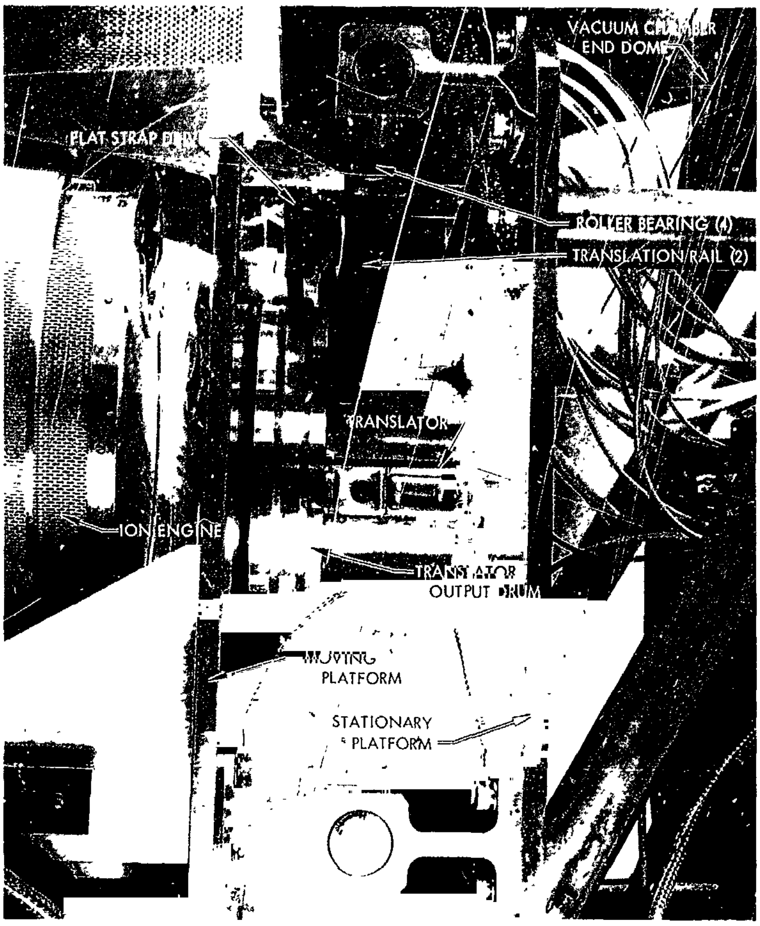

Fig. 2. Translator actuator

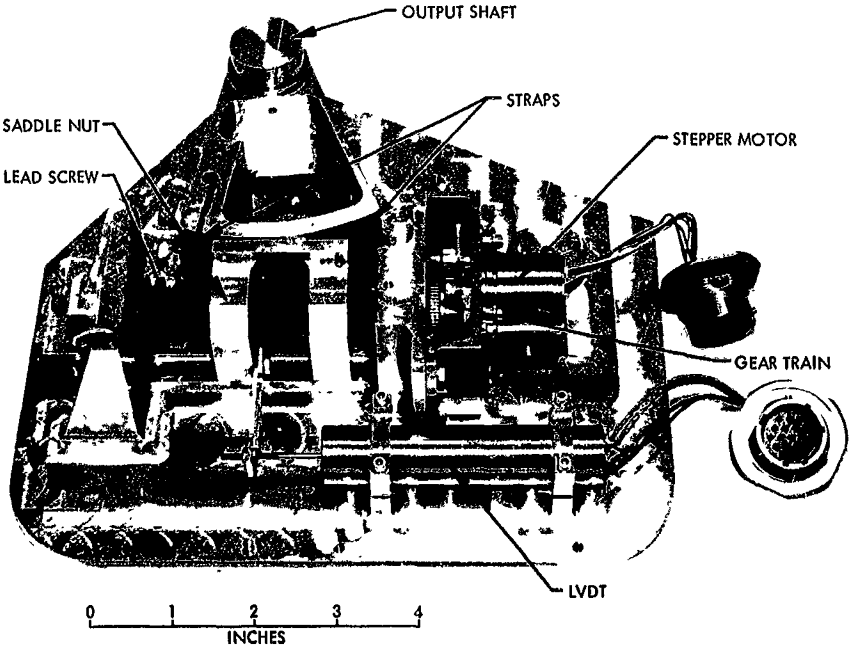

Fig. 3. Gimbal actuator

for a 1000-h test run in February 1969. No consideration was given in this breadboard system to weight reduction (flight requirement of less than 3 lb/actuator) or flight environmental requirements. These will be considered in the flight prototype system now being designed.

The prototype system, which will be ready for system test by the end of calendar year 1969, will be designed to provide two perpendicular directions of translation over a span in each direction of ±13 in. A closed-loop control system will also be provided for the new engine array.

B. Sterilizable Inertial Sensors: Gas Bearing Gyros, *P. J. Hand*

The objective of this task is to perfect a complete family of miniature inertial sensors that will be capable of withstanding both thermal and gas sterilization without either catastrophic failure or significant degradation of performance. Included in this family of inertial sensors are long-life gas bearing gyros of the single-axis, rate-integrating-type, subminiature ball bearing gyros, and high-performance linear accelerometers. All of these inertial sensors have potential applications in advanced planetary spacecraft, entry capsule attitude-control systems, and landed planetary missions.

The gas bearing gyroscopes selected for this development effort are the Honeywell, Inc., high-gain type GG159 and its low-gain, wide-angle counterpart, type GG334S. These gas bearing gyros do not have any bearing wearout conditions during operation and can, therefore, be considered for applications on any very long term planetary mission. The fabrication status and developmental history of both gyro types were covered in SPS 37-51, Vol. III, pp. 53–55.

The GG159E version is the culmination of a development program begun in 1962. This gyro has essentially met all of the design goals for performance through sterilization that were set forth at the beginning of the development effort. The program objective was to fabricate a gyro that would incorporate the major design goals of sterilization capability, high-g shock and vibration capability, low-power spin motor, and high-frequency fluid pump for the gimbal suspension system. Table 2 shows design characteristics of this unit.

Table 2. Design characteristics of the GG159E gyroscope

Parameter	Value
Complete gyro unit[a]	
Diameter (excluding flange), in.	2.105
Length, in.	3.096
Weight, lb	0.997
Angular momentum, g-cm^2/s	100,000
Input/output gain (at operating temperature)	155
Operating temperature, °F	
Nominal	115
Maximum limits	50 to 130
Output axis freedom, deg	+0.55, −0.56
Operating life (minimum)	
Hours	18,000
Start–stop cycles	10,000
Power of gimbal suspension pump (490 Hz, 100 V rms), W	0.6
Spin motor[b]	
Speed, rev/min	24,000
Power (26 V rms, 800 Hz, 2 phase), W	
Start	6.8
Run	3.5
Torque margin (to synchronize), V rms	21
Run-up time, s	15.7
Run-down time, s	56.7
Pickoff[c]	
Frequency, Hz	7200
Voltage, V rms	10.5
Sensitivity, mV/mrad	24.1
Null voltage, mV	1.2
Linearity, %	1.0
Torquer[d]	
Scale factor, deg/h/mA	356.1
Linearity, %	< 0.025
Stability, %	< 0.018
Maximum slew rate, deg/h	> 11,000
Temperature sensitivity (100 to 130°F), %	0.57
Heaters	
Warmup, Ω	265
Control, Ω	140
Sensor (at 115°F), Ω	780

[a] Single-axis, floated, rate-integrating, pumped-fluid gimbal suspension type.
[b] Hydrodynamic gas bearing type.
[c] Moving coil, air-core differential transformer type.
[d] Permanent magnet, moving coil type.

The GG159E1 gyro (SN1) was fabricated and delivered to JPL in September 1968. Table 3 shows a comparison between the design goals and the actual performance of this instrument when subjected to thermal sterilization. The spin motor required 3.5 W of running power, which is well below the 4.0-W goal. In addition, the ability to build a gyro motor using approximately 2.5 W was demonstrated during the fabrication of one of the GG334S wide-angle gyros. Thus, further power reductions are a possibility if required. The decision to remain with a 3.5-W motor was based on obtaining the maximum motor torque margin consistent with the power design goal.

Table 3. Comparison of design and actual performance data of the GG159E gyroscope

Parameter	Design	Actual
FT, deg/h	±0.30	−0.158
MU_{SA}, deg/h/g	±0.50	1.54
MU_{IA}, deg/h/g	±0.46	0.414
Drift stability (rms)		
Run up to run up, deg/h	0.01	0.055
Cooldown to cooldown		
FT and *RT*, deg/h	0.03	0.09
MU_{SA} and MU_{IA}, deg/h/g	0.05	0.064
Random drift (1 σ), deg/h		
Output axis vertical	0.008	0.005
Input axis vertical	0.015	0.005
Elastic restraint, deg/h/mrad	±0.05	−0.042
Anisoelastic coefficient, deg/h/g^2	±0.05	0.02
Change of drift rates with sterilization (each cycle)		
Change in TSF, deg/h/mA	±4.0	0.065 (total)
Change in MU_{SA}, deg/h/g	±0.14	0.198 (max)
Change in MU_{IA}, deg/h/g	±0.14	0.202 (max)
Change in *RT* (total), deg/h	±0.07	0.095 (max)[a]
Change in elastic restraints, deg/h/mrad	±0.015	0.006 (max spread)

[a] Excludes first shift as not being typical.

One notable departure from the design goal was the optimum frequency of 490 Hz obtained for the piezoelectric, hydrostatic, gimbal suspension pump. (The design goal was 400 Hz.) The concept of the high-frequency pump was demonstrated in a previous JPL contract. The object of the current effort was to develop the necessary hardware to implement the new pump design into the GG159E gyro.

No less than seven variables are involved in the resonance of this piezoelectric pump. Among these are spacing, compliance, and mass of the piezo plates, as well as density and viscosity of the flotation fluid. The actual resonant frequency was of secondary importance to the application of this pump into the gyro; therefore, less effort was applied to obtain an exact 400-Hz resonant operation. (This is one area that can be improved in future development.) The pump assembly in the final device showed stable operation throughout the entire test program, including the sterilization cycling. Final test results on the pump were: power 0.6 W, frequency for best operation 490 Hz, and total operating time 585 h.

Prior to sterilization exposure, the gyro was subjected to an environmental test series consisting of: (1) shock, 200 *g* peak, 1.5-ms duration, 5 times in each axis; (2) vibration, 14-*g* rms random noise plus swept sinewave, 10 min in each axis; and (3) static acceleration, 14 *g*, 5 min in each axis. The shifts encountered in the critical parameters of reaction torques (*RT*), fixed torques (*FT*), mass unbalance on the input axis (MU_{IA}), and mass unbalance on the spin reference axis (MU_{SA}) are shown below.

Environment	Δ*RT*, deg/h	Δ*FT*, deg/h	ΔMU_{IA}, deg/h/g	ΔMU_{SA}, deg/h/g
Shock	−0.10	+0.10	+0.63	−0.24
Vibration	−0.02	−0.01	+0.02	+0.16
Acceleration	−0.05	−0.01	+0.06	+0.07

These results verify that, besides survival of the spin motor, the gyro performance was not significantly disturbed by such environments.

After completion of the above tests, the instrument was started into the thermal sterilization cycles. Each of the 6 cycles was 64 h in duration and a temperature of 135°C was sustained at the gyro. Performance data were taken before and after each thermal cycle. These data are presented in graphic form in Fig. 4, which displays, in a chronological sequence, the values of *FT*, MU_{SA}, and MU_{IA} as measured after the final assembly of the gyro and includes the sterilization cycling. The points designated as cooldown 1 through 5 represent a daily cooldown to room ambient (70°F) from the operating temperature of 115°F, and demonstrate the basic daily stability prior to sterilization. These data clearly show

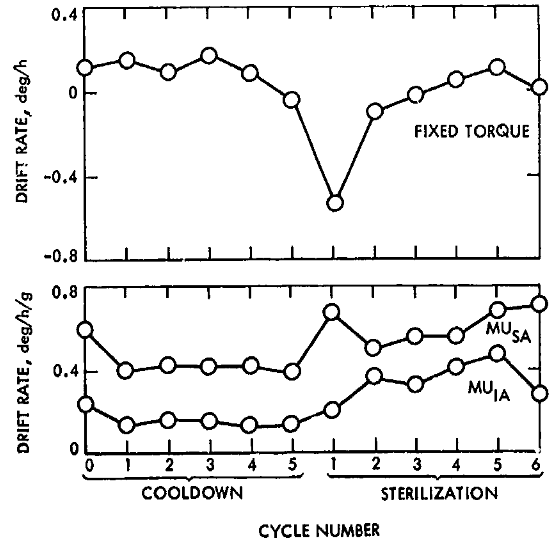

Fig. 4. Gyro drift through sterilization

that, except for the typical first cycle shift, the gyro performance is not significantly degraded by sterilization cycling.

In addition, other parameters, such as elastic restraints and motor performance, are shown in Table 4.

Except for the initial shift of fixed torque as a result of the first cycle (which has happened on other GG159 gyros in the past), no significant performance change will be noted in all of these test results. One item not listed in the table that is of particular interest is the torquer scale factor (TSF), which measured a change of less than 0.02% over the 6 cycles.

Two difficulties were encountered with the instrument after sterilization: an open spin motor rotation detector (SMRD) coil and decreased sensitivity in the eutectic balance capsule. Neither problem was directly related to the performance of the instrument as an inertial sensor. The SMRD winding is used during laboratory testing to observe spin-motor synchronism; it is not used in a flight application. The open SMRD coil was found to be inside the sealed gyro housing. Further investigation would entail a major disassembly of the gyro, and, since the SMRD coil was not related to the performance, the failure was not pursued further.

The balance capsule is used to make final vernier adjustments to the mass unbalance (MU) parameters without going into the gyro case. The capsule has already fulfilled its most important function at the time of initial MU trim; therefore, its decreased sensitivity did not warrant corrective action for this particular unit.

Additional effort to improve the sterilization capability of both the SMRD coil and the balance capsule would be in order for future production of this gyro.

The following conclusions can be drawn from the results of this development task:

(1) The GG159E gyro has successfully demonstrated compliance with the initial design goals of sterilization capability, high-g vibration and shock resistance, a low-power spin motor, and a high-frequency suspension pump.

(2) The GG159E is now a precision inertial sensor capable of application on any space mission requiring either sterilization capability, long life, or both.

(3) Corrective design actions needed to improve future units are very limited in scope and have no significant impact on the performance of the gyro. They are: improvement of the SMRD coil, improvement of the balance capsule, and adjustment of the suspension pump to operate on 400 Hz.

C. Ion Engine Thrust-Phase Attitude Control With Flexible Solar Arrays, *G. E. Fleischer*

1. Introduction

Increasing attention and detailed study have been given recently to the application of solar-array-powered electric-propulsion systems to specific missions to the Jovian planets.[2] Efforts to demonstrate the capability and practicality of an ion-engine-powered spacecraft has been mainly directed toward developing accurate dynamic

Table 4. Performance through sterilization

Parameter	Reference	Post 1	Post 2	Post 3	Post 4	Post 5	Post 6
Random drift (1σ) deg /h							
Output axis vertical	0.005	0.003	0.007	0.001	0.003	0.005	0.003
Input axis vertical	0.008	0.002	0.005	0.002	0.004	0.004	0.003
FT, deg/h	−0.022	−0.552	−0.092	−0.007	0.064	0.125	0.030
MU_{IA}, deg/h/g	0.130	0.208	0.370	0.333	0.423	0.485	0.287
MU_{SA}, deg/h/g	0.484	0.686	0.504	0.563	0.570	0.687	0.709
Elastic restraint, deg/h/mrad	−0.042	−0.046	−0.046	−0.048	−0.046	−0.047	−0.043
Run-up time, s	15.7	15.0	15.1	15.1	15.0	15.3	15.2
Run-down time, s	56.7	53.6	53.4	51.4	52.4	51.8	50.2
Power, W							
Start	6.82	6.50	6.80	6.60	6.70	6.40	6.40
Run	3.50	3.20	3.35	3.40	3.42	3.35	3.40

models of such a system and applying them to the spacecraft attitude-control design problem. This article describes some of the results obtained in assessing the dynamic interaction of large flexible solar panels with an attitude-control system based on ion engine thrust vector control.

2. System Dynamics Model

Attitude control of an electrically propelled craft, primarily due to the presence of very large and flexible solar cell arrays and the continuous force of the thrusters and solar winds, does not allow the use of the usual nitrogen gas or comparable mass-expulsion techniques since they result in unacceptably large system weights over the mission flight times involved. Thrust vector control must then be used for attitude control during powered phases. It becomes necessary, therefore, to provide for translation of the entire ion engine bank in two directions and to gimbal pairs of engines in order to achieve complete three-axis control. Several engine configurations are possible. For example, Fig. 5 shows a five-engine array designed for a Jupiter flyby mission (see *Footnote 2*).

In general, the control block diagram appears as shown in Fig. 6. Attitude error signals are supplied by the usual collection of celestial (sun and Canopus) sensors and transformed to engine coordinates. Control torques are applied to the craft as a consequence of the commanded engine translations and rotations. Stabilization and damping are achieved by feedback compensation about the engine control loop.

A major question has been the definition of an accurate mathematical model for the SPACECRAFT DYNAMICS block. Theoretically, this block must include the effects of what could be very flexible solar panels, or antennas, as well as the motion of relatively rigid but significantly

---

[2] Barber, T. A., et al., *1975 Jupiter Flyby Mission Using a Solar Electric Propulsion Spacecraft*, Mar. 1, 1968 (JPL internal document); also see Refs. 1 and 2.

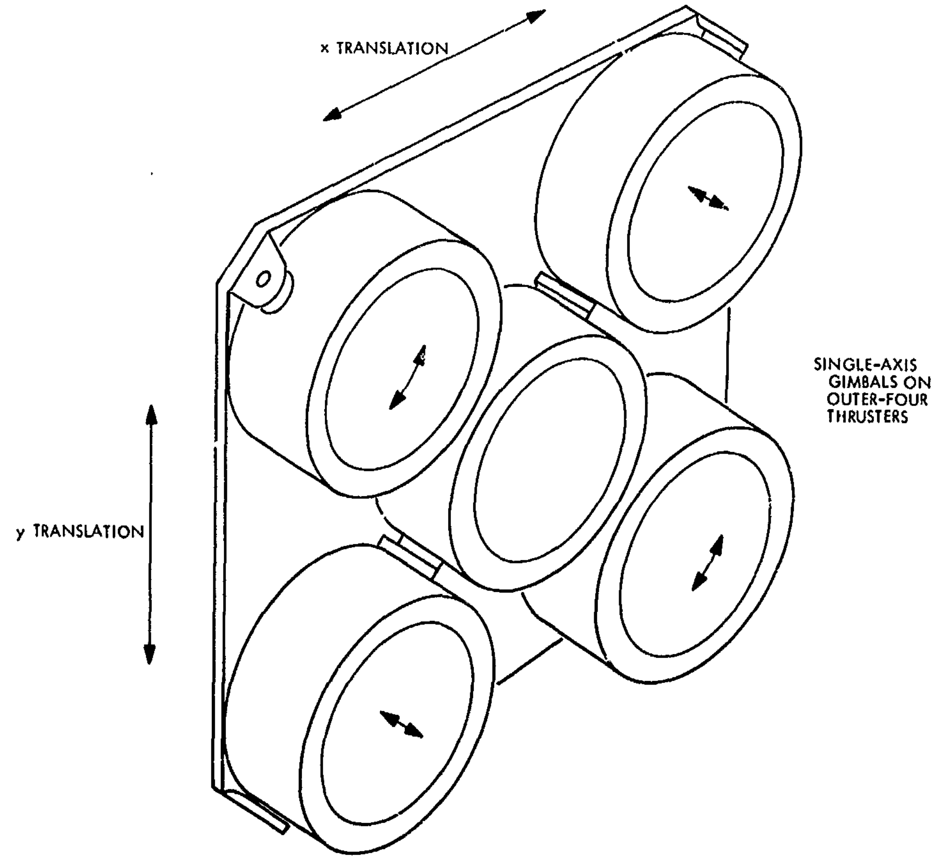

Fig. 5. Powered flight control using two-axis translation and third-axis gimballing

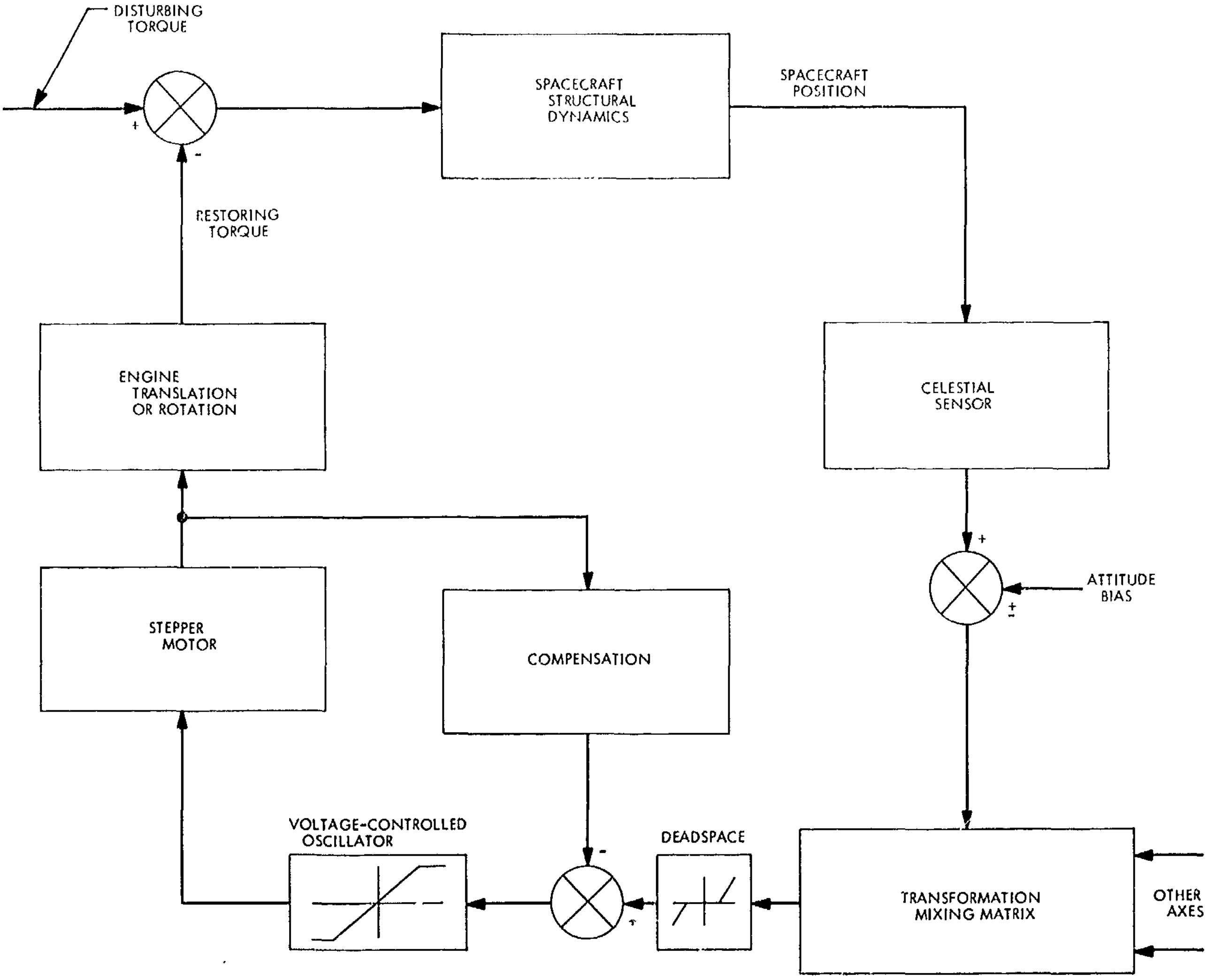

Fig. 6. Basic translation or gimbal control loop

large masses, such as an ion engine assembly or, perhaps, momentum wheels. Each of these interacts with the motions of the spacecraft's rigid central structure, or bus, which normally is the intended beneficiary of rotational control and therefore usually carries both the celestial and inertial sensors.

A great deal of experience and capability has been developed in the analysis of flexible structures using modal deformation coordinates, and they have long been efficiently applied to aircraft, missiles, and spacecraft as well. From the control standpoint, however, a *strictly* modal coordinate approach is not capable of accommodating rotors, nonlinear internal controls, discrete dampers, etc. At the same time, the opposite approach of modeling the system as a large collection of rigid bodies appears to be extremely cumbersome. Computer solutions to the resulting equations may be forced to include irrelevant high-frequency components, drastically increasing run times and therefore cost. Typically, the solution of large matrix equations are also required at each numerical integration step, aggravating even further the computational problem.

Recently, Likins[3] has developed in detail a "hybrid coordinate" approach to the vehicle control problem when flexible appendages are involved. It is based on the assumption that flexible portions of the craft may be accurately characterized by small, linearly elastic deformations and are therefore subject to modal analysis. Furthermore, if the flexible appendages are attached to a

---

[3] Likins, P. W., *Dynamics and Control of Flexible Space Vehicles*, Technical Report 32-1329. Jet Propulsion Laboratory, Pasadena, Calif. (in press); also see Refs. 3 and 4.

rigid base undergoing small motions or which has nearly constant angular velocity, normal modes of vibration can be shown to exist. Discrete coordinates are retained for describing the rigid base motion or the motion of other essentially rigid components, such as gimballed (or translated) engines, rotors, discrete dampers, and the like.

For example, if the spacecraft's rigid bus is assumed to experience a sufficiently small inertial angular velocity, so that second-degree terms and higher derivatives in this variable are negligible, the completely linearized matrix equation describing the flexible appendage becomes

$$M[E - \Sigma_E \Sigma_E^T M/\mathcal{M}]\,\ddot{q} + Kq = -M\Sigma_E\,[\ddot{X} + \ddot{e} - 2\tilde{\dot{e}}\dot{\theta} - (\tilde{e} + \tilde{R})\,\ddot{\theta}] + M\tilde{r}\,\Sigma_L\ddot{\theta} + \lambda \tag{1}$$

where

M = mass matrix of the flexible appendage ($3n \times 3n$) (n is the number of point masses used to model the appendage)

$\mathcal{M}$ = total vehicle mass (scalar)

q = column matrix of appendage deformation coordinates ($3n \times 1$)

K = appendage stiffness matrix ($3n \times 3n$)

X = inertial position of the system center of mass (3×1)

e = position of system mass center with respect to a point fixed in rigid base (bus), not including flexible appendage contributions (3×1)

R = location of appendage attachment point in rigid base (3×1)

$\tilde{r},\tilde{R}$ = skew symmetric matrices locating masses in the flexible appendage ($3n \times 3n$, 3×3)

θ = inertial attitude of rigid base body (3×1)

E = identity matrix, any order

Σ_E = matrix $[E\,E\,E \cdots E]^T$, ($3n \times 3$)

λ = matrix of external forces applied to appendage ($3n \times 1$)

If in Eq. (1) the transformation $q = \Phi\eta$ is substituted followed by a premultiplication of the equation by Φ^T, where Φ is the matrix of eigenvectors of the homogeneous equation, the coefficient matrices of η, $\ddot{\eta}$ are diagonalized. Suitable normalization of the eigenvectors and insertion of a diagonal structural damping matrix results in

$$\ddot{\eta} + 2\,\zeta\omega\,\dot{\eta} + \omega^2\eta = -\Phi^T M\,\{[-\Sigma_E(\tilde{e} + \tilde{R}) - \tilde{r}\,\Sigma_E]\,\ddot{\theta} + \Sigma_E(\ddot{X} + \ddot{e} - 2\,\tilde{\dot{e}}\dot{\theta})\} + \Phi^T\lambda \tag{2}$$

Equation (2) may then be reduced in dimension (η's are uncoupled) to eliminate those modal coordinates η with unwanted high frequencies.

In addition to appendage Eq. (2), a vector equation of motion can be written for the entire vehicle from the basic relation $\mathbf{T} = \dot{\mathbf{H}}$, which in matrix form becomes

$$[I - I_w E]\ddot{\theta} + (\tilde{R}\,\Sigma_E^T + \Sigma_E^T\tilde{r})\,M\Phi\ddot{\eta} + A_E\ddot{u}_E = T - \tau - \tilde{\dot{\theta}}\,I_w\dot{\phi} \tag{3}$$

where

I = total undeformed vehicle inertia matrix (3×3)

I_w = spin-axis moment of inertia for each of 3 identical momentum wheels whose spin axes are parallel to the reference axes (scalar)

τ = $[\tau_1\tau_2\tau_3]^T$, momentum wheel applied torques

$\dot{\phi}$ = $[\dot{\phi}_1\dot{\phi}_2\dot{\phi}_3]^T$, momentum wheel spin rates

T = matrix of torques applied to rigid base (3×1)

For the case of the solar-powered electric-propulsion spacecraft considered here, Eq. (3) includes acceleration (or torque) coupling of the ion engine bank, so that

$$u_E = [y_T x_T \alpha_1 \alpha_2 \alpha_3 \alpha_4]^T$$

where

x_T, y_T = translation coordinates of the engine assembly

$\alpha_1,\alpha_2,\alpha_3,\alpha_4$ = gimbal angles of each ion engine

and A_E is, in general, a matrix (3×6 in this case) of time varying coefficients that reflect the location and geometry of the ion engine assembly with respect to a point fixed in the bus.

To complete the system equations of motion, relations can be written for each of the engine coordinates and each momentum wheel spin coordinate. In matrix form, they appear as

$$A_{EE}\ddot{u}_E + A_E^T \ddot{\theta} + A_\eta \Sigma_E^T M \Phi \ddot{\eta} = \lambda_E(\dot{\theta}, \dot{u}_E, u_E, \ddot{X}, F_i) \tag{4}$$

and

$$I_w[\ddot{\phi} + \ddot{\theta}] = \tau \tag{5}$$

where

A_{EE}, A_η = constant coefficient matrices

λ_E = matrix of velocity and position dependent forcing functions or applied forces (6×1)

F_i = thrust applied by the ion engines (scalars)

The relation $\ddot{X} = F/\mathcal{M}$, where F is the matrix of force components applied to the vehicle (3×1), is also useful.

3. Applications

The hybrid coordinate dynamic model described here has been programmed for attitude-control system simulations on both the IBM 7094 digital computer (using the DSL/90 language) and an Electronic Associates 231-R analog computer. Several solar-array configurations and high-gain antenna structures, designed for a specific flyby mission to Jupiter, Saturn, Uranus, and Neptune, have been analyzed in terms of modal coordinates. Results from these simulations will be presented in subsequent articles.

References

1. *Solar Powered Electric Propulsion Spacecraft Study*, JPL Contract 951144, Hughes Aircraft Co., Culver City, Calif., Dec. 1965.
2. *Solar Powered Electric Propulsion Program Summary Report*, JPL Contract 951144, Hughes Aircraft Co., Culver City, Calif., Dec. 1966.
3. Likins, P. W., and Wirsching, P. H., "Use of Synthetic Modes in Hybrid Coordinated Dynamic Analysis, *AIAA J.*, Vol. 6, pp. 1867–1872, 1968.
4. Likins, P. W., and Gale, A. H., "Analysis of Interactions Between Attitude Control Systems and Flexible Appendages," paper presented at the 19th International Astronautical Congress, Oct. 14–19, 1968.

VIII. Guidance and Control Research

GUIDANCE AND CONTROL DIVISION

A. Preignition Characteristics of Cesium Thermionic Diodes, *K. Shimada*

1. Introduction

Preignition volt–ampere curves of thermionic diodes operating in an electron-rich emission mode exhibit two clearly distinguishable features in their apparent saturation regions characterized by two different rates of current increase as a function of applied voltage. The region having a slower rate is designated the "Schottky-like" region; the remainder is designated the "avalanche" region (SPS 37-51, Vol. III, pp. 82–86). It is apparent that the rate is determined by how the space–charge sheath controls the current flow through the diode since the diode current is space-charge-limited. In the Schottky-like region, the space–charge sheath is controlled mainly by those ions produced at the emitter by surface ionization; in the avalanche region, by those ions produced in the volume. This article describes results obtained from a fixed-gap cesium diode, as well as from a variable-gap cesium diode.

2. Fixed-Gap Diode

A fixed-gap cesium diode, built by Electro-Optical Systems (EOS), Pasadena, California, and designated SN-107, was described in SPS 37-51, Vol. III. The diode has two rhenium plane-parallel electrodes. The electrode area is 2.00 cm^2 and the interelectrode gap is 0.0115 cm.

The diode was operated in an electron-rich emission condition for which two regions of preignition characteristics were clearly discernible. The emitter temperatures were 1284, 1386, 1495, and 1598°K, and the cesium temperatures were between 473–553°K. Typical preignition characteristics were reported previously, and their analyses are given in this article.

The normalized current I/I_0, i.e., the ratio between the measured current I and the apparent saturation current I_0, varies exponentially with applied voltage V. The empirical relationship between I/I_0 and V is

$$I/I_0 = \exp\left[k_1 (V - V_1)\right] + \exp\left[k_2 (V - V_2)\right] \qquad (1)$$

where k_1, k_2, V_1, and V_2 are constants for a given volt–ampere curve taken at fixed emitter temperature T_E and cesium-reservoir temperature T_{Cs}. The first and second exponential terms in Eq. (1) represent the current in the Schottky-like and avalanche regions, respectively. The two regions are clearly distinguishable on I–V curves plotted in semilog form. In general, $k_1 < k_2$, $V_1 \simeq 0$, $V_2 > 0$.

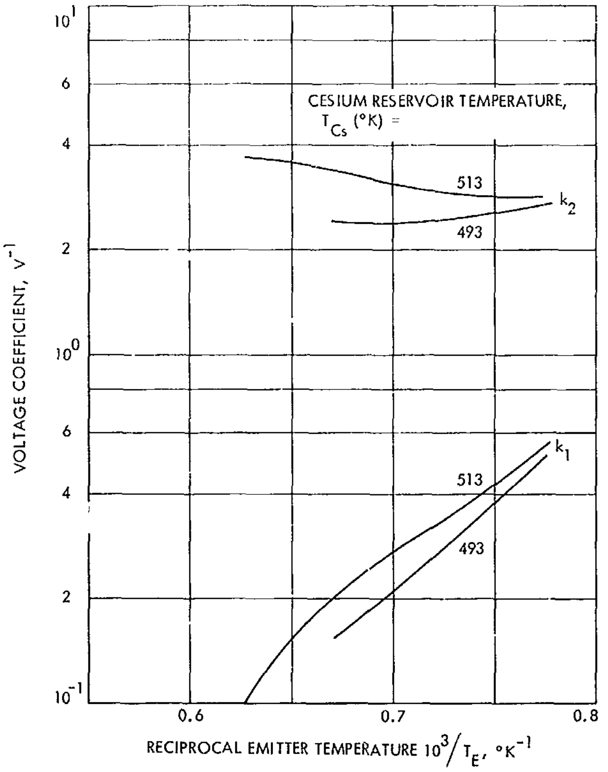

Fig. 1. Voltage coefficients vs $10^3/T_E$ for a fixed-gap diode

Figure 1 shows the dependence of k_1 and k_2 on reciprocal emitter temperature $10^3/T_E$ in the thermionic diode SN-107. The voltage coefficient k_1 increases exponentially with $10^3/T_E$, but varies only slightly with T_{Cs}. The coefficient k_2, on the other hand, does not vary significantly with $10^3/T_E$. These results were in good agreement with those obtained from a similar thermionic converter (SPS 37-50, Vol. III, pp. 122–125), except that k_2 in this converter was smaller than k_1 in the previous one for the same T_{Cs}. This difference was attributed to different interelectrode gaps d which were 0.0115 cm in the SN-107 and 0.0712 cm in the previous diode.

3. Variable-Gap Diode

To further investigate the effect of d on the preignition characteristics, experiments were carried out using a guard-ringed variable-gap thermionic energy converter. This converter was recently acquired from the Marine Engineering Laboratory, Annapolis, Maryland, as surplus equipment. It was fabricated by Thermo-Electron Co., Waltham, Mass., for the Navy, and is equipped with see-through sapphire windows to allow optical measurements of d and T_E. The converter has a separate electron-gun section that is continuously pumped by an appendage pump and, hence, is operable under normal atmosphere. The collector guard ring can eliminate the side-wall effects which ordinarily exist in hardware-type converters such as the SN-107. The variable-gap arrangement allows an effective separation between the surface and volume effects on preignition characteristics.

Volt–ampere curves were obtained for this diode in an electron-rich, unignited mode. The observed T_E ranged between 1173–1373°K, and the T_{Cs} between 453–533°K. The true T_E were not determined because of unknown temperature corrections required for the sapphire window, but the corrections should not have exceeded +10 and −0°K.

The d was varied between zero and 0.142 cm by means of three micrometer screws pushing against the collector flange. A zero-gap condition was established by noting a collector–emitter short; the parallelism was achieved during zero gap adjustments. Subsequently, d was set by the calibrated micrometer screws and occasionally cross-checked against the cathetometer readings. In order to correct for thermal expansions, the zero-gap condition was reestablished whenever the T_E was changed. The maximum error in d would be ±0.005 cm considering electrode surface roughness, parallelism, and measurement errors.

A visual observation of the d during diode operation confirmed that the avalanche region was associated with the *anode-glow* mode of the diode, which was originally found by E. O. Johnson (Ref. 1) and later identified in a thermionic converter by N. S. Rasor (Ref. 2). An increase in the diode current in the avalanche region of the volt–ampere curve was accompanied by increased intensity of a faint orange glow at the collector. The glow appeared to be localized near the center of the collector, and no glow was observed on the guard ring.

Preignition volt–ampere curves obtained at $T_E = 1173$°K and $T_{Cs} = 533$°K are shown in Fig. 2 for various interelectrode gaps ranging between 0.023–0.142 cm. The Schottky-like and avalanche regions are again clearly distinguishable because of the two different slopes of the I–V curve. Note also that the curves in the Schottky-like regions are parallel to one another in Fig. 2 for all values of d. In Fig. 3, where the current is normalized, the Schottky-like regions for six curves at various d converge to a single line. Therefore, the rate of current increase in this region is mainly controlled by the emitter surface; this conclusion is consistent with the previous findings

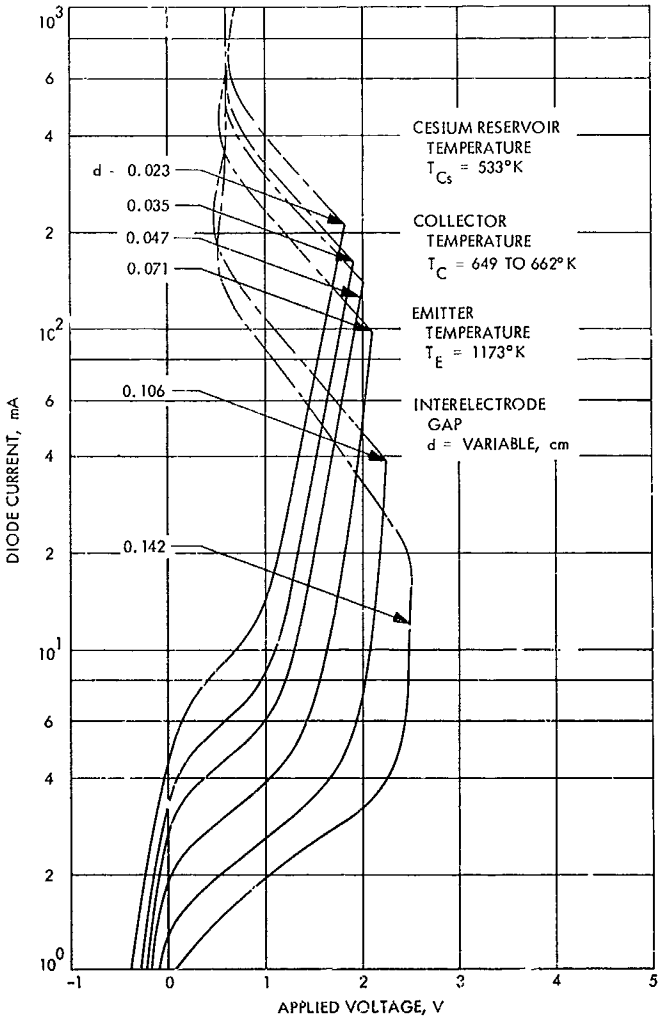

Fig. 2. Preignition volt–ampere curves for a variable-gap diode: semilog plot

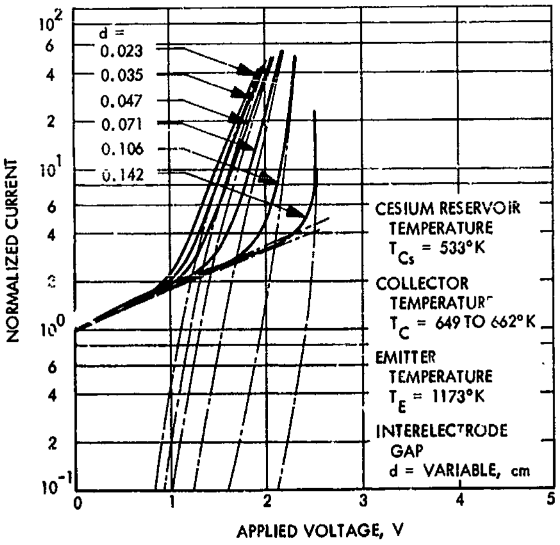

Fig. 3. Preignition volt–ampere curves for a variable-gap diode: normalized plot

with a fixed-gap diode. The voltage coefficients k_1 and k_2 are in agreement with the previous results obtained at similar T_E, T_{Cs}, and d. As is shown in Fig. 3, the rate of current increase becomes larger as d becomes larger; thus k_2 increases with d. This dependence is not surprising since volume ionization takes place in the avalanche region, and, therefore, k_2 may well depend on the product of pressure × distance. Further analysis is required to establish an exact functional relationship.

An additional feature of the *I–V* characteristics that was not found in a fixed-gap diode was revealed with the variable-gap diode. Previously, each observed normalized current could be decomposed into *two* exponential components in that it could be graphically represented as a sum of *two* straight lines in a semilog plot. On the other hand, each current for the variable-gap diode could be graphically resolved into the sum of *one* straight and *one* curved chain line (Fig. 3). Observing that the curved chain line converges toward the current in the avalanche region, and that the bend occurs at a voltage where the transition in normalized current occurs from the avalanche region to the Schottky-like region, one might conclude that a *third* term describing the current at the transition must be added to fit the observed current. The origin of this extra term is not clear at this time.

The electron-rich condition (ion-richness ratio $\beta < 1$) was verified by examining the relationship between the apparent saturation current I_0 and the inverse interelectrode distance $1/d$ (Ref. 3). The linear relationship shown in Fig. 4 confirms that, as expected, the diode was operating in an electron-rich mode.

References

1. Malter, L., Johnson, E. O., and Webster, W. M., "Studies of Externally Heated Hot Cathode Arcs: Part I. Modes of Discharge," *RCA Rev.*, Vol. 12, pp. 415–435, Sept. 1951.
2. Bullis, R. H., *et al.*, "The Plasma Physics of Thermionic Converters," *IEEE Report on the Thermionic Conversion Specialist Conference*, pp. 9–30, Oct. 1965.
3. Warner, C., and Hansen, L. K., "Transport Effects in the Electron-Rich Unignited Mode of Cesium Diodes," *J. Appl. Phys*, Vol. 38, No. 2, pp. 491–500, Feb. 1967.

B. Barrier Heights of Blocking Contacts to Vacuum-Cleaved Photoconducting CdS in the Conducting State, *R. J. Stirn*

1. Introduction

Potential barriers formed at a metal-semiconductor junction when the metal contact has a work function ϕ_m greater than the electron affinity E_A of the semiconductor

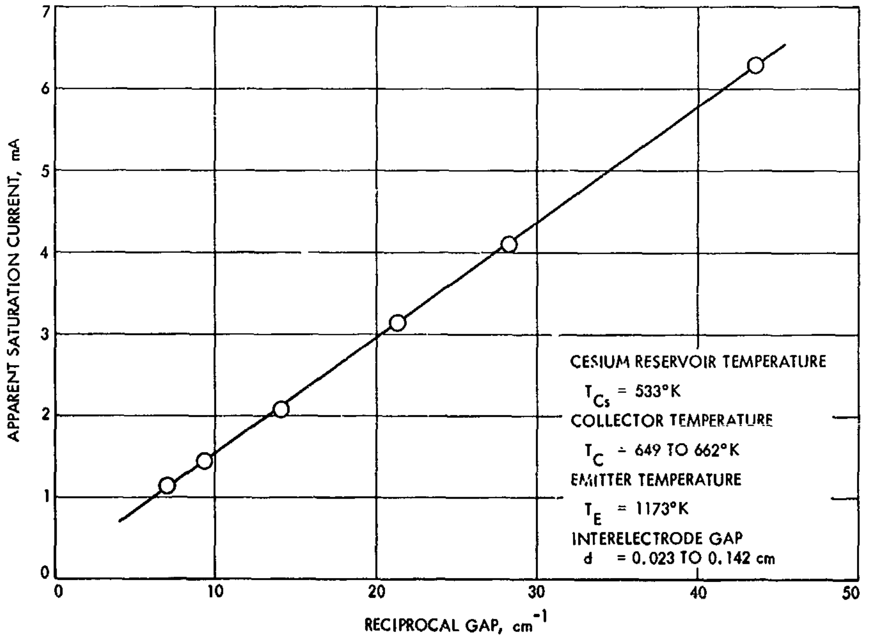

Fig. 4. Apparent saturation current vs reciprocal gap

have been measured for nonphotoconducting cadmium sulfide (CdS) by the techniques of photoresponse and differential capacitance (Ref. 1). The results have been summarized in SPS 37-53, Vol. III, pp. 68–71. Generally, the barrier heights depended upon the metal and ranged from 0.85 eV for Pt and 0.79 eV for Au to 0.36 eV for Cu, with no dependence upon temperature. Also, some preliminary results were given of barrier height measurements on photoconducting CdS, which is of much higher resistivity because of the presence of Cd vacancies. These results showed barrier height values of approximately 0.50 eV at room temperature with little dependence on the metal work function, and, more importantly, showed that the values depended strongly on temperature and photocurrent (light intensity). The results were obtained from an analysis of stationary high-field domains in the range of negative differential conductivity (Ref. 2). It is the purpose of this article to present a summary of the theory, the experimental techniques involved, and additional data.

2. Theory of Stationary High-Field Domains

Under certain conditions of doping and light excitation, field-enhanced excitation of hole traps in photoconducting CdS leads to increasing recombination (i.e., decreasing electron concentration) with increasing applied voltage (field quenching). In this negative differential conductivity (NDC) regime, high-field domains form at the cathode and either remain fixed in place while growing in size or propagate through the crystal in times on the order of seconds per millimeter. The photocurrent saturates or oscillates at low frequency, respectively, in these two cases. The Gunn effect in n-type GaAs is an example of NDC for which the decreasing conductivity with increasing field is caused by increasing scattering of electrons into a subsidiary conduction band having lower carrier mobility. In this case, the domains move with the velocity of sound and the current oscillates in the radio-frequency range.

Although the domains in CdS have many interesting features in relation to bulk properties, it is the fact that one can obtain information about n_c, the carrier concentration near the metal cathode–semiconductor interface, that will be utilized in this investigation. The value of n_c is then related to the barrier height ϕ_B at the cathode by the relation

$$n_c = N_c \exp\left(\frac{-\phi_B}{kT}\right) \tag{1}$$

where N_c is the effective density of states for the semiconductor, k is the Boltzmann constant, and T is the absolute temperature.

Above a critical voltage, the current saturates and the high-field domain can be observed by means in *Subsection 3*. We now wish to examine why the domain forms, i.e., how there can be two regions in the crystal having different field strengths. It has been shown (Ref. 3) that step-like solutions can exist as stationary solutions of Poisson's equation

$$\frac{dE}{dx} = \frac{q}{\epsilon\epsilon_0}(n + n_t - p - p_t) \tag{2}$$

and the transport equation

$$\frac{dn}{dx} = \frac{q}{kT}\left(nE - \frac{j}{q\mu}\right), \tag{3}$$

where

E = electric field

q = electronic charge

j = current density

μ = electron mobility

ϵ_0 = permittivity of free space

ϵ = static dielectric constant

n, p = free electron and hole densities, respectively

n_t, p_t = ionized electron and hole trap densities, respectively

It is required that the electron density have a range that decreases more rapidly than linearly with increasing field (because of enhanced hole excitation), and that the amount of diffusion current be negligible ($dn/dx \approx 0$). The actual solutions to Eqs. (2) and (3) require an appropriate reaction kinetic equation describing the trapping and releasing of carriers, i.e., dn/dt, and necessitate computer computation after reasonable values are assumed for the reaction kinetic coefficients. It will suffice for our purposes to examine the problem graphically.

Image forces at the cathode are neglected for the present so that Eqs. (2) and (3) form an autonomous system, i.e., do not contain the distance from the cathode explicitly. The solutions can, therefore, be discussed in terms of their projection in the n–E plane at any convenient value of x. Since it is experimentally observed that the electric field is constant in the crystal (except at the domain edge and very close to the contact where image forces are no longer negligible), and that diffusion current is negligible, one introduces auxiliary functions $n_1(E)$, for which $dE/dx = 0$, and $n_2(E)$, for which $dn/dx = 0$ (Fig. 5).

The function $n_2(E)$, representing the condition of diffusion neutrality, is obtained from Eq. (3): $n \alpha (1/E)$. When plotted in logarithmic coordinates, as in Fig. 5, the curve $n_2(E)$ is linear with a negative slope of unity. The charge neutrality curve $n_1(E)$, drawn arbitrarily in Fig. 5, shows a constant carrier density (n_i = bulk low-field concentration) up to a certain field strength, above which there is a range where n decreases more rapidly than linearly, so that (as we will show) two singular points, or homogeneous solutions, can exist. It has been shown experimentally that the shape of $n_1(E)$ in Fig. 5 does conform to physical reality for the type of crystals used in this investigation (Ref. 4).

Examination of Eqs. (2) and (3) (with the left-hand sides identically equal to zero) for $n > n_1(E)$ and $n > n_2(E)$ shows that the slope $dn/dE \equiv (dn/dx)/(dE/dx)$ is positive. This fact is symbolized in Fig. 5 by the short arrow in the first quadrant. Similar reasoning leads to the directions shown for the other three short arrows depending on whether n is above or below $n_1(E)$ and $n_2(E)$ at the value of electric field desired. These arrows "point toward" increasing x. Therefore, for the simple case of a nearly homogeneous field at low voltages before current saturation, and under the assumption of a blocking contact at the cathode, the solution curve must lie close to the drift-current curve $n_2(E)$ (since diffusion in CdS is small compared to drift), and must pass from the region of the n–E plane in Fig. 5 near n_c (the carrier concentration at the cathode), to the region for which $E = E_I$ (the homogeneous field) and $n = n_i$, while x varies from the

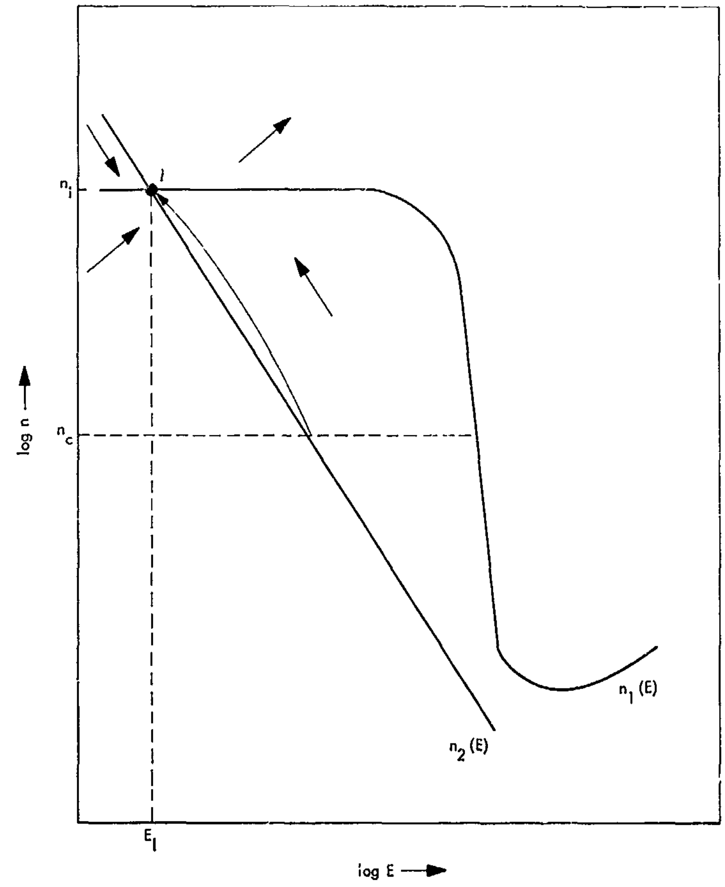

Fig. 5. Symbolized field of direction with charge-neutrality curve n_1 (E) and drift-current curve n_2 (E)

cathode to the edge of the depletion region away from the cathode. Over the rest of the crystal length, the solution curve "stays" near the singular point I, which corresponds to the trivial homogeneous solution $E_I = V_a/L$ where V_a is the applied voltage and L is the electrode separation.

The type of contact at the anode is not important for this investigation; however, if the anode is a neutral contact, the solution curve (Fig. 5) would end at point I for $x = L$. If the anode happened to be blocking (injecting), the curve would dip down (up) in the direction of the third (first) quadrant to values of carrier concentration and electric field below (above) those at point I.

The corresponding current for the simple case just discussed is shown by point A in Fig. 6. The current is slightly below the value expected for an ohmic cathode because of the voltage drop across the depletion region.

When the applied voltage is further increased, the current density j increases, causing the $n_2(E)$ curve to move further away from the origin until, in the region of NDC, a second singular point (II) appears and approaches n_c (Fig. 7a). The current begins to saturate as shown by point B in Fig. 6, since the solution curve (again starting near n_c)[1] is forced closer to point II, remaining close to the value of field E_{II} for larger values of x (Fig. 7c), causing a step-like character to $E(x)$, i.e., two field strengths can exist simultaneously. The corresponding carrier density distribution is shown in Fig. 7b. The high-field domain increases in width with further increasing voltage until it reaches the anode (point C in Fig. 6). At this voltage, point II is exactly at n_c and a homogeneous solution is obtained: $n = n_c$ and $E = E_{II}$ for all x. The case of higher applied voltages involving domains attached to the anode and the point III will not be discussed here.

The values of E_I and E_{II} can be experimentally determined by using the approximation

$$E_{II}l + E_I(L - l) = V_a \tag{4}$$

where l is the domain width. Plotting l versus V_a for a fixed temperature and light intensity yields a straight line with a slope $E_{II} - E_I \cong E_{II}$. The field E_I, which is found to be much less than E_{II} can also be found from the voltage V_0 at which the current in the forward direction equals the saturation current in the reverse direction:

$$E_I = \frac{V_0 - V_0'}{L} \tag{5}$$

where V_0' is the small voltage drop across the barrier. What is most important for our analysis of the barrier height in CdS is that E_{II} is the maximum field within the crystal, that n_{II} is the minimum carrier density, and that the smallest gradients of n and E must lie close to the

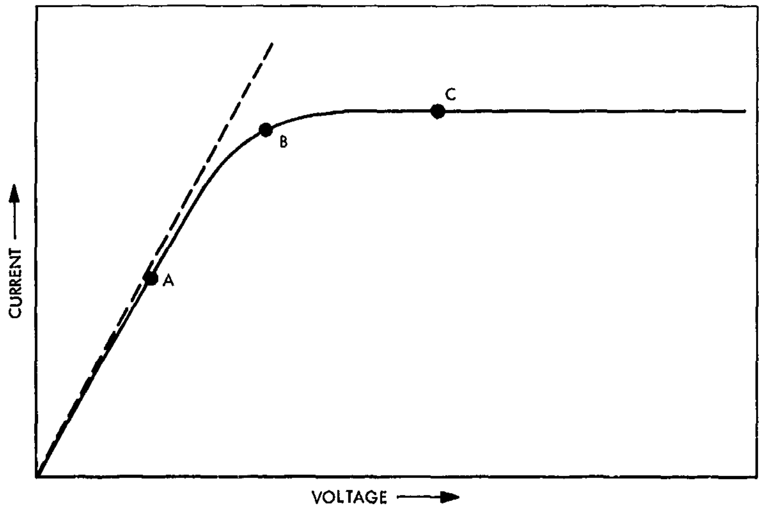

Fig. 6. Reverse current–voltage characteristic in CdS exhibiting stationary high-field domains

---

[1] The separation of n_c and n_{II} in Fig. 7a is greatly exaggerated on the logarithmic scale used. It will be shown later that $n_c \approx n_{II}$.

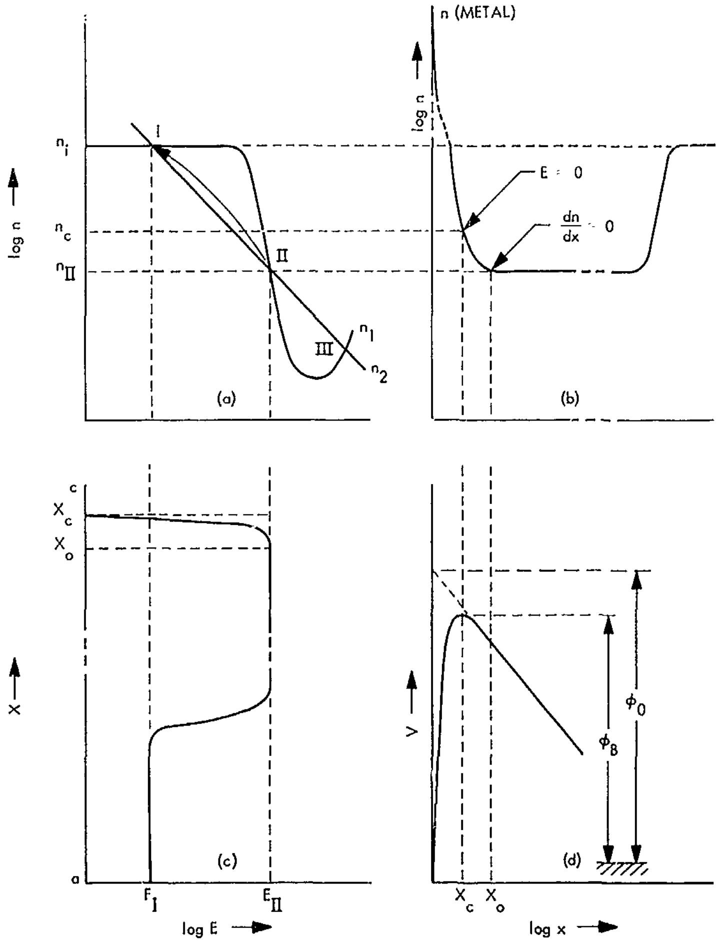

Fig. 7. Carrier concentration vs x and E, electric field vs x, and the potential barrier near the cathode

cathode. Thus, the diffusion current can be neglected within the domain and n_{II} can be calculated from E_{II} and the measured saturation current j_s using the relation

$$j_s = q n_{II} \mu E_{II} \qquad (6)$$

The expected shape of the barrier is shown in Fig. 7d. At x_c (about 50 Å) where the surface field is cancelled by the field due to image forces, the current is given by the diffusion current

$$j = -\mu kT \left(\frac{dn}{dx}\right)_{x=x_c} \qquad (7)$$

which increases with smaller x until the maximum diffusion current is attained. This current is called the thermionic current and is given by (Ref. 5)

$$j_{th} = \frac{q v_{th}}{(6\pi)^{1/2}} N_c \exp\left(-\frac{\phi_B}{kT}\right) \qquad (8)$$

where v_{th} is the thermal velocity of the electrons in the semiconductor. The saturation current densities obtained in this investigation are far larger than one would calculate from Eq. (8) using values of ϕ_B published in Ref. 1, leading to the conclusion that the barrier height is considerably reduced in CdS under conditions of photoconduction. Large tunneling currents could be another explanation. However, this possibility has been explored[2] and it was concluded that the required buildup of positive space charge at the barrier is not possible in these crystals.

---

[2] Böer, K. W., Dussell, G. A., and Voss, P., "Experimental Evidence for a Reduction of the Work Function of Blocking Gold Contacts with Increasing Photocurrents in CdS," to be published in *Phys. Rev.*

From Eqs. (1), (6), and (8), we have

$$n_e = (6\pi)^{1/2} \frac{\mu E_H}{v_{th}} n_H \tag{9}$$

Since $\mu E_H \approx v_{th}$ for the values of E_H found experimentally, $n_e \approx 5\, n_H$ at most.

In this calculation, and in the use of Eq. (6) for determining n_H, the value of the electron mobility is assumed constant up to $E = 40\,\text{kV/cm}$ and to decrease as $1/E$ above 40 kV/cm because of optical phonon scattering of the hot electrons (Ref. 5).

The barrier height of Au electrodes evaporated on CdS crystals which have been exposed to air has been recently determined (Footnote 2). However, it is very desirable to obtain results on vacuum-cleaved surfaces in order to eliminate possible interface effects. The results presented in *Subsection 3* have been performed on such crystals.

3. Experimental Arrangement

The CdS crystals were purchased from the University of Delaware's Department of Physics, where they were grown by sublimation and subsequently doped with Ag and Al by a heat treatment at 900°C for 3 hr. The platelets, whose thickness ranged from 0.05 to 0.10 mm, were initially cut into long slices about 0.5-mm wide with a wire saw. These slices were then mounted in wax on a glass plate with a short section exposed over the edge. This end was cleaved in the vacuum evaporater while the metal to be used as the cathode was being evaporated. Only samples which cleaved *below* the wax line were used, assuring that no metal was deposited on the sides. The remaining slice was then removed by dissolving the wax in benzene and broken to give a length of 0.5 to 1.0 mm. The ohmic contact at the opposite end (anode) was later formed by evaporating indium while the sample was heated to 120°C.

The crystals were mounted in clear epoxy between two thin glass plates so that up to 3000 V could be applied without discharges taking place across the surface. Silver paint was used to form leads to the electrodes. The sample was placed in a windowed double-walled glass dewar that allowed the temperature to be varied between 155°K and room temperature by using a resistance heater and liquid nitrogen at the opposite end of a cold finger.

The crystal was illuminated normal to the largest surface with a beam of monochromatic light with a photon energy equal to the bandgap (511 to 495 nm depending on the temperature). The monochromator slits were set to give a band pass of 6 nm and maximum light intensity of 5×10^{16} photons/cm²/s as measured with a Hilger–Schwarz thermopile. Light intensity was reduced by using calibrated neutral density filters.

The use of band-gap light enables one to see the stationary high-field domain (Fig. 8) because of the Franz–Keldysh effect. This effect, in which the fundamental absorption edge is shifted by a high electric field toward lower energies, is due to the fact that, in the presence of such a field, the electrons of the valence band can penetrate somewhat into the band gap, thus allowing optical transitions to occur to similar states below the conduction band edge. The absorption edge shift makes the area where the field-enhanced recombination occurs, i.e., the domain region, appear darker. The sample was viewed through a 20× microscope equipped with a reticle with which the domain length could be measured for a given voltage. This voltage, and the current through the sample as measured by a Keithley picoammeter, were recorded on an x–y recorder.

4. Experimental Results

A number of samples from a single larger crystal were successfully vacuum cleaved and electroded with evaporated Pt, Au, Ag, Ni, Cu, and Sn. Measurements of the reverse current–voltage characteristics up to 3000 V (saturation occurs at 200–300 V), or for forward currents up to 3×10^{-5} A, were made at some selected temperatures and light intensities. Input power was kept below 1mW to prevent heating the sample. The reverse current–voltage characteristics were always similar to Fig. 6 with the saturation current typically around 10^{-6} A ($j_s \approx 10^{-2}$ A/cm²) at $T = 155$°K. The current at higher temperatures (220–295°K) was actually lower than the current at the lowest temperatures due to the presence of thermal quenching in the photoconductor.

Where possible, the domain width as a function of applied voltage was measured for these samples. A decreasing Franz–Keldysh effect (which is proportional to T^{-2}) made it difficult to see domains at the higher temperatures except for metals with values of E_H above about 80 kV/cm. Figure 9 shows the domain–voltage dependence for Au at $T = 155$°K and various light intensities with $I_0 = 5 \times 10^{16}$/cm²/s. The slopes (equal to $E_H - E_l$) ranged 122–83 kV/cm for this metal contact. Since E_l is less than 1 kV/cm, these slopes were used to approximate E_H in Eq. (6).

Fig. 8. High-field domain in CdS: (a) zero-applied voltage, (b) 500 V, and (c) 1000 V

The Hall mobility field dependence was obtained from Fig. 10 where the low-field values were obtained from Ref. 6. Above 40 kV/cm, the mobility was assumed to decrease as $1/E$ (Ref. 7).

The values of n_e obtained from the analysis described earlier were typically 10^7–10^{10} cm^{-3} depending on the metal contact, temperature, and light intensity. These values are lower (as expected) than the bulk low-field density n_i by about 10^2–10^3.

Values of the effective barrier heights for CdS (in eV) were then calculated using Eq. (1) and the results for a constant photon flux density of 5×10^{15} (cm^{-2} sec^{-1}) are given in Table 1. It is seen that there are relatively small differences between the metals at any one temperature. Except for Pt, there does seem to be some ordering according to the electronegativity of the metal, but the differences are only hundredths of a volt as compared to tenths of a volt differences in the metal electronegativity (or

Table 1. Barrier heights for CdS

Metal	Electro-Negativity	155°K	180°K	220°K	255°K	295°K
Au	2.4	0.30	0.35	0.42	0.47	0.53
Pt	2.2	0.28	0.33	0.36	—	0.50
Ag	1.9	—	0.34	—	0.47	0.53
Cu	1.9	0.27	0.32	—	0.44	—
Ni	1.8	—	0.31	0.37	—	—
Sn	1.8	0.26	0.29	0.35	—	—

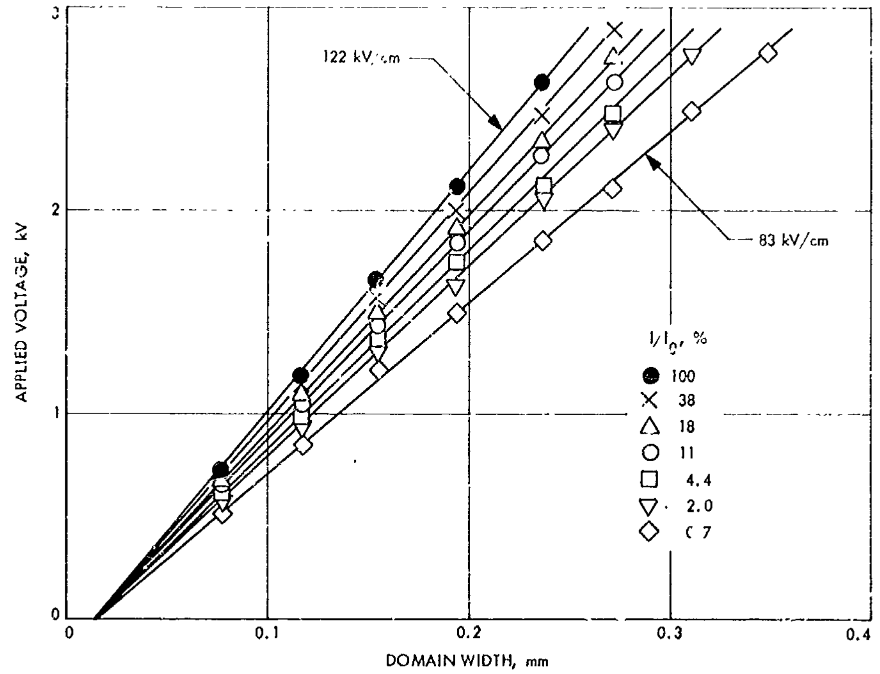

Fig. 9. Domain width vs applied voltage

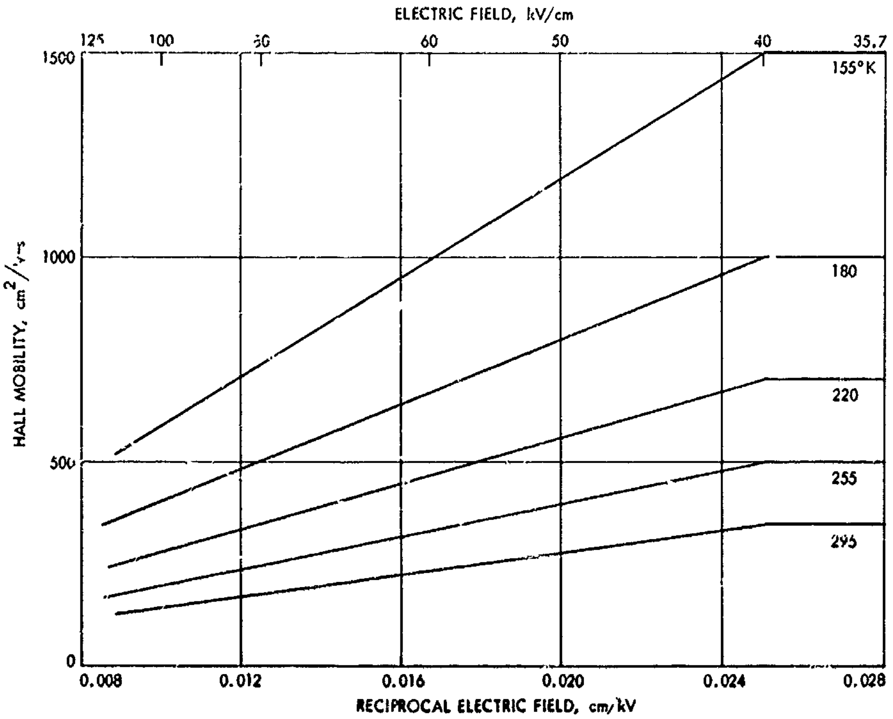

Fig. 10. Assumed field dependence of mobility in CdS

work function). Some differences between the values in Table 1 and published values for lower resistivity CdS were mentioned in the introduction.

The barrier-height temperature dependence observed in the table is shown in Fig. 11 for three of the metals where it is seen that a linear relationship holds.

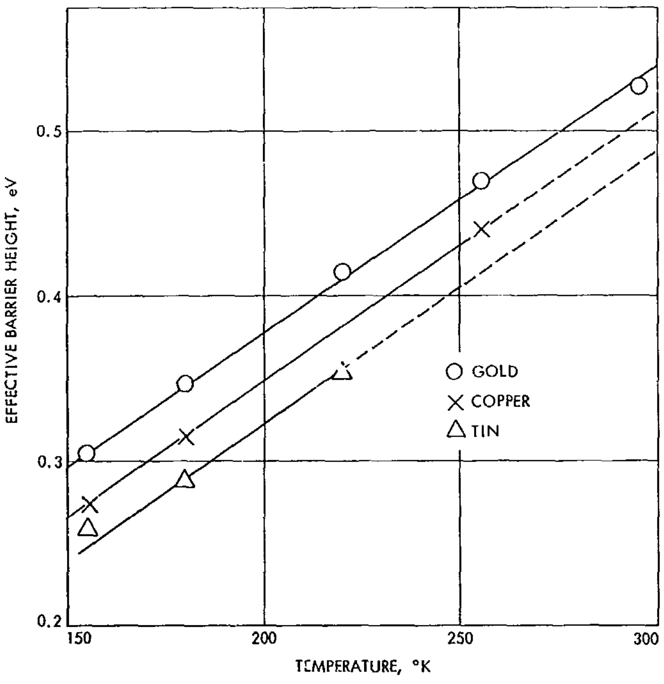

Fig. 11. Temperature dependence of barrier heights on photoconducting CdS for Au, Cu, and Sn

The barrier-height light dependence on CdS for Au and Cu is shown in Fig. 12. Actually, the varying light intensity is only the means to control the amount of photocurrent flowing through the contact, and it is more reasonable to conclude that the barrier height, as measured by the high-field-domain technique, is being affected by the amount of current flow and not directly by the photon flux.

5. Conclusions

In contrast to the situation in nonphotoconducting CdS, barrier heights of blocking contacts on photoconducting CdS depend strongly on temperature and the amount of photocurrent flowing through the contact. In addition, the barrier heights, as measured by the high-field-domain technique, are considerably lower in magnitude than those reported in the literature for semiconducting CdS, allowing considerably higher currents through the contacts, and, thus, higher gain factors than would be expected from the earlier and higher barrier heights. An explanation of this unexpected result is not apparent at this time and may involve subtle changes in the dipole layer at the metal–CdS interface due to the presence of the relatively high photocurrents possible in CdS.

Determination of the barrier heights by more conventional techniques (e.g., by photoresponse measurements) would be very desirable, especially for photocurrents lower than those used in this investigation. However, impurity photoconduction would mask out internal photoemission from the metal contact. Differential capacitance measurements also have their difficulties because of the high impedance of these samples.

References

1. Spitzer, W. G., and Mead, C. A., "Barrier Height Studies on Metal-Semiconductor Systems," *J. Appl. Phys.*, Vol. 34, p. 3061, 1963.
2. Böer, K. W., and Voss, P., "Stationary High-Field Domains in the Range of Negative Differential Conductivity in CdS Single Crystals," *Phys. Rev.*, Vol. 171, p. 899, 1968.
3. Böer, K. W., and Quinn, P. L., "Inhomogeneous Field Distribution in Homogeneous Semiconductors having an *N*-Shaped Negative Differential Conductivity," *Phys. Stat. Sol.*, Vol. 17, p. 307, 1966.
4. Böer, K. W., Döhler, G., Dussell, G. A., and Voss, P., "Experimental Determination of Changes in Conductivity with Electric Field, Using a Stationary High-Field Domain Analysis," *Phys. Rev.*, Vol. 169, p. 700, 1968.
5. Spenke, E., *Electronic Semiconductors,* p. 84. McGraw-Hill Book Company, Inc., New York, 1958.
6. Devlin, S. S., Appendix to Shiozawa, L. R. and Jost, J. M., "Research on II–VI Compound Semiconductors," Final Technical Report for Contract AF 33(657)-7399. USAF Aeronautical Research Laboratories, Wright–Patterson Air Force Base, Ohio, 1965.
7. Böer, K. W., and Bogus, K., "Electron Mobility of CdS at High Electric Fields," *Phys. Rev.*, Vol. 174, 1968.

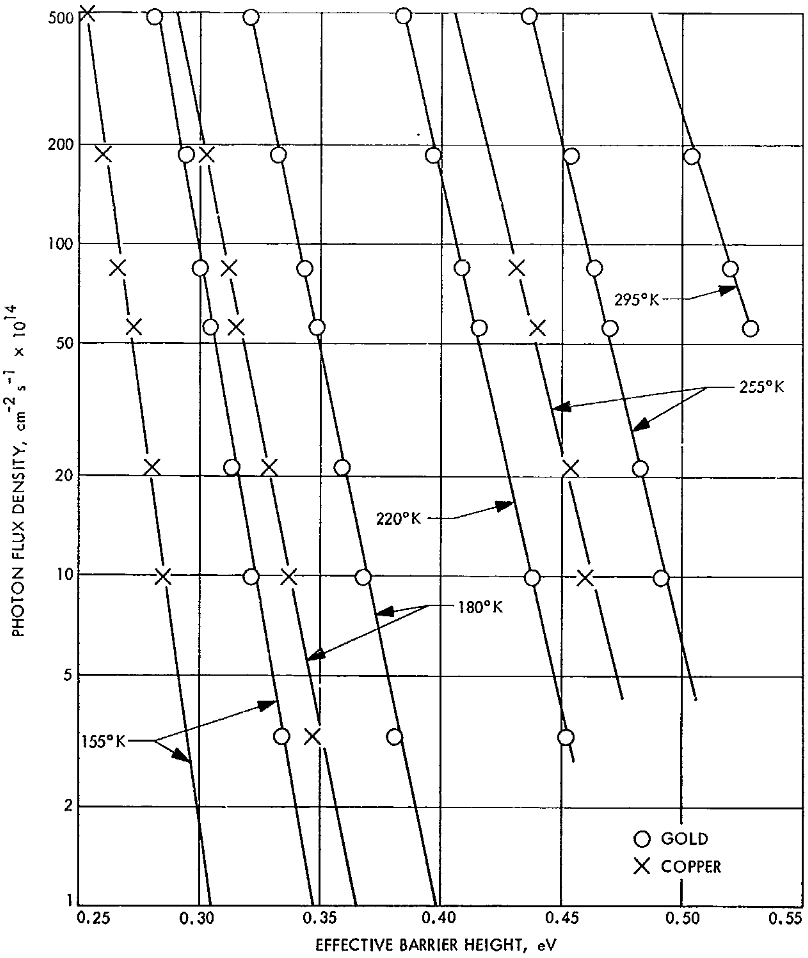

Fig. 12. Barrier-height light dependence on photoconducting CdS for Au and Cu

IX. Electronic Parts Engineering

ENGINEERING MECHANICS DIVISION

A. MOSFET Screening Methodology, *R. A. Summers*

1. Introduction

The metal oxide semiconductor field effect transistor (MOSFET) is a recent development in the transistor field. Its significant features include: (1) a high input impedance comparable to vacuum tubes, and (2) operation at very low power levels. Its use tends to simplify transistor circuitry, and it is somewhat simpler to manufacture.

Because of the significant difference in operating principles and design between MOSFET and conventional bipolar transistors, the method of screening will be different. Two vendors, Fairchild and Siliconix, were selected to develop new screening methods.

Although the approaches by the two vendors were somewhat different, the investigations included:

(1) Gate voltage stresses in the breakdown region.
(2) High-temperature bias tests.
(3) Noise measurement.
(4) Oxide purity tests.
(5) Temperature cycling effects.
(6) Characterization at low temperatures.
(7) Life test to determine degrading effects of various stresses.

The transistors at Siliconix are single enhancement–depletion mode, N-channel units similar to the 2N3631. The Fairchild units are dual enhancement mode, P-channel units similar to the FI0049.

2. Test Results

The test at Siliconix has been concluded. Accidental damage to the high-temperature reverse bias test group invalidated the test sample integrity. However, the following test results were obtained:

Thermal shock. The transistors were tested for resistance to thermal shock by immersing them alternately in boiling water and boiling liquid nitrogen. This test is a screen for marginal internal lead bonds and defective chip-to-header bonds. There were no failures.

Oxide stress test. The absolute maximum rating of the gate to channel voltage is ±60 V. The devices had actual destructive breakdown voltages of 105 to 120 V, which shows adequate safety margin. There was some parameter shift before oxide rupture, but it was too close to breakdown to be useful.

Low-temperature performance. Over the temperature range of +25 to −196°C the MOSFET exhibited the following characteristics:

1. Gain doubled.
2. Pinch-off voltage decreased linearly by 8%.
3. Drain-source breakdown voltage decreased 15%.
4. No deterioration in input resistance.
5. Input capacitance was stable.
6. Drain-source on resistance decreased by 50%.

At Fairchild all the screening tests have been completed, and the parts are in life test. Analysis of data will await completion of the life test. Completion is estimated for March 1969.

B. Power Pulse Method of Screening Resistors,

K. C. Evans

The feasibility of a screening method for resistors is being investigated wherein a short duration power pulse is applied to the part and the resistance variation is monitored during the pulse period. If successful, this method will replace current methods and effect significant savings in screening time and cost.

The current method used for most screening tests is to apply a high-level stress to the part being evaluated with the anticipation that the stress will provide an indication of any defect or weakness in the part. In the past a permanent change in the resistance value has been the indication of defectiveness. By measuring the resistance before and after the screening test, it could be determined that a permanent resistance shift occurred as a result of the high-level stress.

The power pulse method of screening resistors consists of monitoring the resistance change of the test component while it is being subjected to a controlled pulse of maximum nondestructive power. The maximum nondestructive power is defined as that power level which during the test period will bring the temperature of the resistance element up to a specified maximum just below the point where it will cause damage to the resistive material. Generally 5 to 20 times the rated power is applied to the element for a period of 5 s or less. Since the temperature rise in the resistance element is effected over such a short time period, the resulting differential expansion will create stresses in the test unit beyond what would be encountered under normal operating conditions. The effect of these stress conditions on the resistance of the test component is continuously recorded.

The contracted portion of this investigation has been completed. The work included a comparison evaluation on selected resistor types of the power pulse method versus the currently used screening method. The feasibility study has demonstrated that the power pulse method is highly effective. The power pulse screen detected 54 parts of a total 3900 as being abnormal, whereas the conventional screen detected 9 parts of a total 3900. The life test indicated that the power pulse screen detected an additional 15 abnormal parts for a total of 68. In the conventionally screened lot, 30 additional parts were detected for a total 39. This indicates the power pulse method to be about six times more effective in detecting abnormal parts.

The test pulse level for this effort was arbitrarily established at the level necessary to produce a 0.02% permanent change in resistance. Because of differences in rating criteria by manufacturers, as well as differences in configuration and materials, the actual pulse level used ranged from 7 to 70 times rated power for the various types tested. The power pulse method of screening will effect a substantial saving in both time and money. Based on 1,000 resistors to be screened, the power pulse method can be accomplished in one fifth the time and cost of the previous method. Both the potential time and cost savings has prompted further investigation into the use of power pulse screening of resistors.

JPL is purchasing a machine that will screen resistors by the power pulse method. This equipment will provide a maximum of 200 W for resistors up to 20,000 Ω and a maximum of 2,000 V for resistors between 20,000 and 2.0 MΩ. After the proper power level and pulse duration are set up, the machine automatically plots the change in resistance during the power pulse. The resistance monitoring device can indicate resistance fluctuations of as little as 0.001%, so that deviation from the expected change in resistance trace can easily be identified and evaluated to determine if they indicate a nonhomogeneous part. The amount of resistance change or the variation from a normal trace which can be allowed before a part is considered defective varies depending upon the type of resistance element and the degree of the discrimination which is required.

Before the power pulse method can be incorporated into a project screening operation, it will be necessary to establish optimum pulse levels for all types of resistors on the JPL preferred parts list. Testing will be performed and procedures written so that the equipment can be used for project screening.

C. High-Impact Survival of Electronic Parts,

K. R. Bilodeau and K. C. Evans

1. Purpose of Test

Spacecraft electronic equipment capable of withstanding high shock accelerations can benefit the lunar and planetary exploration programs in several ways. The use of such equipment in capsules intended to survive high velocity landings will generally ease design constraints and lead toward increased overall efficiency of the capsule system. Another use is in soft landers, where a hard core could survive an abnormal landing and provide valuable diagnostic information. In other applications, increased reliability of performance after exposure to the normal ground handling and flight environments may be realized (Ref. 1).

The development of such equipment involves two problems on the component part level: (1) ensuring that the component parts used are, by themselves, capable of withstanding high shock accelerations, and (2) ensuring that these parts and their structures are protected by proper mounting and packaging. This test program was initiated to solve the first problem.

2. Test Program

The test program involved rigidly mounting various resistors, capacitors, transistors, diodes, thermistors, relays, fuses, and inductors selected from the Jet Propulsion Laboratory preferred parts list. Various electrical parameter measurements of the mounted parts were then made. After initial measurement, the total number of parts of each part type was divided into three subgroups. Each of the subgroups was subjected to a 2,000 $g \pm 10\%$ square wave with a pulse time of 0.5 to 1.5×10^{-3} s with each subgroup mounted in one of the three distinct axes of the part. Electrical parameter measurements were again made and recorded. The mounted parts were then subjected to a 5,000 g shock with each subgroup mounted in the same axis as before. The parameters were again measured and recorded. The parts were subject to a 10,000-g shock, and final parameter measurements were made and recorded. Those parts which failed by excessive parameter change and those which failed catastrophically were removed from the mounting board, disassembled, and visually inspected.

3. Shock Testing

It is insufficient to define an impact shock by g-level alone. Additional information is required in the form of duration and pulse shape. There are numerous ways in which the damage potential of a shock pulse or the sensitivity to damage of a component may be presented. A concept that is easy to understand was originated at the Naval Ordnance Laboratory (Ref. 2).

According to this concept, the conditions under which a specimen will or will not be damaged may be presented graphically on a plot of velocity change versus acceleration. The shape and location of the curve separating the region of damage and no damage is dependent on the mechanical properties of the specimen and on the shape of the applied shock pulse. Quantitatively, for a given shock pulse shape and direction of loading, there are two ways in which the specimen may escape damage. The peak acceleration may be so low that the component could withstand its steady application, or the velocity change may be so small that the maximum energy that can be supplied to the component is insufficient to produce damaging stresses. In the latter case, the applied acceleration could be extremely high without causing damage.

The remaining factor to consider is pulse shape. Kornhauser (Ref. 2) derives curves that show that a square-wave input provides the greatest amplification factor. Amplification factor is the ratio of maximum dynamic deflection of a system to the maximum static deflection. It can then be concluded that to conduct a severe test, it is best to use a high-level square-wave shock pulse of as long a duration as possible.

4. Equipment

The main piece of equipment is the sling-shot type shock tester (Fig. 1). The tester consists of a pair of guide rails (I-beams), a pretensioning mechanism, a winch, a release mechanism, a test carriage, a copper target, and an impact block. The test carriage travels between the guide rails. It uses a 40-ft long shock-absorber (bungee) cord. The bungee cord is loaded to a small pretension, and the test carriage is pulled by the winch against the tension of the bungee cord to a selected length for desired shock pulse duration. Various bungee cords, each with different diameters, are used to achieve selected impact velocity. Tension force varies linearly with a displacement of up to about 80% elongation. The impact tool is mounted in front of the carriage. Test shocks are produced by impacting the carriage nose against an annealed copper block (target), which is mounted in the impact block. The

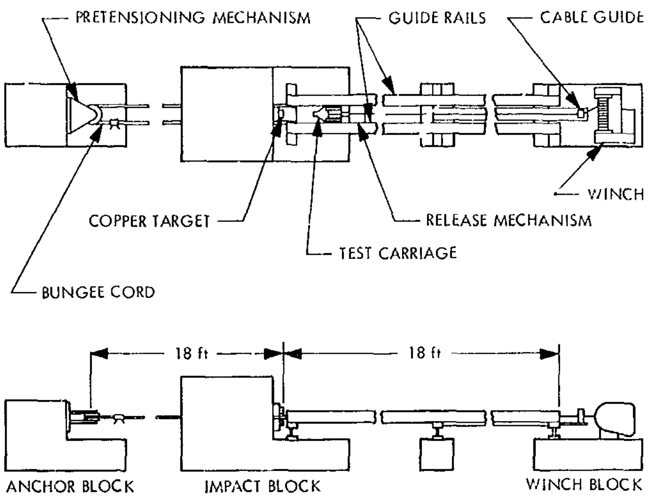

Fig. 1. Sling-shot shock tester configuration

acceleration level is determined mainly by the impact material and the diameter of the impact tool (Ref. 3). The length of the shock is determined by the velocity of impact. The velocity of the test specimen could be increased until depth of penetration in the target is so deep that near plastic deformation of the target is no longer possible, or until the 200 ft/s limit of the tester is obtained.

5. Instrumentation

Two methods of measuring the acceleration level produced by the test were used, and the results were recorded. The first method employed a piezo-electric shock accelerometer. The output was displayed on a memory oscilloscope and simultaneously FM-recorded on 0.5-in. magnetic tape at a speed of 120 in./s, which enabled a frequency response of dc to 100 kHz. Figure 2 shows typical shock curves.

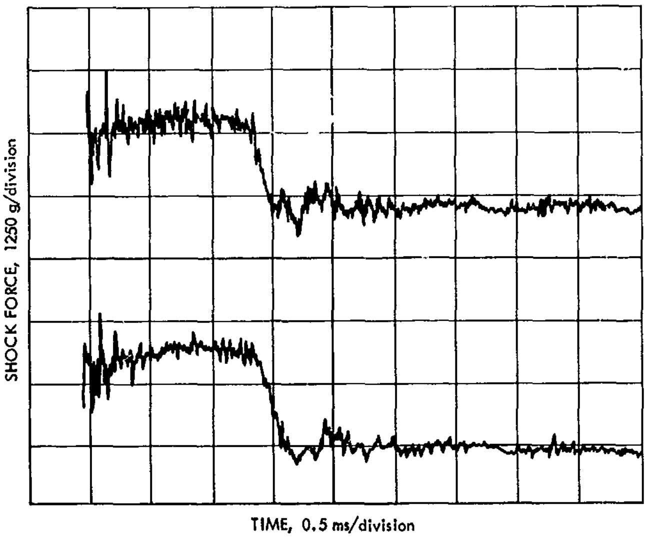

Fig. 2. Typical shock curves

The second method measures the impact velocity v with a set of timing lights placed a few inches in front of the target, and measures the depth d which the impact tool penetrates into the target. Knowing these two quantities and assuming the pulse to be reasonably rectangular, the acceleration level can be calculated from the basic equation for uniformly accelerated motion, $v^2 = 2ad$.

6. Procedure

Parts of known reliability, including resistors (carbon, metal film, wirewound, and trimming), capacitors, diodes, transistors, thermistors, relays, fuses, inductors, and microcircuits, were purchased directly from the manufacturer to assure that the latest manufacturing techniques were used.

All parts except transistors, microcircuits, six diodes and one inductor were mounted by epoxy to aluminum test fixture plates. If the shear stress would be greater than 500 psi, or the tensile stress greater than 750 psi at 10,000 g, a 0.018-in. stainless steel strap was placed over the part. The part was then covered with a coating of polyurethane conformal coating (Solithane 113/300).

The transistors and diodes were mounted separately in a fixture containing holes, into which the transistor or diode can fit. The leads were potted in polyethylene glycol. Power diodes were mounted by their studs in a tapped aluminum fixture and tightened to the specified torque limits.

The inductors were mounted to an aluminum plate, through existing holes, with a strap and two bolts. The microcircuits were mounted to an aluminum plate with adhesive tape.

After mounting, initial parameter measurements were made; then the parts were subjected to 2,000-, 5,000-, and 10,000-g shocks. Parameter measurements were made between each shock level and after the 10,000-g shocks.

7. Test Results

Because of the small sample size tested (15 parts per part type), care was taken to ensure that test samples reflected normal distributions. The following statistics were calculated following each test level on all parameters: mean, median, standard deviation, F test (statistical test of significance of parameter variability), skewness and kurtosis. Histograms were also plotted.

a. Fixed resistors. No catastrophic failures were noted in any of the fixed resistors tested.The mean, median, and standard deviation changed less than 1% as a result of the three levels of shock testing. In all cases the distribution passed the F test at $F_{(0.80)}$. Skewness and kurtosis values were close to normal distributions.

b. Variable trimming resistors. Three parametric failures were noted in the voltage ratio parameter:

(1) One decrease of 81.5% from initial to post 10,000 g.

(2) One increase of 66.8% from initial to post 10,000 g.

(3) One increase of 66.4% from initial to post 10,000 g.

All failures occurred in parts shocked in a direction parallel to the plane of the resistive element. Visual examination yielded no reason for these failures.

The change in the mean of the voltage ratios and resistance of the remaining parts was less than 1%.

The shapes of the distributions were generally normal in skewness but not in kurtosis; however, these values remained constant throughout the tests. The F test was passed at $F_{(0.80)}$.

c. Capacitors. The capacitance and dissipation factor of all parts, with the exception of a few catastrophic failures, changed less than 3%. Two large increases in dissipation factor of 126.6% occurred due to cracking of the glass body on one type tested. One failure occurred at 5,000 g and one at 10,000 g, but both were in shock axes which were perpendicular to the largest surface of the part.

The dissipation of one of the tantalum slug capacitors increased 95% after 10,000-g shock. X-ray analysis revealed that the slug had shifted.

Five catastrophic failures occurred out of the 30 rolled foil capacitors tested. Visual examination revealed that the foil roll shifted when shocked in a direction parallel to the leads causing the internal connecting lead to pierce an insulating wafer and short the capacitor.

d. Transistors. None of the transistors tested failed to the point that the case or the chip was broken or the bonds lifted. Several parts did, however, experience parameter shifts, some of which appeared quite serious. The parameters which did exhibit this change (50% to as high as 1500%) were consistently current measurements. Visual examination, however, failed to reveal the cause.

e. Diodes. Three types of catastrophic failures occurred among the diodes tested. Seven (5 at 2,000 g and 2 at 10,000 g) of the stud-mounted varactors failed when the ceramic spacer on the terminal sheared. One chip of a can-mounted diode cracked at 2,000 g when shocked in an axis perpendicular to the face of the chip. One small diode showed a particularly large increase in forward voltage drop V_F and reverse leakage current I_R measurements. Microscopic examination revealed that the gold ball contact to the chip had shifted.

f. Thermistors. No catastrophic or parametric failures were noted. In the worst case the mean resistance of any part changed less than 4%.

g. Relays. The relays are typically rated for 200 g shock maximum. Some survived the 10,000 g shock pulse. The samples were not tested for contact bounce during the shock pulse. The only requirement was that the relay remained in one contact state before and after the shock pulse and that it was able to function as a relay. Relays by design are basically quite fragile, and are packaged in a very small space. The sample size of this test was too small to make statistically conclusive statements; however, because of the amount of damage sustained it seems unlikely that relays of the types or construction tested can be used at these shock levels.

h. Fuses. No catastrophic failures or appreciable parameter shift occurred.

i. Inductors and transformers. All transformers and inductors that survived behaved in a normal manner. The major problem was providing adequate mounting for the heavier parts. One suggestion would be to completely encapsulate them into a test fixture.

j. Microcircuits. All parts with metal lids to the flat pack failed at 10,000 g when mounted with their faces perpendicular to the shock axis. The failures were caused by the lifting of the metal lid and cracking of the ceramic case. In actual circuit use, the parts would probably be fastened to circuit boards by their leads and conformal coating. This type of mounting could prove to be adequate if it were tested.

8. Conclusions

The best technique of testing electronic components for high-impact survival appears to be to subject the part to a square wave shock of long duration and high magnitude. Components which must withstand up to a 10,000-g shock must be mounted in such a way as to assure that no movement is possible. Component parts selected for high-impact survival must not be constructed in a manner that will allow internal movement of material. Neither can the part be made from fragile materials such as glass, for the mounting of such parts to ensure that there is no movement is difficult without cracking the glass.

References

1. Lonborg, J. O., *High Impact Survival*, Technical Report 32-647. Jet Propulsion Laboratory, Pasadena, Calif., Sept. 30, 1964.

2. Kornhauser, M., "Prediction and Evaluation of Sensitivity to Transient Acceleration," *Journal of Applied Mechanics*, pp. 371–380, Dec., 1954.

3. Lahoti, B., "Improvements on Sling-Shot Shock Testing and Measuring Techniques," presented at 14th Annual Technical Meeting and Equipment Exposition Institute of Environmental Sciences, St. Louis, Mo., April 28–May 1, 1968.

X. Advanced Projects Development

ENGINEERING MECHANICS DIVISION

A. Parachute and Deployment Mortar Jettison Mechanisms, *T. H. Mack*

Mechanisms for jettisoning a parachute and its associated deployment mortar from a planetary landing capsule are under development. The current effort is directed toward a Martian rough-landing mission, but other planetary landing missions are expected to have similar requirements.

For this class of mission, it is necessary to jettison the parachute at impact in such a way that it does not envelop the landed payload and thus interfere with subsequent experiments. The deployment mortar, which is required to deploy the parachute through the wake of the entry body, must be jettisoned so that it does not present a landing hazard for the payload and does not interfere with post-landing antenna patterns.

The conceptual approach that has been taken to provide these functions is as follows:

(1) The deployment mortar is released soon after the peak parachute deceleration loads have passed. The system is at sufficient altitude at this time to ensure that aerodynamic dispersions will separate the mortar and payload impact points sufficiently (Fig. 1a).

(2) At the same time that the mortar is jettisoned, the heavy three-legged parachute bridle (required to carry peak loads) is released. The lander is then attached to the parachute by means of a single line (Fig. 1a).

(3) The parachute is equipped with elastic "jumpers" on some of its suspension lines. The effect is that these lines become shorter than the others when high loads have passed. The parachute/lander system then "glides" at an angle to the vertical, with the parachute leading the lander (Fig. 1b).

(4) At lander impact, the single lander suspension line is severed. By virtue of the gliding geometry, the parachute canopy descends to the surface beyond the lander (Fig. 1c).

Several mechanizations for the mortar and bridle release function have been considered; a prototype of the

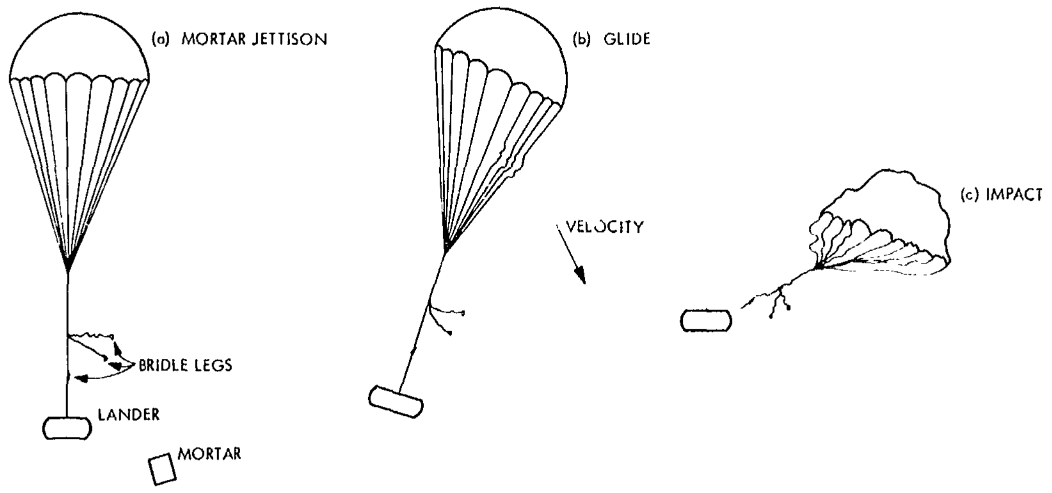

Fig. 1. Parachute and mortar jettison sequence

one selected is shown in Fig. 2. In operation, a pyrotechnic cable cutter would sever a cable passing around the three mortar/bridle clamps about 10 s after parachute deployment. The clamps would then free the mortar as well as the bridle legs. A single line leading from one of the bridle loops to the center of the lander would then become taut, causing the mortar to be thrown off to one side.

Fig. 2. Prototype mortar and bridle release mechanism

The mechanization envisioned for the parachute gliding feature is to "jumper" several of the suspension lines with lengths of elastic shock absorber (bungee) cord. Under high load, these jumpers will stretch sufficiently to allow the suspension lines to take substantially all of the load. At low load, they will effectively shorten the lines and provide the gliding feature.

The final parachute release will be accomplished by using an impact switch to trigger the firing of a pyrotechnic cutter. Much of this hardware was developed during the Capsule System Advanced Development program and will be re-used.

Future plans include performing gliding tests as well as a drop test demonstration of the whole jettison system. This demonstration will employ a parachute typical of the type that might be used in such a mission and a live deployment mortar. The test system will be dropped from a helicopter and allowed to go through the entire functional sequence.

XI. Solid Propellant Engineering

PROPULSION DIVISION

A. Interior Ballistic Design and Experimental Development of a Self-Obturating, Propellant-Actuated Device, O. K. Heiney

1. Introduction

A ballistic launcher capable of deploying a sampling device to a location reasonably remote from a landed vehicle is a potential requirement for proposed future planetary landing systems. Remote deployment would be employed to acquire chemical or mineral specimens uncontaminated by either the presence of the lander or its retro-rocket plume impingement. Device design would be conventional and straightforward except for two additional required characteristics: (1) the system must be self-obturating subsequent to payload ejection, and (2) the system must be compatible with the sterilization requirement. Self-obturation is necessary to prevent (1) possible degradation of the landed vehicle's optical surfaces, and (2) additional area chemical contamination due to combustion products and ejecta associated with ballistic firings.

2. System Design

*a. **Propellant.*** The sterilization requirement is satisfied if a squib and main charge propellant combination can undergo six 56-hr sterilization cycles at 275°F. Surplus squibs from the *Surveyor* program were found to perform adequately after exposure to this environment.

The first main charge propellant investigated, Hercules 8028, was found to be adequate for this application. The propellant, developed during government-funded programs at Hercules, was designed to perform subsequent to extended exposure to high temperatures. It is a rubber-based composite formulation utilizing HMX as the oxidizer. The propellant demonstrates a weight loss of less than 1% and a trace of minor surface discoloration subsequent to exposure to the standard sterilization cycle. Externally, the individual propellant grains did not appear to have been physically degraded; however, the interior ballistic performance of the cycled propellant indicated internal degradation had occurred. This increased tendency of the grains to fragment during the ballistic cycle, although annoying, did not materially inhibit the usefullness of the propellant.

*b. **Launcher.*** The purpose of the launcher is to project an approximately 2-lb claw to acquire a sample which will be returned to the lander and subjected to chemical analysis. For experimental ballistic development, an inert cylinder was used to simulate a retrievable claw. Optimum ballistic design indicated the necessary muzzle velocity of

120 ft/s could best be obtained with a 60 caliber device having a 6-in. stroke. The main charge is 0.8 g of propellant with a web of 0.0048 fired in an initial chamber volume of 0.50 in. The device develops a peak pressure in the area of 5,000 lb. Since it is a requirement that all combustion products be sealed in the bore, a dual development approach was used. A simple lead slug obturation system and a more sophisticated tapered slug and sleeve approach were attempted.

In the lead slug system, shown in Fig. 1a, the payload, D, is propelled down the bore by means of gas pressure on an obturator, A. At stroke completion, the obturator is swaged onto a retainer, B, which is held to the barrel by a locking lug, C. The juncture of the lead obturator and the retainer provides a positive and total gas and debris seal. Subsequent to firing, retained pressure was vented by cracking a relief valve, E, which would not be employed on an operational system. Through a series of firings with sterilized and unsterilized components, this device invariably held the pressure and sealed in all combustion products.

The sliding sleeve system, shown in Fig. 1b, employed a tapered steel projector, F, which, at cycle termination, interfered with, and was stopped by, a tapered aluminum

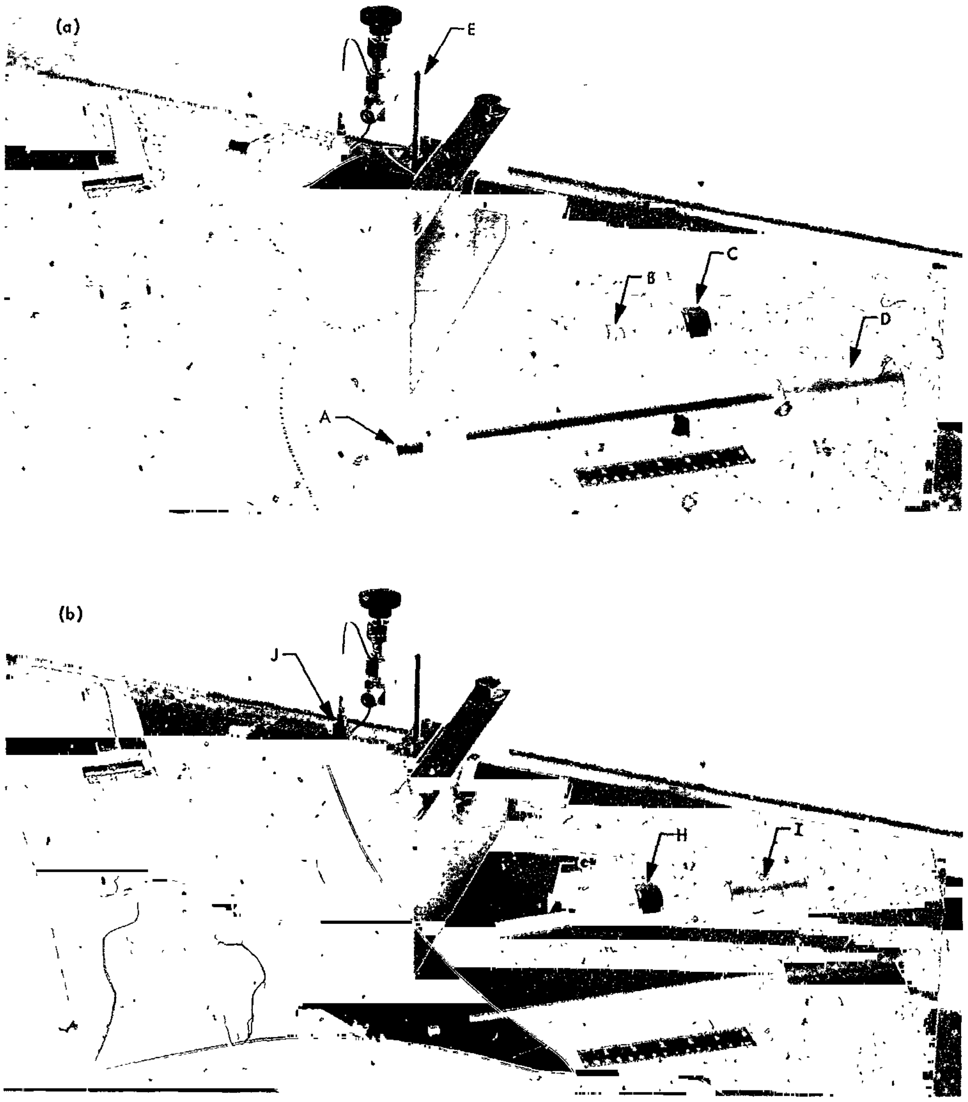

Fig. 1. Ballistic launcher components for: (a) lead-seal and (b) sliding-sleeve systems

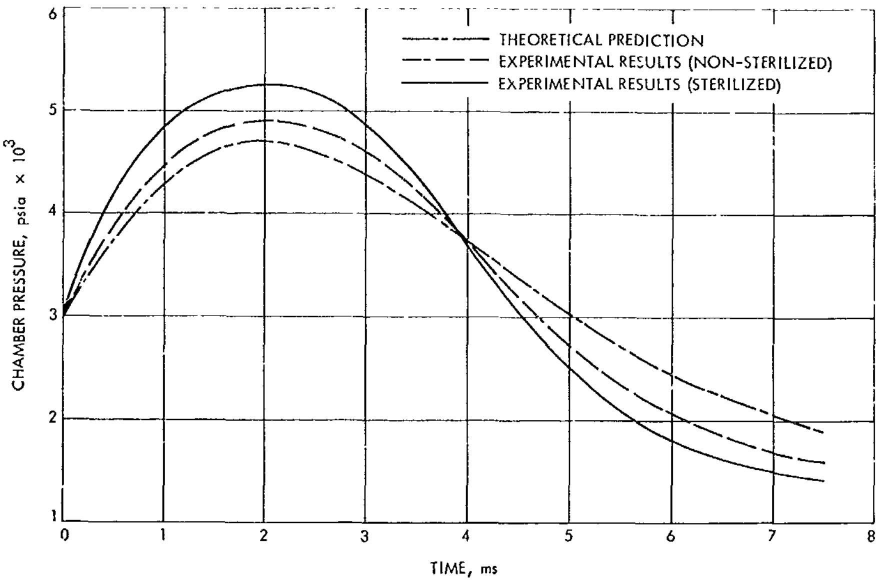

Fig. 2. Theoretical and experimental pressure–time plots

cylinder, G, held in a locking sleeve, I, and retained by a lock nut, H. This system was also effective for holding pressure; however, after several firings the projector became scored and would bleed off gases over a period of several minutes. This would not occur in an operational device since a new projector would be used for each firing.

Pressures were recorded by a Kistler piezometric pressure transducer, J, which fed a charge amplifier, K. The theoretical interior ballistics developed from previous analysis (SPS 37-43, Vol. IV, pp. 167–170) and coded for a digital computer is compared with experimental results and shown in Fig. 2. Note that both sterilized and non-sterilized firings exhibited higher peak pressures than were theoretically predicted. This is due to the squib fracturing a percentage of the propellant grains. For the sterilized system, the effect is more pronounced due to the minor structural degradation experienced during thermal cycling.

Both obturation mechanisms are acceptable and positive, with the lead seal technique being simpler and possibly somewhat more effective.

B. T-Burner Studies, *E. H. Perry*

1. Introduction

The T-burner is, perhaps, the most widely used device for studying combustion instability in solid propellants despite the fact that several important questions surrounding T-burner technique remain unanswered. These questions concern both the possible effects of the T-burner itself on the phenomena under examination, and the equivalence of the various methods of conducting T-burner experiments. Some 200 test firings have now been completed in JPL burners in order to resolve some of these questions and provide a higher level of confidence for future T-burner experiments.

2. Burner and Methods Description

The T-burner, shown in Fig. 3, is a centrally vented cylindrical cavity containing a disk of solid propellant in

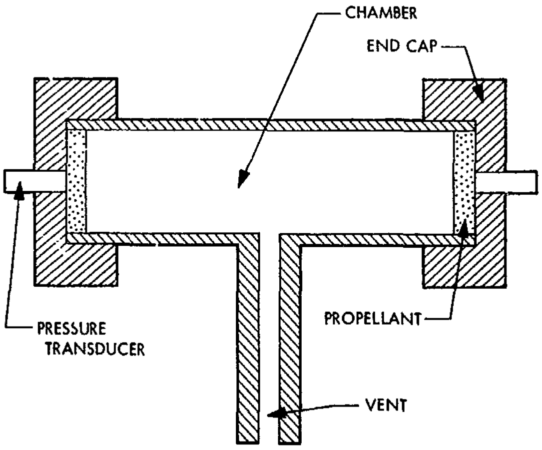

Fig. 3. Cross-sectional view of the T-burner

each end. As the propellant burns, pressure oscillations driven by the burning surface develop in the chamber. These oscillations, observed with pressure transducers behind the propellant, grow exponentially until a limiting amplitude is reached. Remaining near this amplitude until burnout occurs, they then decay exponentially because of losses present in the chamber.

The frequency of the oscillations is controlled by the length of the chamber since, in practice, only the fundamental acoustic mode of the cavity is observed. Frequencies ranging from 250–6000 Hz were obtained in the present experiments by using chambers with lengths varying from 43.5–3.25 in.

The ability of the burning surface to drive such oscillations is measured in terms of the "response function" of the propellant. Knowledge of the response function is the main goal of T-burner experiments since such information permits a calculation of the stability characteristics of a full-scale rocket motor using the same propellant. For a given propellant, the response function depends on mean chamber pressure, initial grain temperature, and the frequency of the oscillations.

Presently, there are two methods, often referred to as the "growth–decay" and "variable-area" methods, of conducting T-burner tests to determine the response function. Using the growth–decay method, one measures how rapidly the oscillations grow during the initial portion of the test and also how rapidly they decay after burnout. The decay rate provides a measure of the losses in the chamber, which are assumed to remain constant during the entire test. Allowing for these losses, one can then calculate how rapidly the oscillations would grow if driven by the burning surface in a lossless chamber. The response function is deduced from these calculations.

In the variable-area method, one measures only how rapidly the oscillations grow. However, in this case the propellant disk covers only a portion of the total cross-sectional area of the chamber. By measuring the growth rate as a function of this area ratio, the response function can be deduced. Further details of these methods are given in Ref. 1.

3. Experimental Comparison of the Two Methods

A comparison of the results obtained by the two methods for the same propellant was undertaken in the present experiments. The propellant used was a PBAN/AP composite, denoted as A-13, supplied by the Naval Weapons Center at China Lake, California. A chamber diameter of 1.5 in., a mean chamber pressure of 315 psia, and an initial grain temperature of 90° F were used in all the tests. For the variable-area tests, area ratios of 1.00, 0.75, and 0.43 were used. Kistler model 603A pressure transducers were used to observe the pressure oscillations in these tests as well as in the others to be discussed later.

The response function determined from these experiments is shown in Fig. 4 as a function of frequency. The upper curve represents values calculated from growth–decay measurements and the lower curve those calculated

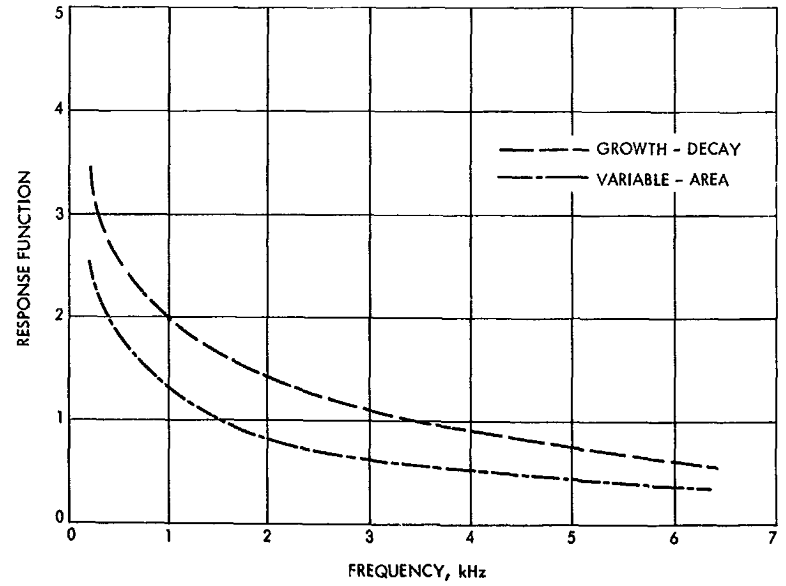

Fig. 4. Response function determined by the two T-burner methods

from variable-area measurements. The poor agreement of the two curves indicates that the two methods of conducting T-burner experiments are not equivalent. Unfortunately, there is no way to determine from these tests which, if either, of the two methods yields correct values for the response function. However, considering the underlying assumptions of the two methods and their relative experimental difficulties, one is inclined to favor the growth–decay method. However, such considerations cannot be taken as conclusive at this time.

4. Effects of Chamber Diameter

Regardless of which method is used, it is clear that the burner itself should have no effect on the response function of the propellant if meaningful results are to be obtained. To determine possible effects of chamber diameter on the response function, values for the A-13 propellant were obtained from tests conducted in burners of different diameter. The growth–decay method was adopted for these tests, and burner diameters of 1.0, 1.5, and 2.5 in. were used. Figure 5 shows the response function determined from these experiments as a function of frequency. It is apparent from these results that the chamber diameter has no effect on response function measurements. This is, perhaps, the most significant, as well as encouraging, fact to emerge from the experiments, since the presence of such effects would greatly reduce the credibility of T-burner results. Thus, it appears that discrepancies among various laboratories on reported values of response functions cannot be attributed to differences in burner diameter, but rather to other, perhaps more subtle, aspects of the test.

5. Comparison of Ignition Procedures

One such aspect is the procedure used for igniting the propellant. For these tests, the normal method was to cover the entire face of the propellant disk with a pyrotechnic igniter paste. Ignition was brought about by passing an electric current through a Nichrome wire in contact with this paste. This method appeared to provide a rapid, simultaneous ignition of both propellant disks in the chamber and resulted in burn times consistent with the known burning rate of the propellant.

In some 30 tests, however, a procedure was followed in which the igniter paste covered only a small portion of the propellant disk. These "spot igniter" tests all had burn times considerably longer than the normal tests, providing perhaps the best evidence that a poor ignition had occurred. More important, however, were the lower rates of growth and decay of the pressure oscillations that accompanied the longer burn times. As a result, the response function calculated from these tests was correspondingly lower. The lower oscillation growth rate was probably due to uneven burning of the propellant, and the lower decay rate due to uneven burnout of the two disks. In any case, it is now evident that ignition procedures can play a rather substantial role in T-burner experiments and should be given careful consideration.

6. Chamber Losses

It is rather apparent that an understanding of the chamber losses is necessary for a complete understanding of the burner. Although the present experiments provide

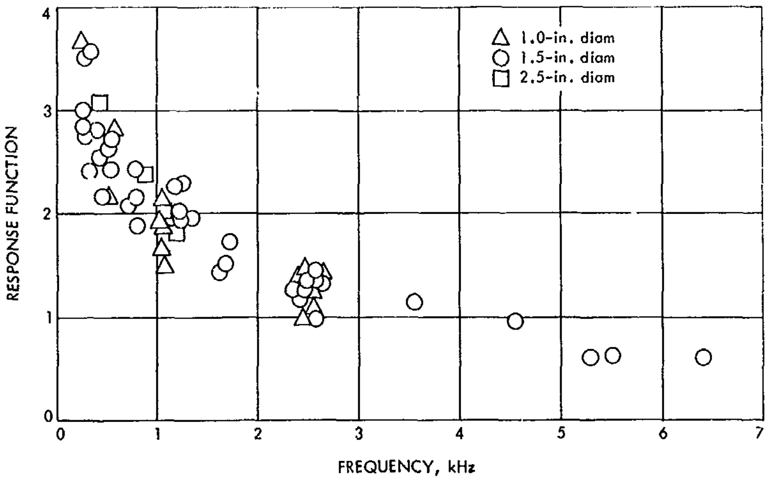

Fig. 5. Response function determined by T-burners of different diameters

some new insights into the nature of these losses, a true understanding of them is still lacking.

The rate of decay of the oscillations after burnout provides a measure of the chamber losses and is measured in terms of a chamber "decay constant." It has generally been assumed that the decay is due to viscous and thermal dissipation at the chamber walls. If this were the case, the losses would be the familiar Kirchkoff–Helmholtz losses of classical acoustics which are proportional to the square root of the frequency and inversely proportional to the chamber diameter. Figure 6 shows decay constants for the three chamber diameters mentioned earlier as a function of frequency. There are two aspects of the losses that are apparent from the figure: (1) the losses increase approximately as the square root of the frequency, as indicated by the dashed line, and (2) the losses show no dependence on chamber diameter.

The latter fact indicates that even though the Kirchkoff–Helmholtz losses are undoubtedly present, other losses either dominate them or at least offset their diameter dependence. Reference 2 provides experimental evidence that large amplitude sound waves are attenuated more strongly than the small amplitude waves generally treated in linear acoustic theory. Since the pressure oscillations present in T-burners are typically very large amplitude waves, the observed chamber losses could arise from such "finite amplitude" effects. However, until further work is done, these are offered only as a possible explanation.

References

1. Beckstead, M. W., and Culick, F. E. C., *A Comparison of Analysis and Experiment for Solid Propellant Combustion Instability*, Technical Publication 4531. Naval Weapons Center, China Lake, Calif., May 1968.
2. Lehmann, K. O., "*Die Dampfungsverluste bei Starken Schallschwingungen in Rohren*," *Ann. Phys.*, Vol. 21, pp. 533–552, 1934.

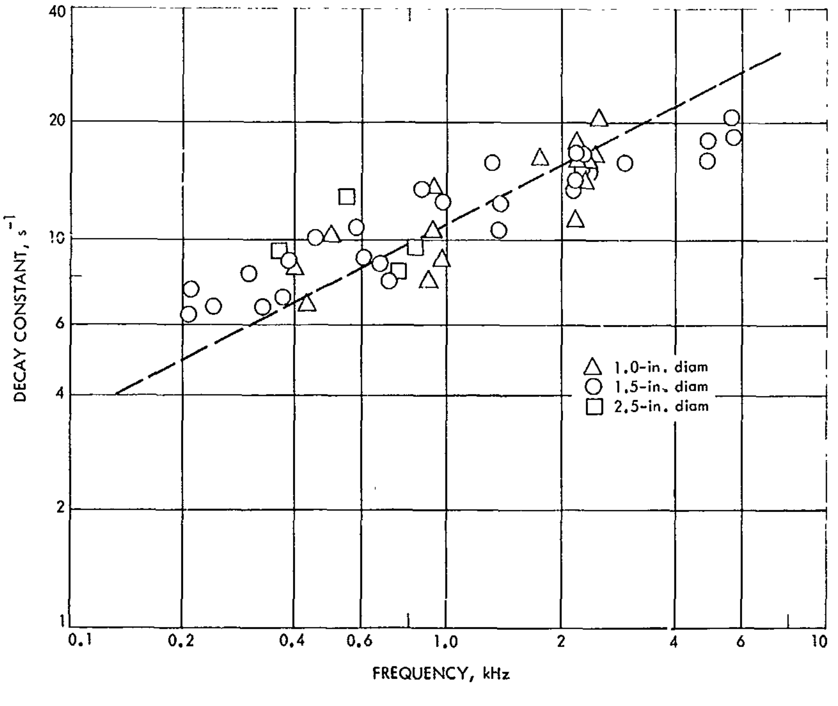

Fig. 6. Chamber decay constants for different diameter burners

XII. Polymer Research

PROPULSION DIVISION

A. A Model for the Effect of Dewetting on Mechanical Behavior of Composites Based on a Parabola-Shaped Void Cavity,

R. F. Fedors and R. F. Landel

1. Introduction

In a previous article (SPS 37-41, Vol. IV, pp. 97–107), a model was proposed which enabled one to relate the stress–strain behavior to the volume dilation, i.e., void formation, for composites which undergo significant strain-induced particle–binder dewetting. It was also demonstrated that the model provided satisfactory agreement with experimental data for SBR[1]–glass bead composites.

The formation of voids leads to two directly observable effects: (1) a relatively large strain-induced dilation, which is a consequence of the formation and growth of voids, and (2) a modified stress–strain response, which is assumed to be related to the continuous decrease, as the voids increase in size, in the fraction of the particle surface area which remains in contact with the binder; it is this latter effect which causes the stress at a given strain level to be lower than it would be in the absence of dewetting. A limit is reached, however, when dewetting occurs to such an extent that the particle surface is essentially no longer in contact with the binder, in which case the stress–strain response of the composite approaches the response of the unfilled binder.

In developing the model, it was assumed that the voids formed were cone-shaped. However, one difficulty of the cone-shaped void is the existence of a discontinuity at the apex of the cone. While such a discontinuity does not affect the calculation of the void volume as a function of the strain or of the fraction of particle surface area remaining in contact with the binder, it may pose problems in other related kinds of calculations, e.g., in stress analysis applications.

For this reason, the previous study has been extended to a consideration of a void having a more realistic parabolic shape, and the purpose of this article is to present these new results.

2. Discussion

a. Development of the model. As in the previous article, we consider a single spherical filler particle imbedded in a binder matrix. Before any strain is imposed on the system, the particle surface is assumed to be completely wetted by the binder as indicated schematically in Fig. 1a. When the composite is strained, dewetting is assumed to occur with the resultant formation of a parabola-shaped cavity on each side of the particle, parallel to the strain axis as indicated in Fig. 1b.

The center of the spherical particle of radius r is located at the origin of a set of x, y, z coordinate axes. The void volume will then consist of the enclosed volume formed

---

[1] SBR = styrene–butadiene rubber.

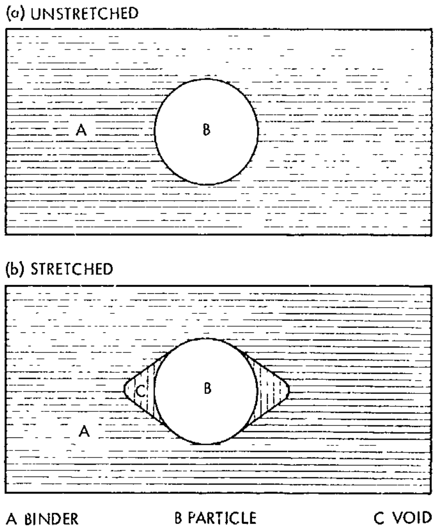

Fig. 1. Schematic representation of a spherical filler particle imbedded in an elastomeric binder

by the intersection of a paraboloid of revolution with a circle of revolution, i.e., a sphere. The dewetted surface area of the particle is then taken as the spherical surface in contact with the void volume. Both the void volume and dewetted surface area will be symmetric with respect to the x-axis and, hence, one can consider the simpler two-dimensional case of the intersection of a circle with a parabola. The quantities of interest are then obtained by permitting both the circle and parabola to revolve about the x-axis.

Figure 2 shows a circle of radius r, with center located at the origin of the x, y axes, intersecting with a parabola symmetrical with respect to the x-axis. The equation of the circle is simply

$$x^2 + y^2 = r^2 \tag{1}$$

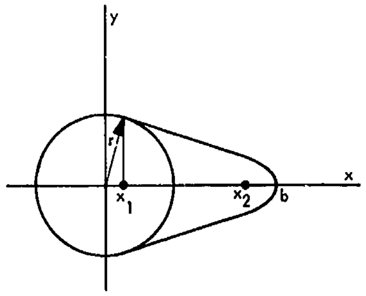

Fig. 2. Details of the parabolic void cavity

We require the parabolic void to simultaneously intersect and be tangent to the circle in the interval $0 \leq x \leq r$, say at the point (x_1, y_1) when the focus of the parabola is at the point $(x_2, 0)$. Further, as x_2 increases, i.e., as the void increases in size, the point of intersection on the x-axis decreases to a limiting value of zero. Because of symmetry, the form of the family of parabolas is taken as

$$y^2 = B(b - x) \tag{2}$$

where B and b are parameters. When $y = 0, x = b$, which represents the maximum separation of the binder from the filler particle. Hence, b $(b \geq r)$ will be referred to as the "length" of the parabolic void, which, as will be shown later, depends directly on the strain. At a fixed value of b, the parameter B is uniquely defined by the condition that the tangent of both the sphere and paraboloid be equal at each point of intersection. Thus, based on this requirement, it is easy to show that the x value at the point of intersection is $B/2$ and further that B is related to b by

$$B = 2\left[b - (b^2 - r^2)^{1/2}\right] \tag{3}$$

Hence, the family of parabolas which define the void shape is given by

$$y^2 = 2\left[b - (b^2 - r^2)^{1/2}\right](b - x) \tag{4}$$

At any value of the parabola "length" b, the fraction of particle surface area remaining in contact with the binder, S_a, is

$$S_a = \frac{x_1}{r} \tag{5}$$

since dewetting is assumed to occur on both sides of the particle.

Only that fraction of the filler which remains in contact with the binder will alter the stress–strain response of the system and, hence, the initial volume loading of filler before dewetting ϕ_0 will, in effect, be reduced according to the fraction of particle surface area enclosed within the void volume. On this basis, the effective volume fraction of filler ϕ_{eff} is given by

$$\phi_{eff} = \frac{\phi_0 x_1}{r} \tag{6}$$

It is assumed, as before, that the separation of the parabola from the particle surface $(b - r)$ is directly proportional to the particle radius and to the effective strain, which is taken to be the difference between the internal strain ϵ_i and the threshold value ϵ_{i0} required to initiate dewetting, i.e.,

$$(b - r) = k_1 r(\epsilon_i - \epsilon_{i0}) \qquad (7)$$

where k_1 is a constant whose magnitude depends on the strength of the filler–binder interaction.

The internal strain is the strain experienced by the binder when an external or overall strain ϵ is imposed on the composite. The relationship between ϵ and ϵ_i can be taken either as

$$\epsilon_i = \frac{\epsilon}{1 - \phi_0^{1/3}} \qquad (8)$$

or as

$$\epsilon_i = \frac{\epsilon}{1 - \phi_0} \qquad (9)$$

depending on the assumption made concerning the manner in which the particles are considered to pack. The latter representation, Eq. (9), is probably a more adequate approximation. Returning to Eq. (6), ϕ_{eff} can now be written as

$$\phi_{eff} = \phi_0[(C_1 + 1) - (C_1^2 + 2C_1)^{1/2}] \qquad (10)$$

where

$$C_1 = k_1 \epsilon_{eff}$$

and ϵ_{eff} is either

$$\frac{\epsilon - \epsilon_0}{1 - \phi_0^{1/3}} \quad \text{or} \quad \frac{\epsilon - \epsilon_0}{1 - \phi_0}$$

as the case may be. This equation can be compared to the expression derived on the assumption of a cone-shaped void,

$$\phi_{eff} = \frac{\phi_0}{1 + C} \qquad (11)$$

where $C = k\epsilon_{eff}$. It is expected that $k_1 \neq k$.

b. Calculation of the void volume. If the void volume per particle is taken as twice the volume of the paraboloid of revolution having a spherical segment as a base, then the relative volume change as a function of the strain is given by

$$\frac{\Delta V}{V_0} = \frac{1}{V_0} \sum_{i=1}^{N} \frac{2\pi n_i r_i^3}{3}$$
$$\times \{C_1[(C_1 + 2)(C_1^2 + 2C_1)^{1/2} - C_1(C_1 + 3)]\} \qquad (12)$$

where n_i is the number of particles of radius r_i and N is the total number of particles present. If the particles are assumed to be monodisperse, then Eq. (12) reduces to

$$\frac{\Delta V}{V_0} = \frac{\phi_0}{2} \{C_1[(C_1 + 2)(C_1^2 + 2C_1)^{1/2} - C_1(C_1 + 3)]\} \qquad (13)$$

which may be compared to the result derived on the basis of a cone-shaped cavity,

$$\frac{\Delta V}{V_0} = \frac{\phi_0}{2}\left(\frac{C^2}{1 + C}\right) \qquad (14)$$

Figure 3 shows a comparison of these equations in the form $2\Delta V/\phi_0 V_0$ versus either C or C_1. Curves 1 and 2 show the behavior of Eq. (13) and (14), respectively, assuming $C = C_1$. As expected, the parabolic void yields a larger value for the volume dilatation at a given strain than does the cone-shaped void. However, there is no *a priori* reason to expect the k values (and hence the C values) will be the same for each model. If one takes $k_1 = 1.93\,k$ ($C_1 = 1.93\,C$), then the dashed curve 3 is obtained, which indicates that in the region of interest,

$$0 \leq \frac{2\Delta V}{\phi_0 V_0} \sim 1.4$$

the two expressions do not markedly differ. The parabolic model predicts a somewhat larger volume increase at small strains and a somewhat smaller increase at large strains than does the cone model. It is probable that either equation can be used to represent experimental data over limited ranges.

c. Effect of dewetting on the modulus. The modulus of a composite, E, in the absence of dewetting can be represented by an equation of the form (SPS 37-41, Vol. IV)

$$\frac{E}{E_0} = \left(\frac{\phi_m}{\phi_m - \phi_0}\right)^n \qquad (15)$$

where E_0 is the modulus of the binder, ϕ_m is the maximum volume fraction of filler which the binder can accept, and

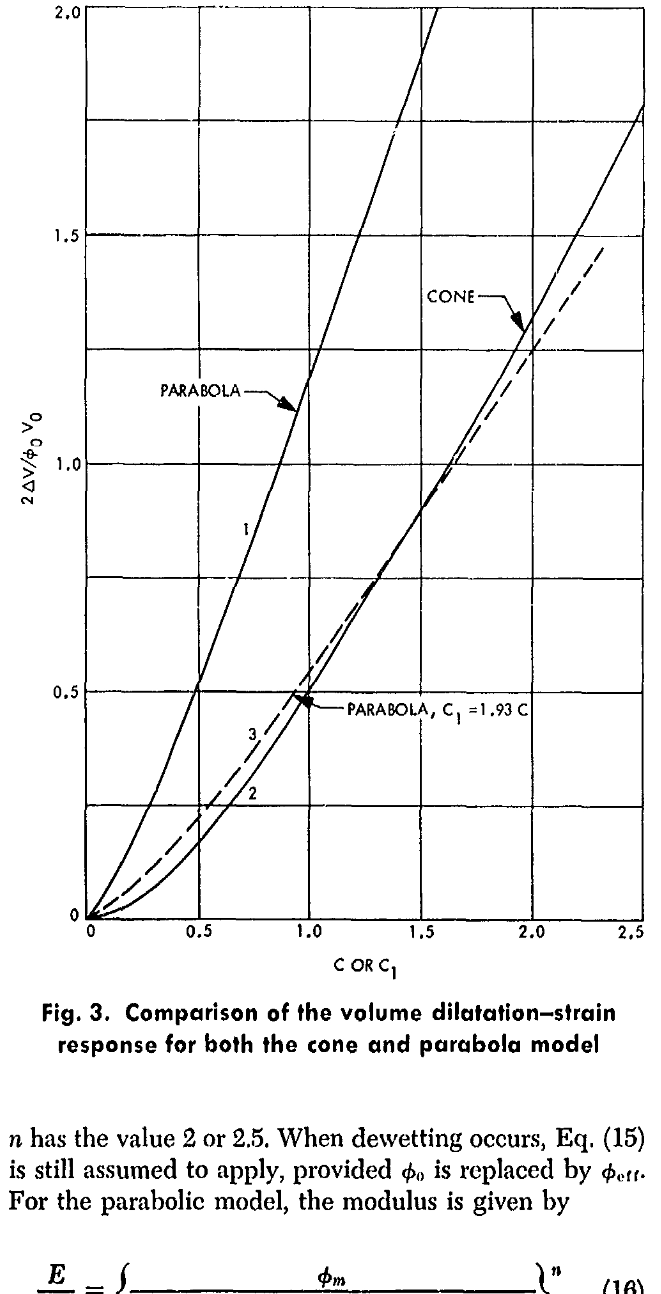

Fig. 3. Comparison of the volume dilatation–strain response for both the cone and parabola model

n has the value 2 or 2.5. When dewetting occurs, Eq. (15) is still assumed to apply, provided ϕ_0 is replaced by ϕ_{eff}. For the parabolic model, the modulus is given by

$$\frac{E}{E_0} = \left\{ \frac{\phi_m}{\phi_m - \phi_0\,[(C_1 + 1) - (C_1^2 + 2C_1)^{1/2}]} \right\}^n \tag{16}$$

which may be compared to the result obtained from the cone model,

$$\frac{E}{E_0} = \left[\frac{\phi_m}{\phi_m - \left(\frac{\phi_0}{1 + C}\right)} \right]^n \tag{17}$$

These equations are compared in Fig. 4 in the form E/E_0 versus C or C_1. The value of ϕ_m was taken equal to 0.63, which is typical for large-size spheres. Values of $\phi_0 = 0.2$ and 0.4 were also used. Previous results (SPS 37-41, Vol. IV) have shown that Eq. (17) adequately describes experimental stress–strain data obtained with SBR–glass bead composites, provided n is set equal to 2 and curves 1 and 2 show the behavior of Eq. (17) for $\phi_0 = 0.4$ and 0.2, respectively. Curves 3 and 4 represent the behavior predicted by Eq. (16) for $\phi_0 = 0.4$ and 0.2, respectively, when n is set equal to 2.5 rather than 2 and C_1 is taken equal to 1.93 C. Comparing curves 1 and 3 for $\phi_0 = 0.2$, it is apparent that the difference is negligible for C_1 or $C > 0.1$. For $\phi_0 = 0.4$, there is a greater divergence, especially for small C_1 or C values, which corresponds to systems at very small strains and/or systems having small k or k_1 values. Reliable data in this region are required to ascertain which model is the more correct. However, for C or $C_1 > 0.5$, the two equations differ at most by only about 6%, and at larger C values, the difference is negligible. Hence, for the SBR–glass bead system, it appears that either model can be employed to describe the stress–strain behavior.

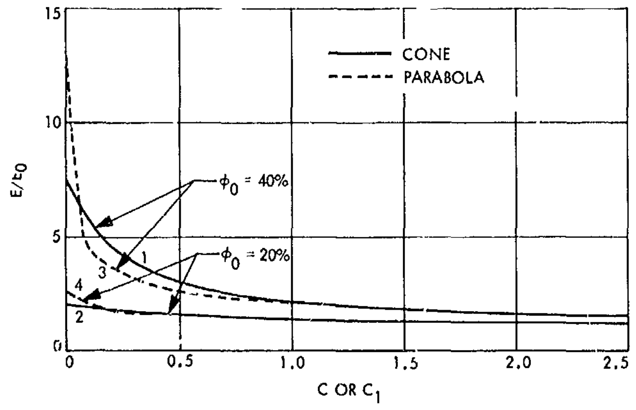

Fig. 4. Comparison of the modulus of a composite as a function of strain for both the cone and parabola model

B. Investigation on Sterilizable Polymer Battery Separators, *E. F. Cuddihy and J. Moacanin*

1. Introduction

Sterilizable battery separators have been prepared from a graft copolymer of poly(potassium acrylate) and polyethylene. This and two preceding articles (SPS 37-50, Vol. III, pp. 166–169, and 37-52, Vol. III, pp. 98–100) report on the continuing efforts to characterize these materials by investigating their chemical and physical properties.

2. Irreversible Dehydration

After service as a separator in Ag–Zn batteries, the initially supple and very elastic membranes are found upon removal to have become brittle, fragile, and easily susceptible to cracking or tearing. Also, these materials become devoid of absorbed water and fail to absorb water from the atmosphere. This is in contrast with the virgin membrane material which equilibriates rapidly in air and at room temperature with large quantities of water (Fig. 5). Further, the elasticity and suppleness of the initial membranes were related to their water content, becoming increasingly brittle as the water content decreased. However, upon exposure to the ambient atmosphere, the virgin membranes quickly resorbed moisture and again became supple and elastic. The loss of hygroscopic properties after battery service was labeled "irreversible dehydration."

The explanation is simple, though it was attendant with a surprising result. The membrane is prepared by grafting chains of poly(potassium acrylate), PKA, on a film of polyethylene (PE). The PE is 50% crystalline and, after grafting, the crystalline content remained unchanged, indicating that all of the grafted PKA was present in the amorphous phase of the PE. The glass transition temperature T_g of PKA is above room temperature, and therefore this material should be hard at ambient conditions. Thus, the incorporation of PKA should render the film brittle. But absorbed water plasticizes the PKA, lowers its T_g below room temperature, making PKA rubbery, and hence the film becomes supple. Thus, the water content directly controls the elastic to brittle property range of the film by its plasticizing action in raising or lowering the T_g of PKA.

In turn, it is a property of the potassium cation to retain in the film sufficient water for plasticization. Reference to Fig. 6, which is reproduced from the literature (Ref. 1), details the influence of the cation on the ability of acrylate–ethylene systems to retain water. Starting with potassium, the propensity for retaining water decreases through sodium, to lithium, and finally to divalent cations, which give almost totally non-hygroscopic properties to the film. Thus, a film prepared with a divalent cation would be brittle at all times in air at room temperature.

Membranes during battery service are exposed to an electrolyte rich in zinc oxide, and it was reasoned that cation exchange between potassium and zinc could occur. This divalent cation would render the film non-hygroscopic and "irreversible dehydration" would result. Analyses for cation identification and concentration were carried out on samples of battery separators both before and after battery service, and the results are given in

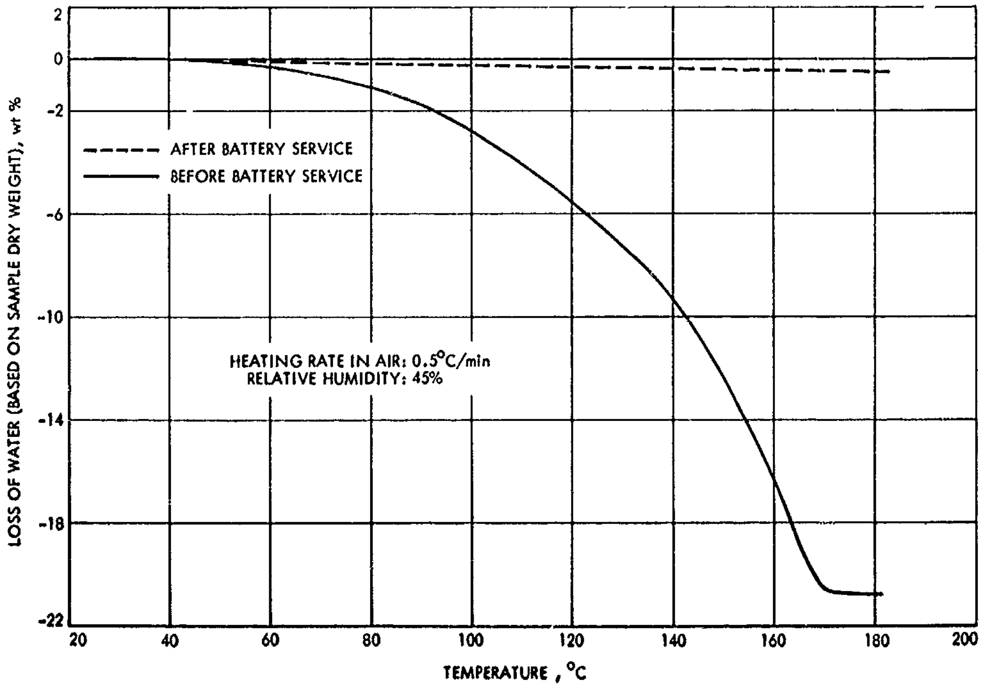

Fig. 5. Thermogravimetric analysis of GX-119 battery separator membranes

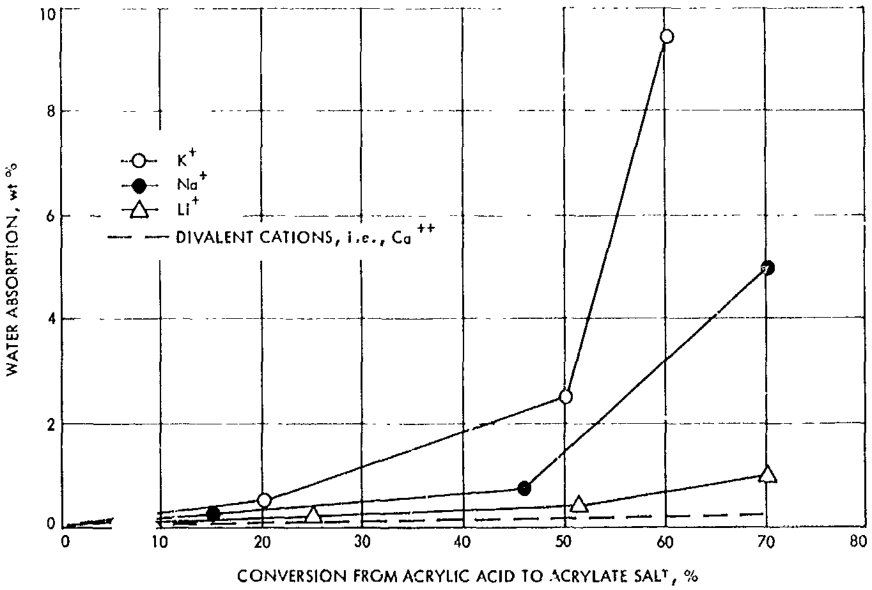

Fig. 6. Retained water content of a 14.8% acrylic acid–85.2% ethylene copolymer after 24-h water immersion at room temperature

Table 1. Expectantly, the separator before service contained dominantly potassium, but the membrane after service contained, quite unexpectedly, not the divalent cation zinc, but the divalent cation calcium. Although the presence of calcium explains why the membranes after battery service are non-hygroscopic, the origin of the calcium is as yet unexplained.

Table 1. Principal cations and their concentrations in GX-119 battery separator membranes before and after battery service

Cation[a]	Sample,[b] wt %	Concentration,[a] meq/g
Before battery service[c]		
K	8.20	2.09
Ca	0.44	0.22
Na	0.23	0.10
Mg	0.14	0.11
Ag	0.005	—
After battery service[d]		
Ca	4.10	2.06
Zn	0.74	0.22
Mg	0.67	0.55
K	0.47	0.12
Ag	0.008	—

[a] Identification and concentration obtained by spectroscopic analysis of the membranes.

[b] Wt. % calculated by employing dry weight of membrane sample.

[c] As received from Southwest Research Institute.

[d] Sections of battery membrane material after service contain a deposit of a blackish substance, presumably Ag_2O. For this study, care was taken to ensure that these sections were eliminated prior to the analysis.

Soaking the poly(calcium acrylate)-containing membranes in mild acid and then in aqueous KOH exchanges potassium for calcium, and the membranes regain their initial suppleness.

3. Zincate

A further point related to the cation exchange is concerned with the state of zinc oxide when dissolved in 40% $KOH-H_2O$ solution. It is currently accepted that zinc oxide reacts with hydroxide to yield the zincate anion $ZnO_2^{=}$, and hence there would be no free zinc ion in solution to exchange with the potassium. This was subsequently tested by placing a piece of membrane containing PKA in a solution of ZnO in distilled and deionized water and another in a 40% $KOH-H_2O$ solution saturated with zinc oxide. Cation exchange to zinc only occurred in the membrane placed in the zinc-oxide water solution, where zinc ions are known to exist. No zinc exchange occurred from exposure in the alkaline solution, indicating the absence of any free zinc ions.

4. Simple Analytical Technique for Acrylate Content

The battery separator membrane assumes non-hygroscopic properties not only in the presence of divalent cations but also when the acrylic part is in the acid state.

Hence, very accurate weighings of the membranes in either state can be made in air without interference from atmospheric moisture. Thus, the difference in weight of a sample when in the acid form and when containing a divalent cation is directly related to the acrylate content. Complete conversion from acid to salt and vice versa can be accomplished usually within an hour by soaking the membranes in either a 5–10% acid solution or a basic solution of the hydroxide or oxide of the desired divalent cation. Confirmation of the complete conversion from one form to the other is easily obtained by the change in the very sensitive and strong IR peaks for the acid at 5.58 μ and the salt at 6.45 μ.

5. Crosslinking

The membranes are prepared by first grafting chains of PKA onto PE and then crosslinking the system with divinylbenzene (DVB). Both reactions are initiated by exposure to γ-radiation from a cobalt 60 source and occur exclusively in the amorphous phase of the PE. The crosslinking is required to ensure that the film stays together when heated during sterilization at temperatures above the PE melting point of 107°C.

The extent of crosslinking can be obtained by measuring the stress–strain curves of the film when swollen in α-chloronaphthalene at 125°C. The high temperature is required to ensure that all the crystalline PE is melted and will therefore give no contribution to the mechanical strength. In addition, the swelling in a good PE solvent is required to disentangle the polymer chains and cause them to separate only to the extent allowed by the crosslinks. Hence, the strength of the film as measured by the initial modulus of the stress–strain curves will now be directly related to the number of crosslink sites.

Stress–strain measurements at 125°C in α-chloronaphthalene were carried out on (1) a membrane both grafted and crosslinked, (2) a membrane just grafted, and (3) a membrane just crosslinked. The results, summarized in Table 2, show that the grafted and crosslinked sample has a crosslink density of 1120×10^{-6} moles crosslink chains/cm^3, the just-grafted sample has a crosslink density of 669×10^{-6} moles crosslink chains/cm^3, while the sample presumably crosslinked with DVB, the crosslinker, was so negligibly crosslinked it couldn't be measured. For comparison, crosslinked rubbers typically have values between $100–200 \times 10^{-6}$ moles crosslink chains/cm^3 while hard, cured epoxy resins have values in excess of 1120×10^{-6}.

The surprisingly high value of 669×10^{-6} for the just-grafted membrane clearly indicates that the grafted chains are actually crosslinking the system. Given now the concentration of these chains in the membrane, as well as the amount of PKA in the film, the molecular weight of the PKA chain is readily calculated to be 780, which corresponds to a degree of polymerization of 7.

Table 2. Mechanical properties at break[a] and crosslinking densities of battery separator membranes for the GX-119 series

Membrane description	Tensile strength, psi	Elongation, %	Crosslink density,[b] moles crosslink chains/cm^3
Both grafted with poly(potassium acrylate) and crosslinked with divinyl benzene	540	29	1120×10^{-6}
Just grafted with poly(potassium acrylate)	445	40	669×10^{-6}
Just crosslinked with divinyl benzene	← Footnote c →		

[a] Stress–strain measurements obtained at 125°C on samples swollen in α-chloronaphthalene. This permits the direct measurement of the contribution to properties from the crosslinked network, and therefore the crosslinking density.

[b] For comparison, rubber has a crosslink density between 100 to 200 moles crosslink chains/cm^3.

[c] Stress–strain measurements unobtainable since sample came apart in α-chloronaphthalene at 125°C.

After grafting, DVB is then incorporated into the film, and the crosslink density increases from 669×10^{-6} to 1120×10^{-6}. Clearly, if this difference of $(1120 - 669) \times 10^{-6} = 451 \times 10^{-6}$ existed in the PE film just crosslinked with DVB, it would have had a reasonable strength, but, in actual fact, it disintegrated in α-chloronaphthalene. Since the amounts of reacted DVB are equal in both cases, the implication is that more of the DVB is consumed in a crosslinking capacity in the presence of acrylate than is in the presence of PE only. Perhaps, in absence of PKA, DVB tends to polymerize into long chains of poly(divinylbenzene) rather than induce crosslinking.

In the early stages of development of these membranes at Southwest Research Institute, the procedure was to crosslink first, followed by grafting. However, inferior products were obtained. Subsequently, the procedure was reversed and greatly improved membrane materials were obtained. Perhaps, as the results here indicate, the crosslinking densities in their initial products were too low, or the DVB in the PE interfered with PKA grafting.

One final point on crosslinking is worth noting. As has been pointed out, the membranes during battery service are experiencing cation exchange from potassium to calcium. This divalent cation, by connecting across two acrylate groups, increases the crosslinking density. If, during battery service, degradative reactions are occurring which destroy the crosslinking introduced by the PKA and DVB, then the cation exchange to calcium would provide offsetting crosslinking and preserve the mechanical strength of the membrane. Some evidence of this was obtained by converting a used battery separator from the calcium salt back to the potassium salt, and noting that, although the elastic and supple properties returned, the material had greatly reduced tear resistance as compared to a membrane that had not seen battery service.

b. Silver Oxide Problem

During battery operation, silver oxide (Ag_2O) is formed on the silver electrode, and this material has a finite solubility (4×10^{-4} molar) in the $KOH–H_2O$ electrolyte. Silver oxide can then freely migrate to the zinc electrode, where it can be reduced to metallic silver. The membrane's intended function, in dividing the cell, is to keep the dissolved silver oxide on the silver electrode's side. However, some silver oxide does permeate the membrane, but also there is a continuous deposition of solid silver oxide within the interior of the membrane. This deposition continues until the volume concentration of the silver oxide builds to a sufficient level where battery performance deteriorates due to the onset of "high-resistant–short-circuiting" across the membrane. Even an insulating solid in thin enough layers can have some measurable electrical conductivity.

This deposition is a failure mode of the battery, as are any problems which arise from metallic silver accumulation at the zinc electrode. In addition, silver oxide dissolved in strong alkaline medium is a strong oxidizing agent, intermediate between the oxidizing powers of permanganate and perchlorate. This can lead to oxidative damage of the membrane, such as oxidative scission of the crosslinking introduced by the PKA and DVB reactions. Perhaps this is the testimony to the desirability of the divalent cation exchange in the membrane to preserve the crosslinking level. Finally, another failure mode, unrelated to silver oxide, is the growth at the zinc electrode of crystalline whiskers whose sharp points can pierce the membrane and provide a direct short-circuit path, which may eventually touch the silver electrode.

Although there is considerable effort being expended to find solutions for each of the failure modes posed by the presence of the dissolved silver oxide, such as perm-selective membranes, one direct approach seems to lie in finding methods to simply reduce silver-oxide solubility —additives, for instance, which would not interfere with battery operation but which would lower or eliminate silver-oxide solubility. The feasibility of this approach was demonstrated by observing that the solubility of silver oxide was reduced by a factor of over 20 in a solution of 40% KOH in a mixed solvent system of 80 vol % water and 20 vol % methanol. Though this solution is compatible with the membrane, it performed poorly as a battery electrolyte, as can be seen from its current–voltage characteristic curve given in Fig. 7. In fact, all solutions containing greater than 5 vol % methanol failed as candidate electrolytes, all giving gaseous products at the negative electrode at an applied potential of only 0.6 V. The Ag–Zn batteries are normally changed at an applied potential of 1.5 to 1.6 V.

Investigations will continue on electrolyte systems which are operational in a Ag–Zn battery and which will have lowered silver-oxide solubility.

Reference

1. Bonotto, S., and Bonner, E. F., *Polymer Preprints*, ACS, Vol. 9, No. 1, p. 537, Apr. 1968.

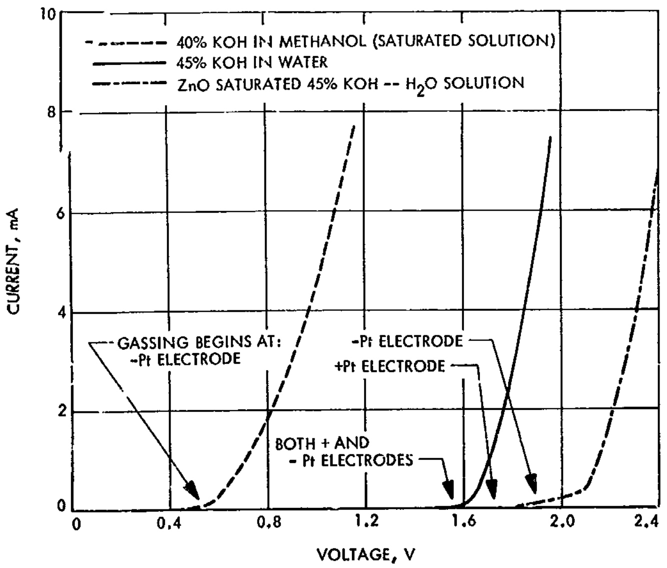

Fig. 7. Current–voltage characteristic curves for various battery electrolytes measured by employing platinum electrodes

C. Creep of Elastomer Undergoing Aging,

J. Moacanin, H. Y. Tom, R. F. Fedors, and R. F. Landel

1. Introduction

A long-standing goal of the research program on the mechanical properties of solid composite propellants and their elastomeric binders has been to be able to predict their properties from molecular parameters characteristic of the binders (Refs. 1 and 2). This goal has now been reached and a comprehensive theory developed (Ref. 3).

For example, modulus values, as well as breaking strengths, can be estimated over wide ranges in time or temperature without using any arbitrary parameters. Though developed in a program related to solid composite propellants, these results also have implications for long time behavior of materials such as sealants for high-speed aircraft fuel tanks, or rubbers for shock mounts. However, in the long time region, i.e., at quasi-equilibrium in terms of the kinetic theory of rubberlike elasticity, there are two main reasons that prevent a straightforward application of this development: (1) the theory in its present form does not account for degradation reactions, which may be too slow to be ascertained from short time measurements; (2) there exist poorly understood slow relaxation processes whose effects are presently accounted for by an empirical equation due to Plazek (Ref. 4).

Plazek studied the creep compliance in shear of natural rubber and styrene-butadiene rubber (SBR), but also found that Thirion's (Ref. 5) stress relaxation data on specimens from the same sheets were in complete accord with his creep data. (Both were very careful to exclude chemical degradation.) The good agreement between the results from these two types of experiments and our own constant strain-rate data confirm the validity of Plazek's equation but, of course, this does not mean that it will be generally valid for all elastomers.

Therefore, a program has been initiated to combine our studies on mechanical properties with those on the chemical reactions of such materials to develop, through an interdisciplinary approach, improved methods of predicting long-term or fatigue behavior of such materials. This article explores in particular the implications of Plazek's work on the interpretation of the creep behavior of slowly degrading systems.

2. Discussion

Plazek showed that, in addition to the usual time–temperature superposition for the viscoelastic response of a crosslinked elastomer, a superposed curve for long time response could be obtained using the apparent molecular weight between crosslinks M_c as a reduction variable. Thus, by carrying out measurements at several temperatures and M_c levels, one can obtain the viscoelastic response for a reference temperature and reference M_c over 9 or 10 decades of logarithmic time.

Plazek's master curve for creep compliance—the starting point for this work—is shown in Fig. 8 and is given by

$$\log J_x\left(\frac{t}{a_x}\right) = \log J_e(M_c) + \log\left[\frac{J_e(M_{ref})}{J_e(M_c)}\right] + \log \psi_x\left(\frac{t}{a_x}\right) \tag{1}$$

where $J_e(M_c)$ is the equilibrium compliance corresponding to M_c, the ratio in the second term represents the vertical shift that brings the response for the specimen onto the level of the reference curve, and ψ is a terminal retardation function which describes the very slow approach to equilibrium. The factor $\log a_x$, which provides the reduced

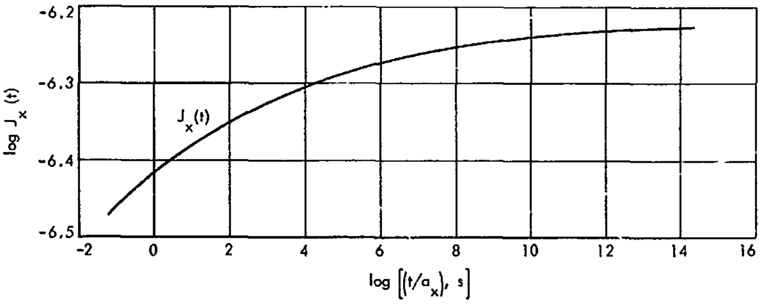

Fig. 8. Logarithmic plot of $J_x(t)$, extended compliance curve resulting from reduction using M_c as a reduction variable, vs logarithm of reduced time t/a_x (M_c varies between 5200 and 20,500)

time scale, represents the horizontal shift necessary to achieve superposition. The shift factor a_x was found to be an exponential function of M_c:

$$a_x = \text{const} \times M_c^m \qquad (2)$$

with $m = 15.4$ for both natural rubber and SBR.

It follows from this development, once the master curve for an elastomer is established and, consequently, the $a_x - M_c$ relationship is known, that M_c is the only parameter needed to predict the creep compliance of a given specimen at time t. Also, one can use the compliance curve to calculate other rheological properties via the distribution of retardation times.

Accepting that the above considerations account for mechanical effects, the relationship between a_x and M_c suggests a method of incorporating the effects of chemical changes into the same formalism. We merely let M_c, and hence a_x, become a time-dependent parameter whose value is determined by the appropriate degradation kinetics.

For studying degradation, it is preferable to use the effective number of chains ν_e as the operational parameter, instead of M_c. The relationship between the two is taken as $\nu_e = \rho / M_c$ moles/cm^3. Note that M_c, the apparent molecular weight of a network chain as defined here, is not the same as M_c', the true molecular weight of an elastically effective chain; in general, $M_c > M_c'$.

For the description of a system undergoing degradation, it is appropriate to use the initial material as reference; then the master curve describes the behavior of the undegraded material. As degradation proceeds, a_x departs from unity:

$$a_x(t) = \left[\frac{M_c(t)}{M_c(0)}\right]^m = \left[\frac{\nu_e(0)}{\nu_e(t)}\right]^m \qquad (3)$$

By an appropriate horizontal shift, i.e., log $a_x(t)$, and vertical shift, i.e., log $J_e(0)/J_e(t)$, in a double logarithmic plot of $J(t)$ versus t, one arrives at the compliance of the degraded material. This statement implies that the state of the system is determined uniquely by the value of $a_x(t)$, and does not depend on its history. This is an approximation whose effect is illustrated in Fig. 9. The two solid curves indicate the compliance–time relationships for elastomers, in the absence of degradation, crosslinked to different extents.

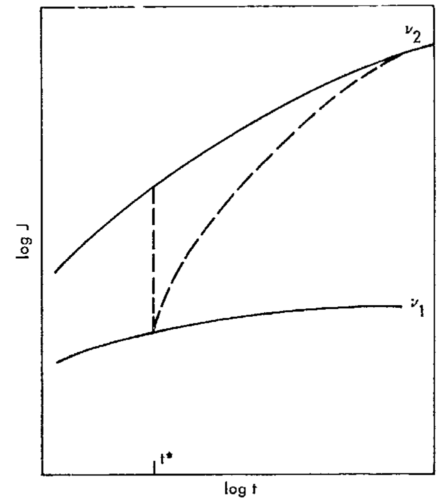

Fig. 9. Implication of the assumption that the network responds instantaneously to changes in ν_e

Now suppose that specimen ν_1 is suddenly degraded to ν_2 at t^*. According to this approximation, it should assume instantaneously the compliance for ν_2 at t^*. Clearly, this is an idealized situation, for a real system would gradually approach the curve ν_2. The approximation should not be too serious, however, as long as the degradation processes are slow, because then $\nu(t + \Delta t)/\nu(t) \approx 1$, i.e., the two curves are close together, and the difference in the paths is very small. Moreover, the approximation overestimates the rate of creep, and, therefore, will lead, for example, to conservative fatigue estimates.

It is to be noted that considerable work has been done on the behavior of elastomers at elevated temperatures (Ref. 6). Under these conditions, ψ_x may approach unity. If so, it can be assumed that the elastomer is at equilibrium (i.e., at J_e) at all times, and, hence, relating changes in the mechanical response to degradation is straightforward.

Initially, there are $\nu(0)$ chains. At time t we suppose that $q(t)$ cuts have occurred, some of which may be multiple cuts on the same chain, leaving $\nu(t)$ elastically effective chains to support the load. These are the chains which have not experienced a single cut. It is necessary, therefore, to derive the relationship between $\nu(t)$ and $q(t)$, i.e., $\nu[q(t)]$, since the mechanical response is determined by $\nu(t)$ whereas chemical kinetics of degradation will yield $q(t)$.

As an illustration of the approach to be taken in incorporating degradation kinetics, let's consider the simple case of first-order kinetics which has been shown to apply to some real systems, e.g., oxidative degradation of natural rubber. If each cut were effective, then

$$\nu(t) = \nu(0) - q$$

and, in accordance with the postulated kinetics,

$$\frac{d\nu(t)}{dt} = -k'\nu(t)$$

or

$$\frac{\nu(t)}{\nu(0)} = \exp(-k't)$$

Also, in view of Eq. (3),

$$a_s(t) = \exp(mk't) \qquad (4)$$

Figure 10 shows the compliance curve for an elastomer where M_c is 20,500, m is 15.4 (the value for natural rubber), and where $\nu(t)/\nu(0) = ½$ after 1 day in one case, and after 1 yr in the other case. It is apparent that, after one half-life, properties deteriorate too rapidly to be of much interest.

Future work will use existing kinetic data for a system like natural rubber to estimate the degradation rate at low temperatures, such as ambient, and then attempt a realistic comparison of the predicted and experimentally determined behavior. Such an analysis is necessary to ascertain the range of conditions where one may expect to be able to separate chemical from purely mechanical contributions to behavior.

References

1. Landel, R. F., and Fedors, R. F., *Processes in Polymeric Solids*, p. 361. Interscience Publishers, New York, 1964.
2. Landel, R. F., *Office of Naval Research Structural Mechanics Series, Mechanics and Chemistry of Solid Propellants*, proceedings of the Fourth Symposium on Naval Structural Mechanics, pp. 575. Pergamon Press, New York, 1967.
3. Fedors, R. F., and Landel, R. F., "A Test of the Predictability of the Properties of Filled Systems," presented at the AIAA Meeting, Washington, D.C., June 1967.
4. Plazek, D. J., *J. Poly. Sci.*, A-2, Vol. 4, p. 745, 1966.
5. Thirion, P., *Proceedings of the International Conference on the Physics of Non-Crystalline Solids*, p. 345. North Holland, Amsterdam, 1965.
6. Tobolsky, A. V., *Properties and Structure of Polymers*, Chapt. V. John Wiley & Sons, Inc., New York, 1960.

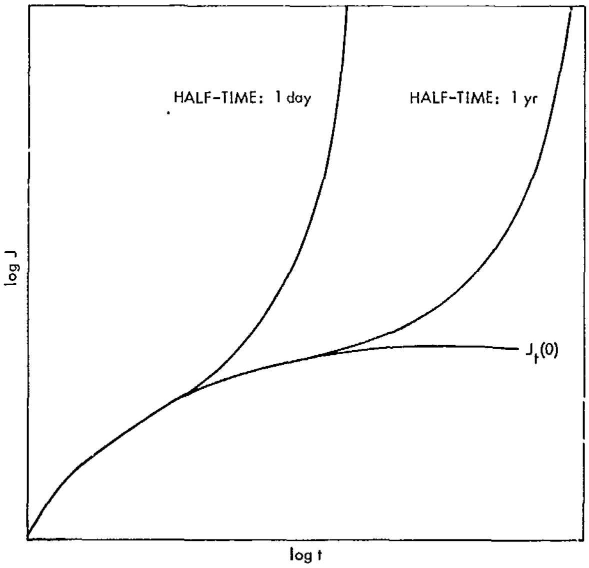

Fig. 10. Compliance curves for networks undergoing degradation

D. Stress Relaxation in Compression of SBR–Glass Bead Composites,

J. Moacanin and H. Y. Tom

1. Introduction

A solid-propellant grain undergoing heat sterilization experiences a complex history of tensile and compressive stresses. A simple test was devised to ascertain the changes which may be taking place in the propellant during sterilization. A cylindrical polyurethane propellant slug was confined to a fixed length in the clamp; the ends of the specimen were bonded to the clamp plates. Starting at room temperature, the specimen was unstressed. As the temperature was gradually raised to 135°C, the specimen experienced compressive stresses (Fig. 11) because its expansion was restricted. While the temperature was maintained at 135°C, stress relaxation took place; the final stress level was about ¼ of its maximum value. At the end of the cycle, when the specimen was cooled to room temperature, it experienced a significant tensile stress. The specimen did not return to its initial unstressed state, because the relaxation at 135°C was caused in part by chemical exchange of the urethane bonds in the binder. At room temperature, however, the rate for this process is too slow to contribute to the overall relaxation process.

These observations could not be interpreted quantitatively, however, because stress relaxation is caused by

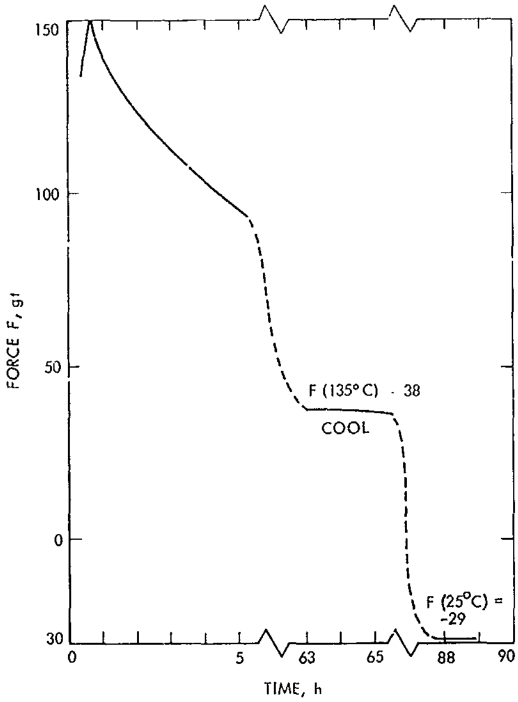

Fig. 11. Stress in a polyurethane propellant test specimen undergoing heat sterilization

the superposition of the following effects: mechanical relaxation, dewetting of filler, and chemical degradation and exchange reactions. To identify and ultimately assess the extent of each contribution, a separate study was conducted on the stress relaxation in compression of styrene–butadiene rubber (SBR) filled with glass beads. For the experimental conditions which were used, chemical degradation and exchange reactions should be negligible. Thus, these experiments enabled us to focus our attention on the contribution of dewetting.

2. Experimental Technique

Styrene–butadiene rubber test specimens loaded with varying amounts of glass (0.000 to 0.339 volume fraction) were prepared, following a slightly modified procedure described previously for thin sheets (SPS 37-32, Vol. IV, pp. 120–125). The test specimens (1.2 cm long × 1.8 cm diameter) were cured in the press for 3 h at 154.5°C, and then let stand in a vacuum chamber for 3 h at 130°C, before removal from the mold. By including the last step, clear bubble-free specimens could be obtained. The effective number of chains ν_e was assumed to be the same for all samples, since the same peroxide concentration was used; determinations of their values by swelling are underway.

The stress relaxometer was constructed with a LVDT load cell (Daytronic, 152A), excited and amplified by a signal conditioner (Daytronic, 300 D with type 71 plug-in module). The output from the force transducer was recorded by a strip chart recorder (Leeds and Northrop, model G). To minimize temperature fluctuations in the load cell, a flow of nitrogen gas maintained at room temperature was circulated past the head. A further precaution against thermal influence was taken by extending the coupling between the head and sample with a long univar rod. The stability of this instrument over a 24-h period was found to be ±20 g.

In a typical experiment, the test specimen was placed between two plates, where one was fixed and the other coupled to the load cell. The sandwiched specimen was then immersed into an oil bath fixed at 50 ±0.5°C. After ½ h, it was gradually compressed until a reasonably high stress was attained. The gage reading corresponding to the initial length l_0 was determined by extrapolating linearly to zero force. The specimen was then allowed to relax at l_0 for at least 10 min before compressing to the desired level.

The stability of the experimental setup was assessed by conducting a control experiment for 24 h with the test specimen held at l_0. No increase in instrument instability or significant oil sorption from the constant temperature were observed.

The following changes would substantially improve the instrumentation. Better temperature control for the electronics would minimize drift and therefore improve long time stability. A clamp to quickly strain the test specimen (< 1 s versus 15–20 s required now) would extend data to short times.

3. Results and Discussion

In earlier articles,[2] various aspects of the mechanical behavior of composite systems in tensile deformation have been discussed in some detail. In particular, strain-induced particle-binder dewetting was described, and a theoretical model was proposed which predicts the isothermal volume dilatation. Pursuant to these investigations, the reinforcing effect of the filler particle is proportional to the loading fraction ϕ and the fraction of the filler surface in contact with the binder. Thus, for

---

[2] SPS 37-32, Vol. IV, pp. 120–125; SPS 37-35, Vol. IV, pp. 93–98; SPS 37-40, Vol. IV, pp. 80–83; and SPS 37-41, Vol. IV, pp. 97–107.

small strains without dewetting, the modulus E for the filled system is related to that of the binder E_0 by

$$\frac{E}{E_0} = \left(1 - \frac{\phi}{\phi_m}\right)^{-2.5} \tag{1}$$

where ϕ_m is the maximum attainable volumetric loading fraction.

As the binder pulls away from the filler surface, the effective loading level for tensile deformation and a spherical filler particle is given by

$$\phi_{eff} = \phi \sin\theta \tag{2}$$

where the angle $\theta = 90\ \text{deg} - \theta$ defined in SPS 37-41, Vol. IV.

This result was obtained by assuming that the void formed is conical in shape. The fraction of particle surface still in contact with the binder is then given by $S_a = \sin\theta$, where the angle θ defines the base of the tensile cone in contact with the sphere (Fig. 12). Using the same model for compression, instead of two cones with their axis parallel to the direction of stress, one obtains a doughnut-shaped body with the axis of revolution parallel to the compressive stress. Carrying out the analysis, we arrive at $S_a = \sin\theta$, leading to

$$\phi_{eff} = \phi\,(1 - \sin\theta) \tag{3}$$

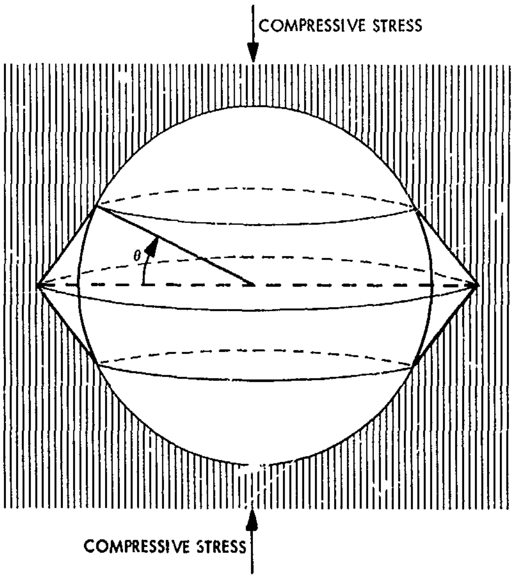

Fig. 12. Schematic of dewetting

Allowing ϕ_{eff} to vary with time, because of dewetting, Eq. (1) can be rewritten as

$$\frac{E}{E_0} = \left(1 - \frac{\phi_{eff}}{\phi_m}\right)^{-2.5} = \left(1 - \frac{\phi}{\phi_m}\right)^{-2.5} \left(1 + \frac{\dfrac{\xi_t}{\phi_m}}{\dfrac{1-\phi}{\phi_m}}\right)^{-2.5} \tag{4}$$

where

$$\phi_{eff}(t) \equiv \phi - \xi_t$$

ϕ being the value for $t = 0$; hence, ξ_t represents the decrease in ϕ for given t. Since by postulate ϕ_{eff} is proportional to S_a, then

$$\frac{\phi_{eff}(t)}{\phi} = 1 - \sin\phi = 1 - \frac{\xi_t}{\phi}$$

or

$$\sin\theta = \frac{\xi_t}{\phi}$$

On the other hand, it was found (SPS 37-41, Vol. IV) that the rate of volume dilation in tension is proportional to the cube root of time $t^{1/3}$. Accepting the same relationship for compression, one can write

$$\frac{\Delta V}{V_0} = \frac{\phi}{2}\,\frac{\sin^3\theta}{1 - \sin^2\theta} = \frac{\phi}{2}\left(\frac{\dfrac{\xi_t^3}{\phi^3}}{1 - \dfrac{\xi_t^2}{\phi^2}}\right) = \beta t^{1/3}$$

Thus

$$\beta^{1/3}\, t^{1/9} = \frac{\left(\dfrac{\phi}{2}\right)^{1/3} \dfrac{\xi_t}{\phi}}{\left(1 - \dfrac{\xi_t^2}{\phi^2}\right)^{1/3}} = \left(\frac{\phi}{2}\right)^{1/3} \frac{\xi_t}{\phi} + 0\left(\frac{\xi_t^3}{\phi^3}\right)^{1/3} \tag{5}$$

Only the term in ξ_t/ϕ need be retained, since the ratio is $\ll 1$. With the proper substitutions, Eq. (4) predicts for compression

$$\frac{\sigma}{\sigma_0} = \left(1 - \frac{\phi}{\phi_m}\right)^{-2.5} \left[1 + \frac{\dfrac{\phi}{\phi_m}}{\dfrac{1-\phi}{\phi_m}} \left(\frac{2\beta}{\phi}\right)^{1/3} t^{1/9}\right]^{-2.5} \tag{6}$$

or

$$\left(\frac{\sigma_0}{\sigma}\right)^{0.4} = \left(1 - \frac{\phi}{\phi_m}\right) + \frac{\phi}{\phi_m}\left(\frac{2\beta}{\phi}\right)^{1/3} t^{1/9} \qquad (7)$$

From Eq. (7), it follows that a plot of $\sigma_0/(\sigma)^{0.4}$ should be linear in $t^{1/9}$, the intercept giving $(1 - \phi/\phi_m)$ and the slope being $\phi/\phi_m(2\beta/\phi)^{1/3}$.

The experimental results for the SBR–glass beads system were treated according to the above scheme. Figures 13 and 14 show the data for 7% and 18% compression, respectively. For the 7% data, the scatter does not allow for a meaningful estimate of the slopes. The intercepts, however, are reasonably well defined. For the 18% data, both the intercepts and the slopes are better defined. The various parameters calculated from the analysis of these plots are given in Table 3.

Inspection of Table 1 shows that the estimates of ϕ from the plots are lower than the filler volume fractions. The deviations are illustrated in Fig. 15. The equation used to calculate the lines is

$$\phi_{\text{eff}} = \frac{\phi_0}{1 + k\epsilon\left(\frac{1}{1 - \phi_0^{1/3}}\right)} \qquad (8)$$

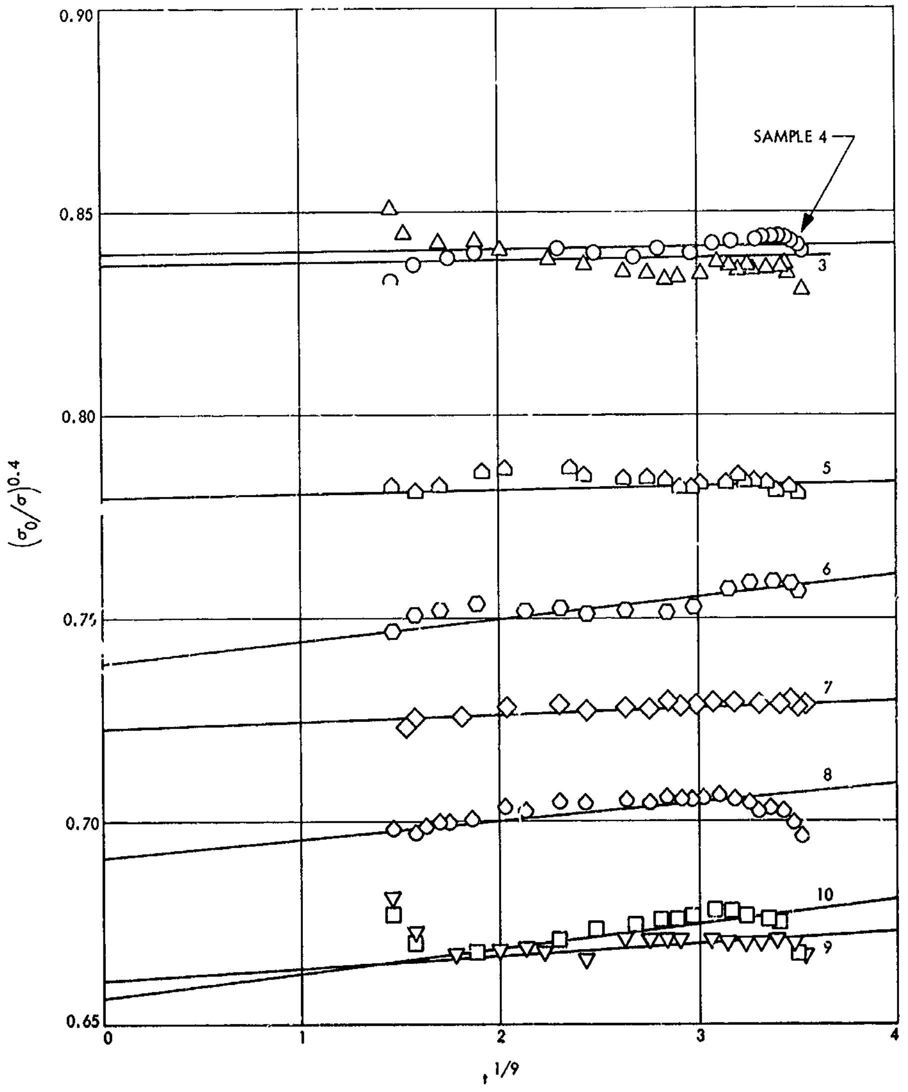

Fig. 13. $(\sigma_0/\sigma)^{0.4}$ vs $t^{1/9}$ for 7% compression

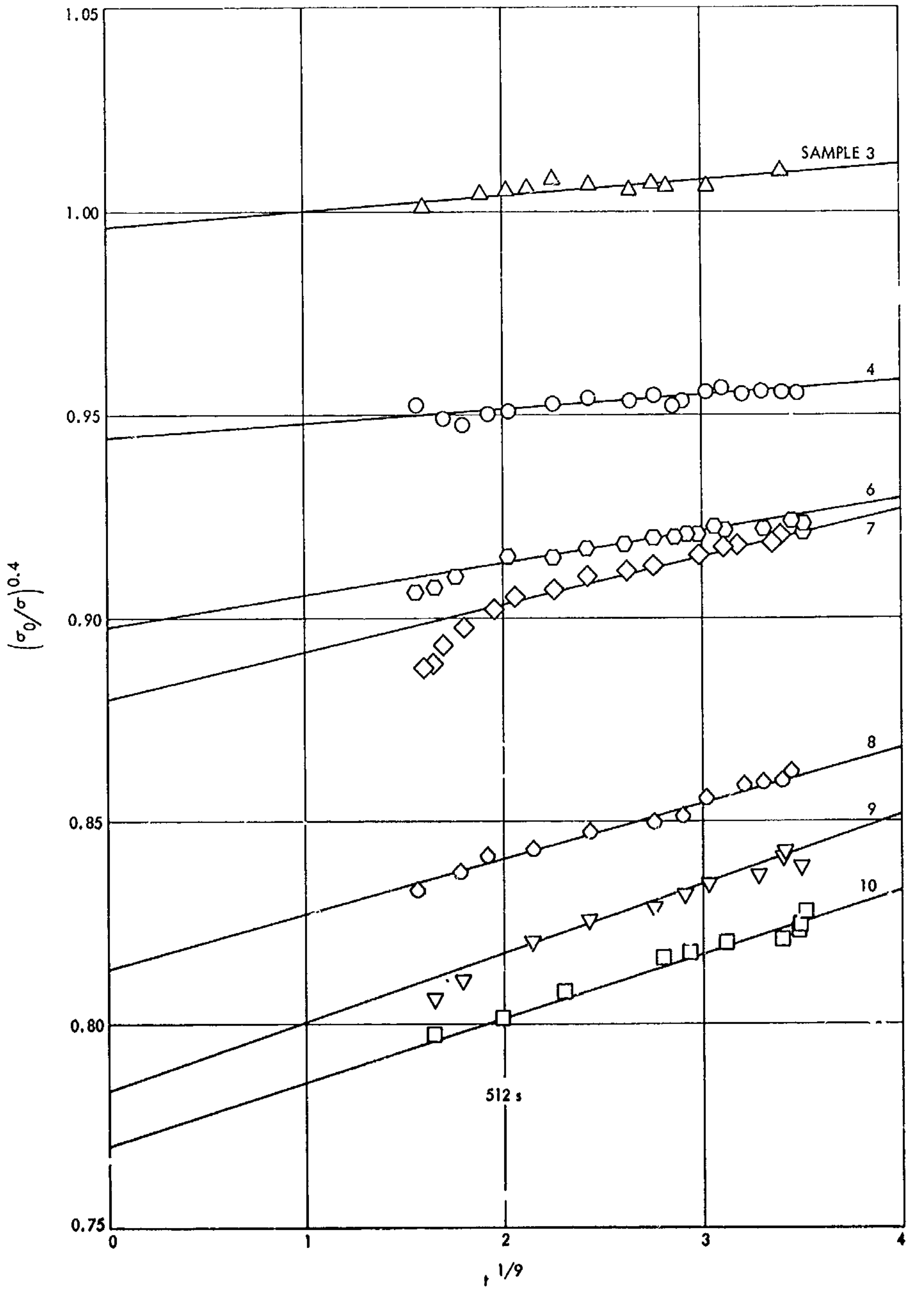

Fig. 14. $(\sigma_0/\sigma)^{0.4}$ vs $t^{1/9}$ for 18% compression

Table 3. Parameters from $(\sigma_0/\sigma)^{0.4}$ vs $t^{1/9}$ plots according to Eq. (7) for 7% and 18% compression

Sample number	Glass-bead volume fraction ϕ	$(1 - \phi/\phi_m)$		$\phi(\phi_m = 0.74)$		$\phi^{2/3}/\phi_m \times (2\beta)^{1/3}$		$(2\beta)^{1/3}$
		7%	18%	7%	18%	7%	18%	18%
3	0.092	(0.84)[b]	(0.97)[c]	0.045	0.02	—	0.004	0.22
4	0.132	0.84	0.954	0.12	0.034	0.004	0.0035	0.20
5	0.169	0.78	—	0.16	—	b	—	—
6	0.204	0.74	0.907	0.19	0.069	0.005	0.0066	0.055
7	0.234	0.724	0.879	0.21	0.09	0.002	0.0117	0.068
8	0.270	0.69	0.814	0.23	0.14	0.005	0.014	0.070
9	0.2[illegible]	0.66(?)	0.779	0.25	0.16	0.003	0.017	0.080
10	0.3[illegible]	0.66	0.756	0.25	0.18	0.012	0.016	0.072

[a] Used ϕ extrapolated.
[b] Bad plot.
[c] Plot gives $\approx$ 1.0, hence $\phi \approx 0$; 0.97 is lower limit of estimate of uncertainty.

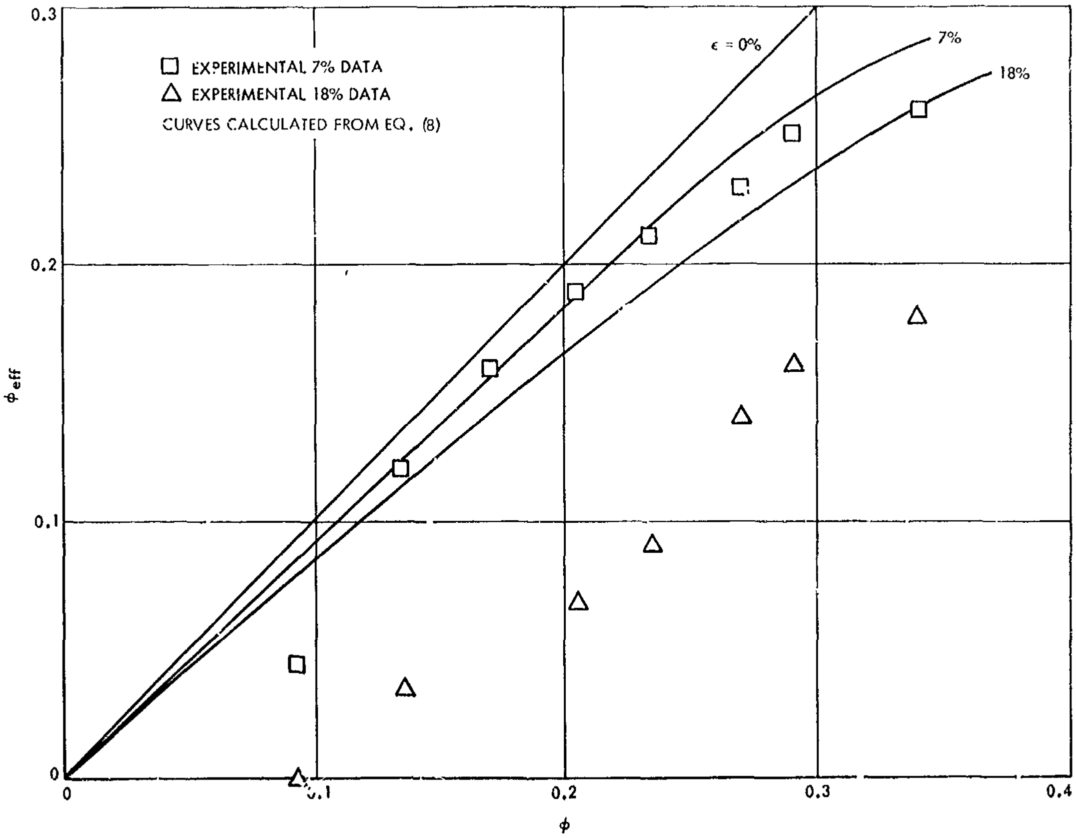

Fig. 15. Comparison of volumetric and effective filler fractions

where $k = 1/2$). Included in the equation is a correction for the fact that in a filled system the total strain is taken up by the binder alone, but does not include dewetting.

The data points in Fig. 15 are the estimates from the plots according to Eq. (7). For 7% compression, the agreement is good. For 18% compression, the points are much below the corresponding curve. This may be the consequence of partial instantaneous dewetting the moment the specimen is strained; thus, ϕ_{eff} corresponding to $t \rightarrow 0$ would be given by the extrapolation. Following this fast initial dewetting, the process then continues gradually at a rate proportional to $t^{1/9}$. This is in qualitative agreement with the previously reported volumetric measurements, where for tensile deformation plots of $\Delta V/V_0$ versus $t^{1/2}$ were linear, with an intercept for $t = 0$ which was proportional to the strain.

The rate constant β for 18% compression was estimated from the data for the five highest loading levels to be about 0.2 (sec^{-1}). This value is in remarkable agreement with about 0.12 obtained from dilatrometric data for tensile deformation (SPS 37-41, Vol. IV). The fact that data from stress relaxation in compression lead to the same rate constant as those from volume measurements in tension strongly supports the basic correctness of the underlying model for dewetting. It also demonstrates that the contribution of dewetting to the mechanical behavior can be factored out.

XIII. Research and Advanced Concepts

PROPULSION DIVISION

A. Further Heat-Transfer Results With an Applied, Transverse Magnetic Field in a Square Channel, *E. J. Roschke*

1. Introduction

Some experimental heat-transfer results for partially ionized argon flowing in a 2- × 2-in. square channel with a transverse magnetic field were presented in SPS 37-51, Vol. III, pp. 130–135. Those results, and all results appearing in previous SPS publications, were for subsonic flow. The purpose of this article is to present some of the earlier data in a different way and compare it to the theory presented by Back.[1] Prominent in this treatment of both experiment and theory is the joule heating parameter S, which arises in the energy equation applicable to this problem. Methods of computing S are given; various methods for correcting S due to departures of the electrical conductivity from scalar values are discussed. In addition, new data for a case of supersonic flow is presented that is of interest because much higher values of S were obtained than in previous tests and much larger increases in heat transfer were measured than before. The apparatus and method of making experiments are described in SPS 37-51, Vol. III, and earlier articles in the SPS series. Symbols used in this article are defined in Table 1.

2. Method of Presenting Heat-Transfer Data

A convenient way of presenting the experimental heat-transfer data is in the form of the non-dimensional heat flux

$$Q^* = \frac{2aq}{k_i\,(T_i - T_w)} \qquad (1)$$

This grouping tends to include the effect of changes in the bulk temperature of the gas that occur when the magnetic field is applied and then varied (see SPS 37-51, Vol. III). It is also one of the dependent variables utilized in the theoretical treatment (see Footnote 1). The effect of the applied magnetic field is emphasized by forming the ratio Q^*/Q^*_0, which represents the ratio of the non-dimensional heat flux with applied field to its value when the applied field is zero.

---

[1] Back, L. H., "Laminar Heat Transfer in Electrically Conducting Fluids Flowing Between Parallel Plates," paper accepted for publication in *Int. J. Heat Mass Transfer.*

Table 1. Nomenclature

a	channel half-height, $2a = 2$ in.
A, C	upper and lower walls of channel, respectively
B	applied magnetic field strength
c	specific heat
E	applied electric field strength
Ek	Eckert number, $Ek = \bar{u}^2/c\,(T_i - T_w)$
H	total enthalpy
Ha	Hartmann number, $Ha = (\sigma/\mu)^{1/2} Ba$
j	current density
K	ratio of applied to induced electric fields, $K = E/\bar{u}B = 0$
k	thermal conductivity (Ref. 2)
$\dot{m}$	mass rate of flow
Pr	Prandtl number (Ref. 2)
q	measured heat flux
Q^*	non-dimensional heat flux, $Q^* = 2aq/k_i\,(T_i - T_w)$
Q_0^*	non-dimensional heat flux at zero magnetic field
Re	Reynolds number based on channel height, $Re = \dot{m}/2a\mu$
S	joule-heating parameter, $S = (Ha)^2 Ek\,(1 - K)^2 Pr$
S'	corrected joule-heating parameter, $S' = S\,(1 + \beta_e\beta_i)$
T	temperature
$\bar{u}$	bulk gas velocity
x	axial coordinate in direction of flow
$\bar{x}$	non-dimensional axial distance, $\bar{x} = (x/2a)/RePr$
β_e	Hall parameter, $\beta_e = \omega_e\tau_e$
β_i	ion-slip parameter, $\beta_i = \omega_i\tau_i$
μ	viscosity (Ref. 2)
σ	scalar electrical conductivity (Ref. 2)
τ_e, τ_i	particle collision times
ω_e, ω_i	particle collision frequencies
Subscripts	
i	inlet conditions
0	conditions at zero magnetic field
w	conditions at wall

In the theoretical treatment, k_i is constant because of the constant-property assumption and T_i may be considered fixed as Q^* changes with changing value of magnetic field B, i.e., changes in the joule heating parameter S. However, in the experimental case, both k_i and T_i vary with S at a selected inlet axial station. In practice, Q^* is calculated presently from

$$Q^* = \frac{2acq}{k_i\,(H_i - H_w)} \tag{2}$$

where c is an effective specific heat taken to be constant; H_i is obtained directly from an energy balance applied to the system in the axial direction. All semi-local bulk flow parameters (such as temperature, velocity, and ionization fraction) are obtained from the energy balance and iteration of the conservation equations; transport properties at the appropriate conditions are taken from Ref. 1. Presently, the inlet station is taken to be the center of the first segment of the four-segment test section (SPS 37-51, Vol. III), partly because the magnetic field distribution becomes approximately flat at that location. All heat-transfer data to be presented later, however, are for the second segment of the test section.

The variation of Q^*/Q_0^* with S at the selected axial station is then of interest for the channel walls perpendicular to the direction of the applied magnetic field.

3. Calculation of the Joule Heating Parameter

The joule heating term j^2/σ in the energy equation may be non-dimensionalized according to

$$S = (Ha)^2 Ek\,(1 - K)^2 Pr \tag{3}$$

Thus, the sign of S is always positive for a horizontal channel whether the direction of B is vertically upward or downward. The calculation of S from Eq. (3) is straightforward when all the bulk properties of the gas are known as a function of axial position. Since there is no applied electric field in the present experiments, $K = 0$.

However, at the considerably high values of applied magnetic field employed here (up to 10,000 G), departures of S from the value expressed by Eq. (3) are to be expected when the electrical conductivity departs from its classic scalar value. One correction commonly used is due to the Hall effect and S then becomes reduced in accordance with

$$S' = \frac{S}{(1 + \beta_e^2)} \tag{4}$$

In these experiments $\beta_e >> 1$ so that $S' \rightarrow 0$; theoretically, no effects of magnetic field on heat transfer would be observed. Since substantial changes in q and Q^* were obtained for negligible S' from Eq. (4), it is concluded that Eq. (4) cannot apply in the present experiments.

Hall and ion-slip effects were discussed in SPS 37-52, Vol. III, pp. 109–112. Those results indicated that $\beta_i \leq 10^{-2}\,\beta_e$ for argon and that the correction factor due to ion-slip alone would be zero when the Hall effect was zero ($\beta_e = 0$). The ion-slip effect, however, is not necessarily zero when the Hall effect is zero if the ions are current carriers (Ref. 2). Those results applied to the present situation yield a corrected value of

$$S' = \frac{S}{(1 + \beta_e \beta_i)} \tag{5}$$

which applies when the Hall current is zero and the component of magnetic field in the flow direction is small compared to the transverse component. The correction factor $(1 + \beta_e \beta_i)$ was successfully used to correlate experimental measurements for argon (Ref. 2) for conditions that may be similar to those in the present experiments.

4. Results for a Case of Subsonic Gas Flow

The results given in SPS 37-51, Vol. III, were obtained by manual calculation; since that time more refined calculations have been performed and many have been reduced to machine computation. The results for tests 107-18H and -19H (taken for the same flow conditions and applied electric power to the gas) are shown in Fig. 1. Values of the non-dimensional heat-flux ratio Q^*/Q_0^* are plotted at corrected values of S' as defined in Eq. (5).

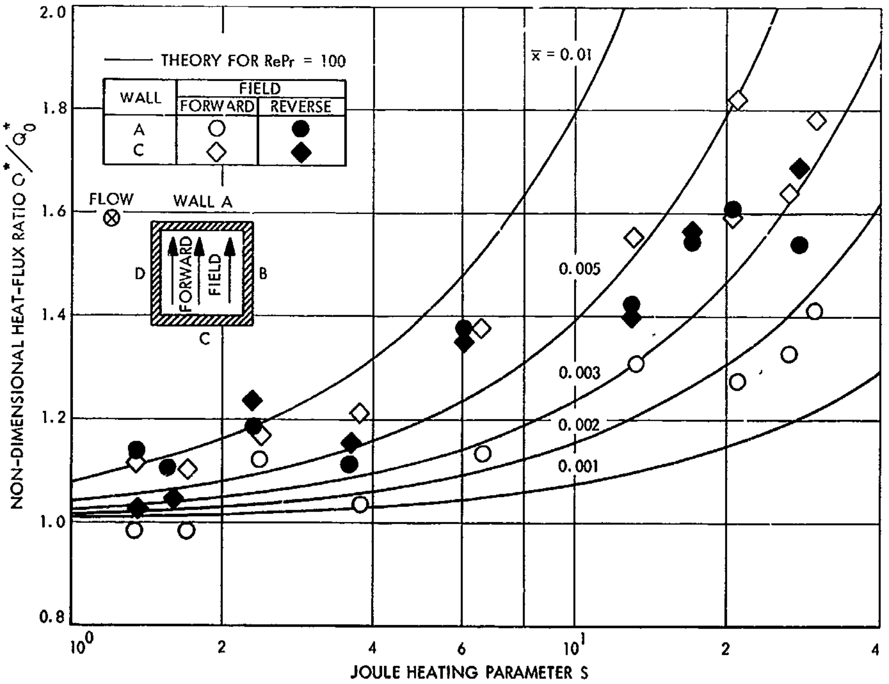

Fig. 1. Non-dimensional heat flux at second segment of test section for subsonic flow, tests 107-18H and -19H

Forward field indicates an applied magnetic field directed vertically upward and vice versa for reverse field In this case, at the highest values of S obtained, $0.25<\beta_e\beta_i<0.30$. It is clear that substantial increases in heat transfer occur with an increase in either S or S'. The relatively good agreement between walls A and C for reverse field is noted; the reason data for wall A at forward field are low has not yet been determined.

Also appearing in Fig. 1 are theoretical predictions adapted from Back (Footnote 1). Each curve represents the variation of Q^*/Q_0^* with S for different nondimensional axial distances from the inlet, as defined by $\bar{x} = (x/2a)/RePr$. Although the curves are indicated for $RePr = 100$, they are virtually independent of $RePr$ for values of $RePr$ greater than 50. For these experiments $82 < RePr < 110$. The trend of the data is in rough agreement with the theory. Experimental values of $\bar{x}$ are not known because the "effective" location at which the flow may be considered to begin is not determined. If the "starting" point of the flow is considered to occur at the center of the first segment of the test section (1 in upstream of the location of these data), values of $0.005 < \bar{x} < 0.006$ would be obtained. The agreement between theory and experiment is sufficiently good to be encouraging.

5. Results for a Case of Initially Supersonic Gas Flow

The results of test 107-26H were of interest because large values of S were obtained. This test was considered to be initially supersonic (before applied field) because the bulk equilibrium Mach number was greater than unity, the flow was accelerating, and the axial pressure distributions were unlike those obtained in the subsonic cases. This is demonstrated in Fig. 2, which is a comparison of results for tests 107-18H and -26H; both tests were conducted with a value of mass flow rate $\dot{m} \simeq 0.007$ lb/s.

The effect of the applied magnetic field on static pressure measured at the wall is shown in Fig. 3. These results differ from equivalent results for test 107-18H (see SPS 37-51, Vol. III) in several important ways: (1) peaking of the pressure distribution still occurs but is much less sharp and occurs further upstream than test 107-18H indicates, (2) the relative increase in pressure in the test section is much greater in the supersonic case compared

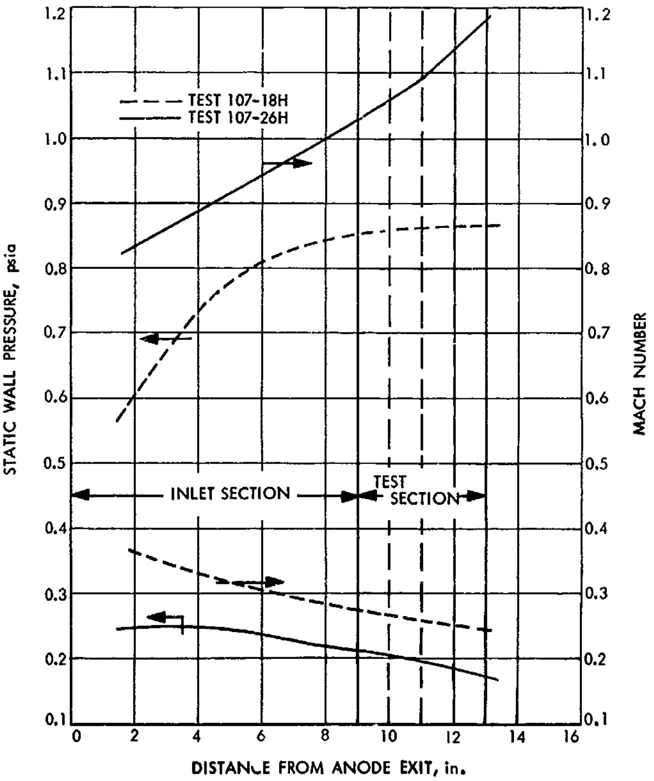

Fig. 2. Comparison of axial distributions of pressure and Mach number for subsonic and supersonic cases with zero applied magnetic field

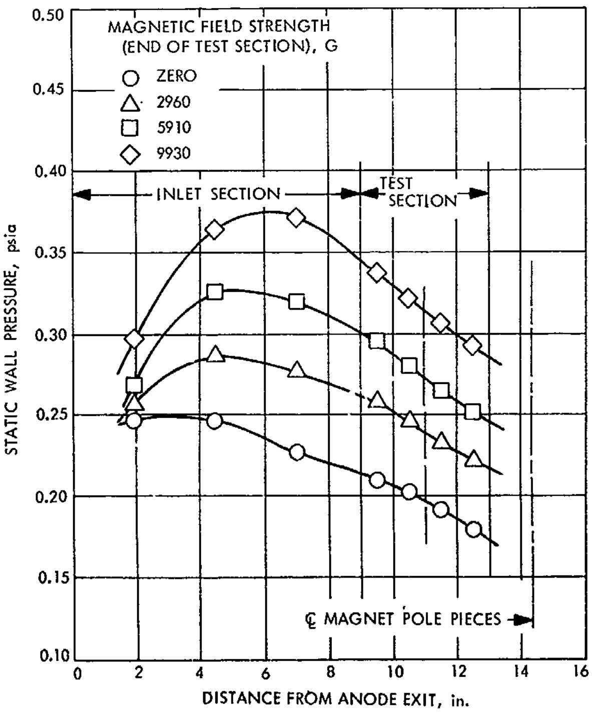

Fig. 3. Effect of magnetic field on axial pressure distribution along side wall B, test 107-26H

to the subsonic case, and (3) the pressure gradient in the test section is somewhat greater in the supersonic case.

Heat-transfer results for this test are shown in Fig. 4 in the same manner as Fig. 1 was depicted; larger values of S' and Q^*/Q^*_0 are evident. In this case, the highest values of S obtained were approximately 250, whereas the corresponding values of $1.5 < \beta_e\beta_i < 3.1$ were computed so that S' was markedly less than S at the highest values of the magnetic field. Values of $RePr$ were similar to those obtained in test 107-18H. Trends of the data (Figs. 1 and 4) are similar. In the latter case, a comparison with theory would tend to indicate a higher value of $\bar{x}$ for the supersonic case than for the subsonic case. Again, one low set of data is evident, this time for wall C with reverse field. In contrast to the subsonic case, better agreement between walls is obtained for forward field than for reverse field.

In test 107-26H, for all but the very lowest values of S', the computed bulk values of Mach number throughout the square channel were less than unity; however, the trends of the Mach number were similar to that shown in Fig. 2 so that the nature of the flow is not clear. It does not appear that the results of Fig. 4 are necessarily typical of supersonic flow. It does appear that flow deceleration due to axial Lorentz forces is relatively greater as the value of the initial Mach number (at zero applied magnetic field) is increased.

6. Conclusions

It is now apparent that joule heating due to an applied magnetic field can cause large increases in heat transfer to the walls of a channel in which a weakly ionized gas is flowing. Trends of the non-dimensional heat flux Q^* increase with the joule-heating parameter S as predicted by theory. The largest increase in Q^* obtained to date has been six times that obtained at zero applied field. Despite the short comings of the theory due to its idealized treatment of incompressible slug flow between infinite parallel plates, it appears that the theory does contain the essential features of the consequences of joule heating.

The values of S computed in these experiments are probably too large because of non-scalar behavior of the electrical conductivity that may occur in strong magnetic

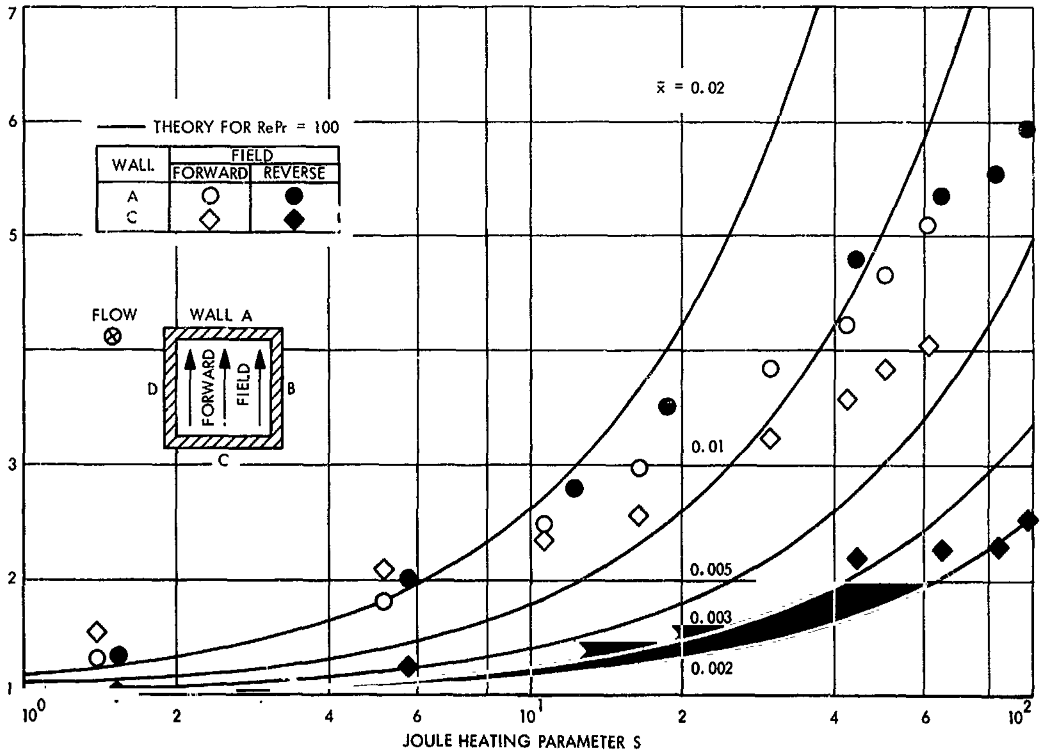

Fig. 4. Non-dimensional heat flux at second segment of test section, test 107-26H; flow initially supersonic at zero magnetic field

fields. Theoretical values of the Hall parameter calculated by usual procedures were much too large to be relevant in the present experimental results; it appears that theoretical values of β_e are one to two orders of magnitude too high. An alternative ion-slip correction suggested in Ref. 2 has been utilized in the form $S' = S/(1 + \beta_e\beta_i)$; this correction yields much more reasonable results since $\beta_i \leq 10^{-2}\beta_e$ in these experiments.

References

1. de Voto, R. S., *Argon Plasma Transport Properties*, Technical Report 217, Stanford University, Department of Aeronautics and Astronautics, Stanford, Calif., Feb. 1965. Also available in *Phys. Fluids*, Vol. 10, pp. 354–364, Feb. 1967.
2. Patrick, R. M., and Brogan, T. R., "One-Dimensional Flow of an Ionized Gas Through a Magnetic Field," *J. Fluid Mech.*, Vol. 5, Part 2, pp. 289–309, 1958.

B. Thermionic Diode Kinetics Experiment,

H. Gronroos

1. Introduction

The thermionic diode kinetics experimental program is part of a continued effort aimed at delineating the problems associated with liquid-metal-cooled thermionic reactors for space powerplant application. This article describes a non-nuclear thermionic reactor system experiment that is now being assembled. The experiment will mainly address itself to the questions of plant dynamics and control. Other parallel evaluations concerned with reactor physics, design and engineering, materials and fabrication, and application studies are not discussed in this article.

The experimental assembly has many features in common with what would be termed a system simulator. However, the assembly is more accurately described as a first step towards a system simulator test. Although the time constants are expected to approximate those existing in a real system, many components are relatively far removed in design from what they probably will be in application.

2. Results of Analytical Investigations

Results of analytical investigations of thermionic reactor system dynamics and control are summarized to clarify the requirements that should be placed on an experimental facility.

a. Open loop stability studies.[2]

(1) The open loop uncontrolled plant is generally inherently stable. However, design modifications to improve marginal stability and increase protection against accidental large reactivity insertions may be required.

(2) The small feedback effects lead to a relatively large change in operating point even for minor perturbations. The self-regulation is inadequate, necessitating active control.

(3) Thermal transients from electric load and reactivity perturbations are damped and can be controlled with conventional controller hardware. This also holds for thermal transients following open circuiting at the reactor terminals. If uncontrolled, this leads to large and fast fuel and emitter temperature increases.

(4) If the cesium pressure is optimized with respect to a given operating point, the characteristic current–voltage curves cross each other. Then, for a given load line, the heat balance characteristic can pass through a maximum and a minimum. Therefore, conditions for self-sustained oscillations can be conjectured for a nuclear reactor application. With a small increase in cesium pressure, at some cost in efficiency, the characteristics are altered sufficiently to prevent such oscillations.

b. Control studies.[3]

(1) Depending on the system application, either constant reactor output voltage control or a specific programmed response control is feasible.

(2) It appears that existing controller hardware technology is sufficient to meet foreseeable controller performance specifications.

(3) A step change in the electric load will cause a voltage spike to occur at the reactor terminals and, therefore, also at the input to the power conditioner. To avoid the spike at the output of the power conditioner, it must be designed to accommodate the spike for the duration of the transient.

The analytical studies have been useful in building up a theoretical understanding of the system behavior but they necessarily employ models that are only approximate

---

[2] SPS 37-45, Vol. IV, pp. 151–162, and Ref. 1.

[3] References 2 and 3.

descriptions of the physical system. There are considerable difficulties in the analytical formulation, particularly for start-up and shut-down and for cases of large perturbations. In addition, computer constraints limit the feasibility of detailed modeling of the complete system.

3. Motivations and Requirements

The cost of in-pile experiments are high and, at this time, several hardware problems remain to be resolved. A non-nuclear experiment aimed at investigating the dynamics and control will give inputs for the reliable design of nuclear experiments, and also for the design of a reactor prototype. An experiment designed to give data for evaluation of system responses to various perturbations and simulated accidents will aid in the evaluation of various control concepts. Also, predictions from analytical models can be compared with experimental information. Particularly, studies of system behavior off nominal operating conditions, such as part electrical load, diode open and short circuiting, loss of cesium, loss of coolant flow, start-up and shut-down, and prompt criticality, are important before any nuclear application is attempted. In addition, hardware specifications will be placed on a firmer basis and breadboarded system components can be placed in line with power-producing thermionic diodes.

The experimental facility should have the following features:

1. Flexibility in simulating various controllers and reactor systems in order to accommodate various design concepts, which implies the use of analog and digital computers on line.
2. Realistic simulation of thermionic diode performance, which implies the use of diodes approximating prototype designs.
3. Adequate instrumentation and data reduction systems.
4. The experiment need not comply with weight and volume limitations applicable to a spacecraft design.
5. A high-current and low-voltage switching unit for introduction of open and short circuits in a diode matrix.
6. Simulation of the heat-transfer characteristics of the heat-rejection loop in actual systems, which implies the use of liquid-metal coolant for the experimental assembly.

4. Experimental Assembly

To accommodate the desired objectives as closely as possible and still stay within reasonable cost, an experimental approach shown in Fig. 5 was chosen. Up to six cylindrical thermionic diodes may be mounted vertically in a single-channel NaK-cooled test bank enclosed in a vacuum chamber. Each diode is independently heated by electron beam power. The associated cesium reservoir is also controlled independently. The NaK heat-rejection loop is enclosed in a housing under nitrogen cover gas. An NaK to nitrogen heat exchanger carries away the waste heat.

The generated electrical power is fed to an electrical coupling unit that consists of a series of specially developed, high-current, pneumatically actuated, mercury switches connecting copper bus bars. Any desired series or parallel electrical interconnection between the diodes in the test bank may be chosen, as well as open and short circuit conditions.

The power-conditioning equipment transforms the low voltage–high current dc power generated by the test diodes to high voltage–low current dc power. The electric load simulates the load to which a thermionic reactor powerplant would be connected.

An analog computer provides the nuclear reactor simulation. Thermocouple readings from the diodes and the coolant loop are fed into the computer and the electrical analog of temperature coefficients of reactivity is generated along with the neutron kinetics. The computer controls the electron beam heater power supply for the diodes. Various reactor control concepts can be programmed on the analog computer. With this computer it is also possible to compensate the cesium reservoir temperature in a desired manner (e.g., for simulation of integral cesium reservoir temperature variations).

The controls for the experimental facility monitors the experimental parameters and incorporates the safety circuitry.

A number of constraints had to be considered to implement the outlined experimental approach. Due to cost the number of diodes must be limited. Six diodes was considered to be the minimum number from which a meaningful matrix may be formed. Eutectic NaK is the most feasible coolant choice and permits the use of stainless steel as construction material. Relatively large cylindrical diodes should be used. Because of the very large current (500 A at 0.5 V and 1800°C emitter temperature for the

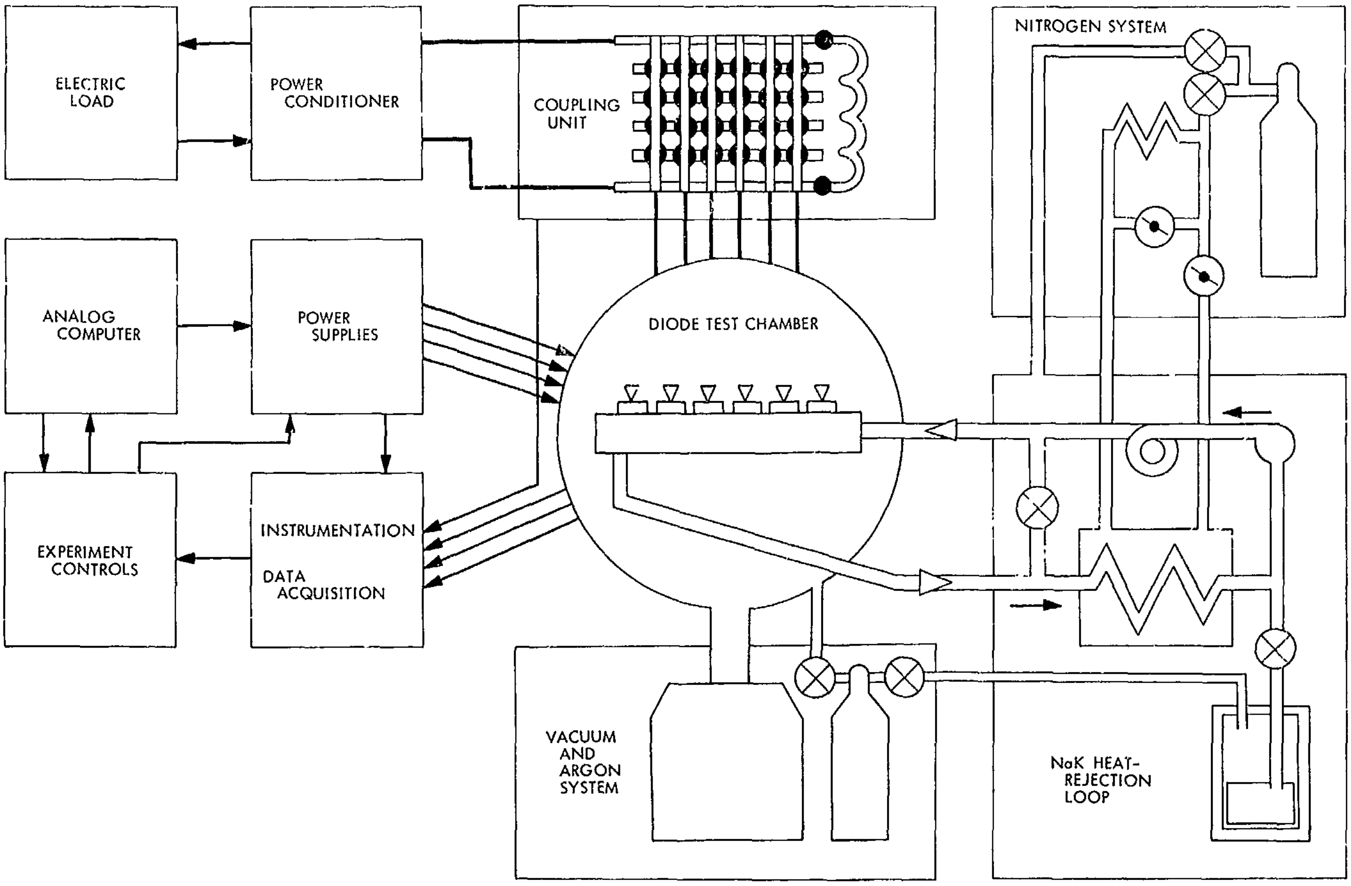

Fig. 5. Schematic of thermionic diode kinetics experiment

chosen diode dimensions), there are difficulties with the switching and power-conditioning units. A separate development effort was necessary for these components.

a. Description of subsystems. The experimental facility consists of two main subsystems: the thermionic diodes with associated equipment and the heat-rejection loop. The analog computer is programmed to give a complete simulation of a thermionic reactor powerplant.

Thermionic diodes. Figure 6 shows a cross-section of a thermionic diode.[4] The emitter is made of rhenium, 0.240 in. thick, 2 in. long, and 0.75 in. outer diameter. The interelectrode gap is 0.010-in. Niobium was chosen as the collector material. The 0.060-in.-thick collector is the inner part of a trilayer construction with 0.060-in. insulator sheath followed by a kovar cladding of 0.020-in. thickness.

The temperature range under normal operating conditions are expected to be: emitter 1900–1500°C, collector 900–600°C, insulator 900–600°C, and cladding 700–600°C. Under open-circuit conditions, the emitter temperature may rise to approximately 2400°C, the collector to 1000°C, and the insulator to 1000°C. The cladding and coolant temperatures will not be allowed to rise appreciably.

Three tungsten–25% rhenium thermocouples are imbedded in the emitter, and three cromel–alumel thermocouples are in the trilayer.

A prototype thermionic diode has been tested and was found to operate well within the specifications. Figure 7 shows some representative test data (Ref. 4).

Test bank, vacuum chamber, and NaK loop. Figure 8 shows the test bank into which the thermionic diodes are installed in the vacuum chamber. All feedthroughs are taken out through one head of the chamber, except for the liquid-metal loop penetrations that come through the side. The frame of the NaK loop outside of the vacuum chamber is shown in Fig. 9. A NaK to nitrogen heat

---

[4] Manufactured by Thermo Electron Corp., Waltham, Mass.

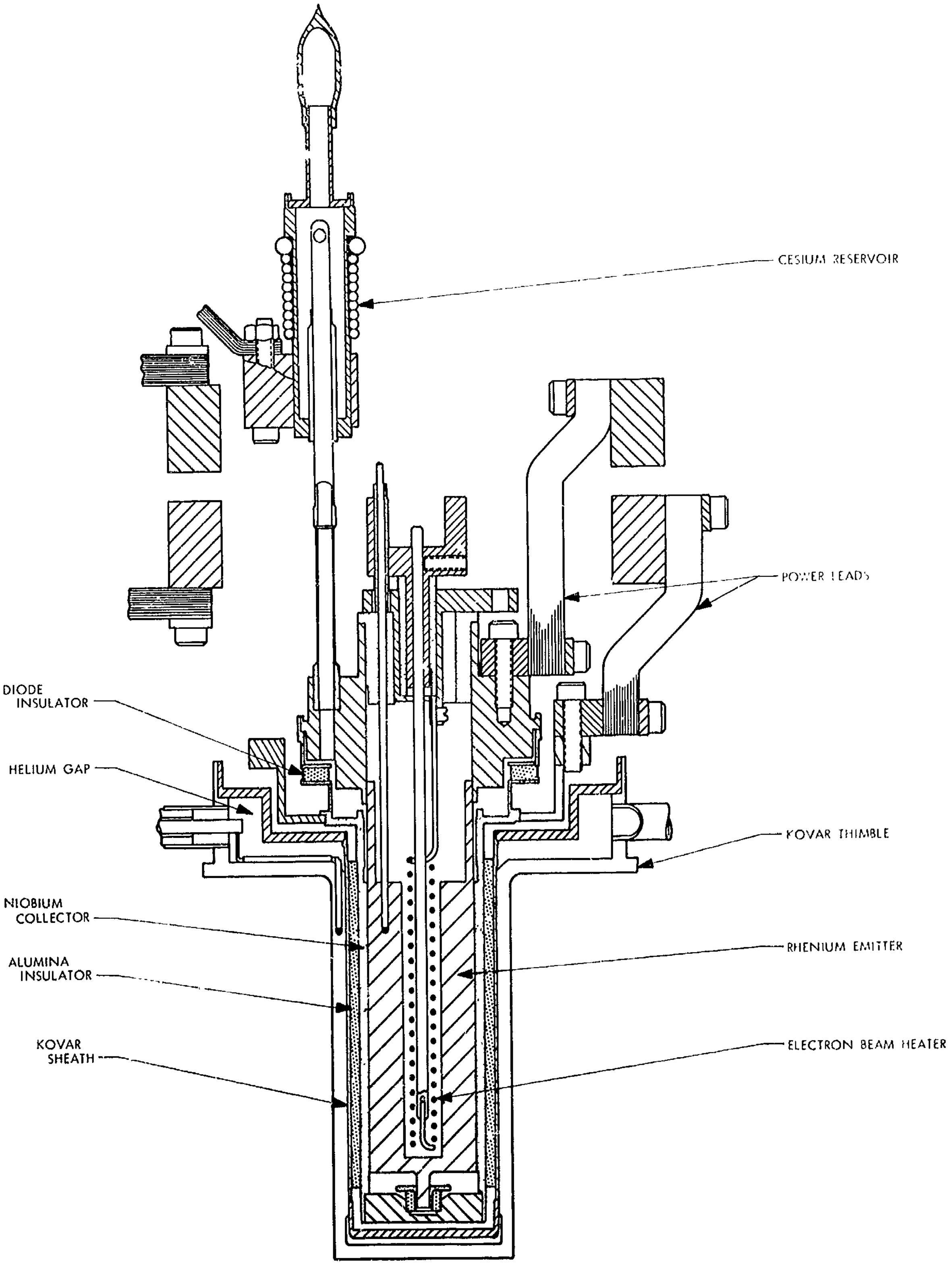

Fig. 6. Cylindrical diode for thermionic diode kinetics experiment

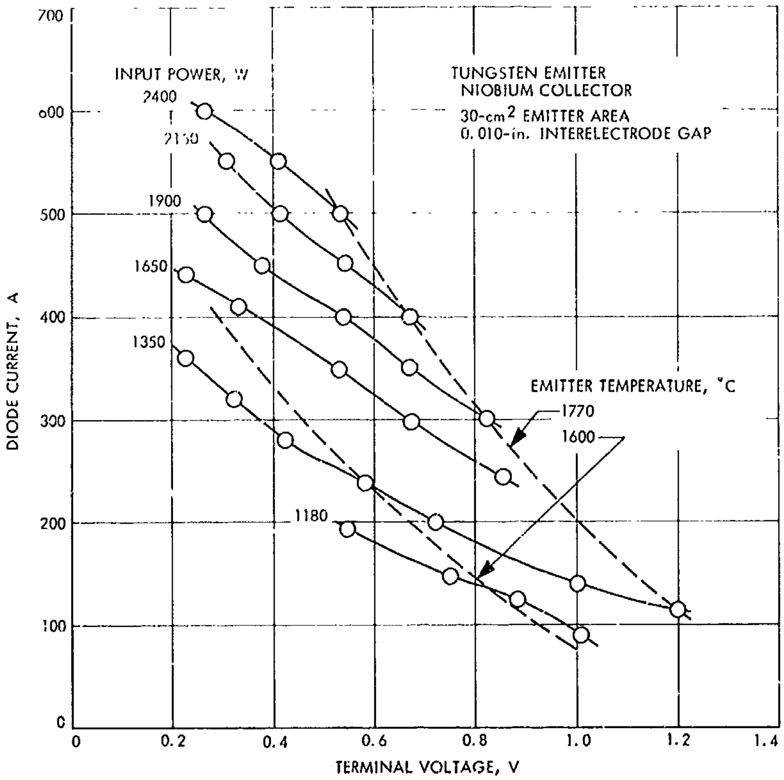

Fig. 7. Test results from prototype diode

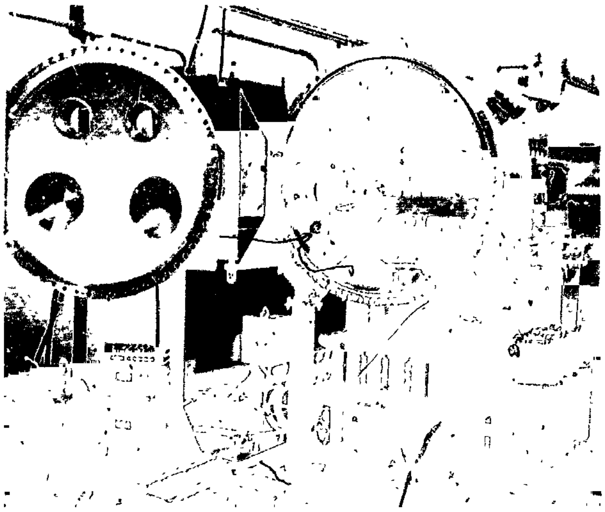

Fig. 8. Test bank and vacuum chamber for thermionic diode kinetics experiment

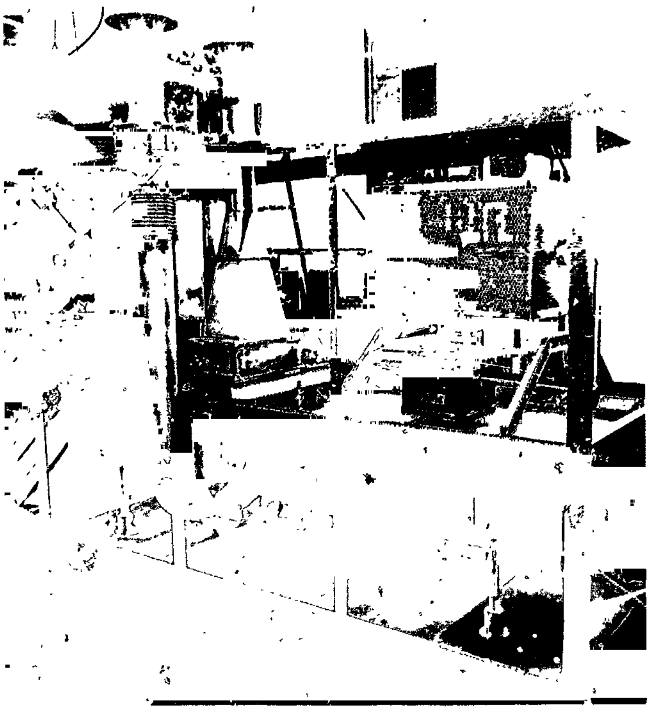

Fig. 9. NaK loop for thermionic diode kinetics experiment

exchanger permits removal of heat up to 25 kW at 1250°F coolant temperature. The electro-magnetic pump has a capacity of 3000 lb/h at 30-psi head, and the preheater provides heat input up to 10 kW. Piping, valves, and test bank are all constructed of 304 stainless steel. Full penetration welded construction is employed. For extra protection, double bellows are used between the vacuum chamber and the external part of the loop.

Diode electric circuitry. The diode electric circuitry consists of copper bus bars leading to the switching unit (Fig. 10). A development effort was necessary to obtain the required high current–low voltage drop (600 A, 5 mV) characteristic for the mercury switches. (This work was also done by the Thermo Electron Corp.) A close-up of the switch is shown in Fig. 11. The circuitry for actuating the switches is such that a selection is made first for the desired coupling pattern, and then all switches are actuated simultaneously.

A special development effort also went into the design of the power conditioner (see *Chapter V-C*). The unit is designed to operate from 1 to 5 V at 700 to 50 A, respectively, and give an output dc voltage of 50 V to a dummy resistive load. A separate cooled resistance coil is connected directly to the switching unit. It is used when the power conditioner is off line.

b. Present status. All major components have been fabricated and assembled. The vacuum tank with accessories, the bank onto which the thermionic diodes are mounted, and the external NaK loop are ready for final joining and welding. All other important auxiliary equipment, such as electron beam heaters with controls, cesium reservoir heaters with controls, and liquid-metal loop-heater power supplies, are available. The instrumentation has been laid out and is being installed. The analog computer has been installed.

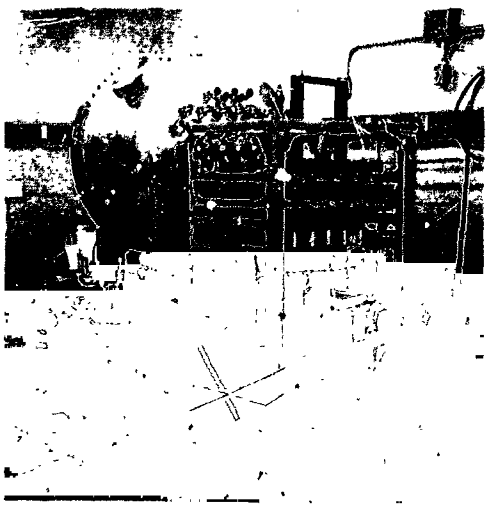

Fig. 10. Coupling unit for thermionic diode kinetics experiment

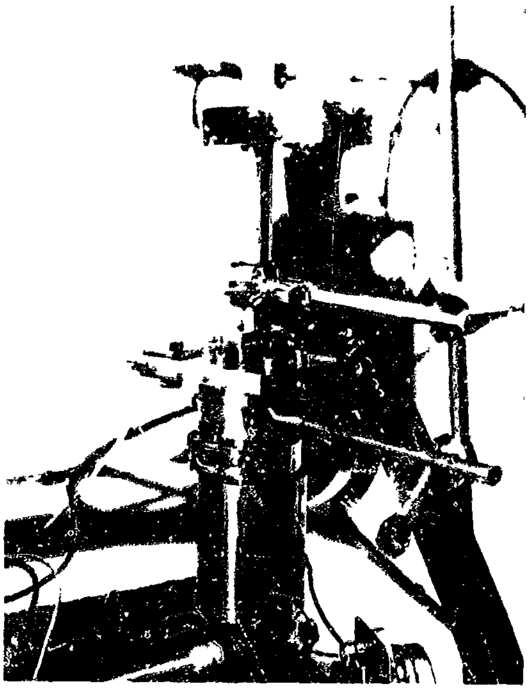

Fig. 11. 600 A pneumatically actuated mercury switch

The various components are now being assembled as a system. The first experiments are expected to begin during fiscal year 1969.

References

1. Schock, A., "Effect of Cesium Pressure on Thermionic Stability," paper presented at the Second International Conference on Thermionic Electrical Power Generation, Stresa, Italy, May 27–31, 1968.
2. Gronroos, H., et al., "A Control System Study for an In-Core Thermionic Reactor," paper presented at the IEEE Thermionic Conversion Specialist Conference, Palo Alto, Calif., Oct. 30–Nov. 2, 1967.
3. Gronroos, H., and Davis, J. P., "Stability and Control Considerations for Thermionic Reactors," paper presented at the Second International Conference on Thermionic Electrical Power Generation, Stresa, Italy, May 27–31, 1968.
4. Peelgren, M., and Speidel, T., "Large Cylindrical Diodes with Rhenium Emitter for Diode Kinetics Experiment," paper presented at the IEEE Thermionic Conversion Specialist Conference, Framingham, Mass., Oct. 21–23, 1968.

C. Liquid–Metal MHD Power Conversion,

D. G. Elliott, D. J. Cerini, and L. G. Hays

1. Introduction

Liquid–metal magnetohydrodynamic (MHD) power conversion is being investigated as a power source for nuclear-electric propulsion. A liquid–metal MHD system has no moving mechanical parts and operates at heat-source temperatures between 1600 and 2000°F. Thus, the system has the potential of high reliability and long lifetime using readily available containment materials such as Nb–1%Zr.

In the MHD cycle being investigated, liquid lithium would be (1) heated at about 150 psia in the reactor or reactor-loop heat exchanger; (2) mixed with liquid cesium at the inlet of a two-phase nozzle, causing the cesium to vaporize; (3) accelerated by the cesium to about 500 ft/s at 15 psia, (4) separated from the cesium; (5) decelerated in an ac MHD generator; and (6) returned through a diffuser to the heat source. The cesium would be condensed in a radiator or radiator-loop heat exchanger and returned to the nozzle by an MHD pump.

2. NaK–Nitrogen Conversion System

The empty-channel electrical tests of the ac generator have been completed. The tests demonstrated the readiness of the instrumentation and electrical control systems for the NaK–nitrogen tests and the ability to set a uniform traveling magnetic field with proper compensation. The only unexpected result was that the core loss,

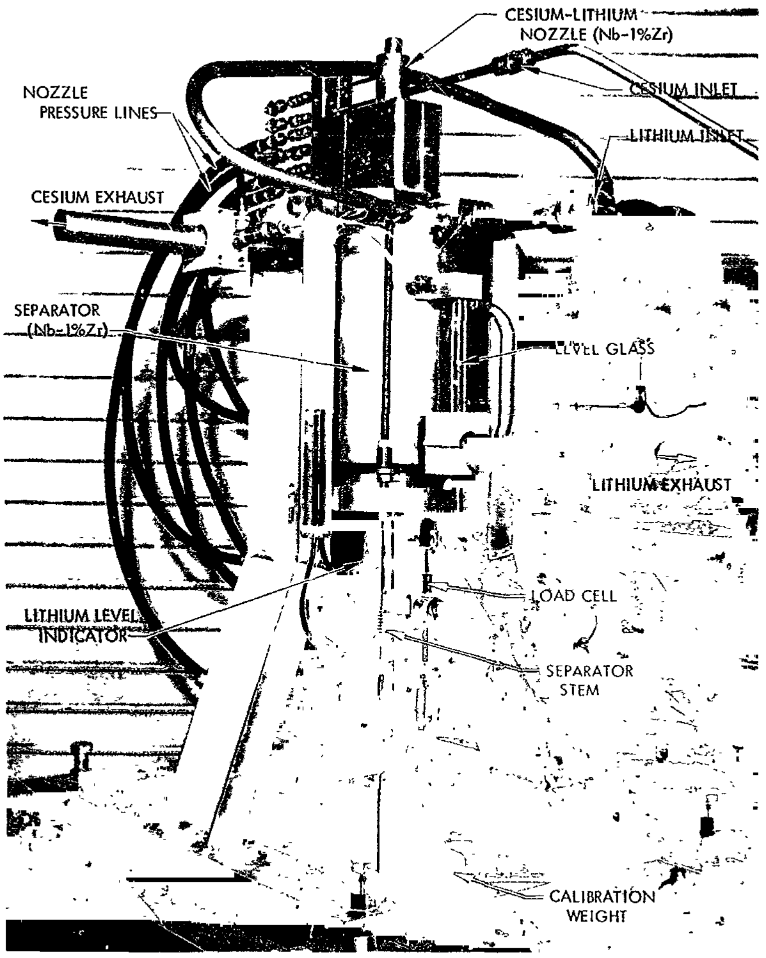

Fig. 12. Cesium–lithium nozzle–separator assembled for hydraulic evaluation

measured at phase currents up to 19 A (rms gap field of 1100 G), was about 5 times the standard value for Hiperco 50. The added loss would reduce the maximum power output from 42 to about 30 kW. The fabrication step causing the high loss will be identified and modified, if possible, in subsequent stators.

Power losses were also measured for the supporting H-frames and for the proposed Hiperco slot plugs. The added core loss due to the H-frames was 6 kW (extrapolated to the intended operating field of 4500 G rms) and was unaffected by annealing and negligibly affected by displacement 1-in. away from the stators. The addition of solid or laminated Hiperco slot plugs increased the core loss by an even larger amount, and also doubled the required coil voltages and produced a nonsinusoidual variation of gap field with time, although the variation of field with distance was smoother. It was decided to employ fiberglass for the H-frames and slot plugs in the NaK tests.

To observe the effect of a conducting sheet in the generator, aluminum plates of various thicknesses were placed in the channel and the exerted force and dissipated power were measured. The values agreed with expected values within the 20% uncertainty of the measurements.

3. Cesium–Lithium Erosion Loop

The auxiliary argon and vacuum systems have been completed. The NaK heat-removal system and controls have been completed and are ready for liquid-metal fill. The control system and console are complete, and control operation is being tested.

Figure 12 shows the two-phase nozzle and separator assembled for water–nitrogen tests. The purpose of the tests is to verify proper operation of the separator and to compare the nozzle thrust measured by the target method (to be used during high-temperature operation) with previous direct measurements (SPS 37-48, Vol. III, pp. 125–129). The best adjustment of the separator exit gap indicated by the tests will be retained in the final welding.

Measurement of the level of 2000°F lithium in the separator discharge chamber will be attempted with a new type of probe shown schematically in Fig. 13. This level indicator operates on the principle that the heat transfer from the liquid phase is much greater than that from the vapor phase. Hence, if the total heat input to an internally cooled probe is measured, it will be directly proportional to the length of the probe in contact with the liquid metal. For the probe of Fig. 13, the heat input is transferred by the heat-pipe action of lithium to a section where the heat is rejected by radiation. Since the area of the radiating section is fixed, the temperature of the radiating section is determined by total heat input and, hence, liquid level. The resultant probe is of very simple and rugged construction and provides a reliable, high-level signal (thermocouple output).

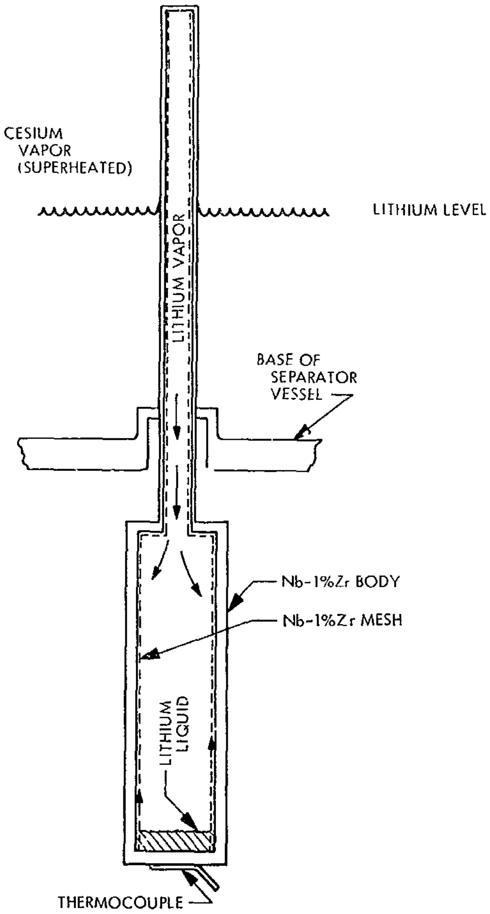

Fig. 13. Differential heat-transfer level indicator for cesium–lithium separator

The approximate relationship (neglecting heat pipe and wall temperature differences) that holds between liquid level and temperature is

$$\pi d_0 (L_0 - L_l) \bar{h}_v (T_l - T_r) + \pi d_0 L_l \bar{h}_l (T_l - T_r) = A_r \sigma \epsilon (T_r^4 - T_e^4)$$

where

d_0 = probe diameter

L_0 = probe length

L_l = liquid level

$\bar{h}_v$ = vapor heat-transfer coefficient

$\bar{h}_l$ = liquid heat-transfer coefficient

T_l = liquid temperature

T_r = radiating temperature

T_e = ambient temperature

A_r = radiating area

ϵ = emissivity

σ = Stefan–Boltzmann constant

For the case $\bar{h}_v << \bar{h}_l$,

$$L_l \approx \frac{A_r \sigma \epsilon (T_r^4 - T_e^4)}{\pi d_0 \bar{h}_l (T_l - T_r)}$$

Thus, for a fixed geometry, the liquid level is a function of the natural convection coefficient $\bar{h}_l$, the lithium temperature T_l, the ambient temperature T_e, and the radiating temperature T_r. During a test the first three parameters will be nearly constant, and T_r will provide a measure of the level. The calculated relation between lithium level and radiating temperature T_r for the geometry of the separator probe is shown in Fig. 14. This calculation included the effect of wall temperature differences and the variation of $\bar{h}_l$ with L_l. A change in level of 3 in. results in a change in thermocouple output of 100°F. Calibration of the probe at one level will be used to establish the actual operating curve.

The predicted behavior was checked with a similar level indicator at lower temperature with water as the heat-pipe fluid. In this probe the heat rejection from the radiator was accomplished by natural convection. The unit was tested by varying the level of Dow-Therm A heated to 250°F with the result shown in Fig. 15. The measured temperature difference agrees with the calculated value within 15%, and the theoretical variation of temperature with level is followed closely.

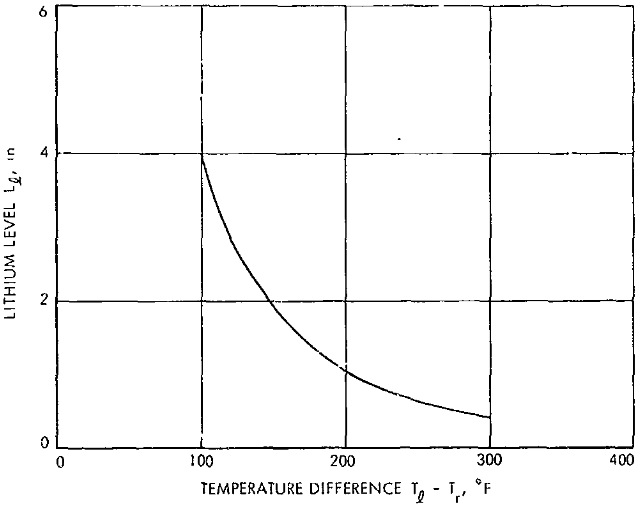

Fig. 14. Lithium level vs temperature difference for separator probe at 2000°F lithium temperature

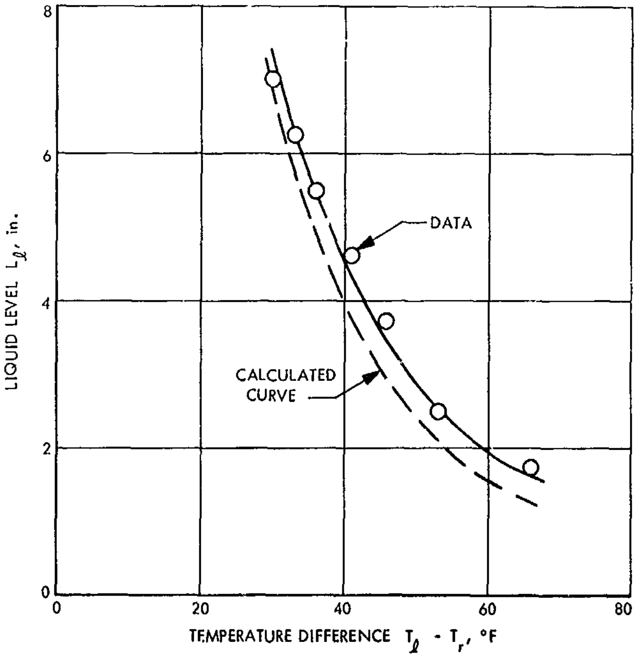

Fig. 15. Comparison of measured and calculated liquid level for differential heat-transfer liquid-level indicator in Dow-Therm A at 250°F

XIV. Liquid Propulsion

PROPULSION DIVISION

A. Combustion Effects in Sprays, *J. Houseman*

1. Introduction

In the area of injector design for liquid-propellant rocket engines, use is made of the experimental data obtained in cold-flow tests with simulated propellants. It is usually assumed that the effects of combustion on impingement and spray formation are small. The mass and mixture ratio distributions in an actual propellant spray are considered to be essentially the same as in a simulant spray.

This article presents experimental data which shows that, under many conditions, this assumption is not valid. This applies particularly to hypergolic propellants. A jet of nitrogen tetroxide impinging upon a jet of hydrazine[1] results in a nonuniform spray in which the oxidizer side is rich in oxidizer while the fuel side is rich in fuel. A sketch of the impingement region is shown in Fig. 1. Since the propellants are considered to be immiscible, liquid phase mixing and chemical reaction take place at the interface between the jets. The formation of gas at the interface prevents mixing of the streams and results in stream separation or "blowing apart" of the jets, which produces a nonuniform spray mixture.

Three mechanisms for stream separation are postulated as follows:

(1) Local boiling of the propellant due to heat released by liquid phase reaction.

(2) Gas evolution due to gaseous products of liquid phase reactions.

(3) Formation of a gas film between the jets due to gas phase reaction.

Theoretical models for these three mechanisms have been developed at JPL and the earliest version (Ref. 1) is shown in Fig. 2. The graph defines a separation-free area on the lefthand side as a function of pressure, propellant injection temperature, and contact time. This contact time is closely approximated by D/V, the orifice diameter divided by the average jet velocity.

An experiment was devised to verify these concepts by measuring the mixture ratio distribution across the spray from an unlike impinging doublet.

---

[1] Elverum, W. G., and Staudhammer, P., *The Effect of Rapid Liquid-Phase Reactions on Injector Design and Combustion in Rocket Motors*, Aug. 25, 1959 (JPL internal document).

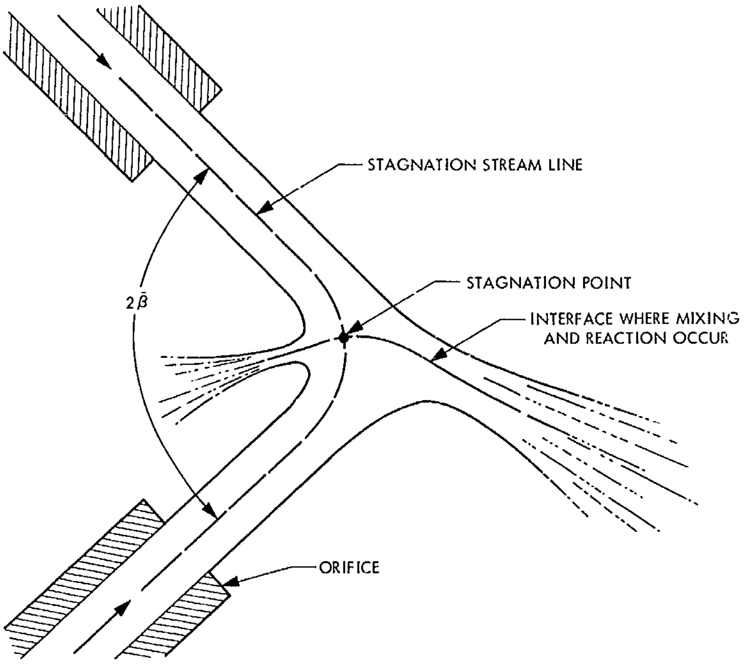

Fig. 1. Jet impingement

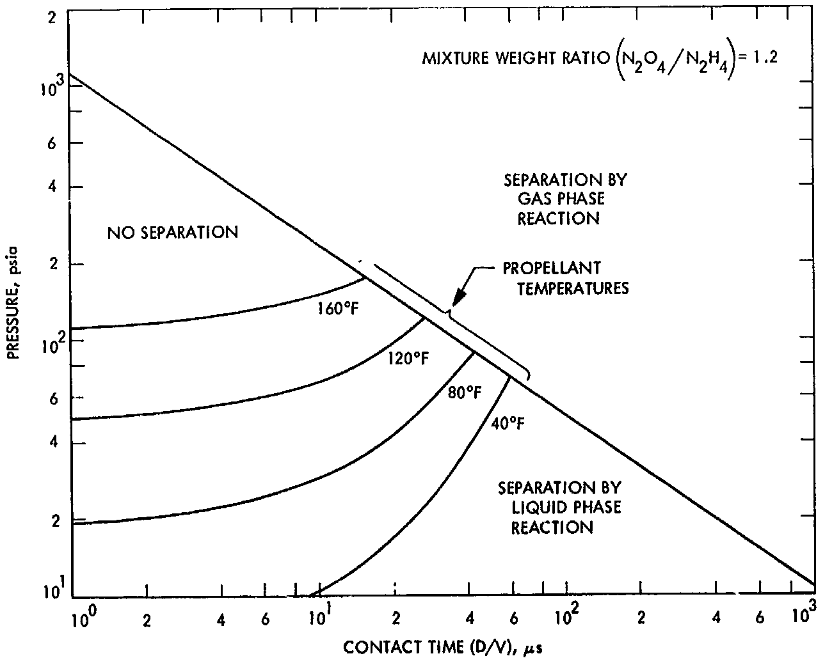

Fig. 2. Stream separation criteria

2. Experimental Procedures

Temperature conditioning of the propellants is achieved by a coil in a water bath, the coil being just ahead of the firing valve. The chamber and sampling probe assembly are shown in Fig. 3. Two sonic orifices and a leak valve in series provide input gas to the quadrupole mass spectrometer.

The gold probe tip extends 0.140 in. upstream of the water-cooled 0.250-in. stainless steel probe to overcome the boundary layer of the tube. Details of the probe are shown in Fig. 4.

In order to determine the mixture ratio at a point, it is only necessary to measure the H_2/N_2 ratio and the O_2/N_2

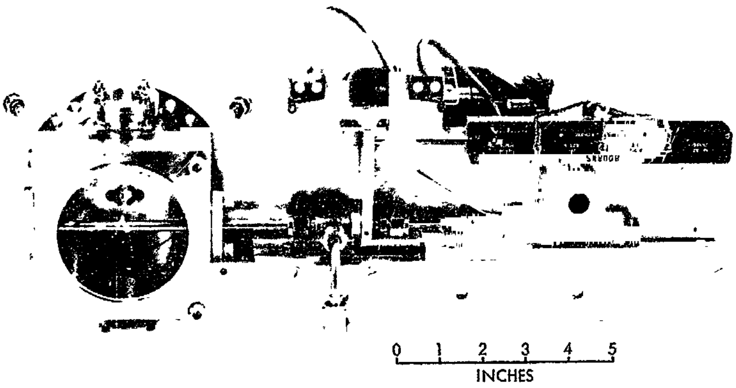

Fig. 3. Engine and sampling probe assembly

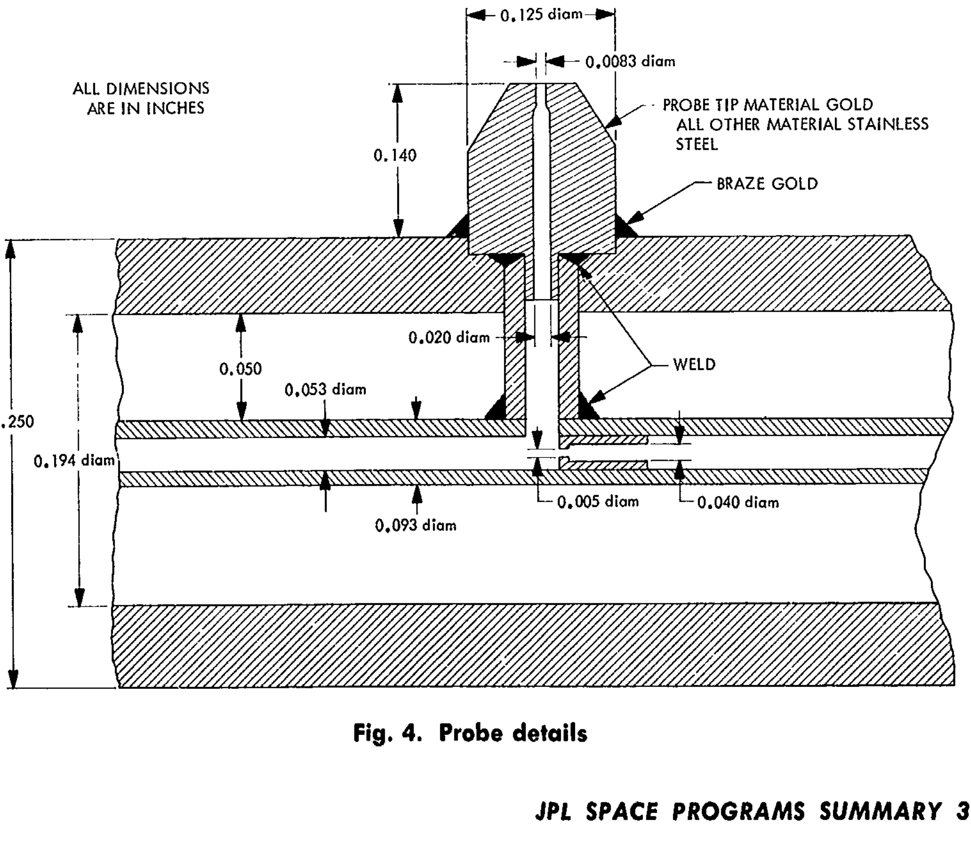

Fig. 4. Probe details

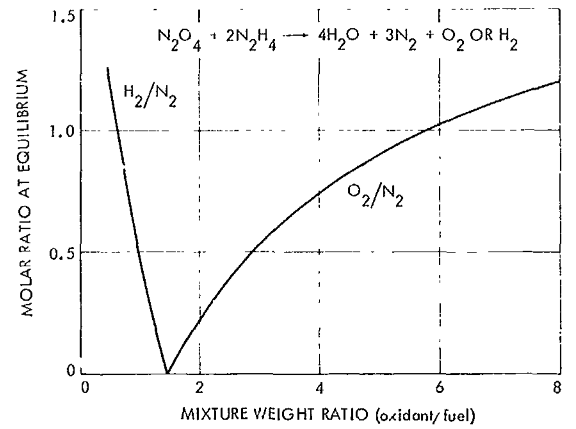

Fig. 5. Equilibrium composition for N_2O_4/N_2H_4 at 300°K

ratio of the sampled gas, as indicated in Fig. 5. The quadrupole mass spectrometer was modified for operation under computer control to obtain a simplified data recording system. As shown in Fig. 6, the normal output consists of a spectrum of up to 50 peaks. The mass numbers are varied from 1 through 50 in a scan by means of a continuous ramp voltage of from 0–10 V. In this experiment, only a few peaks are of interest and only the height of the peak is important, the shape being irrelevant. By setting the ramp voltage at various distinct values corresponding to the top of the peaks of the desired mass numbers, the output of the mass spectrometer will consist of only a few numbers rather than a whole spectrum. This forms the basis for the new method of operation shown on the right side of Fig. 6. A PDP-4 computer was used to generate the ramp voltages to tune the EAI 200 quadrupole to the peaks of interest. The equipment was operated at a scanning speed of one peak per 10 ms.

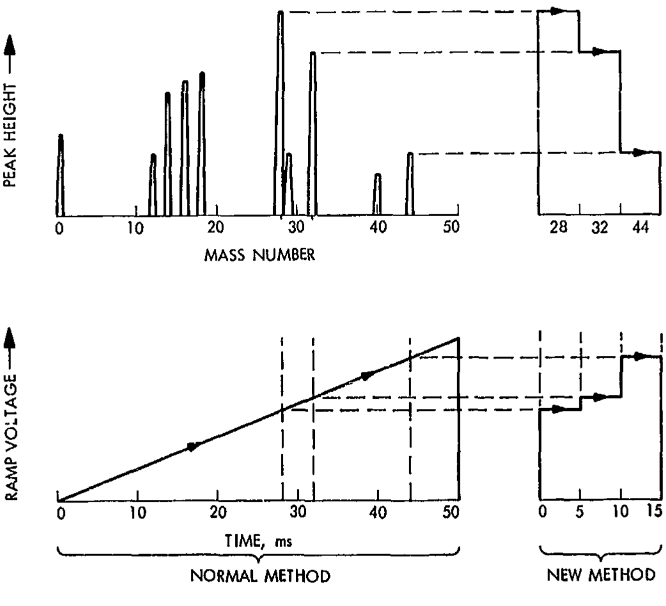

Fig. 6. Mass number selection for quadrupole mass spectrometer

3. Results

A series of 4.0-s firings was carried out with the probe at different positions in the chamber.

The mixture ratio is definitely nonuniform across the spray and only slightly influenced by injection temperature. Data based on both H_2/N_2 and O_2/N_2 measurements are shown in Fig. 7. The mixture ratio varies from 0.6 on the fuel side to 2.2 on the oxidizer side. The data are plotted on a stream-separation criteria plot in Fig. 8 for comparison with a provisional gas evolution model. Separation occurred at all the points shown. The 140°F points are on the correct, i.e., the separated, side of the 140°F line. However, the 40°F points are on the wrong side of the 40°F line. Comparison with the dashed line for separation by gas-phase reaction shows that all points are in the correct region.

Considerable roughness was experienced with the single unlike doublet. Figure 9 shows chamber pressure

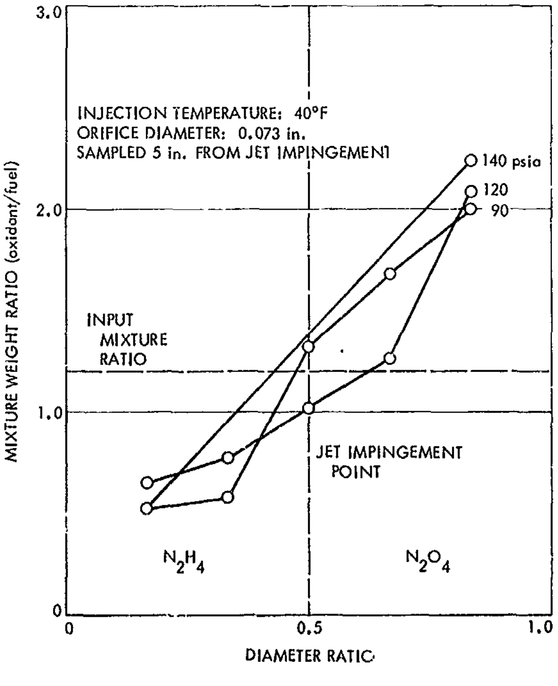

Fig. 7. Stream separation in an unlike doublet

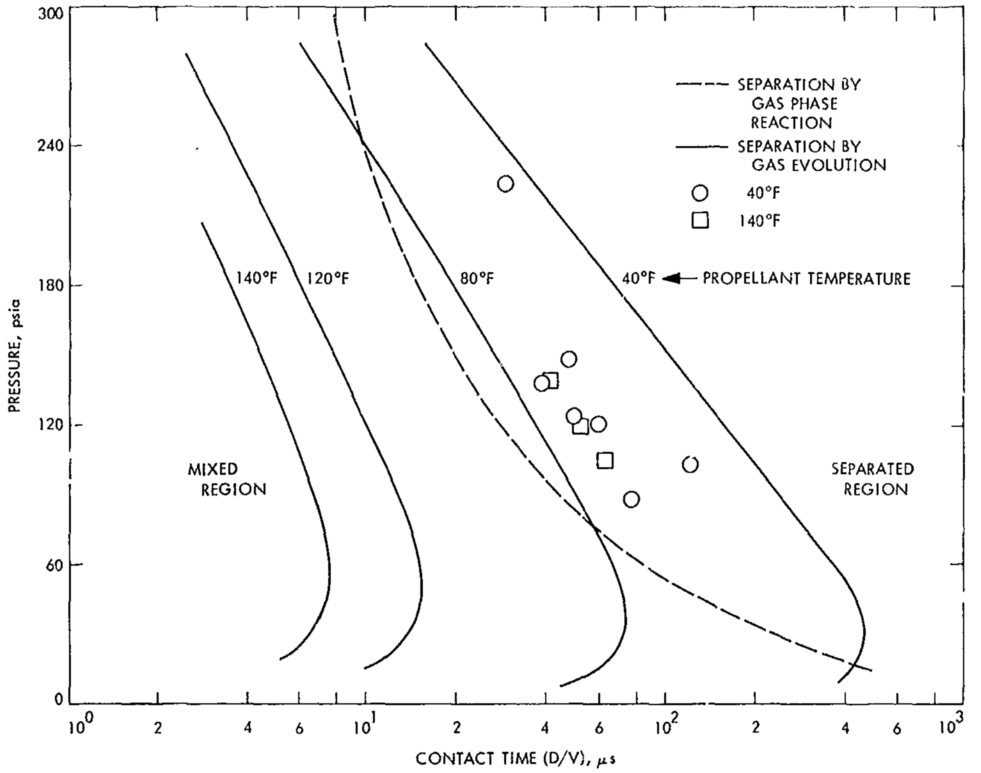

Fig. 8. Gas evolution model

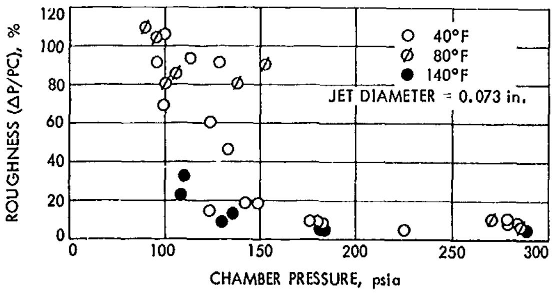

Fig. 9. Roughness with a single unlike doublet

fluctuations (ΔP) up to 100% as a function of average chamber pressures (PC) and propellant temperature. The frequency ranged from 100–250 Hz.

4. Conclusions

The experimental data shows that combustion effects can produce mixture ratio distributions that are significantly different from those obtained in simulated cold-flow tests. When using such cold-flow data, the stream separation criteria should be checked to establish that the element will operate in a non-separated region. This probably applies not only to mixture ratio distributions, but also to mass and drop-size distributions.

Reference

1. Kushida, R., and Houseman, J., *Criteria for Separation of Impinging Streams of Hypergolic Propellants*, Technical Memorandum 33-395. Jet Propulsion Laboratory, Pasadena, Calif., July 15, 1968.

XV. Lunar and Planetary Instruments

SPACE SCIENCES DIVISION

A. A Mars Meteorology Wind Tunnel, *J. M. Conley*

1. Introduction

This article is based on the assumption that it will be desirable for the first Mars lander to be capable of measuring the atmospheric temperatures and wind velocities of Mars. Trade-off studies for the selection of specific instruments for wind measurement have been inconclusive (SPS 37-53, Volume III, pp. 136–143) and more detailed data on the operation of various instrument types under the Mars surface environment are required in order to thoroughly evaluate the instruments for this application. Experimental determination of the heat transfer parameters of immersion thermometers under simulated Mars surface conditions is also necessary. It would, of course, be desirable to simulate all of the relevant environmental parameters, which may include, depending on the instrument under test, gas composition, pressure, and temperature; wind speed; solar radiation; surface temperature; atmospheric dust and gravity. However, if the candidate instruments can be tested under conditions approximating those at the Mars surface, then scaling procedures will allow close estimates of their performance for any given Mars model atmosphere. It does *not* follow that the performance of the various instruments under earth-surface atmospheric conditions can be readily scaled to the Mars conditions since the density ratio of the two atmospheres is of the order of 100 and small errors in the measurements would result in considerable errors when extrapolated to the Mars conditions. Furthermore, scaling procedures applied over this large density ratio would require extremely delicate measurements of forces, temperatures differences, etc., and would not be nearly as convincing as actual operation of the instruments under simulated Mars conditions.

A small wind tunnel capable of simulating the expected Mars surface pressures and wind speed has been built and is described in this article. Original design goals for the tunnel included test section speeds in the range of 0–460 ft/s at gas densities of 10^{-5}–4×10^{-5} g/cm^3 corresponding to Mars surface pressures of 5–20 mbars.

2. Design Studies

a. Basic options. It was required that the system allow simulation of the critical environmental parameters for the aforementioned instrument types. For the anemometers, if both Reynolds numbers and speed are simulated, only small corrections to the data would be required for the other parameters of interest. In later phases, it may be desirable to include atmospheric dust and temperature, but, in many cases, these can be simulated independently of Reynolds number and speed, i.e., with other facilities. For the immersion thermometer work, it would also be desirable to simulate thermal radiation and gas temperature environment. The solar thermal radiation incident on a small sensor can be simulated with a small light source and the infrared radiation by shrouds surrounding the sensor. Gas temperature control can be accomplished by means of a heat exchanger upstream of the sensor. Although these features were not incorporated into the design, they can be added at a later date.

Ideally, the test section would be a black-body, anechoic chamber with linear dimensions of about 10 ft. This would allow testing of sonic anemometer arrays and other large instruments. Such a system is not within the scope of the present program. A rotating arm within a vacuum system was considered but rejected because of the relatively large forces that would arise due to rotation. Thus, a wind tunnel is required.

A minimum test section size of about 1-ft^2 cross section is determined by the rotating-cup anemometer, which has a projected area of about 4 in.^{2}. Thus, a volume flow rate of 460 ft^3/s (27,000 ft^3/min) is desirable. Two pumping techniques were considered: (1) ejector pumps exhausting to the atmosphere, and (2) a recirculating fan operating within a vacuum system. At the maximum anticipated test section pressure, a throughput of about 5×10^5 torr–liter/s would be required. Since a very large, costly high maintenance steam ejection facility would be necessary, this technique was rejected.

No information was available on the performance of commercial fans at the densities of interest. Measurements of the head of a small aircraft fan blade at blade Reynolds numbers approximating those of a larger commercial fan (both of vaned axial construction) indicated that good performance could be obtained down to pressures of approximately 5 mbars of air at a standard temperature, corresponding to the lowest expected Mars surface pressures and fan blade Reynolds numbers. A surplus jet engine compressor might also have been used. Such fans, which operate with supersonic blade tip speeds, are capable of producing a relative total head $\Delta p/p$ of approximately 0.5 per stage, where Δp is the total head and p is the inlet static pressure. In contrast, the commercial fan selected yields only $\Delta p/p = 0.022$ per stage. However, it was inexpensive, readily available, required no expensive modification, and was deemed adequate for the application.

b. Tunnel loop losses. An existing vacuum system and a tank 4 ft in diameter by 16 ft long was available. Even though the disadvantages of an annular construction were realized (Ref. 1), it was the most economical means of achieving the desired test section conditions. Head losses to be considered in the design included those due to skin friction, screens, corners, and diffuser inefficiency.

The desired maximum test section speed of 460 ft/s requires a fan $\Delta p/p = 0.12$, independent of gas density. Loop losses would add to this requirement and any head recovery in the diffuser would lessen it. However, the available vacuum tank allowed space for only a two-stage fan with a $\Delta p/p = 0.044$. Thus, a maximum speed of 280 ft/s could be achieved assuming no friction losses and zero diffuser efficiency. A friction loss of 15% of total head would result in a maximum speed of approximately 265 ft/s. Although this falls far short of the original 460 ft/s design goal, it was considered to be adequate for critical tests required to evaluate the performance of the instruments in question. Higher Reynolds numbers and dynamic pressures can be achieved by operating at higher pressures.

Since turbulence levels of the order of several percent could be tolerated, neither turning vanes nor screens were incorporated into the initial design. However, provisions were made for adding them at a later date if they proved to be necessary.

The diffuser efficiency to be expected was unknown, although criteria established for higher Reynolds numbers than those occurring in the diffuser indicated that boundary layer separation would occur and that diffuser efficiency would be quite low. For design purposes, it was assumed to be zero and any actual head recovery in the diffuser would allow re-setting of the fan-blade pitch to increase the maximum test section speed attainable. The only appreciable skin friction losses occur at and near the test section and were calculated to be approximately 10% of the fan head. Lack of a diffuser at the fan exit would also result in some loss of head. In the absence of screens, the loss around the loop should not exceed 15% of the fan head, excluding that due to diffuser inefficiency.

3. Final Design

Figure 1 is a cross-sectional view of the system, approximately to scale, and Figure 2 is a photograph of the nozzle and test section taken through the 5-ft diam vacuum tank port.

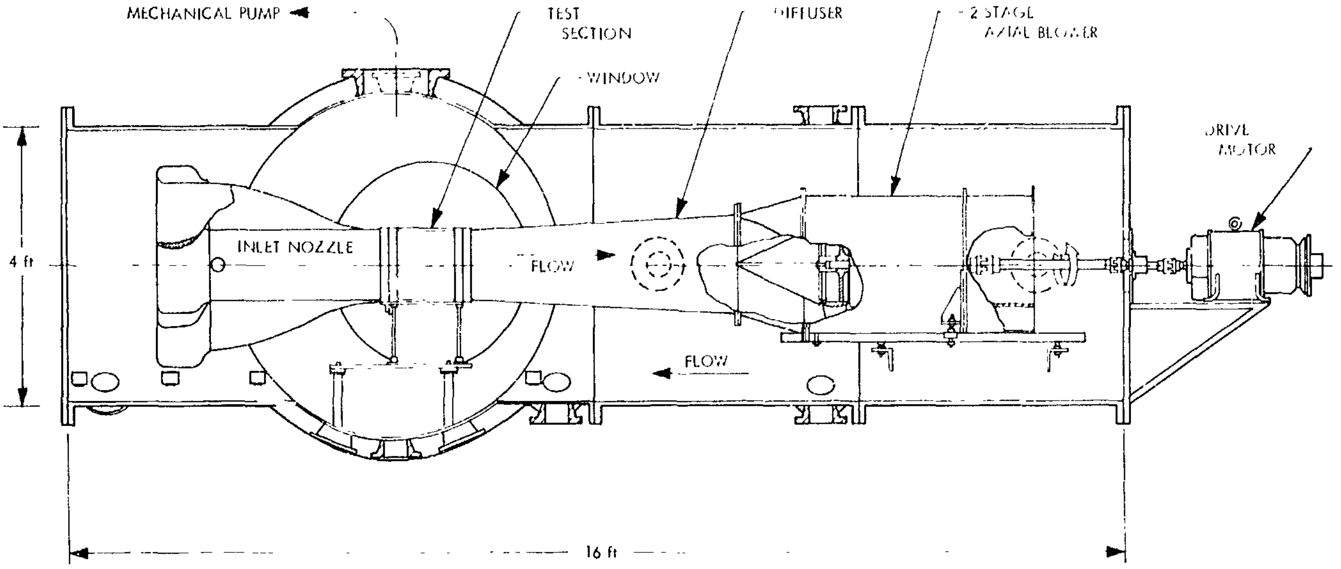

Fig. 1. Mars wind tunnel cross section

Fig. 2. Nozzle and test section

The nozzle entrance is hexagonal in shape. Four of the eight sides taper to zero width at the test section such that, in cross section, the sides appear as two cubic curves of the form $y = ax^3/3$ on the entrance end of the nozzle and $y' = ax'^3$ on the exit end. The alternate sides are of constant 12-in. width. Nozzle length is 36 in. and the curves intersect, with equal slope, at a point 22.8 in. from the entrance. A nozzle entrance bell of 1.5-in. radius is provided. The area of the nozzle entrance was selected to provide approximately equal conductances in the nozzle entrance and in the annulus surrounding it. The contraction ratio is 4.8.

The test section is a 1-ft cube. Plexiglas windows, 8-in. diam, are provided on one side and the top, and a hinged plexiglas door 9-in. wide by 12-in. high forms the other side. A removable bottom plate can be readily replaced for various model configurations. No traverse mechanism has been provided, although it would be highly desirable since the system now must be vented in order to move a model or probe. Pumpdown time from one atmosphere to 10 mbars is approximately 3 min with the existing 300 ft^3/min mechanical pump. On the basis of the data given in Ref. 2, the test section profile should be reasonably flat for speeds down to approximately 1 ft/s.

The diffuser half-angle is 3 deg and it is coupled to the fan by a transition section 1-ft long.

The fan is a two-stage, vaned axial 23.25-in. diam blower with a 14-in. hub. It is nominally rated at 50 hp, 3450 rev/min, 12,000 ft^3/min at 18 in. of water Δp. Variable-pitch blades allow some latitude in the fan characteristics.

The direct drive motor is a silicon-controlled rectifier controlled variable speed dc motor with tachometer feedback. Although only 1 hp is required to drive the tunnel at the highest expected Mars atmosphere surface density, the high moment of inertia of the fan would result in a 10-min acceleration time to full speed and a similar deceleration time. For this reason, and also to allow operation at high Reynolds numbers, a 5-hp drive motor was chosen. Under constant load, its speed is stable at ±1% of set speed from 20–3500 rev/min. The motor is coupled through the vacuum tank end plate by an oil-lubricated, graphite-to-ceramic, rotating seal.

4. System Performance

The maximum test section speed achieved at 3450 rev/min, as measured by means of a pitot was found to be 240 ft/s at an air density of 2×10^{-5} g/cm^3. Adjustment of the fan blade pitch should increase this to approximately 280 ft/s. Since this is in nearly exact agreement with the result of applying Bernoulli's equation to the characteristics published by the fan manufacturer, it must be assumed either that the diffuser head recovery balances the friction loss or that both are negligible. However, these are preliminary data and further measurements will be required since the fan inlet density is not known. The instrumentation necessary for more precise measurements is now being installed and more detailed performance information, including profiles and turbulence data, will be available in the near future.

The leak rate of the vacuum system results in a pressure increase of approximately 0.015 mbars/hr. This is much less than the rates associated with temperature changes due to venting and pumping down the system. It is not known how much of this leak rate is due to the rotating seal, but, since the total leak rate is negligible, the seal must be considered to be satisfactory. No seal wear has been detected after approximately 16 hr of operation.

The system can be operated easily by one man and should require very little maintenance. Although measurements of the test section speed profiles would be facilitated by a traverse system, the effort required to design and build one would not be justified at this time.

References

1. Pankhust, R. C., and Holder, D. W., *Wind Tunnel Technique*, Sir Isaac Pitman and Sons, Ltd., London, 1952.
2. Prandtl, L., and Tietjens, O. G., *Applied Hydro- and Aeromechanics*, Dover Publications, Inc., New York, N. Y., 1957.

XVI. Space Instruments

SPACE SCIENCES DIVISION

A. A Low-Noise Charge-Sensitive Video Preamplifier for Use With the SEC Camera Tube, *D. F. Stout*

1. Introduction

Handling of slow scan video information from the secondary electron conduction (SEC) camera tube requires an extension of techniques used with slow scan vidicons. At standard scanning rates (30 frames/s) the signal current from the target of an SEC camera tube has a signal-to-noise ratio of only 50 to 100. At slow scan speeds, similar to those used on *Mariner* television systems, the signal-to-noise ratio from the SEC camera tube is severely degraded. Work has been performed to overcome this drawback to a potentially useful spacecraft imaging camera tube.

2. Approach

The first consideration was to develop a television system that would effectively scan the SEC camera tube at high speeds and, at the same time, possess line and frame times which would be compatible with the spacecraft data handling capability. Two approaches to achieve the above result are being explored.

1. *Beam chopping.* This method allows the read beam to be on for only a short portion of the time it is scanning across each picture element (pixel). This generates pulses with amplitudes proportional to the quantity of charge stored on each pixel.
2. *Beam position modulation.* This technique utilizes a small fast vertical beam movement during the time the beam is slowly sweeping horizontally over each pixel. Again, this produces pulses of video information during the short vertical movement of the beam.

Either method results in fast low-noise pulses of video information. For a 1000-× 1000-pixel raster, these pulses contain from approximately 10^{-16} to 10^{-14} C/pulse. An optimum method of preamplification was needed, so that the signal-to-noise ratio of this information would not be degraded. An extensive survey of various methods of low-noise preamplification was made prior to designing a charge-sensitive amplifier.

3. Preamplifier Design

Accuracy in charge measurements is enhanced by making these measurements independent of variations in source capacitance, amplifier input capacitance, and stray wiring capacitance. This is accomplished by making the effective amplifier input capacitance very large and also dependent only on passive temperature stable components.

The standard configuration (Fig. 1a) for such a device is a high-gain, high-quality, wide-bandwidth operational amplifier with a feedback network whose prime elements are a parallel capacitance C_f and resistor R_f.

The output of the circuit shown in Fig. 1a for an input charge impulse of magnitude Q is

$$e_2(t) = \frac{Q \exp\left[-t/(R_f C_f)\right]}{C_f}$$

The capacitor C_f should be as small as possible so that e_2 is sufficiently above noise before going to the next amplifier.

The capacitor C_f can be treated as if it were a Miller capacitance $C_f(1-A)$. If gain A approaches infinity, then essentially all incoming charge is deposited on C_f. The input impedance is therefore nearly zero for the charge pulse. For these reasons the device is called a charge-sensitive amplifier.

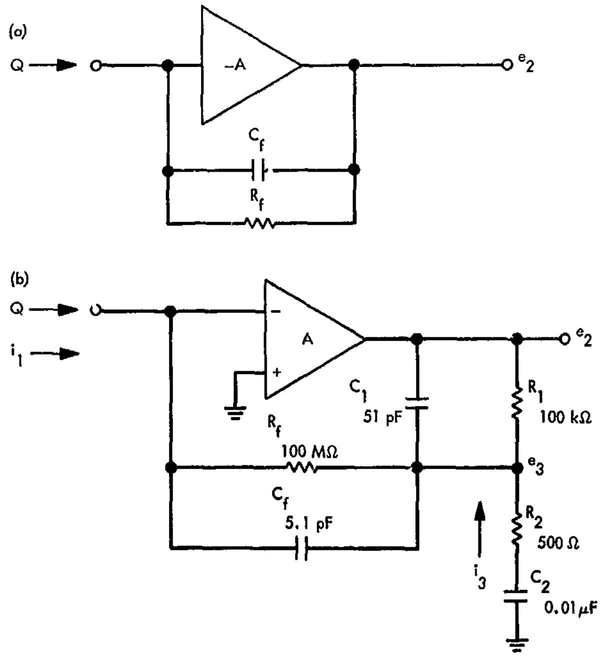

Fig. 1. Charge-sensitive amplifiers: (a) basic, (b) modified

For the SEC camera tube, C_f must be only 0.1 pF if e_2 is to remain greater than 1 mV for all expected charge pulses. This would make C_f very difficult to realize with the required accuracy and stability. It would be better if C_f could be at least several picofarads.

If a 100:1 attenuator is placed between e_2 and the feedback network impedance Z_f, then several significant changes are made to the feedback circuit requirements: (1) R_f must be lowered in resistance 100 times, and (2) C_f must be raised in capacitance by 100 times. These changes will make the charge-to-voltage conversion gain identical with that of the original preamplifier. The new circuit diagram is shown in Fig. 1b.

Thus, C_f looks like 5.1 pF/100 = 0.051 pF as far as the conversion gain is concerned. Conversely, to the input, C_f appears to be $A_L\,C_f = 0.56\ \mu\text{F}$, where A_L = loop gain $= 0.01\,A = 1.1 \times 10^5$. It is obvious that stray capacitance is negligible compared to 0.56 μF and should therefore have little effect on the conversion gain.

4. Attenuator Design

The attenuator requires careful design since it performs the pulse shaping for the entire preamplifier. This attenuator is sometimes referred to as a lead–lag network because over a given frequency range the phase shift is approximately zero. In the time domain, the parameters of the attenuator are chosen such that the rise and fall times are both 5 μs.

Some basic assumptions regarding the total television system must first be made before the attenuator design can be determined.

1. The picture format dimensions are chosen to be 1000 × 1000 pixels.
2. The sweep speed is 50 ms for the active portion of each line. This means the beam will reside over each pixel for 50 μs.
3. The duty cycle for beam chopping or beam position modulation is 2% so that the charge pulses have a width of 1 μs.

These assumptions are used to determine the preamplifier pulse shaping. With 49 μs between pixels, adequate time is available to form a good quality gaussian pulse with rise and fall times of several microseconds. A gaussian pulse shape has very good characteristics upon which to perform an accurate analog-to-digital conversion. The pulse shape and time constants chosen are adequate to assure that the baseline will be within 1% of zero before the next pulse occurs.

The transfer function of the attenuator is

$$\frac{E_3(s)}{E_2(s)} = \frac{(1 + T_1 s)(1 + T_2 s)}{T_1 T_2 s^2 + (T_1 + T_2 + T_{12})s + 1}$$

$$= \frac{(1 + T_1 s)(1 + T_2 s)}{(1 + T_3 s)(1 + T_4 s)}$$

where

$T_1 = R_1 C_1 = 5 \times 10^{-6}$ s = pulse rise time

$T_2 = R_2 C_2 = 5 \times 10^{-6}$ s = pulse fall time

$T_{12} = R_1 C_2$

The magnitude of the attenuation is

$$\left| \frac{e_3}{e_2} \right| = \frac{T_1 + T_2}{T_1 + T_2 + T_{12}} = 0.01$$

Rearranging,

$$T_{12} = \frac{T_1 + T_2}{\left| \frac{e_3}{e_2} \right|} - T_1 - T_2 = 9.9 \times 10^{-4}$$

For physical size considerations, C_2 is first chosen to be 0.01 μF. The other components then become as shown in Fig. 1b.

A Bode plot of the attenuator transfer function is shown in Fig. 2. Also shown on the same figure is the response as predicted by the CIRCS computer-aided circuit-analysis program. Figure 3 shows the phase plot as obtained with the CIRCS program, which is executed on the IBM 1620 computer.

5. Preamplifier Analysis With Attenuator Included

By assuming the operational amplifier has infinite gain, infinite input impedance, and zero output impedance, the analysis is greatly simplified. From Fig. 1b and the above three assumptions, the following equations are derived:

$$E_3 = I_1 Z_f = I_3 Z_2$$

or

$$I_1 = \frac{I_3 Z_2}{Z_f}$$

and

$$E_2 = I_3 (Z_1 + Z_2)$$

The transimpedance becomes

$$\frac{E_2}{I_1} = \frac{I_3(Z_1 + Z_2)}{I_3 Z_2 / Z_f} = \frac{Z_f(Z_1 + Z_2)}{Z_2} \tag{1}$$

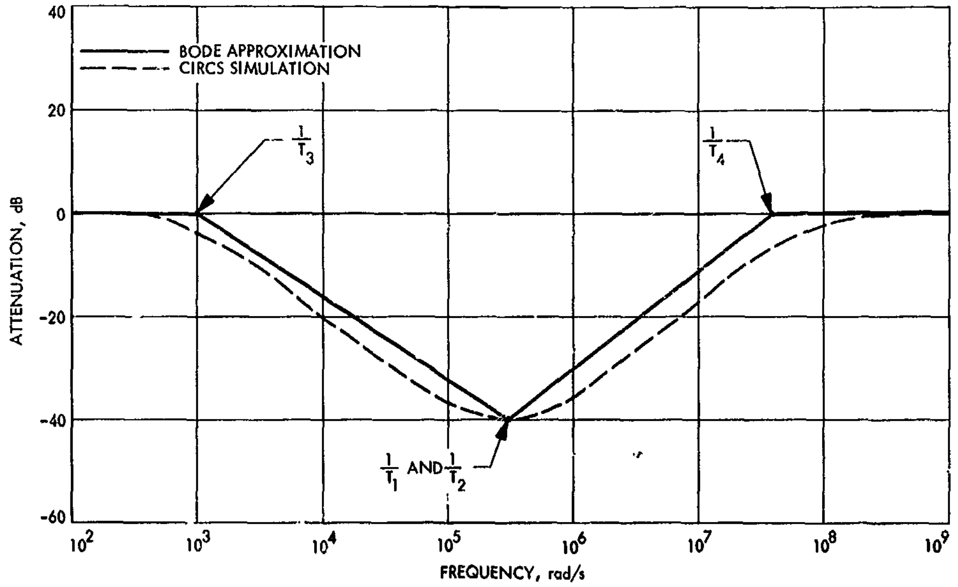

Fig. 2. Attenuation of lead–lag network

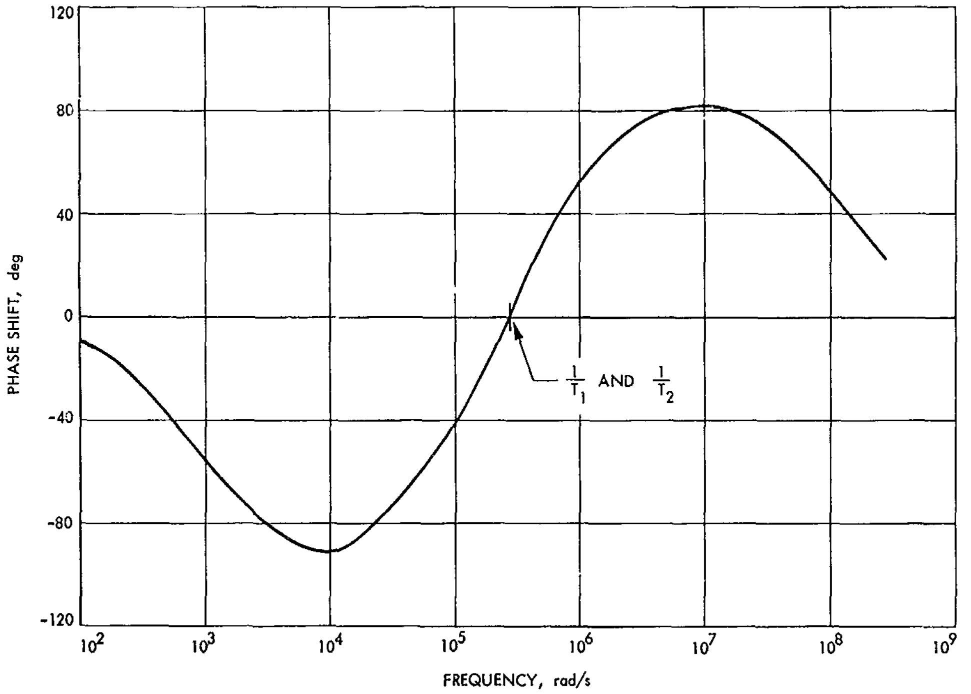

Fig. 3. Phase shift of lead–lag network

The input current I_1 is assumed to be an impulse of magnitude Q. By changing to the s domain and assuming $Z_2 \ll Z_1$, Eq. (1) becomes

$$E_2(s) = \frac{Q R_1}{C_f R_2}\left[\frac{sT}{(1+sT)^2}\right] \tag{2}$$

where $T = T_1 = T_2 = 5$ μs. The inverse transform of Eq. (2) is

$$e_2(t) = \frac{Q R_1}{C_f R_2}\left[\frac{t \exp(-t/T)}{T}\right]$$

The peak voltage of the output pulse is

$$e_2(\text{peak}) = \frac{Q R_1}{e C_f R_2}$$

where $e = 2.718 =$ natural logarithm base.

A peak output voltage greater than 1 mV was desired for the minimum detectable charge pulse (2×10^{-16} C). By choosing $C_f = 5.1$ pF, which is a practical lower limit for this capacitor, the minimum peak output voltage e_2 becomes 2.88 mV. For a pulse of 2×10^{-14} C, the maximum peak output voltage is 0.288 V. With a ×4 buffer amplifier, the pulse amplitude range is approximately 0.0115 to 1.15 V.

6. Feedback Resistor R_f

Current in the attenuator is several orders of magnitude larger than that in Z_f. For this reason the time constant of Z_f does not significantly affect the preamplifier output pulse shape. Therefore, R_f can be chosen from noise considerations.

Feedback resistor R_f injects noise current into the first stage field-effect transistor (FET) with magnitude

$$i_n = \left(\frac{4kT}{R_f}\right)^{1/2} \text{A/(Hz)}^{1/2} \tag{3}$$

where

$k =$ Boltzmann constant $= 1.38 \times 10^{-23}$ J/°K

$T =$ temperature, °K

The channel noise of good quality n channel FETs is approximately 4×10^{-14} A at the frequencies of interest here (i.e., approximately 20–100 kHz). Equation (3) can be rearranged to find the resistance that will produce this much current:

$$R_{f,\min} = \frac{4kT}{i_n^2} = 10.4\,\mathrm{M}\Omega$$

The actual value used in the breadboard preamplifier was 100 MΩ. Therefore, R_f is a negligible noise source.

7. FET Cascode Design

The input stage of the preamplifier uses a cascode configuration for several reasons.

1. (1) Input capacitance, which is mostly unwanted Miller capacitance and likewise temperature sensitive, is decreased several orders of magnitude. Stability of these first two stages is thereby enhanced. This is important because the overall stability of the entire amplifier is critically dependent on the stability of each stage. The phase shift of each stage must be carefully controlled if the overall phase margin is to be adequate.
2. (2) Bandwidth is also increased without sacrificing the superior low-noise characteristics of the first FET.

The cascode stage gain is simply the product of the common base stage (second FET) transconductance and the load resistance: $A_v = (3 \times 10^{-3})\,(3 \times 10^{3}) = 9$.

To verify the gain and stability of the cascode configuration, an equivalent circuit of the stage was modeled for use with the ECAP computer-aided circuit-analysis program. This model is shown in Fig. 4. The results of this simulation, as run on the IBM 7094 computer, are shown in Figs. 5 and 6. The large gain and phase margins indicate a very good stability for the stage.

Since the two FETs in the cascode stage only provide a voltage gain of 9, the second stage must also be a low-noise device. A p-channel 2N2497 FET was chosen because it will also shift the dc bias level to zero. The following μA709 needs this zero bias so that its output quiescent bias will be zero. Both the input node and the output node of the charge-sensitive amplifier are biased at zero. This allows dc-coupled feedback through the attenuator and R_f to achieve a high degree of dc stability. A 100% change in any single-loop gain parameter that affects bias will cause only a $100\%/1.1 \times 10^5 = 0.00091\%$ change in the bias levels. The same stability is also achieved for the charge-to-voltage conversion gain of the amplifier. This gain is nominally $0.288\ \mathrm{V}/2 \times 10^{-14}\ \mathrm{C}$. The schematic of the complete charge-sensitive amplifier is shown in Fig. 7.

8. Initial Experimental Results

A breadboard version of the charge-sensitive amplifier has been fabricated and partially tested. The results of several of these tests are summarized.

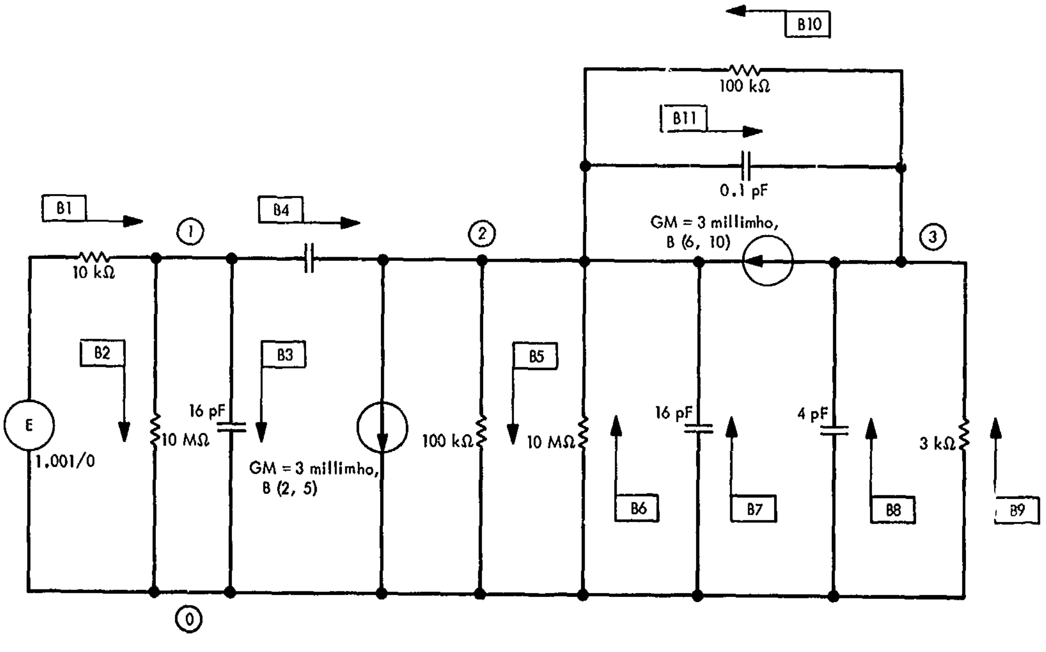

Fig. 4. 2N4869A FET cascode pair modeled for ECAP

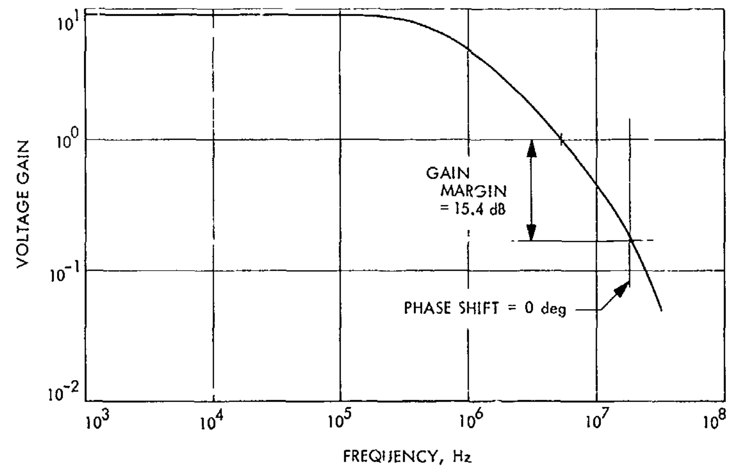

Fig. 5. Frequency characteristics of FET cascode stage

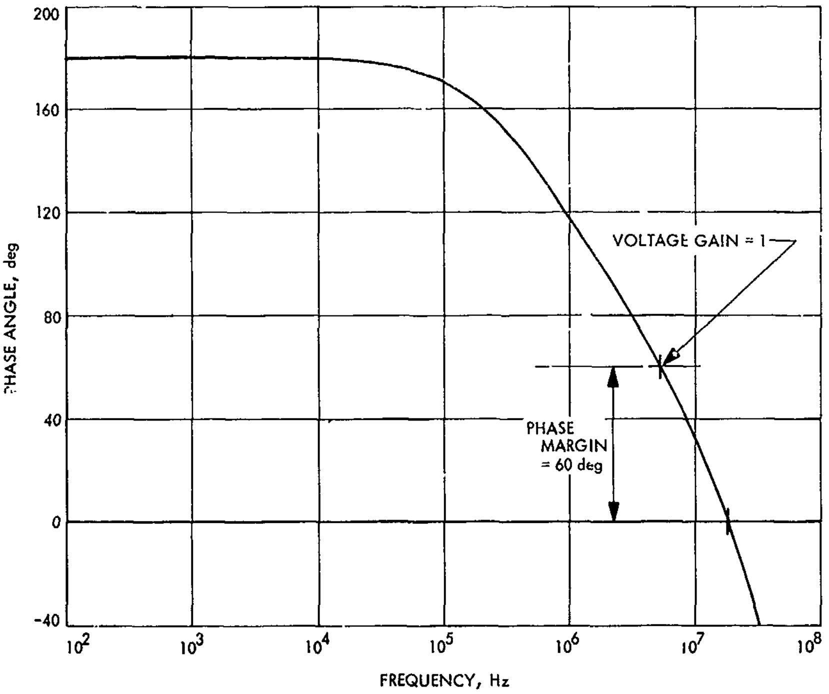

Fig. 6. Phase characteristics of FET cascode pair

Linearity test. By coupling to the input of the charge-sensitive amplifier through a 30-pF capacitor, the conversion gain can be measured. The charge transferred across the capacitor C is simply $Q = CV$, where V is the peak pulse voltage appearing on the generator side. The graph of peak voltage output (after the ×4 buffer) as a function of charge input is shown in Fig. 8.

Noise test. Signal-to-noise ratio was measured at the preamplifier output terminal as a function of input stray capacitance. The minimum stray capacitance of the device (in its present layout) is 35 pF. Coupled with this, a 30-pF output capacitance of an SEC camera tube would give a signal-to-noise ratio of 180.

Signal was defined as the peak pulse voltage resulting from the charge pulse input. Noise was measured by removing the generator and connecting a true rms voltmeter to the preamplifier output terminal. Figure 9 shows the results of this test.

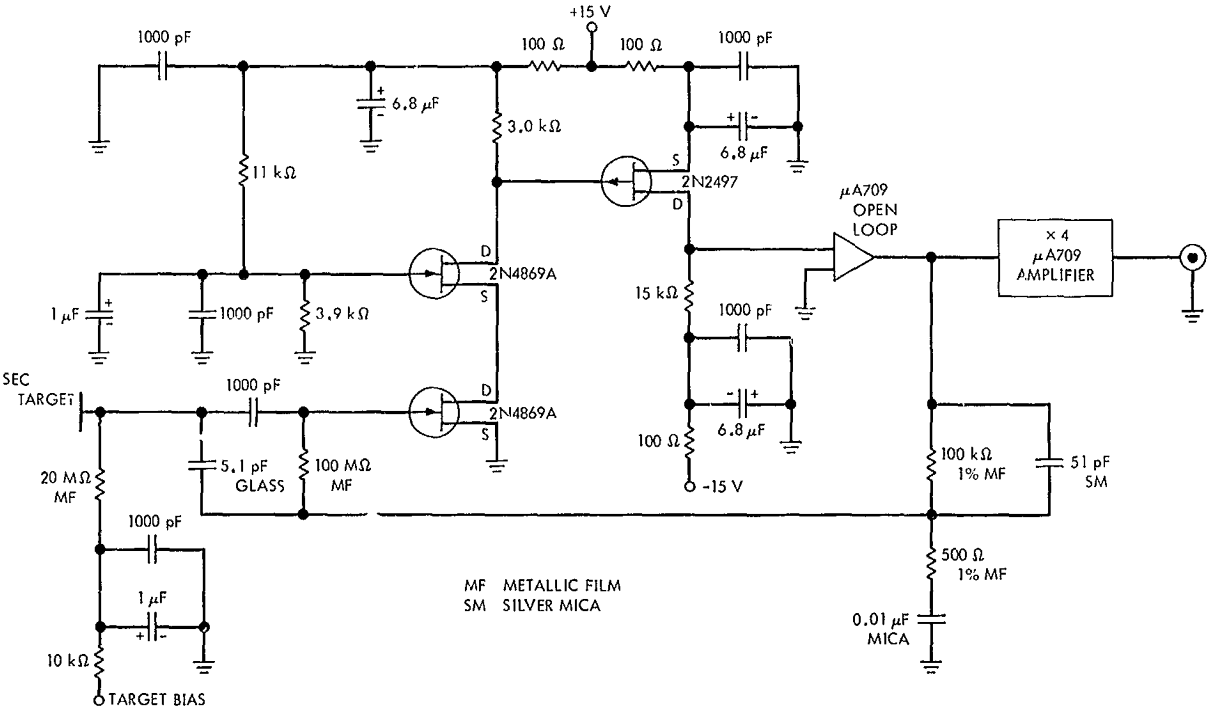

Fig. 7. Charge-sensitive amplifier

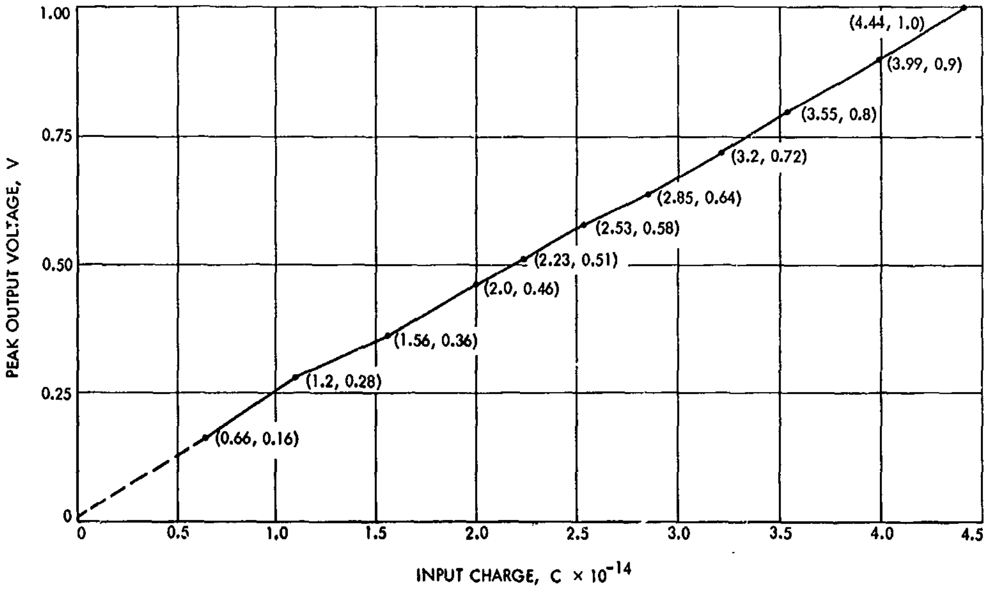

Fig. 8. Linearity of charge-sensitive amplifier

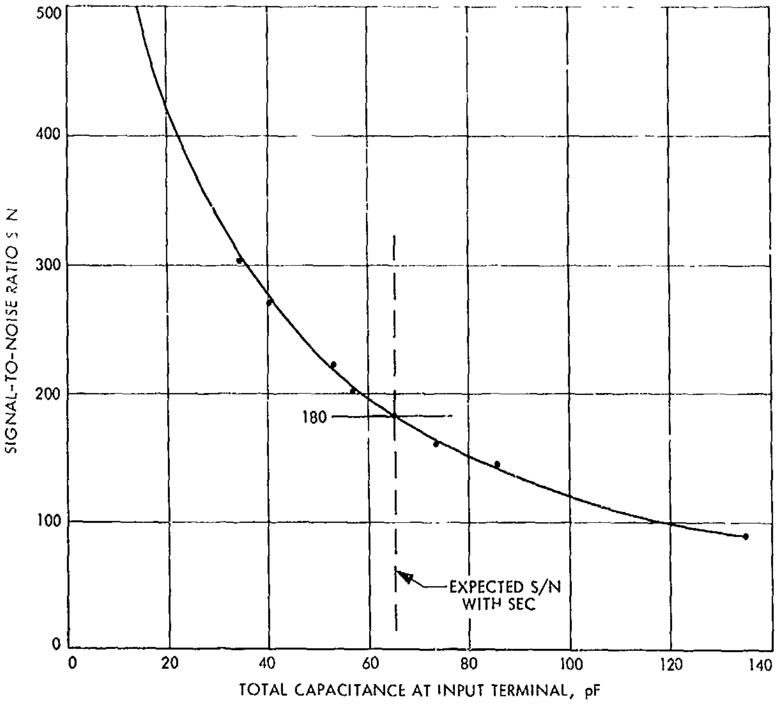

Fig. 9. Signal-to-noise ratio of preamplifier

9. Conclusions

The charge-sensitive preamplifier is capable of making the SEC camera tube compatible with a slow-scan television system. The circuit parameters chosen in this first iteration of such a device should be compatible with present *Mariner* television system timing parameters, i.e., 50-ms line time and 945 pixels/line. The dynamic range of the preamplifier covers the two orders of signal current magnitude expected for the above scan speed. Thus, charge pulses from 2×10^{-16} to 2×10^{-14} C/pulse will produce amplifier output pulses from approximately 0.010 to 1.0 V. The experimental preamplifier signal-to-noise ratio of 180 is adequate when coupled to the SEC camera tube that has a signal-to-noise ratio of only 50–100.

B. Alignment of the Flight-Model Infrared Interferometer, *F. L. Murphy*

1. Introduction

The design, development, and construction of the flight-model infrared interferometer were presented in SPS 37-43, Vol. IV, pp. 253–257, and SPS 37-52, Vol. III, pp. 142–148. In this article, the procedure in the optical alignment of the instrument is discussed in three areas: (1) cat's-eye retroreflector, (2) fore-optics, and (3) servo-drive.

2. Cat's-Eye Retroreflector Alignment

Fabrication and assembly of the cat's eye constitute as much of the critical requirements as does the final optical test for focusing. Therefore, the mechanical assembly will be described along with optical alignment procedures.

The cat's-eye retroreflector consists of a secondary mirror assembly, quartz support tube, primary mirror, and differential thread adjustment housing. Its function, shown by the optical diagram in Fig. 10, is similar to that of a cube-corner reflector, namely to reflect rays in the direction opposite to their incidence.

The secondary mirror is placed at the approximate focal point of the primary mirror; its position must be maintained to within 1 μm. Adjustment of the final position is accomplished by the differential thread adjustment of the primary mirror.

Since the rotation of the differential adjusting ring provides linear motion of the primary mirror, it was necessary to machine this assembly to the closest tolerance

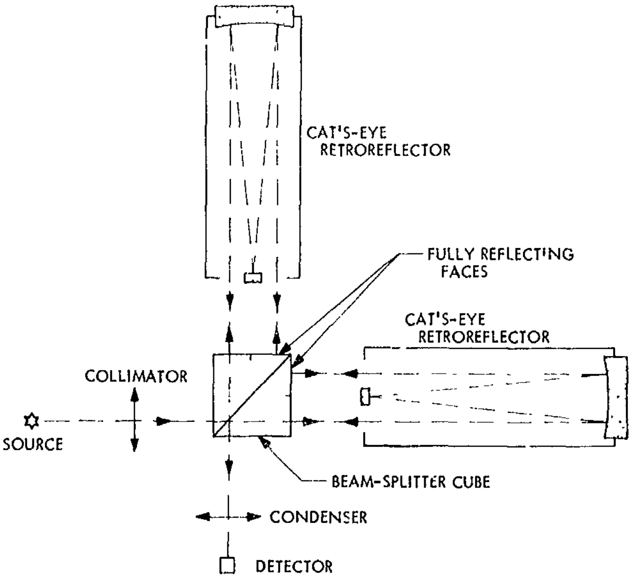

Fig. 10. Optical diagram of interferometer

possible, maintaining perpendicularity with the optical centerline and obtaining minimum backlash in the threads. To guarantee minimal backlash, the unit is spring-loaded. The quartz tube support was bonded into position with relation to the optical centerline while still on the machining spindle.

Assembly of the secondary mirror required the use of a fixture to accurately align the mirror, the piezoelectric transducer, the transducer support, and the quartz support while bonding as a unit.

The primary mirror is located 5.217 in. from the secondary mirror and must be positioned within 0.001 in. so that a minimum of differential thread movement would be required for the final adjustment. This positioning was verified by mechanical measurement.

The cat's eye was mounted on a special indexing head, providing bi-axial rotation and two-directional traverse, at the end of an optical bench. It was offset with respect to the bench centerline by one-half the radius of the quartz support tube. Alignment with the bench centerline required replacement of the primary mirror with an optical flat mirror of the same optical quality and then re-imaging a source upon itself.

A special fixture was used to hold the secondary assembly in position while making adjustments for proper placement. The secondary image was centered by observing it with a telescope from behind the primary mirror through a small hole in its center. The secondary to primary mirror axes were held coincident within 0°3′26″ and, upon proper placement of the secondary, the fixture became a means for support during bonding. After bond curing, the fixture was removed and again the secondary image was viewed for verification of placement.

It had been thought that a vibrating Ronchi ruling test could be used for final primary to secondary mirror placement (SPS 37-43, Vol. IV), but this method proved to be of insufficient accuracy. The test did provide a means of calculating reflective loss through the cat's-eye system. Fine adjustment was done with the single cat's-eye interferometer arrangement as described in SPS 37-52, Vol. III.

3. Fore-optics Alignment

The fore-optics consist of seven 90-deg off-axis paraboloidal mirror segments, a chopper with half reflective and half transmitting window, two detectors, the photomultiplier, and the reference sources and black body source.

The function of the fore-optics is shown in Fig. 11, where the interferometer detector and reference detector alternately "see" the planet or the black body source as determined by the chopper window position.

The specifications require the incoming, as well as the black body, radiation to form an image on this chopper window of 1.1-mm diameter. This requires a 1.25-deg look angle. Therefore, the main alignment requirement was to have the four main mirror segments focus collimated radiation entering the aperture on the chopper window, and transmit this radiation to the interferometer normal to the beam-splitter face with an accuracy of ±1 arc min.

The first approach to the alignment of the fore-optics was to align the planet-to-interferometer channel in relation to the chopper by means of an autocollimator. It had been hoped to reflect the collimator source in and out of the system by placement of an optical flat mirror in the interferometer at the beam-splitter position. This was not possible due to the large reflective losses through the autocollimator–fore-optics combination. Therefore, a laser module was placed and aligned on the interferometer centerline at the beam-splitter location and beamed through the planet-to-interferometer channel to the outside (Fig. 12), where a target and optical flat mirror were alternately viewed. When the planet-to-interferometer mirrors were aligned properly, the target showed on

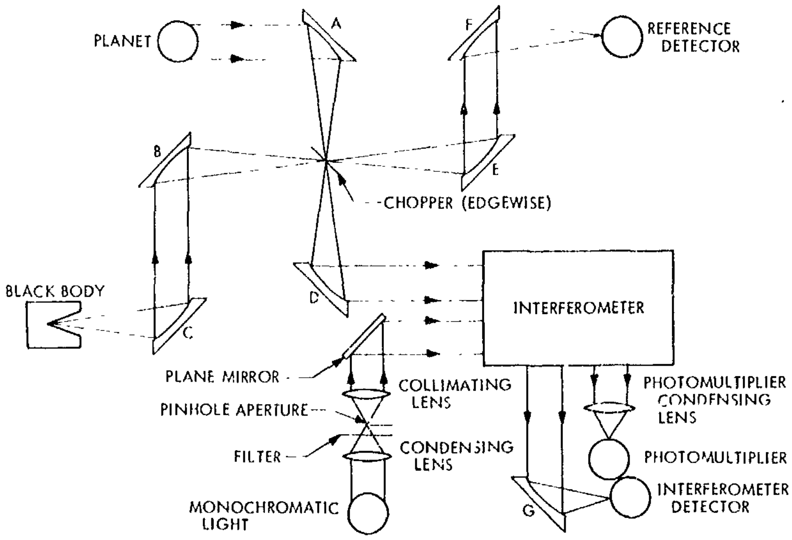

Fig. 11. Fore-optics of interferometer

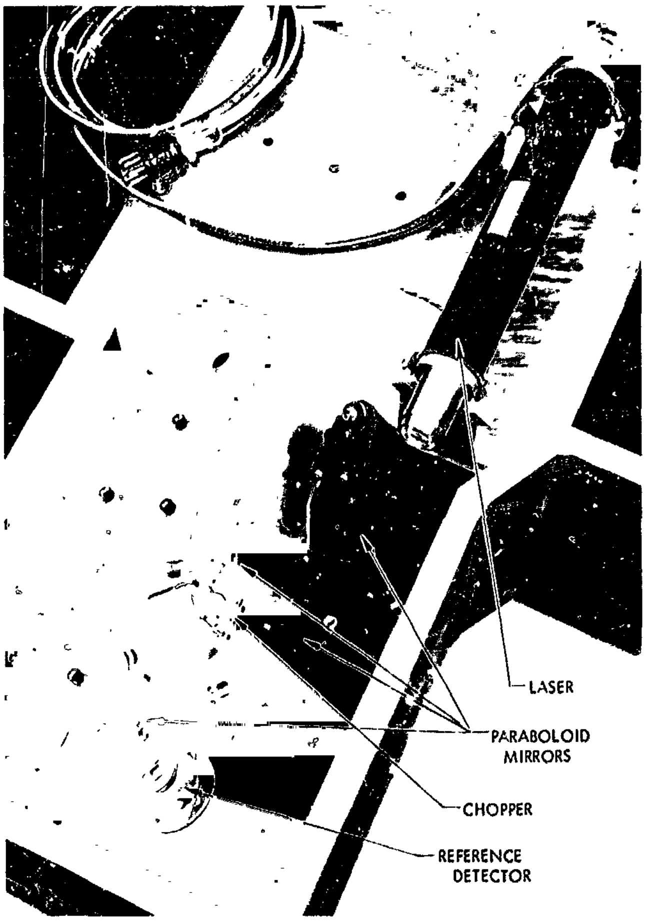

Fig. 12. Laser position for alignment

center and the mirror visually showed on center by reflecting the beam upon itself. The focal point in relation to the chopper window was obtained by both visual and mechanical measurement, using a laser beam expander.

With the laser module still in the beam-splitter position, the black body channel was also aligned by using the reflected half beam off the chopper window.

In order to align the reference detector channel, it was necessary to have an external source and observe the reflected beam from the chopper window. An external source is also necessary for placement of the servo-drive; therefore, another laser module was placed and aligned on the system optical centerline using the internal laser as its target. With both units *on*, the beams coincided.

The planet-to-interferometer channel alignment was verified with a photomultiplier, with the chopper running and forming a square-wave scope reading as shown in Fig. 13. Proper chopping was indicated by equal volume under the square wave, and proper focus was indicated by parallel sides forming the square wave.

With all channels satisfactorily aligned, the system was now ready for acceptance of the servo-drive. The internal laser was removed and the servo was completely assembled, except for the beam splitter, and placed into the system. The optically machined pads on this servo unit, which locate the beam-splitter cube in relation to the cat's eyes, were used for placement of an optical flat

Fig. 13. Square-wave chopper alignment verification

mirror to reflect the external laser beam upon itself when the servo-drive was in its proper place. To observe this, a pin hole was placed in the incoming target.

The beam-splitter cube was placed in position as was the phototube housing and reference sources. The infrared detector will not be placed into the system until after system testing. The external laser will be left in position and used as a source for system tests.

4. Servo-Drive Alignment

The servo-drive unit contains the cat's eyes, one of which is mounted into a moving housing that, when stepped, creates an optical path difference in relation to the stationary cat's eye. The unit locates the beam-splitter cube in relation to both cat's eyes.

The unit must function within the following specifications:

(1) Provide 4 cm of optical path difference.

(2) Maximum tilt of the optical axis of any optical element not to exceed 1 arc min from the normal to the beam splitter.

(3) The lateral separation of the geometric axis of the elements not to exceed 0.5 mm.

(4) Roll about the normal to the beam splitter of any optical element not to exceed 5 arc min.

The servo-drive was built and aligned by Aeroflex Laboratories. Alignment was observed and verified to fall within the specifications except for the 4 cm of optical path difference, which was short by a negligible amount.

All alignment procedures were conducted with the use of an autocollimator and optical flat mirrors. With the main housing placed and leveled on an indexing head, the autocollimator was zeroed when viewing a mirror placed against the beam-splitter cube support pads perpendicular to the moving cat's-eye optical axis.

Neither the cat's eye nor the beam splitter was used during the alignment; instead, a fixture that simulated the weight and center of gravity of the cat's eye was mounted in the moving structure. Attached to the mounting surface of this structure was a mirror that defined the optical axis direction in relation to the beam-splitter pads, which indicated 16 arc sec from the normal. This was a total reading of the structure through its total travel.

The main structure was moved 90 deg and, viewing a mirror placed on the beam-splitter pads perpendicular to the stationary cat's-eye axis, a deviation of 9 arc sec was observed with relation to zero position. Placement of a mirror on the stationary cat's-eye mounting surface indicated 10 arc sec of deviation.

The autocollimator was shifted by means of a transfer mirror in order to observe a mirror placed on the moving structure and normal to its axis. Translating the moving structure to its extreme limits, roll was observed and found to be 5-arc sec deviation.

Lateral separation was measured by mechanical means and 0.002-in. deviation was found between all optical elements.

5. Present Status

The interferometer is now aligned as well as available techniques permit. System testing is in progress with reference fringes being produced by the instrument. As testing continues, it may be found that finer adjustment will have to be incorporated in order to obtain the desired final results.

XVII. Lunar and Planetary Sciences

SPACE SCIENCES DIVISION

A. Meteoritic Sampling of the Solar Wind,

H. C. Lord, III

The retention of low-energy ions incident upon silicate surfaces has been described in SPS 37-48, Vol. III, pp. 155–157. Furthermore, it was predicted that natural silicate samples exposed to a solar wind irradiation should retain both hydrogen and helium, the predominant solar wind species, Table 1 (Ref. 1).

A small number of meteorites have been known for some time to contain an inert gas fraction with an isotopic and elemental composition essentially the same as the solar values. Furthermore, the helium concentration was on the order of 10^{-2} cm^3/g, a factor of 10^3 greater than typical meteoritic helium concentrations. The meteorites containing this high concentration of unfractionated gas do not belong to any particular type, but rather only show in a typical light–dark structure. It is found that this solar primordial fraction is present only in the dark phase. Chemically the phases are essentially the same except for trace element variations and an enrichment of carbon in the dark phase.

Table 1. Pertinent solar wind parameters

Ion[a]	Average abundance	Average energy, keV
H^+	96.5%	0.9
$^4He^{2+}$	$4.4^{+}\%$	1.8
$^4He^{1+}$	3.0×10^{-3} $^4He^{2+}$	3.6
$^3He^{2+}$	1.3×10^{-3} $^4He^{2+}$	1.3
O	1.5×10^{-2} to 4×10^{-2} $^4He^{2+}$	2.4 ($^{16}O^{6+}$)

[a] No other elements have been definitely identified, but both C and Ne appear to be present.

Eberhardt, et al. (Ref. 2), when studying separated minerals and grain sizes in Khor Temiki, discovered that HF etching of the individual grains radically reduced the gas concentration. Furthermore, the primordial gas content (in cm^3/g) was found to decrease with increasing grain size. These characteristics suggest that a low-energy particle irradiation, like the solar wind, was the cause.

An 87.2-mg sample of Pesyanoe (a known solar primordial gas containing meteorite) was heated in 100°C steps, with the evolved gas at each step measured with a thermal conductivity detector gas chromatograph. The gas release results are shown in Fig. 1; as seen, both

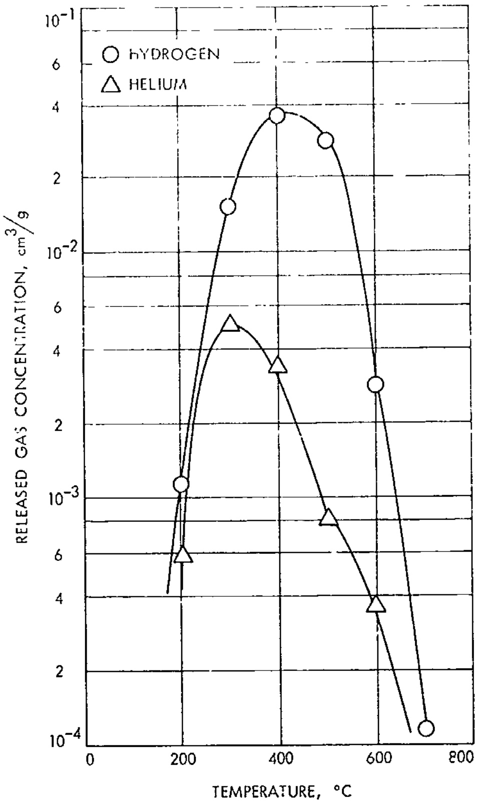

Fig. 1. Differential gas release from Pesyanoe

hydrogen and helium were detected. The absolute concentrations of each species observed is listed in Table 2, along with the results of a separate analysis. The He/H value obtained is compared with other pertinent extraterrestrial values. This He/H value of 0.061 is seen to be the same order of magnitude as that expected for the solar wind. The integrated gas release curves of the hydrogen and helium in Pesyanoe can be compared with the results obtained for low-energy ion injection into forsterite (SPS 37-48, Vol. III). It is seen that the curves are essentially the same.

Table 2. Gas composition of Pesyanoe solar wind

Source	Helium, cm^3/g	Hydrogen, cm^3/g	He/H
This work[a]	1.0×10^{-2}	8.4×10^{-2}	0.061
Zahringer (Ref. 3)	0.7×10^{-2}	—	—
Solar	—	—	0.160
Solar, photosphere (Ref. 4)	—	—	0.090
Solar wind (Ref. 1)	—	—	0.045

[a] Error ±20%.

Further work is now in progress to analyze other gas-rich meteorites as well as to study the isotopic composition of the released hydrogen. The solar D/H value is thought to be $<4 \times 10^{-5}$ (Ref. 5), while the terrestrial value is 1.56×10^{-4}. Analysis of the solar wind component will then give a value for the solar corona. It is proposed that detection of solar wind implanted hydrogen and helium is an unambiguous identification for extraterrestrial material. This is the first reported detection of solar wind hydrogen in extraterrestrial material.

References

1. Bame, S. J., et al., "Solar Wind Ion Composition," *Phys. Rev. Lett.*, Vol. 20, pp. 393–395, 1968.
2. Eberhardt, P., Geiss, J., and Grogler, N., "Further Evidence on the Origin of Trapped Gases in the Meteorite Khor Temiki," *J. Geophys. Res.*, Vol. 70, pp. 4375–4378, 1965.
3. Zahringer, J., "Ueber die Uredelgase in den Achondriten Kapoeta und Staroe Pesjanoe," *Geochim. Cosmochim. Acta*, Vol. 26, pp. 665–680, 1962.
4. Neugebauer, M., and Snyder, C. W., "*Mariner II* Observations of the Solar Wind: I. Average Properties," *J. Geophys. Res.*, Vol. 71, pp. 4469–4484, 1966.
5. Kinman, T. D., "An Attempt to Detect Deuterium in the Solar Atmosphere," *Mon. Not. Roy. Astron. Soc.*, Vol. 116, p. 77, 1956.

XVIII. Bioscience

SPACE SCIENCES DIVISION

A. Organic Analysis of Soil by Pyrolysis–Gas Chromatography–Mass Spectrometry—A Candidate Experiment for a Mars Lander,

P. G. Simmonds, G. P. Shulman, and C. H. Stembridge

1. Introduction

One of the experiments suggested for the unmanned biological exploration of Mars involves the organic analysis of the Mars soil by an automated pyrolysis–gas chromatography–mass spectrometry system[1] (Refs. 1, 2, and 3). The proposed experiment consists of the following basic steps:

(1) A sample is heated in an inert atmosphere at a temperature sufficient to degrade and/or volatilize the organic matter present.

(2) The complex mixture of volatile products is then fractionated by gas chromatography and the individual components identified by mass spectrometry.

(3) The chemical composition of the organic matter contained in the original sample is inferred from the type of volatile pyrolysis compounds obtained and the pyrolysis conditions.

This system not only offers the advantage of operational simplicity as compared to wet chemical procedures of the kind normally used for the analysis of soils and sediments (Ref. 4), but also permits investigation of normally intractable polymeric materials such as humic acid. A California desert soil containing less than 1% organic matter was selected as a suitably complex test sample to study the feasibility of the technique for the bio-organic analysis of soils.

2. Experimental Technique

A schematic of the laboratory apparatus is shown in Fig. 1. It should be understood that the present experimental arrangement is designed for analytical convenience and is intended to provide only the fundamental guidelines for a flight instrument. Experimentally, a 15 mg sample of desert soil containing 0.34% organic matter (Allison method, Ref. 5) was placed in a 3 × 0.159 cm OD stainless steel tube that was sleeved by a small pyrolysis furnace. This sample tube was connected directly to a 152 × 0.0005 m ID capillary column via a stainless-steel swagelock union. Carrier gas entered the sample tube through a capillary gas line that is silver soldered into the small volume union at its mid-point. The chromatographic column was coated with a 10% solution of DC200 silicone/Igepal C0990 (20:1) (Ref. 6). The sample tube was heated to 500°C in 15 s by the pyrolysis furnace

---

[1] *The Biological Exploration of Mars—A Plan for the First Three Missions.* Edited by H. Ford, Aug. 1967 (JPL internal document).

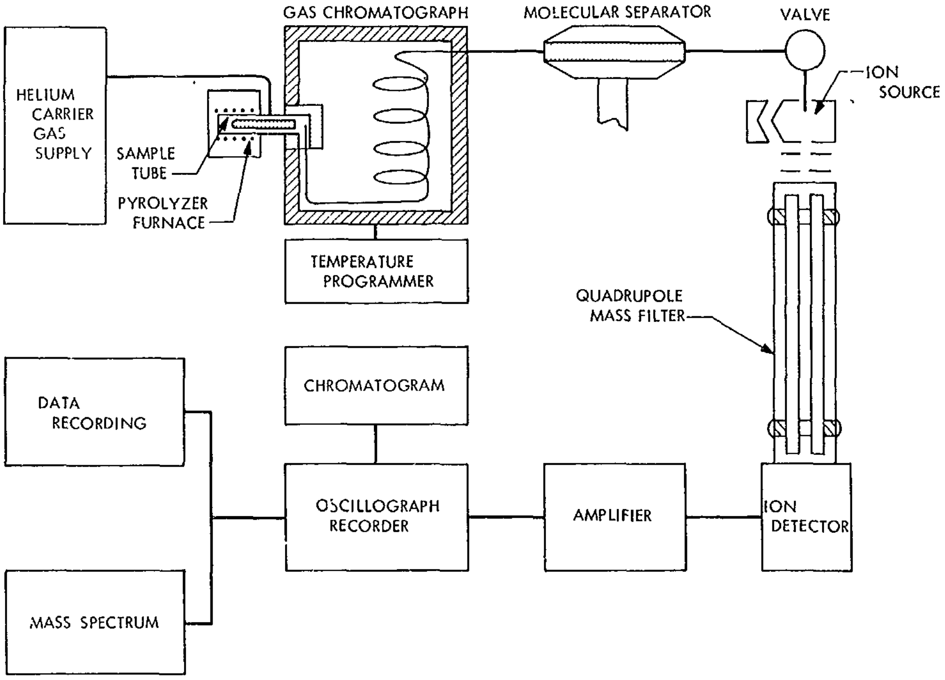

Fig. 1. Pyrolysis–gas chomatograph–mass spectrometer system

and the pyrolysate passed into the column under flow of helium. The column was temperature programmed from 30–185°C at 4°/min, and the eluted sample passed through a single-stage molecular separator (Ref. 7) directly into the ion source of an Electronic Associates, Inc. quadrupole mass spectrometer. The mass spectrometer was adjusted to scan the mass range 10–250 atomic mass units. An ion-current detector monitored the mass range of interest, and the output signal was displayed on a potentiometric recorder that served as a measure of the chromatographic peak intensity. The mass spectra were recorded simultaneously on an oscillograph and six-channel tape system. The tape storage system can subsequently be subjected to automated data processing for spectral recognition by a computer technique developed for mass spectrometry systems (Refs. 8, 9, and 10). The individual pyrolysis products separated by the gas chromatograph were identified by a comparison of their mass spectrometric fragmentation patterns with those in a reference library.

3. Results and Discussion

In order to reconstitute the identity of the principle classes of organic compounds present in the original sample, pyrolyses of pure compounds of biological interest were performed. A library of representative pyrolysis fragments can now be established for the thermal degradation of the major classes of terrestrial bio-organic matter. Table 1, which summarizes this data, was compiled from both work performed in this laboratory and comprehensive literature surveys.

When pyrolysed, amino acids generally lose carbon dioxide to yield an intermediate amine that dehydrogenates to form the corresponding nitrile in high yield. Alternative decomposition by deamination and reduction yields the alkyl or aryl residues of the original amino acids (Refs. 11–14) or their decarboxylation products. Peptides and proteins yield the same major components identified from free amino acids. Carbohydrates decompose smoothly to a series of furans including furfural and furfuryl alcohol (Refs. 15 and 16). As a general rule, lipids (Ref. 17) form a series of alkenes and alkanes; e.g., tristearin pyrolyses to acrolein in addition to a mixture of straight-chain C_2–C_{18} alkenes and alkanes with the alkenes predominating, except C_{17}, as expected. The presence of iron-containing minerals causes some cyclization and isomerisation during pyrolysis of lipids. Porphyrins thermally fragment to a series of pyrroles characteristic of the class (Refs. 18 and 19). Hydrocarbons decompose to lower molecular weight aromatic and aliphatic hydrocarbons, with a high degree of unsaturation (Refs. 20 and 21). When pyrolysed, the purine and pyrimidine bases of nucleic acids decompose extensively to form acetonitrile, methacrylonitrile and substantial amounts of hydrogen cyanide (Ref. 22); the carbohydrate moiety of

Table 1. Analysis of bio-organic compounds

Class of compound	Typical degradation products
Polypeptide and free amino acids[a] 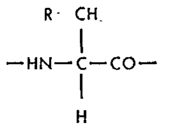 $-HN-\overset{R-CH_2}{\underset{H}{C}}-CO-$	RCH$_3$, RCH = CH$_2$, RCN, RCH = CH—CN Note: R = aromatic, heteroaromatic, aliphatic, or substituted aliphatic
Carbohydrate[b]	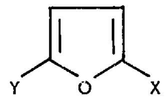 And aliphatic ketones and aldehydes Note: X or Y = H, CH$_3$, CHO, or CH$_2$OH.
Lipid[c] R(CO$_2$)$_3$C$_3$H$_5$	CH$_2$ = CH-CHO, and straight-chain alkenes and alkanes
Porphyrin[d]	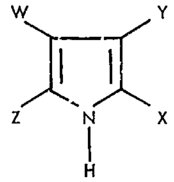 And lower aliphatic nitriles aliphatic-branched alkenes and alkanes Note: X, Y, W or Z = H or alkyl
Hydrocarbon[e] R(CH$_2$)$_n$ CH$_3$	R(CH$_2$)$_{n-1}$ CH = CH$_2$, R(CH$_2$)$_{n-1}$ CH$_3$, etc. Note: R = aromatic, aliphatic, straight chain, or branched
Nucleic acid[f]	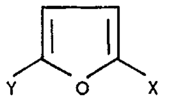 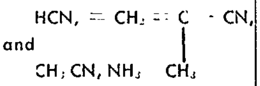 HCN, $CH_2=\underset{CH_3}{C}-CN$, and CH$_3CN, NH_3$ Note· X or Y = H, CH$_3$, CHO, and CH$_2$OH

[a] References 11, 12, 13, 14.
[b] References 15, 16.
[c] Reference 17.
[d] References 18, 19.
[e] References 20, 21.
[f] Reference 22.

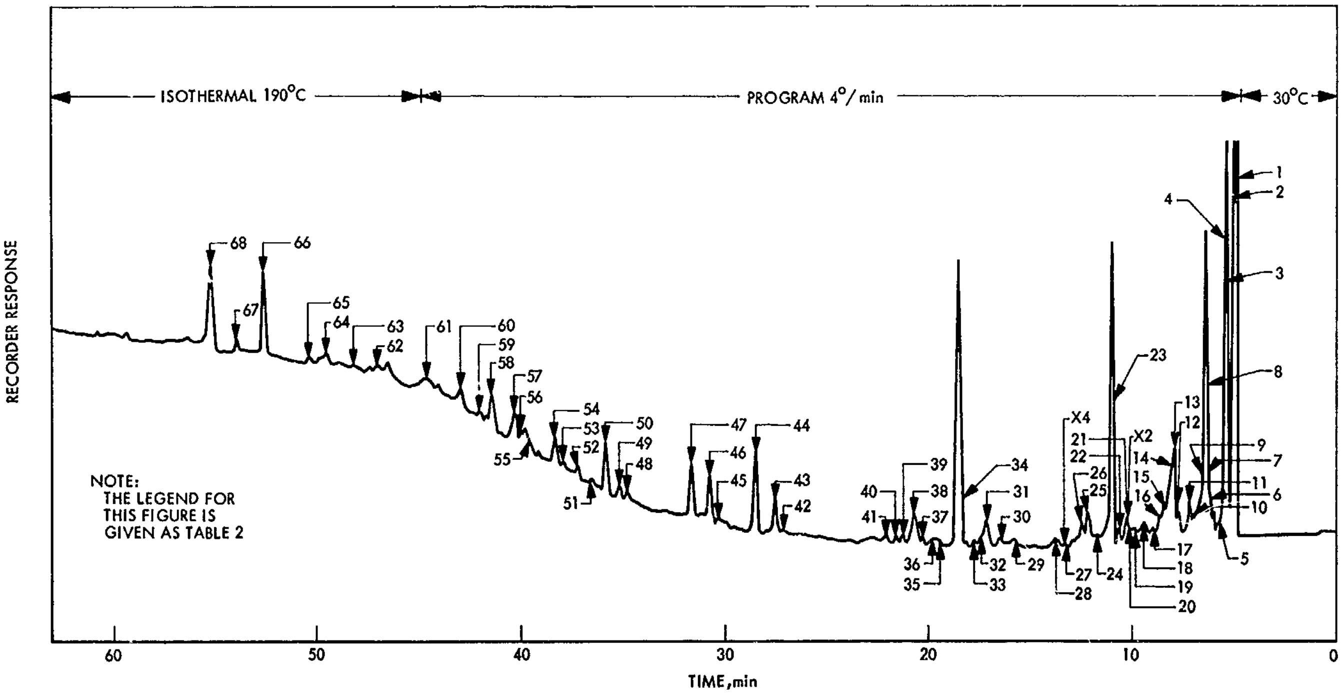

NOTE:
THE LEGEND FOR THIS FIGURE IS GIVEN AS TABLE 2

Fig. 2. Gas chromatograph of desert soil pyrolysate

nucleotides decompose as expected to substituted furans. At present, it is not possible to characterize the individual nucleic acid base.

A chromatogram of the pyrolysis products of the desert soil sample is shown in Fig. 2. These compounds are listed in Table 2, which is keyed to the peaks shown in Fig. 2. Identification of individual compounds was made by comparison of their mass spectra with the spectral library. Peak number 34 (Fig. 2), identified in Table 2 as toluene, represents approximately 2.5×10^{-8} g of material. In Table 3 the various pyrolysis fragments have been assigned to those classes of compounds from which they probably originated. In most cases, there is at least one characteristic series of products for each class. For example, aliphatic nitriles are formed by thermal degradation of amino acids, whether free or part of a polypeptide chain. It is apparent, however, that certain products such as the aliphatic alkanes and alkenes may originate from more than a single class of compound. For example, the identification of butene is *prima facie* evidence of the presence of polypeptide, lipid, or hydrocarbon classes; however, if a series of aliphatic and ring-substituted aliphatic nitriles are detected in addition to butene, then it becomes more reasonable to infer the presence of either polypeptides or free amino acids. An alkene with a carbon number greater than C_6 dictates a choice between lipids and hydrocarbons. These may be distinguished readily since naturally-occurring hydrocarbons contain large amounts of aromatic or branched aliphatic structures, in contrast to the fatty acid pyrolysate.

Certain pyrolysis products appear to be specific for a single class of compound. Thus, phenylacetonitrile is an exclusive product of phenylalanine and of polypeptides containing this amino acid. Similarly, indole and methyl indole have been observed only in tryptophan pyrolyses. Disubstituted pyrroles are characteristic for porphyrins, while the lower aliphatic mercaptans are, apparently, unique thermal fragments from the sulfur-containing amino acids. It is conceivable that mercaptans may also originate from hydrocarbon material with a high indigenous sulfur content; however, in this case, some aromatic sulfur compounds would also be expected. Furans and substituted furans are characteristic for carbohydrate moieties.

Table 2. Compounds identified from gas chromatograph of desert soil pyrolysate (Fig. 2)

Peak No.	Compound	Peak No.	Compound	Peak No.	Compound
1	Carbon dioxide, methane ethane	23	Benzene	46	Styrene
2	Propene, carbonyl sulfide	24	2-butenal	47	2-furaldehyde
3	Butene, hydrogen sulfide	25	Dimethyl furan	48	Unidentified
4	Methanethiol, methyl propane, dimethyl sulfide	26	Methyl pentene	49	Dimethyl hexadiene
		27	Unidentified	50	Isopropyl benzene + unidentified
5	Methyl butene	28	Hexene	51	Unidentified
6	Propanal, methanol	29	Unidentified	52	Methyl styrene
7	Acrolein	30	Dithiabutane	53	Unidentified
8	Furan, acetone	31	C_6 branched alkane	54	Methyl furaldehyde
9	2-methyl propanal	32	Pyrrole	55	Unidentified (amine)
10	Butanone	33	Unidentified	56	C_9 olefin
11	Dimethyl butene	34	Toluene	57	Furfuryl alcohol
12	Methyl propenal	35	Methyl pyrrole	58	Benzonitrile
13	Ethanenitrile	36	Unidentified	59	Indene
14	Acrylonitrile	37	C_7 branched alkene	60	Phenyl acetonitrile
15	Pentene	38	Unidentified	61	Phenol
16	2-methyl furan	39	Dimethyl pentene	62	o- or m cresol
17	Butanal	40	Dimethyl pyrrole	63	p-cresol
18	Pentanone propanenitrile	41	Pyridine	64	Dimethyl phenol
19	Methyl butadiene	42	Methyl pyridine	65	Unidentified
20	Methacrylonitrile	43	Ethyl benzene	66	Alkyl benzene
21	Valeraldehyde	44	Dimethyl benzene	67	Alkyl phenol
22	Butanenitrile	45	2-methyl pyrazine	68	Indole

Table 3. Assignment of pyrolysis fragments to biological classes

Protein[a]	Carbohydrate[a]	Nucleic acid	Lipid		
			Fats and waxes[a]	Hydrocarbon	Porphyrin[a]
Characteristic series					
Ethane nitrile	Acrolein		Ethene		Pyrrole
Acrylonitrile	Propanal		Propene		Methylpyrrole
Propanenitrile	Acetone		Butene		Dimethylpyrrole
Methacrylonitrile	2-methylpropanal		Pentene		
Butanenitrile	Butanone		Hexene		
Benzonitrile	2-methylpropenal		C_6 alkene		C_6 alkene
Phenylacetonitrile	Butanal		C_7 alkene		C_7 alkene
	Pentanone		C_9 alkene		C_8 alkadiene
	Pentanal				C_9 alkene
Ethene	2-butenal				
Propene					
Methylpropane					
Methylbutene					
Methylpentene	Furan				
Benzene	2-methylfuran				
Toluene	Dimethylfuran				
Ethylbenzene	Furfural				
Styrene	Methylfurfural				
Propylbenzene	Furfuryl alcohol				
Methylstyrene					
Individual compounds					
Phenol[b]	Methylbutadiene	Methanol[b]	Acrolein[b]	Dimethylbenzene	
Cresols[b]	Benzene	Acrylonitrile		Alkylbenzene	
Xylenol[b]		Ethanenitrile		Methylpentene	
Indole[b]		Methacrylonitrile		Dimethylbutene	
Indene		Butanenitrile			
Methanethiol[b]		Pyridine			
Dimethyl sulfide[b]		Methylpyridine			
Dimethyl disulfide[b]		2-methylpyrazine[b]			
Pyrrole					
Methylpyrrole					
Pyridine					
Methylpyridine					

[a] Presence established.
[b] Characteristic.

4. Conclusion

A considerable amount of work remains to be done in establishing the precise pyrolytic pathways and mechanisms of pyrolysis for specific macromolecules of biological interest. It is anticipated that detailed studies of this kind will establish a substantial library of thermal fragments unique to the pyrolysate of a single bio-organic class, and, more specifically, to individual members of the class. Based on the above observations and a critical study of the individual pyrolysis products from Table 3, it is possible to infer that all the biochemically important classes of compounds are present in the desert soil sample. This is not surprising since microbiological surveys in this area have clearly established the existence of approximately 5×10^5 microorganisms per gram of soil (SPS 37-34, Vol. IV, pp. 193–202). The present work is sufficiently encouraging to justify the conclusion that the primary objectives of the pyrolysis–gas chromatography–mass spectrometry experiment are attainable. A preliminary investigation of the Precambrian Fig Tree shale (age 3.1×10^9 yr) by this technique indicates that the pyrolysate is, predominately, a mixture of hydrocarbons with a surprising lack of any heteroatom fragments. This work will be continued to include other shales and also meteorites and will be reported in a future article.

References

1. Oyama, V. I., *Proceedings of the Thirteenth Lunar and Planetary Exploration Colloquium,* Vol. 3, Part 2, p. 29, North American Aviation S&ID, Downey, Calif., 1963.
2. Bentley, K. E., *et al., AAS Sci. Tech.,* Vol. 2, p. 93, 1964.
3. Rea, D. G., National Academy of Sciences Publication 1296, p. 347, 1966.
4. Degens, E. T., and Reuter, J. H., in *Advances in Organic Geochemistry,* No. 15, p. 377. Edited by U. Colombo and G. D. Hobson. The MacMillan Company, New York, 1964.
5. Allison, L. E., *Soil Sci. Soc. Amer. Proc.,* Vol. 24, p. 36, 1960.
6. Teranishi, R., and Mon, T. R., *Anal. Chem.,* Vol. 36, p. 1490, 1964.
7. Ryhage, R., *Anal. Chem.,* Vol. 36, p. 759, 1964.
8. Boettger, H. G., "Automated Data Reduction of High-Resolution Mass Spectra of Organic Compounds," Abstract 233, presented at Pacific Conference on Chemistry and Spectroscopy, Anaheim, Calif., 1967.
9. Boettger, H. G., "An Advanced Data Processing System for Fast Scanning High-Resolution Mass Spectrometers," Paper 31, presented at the fifteenth Mass Spectrometry and Allied Topics Conference, Denver, Colo., 1967.
10. Hites, R. A., and Biemann, K., *Anal. Chem.,* Vol. 40, p. 1217, 1968.
11. Kanomata, K., and Mashiko, Y., *Nippon Kagaku Zasshi,* Vol. 87, p. 57, 1966.
12. Vollmin, J., *et al., Microchem. J.,* Vol. II, p. 73, 1966.
13. Merritt, C., Jr., and Robertson, D. H., *J. Gas Chromatography,* Vol. 5, p. 96, 1967.
14. Shulman, G. P., and Simmonds, P. G., *Chem. Comm.,* p. 1040, 1968.
15. Kata, K., *Arg. Biol. Chem.,* Vol. 31, p. 657, 1967.
16. Kata, K., and Komorita, H., *Arg. Biol. Chem.,* Vol. 32, p. 21, 1968.
17. Janak, J., *Nature,* Vol. 185, p. 684, 1960.
18. Levy, R. L., *et al., J. Gas Chromatography,* Vol. 2, p. 254, 1964.
19. Whitten, D. G., Bentley, K. E., and Kuwada, D., *J. Org. Chem.,* Vol. 31, p. 322, 1966.
20. Holman, R. T., Deubig, M., and Hayes, H., *Lipids,* Vol. 1, p. 247, 1966.
21. Henderson, W., *et al., Nature,* Vol. 219, p. 1012, 1968.
22. Jennings, E. C., and Dimick, K. P., *Anal. Chem.,* Vol. 34, p. 1543, 1962.

XIX. Physics

SPACE SCIENCES DIVISION

A. Jupiter's Red Spot and the Solar Wind,

M. Eikrem[1] and M. Neugebauer

During the past few months, there have been some interesting discussions in the scientific literature concerning the possible origin of variations in the intensity of Jupiter's red spot. First, Graf, Smith, and McDevitt (Ref. 1) suggested that the red-spot variations were correlated with the Zurich sunspot number; the data on which their argument was based are shown in Fig. 1. The suggested coupling agent was the ultraviolet radiation associated with solar activity.

The fact that the red-spot data have at least two maxima per 11-yr solar cycle led T. S. Smith (Ref. 2) to suggest that solar flare protons are a more probable cause of variations in the red spot. However, Jupiter's strong magnetic field may prevent all but the highest rigidity protons from reaching the relatively low magnetic latitude of the red spot.

Further analysis at JPL has led to the suggestion that variations in the solar wind, rather than in solar flare protons or ultraviolet radiation, may be the cause of red-spot variations. Because no direct measurements of the solar wind were made before the current decade, geomagnetic activity was selected as a measure of the solar wind. Although the details of the interaction of the solar wind with the earth's magnetic field are not yet completely clear, the mechanism which converts solar wind variations into geomagnetic activity, auroral activity, and enhanced precipitation of geomagnetically trapped radiation should also operate at Jupiter, if the solar wind exists at 5 AU. The location and shape of the Jovian red spot are suggestive of a magnetic anomaly at which enhanced precipitation of trapped particles might occur (similar to the earth's south Atlantic anomaly).

In Fig. 2, the red-spot intensity and geomagnetic data are plotted together versus time for the years 1892 through 1947. For each opposition of Jupiter with the earth and su [illegible] ed-spot intensity is given by Peek's (Ref. 3) qu [illegible] e index, which ranges from 0 = invisible to 8 = [illegible] dark and conspicuous," and geomagnetic activity is represented by a 2-mo average of the geomagnetic character index C_i (Ref. 4) for the month of and the month preceding the opposition. This particular 2-mo average was chosen because at opposition the earth and Jupiter sample nearly the same radially flowing solar wind plasma with a 10- to 20-day time delay required for the plasma to travel from the orbit of earth to the orbit of Jupiter.

---

[1] JPL summer employee.

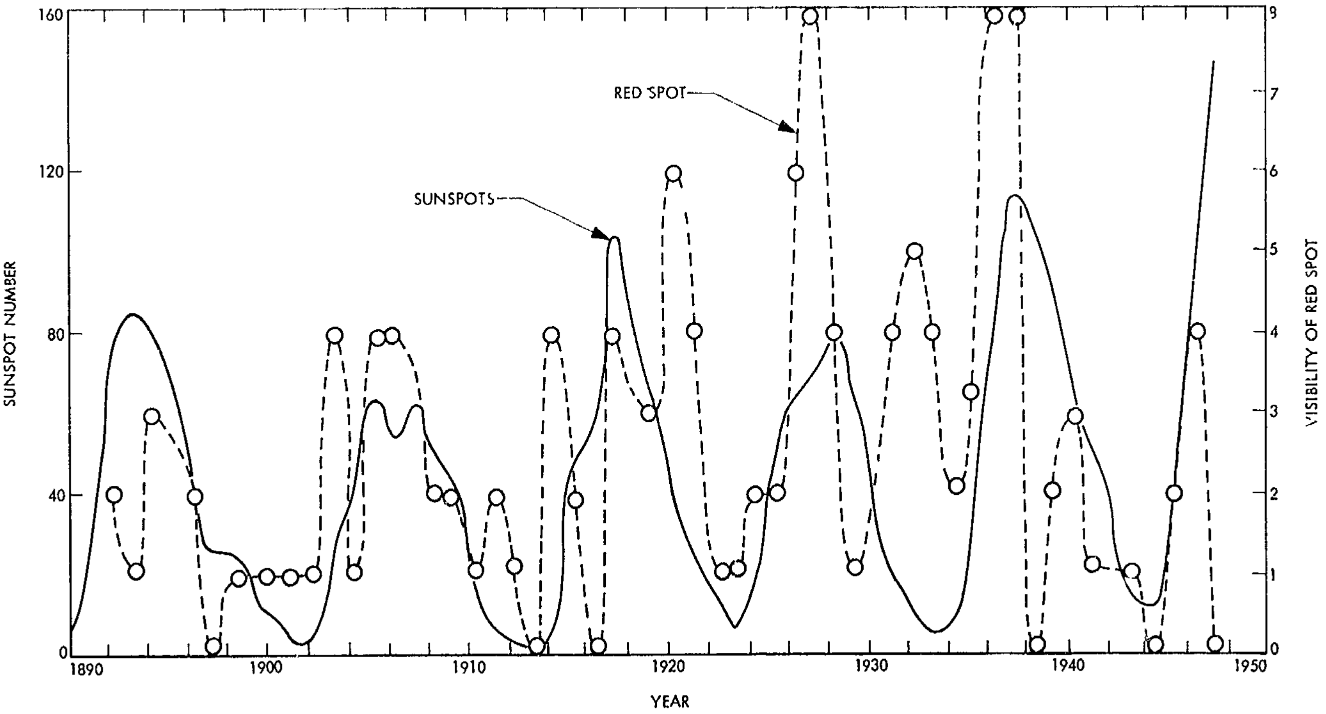

Fig. 1. Smoothed yearly-average Zurich sunspot number and relative intensity of Jovian red spot between 1892 and 1947

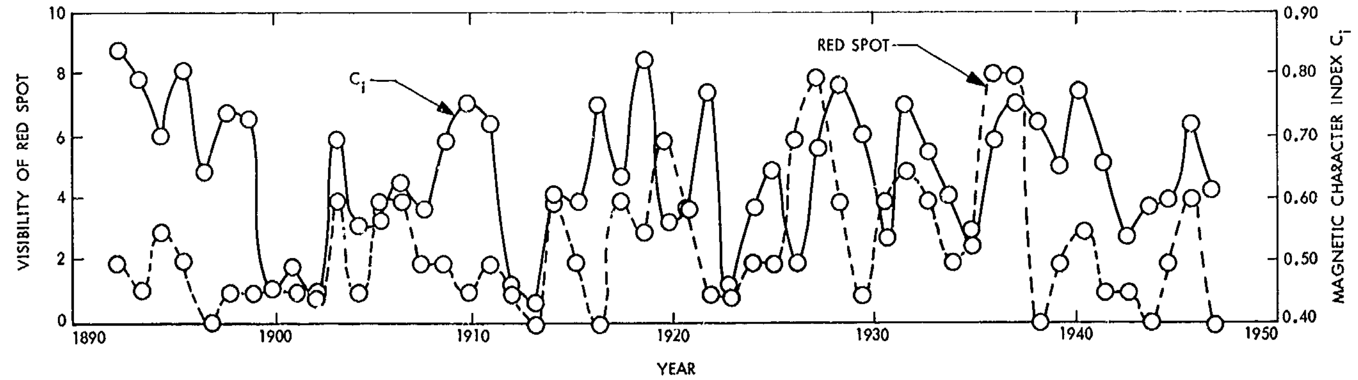

Fig. 2. Two-month average geomagnetic character figure C_i and relative intensity of Jovian red spot between 1892 and 1947

Figure 2 shows a fairly convincing correlation between the 2-mo C_i and red-spot intensity for the years 1900–1908, and after 1922. The yearly-average C_i (not plotted) correlates very well the red-spot data before 1900. For those intervals, the C_i–red spot correlation is appreciably better than the corresponding sunspot–red spot correlation shown in Fig. 1.

Recently, it has been suggested that the termination of the solar wind by a shock transition to subsonic flow may occur as close to the sun as ~ 5 AU, or the orbit of Jupiter (Ref. 5). It is tempting to speculate that the years 1909–1911, 1916, 1918, and 1922, which show no correlation between C_i and red-spot intensity, correspond to periods when Jupiter was outside the shock. The fact that the periods of very poor correlation are generally periods of low red-spot intensity supports this speculation.

In conclusion, although the data in Fig. 2 do not show a statistically significant correlation between the red-spot intensity and C_i for the entire period 1891–1947, the correlation during some periods is quite striking. The resultant suggestion that the great red spot is associated with a magnetic anomaly could be tested by proposed spacecraft missions to Jupiter.

References

1. Graf, E. R., Smith, C. E., and McDevitt, F. R., *Nature*, Vol. 218, p. 857, 1968.
2. Smith, T. S., *Nature*, Vol. 219, p. 357, 1968.
3. Peek, B. M., *The Planet Jupiter*. Faber and Faber, Ltd., London, England, 1958.
4. *Handbook of Geophysics and Space Environments*. Air Force Cambridge Research Laboratories, Bedford, Mass., 1965.
5. Hundhausen, A. J., *Planet. Space Sci.*, Vol. 16, p. 783, 1968.

B. An ICR Study of the Ion-Molecule Thermal Reaction Rates of H_2, D_2, and HD,

D. D. Elleman, J. King, Jr., and M. T. Bowers

1. Introduction

The measurement of the ion-molecule thermal rates in the gas phase Reactions I–III has been of considerable interest for some time.

$$H_2^+ + H_2 \xrightarrow{K_1} H_3^+ + H \qquad \text{(I)}$$

$$D_2^+ + D_2 \xrightarrow{K_2} D_3^+ + D \qquad \text{(II)}$$

$$HD^+ + HD \xrightarrow{K_3 a} H_2D^+ + D \qquad \text{(IIIa)}$$

$$HD^+ + HD \xrightarrow[K_3 b]{} HD_2^+ + H \qquad \text{(IIIb)}$$

Harrison has developed a pulsing technique for studying thermal energy ion-molecule reaction rates and has reported thermal values for K_1 and K_2 (Refs. 1 and 2). (In private communication, Harrison later reported that these values for K_1 and K_2 are probably too low by a factor of 2.) Stevenson and Schiesler (Ref. 3) and Reuben and Friedman (Ref. 4) have used high pressure (hp) mass spectrometry to obtain rate constants at higher energies for Reactions I, II, and III.

This article reports the results of a study of reactions I–III, using ion cyclotron resonance (ICR) spectroscopy (Refs. 5, 6, 7, and SPS 37-53, Vol. III, pp. 149–151). A brief description of the ICR spectrometer and of the ICR technique was given in SPS 37-46, Vol. IV, pp. 205–208.

2. Experimental Techniques

Previous work using ICR single resonance techniques has shown that it is possible to determine the thermal energy rates of ion-molecule reactions (Ref. 8 and Footnotes 2 and 3). A description of this technique will be given here so as to aid in the evaluation of the rate constants that are reported.

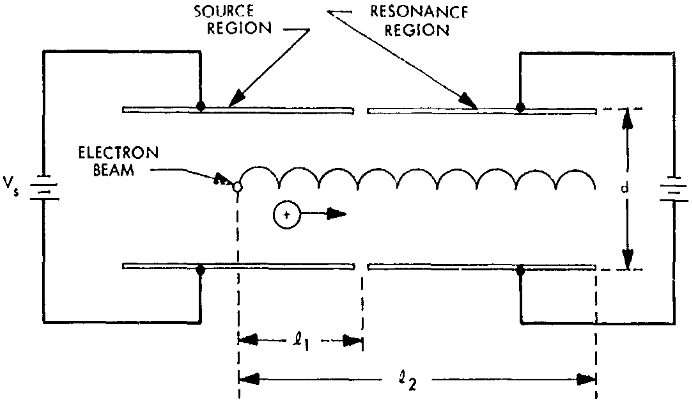

Fig. 3. Side view of ICR cell showing parameters for kinetic analysis (magnetic field is parallel to electron beam)

Figure 3 shows the geometry of the ICR cell required for a kinetic analysis. Separate drift voltages v_s and v_p are applied to the source and resonance regions of the cell. The arrow indicates the direction of ion drift for the crossed field geometry. The drift velocities (in m/sec) in the source and resonance regions are

$$v_{sd} = \frac{V_s}{Bd} \qquad (1)$$

$$v_{rd} = \frac{V_r}{Bd} \qquad (2)$$

where d is the spacing between the plates in meters, V_s and V_r are the voltages in practical volts across the plates, and B is the magnetic field in Wb/m². If the effects of fringing fields are neglected, then the times at

---

[2] Bowers, M. T., Elleman, D. D., and Beauchamp, J. L., *J. Phys. Chem.*, Vol. 72, p. 3599, 1968.

[3] Bowers, M. T., Elleman, D. D., and King, Jr., J., *J. Chem. Phys.* (in press).

which the ion enters τ and leaves τ', the resonance region, are given by

$$\tau = \frac{l_1}{v_{sd}} \tag{3}$$

$$\tau' = \frac{l_1}{v_{sd}} + \frac{l_2 - l_1}{v_{rd}} \tag{4}$$

where l_1 and l_2 are shown in Fig. 3.

Beauchamp (Ref. 8) and Bowers, Elleman, and Beauchamp (Footnote 2) have developed an equation which relates the intensity of the primary ion I_p and secondary ion I_s to the reaction rate constant K in the limit where $nK\,\tau'_s \ll 1$ and $nK\,\tau'_p \ll 1$. The subscripts p and s on τ' refer to the primary and secondary ion exit times and n is the number of neutral molecules per unit volume in the cell. The resulting equation is

$$\frac{nK}{2} = \frac{1}{\left(1 + \frac{m_s}{m_p}\frac{I_p}{I_s}\right)(\tau'_p + \tau_p)} \tag{5}$$

where m_s and m_p are the masses of the secondary and primary ions, respectively. In the development of Eq. (5), it has been assumed that the line widths of the primary and secondary ions are equal; experiments to date have shown that this is a valid approximation.

It is convenient to rewrite Eq. (5) in terms of known instrument parameters when using the expression to measure the rate constant K. Generally, for ease of operation, the drift voltages in the source and resonance regions are set equal so that

$$V = V_R = V_s \tag{6}$$

It is then possible to express $\tau_p + \tau'_p$ in terms of known measurable quantities so that

$$\tau_p + \tau'_p = \frac{l_1 + l_2}{v_p} = \frac{B_p}{v}\,d(l_1 + l_2) \tag{7}$$

where B_p is the value of the magnetic field at the resonance condition for the primary ion. Equations (5) and (7) can be combined and simplified and the values for l_1, l_2, and d can be used to give

$$\frac{nK}{2} = \frac{V}{\left(1 + \frac{m_s}{m_p}\frac{I_p}{I_s}\right) B_p\, 2.224 \times 10^{-3}} \tag{8}$$

Data is then taken by varying the drift voltage V and measuring the resulting changes in the intensities I_p and I_s of the primary ion and secondary ion. A plot of

$$\left(1 + \frac{m_p}{m_s}\frac{I_p}{I_s}\right)^{-1}$$

versus V^{-1} is made and the slope S is obtained. Equation (8) is then rewritten in the form

$$\frac{nK}{2} = \frac{S}{2.24 \times 10^{-3} B_p} \tag{9}$$

The rate constant is then readily obtained from Eq. (9) if n, the number of neutral molecules per unit volume, is known.

The JPL spectrometer has been calibrated for n by measuring, with the technique described above, the well known rate constant of methane in the reaction

$$CH_4^+ + CH_4 \xrightarrow{K_m} CH_5^+ + CH_3 \tag{IV}$$

The value of n determined from the pressure measurement of the ionization gage attached to the cell was compared to the value of n calculated from the ICR-measured value of K_m and the accepted literature value of K_m.[2] It was determined that the ion gage value of n was low by a factor of 3.5, and all subsequent ion gage measurements of n have been corrected by this factor. Corrections for differences between the gage, calibrated for N_2, and the sample gas are made by multiplying the ion gage reading by the ratio $\sigma_i(N_2)/\sigma_i(i)$, where $\sigma_i(N_2)$ is the ionization cross section of N_2 gas and $\sigma_i(i)$ the ionization cross section of the sample gas. It is assumed that the collection efficiency of the ion gage is equal for all ions.

The ICR experiments on hydrogen and deuterium were performed at a pressure of 2×10^{-6} torr; the gas was weakly ionized by a 45-eV electron beam of 0.1 μA. The resulting ion current down the cell was in the range of 1×10^{-11} A. The gases were Matheson Research grade and were used without further purification.

3. Experimental Results

The experimental plots for Reactions I–III are given in Fig. 4. As can be seen, a straight line that passes through the origin fits the experimental points for a relatively large range of V. The resulting rate constants calculated from

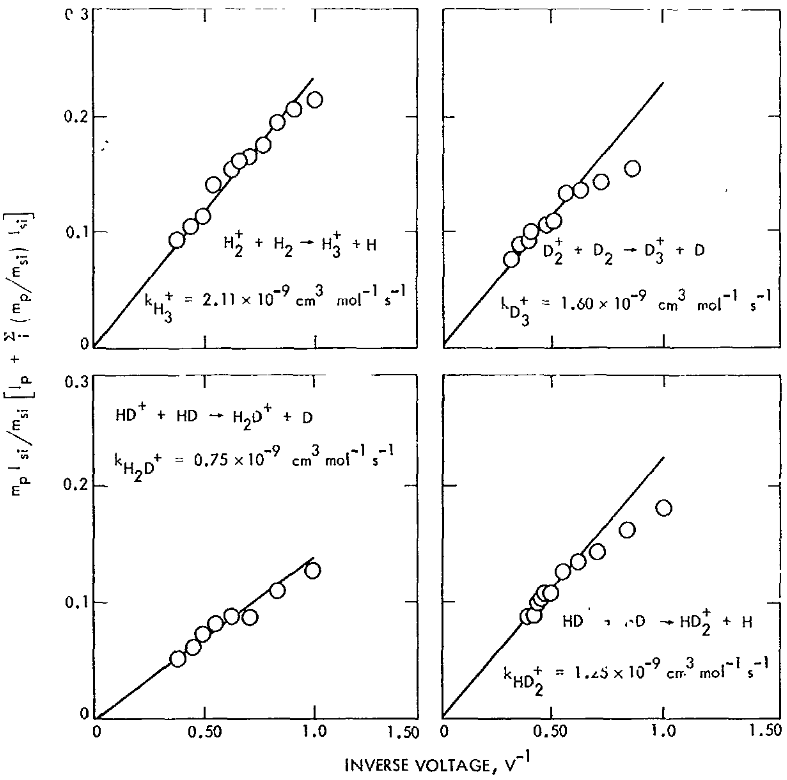

Fig. 4. $m_p I_{si}/m_{si}\left[I_p + \sum_i (m_p/m_{si}) I_{si}\right]$ vs (drift voltage)$^{-1}$ for various isotopic hydrogen reactions. (Straight line was used to determine rate constants according to Eq. 9)

this ICR data are listed in Table 1, along with data from other workers for comparison.

The values K_1(ICR) and K_2(ICR) = 2.11 and 1.6 × 10^{-9} cm^3 molecule^{-1} sec^{-1} obtained from Fig. 4 are in good agreement with previously reported data. Harrison, et al., (Ref. 1) reported thermal rate constants obtained from pulsed work of K_1(pulse) and K_2(pulse) = 0.59 and 0.58 × 10^{-9} cm^3 molecule^{-1} sec^{-1}. In a more recent paper, Gupta, et al. (Ref. 2) have reviewed many of the thermal rate constants reported in Ref. 1. Most of the proton transfer reactions in Ref. 1 were too low by a factor of approximately 2. While revised values of K_1 (pulse) and K_2 (pulse) were not reported by Gupta, et al. (Ref. 2), Harrison has indicated that the initially reported values in Ref. 1 are also probably too low by approximately a factor of 2. In addition, Harrison, et al. (Ref. 1) report K_1 (pulse)/K_2 (pulse) = 1.01, compared with the value of 1.33 reported for that ratio here. Beuben and Friedman (Ref. 4) have reported K_1 (hp) and K_2 (hp) = 2.02 and 1.44 × 10^{-9} cm^3 molecule^{-1} sec^{-1} at 1.4-eV exit ion energy with K_1/K_2 = 1.43 in fair agreement with the ratio reported here. Reuben and Friedman (Ref. 4) also give values of K_1 and K_2 as a function of energy and report both K_1 and K_2 decrease with energy above 1.4-eV exit ion energy. The energy dependence of Reactions I–III as determined by ICR is quite complex, and the energy dependence results will be presented at a later date.

Table 1. Thermal reaction rate constants for H_2, D_2, and HD

Reaction	$K \times 10^{-9}$, cm^3 molecule^{-1} sec^{-1}			
	ICR	Pulse[a]	High pressure[b]	Theory[c]
$H_2^+ \rightarrow H_3^+$	2.11	0.59	2.02	2.08
$D_2^+ \rightarrow D_3^+$	1.60	0.58	1.44	1.45
$HD^+ \rightarrow H_2D^+$	0.75	--	0.75	1.66
$HD^+ \rightarrow HD_2^+$	1.25	—	0.91	

[a] Ref. 1. These values should probably be multiplied by approximately 2. See Ref. 2.

[b] Ref. 4. Data are the lowest energy reported (1.4-eV exit ion energy).

[c] Ref. 9.

The rate constants for the HD^+ reactions were determined to be K_{3a} (ICR) and K_{3b} (ICR) = 0.75 and 1.25 $\times 10^{-9}$ cm^3 molecule^{-1} sec^{-1} with a ratio $k_{3a}/k_{3b} = 1.67$. Reuben and Friedman (Ref. 4) report values of K_{3a} and $K_{3b} = 0.75$ and 0.91×10^{-9} cm^3 molecule^{-1} sec^{-1} with the ratio $K_{3a}/K_{3b} = 1.21$. The agreement is fair.

The existence of a significant isotope effect in Reactions IIIa and IIIb indicates that either a relatively long-lived complex is formed in the hydrogen molecule–parent ion system or there is preferential orientation in a shorter-lived complex (Refs. 4, 10, and 11). There is evidence from photochemical studies (Ref. 12), however, that both a stripping mechanism and a complex mechanism are simultaneously occurring at low energies in Reactions I–III. The rate constants reported here merely reflect the total rate of formation of $(H,D)_3^+$ ions from the $(H,D)_2^+$ + $(H,D)_2^+$ reactant at thermal energies.

References

1. Harrison, A. G., Myher, J. J., and Thynne, J. C. J., "Ion-Molecule Reactions in the Gas Phase," *Advan. Chem.*, Series 58, Chapt. 10, 1966.
2. Gupta, S. K., Jones, E. G., Harrison, A. G., and Myher, J. J., *Can. J. Chem.*, Vol. 45, p. 3107, 1967.
3. Stevenson, D. P., and Schiesler, D. O., *J. Chem. Phys.*, Vol. 29, p. 282, 1958.
4. Reuben, B. G., and Friedman, L., *J. Chem. Phys.*, Vol. 37, p. 1636, 1962.
5. Beauchamp, J. L., Anders, L. R., and Baldeschwieler, J. D., *J. Am. Chem. Soc.*, Vol. 89, p. 4569, 1967.
6. Baldeschwieler, J. D., *Science*, Vol. 159, p. 263, 1968.
7. Fluegge, R. A., *Cornell Aeronautical Lab Report UA-1854-P-1*. U.S. Department of Commerce Clearing House for Federal Scientific and Technical Information, Washington, D.C., Feb. 1967.
8. Beauchamp, J. L., Ph.D. Thesis, Harvard University, Cambridge, Mass., 1967.
9. Gioumousis, G., and Stevenson, D. P., *J. Chem. Phys.*, Vol. 29, p. 294, 1958.
10. Klein, F. S., and Friedman, L., *J. Chem. Phys.*, Vol. 41, p. 1789, 1964.
11. Friedman, L., *J. Chem. Phys.*, Vol. 41, Chapt. 7, 1964.
12. Chupka, W. A., Russell, M. E., and Refaey, K., *J. Chem. Phys.*, Vol. 48, p. 1518, 1968.

C. Compressional Waves in the Solar Wind,

T. W. J. Unti

The search continues for a clear example of a magnetosonic wave. In the *Mariner V* magnetometer readings there are several promising segments of data. These segments are being processed for computer analysis.

As an example, day 206 contains a 12-h run of field and plasma data, during which the average field, bulk velocity, and average density remain almost constant. The amplitude of the field fluctuation is about one third the amplitude of the average field, with corresponding reasonably small amplitudes in the velocity and density fluctuations. This data sector will be divided into 12 1-h segments, and each segment will be analyzed independently.

If a linearly polarized longitudinal wave is present, the field will oscillate primarily in a single direction. Each 1-h subset, therefore, is examined for its line of oscillation. Consecutive data segments that are found to have the same, or nearly the same, line of oscillation are combined into a single data set. It is hoped that several subsets will coalesce in this manner. Such an extension of data sets may be indicative of wavelike phenomena.

But if the oscillations actually represent a compressional wave, the magnetic field and plasma must obey interrelations imposed by the hydromagnetic equations. If the magnetic field is given, the wave velocity of the particles is already determined by the equations. This suggests the following test: The magnetic field data are used, with the hydromagnetic equations, to predict the velocity fluctuations for a sonic wave. The curve obtained is then compared to the actual velocity measurements. If the curves agree, it may be concluded that sonic waves are present.

This will constitute the main test for magnetosonic waves, but a second test can be applied for verification. The density fluctuations are also determined by the field, through the hydromagnetic equations. Again, the computed density will be compared to the actual density measurements.

Various difficulties prevent a straightforward solution to the problem. In order to calculate the sonic wave velocity, the specific heat ratio and the electron temperature must be known. These quantities are not measured directly and must be inferred from the available information, perhaps by a least-squares technique relating all the wave parameters by means of the hydromagnetic equations. Also, it has been theoretically demonstrated by Barnes that, in contrast to Alfvén waves, sonic waves damp very quickly. Therefore, all the quasi-periodic structures evident in the *Mariner V* data may be Alfvén waves and/or other phenomena.

D. Debever Vectors in Dyadic Notation,

B. K. Harrison[4]

One way to express the Petrov algebraic classification of the Weyl curvature tensor in differential geometry is to use the concept of *Debever vectors.* A Debever vector is a real null vector which satisfies a certain equation with the Weyl tensor. For the most general Weyl tensor (Petrov Type I), there are four distinct Debever vectors. If two or more Debever vectors are parallel (degenerate), the Weyl tensor is said to be degenerate, or of an algebraically special type.

Table 2 (Ref. 1) shows the different types of Petrov classification, the number of independent Debever vectors, and the equation satisfied by the degenerate Debever vectors The bracket in the second column shows the number of degenerate vectors along with the number of nondegenerate vectors; [211], for example, means that there are two parallel vectors, which are thus degenerate, with two others not parallel to the first vectors or to each other. The degenerate vectors for a given type satisfy the equation for that type; the others satisfy the general equation (that for Type I). Brackets on indices represent antisymmetrization.

Table 2. Classification of Weyl tensor

Petrov type	Arrangement of vectors	Equations satisfied by Debever vectors
I	[1111]	$k_{[a}C_{b]cd[e}k_{f]}k^c k^d = 0$
II	[211]	$C_{bcd[e}k_{f]}k^c k^d = 0$
D	[22]	$C_{bcd[e}k_{f]}k^c k^d = 0$
III	[31]	$C_{bcd[e}k_{f]}k^d = 0$
N	[4]	$C_{bcde}k^e = 0$
0	–	$C_{bcde} = 0$

For purposes of analysis, it is desirable to represent Debever vectors and their equations in the dyadic formulation of Wahlquist and Estabrook (Ref. 2). We use the following notation. The null vectors k_μ will be written $k_\mu = (1,\mathbf{u})$, where $\mathbf{u}$ is a real unit 3-vector.(Since k_μ is real and null, its time component is nonzero and can be taken as unity.) The Weyl tensor is written in terms of components with respect to a local orthonormal frame, and the components are written in the form of dyadics **A** and **B** (Ref. 2):

$$A_{ab} = C_{oaob} = -\frac{1}{4}\epsilon_{acd}\epsilon_{bfg}C^{cdfg} \tag{1}$$

$$B_{ab} = \frac{1}{2}\epsilon_{bcd}C_{oacd} \tag{2}$$

We also define a complex dyadic $\mathbf{C} = \mathbf{A} + i\mathbf{B}$. Indices are raised and lowered for the component indices with the Minkowski metric tensor.

We now write the equations of Table 2 for the Debever vectors in dyadic form. We find that they can be expressed in terms of a single dyadic equation for **C** and **u** for each Petrov type. It is to be remembered that **u** is real, $\mathbf{u}^2 = 1$, and that **C** is traceless and symmetric.

Type I.

$$\mathbf{C} - (\mathbf{C}\cdot\mathbf{u})\mathbf{u} - \mathbf{u}(\mathbf{u}\cdot\mathbf{C}) + i\mathbf{C}\times\mathbf{u} - i\mathbf{u}(\mathbf{u}\cdot\mathbf{C}\times\mathbf{u})$$
$$+\frac{1}{2}(\mathbf{u}\cdot\mathbf{C}\cdot\mathbf{u})(\mathbf{I} + \mathbf{u}\mathbf{u} + i\mathbf{I}\times\mathbf{u}) = 0,$$
$$\mathbf{u}(\mathbf{u}\cdot\mathbf{C}\cdot\mathbf{u}) - \mathbf{u}\cdot\mathbf{C} - i\mathbf{u}\cdot\mathbf{C}\times\mathbf{u} \neq 0 \tag{3}$$

There are four noncoincident solutions for **u** in general.

Type II.

$$\mathbf{C} - (\mathbf{C}\cdot\mathbf{u})\mathbf{u} + i\mathbf{C}\times\mathbf{u}$$
$$+\frac{1}{2}(\mathbf{u}\cdot\mathbf{C}\cdot\mathbf{u})(\mathbf{I} - \mathbf{u}\mathbf{u} + i\mathbf{I}\times\mathbf{u}) = 0,$$
$$\mathbf{u}\cdot\mathbf{C}\cdot\mathbf{u} \neq 0 \tag{4}$$

The single solution of this equation represents the pair of coincident Debever vectors. The other two Debever vectors satisfy Eq. (3).

Type D. The Debever vectors are coincident in pairs; each vector satisfies Eq. (4).

Type III.

$$\mathbf{C} - (\mathbf{C}\cdot\mathbf{u})\mathbf{u} + i\mathbf{C}\times\mathbf{u} = 0, \qquad \mathbf{C}\cdot\mathbf{u} \neq 0 \tag{5}$$

---

[4] Resident research associate assigned to JPL.

The single solution of this equation represents the triplet of coincident Debever vectors. The other Debever vector satisfies Eq. (3).

Type N.

$$\mathbf{C} + i\mathbf{C} \times \mathbf{u} = 0, \qquad \mathbf{C} \neq 0 \tag{6}$$

The solution of this equation gives the four coincident Debever vectors.

Type O.

$$\mathbf{C} = 0 \tag{7}$$

This is the conformally flat case.

If we now define a dyadic $\mathbf{D}$,

$$\mathbf{D} = \mathbf{C} + \frac{1}{2}(\mathbf{u} \cdot \mathbf{C} \cdot \mathbf{u})\mathbf{I} \qquad (= \mathbf{D}^T) \tag{8}$$

we note

$$\mathbf{C} = \mathbf{D} - \frac{1}{3}(Tr\mathbf{D})\mathbf{I} \tag{9}$$

and find Eq. (4) to yield

$$\mathbf{D} - (\mathbf{D} \cdot \mathbf{u})\mathbf{u} + i\mathbf{D} \times \mathbf{u} = 0 \tag{10}$$

Instead of solving this equation for $\mathbf{u}$, let us find the possible form of $\mathbf{D}$. We write

$$\begin{aligned}\mathbf{D} = {} & -3\alpha\mathbf{uu} + \zeta\mathbf{vv} + \xi\mathbf{ww} + \delta(\mathbf{uv} + \mathbf{vu}) \\ & + \epsilon(\mathbf{uw} + \mathbf{wu}) + \eta(\mathbf{vw} + \mathbf{wv})\end{aligned} \tag{11}$$

where $(\mathbf{u}, \mathbf{v}, \mathbf{w})$ form a positive orthonormal triad. Equation (10) yields

$$\eta = \zeta i, \qquad \xi = -\zeta, \qquad \delta = -\epsilon i \tag{12}$$

Then if

$$\mathbf{y} = \frac{1}{(2)^{1/2}}(\mathbf{w} - i\mathbf{v}) \tag{13}$$

we find

$$\mathbf{D} = -3\alpha\mathbf{uu} - 2\zeta\mathbf{yy} + \epsilon(2)^{1/2}(\mathbf{uy} + \mathbf{yu}) \tag{14}$$

and

$$\mathbf{u} = i\mathbf{y} \times \bar{\mathbf{y}} \tag{15}$$

(Bar denotes complex conjugate.)

We note that

$$\mathbf{y}^2 = 0, \mathbf{y} \cdot \bar{\mathbf{y}} = 1, \text{and } \mathbf{u} \cdot \mathbf{y} = 0 \tag{16}$$

Then, with $\beta = -2\zeta$, and $\gamma = \epsilon(2)^{1/2}$, we have from Eqs. (9) and (14)

$$\mathbf{C} = \alpha(\mathbf{I} - 3\mathbf{uu}) + \beta\mathbf{yy} + \gamma(\mathbf{uy} + \mathbf{yu}) \tag{17}$$

This is the general form $\mathbf{C}$ must have to be algebraically special (i.e., not of Type I), with $\mathbf{u}$ and $\mathbf{y}$ satisfying Eqs. (15) and (16). Further restrictions, such as $\mathbf{u} \cdot \mathbf{C} \cdot \mathbf{u} = 0$, restrict $\mathbf{C}$ to be more special than Type II.

If we note that

$$\mathbf{I} = \mathbf{y}\bar{\mathbf{y}} + \bar{\mathbf{y}}\mathbf{y} + \mathbf{uu} \tag{18}$$

and define

$$\mathbf{z} = -\alpha\bar{\mathbf{y}} - \frac{1}{3}i\gamma\mathbf{y} \times \bar{\mathbf{y}} - \frac{1}{6}\beta\mathbf{y} \tag{19}$$

we can write $\mathbf{C}$ in Eq. (17) in the form

$$\mathbf{C} = -3\mathbf{yz} - 3\mathbf{zy} + 2(\mathbf{y} \cdot \mathbf{z})\mathbf{I} \tag{20}$$

This is the form obtained by Wahlquist[5] from a consideration of the Cayley–Hamilton equation for $\mathbf{C}$.

By analysis of the two forms for $\mathbf{C}$, Eqs. (17) and (20), we now construct Table 3, summarizing the conditions

Table 3. Conditions for C to be a given Petrov type

Petrov type	Conditions for Eq. (17)	Conditions for Eq. (20)
II	$\alpha \neq 0,\ \gamma^2 \neq -3\alpha\beta$	$\mathbf{y} \cdot \mathbf{z} \neq 0,\ \mathbf{z}^2 \neq 0$
D	$\alpha \neq 0,\ \gamma^2 = -3\alpha\beta$	$\mathbf{y} \cdot \mathbf{z} \neq 0,\ \mathbf{z}^2 = 0$
III	$\alpha = 0,\ \gamma \neq 0$	$\mathbf{y} \cdot \mathbf{z} = 0,\ \mathbf{z}^2 \neq 0$
N	$\alpha = \gamma = 0,\ \beta \neq 0$	$\mathbf{y} \cdot \mathbf{z} = 0,\ \mathbf{z}^2 = 0,\ \mathbf{z} \neq 0$
0	$\alpha = \gamma = \beta = 0$	$\mathbf{z} = 0$

---

[5] Unpublished notes on algebraic classifications of the Weyl tensor dyadic, 1967.

for **C** to be each of the special types. The conditions for Eq. (20) have been given by Wahlquist;[5] those for Eq. (17) are obtained by substituting Eq. (17) into Eqs. (3)–(6), or by consideration of the related inequalities, and by noting that **z** must satisfy $\mathbf{z}^2 = 0$ for Type D.

We note in Types II, III, and N, in which there is one degenerate Debever vector, that it is given by Eq. (15), $\mathbf{u} = i\mathbf{y} \times \overline{\mathbf{y}}$. In Type D, in which there are two degenerate Debever vectors, we can write

$$\mathbf{z} = k\mathbf{w} \tag{21}$$

where $\overline{\mathbf{w}} \cdot \mathbf{w} = 1$, and $\mathbf{w}^2 = 0$.

Then the second Debever vector can be shown to be

$$\mathbf{t} = i\mathbf{w} \times \overline{\mathbf{w}} \tag{22}$$

where **w** may be expressed in terms of **y** and **u**:

$$\mathbf{w} = -\mathbf{y}\cos^2\theta + \overline{\mathbf{y}}\sin^2\theta + \mathbf{u}(2)^{1/2}\sin\theta\cos\theta,\ 0 < \theta \leq \frac{\pi}{2} \tag{23}$$

where θ is a real parameter.

We then find, from Eqs. (22) and (23), that

$$\mathbf{t} = \frac{(2)^{1/2}}{2}\sin 2\theta\,(\mathbf{y} + \overline{\mathbf{y}}) + \mathbf{u}\cos 2\theta \tag{24}$$

Note that, if $\theta = \pi/2$, $\mathbf{t} = -\mathbf{u}$, but $\mathbf{w} \cdot \mathbf{y} = 1 \neq 0$, the space parts of the two Debever vectors may be antiparallel in Type D. We also note, with Wahlquist (Footnote 5), that an alternative form for **C** in Type D is

$$\mathbf{C} = \sigma\left(\mathbf{I} - \frac{3\mathbf{ss}}{\mathbf{s}^2}\right) \tag{25}$$

where **s** is complex.

It is easily shown from Eqs. (20)–(24) that

$$\sigma = -k\mathbf{y} \cdot \mathbf{w} = -k\sin^2\theta \tag{26}$$

and

$$\begin{aligned}\mathbf{s} &= \pm m\,\frac{i\mathbf{y} \times \mathbf{w}}{\mathbf{y} \cdot \mathbf{w}} \\ &= \pm m(\mathbf{u} - (2)^{1/2}\cot\theta\,\mathbf{y})\end{aligned} \tag{27}$$

where $m = (\mathbf{s}^2)^{1/2}$. If $n = (\mathbf{s} \cdot \overline{\mathbf{s}})^{1/2}$ and $\mu = \pm 1$, then

$$\left\{\begin{matrix}\mathbf{u} \\ \mathbf{t}\end{matrix}\right\} = \frac{1}{n^2 + m\overline{m}}\left[\mu(\overline{m}\mathbf{s} + \overline{m}\mathbf{s}) + i\mathbf{s} \times \overline{\mathbf{s}}\right] \tag{28}$$

where $\mu = 1$ gives **u** and $\mu = -1$ gives **t**.

References

1. Pirani, F. A. E., *Introduction to Gravitational Radiation Theory*, (1964 Brandeis Lecture Notes), p. 321. Prentice–Hall, Inc., New York, 1965.
2. Wahlquist, H. D., and Estabrook, F. B., *Rigid Motions in Einstein Spaces*, Technical Report 32-868, p. 31. Jet Propulsion Laboratory, Pasadena, Calif., Mar. 15, 1966.

E. Dielectric Function of a Low-Density Electron Gas, *J. S. Zmuidzinas*[6]

Considerable insight into the physical properties of a metal can be obtained by studying a simple model of the metal consisting of a cold electron gas in a uniform neutralizing background of ions. The behavior of this idealized system is conveniently described by the dielectric function $\epsilon(\underset{\sim}{k},\omega)$ which measures the response of the system to a weak external electric field of frequency ω.

The dielectric function in the random-phase approximation (RPA) is given as (Ref. 1)

$$\epsilon_{RPA}(\underset{\sim}{k},\omega) = 1 - \frac{4\pi e^2}{\hbar k^2 V}\,\chi^0(\underset{\sim}{k},\omega) \tag{1}$$

where e is the electronic charge, V is the volume occupied by the electron gas, and the density–density response function χ^0, in this approximation, is

$$\chi^0(\underset{\sim}{k},\omega) = \Sigma_{\underset{\sim}{q}\sigma}\,\frac{n^0_{\underset{\sim}{q}\sigma} - n^0_{\underset{\sim}{q}+\underset{\sim}{k}\sigma}}{\omega - \omega^0_{\underset{\sim}{q}\underset{\sim}{k}} + i\eta}, \qquad \eta \to 0^+ \tag{2}$$

with

$$\omega^0_{\underset{\sim}{q}\underset{\sim}{k}} = \frac{\hbar}{2m}\left[(\underset{\sim}{q} + \underset{\sim}{k})^2 - \underset{\sim}{q}^2\right]$$

where m is the electron mass.

---

[6] The author wishes to acknowledge fruitful discussions with Dr. M. M. Saffren.

The zero-temperature Fermi distribution functions n^0 arise in Eq. (2) from linearizing the equations of motion for the particle-hole operators about the ground state of a non-interacting Fermi gas; for both spin orientations σ, one has

$$n_{\underset{\sim}{k}\sigma} = \begin{cases} 1, & \text{if } |\underset{\sim}{k}| < k_F \\ 0, & \text{if } |\underset{\sim}{k}| > k_F \end{cases}$$

where

$$k_F = (3\pi^2 n)^{1/3}$$

is the Fermi wavenumber, and n is the electron density. As is well known, the RPA expression (Eq. 1) for the dielectric function is valid only in the high-density limit (n large or $r_s = e^2 m n^{-1/3} \hbar^{-2} \ll 1$). Unfortunately, this limit is not representative of the actual metallic densities ($2 \lesssim r_s \lesssim 6$). Calculations of ϵ in the latter density regime are much more difficult, since the kinetic and the potential energies are comparable there, and neither can be treated as small in the first approximation. In the low-density regime ($r_s \gg 1$), matters are again simpler, since here the Coulomb energy dominates, and hence the strong-coupling methods are appropriate.

According to Wigner (Ref. 2), the electron gas solidifies into a lattice in the low-density limit. While this limit, too, is not representative of the actual metals, its study nevertheless is likely to be profitable, since it may throw some light on the poorly understood lattice–gas transition which is thought to occur at $r_s \sim 4$ (Ref. 3 and SPS 37-28, Vol. IV, pp. 132–134) as the electron density is increased from $r_s \gg 1$. In this article, we determine the RPA dielectric function in the low-density limit (LDL).

The simplest way of calculating ϵ in LDL is to linearize the particle-hole equations of motion not about the Fermi ground state but about the state of the electron lattice. Mathematically, this amounts to replacing n^0 in Eq. (2) by a distribution function appropriate to the electron lattice, determined as follows.

Let $|\Omega>$ be the ground state of the electron lattice:

$$|\Omega> = \mathcal{N} \Big[\prod_{i\sigma} \psi_\sigma(\underset{\sim}{x}_i)^\dagger \Big] |0>$$

Here $\mathcal{N}$ is a normalization constant, adjusted to make $<\Omega|\Omega> = 1$; the product on i runs over all lattice sites ($N/2$ in number for each spin) in some fixed order; $\psi_\sigma(\underset{\sim}{x}_i)^\dagger$ are electron creation operators; and $|0>$ is the electron vacuum. The state $|\Omega>$ is an exact eigenstate of the interaction Hamiltonian and has the lowest possible eigenvalue if the electrons form a body-centered lattice (Ref. 2). However, the expectation value of the kinetic energy is infinite in this state. To avoid this infinity, one may "smear out" the lattice by making the substitution

$$\psi(\underset{\sim}{x}_i) \rightarrow \tilde{\psi}(\underset{\sim}{x}_i) = \int d^3x\, f(\underset{\sim}{x} - \underset{\sim}{x}_i)\, \psi(\underset{\sim}{x}_i)$$

where

$$f(\underset{\sim}{x}) = (\pi^{1/2} \ell)^{-3} \exp\left(\frac{-x^2}{\ell^2}\right)$$

and ℓ is taken much smaller than the lattice spacing $r_0 = n^{-3/2}$. The distribution function is defined as

$$n_{\underset{\sim}{k}\sigma} = V^{-1} \int d^3x \int d^3y \exp i\underset{\sim}{k} \cdot (\underset{\sim}{x} - \underset{\sim}{y}) \;\; <\Omega|\psi_\sigma(\underset{\sim}{x})^\dagger\, \psi_\sigma(\underset{\sim}{y})|\Omega>$$

Using the approximation $\ell \ll r_0$, we find

$$<\Omega|\psi_\sigma(\underset{\sim}{x})^\dagger\, \psi_\sigma(\underset{\sim}{y})\,|\Omega> \simeq [(2\pi)^{1/2} \ell]^3 \sum_i f(\underset{\sim}{x} - \underset{\sim}{x}_i)\, f(\underset{\sim}{y} - \underset{\sim}{x}_i)$$

and hence

$$n_{\underset{\sim}{k}\sigma} = \frac{1}{2} n [(2\pi)^{1/2} \ell]^3 \exp\left(\frac{-k^2 \ell^2}{2}\right) \tag{3}$$

The distribution function Eq. (3) is Maxwellian with "temperature" T determined by $\ell^2 k^2/2 = mv^2/2\kappa T$:

$$T = \hbar^2/m\kappa\ell^2$$

where κ is the Boltzmann constant. Physically, T measures the kinetic energy which an electron acquires by virtue of its localization in a volume $\sim \ell^3$ centered about its lattice site.

Using Eq. (3) in Eq. (2), we find the following expression for the dielectric function in the LDL:

$$\epsilon_{LDL}(\underset{\sim}{k},\omega) = 1 - \omega_p^2 \frac{m^2 \ell}{2^{1/2} \hbar^2 k^3} [Z(x_+) - Z(x_-)] \tag{4}$$

where

$$\omega_p = (4\pi n e^2/m)^{1/2}$$

is the electron plasma frequency,

$$x_\pm = \frac{\ell}{2^{1/2}k}\left(\frac{m\omega}{\hbar} \pm \frac{1}{2}k^2 + i\eta\right)$$

and Z is the plasma dispersion function (Ref. 4)

$$Z(\xi) = \pi^{-1/2}\int_{-\infty}^{\infty}\frac{\exp(-x^2)\,dx}{x-\xi}$$

In the long-wavelength limit, Eq. (4) reduces to

$$\epsilon_{LDL|k\to 0} = 1 - \frac{\omega_p^2}{\omega^2}\left(1 + 3\frac{k^2}{k_T^2}\right) + 0(k^4) \qquad (5)$$

where

$$k_T = \frac{m\ell\omega}{\hbar} \qquad (6)$$

Equation (5) shows that the electron gas supports collective oscillations at the plasma frequency ω_p. Following Saffren's arguments (SPS 37-28, Vol. IV), one may regard the lattice electrons as moving in a harmonic–oscillator potential

$$V = \frac{e^2 \underset{\sim}{x}^2}{2R^3} = \frac{m\Omega^2 r^2}{2}$$

Where $R = r_s a_0$ and $a_0 = \hbar^2/me^2$ is the Bohr radius. One can then write ℓ^2 in $f(\underset{\sim}{x})$ as

$$\ell^2 = \frac{2\hbar}{m\Omega} = 2r_s^{3/2}\,a_0^2$$

Substitution of this expression into Eq. (6) gives

$$k_T^2 = 8\pi r_s^{-3/2}\,a_0^{-2}$$

The high-density *RPA* expression for ϵ in the long-wave limit is (Ref. 5)

$$\epsilon_{RPA|k\to 0} = 1 - \frac{\omega_p^2}{\omega^2}\left(1 + \frac{9}{5}\frac{k^2}{k_{FT}^2}\right) + 0(k^4) \qquad (7)$$

where

$$\begin{aligned} k_{FT}^2 &= 4\pi^{-1}\,a_0^{-1}\,k_F \\ &= 4\pi^{-1}\,(3\pi^2)^{1/3}\,r_s^{-1}\;a_0^{-2} \qquad (8) \end{aligned}$$

It is easy to verify that Eqs. (5) and (7) agree to order k^2 *only* when

$$r_s = \left[\frac{6\pi^2}{5\,(3\pi)^{1/3}}\right]^2 \simeq 16$$

Thus, in general, the high- and low-density random-phase approximations to $\epsilon(k \to 0)$ are different, and hence care must be exercised when performing extrapolations of these approximations away from their respective regions of validity.

References

1. Pines, D., and Nozières, P., *The Theory of Quantum Liquids*, Vol. I, pp. [illegible] and 283. W. A. Benjamin, Inc., New York, 1966.
2. Wigner, E., *Trans. Faraday Soc.*, Vol. 34, p. 678, 1938.
3. Carr, Jr., W. J., *Phys. Rev.*, Vol. 122, p. 1437, 1961.
4. Fried, B. D., and Conte, S. D., *The Plasma Dispersion Function*. Academic Press, New York, 1961.
5. Hubbard, J., *Phys. Lett.*, Vol. 25A, p. 709, 1967.

F. The Microwave Spectrum of the OD Free Radical, *R. L. Poynter*

1. Introduction

A few free radicals have been studied by microwave spectroscopic methods since the pioneering work on OH of Dousmanis, Sanders, and Townes (Ref. 1) in 1955. In particular, Powell and Lide[7] (Ref. 2) have studied SO, CF_2, and Powell and Johnson[8] have studied ClO. The OH and OD radicals are still of considerable interest, however, since they are amenable to an accurate theoretical analysis and their absorption frequencies are of importance to radio astronomy. Attempts to observe the low microwave frequency transitions by radio astronomy have been successful, but only after the characteristic transitions have been precisely located and identified in

---

[7] Powell, F. X., and Lide, Jr., D. R., "Microwave Spectrum of the CF_2 Radical," *J. Chem. Phys.* (in press).

[8] Powell, F. X., and Johnson, D., "The Microwave Spectrum of the ClO Radical," *J. Mol. Spectrosc.* (in press).

the laboratory (Refs. 3–5 and SPS 37-47, Vol. III, pp. 200–207). Radio astronomers have been reluctant to conduct searches over the radio spectrum based only on predictions computed from the early microwave OH and OD studies due to the length of time required to tune the narrow-band maser receivers which are used in radio astronomy.

We have found that the OH and OD radical frequencies can be accurately predicted from our new data. We have reported an analysis of the OH spectrum (SPS 37-47, Vol. III) in which we were able to make very good predictions of the astronomically interesting transitions at low microwave frequencies. In this article, we present a similar analysis of the OD spectrum in which we have been able to accurately predict and *observe* six new $\Delta F = 0$ transitions belonging to the OD radical.

At this time, we have not been able to observe any of the much weaker $\Delta F = \pm 1$ transitions, and, therefore, three out of the four hyperfine coupling constants remain undetermined. Although this severely limits our ability to predict the frequencies of any of the $\Delta F = \pm 1$ hyperfine transitions, it in no way affects our results for the $\Delta F = 0$ hyperfine transitions.

2. Experimental Techniques

The microwave spectrometer and absorption cell employed in this work were briefly described in SPS 37-51, Vol. III, pp. 193–197, and further details will be described in a later article. Here, we only point out a few changes that have been made.

The OD free radicals were generated by the fast chemical reaction of deuterium atoms with NO_2. The deuterium atoms were generated by an electrodeless discharge in gaseous D_2, which was mixed with a trace amount of either O_2 or NO_2 as a controlled impurity gas. The impurity was added to enhance the number of deuterium atoms produced by the discharge.

The spectrometer consists of the usual klystron oscillator for the microwave signal source, an absorption cell, a crystal detector which is used to drive a 100-kHz narrow-band amplifier, and a phase-sensitive detector. The absorption cell consists of two parallel stainless steel plates which are separated by a nominal 0.5 cm. These plates are mounted inside a large vacuum chamber, where the reacting gases can be controlled by a suitable pumping and inlet manifold system.

Frequency measurements are made by a slightly different method than previously reported. A frequency synthesizer (500-MHz) was used in combination with a narrow-band, high-power, high-frequency amplifier to drive a crystal harmonic multiplier. The beat frequency signal of the microwave klystron output with one of the crystal multiplier harmonics was detected by a fixed-tuned, narrow-band, crystal-controlled receiver. This method is very rapid and sufficiently accurate to give overall absorption frequency measurements to within ± 0.01 MHz at a microwave frequency of 38 GHz. However, the actual limitation to absorption measurement accuracies arises from the line widths, which are about 0.20 MHz. Greater accuracies could be obtained, but they are not required in the present application.

3. Energy Levels and Frequencies

The basic Hamiltonian given by Van Vleck (Ref. 6) and Frosch and Foley (Ref. 7) was used to calculate the molecular energy levels. Two centrifugal distortion terms were also included in the Hamiltonian to account for the observed spectrum (SPS 37-51, Vol. III). The complete matrix for the lambda doubling in OD is identical in form to that employed for the analysis of OH, except for a change in the nuclear spin from ½ to 1. A nuclear spin of 1 will also change the number of F energy levels from 2 to 3, precipitating a change in the computer logic details.

The complete Hamiltonian matrix is exactly diagonalized by a computer program, and the resulting energy levels are then employed to compute the molecular frequencies. The unitary transformation matrix used in the Hamiltonian diagonalization is retained and used to calculate the transition intensities. The accuracy of the results has been checked by writing a fourth-order perturbation-type computer program. Both programs converge to the same results. Further checks were employed by writing these programs in successive stages, with and without nuclear hyperfine interactions. The first-stage computation involved only the pure lambda doubling. These results were checked by comparing with the pure lambda doubling frequencies as derived from the experimental results. When the proper convergence was obtained, the nuclear hyperfine splitting terms were added. These results were checked directly against the observed spectra.

To analyze the observed frequencies, it is necessary to change the molecular parameters, compute a predicted spectrum, and compare the predictions with experimental observations. Corrections to the initial parameters are computed from the differences between the observed and predicted spectra. This is essentially an iterative process, which is best handled by employing least-squares methods. Thus, the energy level/frequency program was compressed to bare essentials and merged with a standard least-squares program.

The combination of these programs permitted a rapid evaluation of our experimental data. It was possible to show whether or not various theoretical terms were important in explaining the observed spectrum.

The least-squares-computed spectral parameters could be used in the full program to predict all of the absorption lines which would fall in the microwave region accessible to our spectrometer. We also computed the expected laboratory intensities, to determine whether or not we could reasonably expect to see any of the predicted lines. Further details of the analytical and computational results will be reported later.

4. Results

We *assumed* the same optical spectral constants which DST used. The validity of this assumption will be examined later. We then calculated approximate values for the remaining lambda doubling parameters from the results of Dousmanis, Sanders, and Townes. All parameters were then inserted into the least-squares program, along with the prior-observed frequencies. This process resulted in a "refined" set of molecular parameters. It also showed that three of the molecular constants were very insensitive parameters in fitting the lambda doubling spectrum. These constants were (1) the energy difference between the Σ and the π electronic states, (2) the rotational constant for the Σ state, B_Σ, and (3) either (but *not* both) the rotational constant for the π state *or* the spin-orbit coupling constant, A. These three constants were held fixed at the values obtained from optical spectroscopic results. On this basis, it was possible to obtain a fair fit of the spectrum. This fit also showed that a number of the observed frequencies reported by Dousmanis, Sanders, and Townes were in error. This forced us to remeasure all of the frequencies that had been reported, since there was no simple way of determining which of those frequencies were incorrect.

In this process, we were able to resolve all of the $^2\pi_{3/2}$ transitions into the expected triplets for the first time. We were thus able to obtain a very precise value for the d nuclear hyperfine coupling constant. In addition, we could now predict all of the expected microwave transitions which would fall below 40 GHz. Six predicted lines were accessible to measurement with our spectrometer. They were observed very close to their predicted locations. The complete set of absorption lines is presented in Table 4. This set of lines (30) was then used to compute a "final" set of molecular constants which are presented in Table 5. The quality of the derived constants can be judged from the extremely close agreement obtained between the calculated and observed frequencies. If the agreement were to a nominal 0.5 MHz, it would be a good fit by microwave spectroscopic standards. The

Table 4. Comparison of calculated and observed OD transitions

Assignment		Frequency, MHz		Frequency difference (observed − calculated), MHz
J	$F \rightarrow F'$	Calculated	Observed	
$^2\pi_{1/2}$ electronic state				
5/2	3/2	8110.740	8110.72	−0.020
	5/2	8117.999	8117.99	−0.009
	7/2	8128.160	8128.13	−0.030
7/2	5/2	9578.933	9578.90	−0.033
	7/2	9586.279	9586.32	+0.041
	9/2	9595.723	9595.74	+0.017
9/2	7/2	10192.22	10192.21	−0.011
	9/2	10199.53	10199.56	+0.029
	11/2	10208.47	10208.50	+0.035
11/2	9/2	9914.722	9914.70	−0.022
	11/2	9921.936	9921.95	+0.014
	13/2	9930.462	9930.44	−0.022
$^2\pi_{3/2}$ electronic state				
11/2	9/2	8671.548	8671.60	+0.052
	11/2	8672.409	8672.37	−0.039
	13/2	8673.426	8673.35	−0.076
13/2	11/2	12917.03	12917.08	+0.051
	13/2	12918.10	12918.13	+0.026
	15/2	12919.34	12919.33	−0.014
15/2	13/2	18009.39	18009.46	+0.073
	15/2	18010.66	18010.63	−0.034
	17/2	18012.11	18012.13	+0.017
17/2	15/2	23907.01	23907.08	+0.068
	17/2	23908.48	23908.44	−0.039
	19/2	23910.12	23910.04	−0.080
19/2	17/2	30565.34	30565.42	+0.083
	19/2	30566.98	30566.95	−0.029
	21/2	30568.79	30568.72	−0.074
21/2	19/2	37940.59	37940.58	−0.012
	21/2	37942.39	37942.43	+0.037
	23/2	37944.37	37944.36	−0.006

constants of Table 5 give an agreement of almost 5 to 10 times better than this, which is an excellent fit! It should also be pointed out that the same centrifugal distortion effects, D and δ, that occur in OH must also be used here to compute the results shown in Table 4.

The very close fit between the computed and observed spectral lines gives confidence that other microwave absorption lines can be reliably predicted. A complete list of the $\Delta F = 0$ lines which may be of interest for radio astronomy is given in Table 6. The $\Delta F = \pm 1$ lines have been omitted because there is insufficient experimental data available to determine the three nuclear hyperfine coupling constants, a, b, and c, which are required to predict the line frequencies. These constants have no affect upon the $\Delta F = 0$ transitions.

Table 5. Least-squares-evaluated molecular constants for the OD molecule

Constant	MHz
E_σ[a]	9.797981×10^8
B_σ[a]	2.70713×10^5
B_π[a]	2.95836×10^5
$A_{\text{spin-orbit}}$	$-4.16227 \times 10^6 \pm 0.000151$[b]
$<\Sigma \mid BLy \mid \pi>$	$2.005746 \times 10^5 \pm 0.000037$[b]
$<\Sigma \mid (2B + A)Ly \mid \pi>$	$-1.890918 \times 10^6 \pm 0.000038$[b]
$D_{\text{centrifugal-distortion}}$	30.096 ± 0.018[b]
δ	-2.865 ± 0.028[b]
λ[c]	-14.0693 ± 0.024[b]
$d_{\text{hyperfine}}$	8.747 ± 0.017[b]

[a] These constants are obtained from the optical spectroscopic constants that DST used, under the *assumption* that they picked the best values.

[b] "Error limits" quoted are the standard deviation. No "scale" factors have been used as yet.

[c] λ accuracy is determined by uncertainty in B_π.

References

1. Dousmanis, G. C., Sanders, Jr., T. M., and Townes, C. H., "Microwave Spectra of the Free Radicals OH and OD," *Phys. Rev.*, Vol. 100, p. 1735, 1955.
2. Powell, F. X., and Lide, Jr., D. R., "Microwave Spectrum of the SO Radical," *J. Chem. Phys.*, Vol. 4, p. 1413, 1964.
3. Ehrenstein, G., Townes, C. H., and Stevenson, M. J., "Ground State Λ-Doubling Transitions of OH Radical," *Phys. Rev. Lett.*, Vol. 3, p. 40, 1959.
4. Weinreb, S., Barrett, A. H., Meeks, M. L., and Henry, J. C., "Radio Observations of OH in the Interstellar Medium," *Nature*, Vol. 200, p. 829, 1963.
5. Zuckerman, B., Palmer, P., Penfield, H., and Lilley, A. E., "Detection of Microwave Radiation from the $^2\pi_{1/2}$, $J = 1/2$ State of OH," *J. App. Phys.*, Vol. 153, p. L69, 1968.
6. Van Vleck, J. H., *Phys. Rev.*, Vol. 33, p. 467, 1929.
7. Frosch, R. A., and Foley, H. M., *Phys. Rev.*, Vol. 88, p. 1337, 1952.

Table 6. OD lambda doubling transitions ($\Delta F = 0$)

J	$F(I)$	$F(F)$	Frequency, MHz	$A(F, FP)$, s^{-1}	Intensity, cm^{-1}
$^2\pi_{1/2}$ electronic state					
0.5	0.5	0.5	3093.647	3.17×10^{-10}	2.81×10^{-6}
0.5	1.5	1.5	3111.141	3.22×10^{-10}	2.86×10^{-6}
1.5	0.5	0.5	5887.786	4.56×10^{-10}	3.49×10^{-6}
1.5	1.5	1.5	5894.695	4.58×10^{-10}	3.50×10^{-6}
1.5	2.5	2.5	5906.210	4.61×10^{-10}	3.52×10^{-6}
2.5	1.5	1.5	8110.742	5.46×10^{-10}	3.25×10^{-6}
2.5	2.5	2.5	8118.001	5.48×10^{-10}	3.26×10^{-6}
2.5	3.5	3.5	8128.162	5.50×10^{-10}	3.28×10^{-6}
3.5	2.5	2.5	9578.938	5.41×10^{-10}	2.27×10^{-6}
3.5	3.5	3.5	9586.283	5.42×10^{-10}	2.28×10^{-6}
3.5	4.5	4.5	9595.727	5.44×10^{-10}	2.28×10^{-6}
4.5	3.5	3.5	10192.229	4.51×10^{-10}	1.21×10^{-6}
4.5	4.5	4.5	10199.539	4.52×10^{-10}	1.21×10^{-6}
4.5	5.5	5.5	10208.473	4.53×10^{-10}	1.22×10^{-6}
5.5	4.5	4.5	9914.733	3.12×10^{-10}	4.87×10^{-7}
5.5	5.5	5.5	9921.946	3.13×10^{-10}	4.88×10^{-7}
5.5	6.5	6.5	9930.472	3.14×10^{-10}	4.89×10^{-7}
6.5	5.5	5.5	8753.001	1.70×10^{-10}	1.40×10^{-7}
6.5	6.5	6.5	8760.091	1.71×10^{-10}	1.40×10^{-7}
6.5	7.5	7.5	8768.271	1.71×10^{-10}	1.41×10^{-7}
7.5	6.5	6.5	6737.080	6.38×10^{-11}	2.52×10^{-8}
7.5	7.5	7.5	6744.035	6.40×10^{-11}	2.53×10^{-8}
7.5	8.5	8.5	6751.917	6.42×10^{-11}	2.54×10^{-8}
8.5	7.5	7.5	3907.517	1.05×10^{-11}	1.81×10^{-9}
8.5	8.5	8.5	3914.336	1.05×10^{-11}	1.82×10^{-9}
8.5	9.5	9.5	3921.957	1.06×10^{-11}	1.83×10^{-9}
9.5	8.5	8.5	307.800	4.40×10^{-15}	3.04×10^{-13}
9.5	9.5	9.5	314.489	4.69×10^{-15}	3.24×10^{-13}
9.5	10.5	10.5	321.881	5.03×10^{-15}	3.47×10^{-13}
10.5	9.5	9.5	4019.392	8.52×10^{-12}	2.15×10^{-10}
10.5	10.5	10.5	4012.827	8.48×10^{-12}	2.14×10^{-10}
10.5	11.5	11.5	4005.636	8.43×10^{-12}	2.13×10^{-15}
$^2\pi_{3/2}$ electronic state					
1.5	0.5	0.5	310.143	5.66×10^{-11}	9.41×10^{-9}
1.5	1.5	1.5	310.232	5.66×10^{-13}	9.42×10^{-9}
1.5	2.5	2.5	310.381	5.67×10^{-13}	9.43×10^{-9}
2.5	1.5	1.5	1190.580	1.34×10^{-11}	1.79×10^{-7}
2.5	2.5	2.5	1190.819	1.34×10^{-11}	1.79×10^{-7}
2.5	3.5	3.5	1191.154	1.34×10^{-11}	1.79×10^{-7}
3.5	2.5	2.5	2822.022	9.63×10^{-11}	9.40×10^{-7}
3.5	3.5	3.5	2822.452	9.63×10^{-11}	9.40×10^{-7}
3.5	4.5	4.5	2823.004	9.64×10^{-11}	9.41×10^{-7}
4.5	3.5	3.5	5304.021	3.94×10^{-10}	2.57×10^{-6}
4.5	4.5	4.5	5304.663	3.94×10^{-10}	2.58×10^{-6}
4.5	5.5	5.5	5305.448	3.94×10^{-10}	2.58×10^{-6}
5.5	4.5	4.5	8671.537	1.15×10^{-9}	4.61×10^{-6}
5.5	5.5	5.5	8672.398	1.15×10^{-9}	4.61×10^{-6}
5.5	6.5	6.5	8673.414	1.15×10^{-9}	4.61×10^{-6}
6.5	5.5	5.5	12917.015	2.70×10^{-9}	6.05×10^{-6}
6.5	6.5	6.5	12918.089	2.70×10^{-9}	6.05×10^{-6}
6.5	7.5	7.5	12919.329	2.70×10^{-9}	6.05×10^{-6}
7.5	6.5	6.5	18009.369	5.41×10^{-9}	6.21×10^{-6}
7.5	7.5	7.5	18010.647	5.41×10^{-9}	6.21×10^{-6}
7.5	8.5	8.5	18012.095	5.41×10^{-9}	6.21×10^{-6}
8.5	7.5	7.5	23906.992	9.67×10^{-9}	5.21×10^{-6}
8.5	8.5	8.5	23908.459	9.67×10^{-9}	5.21×10^{-6}
8.5	9.5	9.5	23910.100	9.68×10^{-9}	5.21×10^{-6}
9.5	8.5	8.5	30565.316	1.59×10^{-8}	3.67×10^{-6}
9.5	9.5	9.5	30566.958	1.59×10^{-8}	3.67×10^{-6}
9.5	10.5	10.5	30568.772	1.59×10^{-8}	3.67×10^{-6}
10.5	9.5	9.5	37940.569	2.44×10^{-8}	2.21×10^{-6}
10.5	10.5	10.5	37942.371	2.44×10^{-8}	2.21×10^{-6}
10.5	11.5	11.5	37944.344	2.44×10^{-8}	2.21×10^{-6}

N69-26204

XX. Communications Systems Research

TELECOMMUNICATIONS DIVISION

A. Sequential Decoding: Short Constraint Length Convolutional Codes, *J. A. Heller*

1. Introduction

Much of the past interest in convolutional codes has been in the use of these codes with sequential coding. There the problem of finding "good" codes is not pressing, because arbitrarily small error probabilities can (albeit at the expense of some erasure probability) be had by using almost any code of sufficiently long constraint length. The complexity of a sequential decoder is not very sensitive to constraint length.

Recently, Viterbi (Ref. 1) described a decoder for convolutional codes which was subsequently shown to be maximum likelihood (Ref. 2). The number of operations required by the Viterbi algorithm per decoded bit is a constant for any given constraint length K and increases exponentially with K. This contrasts with brute force maximum likelihood decoding where the decoder complexity goes up exponentially with block length which is typically many times K.

The Viterbi algorithm, while not practical for large K, may perhaps be useful in the range $K = 4$ to 10. Since it is limited to small K, finding good short constraint length codes becomes important. The Viterbi algorithm has several advantages over sequential decoding for small K. First, the time to decode is fixed; hence buffering of the received data is unnecessary. Second, decoding progresses at the received data rate; there is no need for the decoder to be 10 to 20 times faster than the incoming data rate as is necessary in sequential decoding to combat buffer overflow. Third, resynchronization by inserting a known single-constraint-length-long sequence into the data stream periodically is unnecessary. The most important result is that for systems giving a bit error probability of about 5×10^{-3}, such as prevails in the *Mariner* Mars 1969 high rate telemetry system, convolutional codes with short constraint length decoded by the Viterbi algorithm yield a gain of about 1 dB over the use of biorthogonal codes. Also, with the Viterbi algorithm there are no erasures. And the bandwidth expansion is not high. Hence, the use of short constraint convolutional codes is very attractive in future telemetry systems.

2. Properties of Convolutional Codes

Figure 1 shows a typical binary (nonsystematic) convolutional coder. The code rate is $R_N = 1/v$. In Figure 1 $R_N = 1/3$ bits/code symbol. The code itself is determined by the connections between the shift register stages and the mod-2 adders. It is usually specified by v connection

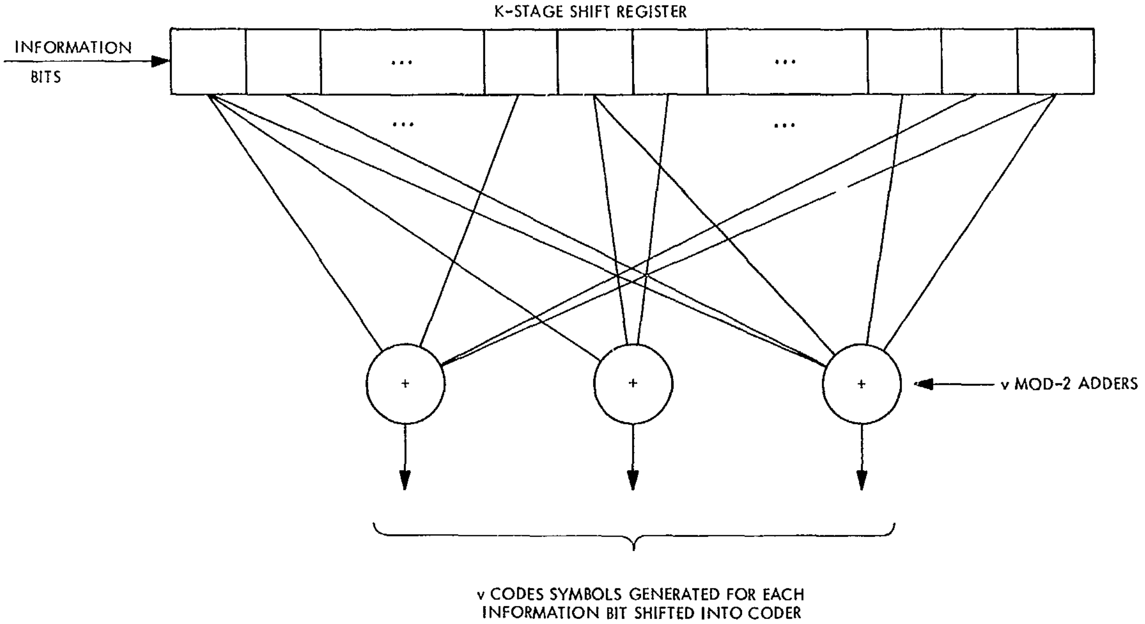

Fig. 1. Binary convolutional coder

vectors, one for each adder, $\mathbf{g}_1, \mathbf{g}_2, \cdots, \mathbf{g}_v$. The jth component of $\mathbf{g}_i$ is a 1 if stage j of the shift register is connected to the ith adder, otherwise it is 0. A more compact method of specifying the code is a Kv component vector $\mathbf{f}$ which contains the components of the connection vectors interleaved, that is,

$$f_1 = g_{11},\ f_2 = g_{21},\ \cdots,\ f_v = g_{v1}$$

$$f_{v+1} = g_{12},\ \cdots,\ f_{Kv} = g_{vK}$$

Convolutional codes are special cases of group codes. The generator matrix, G, of a convolutional code is shown in Fig. 2. The first row of the matrix is the vector $\mathbf{f}$ followed by zeros. Each succeeding row is the previous row shifted v places to the right with the vacated elements filled with zeros. The number of rows L in the matrix is the length of the input information stream. It follows that there are $(K + L - 1)\,v$ columns in G; this is the block length of the code. The $(K + L - 1)\,v$ element code word y is related to the L element input sequence x by

$$y = xG \tag{1}$$

The code is thus the set of all 2^L linear combinations of the rows of G.

The problem of finding the best code, in the probability of error sense, for a given K is difficult if not impossible.

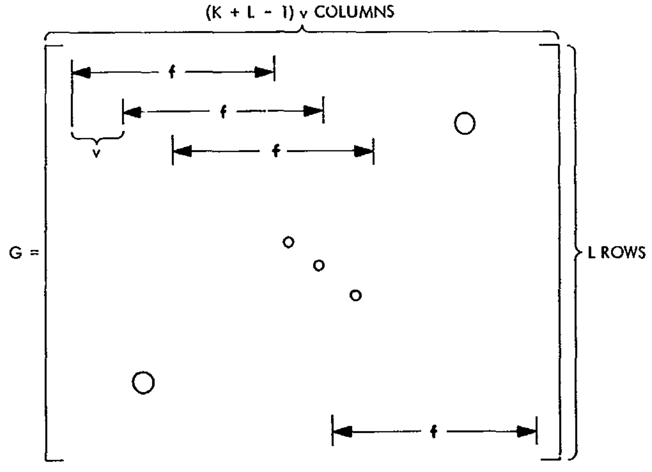

Fig. 2. Convolutional code generator matrix

Other criteria such as maximizing the minimum code word distance do not guarantee that error probability is minimized (this has been shown by simulation). However, low error probability seems at least to be well, if not perfectly, correlated with large minimum distances; that is, a large minimum distance implies that all code word distances are large.

An upper bound on minimum code-word distance for systematic codes has been obtained previously (SPS 37-50, Vol. III, pp. 248–251), and will be stated here for nonsystematic codes. Since a linear convolutional code is a group code, the set of distances from the kth code word to all other code words is independent of k. Thus without loss of generality assume the all-zero code word (corresponding to the all-zero information sequence) is the correct code word. It is a well-known property of group codes that the total number of ones summed over all code words is less than or equal to the total number of zeros (Ref. 3), with equality when no column of G is all zero. The minimum distance must be less than or equal to the average distance, and distance is simply the number of ones in a code word. There are 2^L code words of which $2^L - 1$ are nonzero. The average number of ones in the $2^L - 1$ nonzero code words is thus

$$\frac{2^L}{2^L - 1}\left[\frac{(K + L - 1)\,v}{2}\right]$$

Hence d_m, the minimum distance, is upper bounded by this quantity.

$$d_m \leq \frac{2^L}{2^L - 1}\left[\frac{(K + L - 1)\,v}{2}\right] \qquad (2)$$

This bound is true for input sequences of any length L. It is also true for nonzero sequences of length $h < L$. Therefore, a tighter bound can be obtained by minimizing on h

$$d_m \leq \min_{h} \frac{2^h}{2^h - 1}\left[\frac{(K + h - 1)\,v}{2}\right] \qquad (3)$$

It has been shown that the minimum occurs at a value of h that varies as log K (SPS 37-50, Vol. III, pp. 248–251). As a limiting case, for large K, Eq. (3) reduces to

$$d_m \lesssim \frac{Kv}{2} \qquad (4)$$

which says that for large K the minimum distance is less than about half a constraint length of code symbols. For $K \lesssim 10$, the optimum h, h_0, will be from 2 to 4. When $h = 1$, we have the bound $d_m \leq Kv$ which can be achieved with a code with 2 code words (G has one row, namely **f**) with all elements of **f** equal to 1.

Equation (3) can be considered as a sequence of upper bounds for nonzero input sequences of length $h = 1$ to L (we may take $L = \infty$ since there is no need to segment the data into blocks in the Viterbi algorithm). This suggests the following *ad hoc* scheme which has been useful in generating small K codes with a minimum distance equal to or near the upper bound. Let $d(h)$ be the *actual* minimum distance for a convolutional code of block length h.

Initially choose all Kv elements of the connection vectors, $\mathbf{g}_i$, equal to 1. Then as previously stated, $d(1) = Kv$. Looking at the generator matrix with two rows; however, it is clear that $d(2) = 2v$, which is the weight of the code word corresponding to the input sequence 11. Now change generator elements from 1 to 0 in such a way that each zero is surrounded by ones. Each time this is done, $d(1)$ will drop by 1, and $d(2)$ will increase by 2.

Continue this until min $\{d(1), d(2)\}$ is maximized. This minimum will then be the integer part of the right side of Eq. (3) for $h = 2$. If $K \lesssim 4$ this will be sufficient to achieve the upper bound of Eq. (3). For K up to about 6 the bound can be achieved simply by trying several permutations of the zeros in the connection vectors. For $K > 6$, h_0 gets larger, and $d(j)$ for $j > 2$ must be considered. The manipulations soon become too unwieldy for hand computation.

As an example of this procedure consider generating a $K = 4$, rate ⅓ ($v = 3$) code. Equation (3) yields $d_m \leq 10$ at $h_0 = 2$. Start out with

$$\mathbf{g}_1 = \mathbf{g}_2 = \mathbf{g}_3 = 1111$$

This yields $d(1) = 12$ and $d(2) = 6$. Now make the following change

$$\mathbf{g}_1 = \mathbf{g}_2 = 1111, \qquad \mathbf{g}_3 = 1011$$

Now $d(1) = 11$, $d(2) = 8$. Finally let

$$\mathbf{g}_1 = 1111, \qquad \mathbf{g}_2 = 1101, \qquad \mathbf{g}_3 = 1011$$

Then we have $d(1) = d(2) = 10$. A simple check ensures that $d(i) \geqq 10$, $i > 2$. This code is the $K = 4$ code used in the computer simulation described in the next two sections.

Using the Viterbi algorithm, convolutional codes require 2^{K-1} likelihood comparisons to decode one bit. K-bit binary block codes when encoded and decoded optimally require $(1/K)(2^K - 1)$ comparisons per bit. In the first analysis it is thus meaningful to compare the performance of a K-bit block code with a constraint length K convolutional code.

For the white gaussian noise channel a biorthogonal code is very nearly optimum. As an example, for a 4-bit biorthogonal code, the minimum distance (in terms of signal energy-to-noise ratio) is $2E_b\ N_0$, where E_b/N_0 is the energy per bit to noise ratio. There are 14 signals at the minimum distance.

The $K = 4$ convolutional code previously described has $d_m = 10$. Since there are 3 code symbols per bit, the minimum distance in signal energy is $(10/3)\,E_b/N_0 = 3.33E_b/N_0$. Furthermore there are only 4 code words at this distance at any given decoding step. All other code words are at a greater distance.

3. The Decoding Algorithm

The Viterbi algorithm is well documented (Refs. 1 and 2), and the details will not be repeated here. Suffice it to say that operating on an infinite stream of input data the algorithm never makes final bit decisions. A step in the decoding process consists of generating the likelihoods for 2^K possible bit streams and narrowing this down to 2^{K-1} using 2^{K-1} pairwise comparisons. Each comparison is in many ways similar to a "look forward" step in sequential decoding. The comparisons can be done in parallel. In practice the decoder makes bit decisions after a delay of several constraint lengths. The algorithm seems in the first analysis to be quite amendable to special-purpose machine implementation. The major operations in a step are "add," "compare," "shift," and "register exchange." The principal memory required is 2^{K-1} shift registers of length about 3 to 5 constraint lengths.

As far as synchronization is concerned, the decoder needs only branch synchronization, i.e., it must know which code symbols corresponds to the first adder output in the coder. Since the decoder retains bit stream outputs corresponding to all coder states, the decoder will with high probability synchronize within several constraint lengths when started in an arbitrary place in the received data stream.

4. Experimental Results

The Viterbi decoder was simulated on a SDS 930 computer. Received data was generated in 1000-bit blocks, and the decoder was started unsynchronized at the beginning of each of these blocks. The codes used were rate ⅓, and the channel simulated was a binary input 8-level quantized output white gaussian noise channel. The quantization levels were chosen as in Ref. 4. After allowing 50 bits for resynchronization, the counting of decoding errors was started. Each of the 2^{K-1} decoder output bit streams was 48 bits long. After a decoding step, a decision was made on the oldest bit in the bit stream, by choosing the one corresponding to the most likely stream.

Three codes with different constraint lengths were tested for several values of E_b/N_0. At least 200,000 bits were decoded for each point. The bit error probabilities for the $K = 4$, 6, and 8 codes are shown in Figs. 3, 4, and 5, respectively. The code generators used are also shown in the figures. The $K = 4$, $d_m = 10$ code has already been described. For $K = 6$, Eq. (3) yields an upper bound of 13 on d_m. This d_m is actually achieved with the code shown. This code was also generated using the *ad hoc* scheme and some trial and error. Later, a search program was written to generate all $K = 6$, $v = 3$ codes with $d_m = 13$. Of several tested, the one shown in Fig. 4 proved the best.

At $K = 8$, the bound yields $d_m \leqq 17$. No $d_m = 17$ code was found by hand calculation, and a machine search has not yet been tried. The code used has $d_m = 16$ and is by no means necessarily the best $K = 8$ code. It was, in fact, the only one tested.

Also shown in Figs. 3, 4, and 5 are the corresponding K-bit biorthogonal code bit error probabilities (Ref. 5).

5. Conclusions

The error probability curves of Figs. 3, 4, and 5 clearly indicate that constraint length K convolutional codes perform considerably better than K-bit biorthogonal codes. For instance at $K = 6$ and $P_E = 10^{-3}$ about 1 dB is to be saved. There is also the fact that bandwidth and energy per code symbol required by convolutional codes is independent of K while for biorthogonal codes bandwidth goes as $2^{K-1}/K$ and energy per symbol as $K2^{-(K-1)}$. Included in Fig. 3 is the bit error probability curve for a $K = 7$ biorthogonal code. Observe that a $K = 4$ convolutional code is superior to a $K = 7$ biorthogonal code.

References

1. Viterbi, A. J., "Error Bounds for Convolutional Codes and an Asymptotically Optimum Decoding Algorithm," *IEEE Trans. Inf. Theory*, IT-11, January 1965.
2. *Final Report on a Coding System Design for Advanced Solar Missions*, NASA Contract NAS2-3637. Codex Corp., Watertown, Mass., December 1967.
3. Peterson, W. W., *Error-Correcting Codes*. M.I.T. Press and John Wiley & Sons, Inc., New York, 1961.
4. Jacobs, I. M., "Sequential Decoding for Efficient Communication From Deep Space," *IEEE Trans. Commun. Tech.*, COM-15, August 1967.
5. Golomb, S. W., et al., *Digital Communications With Space Applications*. Prentice-Hall, Inc., Englewood Cliffs, N.J., 1964.

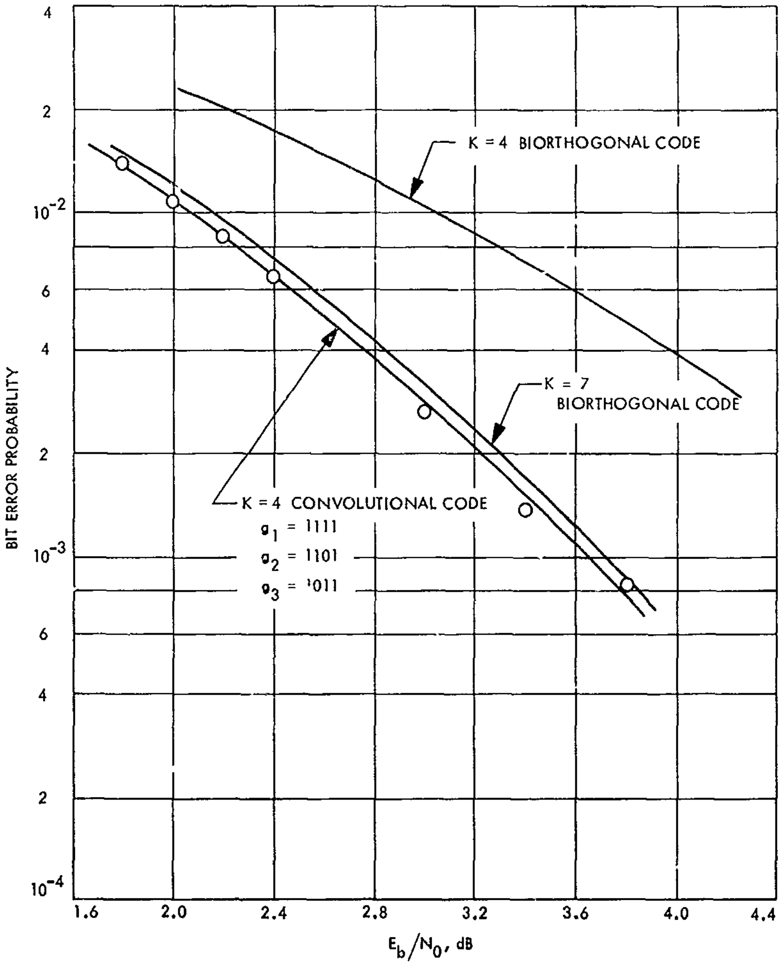

Fig. 3. Bit error probabilities for $K = 4$ codes and a comparison with a $K = 7$ biorthogonal code

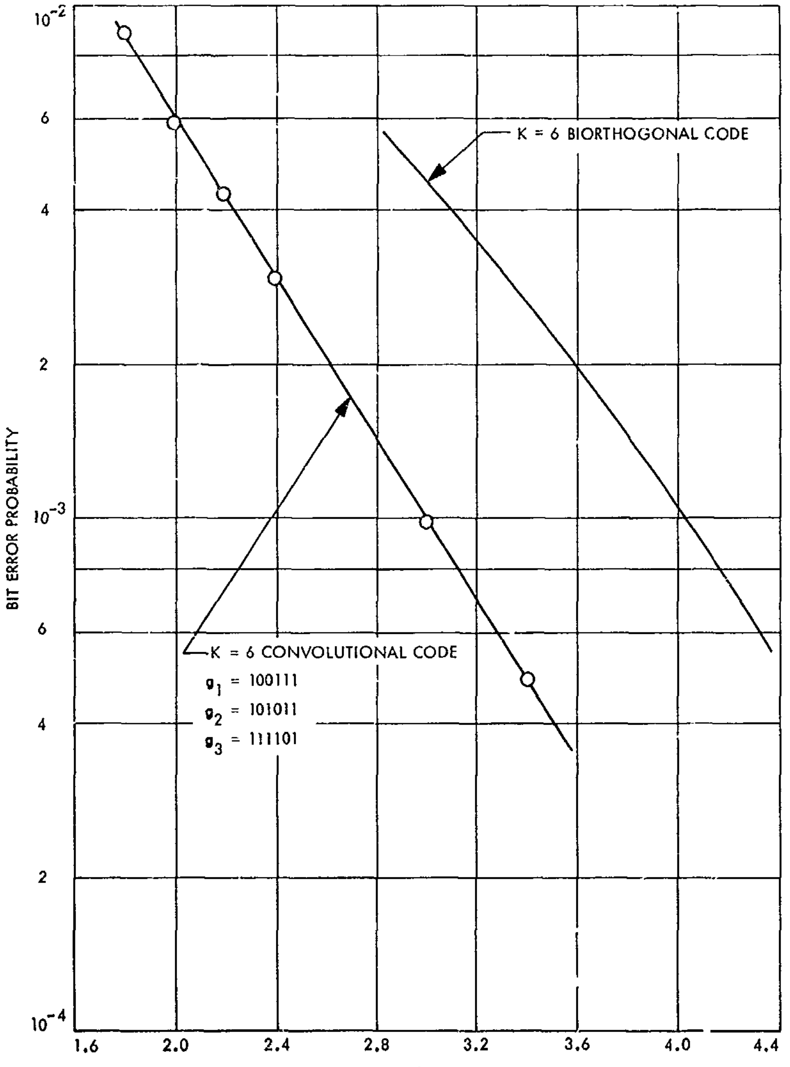

Fig. 4. Bit error probabilities for $K = 6$ codes

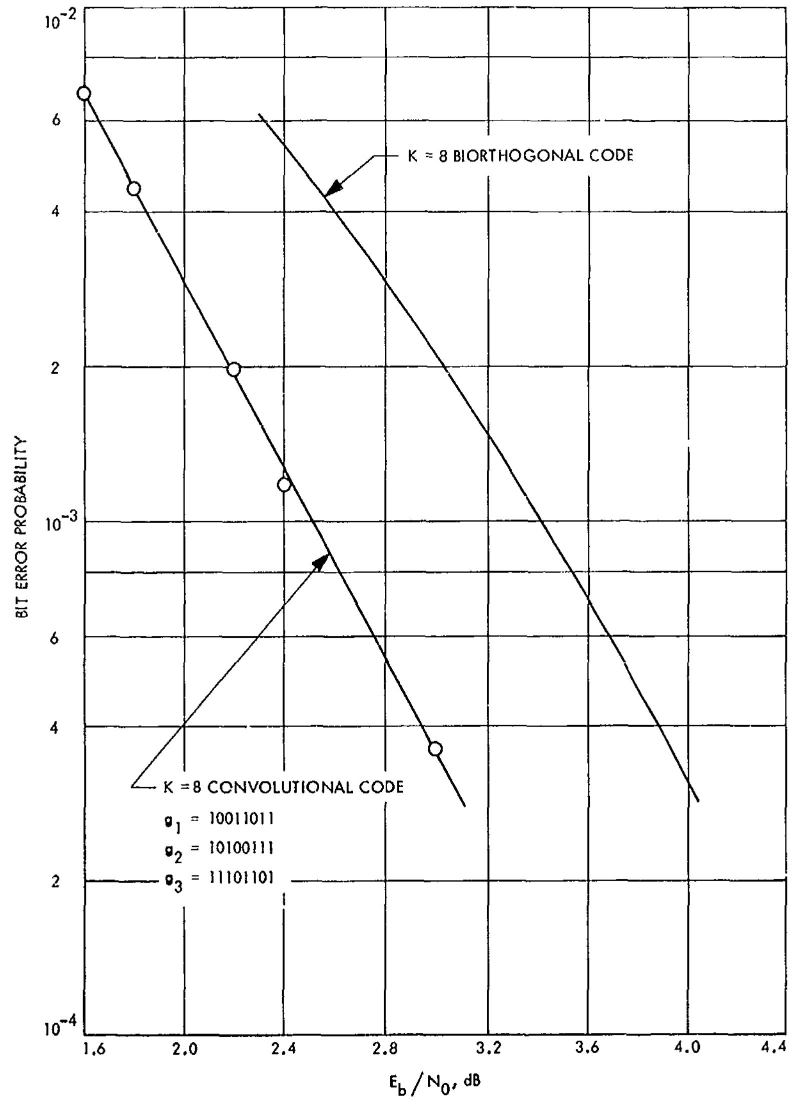

Fig. 5. Bit error probabilities for $K = 8$ codes

B. Coding and Synchronization Studies: Dynamics of Second-Order Phase-Locked Loops,

W. C. Lindsey[1]

1. Introduction

This article discusses some recent results obtained relative to the statistical dynamics of the phase-error process in second-order phase-locked loops.[2] Briefly, the problem can be described as follows: The phase-error process $\tilde{\phi}(t)$ in a phase-locked loop system undergoes diffusion much like a particle in Brownian motion (Ref. 1); hence, the variance of the phase-error becomes infinite in the steady state. Previous work (Refs. 2, 3, and 4) on determining the probability distribution of the phase-error in the steady state of a first-order loop was accomplished by reducing the phase-error modulo 2π to a $\phi(t)$ process. Such a reduction ignores how many cycles have slipped with the passage of time so that diffusion of the phase-error is taking place. For finding telemetry error probabilities, that is all that is needed; for estimating tracking accuracy, however, the $\tilde{\phi}(t)$ process itself must be studied. To completely describe the $\tilde{\phi}(t)$ process, one must account for that component of the variance of the phase-error which causes diffusion, i.e., cycle slipping.

---

[1] Consultant, Electrical Engineering Dept., University of Southern California.

[2] Lindsey, W. C., "Nonlinear Analysis and Synthesis of Generalized Tracking Systems," *Proc. IEEE* (in press). Also USC EE317, University of Southern California, Los Angeles, Calif., Dec. 1968.

This is perhaps best described by evaluating the diffusion coefficient, i.e., the rate with which the variance of the phase-error is approaching infinity, and in some way combine this component of the variance with the variance of the phase-error reduced modulo 2π.

For a second-order loop, this article discusses an approximate solution for the steady-state distribution of the phase-error reduced modulo 2π and establishes the regions of validity of this solution by comparing it with experimental results. Also, formulas are presented for (1) the diffusion coefficient of the phase-error process, (2) the expected values of the time intervals between phase jumps, (3) the expected number of phase jumps per unit time, (4) the expected number of phase jumps "to the right" and "to the left," (5) the expected value of the phase-error rate in the steady state, and (6) the mean-squared value of the phase-error rate in the steady state. In the limit, as the system damping approaches infinity, the results are then valid for the first-order loop.

2. Loop Model and Phase-Error Density Reduced Modulo 2π

For a phase-locked loop system with loop filter,

$$F(p) = \frac{1 + \tau_2 p}{1 + \tau_1 p} \tag{1}$$

it has been recently shown (Footnote 2) that the probability distribution of the phase-error reduced modulo 2π is given to a good approximation by

$$p(\phi) = \frac{\exp[\beta\phi + \alpha\cos\phi]}{4\pi^2 \exp[-\pi\beta]\,|I_{j\beta}(\alpha)|^2} \times \int_{\phi}^{\phi+2\pi} \exp[-\beta x - \alpha\cos x]\,dx \tag{2}$$

where $I_v(x)$ is the imaginary Bessel function of order v and argument x and ϕ belongs to any interval of width 2π centered about any lock point $2n\pi$; n is any integer. The parameters α and β, which characterize Eq. (2), are related to the various system parameters through

$$\left.\begin{aligned} F_1 &= \tau_2/\tau_1 \\ \beta &= \Omega_0 - AK(1 - F_1)\overline{\sin\phi} \\ \alpha &= \left(\frac{r+1}{r}\right)\rho - \frac{1}{r\sigma_G^2} \end{aligned}\right\} \tag{3}$$

where $G = \overline{\sin\phi} - \sin\phi$, the overbar denotes statistical average, Ω_0 represents the amount of loop detuning or frequency offset, ρ is the signal-to-noise ratio in the loop bandwidth, and

$$w_L \approx \frac{r+1}{2\tau_2}, \qquad \text{if } r\tau_1 >> \tau_2$$

The parameter

$$r = AK\tau_2^2/\tau_1 = (\zeta/4)^{1/2}$$

where ζ is the "loop damping" and AK represents open loop gain. Moments of $\sin\phi$ (Footnote 2) are given by

$$\left.\begin{aligned} \overline{\sin\phi} &= \frac{\beta}{\alpha} - \frac{\sinh\pi\beta}{\pi\alpha}|I_{j\beta}(\alpha)|^{-2} \\ \overline{\sin^2\phi} &= \frac{1}{2\alpha} Re\left[\frac{2I'_{j\beta}(\alpha)}{I_{j\beta}(\alpha)}\right] - \frac{\beta}{\alpha}\left[2\,\overline{\sin\phi} - \frac{\beta}{\alpha}\right] \\ \overline{\cos\phi} &= Re\left[\frac{I_{j\beta+1}(\alpha) + I_{j\beta-1}(\alpha)}{2I_{j\beta}(\alpha)}\right] \end{aligned}\right\} \tag{4}$$

with

$$\sigma^2_{\sin\phi} = \overline{\sin^2\phi} - [\overline{\sin\phi}]^2 \tag{5}$$

and $Re[\cdot]$ denotes the real part of the quantity in the brackets. It is clear from Eqs. (2) and (4) that $p(\phi)$ will be symmetric when the loop is designed such that $\beta = 0$. It is easily shown that in the limit, as r approaches infinity, Eq. (2) reduces to a result given by V. I. Tikhonov (Refs. 2 and 3) for a first-order loop.

The expected value of the phase-error can be found from Eq. (2) and the well-known Bessel function expansions of $\exp(\pm x\cos\phi)$. Without going into details (Footnote 2), we have

$$\left.\begin{aligned} \overline{\phi} &= \int_{-\pi}^{\pi} \phi p(\phi)\,d\phi \\ \overline{\phi} &= \frac{2\sinh\pi\beta}{\pi|I_{j\beta}(\alpha)|^2} \sum_{m=1}^{\infty} \frac{m I_m(\alpha)}{m^2 + \beta^2} \\ &\quad \times \left[\frac{I_0(\alpha)}{\beta} + \frac{I_m(\alpha)}{4m} + \sum_{\substack{k=1 \\ k\neq m}}^{\infty} \frac{2m(-1)^k I_k(\alpha)}{m^2 - k^2}\right] \end{aligned}\right\} \tag{6}$$

It is clear from Eq. (6) that with $\beta = 0$, $\bar{\phi} = 0$. Furthermore, $\overline{\phi^2}$ is given (Footnote 2) by

$$\overline{\phi^2} = \int_{\pi}^{\pi} \phi^2 p(\phi)\, \phi$$

$$= \frac{\sinh \pi\beta}{\pi |I_{j\beta}(\alpha)|^2} \left\{ \frac{I_0(\alpha)}{\beta} \left[\frac{\pi^2 I_0(\alpha)}{3} + 4 \sum_{k=1}^{\infty} \frac{(-1)^k I_k(\alpha)}{k^2} \right] + 2\beta I_0(\alpha) \sum_{k=1}^{\infty} \frac{I_k(\alpha)}{k^2(\beta^2 + k^2)} \right.$$

$$\left. + 2\beta \sum_{k=1}^{\infty} \frac{(-1)^k I_k(\alpha)}{\beta^2 + k^2} \left[\left(\frac{\pi^2}{3} + \frac{1}{2k^2} \right) I_k(\alpha) + 4 \sum_{\substack{m=1 \\ m \neq k}}^{\infty} \frac{(-1)^m (k^2 + m^2) I_m(\alpha)}{(k^2 - m^2)^2} \right] \right\} \qquad (7)$$

The variance $\sigma_{\phi}^2 = \overline{\phi^2} - (\bar{\phi})^2$ is minimized when the loop is designed such that $\beta = 0$ and α is maximized (Footnote 2). For this case, from Eqs. (6) and (7), we have

$$\sigma_{\phi}^2 = \frac{\pi^2}{3} + \frac{4}{I_0(\alpha)} \sum_{k=1}^{\infty} \frac{(-1)^k}{k^2} I_k(\alpha) \qquad (8)$$

Finally, the expected value of the phase-error rate $\dot{\phi}$ and the mean-squared value (Footnote 2) are given, respectively, by

$$\left.\begin{aligned} \overline{\dot{\phi}} &= \Omega_0 - AK\overline{\sin\phi} \\ \overline{\dot{\phi}^2} &= K_{00}^2 [\alpha^2 \overline{(\sin\phi)^2} + \beta^2 - 2\alpha\beta \overline{\sin\phi}] \\ \sigma_{\dot{\phi}}^2 &= K_{00}^2 \alpha^2 \sigma_{\sin\phi} + 2K_{00}(1 - K_{00}\beta^2) \end{aligned}\right\} \qquad (9)$$

where

$$K_{00} = \frac{\rho(r+1)^2}{2w_L r^2}$$

The above equation, which relates to $\sigma_{\dot{\phi}}$ to $\sigma_{\sin\phi}$, may be interpreted as an "uncertainty hyperbola."

Figure 6 illustrates a plot of the variance of the phase-error σ_{ϕ}^2 reduced modulo 2π for various values of r with $\beta = 0$. For purposes of checking the validity of the approximation which lead to Eq. (2), we have plotted various values of variance of the phase-error obtained by direct measurement in the laboratory (Ref. 5). From Fig. 6 it is clear that, for most practical purposes, Eq. (2) characterizes the distribution $p(\phi)$ for all $\rho > 0$ dB when $r = 2$, $\Omega_0 = 0$. The larger the value of r, the better the approximation.

---

3. Statistical Dynamics of the Phase-Error Process $\tilde{\phi}(t)$

One method of accounting for the fact that the loop actually skips cycles is to evaluate the rate at which the actual process at work in the loop undergoes diffusion. This parameter, the so-called diffusion coefficient D (Footnote 2 and Ref. 1), is $(2\pi)^2$ times the total average number $\bar{S}$ of phase jumps per unit of time has been shown (Footnote 2) to be given by

$$D = \frac{4w_L r^2}{\rho(r+1)^2} \frac{\cosh \pi\beta}{|I_{j\beta}(\alpha)|^2} = (2\pi)^2 \bar{S} \qquad (10)$$

In *Section 4*, we shall see that the variance of the phase error $\tilde{\phi}(t)$ at time t starting from zero error at time $t = 0$ is

$$V = \overline{\phi^2} + Dt \qquad (11)$$

since the cross term $E[4\pi\phi(t)k(t)]$ is essentially zero. This last fact follows from the fact that $E[\phi(t)] = 0$ while $\tilde{\phi}(t)$ is essentially independent of $k(t)$. Here, $k(t)$ is the unique integer with

$$\tilde{\phi}(t) = \phi(t) + 2\pi k(t)$$

Figure 7 illustrates a plot of the normalized diffusion coefficient for various values of ρ and r with $\beta = 0$. From this figure, it is seen that diffusion will not appreciably effect the measurement in a finite time if $\rho > 3$. Via Eq. (11), Eqs. (6) and (10) can be used to account for the effects in which cycle-slipping produces errors in Doppler measurements.

The expected time interval between successive cycle slipping events is given (Footnote 2) by

$$\Delta T = \frac{\pi^2 \rho(r+1)^2}{r^2 w_L} \frac{|I_{j\beta}(\alpha)|^2}{\cosh \pi\beta}$$

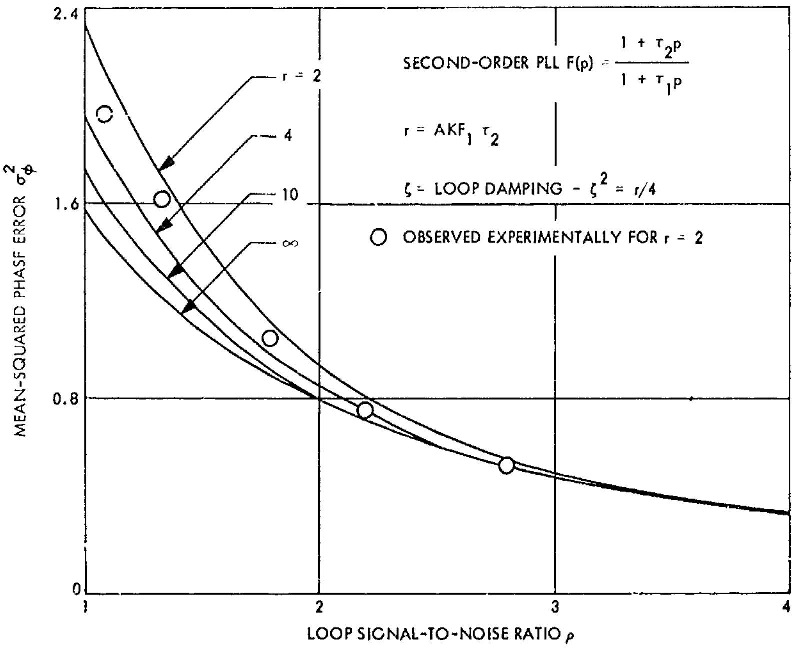

Fig. 6. Variance of the phase-error versus loop signal-to-noise ratio ρ for various values of r

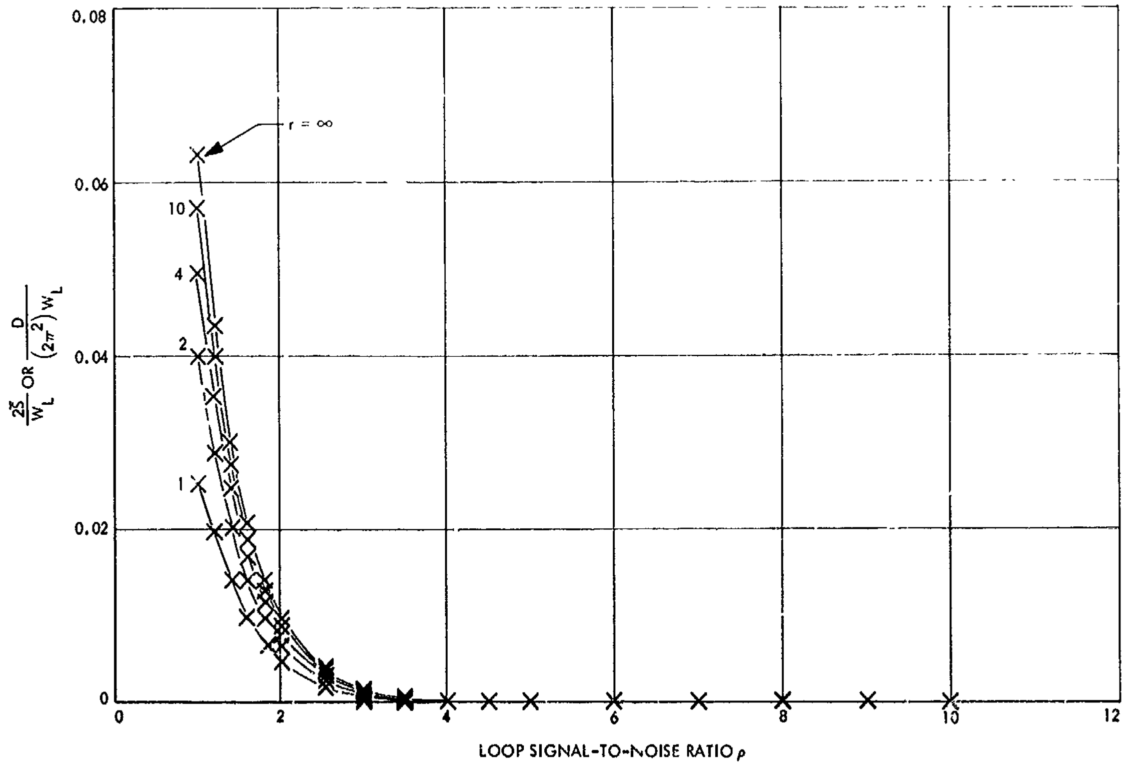

Fig. 7. Diffusion coefficient

where it can be and has been assumed that the successive instants in time when phase synchronization is lost are statistically independent.

In the case where $\Omega_0 \neq 0$, the case of greatest practical interest, the average number of phase jumps "to-the-right," say I_+, is of interest. Formulas for I_+ and I_- are given (Footnote 2) by

$$I_\pm = \frac{\exp(\pm\beta\pi)\, I}{2 \sinh \pi\beta} \tag{12}$$

where I is the (net) average number of phase jumps per unit time; i.e.,

$$I = I_+ - I_- = \left[\frac{\rho\,(r+1)^2}{w_L\,(r\pi)^2}\right]^{-1} \frac{\sinh \pi\beta}{|I_{j\beta}(\alpha)|^2} \tag{13}$$

Both I_+ and I_- are zero for the unstressed loop with $\Omega_0 = 0$. The quantity I is related to the total expected number of phase jumps per unit time $\overline{S}$ through the equation

$$I = \frac{\sinh \pi\beta}{\cosh \pi\beta}\,\overline{S} = (\tanh \pi\beta)\,\overline{S} \tag{14}$$

4. Statistical Dynamics of the Phase-Error Process $\tilde{\phi}(t)$

The actual loop phase error $\tilde{\phi}(t)$ is related to the reduced modulo 2π process $\phi(t)$ through

$$\tilde{\phi}(t) = 2\pi k + \phi(t) \tag{15}$$

where

$$k = \left[\frac{\tilde{\phi}(t) - \phi(t)}{2\pi}\right] \tag{16}$$

is the largest integer which does not exceed the bracketed ratio. Thus, k is a discrete random variable which takes on integer values at random points in time. The mean-squared value of the $\tilde{\phi}(t)$ process is given by

$$\sigma^2_{\tilde{\phi}}(t) = \sigma^2_{\phi}(t) + (2\pi)^2 \sigma^2_k + 2\pi\,[\overline{k\phi} - \bar{k}\bar{\phi}] \tag{17}$$

The event that k cycles are slipped in t seconds will be denoted by $\mathcal{S}$. If we assume that $\mathcal{S}$ is a Poisson-type process, then the quantity $\overline{S}$, representing the total average number of phase jumps per unit time, can be used to produce a probabilistic model for the phase jumping process that causes diffusion of the phase error process $\tilde{\phi}(t)$. Namely,

$$P(\mathcal{S}) = P(k) = \frac{(\overline{S}t)^k \exp[\overline{S}t]}{k!} \tag{18}$$

The mean of k is

$$\bar{k} = \overline{S}t \tag{19}$$

and the variance is also given by

$$\sigma_k^2 = \overline{k^2} = \sigma_k^2 = \overline{S}t \tag{20}$$

Experimental justification that supports the Poisson assumption is given in Ref. 5 and SPS 37-43, Vol. III, pp. 76–80. Thus, the mean-squared value of $\tilde{\phi}(t)$ becomes

$$\sigma^2_{\tilde{\phi}}(t) = \sigma^2_{\phi}(t) + (2\pi)^2 \overline{S}t + 2\pi\,[\overline{k\phi} - \bar{k}\bar{\phi}] \tag{21}$$

and in the steady state, $\tilde{\phi}(t)$ has infinite variance. Now, $D = (2\pi)^2\,\overline{S}$ represents the diffusion coefficient of the $\tilde{\phi}(t)$ process, i.e., the rate at which $\tilde{\phi}(t)$ is undergoing diffusion. Furthermore, if the random variables k and ϕ are independent, as is reasonable, we can write

$$\lim_{t \to \infty} \Delta\sigma^2_{\tilde{\phi}} = \sigma^2_{\tilde{\phi}}(t + T) - \sigma^2_{\tilde{\phi}}(t) = DT \tag{22}$$

Finally, the probability of loosing phase-lock in t seconds (i.e., the probability of slipping one or more cycles) is given by

$$P[\mathcal{S} \geq 1] = 1 - \exp[-\overline{S}t] \tag{23}$$

This result should prove useful in the design of phase-coherent doppler tracking systems.

References

1. Wax, N., *Selected Papers on Noise and Stochastic Processes*, Dover Publications, Inc., N. Y., 1954.
2. Tikhonov, V. I., "The Effects of Noise on Phase-Lock Oscillation Operation," *Automat. Rem. Cont.*, Vol. 22, No. 9, 1959.
3. Tikhonov, V. I., "Phase-Lock Automatic Frequency Control Application in the Presence of Noise," *Automat. Rem. Cont.*, Vol. 23, No. 3, 1960.
4. Viterbi, A. J., "Phase-Locked Loop Dynamics in the Presence of Noise by Fokker-Planck Techniques," *Proc. IEEE*, Vol. 51, No. 12, pp. 1737–1753, Dec. 1963.
5. Charles, F. J., and Lindsey, W. C., "Some Analytical and Experimental Phase-Locked Loop Results for Low Signal-to-Noise Ratios," *Proc. IEEE*, Vol. 55, No. 9, pp. 1152–1166, Sept. 1966.

C. Coding and Synchronization Studies: On Solution to the Second-Order Phase-Locked Loop, *J. K. Holmes*

1. Introduction

Understanding of phase-locked loop (PLL) operation began in 1955 with the now classical paper by R. M. Jaffe and E. Rechtin (Ref. 1). Starting with their basic linear analysis, there have been a wealth of papers concerning extensions, refinements, applications, and new approaches in the analysis of PLLs, as well as other automatic phase control devices.

This present article is concerned with computational simplification and an elaboration of the analysis initiated in a previous article (SPS 37-49, Vol. III, pp. 297–300), in which an expression for the variance and probability density function of the phase error was obtained for a second-order PLL. The solution was simplified with the introduction of a mean-square fit approach to approximate a certain unknown conditional mean. This idea, along with an extension and generalization of a technique due to A. J. Viterbi (Ref. 2), and some aspects of R. C. Tausworthe's "linear-spectral theory" (Ref. 3), allowed the development of a good approximation to the stationary phase-error variance reduced modulo 2π.

Recently, W. C. Lindsey,[3] using the mean-square approach introduced in SPS 37-49, Vol. III, has developed a generalization to Nth order loops and has considered many other aspects associated with the nonstationary case. An additional list of references on the subject of PLLs can be found in Refs. 2, 3, and 4.

2. Derivation

The equation of operation, for zero initial detuning and no modulation, is given in operator form by (Ref. 3)

$$\phi(t) + AK\frac{F(s)}{s}\sin\phi(t) = -K\frac{F(s)}{s}n(t) \tag{1}$$

where s is the Heaviside operator d/dt, $\phi(t)$ is the phase-error $\theta(t) - \hat{\theta}(t)$, and $K = k_1 k_m k_{vco}$. The PLL model under consideration is shown in Fig. 8. For the practical integrator, we have the following loop filter:

$$F(s) = \frac{1 + \tau_2 s}{1 + \tau_1 s} \qquad \tau_1, \tau_2 > 0 \tag{2}$$

where τ_1 and τ_2 are real nonnegative parameters. Substituting Eq. (2) into Eq. (1) yields

$$\begin{aligned} &s(1 + \tau_1 s)\phi(t) \\ &\quad + AK(1 + \tau_2 s)\sin\phi(t) = -K(1 + \tau_2 s)n(t) \end{aligned} \tag{3}$$

To avoid obtaining an equation involving the derivative of white noise, let

$$\phi(t) = \tau_2 \dot{u}(t) + u(t)$$

Then Eq. (3) is equivalent to the third-degree equation

$$\left(1 + \tau_2\frac{d}{dt}\right)(\tau_1\ddot{u} + \dot{u} + AK\sin[\tau_2\dot{u} + u] + Kn(t)) = 0 \tag{4a}$$

However, it is sufficient, as far as the solution for $\phi(t)$ is concerned, to solve

$$\mathcal{L}[u] \overset{\Delta}{=} \tau_1\ddot{u} + \dot{u} + AK\sin[\tau_2\dot{u} + u] = -Kn(t) \tag{4b}$$

as long as $\phi(0) = \dot{\phi}(0) = 0$ and $\mathcal{L}[u(0)] = -Kn(0)$.

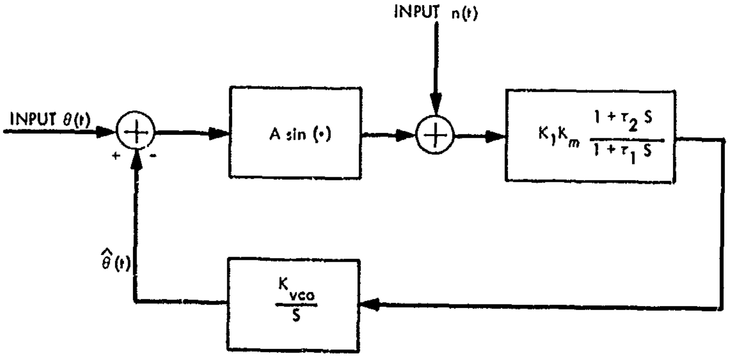

Fig. 8. Mathematically equivalent model for the second-order phase-locked loop

---

[3] Lindsey, W. C., "Nonlinear Analysis and Synthesis of Generalized Tracking Systems," *Proc. IEEE* (in press).

We can now form a Markov vector process in $\mathbf{y}(t)$ where the components are $y_0(t) = u(t)$ and $y_1(t) = \dot{u}(t)$. We have, using Eq. (4a),

$$\left.\begin{aligned} \frac{dy_0}{dt} &= y_1 \\ \frac{dy_1}{dt} &= -\frac{AK}{\tau_1}\sin(\tau_2 y_1 + y_0) - \frac{K}{\tau_1}n(t) - \frac{1}{\tau_1}y_1(t) \end{aligned}\right\} \qquad (5)$$

The Fokker–Planck equation to this system of equations can be shown to be (SPS 37-49, Vol. III)

$$\frac{\partial p}{\partial t} = -y_1\frac{\partial p}{\partial y_0} + \frac{\partial}{\partial y_1}\left\{\left[\frac{AK}{\tau_1}\sin(\tau_2 y_1 + y_0)\right]p\right\} + \frac{1}{\tau_1}\frac{\partial}{\partial y_1}(y_1 p) + \frac{K^2N_0}{4\tau_1^2}\frac{\partial^2}{\partial y_1^2}(p) \qquad (6)$$

where we consider the class of solutions that have continuous first-order derivatives in t and y_0 and a continuous second-order derivative in y_1. The notation $p(y_1, y_0, t)$ denotes the joint probability density function of $\mathbf{y}_t = [y_0(t), y_1(t)]$ at time t. In order to obtain an equation in $p(\phi, t)$, we make the following change of variables. Let $z = y_0$ and $\phi = \tau_2 y_1 + y_0$, then we obtain

$$\frac{\partial p}{\partial t}(\phi, z, t) = -\frac{1}{\tau_2}(\phi - z)\left(\frac{\partial p}{\partial z} + \frac{\partial p}{\partial \phi}\right) + \tau_2\frac{\partial}{\partial \phi}\left\{\left[\frac{AK}{\tau_1}\sin\phi + \frac{1}{\tau_1\tau_2}(\phi - z)\right]p\right\} + \frac{K^2N_0\tau_2^2}{4\tau_1^2}\frac{\partial^2 p}{\partial \phi^2} \qquad (7)$$

This equation appears impossible to solve in terms of known functions. Hence, we are led to obtain an approximation for the density of ϕ. In fact, let us find only the stationary density function with $\partial p/\partial t = 0$ in Eq. (7). First, we integrate out the variable z noting that $p(\phi, z)\big|_{z=\pm\infty} = 0$, which follows from the fact that

$$F(\phi, -\infty, t) = F(\phi, \infty, t) = 0$$

and from the continuity of $p(\phi, z, t)$. We then have

$$\left(\frac{1}{\tau_1} - \frac{1}{\tau_2}\right)\frac{\partial}{\partial \phi}\left(\phi p(\phi) - \int_{-\infty}^{\infty} zp(\phi, z)\,dz\right) + \frac{\tau_2 AK}{\tau_1}\left(\frac{\partial}{\partial \phi}\right)[\sin\phi\, p(\phi)] = 0 \qquad (8)$$

Furthermore, since $z = \phi - \tau_2 y_1$, we see that

$$\int_{\infty}^{\infty} zp(\phi, z)\,dz = p(\phi)[\phi - \tau_2 E(y_1|\phi)]$$

so that Eq. (8) becomes

$$\left(\frac{\tau_2}{\tau_1} - 1\right)\frac{\partial}{\partial \phi}[E(y_1|\phi)\,p(\phi)] + \frac{\tau_2 AK}{\tau_1}[\sin\phi\, p(\phi)] + \frac{K^2N_0}{4}\left(\frac{\tau_2}{\tau_1}\right)^2\frac{\partial^2 P(\phi)}{\partial \phi^2} = 0 \qquad (9)$$

This equation cannot be solved exactly either since $E(y_1|\phi)$ requires the joint distribution function of y_1 and ϕ, which is not available. However, a generalization of the method of Viterbi's (Ref. 2) can be used to obtain a more workable form of this conditional expectation term. Multiply both sides of the differential equation for $y_1(t)$ (Eq. 5) by $\exp(t/\tau_1)$ and integrate from t^+ to a. We obtain

$$y_1(t^+) = y_1(a)\exp\left(\frac{a - t^+}{\tau_1}\right) + \frac{AK}{\tau_1}\int_{t^+}^{a}\exp\left(\frac{t' + t^+}{\tau_1}\right) \times \sin\phi(t')\,dt' + \frac{K}{\tau_1}\int_{t^+}^{a} n(t')\exp\left(\frac{t' - t^+}{\tau_1}\right)dt'$$

Forming $E[(\cdot)|\phi_t]$, and noting

$$E[n(t')|\phi_t, t' > t] = 0$$

we have, letting $t' = t^+ + \tau$,

$$E[y_1(t^+)|\phi_t] = \frac{AK}{\tau_1}\int_0^{a-t^+}\exp\left(\frac{\tau}{\tau_1}\right)E \times [\sin\phi(t^+ + \tau)|\phi(t)]\,d\tau + E\left[y_1(a)\exp\left(\frac{a - t^+}{\tau_1}\right)\bigg|\,\phi(t)\right]$$

It can be shown that

$$\lim_{a\to\infty} E\left[y_1(a)\exp\left(\frac{a - t^+}{\tau_1}\right)\bigg|\,\phi(t)\right] = 0, \qquad \text{if } \tau_1 > 0 \qquad (10)$$

Hence, we have, assuming continuity in the $\phi(t)$ process,

$$E(y_1|\phi) = \frac{AK}{\tau_1}\int_0^{\infty}\exp\left(\frac{\tau}{\tau_1}\right)E[\sin\phi(t + \tau)|\phi(t)]\,d\tau \qquad (11)$$

Hence, the evaluation of $E(y_1|\phi)$ has been reduced to evaluating $E[\sin\phi(t + \tau)|\phi(t)]$.

In order to proceed, it is necessary to approximate the conditional expectation term in Eq. (11). First, note that

$$\lim_{\tau \to 0} E\,[\sin\phi\,(t+\tau)\,|\,\phi\,(t)] = \sin\phi\,(t)$$

Secondly, results of simulation studies indicate the following relationship for $\tau > 0$:

$$E\,[\sin\phi\,(t+\tau)\,|\,\phi\,(t)] \cong f\,(\tau)\sin\phi\,(t)$$

Consequently, we are led to try an approximation of the form

$$E\,[\sin\phi\,(t+\tau)\,|\,\phi\,(t)] = C\,(\tau)\sin\phi\,(t)$$

A reasonable method of estimating $C\,(\tau)$ is to minimize the mean-square error between $C\,(\tau)\sin\phi\,(t)$ and $E\,[\sin\phi\,(t+\tau)\,|\,\phi\,(t)]$. To simplify the notation for the following minimization, let $\phi_2 = \phi\,(t+\tau)$ and $\phi_1 = \phi\,(t)$, and denote E_{ϕ_1} as the ensemble average over ϕ_1 and E_{ϕ_2} as the ensemble average over ϕ_2, given ϕ_1. With this notation, we then seek $C\,(\tau)$ such that

$$E_{\phi_1}\{[E_{\phi_2}(\sin\phi_2\,|\,\phi_1) - C\,(\tau)\sin\phi_1]^2\}$$

is a minimum. Performing the minimization, it is found that the optimum $C\,(\tau)$, say $C_0\,(\tau)$, is given by

$$C_0\,(\tau) = \frac{E\,(\sin\phi_1\sin\phi_2)}{E\,(\sin^2\phi_1)} = \frac{R_{\sin\phi}\,(\tau)}{R_{\sin\phi}\,(0)} \qquad (12)$$

Hence, with the above mean-square fit to the term $E\,(\sin\phi_2\,|\,\phi_1)$, Eq. (11) becomes

$$E\,(y_1\,|\,\phi) = \frac{AK\sin\phi}{\tau_1 R_{\sin\phi}\,(0)} \int_0^\infty \exp\left(\frac{\tau}{\tau_1}\right) R_{\sin\phi}\,(\tau)\,d\tau \qquad (13)$$

It might appear that this expression for the conditional mean is divergent; however, as discussed below, the effect of the exponential in the integrand of Eq. (14) is negligible and, in fact, the integral is finite. Since the moments in Eq. (12) cannot be determined exactly, an approximation will be made similar to that used in linear spectral theory (Ref. 3). In this theory, it is assumed that a function $\gamma\,(s)\,\gamma\,(-s)$ exists such that

$$\gamma\,(s)\,\gamma\,(-s) = \frac{S_{\sin\phi}\,(s)}{S_\phi\,(s)}$$

where $S_\phi\,(s)$ is the spectral density of ϕ, etc. Furthermore, if $F\,(s)$ is very narrow band, $\gamma\,(s) = \gamma$ (a constant) and we have

$$\gamma^2 \int_0^\infty R_\phi\,(\tau)\,d\tau = \int_0^\infty R_{\sin\phi}\,(\tau)\,d\tau$$

A determination of γ^2 is not necessary since it will be seen later to cancel out. A tedious calculation shows that $R_\phi\,(\tau)$ is dominated by the exponential term

$$\exp\left(\frac{-r\,|\tau|}{2\tau_2}\right)$$

where $r = AK\tau_2^2/\tau_1$, and for "normal" design we select the parameters so that

$$\frac{r}{2\tau_2} >> \frac{1}{\tau_1}$$

Consequently, the exponential term in Eq. (13) is negligible in its effect on the integral for normal design. We neglect this term, $\exp\,(\tau/\tau_1)$, in the ensuing development. At this point then, we have

$$E\,(y_1\,|\,\phi) = \frac{AK\gamma^2\sin\phi}{\tau_1 R_{\sin\phi}\,(0)} \int_0^\infty R_\phi\,(\tau)\,d\tau \qquad (14)$$

The final approximation to be made is to assume $\phi\,(t)$ is a gaussian random process in order to estimate $R_{\sin\phi}\,(0)$ for all signal-to-noise ratios (SNRs) of interest. (By using the gaussian assumption, we reduce the calculation of the phase-error density and its variance to a simple calculation for all normal parameter values. The correctness of this assumption is borne out by the comparison depicted in Fig. 9.) Then, by Price's Theorem (Ref. 5), we have

$$R_{\sin\phi}\,(0) = \exp\,(-\sigma_\phi)\sinh\,(\sigma_\phi^2) \qquad (15)$$

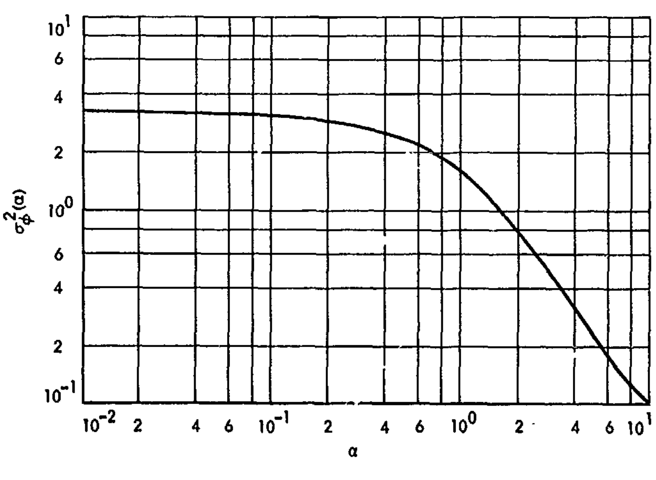

Fig. 9. Loop phase-error variance σ_ϕ^2 versus SNR

Also,

$$\int_0^{\infty} R_\phi(\tau)\, d\tau = \frac{1}{2}\int_{-\infty}^{\infty} R_\phi(\tau)\, d\tau = \frac{1}{2} S_\phi(0) \qquad (16)$$

Now using the spectral equation (Ref. 3), we obtain

$$S_\phi(0) = \frac{N_0}{2A^2\gamma^2}$$

Hence, our approximation for $E(y_1 \mid \phi)$ is finally given by

$$E(y_1 \mid \phi) = \frac{N_0 K}{4A\tau_1} \frac{\exp(\sigma_\phi^2)}{\sinh \sigma_\phi^2} \sin\phi \qquad (17)$$

and we see that, as promised, our result does not depend on γ^2.

Since our goal is to obtain the density function of ϕ, modulo 2π, we define $P(\phi)$ as the sum of all $p(\phi + 2\pi n)$ and normalize it to integrate to one. Therefore, let

$$P(\phi) = \sum_{k=-\infty}^{\infty} p(\phi + 2\pi k)$$

Then, from Eq. (9), we have for $P(\phi)$

$$\left(\frac{\tau_2}{\tau_1} - 1\right) \frac{d}{d\phi}\left[E(y_1 \mid \phi) P(\phi)\right] + \frac{\tau_2 AK}{\tau_1} \frac{d}{d\phi}\left[\sin\phi\, P(\phi)\right] + \frac{K^2 N_0}{4}\left(\frac{\tau_2}{\tau_1}\right)^2 \frac{d^2}{d\phi^2} P(\phi) = 0 \qquad (18)$$

From Eqs. (17) and (18) it can be shown that

$$P(\phi) = \frac{\exp\left\{\dfrac{4A}{KN_0\tau_2}\left[\tau_1 - (\tau_1 - \tau_2)\beta\right]\cos\phi\right\}}{2\pi I_0\left\{\dfrac{4A}{KN_0\tau_2}\left[\tau_1 - (\tau_1 - \tau_2)\beta\right]\right\}} \qquad (19)$$

where

$$\beta = \frac{N_0 \exp(\sigma_\phi^2)}{4A^2\tau_2 \sinh \sigma_\phi^2} \qquad (20)$$

Subsection 3 demonstrates the method for obtaining σ_ϕ^2 versus $N_0/4A^2$ and, hence, through Eq. (20) the value of β.

In the high SNR case (SNR $\gtrsim$ 10 dB), β is given quite accurately by $\beta = 1/(1 + r)$ and the stationary phase-error probability density for high SNRs becomes

$$P(\phi) = (2\pi)^{-1}\left\{I_0\left[\left(\frac{4A\tau_1}{KN_0\tau_2}\right)\left(\frac{AK\tau_2^2 + \tau_2}{AK\tau_2^2 + \tau_1}\right)\right]\right\}^{-1} \times \exp\left[\left(\frac{4A\tau_1}{KN_0\tau_2}\right)\left(\frac{AK\tau_2^2 + \tau_2}{AK\tau_2^2 + \tau_1}\right)\cos\phi\right] \qquad (21)$$

or, letting $r \cong AK\tau_2^2/\tau_1$, and noting $r >> \tau_2/\tau_1$, we have, to a good approximation for high SNRs, the following expression:

$$P(\phi) = (2\pi)^{-1}\left\{I_0\left[\frac{4A^2\tau_2}{N_0(r+1)}\right]\right\}^{1} \exp\left[\frac{4A^2\tau_2}{N_0(r+1)}\right] \qquad (22)$$

As a partial check on our answer, note from Eq. (21) that if $\tau_1 = \tau_2$, then $F(s) = 1$ (i.e., a first-order loop), and $P(\phi)$ is given by

$$P(\phi) = (2\pi)^{-1}\left[I_0\left(\frac{4A}{KN_0}\right)\right]^{-1} \exp\left(\frac{4A}{KN_0}\cos\phi\right) \qquad (23)$$

the exact result for the first-order loop (Ref. 2). Further, if we let K and $\tau_1 \to \infty$ such that $K/\tau_1 \to K'$, $F(s)$ becomes $F(s) = (1 + \tau_2 s)/s$ (i.e., the perfect second-order loop), and we obtain in this case

$$P(\phi) = (2\pi)^{-1}\left\{I_0\left[\left(\frac{4A^2}{N_0}\right)\left(\frac{1}{AK\tau_2 + 1/\tau_2}\right)\right]\right\}^{-1} \times \exp\left[\left(\frac{4A^2}{N_0}\right)\left(\frac{1}{AK\tau_2 + 1/\tau_2}\cos\phi\right)\right] \qquad (24)$$

which agrees with Viterbi's results (Ref. 2) derived for the high SNR case.

3. Comparison of Results

It is of interest to compare the results of this mean-square fit to the conditional mean (MSFCM) method with that of some experimental data reported by F. G. Charles and W. C. Lindsey (Ref. 4), as well as with some previous results. The PLL used in Ref. 4 had the following relevant parameters:

$$\tau_1 = 45.2$$

$$\tau_2 = 0.125$$

$$AK = 5{,}800$$

$$r = 2.0$$

The density function $P(\phi)$ in Ref. 4, was obtained experimentally and the variance was computed from this.

In order to obtain a numerical value for the variance from the method presented in Ref. 4, a knowledge of $\sigma_\phi^2(\alpha)$ is required where

$$\sigma_\phi^2(\alpha) = \int_{-\pi}^{\pi} \phi^2 \frac{\exp(\alpha \cos\phi)}{2\pi I_0(\alpha)}\, d\phi \tag{25}$$

This method deviates from that given in SPS 37-49, Vol. III, pp. 297–300, in that a simplification is introduced here that makes the evaluation of the variance a simple matter not requiring the use of a computer.

A graph of $\sigma_\phi^2(\alpha)$ versus α is given in Fig. 10. From Eqs. (19) and (20), assuming $\tau_1 >> \tau_2$, we have

$$\alpha = \left(\frac{4A^2\tau_1}{N_0\tau_2}\right)\left[\left(1 - \frac{N_0}{4A^2}\cdot\frac{2}{1-e^{-2\sigma_\phi^2}}\right)\right] \tag{26}$$

Hence, once σ_ϕ^2 and α are specified from Fig. 10, $N_0/4A^2$ can be computed from Eq. (26). The SNR A^2/N_0W_L is then given by

$$SNR = \left(\frac{4A^2}{N_0}\right)\left(\frac{\tau_2}{r+1}\right) \tag{27}$$

and, hence, one has a simple method of obtaining the relationship between σ_ϕ^2 and SNR. Using this method, the variance was computed and plotted in Fig. 9. As can be seen from the figure, both the spectral method and the MSFCM method provide relatively close fits. In fact, the MSFCM method yields negligible errors for SNR ≧ 2 dB, which encompasses the useful range of interest. For SNR ≧ 10 dB, the linear spectral method, the MSFCM method, and the linear method, as well as the others, all converge to essentially the same curve.

References

1. Jaffe, R. M., and Rechtin, E., "Design and Performance of Phase-Locked Circuits Capable of Near-Optimum Performance over a Wide Range of Input Signals and Noise Levels," *Trans. PIGIT*, Mar. 1955.
2. Viterbi, A. J., *Principles of Coherent Communication*. McGraw-Hill Book Co., New York, 1966.
3. Tausworthe, R. C., *Theory and Practical Design of Phase-Locked Receivers, Vol. I*, Technical Report 32-819. Jet Propulsion Laboratory, Pasadena, Calif., Feb. 1966.
4. Charles, F. G., and Lindsey, W. C., "Some Analytical and Experimental Phase Locked Loop Results for Low Signal-to-Noise Ratios," *Proc. IEEE*, Vol. 55, No. 9, pp. 1152–1166, Sept. 1966.
5. Price, R., "A Useful Theorem for Nonlinear Devices Having Gaussian Inputs," *Trans. PIGIT*, IT-4, June 1958.
6. Middleton, D., *Introduction to Statistical Communication Theory*, Sections 1.3 and 1.4-3. McGraw-Hill Book Co., New York, 1960.

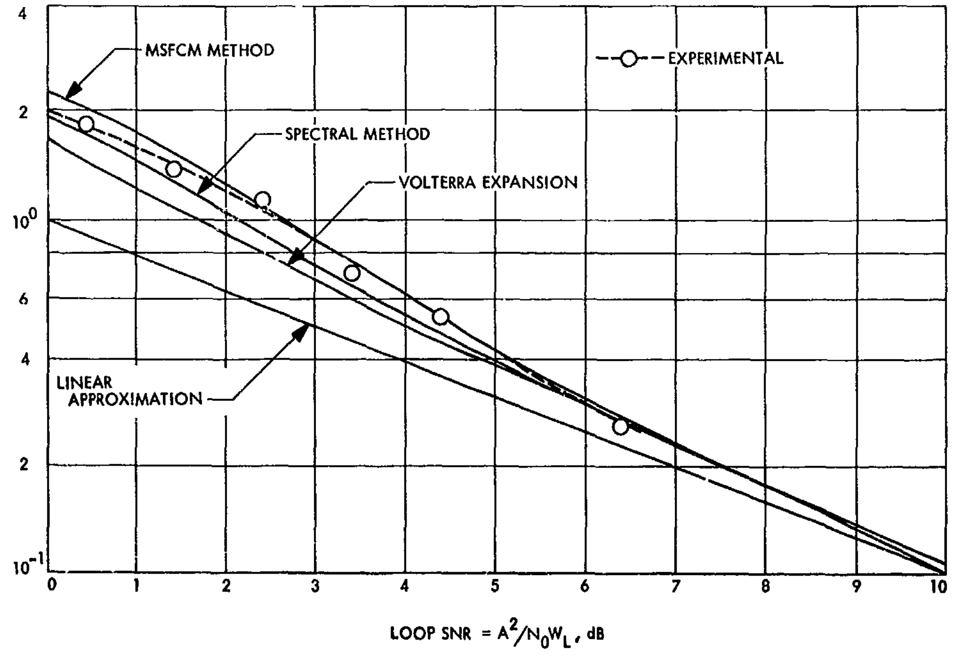

Fig. 10. $\sigma_\phi^2(\alpha)$ **versus** α

D. Coding and Synchronization Studies: Power Allocation Length Into Rapidly Varying Phase Error, *W. C. Lindsey*[1] *and J. F. Hayes*

1. Introduction

In a recent paper (Ref. 1) design trends were established for the allocation of power between the carrier and the information-bearing portion of a transmitted signal. Both one-way and two-way phase coherent communication systems were considered. This work was predicated on data rates high enough that any error in estimating the phase of the radio-frequency carrier could be taken to be constant over the duration of one signaling interval. In the present work the same problem is considered; however, the assumption that the phase error is constant over a symbol time is removed and the phase error is allowed to change appreciably over the signaling interval. In both works it is assumed that reference phase is derived exclusively from the carrier. Alternate approaches that envision deriving the reference phase from the data portion of the transmitted signal lead to quite different results (Ref. 2).

Rapidly varying phase errors are known to affect the operation of command and telemetry systems in deep-space communication systems. Consequently, a theory for predicting their deleterious effects on system performance is needed when carrying out a particular design or in the testing of a fabricated system to see that system performance meets specification. In this article we draw heavily upon the notation introduced in Ref. 1. We also assume that the subcarrier and bit-sync jitter produce negligible effects on the detection process. Procedures for handling these effects, if appreciable, have been reported in Ref. 3.

2. System Model

We consider binary phase-shift-keyed signaling for which the transmitted signals are of the form

$$\rho(t) = (2P)^{1/2} \sin[\omega t + (\cos^{-1} m)\, x_k(t)], \qquad k = 1, 2 \tag{1}$$

where $x_k = \pm 1$, P is the total transmitted power, and m is the modulation factor which serves to apportion power between the carrier and the side-bands. The signal $\rho(t)$ is disturbed in the channel by additive white gaussian noise with a single-sided power density spectrum N_0 W/hz. The signal also suffers a random phase shift $\theta(t)$ in the channel. The received signal is demodulated at the receiver by means of a reference carrier preceded by a phase-locked loop (PLL). This demodulation produces (Ref. 1)

$$y(t) = x_k(t)\,[(1 - m^2)P]^{1/2} \cos\phi(t) + n'(t) \tag{2}$$

where

$$\phi(t) \triangleq \theta(t) - \hat{\theta}(t)$$

is the error between the phase shift in the channel $\theta(t)$ and the estimate $\hat{\theta}(t)$ of this phase shift given by the PLL, and $n'(t)$ is white gaussian noise with single-sided power density spectrum N_0 W/hz. The decision on the transmitted signal is made by correlating $y(t)$ with the possible received signals. Therefore we form

$$q = \int_0^T y(t)\,[x_1(t) - x_2(t)]\,dt \tag{3}$$

If $q \geq 0$, we decide that x_1 was transmitted; otherwise we take the transmitted signal to be $x_2(t)$.

3. System Error Probability

For a given realization of the random process $\phi(t)$, $0 \leq t \leq T$, q is normally distributed with mean

$$\mu = \pm 2\,[(1 - m^2)P]^{1/2} \int_0^T \cos\phi(t)\,dt$$

and variance $\sigma^2 = 2TN_0$. The conditional probability of error has been shown (Ref. 1) to be given by

$$P_E[\phi(t), 0 \leq t \leq T] = \int_{[R(1-m^2)Y]^{1/2}}^{\infty} \frac{\exp(-x^2/2)}{(2\pi)^{1/2}}\,dx \tag{4}$$

where

$$R \triangleq 2\left(\frac{PT}{N_0}\right)$$

$$Y \triangleq \frac{1}{T}\int_0^T \cos\phi(t)\,dt$$

The average probability of error is found by averaging over the random variable Y.

However, the exact computation of the probability density $f_Y(y)$ appears to be a formidable problem. In order to circumvent this difficulty we assume that the phase error is small enough so that the linear PLL theory can be used. For most practical situations this assumption

---

[1] Consultant, Electrical Engineering Dept., University of Southern California.

is valid. The consequences of this assumption are twofold: First, from the linear phase-locked loop theory (Ref. 4) we know that $\phi(t)$ is a gaussian process; second we can make the approximation (valid for the linear region of operation)

$$Y = 1 - \frac{1}{2T}\int_0^T \phi^2(t)\,dt \qquad (5)$$

Thus the computation of $f_Y(y)$ reduces to computing the probability density of the integral of the square of a gaussian process.

In the case of a first-order PLL, a useful approximation to this density is known (Ref. 5). The PLL tracks a carrier of power m^2P immersed in white gaussian noise with power density spectrum N_0 W/hz. The correlation function of $\phi(t)$ is

$$R_\phi(\tau) = \frac{B_L N_0}{m^2P}\exp\left[-4B_L|\tau|\right] \qquad (6)$$

where B_L is the equivalent noise bandwidth of the loop (Ref. 1). The probability density $f_Z(z)$ of the random variable

$$z = \frac{m^2P}{N_0B_LT}\int_0^T \phi^2(t)\,dt \qquad (7)$$

is well approximated by (Ref. 6)

$$f_Z(z) = \frac{1}{(\pi\delta)^{1/2}}\exp(2/\delta)\,z^{-3/2}\exp\left[-\frac{1}{\delta}\left(z + \frac{1}{z}\right)\right], \qquad 0 \leqq z \leqq \infty \qquad (8)$$

where $\delta = 1/TB_L$ is the ratio of the system data rate $1/T$ to the bandwidth of the carrier tracking loop B_L. The density given by Eq. (8) is extremely accurate for $\delta \leqq 5$, the case of interest here. We further assume that the data is modulated onto a square-wave subcarrier whose fundamental frequency is sufficiently large so that the power in the modulation does not enter into the bandwidth of the loop. If, in fact, this is not the case, any appreciable sideband power which exists around the carrier would act as a self-noise in the loop and tend to introduce more jitter on the reference phase. Such designs are usually not interesting in practice, even though the analysis is relatively straightforward.

Averaging Eq. (4) over the random variable Z we find

$$P_E = \int_0^\infty f_Z(z)\int_{A(z)}^\infty \frac{1}{(2\pi)^{1/2}}\exp(-y^2/2)\,dy\,dz \qquad (9)$$

where

$$A(z) = [R(1 - m^2)]^{1/2}\left(1 - \sigma_\phi^2\frac{z}{2}\right)$$

$$\sigma_\phi^2 = \frac{N_0B_L}{m^2P}$$

In the limit as δ approaches infinity Eq. (14) becomes

$$P_E = \frac{1}{(2\pi)^{1/2}}\int_{[R(1-m^2)]^{1/2}}^\infty \exp(-y^2/2)\,dy \qquad (10)$$

which checks with the case for perfect phase synchronization.

4. Numerical Results

The double integral in Eq. (9) has been evaluated over a range of values for the parameters m, δ, and R. In Fig. 11 we plot P_E as a function of $m^2 = P_c/P$, with R as a parameter, for several different values of δ. These curves exhibit the same behavior (Ref. 1) as those plotted for the case of slowly varying phase error. For each value of R and δ there is an optimum modulation factor, e.g., m_0, for which the probability of error is minimum. Also, m_0 decreases as δ increases. In Fig. 12 we plot m_0^2 as a function of R with δ as a parameter. Finally, in Fig. 13 we show the minimum probability of error P_{E_0} corresponding to m_0 as a function of R with δ as a parameter. These results may be compared with those obtained in Ref. 1 for the case where $\phi(t)$ is constant for $0 \leqq t \leqq T$. They may be further used to design phase-coherent systems with $\delta < 1$.

5. Conclusions

As we have seen here and in Refs. 1 and 3, the phase-error introduced into the data detection process by a radio-frequency carrier tracking loop produces deleterious effects on system performance. As opposed to the problem considered in Ref. 1, this paper has treated the case where this error may vary over the duration of the received symbol. Useful design trends and results were established for the situation where the error $\phi(t)$ may be considered gaussian. For most practical applications this assumption is valid.

References

1. Lindsey, W. C., "Optimal Design of One-Way and Two-Way Coherent Communication Links," *IEEE Trans. Comm. Tech.*, Vol. COM-14, No. 4, pp. 418–431, August 1966.
2. Van Trees, H., "Optimum Power Division in Coherent Communication Systems," *IEEE Trans. Space Elect. Telem.*, Vol. SET, pp. 1–9, March, 1964.

3. Lindsey, W. C., "Determination of Modulation Indexes and Design of Two-Channel Coherent Communication Systems," *IEEE Trans. Comm. Tech.*, Vol. COM-15, No. 2, pp. 229–237, April, 1967.

4. Viterbi, A. J., *Principles of Coherent Communication*, McGraw-Hill Book Co., Inc., New York, 1966.

5. Grenander, U., Pollak, H. O., and Slepian, D., "The Distribution of Quadratic Forms in Normal Variates: A Small Sample Theory With Applications to Spectral Analysis," *J. Soc. Ind. Appl. Math.*, pp. 374–401, December 1959.

6. Slepian, D., "Fluxuations of Random Noise Power," *Bell System Technical Journal*, pp. 163–184, January 1958.

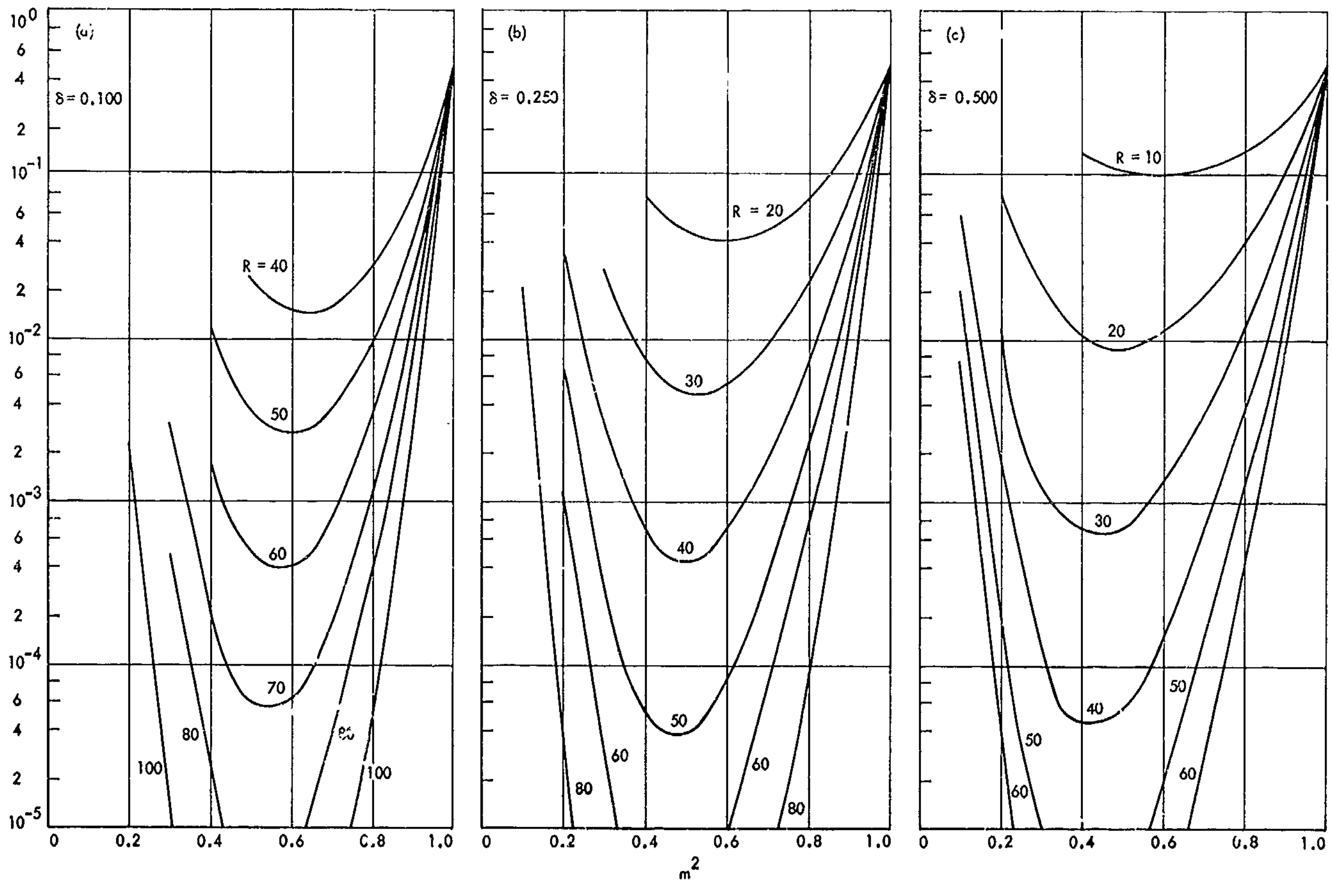

Fig. 11. Error probability P_E versus modulation factor m for various values of R: (a) $\delta = 0.1$, (b) $\delta = 0.5$, (c) $\delta = 0.25$

Fig. 12. Optimum modulation factor m_0 versus R for various values of δ

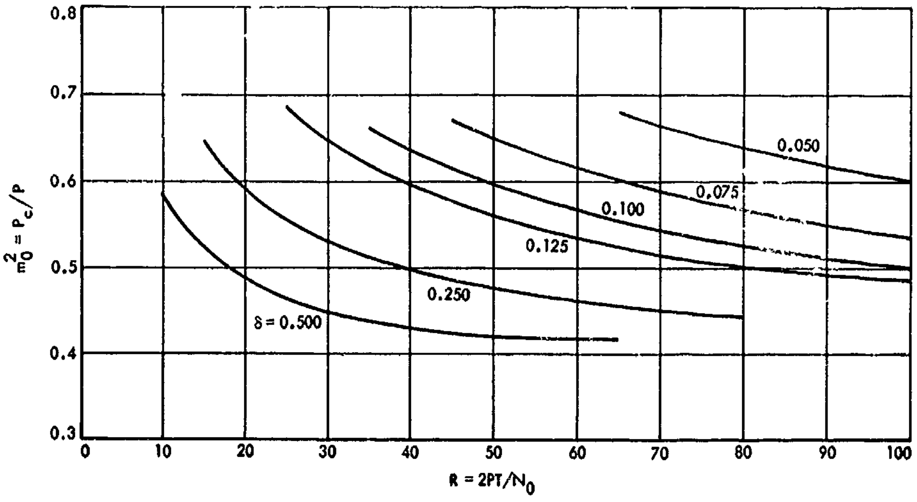

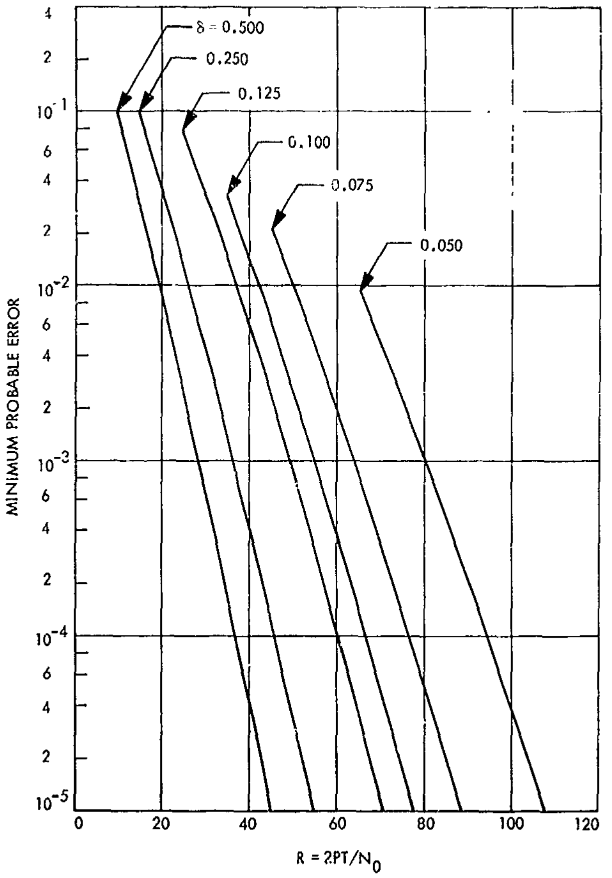

Fig. 13. Minimum error probability P_{E_0} versus R for various values of δ

E. Propagation Studies: Absolute Time by Pulsar,

G. A. Morris, Jr.

1. Introduction

Rapidly pulsating radio stars were reported early this year by the radio-astronomy group at Cambridge (Ref. 1). Further investigation confirms that the periods of these sources are quite regular, and several sources have been identified. The regular pulsations of these sources suggest they might be useful as an inexpensive means of determining absolute time among the Deep Space Network stations.

In order to be useful in determining absolute time these sources must have excellent long- and short-term stability. To be useful from an operational standpoint it must be possible to predict the arrival time of a pulse and also to make an accurate measurement of the arrival time in a short period of observation.

To obtain information about the usefulness of these sources an observational program was started in early August at S-band. The object of this program is to examine all pulsars as they are discovered to determine their usefulness as an absolute time standard. It is preferable to use sources with a large stable flux density in order to increase the signal-to-noise ratio and therefore reduce the time required to make an estimate of pulse arrival time. The pulse shape should be stable and, if possible, should have a structure that can be used to estimate arrival time readily. As of November 1, four sources have been found which satisfy the above criteria. Time versus average flux plots of these sources are shown in Fig. 14. Although individual pulses are generally too weak to be observed, averages of many pulses are easily detectable. Regular weekly observations of these sources will be made for a period of at least 1 yr. The difference between predicted and measured arrival times will be minimized in the least-squares sense, using differential correction techniques to confirm the source's celestial position and pulse period. Right ascension, declination, distance, period, and galactic rotation are among the parameters to be estimated by the least-squares fit. This information is required before accurate predictions of pulse arrival time can be made. Further, this information is valuable in determining the inherent stability of period and celestial position for possible optical identification.

2. System Description

A block diagram of the system is shown in Fig. 15. The only special equipment required is the pulsar timer, which supplies one interrupt to the computer per pulsar period and 5000 sampling pulses to the analog-to-digital converter every period. The 1-pulse/s signal from the cesium clock is used to start the timer on an exact second so that arrival time measurements may be made. The synthesizer used to determine the period is driven from the cesium clock 1-MHz output so that stability of period is obtained. Data is obtained by sampling the signal 5000 times per period and integrating the data for 500 periods. Data is normally taken for 1 h. Then the synthesizer is changed to a new frequency to correct for variations in the apparent period of the pulsar caused by the orbital and rotational motions of the earth. Data is recorded on magnetic tape, after being integrated over 500 pulses, for later analysis in the least-squares fit.

3. Variance–Covariance Analysis

A variance–covariance analysis was performed to determine how accurately several parameters could be measured for the source CP0950, assuming arrival time

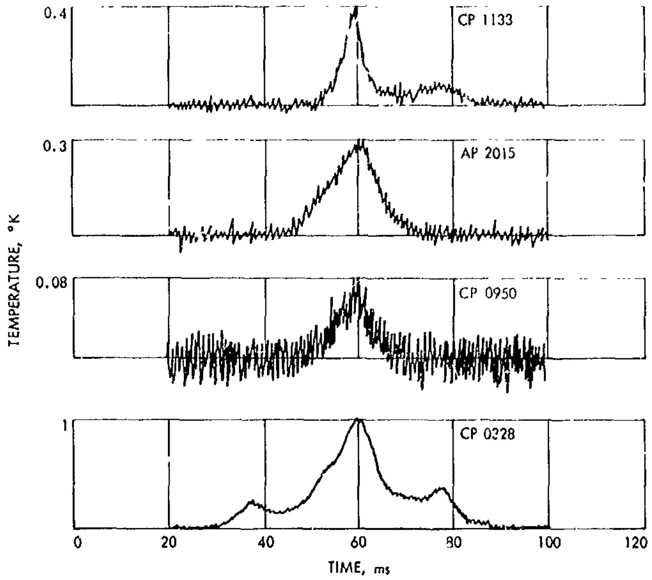

Fig. 14. Time versus flux of S-band pulsars

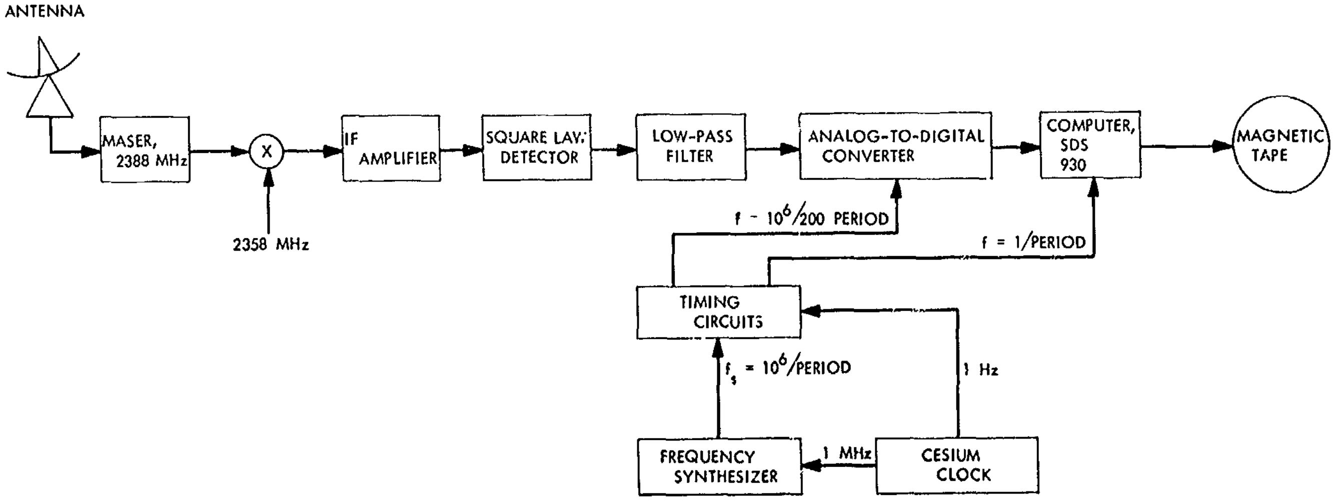

Fig. 15. Block diagram of pulsar system

measurements accurate to 100 μs. Present data indicates this is a reasonable estimate of accuracy. The standard deviations for position and period are shown in Table 1.

Table 1. Variance–covariance analysis based on arrival time measurement accurate to 100 μs for CP0950

Parameter	Standard deviation
Period	3.07×10^{-13} sec
Right ascension	0.00293 arc sec
Declination	0.00763 arc sec

A simplified earth orbit was used, and the source was assumed to have no proper motion, no radial acceleration, and a constant period. The position obtained by this technique, after 1 yr, should be of great benefit in making an optical identification. The standard deviation of the period ranks with the cesium standard as to stability.

Reference

1. Hewish, A., et al., "Observation of a Rapidly Pulsating Radio Source," *Nature*, Vol. 217, pp. 709–713, 1968.

F. Communications Systems Development: Effects of Phase-Locked Loop Dynamics on Phase-Coherent Communications,

I. F. Blake[5] *and W. C. Lindsey*[6]

1. Introduction

In a recent paper (Ref. 1) one of the authors analyzed the performance of a phase-coherent receiver preceded by a bandpass limiter. Two expressions for the error probability were given for the cases: (1) where the phase error varies rapidly over the symbol interval, and (2) where the phase error remains essentially constant over the symbol interval. The parameter which essentially characterizes how fast the phase error varies relative to the symbol time T is the ratio of the system data rate $\mathcal{R}$ to the bandwidth W_{Lo} of the loop at the design point; i.e., $\delta = \mathcal{R}/W_{Lo}$. In practice, the question naturally arises as for what region of δ will case (2) analysis be valid. It is also of interest to understand how the error rate changes as the parameter δ varies over all regions of the phase-error variations. Consequently, the purpose of this article is to present an analysis which deals with the general case of the phase-error variation for all values of δ. The results are particularly useful in the design of medium-rate phase-coherent communication systems used for space communication, e.g., *Mariner*- and *Pioneer*-type telecommunications systems.

2. System Model

If the received signal is tracked by means of a phase-locked loop, the output of the phase detector can be written as

$$y(t) = x_k(t)\cos\phi(t) + n(t) \tag{1}$$

where $\phi(t)$ is the time-varying phase error in the loop, and $n(t)$ is white gaussian noise of two-sided spectral density $N_0/2$ watts/sec (Ref. 1). The signals

$$x_k(t), \qquad k = 1,2$$

are constant over the bit interval of duration T sec:

$$x_1(t) = +A$$

$$x_2(t) = -A$$

The correlator output, on which the decision as to whether $x_1(t)$ or $x_2(t)$ was sent is based, can be shown to be given by (Ref. 1)

$$q_k = \int_0^T [x_k(t)\cos\phi(t) + n(t)]\,[x_2(t) - x_1(t)]\,dt \tag{2}$$

If q_k is negative, we decide that $x_1(t)$ was sent, and if positive, $x_2(t)$. It is assumed that the signal-to-noise ratio in the tracking loop is such that the phase error process $\phi(t)$ is gaussian with correlation function

$$R_\phi(\tau) = \frac{1}{\rho_L}\exp[-\gamma|\tau|] = \sigma_L^2\exp[-\gamma|\tau|] \tag{3}$$

This assumption is justified in the case of a first-order loop with no bandpass limiter preceding it. For the case under consideration here, it is an approximating assumption essential for the analysis. The agreement of known experimental and theoretical results tend to support its use.

The parameter γ in Eq. (3) is defined later in terms of loop and filter parameters in Eq. (11). When the loop is preceded by a band-pass limiter, the quantity σ_L^2 in Eq. (3) is well approximated in the region of interest in practice by (Ref. 1)

$$\frac{1}{\sigma_L^2} = \rho_L$$

$$= \frac{3z}{\Gamma(1 + 2/\mu)}$$

$$\Gamma = \frac{1 + 0.345\,zy}{0.862 + 0.690\,zy}$$

$$z = \frac{P_c}{N_0 b_{LO}}$$

$$y = \frac{b_{LO}}{b_H}$$

$$\mu = \frac{(\Upsilon_0)^{1/2}\exp\left(-\frac{\Upsilon_0 y}{2}\right)\left[I_0\left(\frac{\Upsilon_0 y}{2}\right) + I_1\left(\frac{\Upsilon_0 y}{2}\right)\right]}{z^{1/2}\exp\left(-\frac{zy}{2}\right)\left[I_0\left(\frac{zy}{2}\right) + I_1\left(\frac{zy}{2}\right)\right]}$$

$$\Upsilon_0 = \frac{P_c O}{N_0 B_{LO}} \tag{4}$$

---

[5] Resident Research Associate, NASA–NRC.

[6] Consultant, Electrical Engineering Dept., University of Southern California.

where P_c is the carrier power, b_L and b_H are loop and IF amplifier (in the double heterodyne receiver) bandwidths ($w_H = 2b_H$, $w_L = 2b_L$) (Ref. 1). The subscript 0 refers to the values of the loop parameters at the design point, which is defined as $z_0 = \Upsilon_0$ = constant. The parameter μ is the ratio of the limiter suppression factor at the design point to its value at any other point and

$$I_k(x), \qquad k = 1, 2$$

are modified Bessel functions of order k. The parameter zy is the signal-to-noise ratio at the output of the receiver IF amplifier.

3. Error Probability Calculations

If the parameter z is sufficiently large, the cosine term in Eq. (1) can be replaced by the approximation

$$\cos\phi(t) \cong 1 - \frac{\phi^2(t)}{2} \tag{5}$$

It turns out that in practice this approximation is sufficiently accurate in the region of interest. The decision variable becomes

$$q_k = \beta_k T - \frac{1}{2}\beta_k \int_0^T \phi^2(t)\,dt - 2A\int_0^T n(t)\,dt \tag{6}$$

where

$$\begin{aligned} \beta_k &= x_k(t)\,[x_2(t) - x_1(t)] \\ &= -2A^2, \qquad k = 1 \\ &= +2A^2, \qquad k = 2 \end{aligned} \tag{7}$$

Define the new decision variable

$$\begin{aligned} z_k &= -\frac{(q_k - \beta_k T)}{\frac{1}{2}\beta_k T} \\ &= \frac{1}{T}\int_0^T \phi^2(t)\,dt + \frac{2A}{\frac{1}{2}\beta_k T}\int_0^T n(t)\,dt \end{aligned} \tag{8}$$

where now it is decided that $x_1(t)$ was sent if $z_k > 2$, and $x_2(t)$, otherwise. The second term on the right-hand side of Eq. (8) is a gaussian random variable with mean zero and variance

$$\sigma^2 = \frac{2N_0}{A^2T} \triangleq \frac{2}{R} \tag{9}$$

The probability density of the first integral in Eq. (8) is very difficult to determine. However, a useful approximation to it has been found (Ref. 2):

$$\begin{aligned} g(x) = \rho_L\left(\frac{\beta_L}{2\pi}\right)^{1/2} e^{\beta_L}(\rho_L x)^{-3/2} \\ \times \exp\left[-\frac{\beta_L}{2}\left(\rho_L x + \frac{1}{\rho_L x}\right)\right], \qquad x \geqq 0 \end{aligned} \tag{10}$$

where

$$\begin{aligned} \beta_L &= \frac{\gamma T}{2} \\ &= \frac{1}{\delta}\left(\frac{1 + r_{0/\mu}}{1 + r_0}\right) \end{aligned} \tag{11}$$

where γ is the parameter appearing in the exponent of the correlation function in Eq. (3), r_0 is a loop parameter, μ is as defined in Eq. (4), and

$$\delta = \frac{\mathscr{R}}{W_{LO}} = \frac{\mathscr{R}}{2b_{LO}} \tag{12}$$

The density in Eq. (10) is a unimodal function which is zero at the origin and a maximum at

$$x = \frac{1}{2}\left[\frac{9}{\beta_L^2\rho_L^4} + \frac{4}{\rho_L^2}\right]^{1/2} - \frac{3}{2\beta_L\rho_L^2} \tag{13}$$

The approximation to the true density becomes very close for $\beta_L > 5$. As $\beta_L \to \infty$, the maximum tends to $x = 1/\rho_L$ and the function tends to a delta function at this point. As $\beta_L \to 0$, $g(x)$ tends to a delta function at the origin. Similarly, for fixed β_L as $\rho_L \to \infty$, the function tends to a delta function at the origin. Notice that in order to make the approximation to the cosine valid, ρ_L should be at least 3 or larger.

If it is assumed that the two integrals in Eq. (8) are independent random variables (an approximation which can be partially justified on physical grounds for the case of interest here), then the probability density of the random variable z_k can be written as

$$p(z_k) = \int_0^\infty \frac{1}{(2\pi\sigma)^{1/2}} \exp\left[-\frac{(z_k - x)^2}{2\sigma^2}\right] g(x)\,dx \tag{14}$$

Assuming $x_1(t)$ was sent, the probability of error

$$P_E = \text{prob}\,[z_k > 2]$$

$$= \int_2^\infty \int_0^\infty \frac{1}{(2\pi\sigma)^{1/2}} \exp\left[-\frac{(z-x)^2}{2\sigma^2}\right] g(x)\,dx\,dz \tag{15}$$

Interchanging the integration yields

$$P_E = \int_0^\infty \text{erfc}\left(\frac{2-x}{\sigma}\right) g(x)\,dx \tag{16}$$

where erfc(•) is the complementary error function

$$\text{erfc}(y) = \int_y^\infty \frac{1}{(2\pi)^{1/2}} \exp(-\mu^2/2)\,du \tag{17}$$

Notice that as $\rho_L \to \infty$, $P_E \to \text{erfc}\,(2R)^{1/2}$ which coincides with the result obtained in Eqs. (24) and (38) of Ref. 1 under this condition.

From the results of Ref. 2 it appears that the density function of Eq. (10) becomes a poor approximation as β_L decreases much below unity. Since

$$\beta_L = \frac{1}{\delta}\left(\frac{1 + r_0/\mu}{1 + r_0}\right) \tag{18}$$

this corresponds to δ being greater than

$$\left(\frac{(1 + r_0/\mu)}{1 + r_0}\right)$$

The parameter μ is a function of $x(= z/2)$ and other parameters. To find the region of validity of the curves, consider first Fig. 16, where $R = 4.8$. For $x = 4$, $\mu \cong 0.5$ and the curve is valid for $\delta < 2$. For $x = 300$, $\mu \cong 0.078$ and the curve is valid for $\delta < 9$. Drawing a straight line between these points gives a good approximation to the region of validity. The same limits hold for Fig. 17 also.

4. Results and Conclusions

That component of the error probability, assuming phases reduced modulo 2π, has been evaluated based upon the approximation that

$$\cos\phi(t) = 1 - \frac{\phi^2(t)}{2}$$

This does not imply the assumption that $\phi(t)$ is small, i.e., linear PLL theory holds. If linear PLL theory were

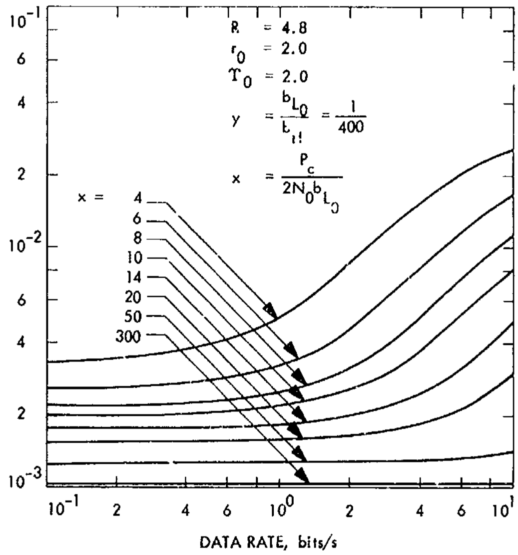

Fig. 16. Error probability versus data rate (phase error varies over bit interval), $R = 4.8$

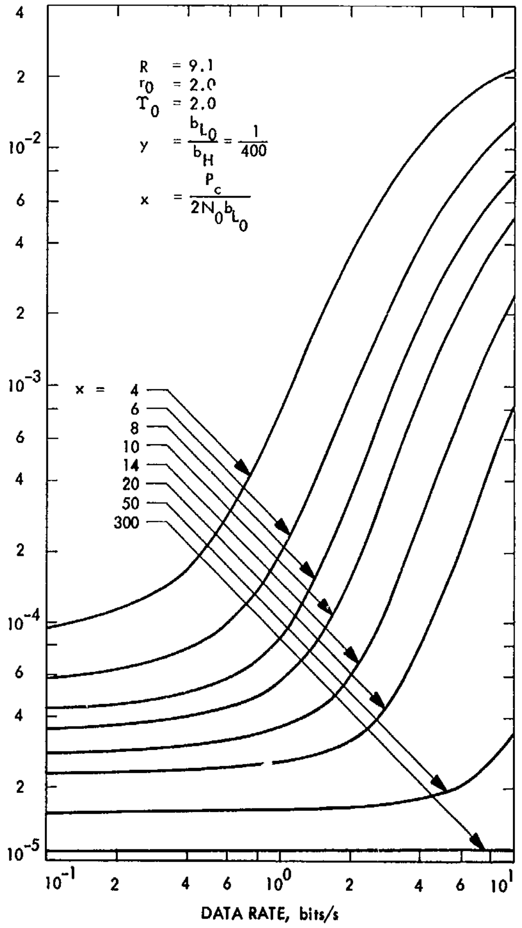

Fig. 17. Error probability versus data rate (phase error varies over bit interval), $R = 9.1$

invoked $\cos\phi(t)$ would be replaced by $\cos\phi(t) = 1$ and $\sin\phi(t) \simeq \phi(t)$. On the other hand, in order to describe the statistics of

$$Y = \frac{1}{T}\int_0^T \cos\phi(t)\,dt$$

$$\cong 1 - \frac{1}{2T}\int_0^T \phi^2(t)\,dt$$

it has been necessary assume that $\phi(t)$ is gaussian. In principle, however, this assumption is not at all restrictive since the variance of the actual ϕ process at work in the loop can be substituted into the probability distribution $f_Y(y)$. Thus the nonlinear effects of the loop are taken into account.

Figures 16 and 17 illustrate the performance of a binary phase-shift-keyed communication system when $\phi(t)$ varies over the symbol interval. The signal-to-noise ratio $R = ST_0/N_0$ has been set such that the error probability of the system would be 10^{-3} (Fig. 16) and 10^{-5} (Fig. 17) in a perfectly synchronized system. For values of $4 \leq \delta \leq 5$ the results check, for all practical purposes, with those given previously (Ref. 1) where it is assumed that $\cos\phi$ is essentially constant over the symbol interval. For $\delta < 4$ the results presented here begin to deviate appreciably from those where $\cos\phi$ is assumed constant; hence, the model introduced here will be useful in designing and testing of phase-coherent systems which operate with $\delta < 4$, the low-rate end of the region of δ.

References

1. Lindsey, W. C., "Performance of Phase Coherent Receivers Preceded by Bandpass Limiters," *IEEE Trans. Comm. Tech.*, Vol. COM-16, No. 2, pp. 245–251, April 1968.
2. Grenander, U., Pollak, H. O., and Slepian, D., "The Distribution of Quadratic Forms in Normal Variates: A Small Sample Theory With Applications to Spectral Analysis," *J. Soc. Ind. Appl. Math.*, Vol. 7, No. 4, pp. 374–401, Dec. 1959.

G. Communications Systems Development: Efficiency of Noisy Reference Detection,

R. C. Tausworthe

1. Introduction

Lindsey (Ref. 1) has published results which, for a given modulation index, relate the observed signal-to-noise ratios (SNR) to equivalent signal losses caused by the noisy demodulation process. Recent measurements of the performance of the 8⅓-bits/s *Mariner* Mars 1969 engineering telemetry instituted a reevaluation of these analyses. The following report is a tabulation of the method for determining the demodulation efficiency as a function of loop phase error. Performance is then related to these efficiencies through the modulation index. This method was chosen because of the flexibility it affords when many indices, bandwidths, etc., are being considered.

2. Efficiency Equations

The output of a coherent amplitude detector is a process of the form (Fig. 18)

$$z(t) = P^{1/2}\,m(t)\,g(\phi) + n(t) \tag{1}$$

in which $n(t)$ is wide-band noise normalized to have the same two-sided spectral density $N_0 = N_+/2$, as the input noise; $P = A^2$ is the rms detected sideband power; $g(\phi)$ is the detector phase characteristic, normalized so that $g(0) = 1$; and $m(t)$ is the detected modulation process, normalized so that $E(m^2(t)) = 1$. The modulation waveform we shall assume is one of M messages $\{m_k(t)\}$, for $0 \leq t < T$.

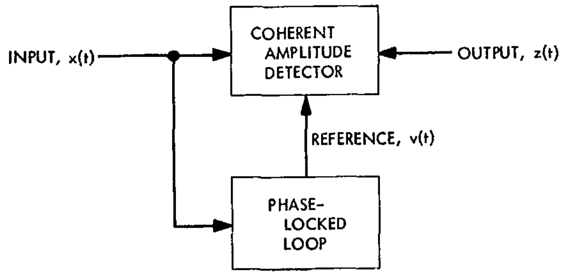

Fig. 18. Coherent detection by loop-derived reference

The process $z(t)$ is the input to a set of correlators, whose outputs at the end of a T-sec message are

$$w_k = \frac{A}{T}\int_0^T m(t)\,m_k(t)\,g(\phi(t))\,dt + N(T) \tag{2}$$

$N(T)$ then is a gaussian random variable with variance

$$\sigma_N^2 = \frac{N_0}{T} \tag{3}$$

We shall also assume that the phase-error process is derived from a phase-locked loop tracking the carrier or subcarrier. The loop bandwidth will be denoted w_L

and the phase-error density $p(\phi)$. The integral term of Eq. (2) can be written as a mean value plus a variational term

$$w_k = A(r_k\mu + \nu_k) + N(T) \tag{4}$$

in terms of the normalized cross-correlation r_k between the incoming message $m(t)$ and the kth stored one, $m_k(t)$, where $\mu = E[g(\phi)]$, the ν_k are random variables which depend on the value of k, and $\mathbf{v} = (\nu_1, \cdots, \nu_m)$ possesses some distribution $p(\mathbf{v})$. The actual overall probability of error is the average conditional error probability

$$\overline{P}_E = \int Pr[\text{error} | \nu_1, \cdots, \nu_m] \, p(\nu_1, \cdots, \nu_m) \, d\nu_1 \cdots d\nu_m \tag{5}$$

The difficulty in specifying the characteristics of $p(\nu_1, \cdots, \nu_m)$ lead to approximations for Eq. (5).

First, if the loop response is considerably more rapid than the integration time T (i.e., $\delta = 2/w_L T << 1$) then the correlator output tends to the average

$$\nu_k \approx 0 \tag{6}$$

in which case the outputs appear all to have an equivalent constant factor $E[g(\phi)]$ multiplying the signal amplitude A. Performance is then the same as it would be if the signal power were reduced by the factor $E^2[g(\phi)]$. The error rate will fit the usual maximum likelihood theory, giving rise to a probability of error as a function of the matched filter SNR parameter ρ_{mf}:

$$\rho_{mf} = \frac{PT}{N_+} E^2[g(\phi)] = RE^2[g(\phi)] \tag{7}$$

in which $R = PT/N_+$ is the undegraded value of ρ_{mf}. In this case, it is easy to see that the detector efficiency η is merely

$$\eta_0 = E^2[g(\phi)] = \mu^2 \tag{8}$$

A second approximation can be made when the loop is very sluggish with respect to the message (i.e., $\delta = 2/w_L T >> 1$). Then, over the interval $(0, T)$, the phase error is nearly constant (but randomly distributed according to $p(\phi)$). In this case, the correlator outputs are very nearly

$$w_k = Ar_k g(\phi) + N(T) \tag{9}$$

so that the averaged error probability yields the overall error rate

$$\overline{P}_E(R^{1/2}) = \int P_E(R^{1/2} g(\phi) | \phi) \, p(\phi) \, d\phi \tag{10}$$

The degradation is then clearly

$$\eta_\infty = \frac{1}{R} \{\overline{P}_E^{-1} [P_E(R^{1/2})]\}^2 \tag{11}$$

Because of the convexity of the function $Pr[E|\mathbf{v}]$, it follows that the actual efficiency is bounded by Eqs. (8) and (11):

$$\eta_\infty \leq \eta_\delta \leq \eta_0 \tag{12}$$

3. Error Probability

Since Eq. (11) requires it, let us consider the error probability function. For no coding and antipodal binary signals, the error rate is

$$P_E = \frac{1}{2} \operatorname{erfc}(R)^{1/2} \tag{13}$$

For orthogonal, equi-energy signals, the error rate is

$$\begin{aligned} P_E &= \frac{1}{(2\pi)^{1/2}} \int_{-\infty}^{+\infty} \exp(-y^2/2) \\ &\quad \times \left[\frac{1}{(2\pi)^{1/2}} \int_{-\infty}^{v+(2R)^{1/2}} \exp(-v^2/2) \, dv \right]^{M-1} dy \\ &\approx \frac{M-1}{2} \operatorname{erfc}\left(\frac{R}{2}\right)^{1/2} \end{aligned} \tag{14}$$

As a function of R, biorthogonal codes behave much the same (Ref. 2) as Eq. (14) indicates. Thus, for the three cases (no coding, orthogonal, biorthogonal) we have

$$P_E(R_1^{1/2}) \approx P_E(R_0^{1/2}) \frac{\operatorname{erfc}(\lambda R_1)^{1/2}}{\operatorname{erfc}(\lambda R_0)^{1/2}} \tag{15}$$

for any values R_0 and R_1 of R. The coefficient λ relates to the coding:

$$\lambda = \begin{cases} 1, & \text{uncoded} \\ \dfrac{1}{2}, & \text{coded (orthogonal/biorthogonal)} \end{cases} \tag{16}$$

We can set $R_0^{1/2} = R^{1/2}$ and $R_1^{1/2} = R^{1/2} g(\phi)$, above, to evaluate Eq. (10):

$$\overline{P}_E(R^{1/2}) = \frac{P_E(R^{1/2})}{\operatorname{erfc}(\lambda R)^{1/2}} \int_{-\pi}^{\pi} \operatorname{erfc}(\lambda R)^{1/2} g(\phi))\, p(\phi)\, d\phi \tag{17}$$

But the same error rate would occur if the value of R were R_{eq} and no degradation were allowed:

$$\overline{P}_E(R^{1/2}) = P_E(R_{eq}^{1/2}) = \frac{P_E(R^{1/2})}{\operatorname{erfc}(\lambda R)^{1/2}} \operatorname{erfc}(\lambda R_{eq})^{1/2} \tag{18}$$

It is then clear that

$$R_{eq} = \frac{1}{\lambda}\left\{\operatorname{erfc}^{-1}\left[\int_{-\pi}^{\pi} \operatorname{erfc}((\lambda R)^{1/2} g(\phi))\, p(\phi)\, d\phi\right]\right\}^2 \tag{19}$$

and, correspondingly, that

$$\eta_\infty = \frac{1}{\lambda R}\left\{\operatorname{erfc}^{-1}\left[\int_{-\pi}^{\pi} \operatorname{erfc}((\lambda R)^{1/2} g(\phi))\, p(\phi)\, d\phi\right]\right\}^2 \tag{20}$$

Thus, it remains only to evaluate Eqs. (8) and (20) for given $g(\phi)$ and $p(\phi)$ to obtain limits on η_δ.

4. Carrier-Extraction Degradation

For the carrier-extraction process the detector characteristic is

$$g(\phi) = \cos\phi \tag{21}$$

and the phase-error distribution, based on the first-order loop theory, is approximately (Ref. 3)

$$p(\phi) = \frac{\exp(\rho\cos\phi)}{2\pi I_0(\rho)} \tag{22}$$

in terms of the loop equivalent SNR (Ref. 4)

$$\rho = \frac{P_c}{N_0 w_L \Gamma} \tag{23}$$

Based on this ρ, a certain loop phase error σ^2 is present in the loop:

$$\sigma^2 \approx \frac{\pi}{3} + \frac{4}{I_0(\rho)} \sum_{n=1}^{\infty} \frac{(-1)^n I_n(\rho)}{n^2}$$

$$\sim \frac{1}{\rho}, \qquad \text{as } \rho \to \infty \tag{24}$$

It also follows that the degradation for $\delta << 1$ is

$$\eta_0 = \left(\frac{I_1(\rho)}{I_0(\rho)}\right)^2 \tag{25}$$

The value for η_∞ has been obtained by numerical integration, and appears along with the η_0 of Eq. (25) in Fig. 19, cross-plotted as a function of the loop error. It may be noted that when σ^2 is small, the two bounds converge approximately to the gaussian-phase-error result

$$1 - \eta_0 \sim \frac{1}{\rho} \sim \sigma^2 \sim 1 - \exp(-\sigma^2) \tag{26}$$

But as degradation becomes an appreciable percent, the two separate and depend not only on σ^2, but on λR as well. Because of the increasing steepness of P_E with λR, the degradation for $\delta >> 1$ becomes more drastic as λR increases. The degradation for $\delta << 1$ is, however, independent of λR.

5. Subcarrier-Loop Degradation

Assuming that the subcarrier is a square wave, the detector characteristic becomes triangular:

$$g(\phi) = 1 - \frac{2}{\pi}|\phi|, \qquad \text{for } |\phi| \leq \frac{3\pi}{2} \tag{27}$$

The approximate loop error density (based on a first-order loop) is again related (SPS 37-31, Vol. IV, pp. 311–325) to the loop equivalent SNR by

$$p(\phi) = \begin{cases} \dfrac{1}{C}\exp\left[-\dfrac{2\rho}{\pi^2}\phi^2\right], & \text{for } |\phi| \leq \pi/2 \\ \dfrac{1}{C}\exp\left[-\rho\left(1 - \dfrac{2(\phi-\pi)^2}{\pi^2}\right)\right], & \pi/2 \leq \dfrac{3\pi}{2} \end{cases}$$

$$C = \frac{\pi^{3/2}}{(2\rho)^{1/2}}\left\{\operatorname{erf}\left(\frac{\rho}{2}\right)^{1/2} + e^{-\rho} h\left(\frac{\rho}{2}\right)^{1/2}\right\} \tag{28}$$

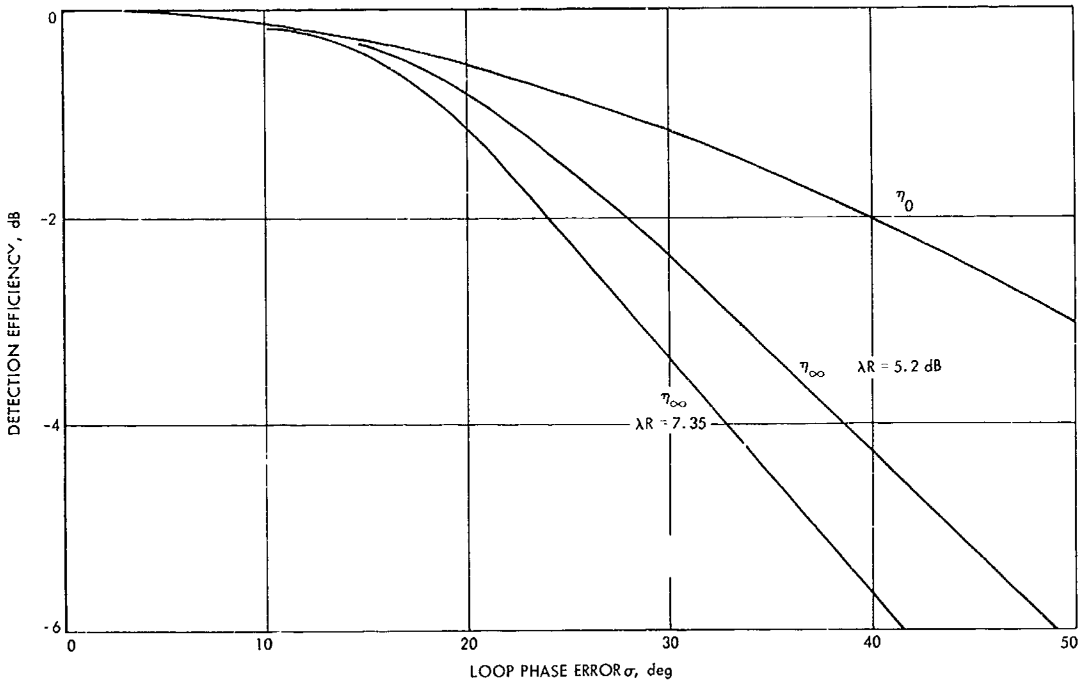

Fig. 19. Loop-derived reference degradation bounds for carrier tracking loop

where the imaginary error function

$$h(x) = \frac{2}{\pi^{1/2}} \int_0^x e^{t^2}\, dt$$

$$= \frac{2}{\pi^{1/2}} x \sum_{n=0}^{\infty} \frac{x^{2n}}{n!\,(2n+1)} \tag{29}$$

The phase-error variance is then

$$\sigma^2 = \left(\frac{\pi}{2}\right)^{5/2} \frac{\pi}{\rho^{3/2} C} \left\{ \operatorname{erf}\left[\left(\frac{\rho}{2}\right)^{1/2}\right] + (4\rho - 1)\, h\left[\left(\frac{\rho}{2}\right)^{1/2}\right] - 4\left(\frac{2\rho}{\pi}\right)^{1/2} e^{-\rho/2} \left(1 - e^{-\rho/2}\right) \right\} \tag{30}$$

and the low-rate efficiency can be straightforwardly obtained as

$$\eta_0 = \frac{\operatorname{erf}\left[\left(\frac{\rho}{2}\right)^{1/2}\right] - e^{-\rho}\, h\left[\left(\frac{\rho}{2}\right)^{1/2}\right]}{\operatorname{erf}\left[\left(\frac{\rho}{2}\right)^{1/2}\right] + e^{-\rho}\, h\left[\left(\frac{\rho}{2}\right)^{1/2}\right]} \times \left\{ 1 - \frac{\left(1 - e^{-\rho/2}\right)^2}{\left(\frac{\pi\rho}{2}\right)^{1/2} \left\{ \operatorname{erfc}\left[\left(\frac{\rho}{2}\right)^{1/2}\right] - e^{-\rho}\, h\left[\left(\frac{\rho}{2}\right)^{1/2}\right] \right\}} \right\} \tag{31}$$

Again, the values for η_∞ have been obtained by numerical integration, and the two different behaviors plotted in Fig. 20 for comparison. As was evident in the previous case as well, the two degradations at low σ^2 behave like

$$\eta_0 = \left[1 - \left(\frac{2}{\pi}\right)^{3/2} \sigma\right]^2 \approx 1 - 2\left(\frac{2}{\pi}\right)^{3/2} \sigma \tag{32}$$

as would be predicted by a gaussian ϕ-process theory.

6. Interpolation Between η_0 and η_∞

For a given normalized code-word rate $\delta = 2/w_L T$, the actual efficiency η_δ lies between η_0 and η_∞. To compute η_δ exactly is an extremely difficult task, since the statistics of ϕ_k required by Eq. (4) are unknown. What we shall develop here is an interpolation formula for η_δ, rather than a direct evaluation of the efficiency. One very good approximation of the error probability in the vicinity of R_0 is obtained by a Taylor expansion of $\ln [P_E (R_1^{1/2})]$:

$$P_E (R_1^{1/2}) \approx P_E (R_0^{1/2})\, e^{\lambda (R_0 - R_1)} \tag{33}$$

for two comparative values R_0 and R_1 of $R = PT/N_+$, for both no-coding and orthogonal/biorthogonal coding, according to the value of λ. We take R_0 to be the value

$$R_0 = R\mu^2 = R\, E^2 [g(\phi)] \tag{34}$$

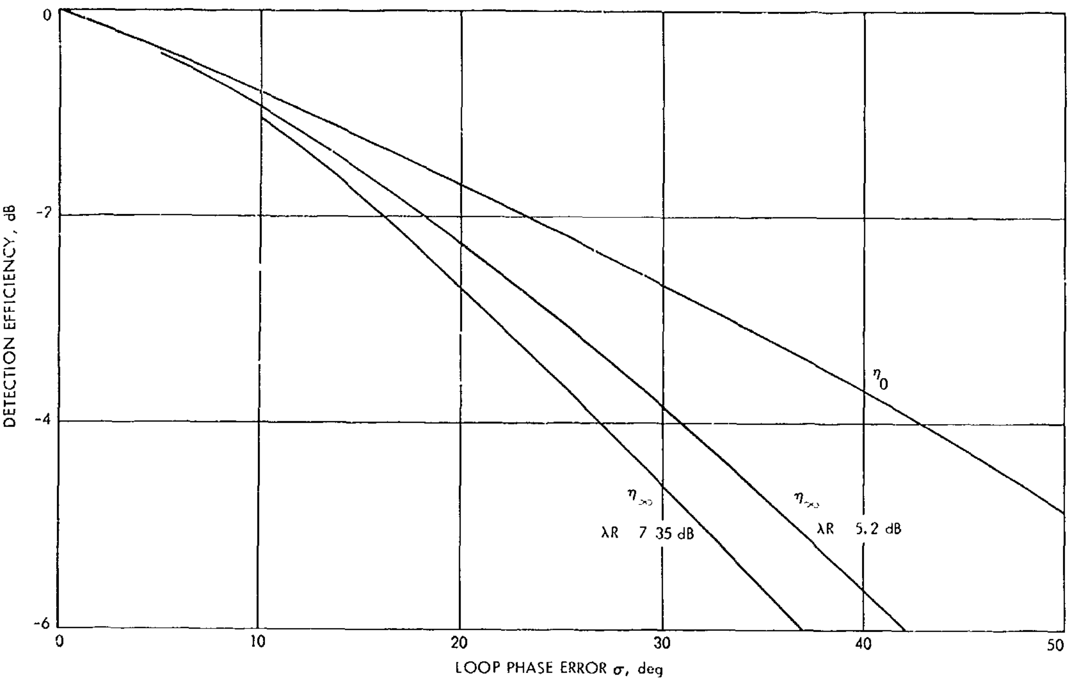

Fig. 20. Loop-derived reference degradation bounds for subcarrier-tone-tracking loop

corresponding to η_0, and take R_1 to be the apparent SNR corresponding to the correct word in Eq. (4):

$$R_1 = R(\mu + \nu)^2 \tag{35}$$

Then we can equate the observed error probability as having occurred with an equivalent value of $R = R_{eq}$, with no reference phase error:

$$\begin{aligned} P_E(R_{eq}^{1/2}) &= \int P_E(R_1^{1/2} | \nu)\, p(\nu)\, d\nu \\ &= P_E(R_0^{1/2}) \int \exp\Bigg\{ - \lambda R_0 \\ &\quad \times \left[\left(\frac{\nu}{\mu}\right)^2 + 2\left(\frac{\nu}{\mu}\right)\right]\Bigg\}\, p(\nu)\, d\nu \end{aligned} \tag{36}$$

The form of P_E displayed in Eq. (33) then provides

$$\lambda(R_0 - R_1) = \ln \int \exp\left\{- \lambda R_0 \left[\left(\frac{\nu}{\mu}\right)^2 + 2\left(\frac{\nu}{\mu}\right)\right]\right\} p(\nu)\, d\nu$$

$$\begin{aligned} \lambda R(\eta_0 - \eta_\delta) &= \ln \int \Bigg\{1 - \lambda R_0 \left[\left(\frac{\nu}{\mu}\right)^2 + 2\left(\frac{\nu}{\mu}\right)\right] \\ &\quad + \frac{\lambda^2 R_0}{2}\left[\left(\frac{\nu}{\mu}\right)^2 + 2\left(\frac{\nu}{\mu}\right)\right]^2 + \cdots \Bigg\}\, p(\nu)\, d\nu \\ &= \ln\left\{1 - \lambda R_0 \left(\frac{\sigma_\nu}{\mu}\right)^2 + 2\lambda^2 R_0^2 \left(\frac{\sigma_\nu}{\mu}\right)^2 + \cdots\right\} \\ &= \left(\frac{\sigma_\nu}{\mu}\right)^2 [2\lambda^2 R_0^2 - \lambda R_0] + \cdots \end{aligned} \tag{37}$$

When σ_ν^2 is small, the first term will dominate the behavior of Eq. (37). Hence, as a result, we see that

$$\frac{\eta_0 - \eta_\delta}{\eta_0 - \eta_\infty} \approx \left(\frac{\sigma_\nu}{\sigma_{\nu,\infty}}\right)^2 = a \tag{38}$$

in which $\sigma_{\nu,\infty}^2$ is the variance of ν as $\delta \rightarrow \infty$. Hence, the interpolation formula we seek is

$$\eta_\delta = (1 - a)\,\eta_0 + a\eta_\infty \tag{39}$$

and is valid whenever Eq. (37) is dominated by its first term.

The parameter a defined by Eq. (38) involves only the expectation of the square of

$$\nu = \frac{1}{T}\int_0^T \{g(\phi(t)) - E[g(\phi)]\}\, dt \tag{40}$$

which is given straightforwardly by (Ref. 5)

$$\sigma_\nu^2 = \delta \int_0^{2/\delta} \left(1 - \frac{\delta x}{2}\right) [R_{g(\phi)}(x/w_L) - R_{g(\phi)}(\infty)]\, dx \tag{41}$$

The asymptotic values of σ_ν^2 at very small and very large δ then verify our previous intuitive claim:

$$\sigma_\nu^2 \approx \begin{cases} \delta \displaystyle\int_0^\infty [R_{g(\phi)}(x/w_L) - R_{g(\phi)}(\infty)]\, dx, & \text{as } \delta \rightarrow 0 \\ \sigma_g^2, & \text{as } \delta \rightarrow \infty \end{cases} \tag{42}$$

It thus remains only to evaluate σ_ν^2 at a particular value of δ. The ratio of the two variances σ_ν^2 and σ_g^2 then give the parameter a. But because the loop is nonlinear, $R_{g(\phi)}(\tau)$ is not known, although there are several approximations available for calculation of $R_\phi(\tau)$. We can model $\phi(t)$ as a gaussian process having the same variance and bandwidth as the ϕ-process and thereby evaluate the autocorrelation of $g(\phi)$ in terms of that of $\phi(t)$ by Price's Theorem (Ref. 6). For example, if $g(\phi) = \cos\phi$, then

$$\begin{aligned} R_{\cos\phi}(\tau) - R_{\cos\phi}(\infty) &= 2e^{-\sigma_\phi^2} \sinh^2\left(\frac{1}{2} R_\phi(\tau)\right) \\ &\approx \frac{1}{2} e^{-\sigma_\phi^2} R_\phi^2(\tau) \end{aligned} \tag{43}$$

while, if $g(\phi)$ is the triangular function present in square-wave subcarrier extraction, then

$$\begin{aligned} R_{\mathrm{tri}(\phi)}(\tau) - R_{\mathrm{tri}(\phi)}(\infty) &= \\ \left(\frac{2}{\pi}\right)^3 \Bigg[R_\phi(\tau) \sin^{-1}(R_\phi(\tau)) \sin^{-1}\left(\frac{R_\phi(\tau)}{\sigma_\phi^2}\right) \\ + (\sigma_\phi^4 - R_\phi^2(\tau))^{1/2} - \sigma_\phi^2 \Bigg] \end{aligned} \tag{44}$$

Further, we can model the correlation function of ϕ by the simple first-order loop result

$$R_\phi(\tau) = \sigma_\phi^2 \exp(-2w_L|\tau|) \tag{45}$$

and thereby evaluate the parameter a.

At best, the evaluation of a requires numerical integration. of σ_ϕ^2 is small in the carrier loop case, however, the approximation in Eq. (43) can be used to give

$$\begin{aligned} a\,(\text{carrier loop}) &= \delta \int_0^{2/\delta} \left(1 - \frac{\delta x}{2}\right) e^{-4x}\, dx \\ &= \frac{\delta}{4}\left[1 - \frac{\delta}{8}(1 - e^{-8/\delta})\right] \end{aligned} \tag{46}$$

and is independent of σ_ϕ^2. This a is plotted in Fig. 21. The numerically integrated, more exact value at $\sigma_\phi^2 = 1$ is almost indistinguishable from Eq. (46).

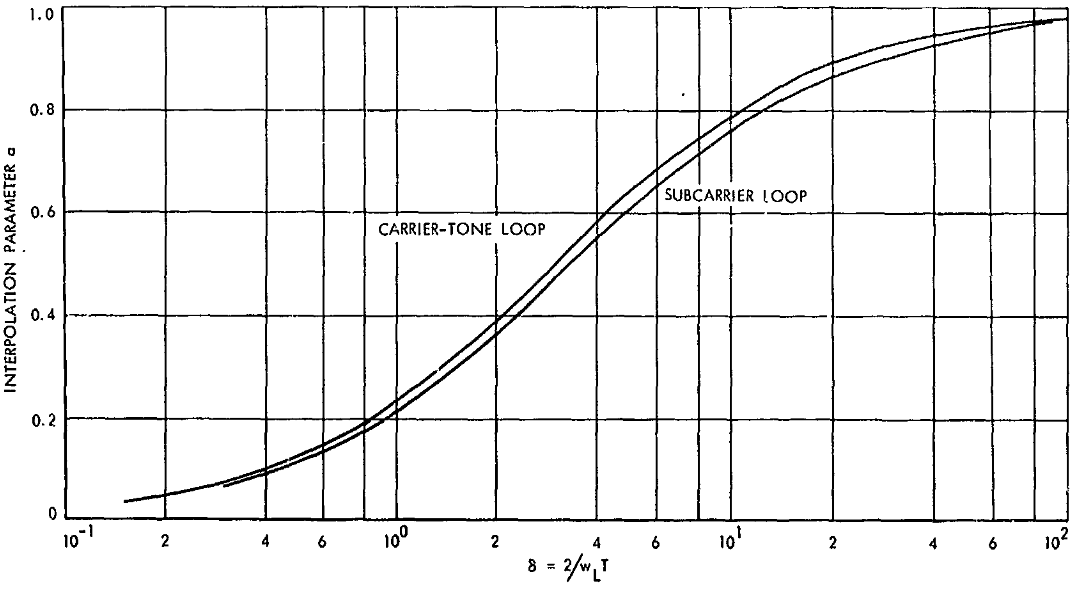

Fig. 21. Interpolation parameter a for sine wave (carrier tone) and square wave (subcarrier tone) loops as a function of the normalized data word rate

In the triangular subcarrier case, a reduces to the integral

$$a\,(\text{subcarrier}) = \frac{\delta}{\pi - 2}\int_0^{4/\delta}\left(1 - \frac{\delta x}{4}\right)\left[e^{-x}\sin^{-1}(e^{-x}) + (1 - e^{-2x})^{1/2} - 1\right]dx \qquad (47)$$

which is also independent of σ_ϕ^2. The variation of a with δ is depicted also in Fig. 21. The approximate expression

$$a\,(\text{subcarrier loop}) = \frac{0.09135\,\delta + \delta^2}{1 + 3.3718\,\delta + \delta^2} \qquad (48)$$

provides a simple formula for amazingly accurate results.

7. Conclusions

The efficiency of a coherent amplitude detector lies somewhere between limits set by two extreme theories, depending on the value of $\delta = 2/w_L T$. In the discussion we have considered (by assumption of the form $p(\phi)$ only) the effects of wide-band input noise. However, if there were other processes causing phase error, such as loop voltage-controlled oscillator noise, detection instabilities, etc., they can be considered as an equivalent phase-error term to be included in $p(\phi)$.

As long as the loop SNR, ρ, is greater than 10, $p(\phi)$ is very nearly gaussian, and a normal density can be substituted for $p(\phi)$, with the other instabilities reflected in the value of σ^2.

References

1. Lindsey, W. C., *Performance of Phase-Coherent Receivers Preceded by Bandpass Limiters*, Technical Report 32-1162. Jet Propulsion Laboratory, Pasadena, Calif., Sept. 1967.
2. Golomb, S. W., et al., *Digital Communications With Space Applications*, pp. 120–131. Prentice-Hall, Inc., Englewood Cliffs, N.J., 1964.
3. Viterbi, A. J., *Principles of Coherent Communications*, pp. 86–96. McGraw-Hill Book Co., Inc., New York, 1966.
4. Tausworthe, R. C., *Theory and Practical Design of Phase-Locked Receivers. Vol. I*, Technical Report 32-819. Jet Propulsion Laboratory, Pasadena, Calif., Feb. 1966.
5. Davenport, W. B., and Root, W. L., *Random Signals and Noise*, Sec. 6-5. McGraw-Hill Book Co., Inc., New York, 1958.
6. Price, R., "A Useful Theorem for Nonlinear Device Having Gaussian Inputs," *IRE Trans. Info. Theory*, Vol. IT-4, pp. 69–72, June 1958.

H. Information Processing: Limiters in Phase-Locked Loops: A Correction to Previous Theory, *R. C. Tausworthe*

1. Introduction

In 1953 Davenport (Ref. 1) published a now-classic paper which showed that at very large values, the asymptotic output signal-to-noise ratio (SNR) of a limiter is twice its input SNR. Because of this, it was supposed that the same improvement ultimately should be evident in the performance of a phase-locked loop tracking the limiter output. In fact, the author (Ref. 2) used this result (erroneously, but subtly so) to derive a limiter performance factor Γ. Recently, however, G. D. Forney (Ref. 3) has presented a simple argument to show that the asymptotic factor of 2 is not realized in loop performance, although it is indeed present in output SNR. In this article, the author extends the asymptotic result to rederive the equivalent limiter performance factor.

2. Loop Theory and Noise Components

We shall assume (Fig. 22) that a loop has incident a sinusoid in wide-band noise, and we shall express this process in the form (Ref. 4)

$$y(t) = \alpha\, 2^{1/2}\sin(\omega_0 t + \theta) + n_Q(t)\, 2^{1/2}\sin(\omega_0 t + \hat{\theta}) + n_I(t)\, 2^{1/2}\cos(\omega_0 t + \hat{\theta}) \qquad (1)$$

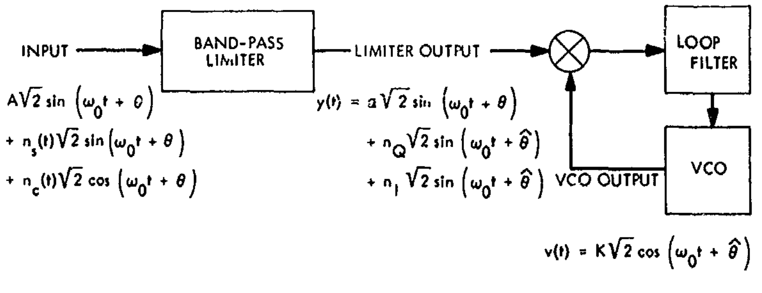

Fig. 22. The bandpass limiter phase-locked loop

where $n_I(t)$ and $n_Q(t)$ are independent wide-band in-phase and quadrature components [with respect to the voltage-controlled oscillator (VCO) output] of the input noise process, α is the rms signal amplitude, and $\hat{\theta}$ is the loop estimate of the input phase process θ. The VCO output we shall take to be of the form

$$v(t) = K 2^{1/2} \cos(\omega_0 t + \hat{\theta}) \tag{2}$$

so that the phase detector output is

$$z(t) = <y(t)\, v(t)> = K[\alpha \sin\phi + n_I(t)] \tag{3}$$

with $\phi = \theta - \hat{\theta}$, the loop phase error. The terms enclosed in "< >" refer to the "low-pass part of" the expression.

The important point in Eq. (3) is that the only noise having any effect on loop performance is the noise in phase with the VCO. The resulting linear theoretical phase error is then

$$\sigma_\phi^2 = \frac{S_{n_I n_I}(0)\, w_L}{\alpha^2} \tag{4}$$

where $S_{n_I n_I}(j\omega)$ is the spectral density of the process $n_I(t)$ and w_L is the loop bandwidth (Ref. 2).

In previous analyses, it has always been assumed that the input noise process has components of equal spectral density, each equal to that of the input process. However, *the noise components at the limiter output do not have equal spectra*; this is the point that was overlooked in extending Eq. (4) to the limiter-loop case. Hence, to correct the result published in Ref. 2, the value of $S_{n_I n_I}(0)$ merely has to be reevaluated.

3. Limiter Output Noise

Let the input to an ideal bandpass limiter be

$$x(t) = A 2^{1/2} \sin(\omega_0 t + \theta) + n_s(A) 2^{1/2} \sin(\omega_0 t + \theta) + n_c(t) 2^{1/2} \cos(\omega_0 t + \theta) \tag{5}$$

where A is the rms signal amplitude, and $n_s(t)$ and $n_c(t)$ are independent, zero mean, quadrature gaussian noise processes with respect to the input signal, having identical variances and spectra

$$\left.\begin{aligned} \sigma_{n_c}^2 &= \sigma_{n_s}^2 = \sigma_n^2/2 \\ N_{0c} &= N_{0s} = N_0 \end{aligned}\right\} \tag{6}$$

It follows directly that the fundamental-zone limiter output is of the form

$$\begin{aligned} y(t) &= \frac{2^{3/2} L}{\pi} \left\{ \left(\frac{[A + n_s(t)]}{A(t)} \right) 2^{1/2} \sin(\omega_0 t + \theta) + \left(\frac{n_c(t)}{A(t)} \right) 2^{1/2} \cos(\omega_0 t + \theta) \right\} \\ &= \frac{2^{3/2} L}{\pi} \{ [\alpha + n_1(t)]\, 2^{1/2} \sin(\omega_0 t + \theta) + n_2(t)\, 2^{1/2} \cos(\omega_0 t + \theta) \} \end{aligned} \tag{7}$$

where L is the limiter clipping level, and $A(t)$ is the process

$$A(t) = [(A + n_s(t))^2 + n_c^2(t)]^{1/2} \tag{8}$$

For convenience, we shall normalize $L = \pi / 2^{3/2}$ to give unity output power in the fundamental harmonic zone. Previous calculations (Ref. 1 and SPS 37-44, Vol. IV, pp. 303–307) have shown that the mean signal level is

$$\begin{aligned} \alpha^2 &= \frac{\pi}{4} \rho_H \exp(-\rho_H) [I_0(\rho_H/2) + I_1(\rho_H/2)]^2 \\ &\approx \frac{0.7854\rho_H + 0.4768\rho_H^2}{1 + 1.0240\rho_H + 0.4768\rho_H^2} \end{aligned} \tag{9}$$

in terms of the input SNR, $\rho_H = A^2/N_0 w_H$, the input process bandwidth w_H and the modified Bessel functions of the first kind, $I_n(x)$.

The second term of Eq. (7) is noise whose variance is

$$\sigma_2^2 = E\left\{ \frac{n_c^2(t)}{A^2(t)} \right\} \tag{10}$$

This expectation involves the evaluation of a somewhat tedious, but straightforward, double integral. The result is the simple expression

$$\sigma_2^2 = \frac{1}{2\rho_H} [1 - \exp(-\rho_H)] \tag{11}$$

The noise component $n_1(t)$ appearing in Eq. (7) is uncorrelated with $n_2(t)$; so its variance is

$$\sigma_1^2 = 1 - \alpha^2 - \sigma_2^2 \tag{12}$$

4. Limiter Noise In-Phase With the VCO

The reader will note that the expressions for the loop input $y(t)$ given in Eqs. (1) and (7) are slightly different.

When multiplied by the VCO output in Eq. (2), the relevant loop noise $n_I(t)$ is

$$n_I(t) = n_1(t)\sin\phi + n_2(t)\cos\phi \tag{13}$$

whose variance is then

$$\sigma_I^2 = \sigma_2^2 + (\sigma_1^2 - \sigma_2^2)\,E(\sin^2\phi) \tag{14}$$

5. Phase-Locked Loop Variance

The variance in Eq. (4) can now be evaluated by noting that, according to the definition of the in-phase noise bandwidth w_I,

$$S_{n_I n_I}(0) = \frac{1}{w_I}\int_{-\infty}^{+\infty} S_{n_I n_I}(jw)\,\frac{dw}{2\pi} = \frac{\sigma_I^2}{w_I} \tag{15}$$

and therefore

$$\begin{aligned}\sigma_\phi^2 &= \frac{\sigma_I^2 w_L}{w_I \alpha^2}\\ &= \frac{N_0 w_L}{A^2}\left(\frac{w_H\rho_H}{w_l\rho_l}\right)\left(\frac{w_l\sigma_I^2}{w_I(1-\alpha^2)}\right)\end{aligned} \tag{16}$$

The ratio $w_l\rho_l/\rho_H w_H$ is the Springett factor (SPS 37-36, Vol. IV, pp. 241–244), previously defined as $1/\Gamma$, which relates output and input spectral densities. The only unknown in Eq. (16) is the ratio w_l/w_I. Asymptotically, as $\rho_H \to \infty$, all the output noise comes from $n_2(t)$, so $w_I = w_l/2$ (the limiter output bandwidth w_l differs by a factor of 2 from that of the baseband process); and as $\rho_H \to 0$, both noises $n_1(t)$ and $n_2(t)$ have the same spectra, so again $w_I = w_l/2$.

Insertion of the value for σ_I^2 and the linear-theoretical assumption $\sin^2\phi \approx \phi^2$ yield

$$\sigma_\phi^2 = \frac{N_0 w_L}{A^2}\Gamma \,\cdot \tag{17}$$

in which Γ is the true limiter performance factor

$$\Gamma = \frac{\left(\dfrac{w_H\rho_H}{w_l\rho_l}\right)\left[\dfrac{1-\exp(-\rho_H)}{(1-\alpha^2)\rho_H}\right]\left(\dfrac{w_l}{w_I}\right)}{1+\left(\dfrac{2w_L}{w_H\rho_H}\right)\left(\dfrac{w_H\rho_H}{w_l\rho_l}\right)\left[\dfrac{1-\exp(-\rho_H)}{(1-\alpha^2)\,2\rho_H} - 1\right]\left(\dfrac{w_l}{w_I}\right)} \tag{18}$$

In limiting cases, Γ behaves as follows:

$$\Gamma \sim \frac{\frac{1}{2}(2)}{1+0} = 1, \qquad \rho_H \text{ very large} \tag{19}$$

as predicted by the Forney result, and

$$\Gamma \sim \frac{1.16}{1 + 0.335\dfrac{w_L}{w_H}} < 1.16\,, \qquad \rho_H \text{ very small} \tag{20}$$

The conclusion reached is that *the effect of a limiter on loop performance is less than 16% (0.66 dB) in effective input SNR!* Under the assumption that $w_H > 10\,w_L$, the dependence of Γ on w_L/w_H disappears for practical purposes (within 0.1 dB). A rational function approximation emulating the cross-over behavior of Eq. (18) near $\rho = 0.5$ (Fig. 23), is

$$\Gamma = \frac{1+\rho_H}{0.862+\rho_H} \tag{21}$$

With this approximation, the linear-theoretical limiter performance follows directly.

6. Nonlinear Loop Theory

The only alteration that must be made to make the derivation of Γ general enough for the linear-spectral loop theory (Ref. 2, Chapt. 9) is the estimation of $E(\sin^2\phi)$ in Eq. (14) by a more accurate value. But the only change which would result in Γ would be a factor

$$\frac{E[\sin^2\Phi]}{E[\Phi^2]} = \frac{(1-\exp(-2\sigma_\Phi^2))}{2\sigma_\Phi^2} \leq 1 \tag{22}$$

(under the assumptions of Ref. 2, Chapt. 9) inserted into the second denominator term of Eq. (18), which we have agreed, for $w_H > 10\,w_L$, is negligible anyway. Hence, the nonlinear theory is also essentially unaltered from the previously published results, except for the new Γ that must be used.

References

1. Davenport, W. B., "Signal-to-Noise Ratios in Band-Pass Limiters," *Journal of Applied Physics,* Vol. 24, No. 6, pp. 720–727, June 1953.
2. Tausworthe, R. C., *Theory and Practical Design of Phase-Locked Receivers,* Technical Report 32-819. Jet Propulsion Laboratory, Pasadena, Calif., February 15, 1966.
3. Forney, G. D., *Coding in Coherent Deep-Space Telemetry.* McDonnell Douglas Astronautics Corp., Santa Monica, Calif., March 19, 1967.
4. Davenport, W. B., and Root, W. L., *Random Signals and Noise,* pp. 158–165. McGraw-Hill Book Co., Inc., New York, 1958.

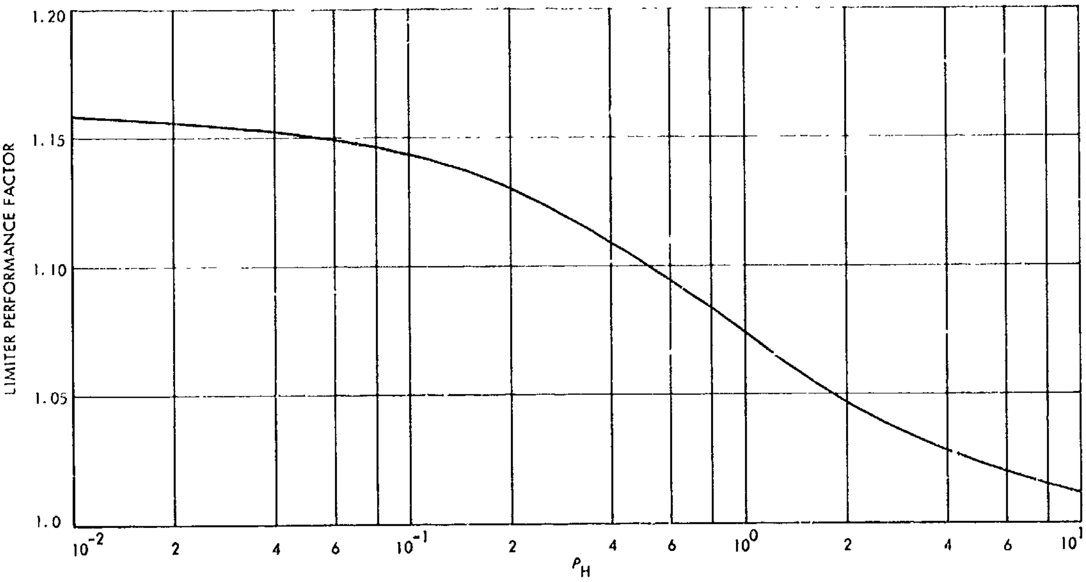

Fig. 23. Variation of the parameter Γ with limiter input SNR, $\rho_H = A^2/N_0w_L$

XXI. Communications Elements Research

TELECOMMUNICATIONS DIVISION

A. System Studies for 90-GHz Space Communications Systems: Atmospheric Effects on Millimeter Wave Propagation, *T. Sato*

The 60-in. radio telescope used for radio astronomy experiments (SPS 37-49, Vol. III, pp. 329–338) is being converted into a radio sextant. An optical tracker automatically tracks the sun in both hour angle and declination by generating error signals for the antenna servo. The error-sensing elements attached to the telescope consist of two photoconducting cells per channel. When the sun is centered, both cells are illuminated equally and produce equal resistances; no error signal is then produced. If the sun's image shifts, the cells are illuminated unequally, thereby producing an error signal. The error signal to the digital processor generates pulses that are fed to the stepping motor in a direction to remove the angular error in pointing.

The 90-GHz nodding subdish radiometer mounted on the 60-in. radio telescope receives emissions from the sun. The slant path through the atmosphere changes with the position of the sun. The temperature of the antenna when pointed at the sun is given by

$$T_a(\phi) = T'_a 10^{-a_0/10 \sec\phi} + T_s(\phi)$$

where T'_a is the antenna temperature with no intervening atmosphere, a_0 is the zenith attenuation in decibels, ϕ is the zenith angle, and $T_s(\phi)$ is the sky temperature. Use of the nodding subdish radiometer balances out the $T_s(\phi)$ component. The expression for the received temperature is then given by

$$\log T_a(\phi) = -\frac{a_0}{10 \sec\phi} + \log T'_a$$

The absolute zenith attenuation can then be determined from measurements of the received power and the zenith angle without knowledge of the solar temperature or antenna gain. Certain weather conditions may invalidate the secant law giving an average value for the zenith attenuation.

B. Spacecraft Antenna Research: RF Breakdown Characteristics of S-Band Sterilizable High-Impact Antennas, *K. Woo*

The power-handling capabilities of the S-band sterilizable high-impact antennas (coaxial cavity,[1] cupped

---

[1] SPS 37-40, Vol. IV: discussion on pp. 201–206; photograph in Fig. 5, p. 202.

turnstile,[2] square cup,[3] and circular cup[4]) have been investigated at very low pressures. The antennas were each tested in the vacuum chamber of the JPL voltage breakdown facility with dry air, 100% carbon dioxide, and a mixture of 50% carbon dioxide and 50% argon.

The ionization breakdown power level at 2298 MHz of each antenna was obtained as a function of pressure near and at the point where the breakdown power is minimum, such as shown in Fig. 1 (obtained for the coaxial cavity radiator). The minimum ionization breakdown power levels at 2298 MHz for all the antennas were found within the pressure range of 1.5 to 2.5 torr. The multipacting breakdown power levels at 2298 MHz of all the antennas were tested around 5×10^{-5} torr. The multipacting breakdown and minimum ionization breakdown power levels for all the antennas are summarized in Table 1.

Each value given in Table 1 represents the power that each antenna actually received, i.e., the power fed into the antenna minus the power reflected back due to mismatch. The values to which "$>$" signs are attached represent the peak levels to which those antennas were tested due to power limitations imposed by either the output of the RF generator or the feeding hybrid (if used) or by other difficulties.

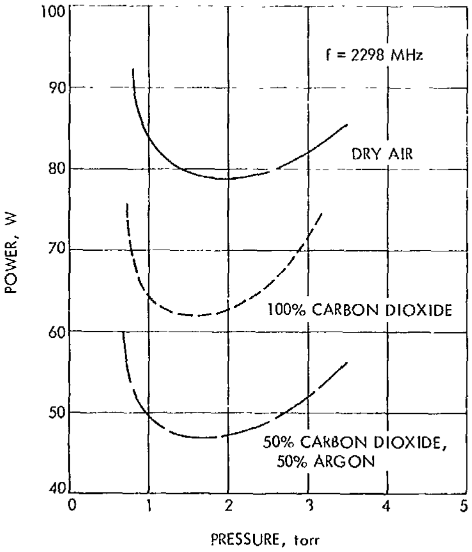

Fig. 1. Ionization breakdown characteristic of coaxial cavity radiator

The power levels for the square cup and circular cup radiators represent only momentary power; i.e., the power was shut off immediately after it was applied to those antennas. When a steady power was applied, those antennas experienced a thermal breakdown (hence, degradation of electrical performance) at relatively low power levels. The thermal breakdown was in the form of charring of the foam in the vicinity of the feed probe due to the accumulation of heat resulting from the poor thermal conductivity of the foam. Figure 2 shows the charred area around the feed of the square cup radiator after removal of the foam. Test results at 2.0 torr showed that a square cup radiator potted with Stafoam AA630 would sustain at least 3 h of continuous operation at the 50-W level, but would suffer thermal breakdown (voltage standing-wave

Table 1. Ionization and multipacting breakdown power levels and locations for the S-band sterilizable high-impact antennas[a]

Antenna	Ionization breakdown				Multipacting breakdown			
	Minimum breakdown power, W, for indicated atmosphere			Location of breakdown	Breakdown power, W, for indicated atmosphere			Location of breakdown
	A	B	C		A	B	C	
Coaxial cavity	79	62	47	Around the probes	> 130	> 130	> 130	None observed
Cupped turnstile	31	23	17	At balun split	> 130	> 130	> 130	None observed
Square cup[b]	> 560	> 560	> 560	None observed	> 560	> 560	> 560	None observed
Circular cup[b]	> 560	> 560	> 560	None observed	> 560	> 560	> 560	None observed

[a] Atmosphere A: dry air.
Atmosphere B: 100% carbon dioxide.
Atmosphere C: 50% carbon dioxide, 50% argon.
[b] Potted with Stafoam AA630 or Eccofoam PT.

---

[2] SPS 37-42, Vol. IV: discussion on pp. 180, 181; photograph in Fig. 1, p. 181.

[3] SPS 37-49 and -53, Vol. III: discussion on pp. 345–347 (37-49) and pp. 164–166 (37-53); photographs in Figs. 32, p. 346 (37-49) and 5, p. 165 (37-53).

[4] SPS 37-47, Vol. III: discussion on pp. 240–242; photograph in Fig. 4, p. 240 and Fig. 5, p. 241.

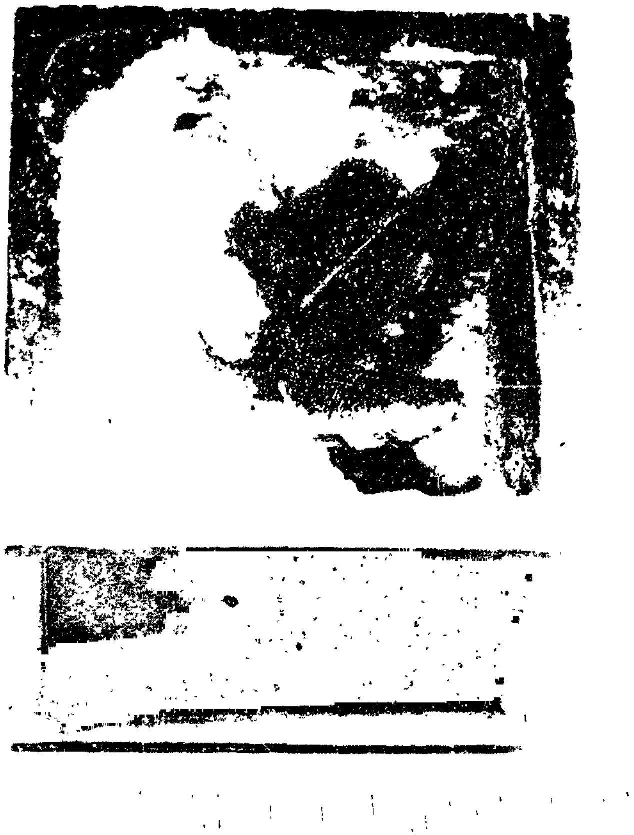

Fig. 2. Square cup radiator after thermal breakdown

ratio changed from 1.8 to 4.6) after 5 min of operation at the 100-W level. The same antenna potted with Eccofoam PT would sustain at least 3 h of continuous operation at the 40-W level.

On the basis of the test results, it can be seen that, for high-power operation, the ionization breakdown is the problem area for the coaxial cavity and cupped turnstile antennas, and the thermal breakdown is the problem area for the square cup and circular cup antennas. To improve the power-handling capabilities of the existing antennas, the following modifications are recommended:

Antenna	Recommendation
Coaxial cavity	Widen cavity and enclose feed probes with high-thermal-conductivity dielectric
Cupped turnstile	Redesign balun
Square cup	Improve thermal conductivity and reduce loss of potting dielectric
Circular cup	

C. Radiation From a Horizontal Electric Dipole Antenna Located in a Cylindrically Stratified Plasma, *R. Woo*

1. Introduction

In SPS 37-47, Vol. III, pp. 247–257, the wake of a Mars entry capsule was represented by a cylindrical plasma column and the problem of a horizontal electric dipole located in the wake was formulated. In SPS 37-50, Vol. III, pp. 312–316, the representation of the wake was improved by surrounding the plasma column with a plasma shell of different electron density than that of the column. Here the wake will be represented by a cylindrically stratified plasma. The problem of a horizontal electric dipole located in the wake will be formulated using a scheme that readily lends itself to computer calculation.

2. Integral Formulation of Fields for Horizontal Dipole

The regions are numbered i, where $i = 1, 2, 3, \cdots, N+1$. Region $N + 1$ is free space.

The free-space region $i = N + 1$ is characterized by permittivity ϵ_0 and permeability μ_0. According to the magneto-ionic theory description for a homogeneous, isotropic, and lossless plasma, the plasma region i is represented by a medium whose permittivity ϵ_i is given by (Ref. 1)

$$\epsilon_i = \left[1 - \left(\frac{\omega_{pi}}{\omega}\right)^2\right]\epsilon_0 \tag{1}$$

where

$$\omega_{pi}^2 = \frac{n_i e^2}{m\epsilon_0} \tag{2}$$

with n_i representing the electron density, e the electron charge, m the electron mass, and ω_{pi} the electron plasma frequency. The propagation constant of region i is then given by

$$k_i^2 = \omega^2 \mu_0 \epsilon_i$$

Assuming a time dependence of $e^{j\omega t}$, the respective electric and magnetic field intensities, **E** and **H**, are related to the electric ($\boldsymbol{\pi}$) and magnetic ($\boldsymbol{\pi}^*$) Hertz potentials through the following equations:

$$\mathbf{E} = \nabla \times \nabla \times \boldsymbol{\pi} - j\omega\mu_0 \nabla \times \boldsymbol{\pi}^* \tag{3}$$

$$\mathbf{H} = \nabla \times \nabla \times \boldsymbol{\pi}^* + j\omega\epsilon \nabla \times \boldsymbol{\pi} \tag{4}$$

where ϵ is the intrinsic permittivity of the medium.

The electric dipole of moment Il is assumed to be located at (ρ_0, ϕ_0, z_0) and oriented in the x direction in plasma region m (Fig. 3). The x component of π, π_{xm}, will therefore represent the primary field and satisfy the following equation:

$$(\nabla^2 + k_m^2)\,\pi_{xm} = -\frac{Il}{j\omega\epsilon_m}\,\delta(\phi - \phi_0)\,\delta(z - z_0)\,\frac{\delta(\rho - \rho_0)}{\rho} \tag{5}$$

where δ is the Dirac delta function and the subscript m refers to the region m. Since both E_z and H_z will be present in the secondary fields, the respective z components of π and π^*, π_{zi} and π_{zi}^*, will be used for region i and will satisfy the following wave equations:

$$(\nabla^2 + k_i^2)\,\pi_{zi} = 0 \tag{6}$$

$$(\nabla^2 + k_i^2)\,\pi_{zi}^* = 0 \tag{7}$$

Integral representations for the Hertz potentials can be written using a Fourier integral in the z direction and a Fourier series in the ϕ direction (Ref. 2). For the primary field in region m,

$$\pi_{xm} = \frac{Il}{j\omega\epsilon_m}\,\frac{1}{8\pi j} \times \sum_{n=-\infty}^{\infty} \int_{-\infty}^{\infty} H_n^{(2)}(\lambda_m\rho)\,J_n(\lambda_m\rho_0)\,e^{-jn(\phi-\phi_0)}\,e^{-jh(z-z_0)}\,dh \tag{8}$$

where

$$\lambda_m^2 = k_m^2 - h^2$$

J_n is the nth-order Bessel function of the first kind and $H_n^{(2)}$ is the nth-order Hankel function of the second kind. Equation (8) is for $\rho > \rho_0$; when $\rho < \rho_0$, ρ and ρ_0 must be interchanged in the equation. For the secondary fields, the following results apply for region i:

$$\pi_{zi} = \sum_{n=-\infty}^{\infty} \int_{-\infty}^{\infty} [a_n^{(i)} J_n(\lambda_i\rho) + c_n^{(i)} H_n^{(2)}(\lambda_i\rho)] \times e^{-jn\phi}\,e^{-jh(z-z_0)}\,dh \tag{9}$$

$$\pi_{zi}^* = \sum_{n=-\infty}^{\infty} \int_{-\infty}^{\infty} [b_n^{(i)} J_n(\lambda_i\rho) + d_n^{(i)} H_n^{(2)}(\lambda_i\rho)] \times e^{-jn\phi}\,e^{-jh(z-z_0)}\,dh \tag{10}$$

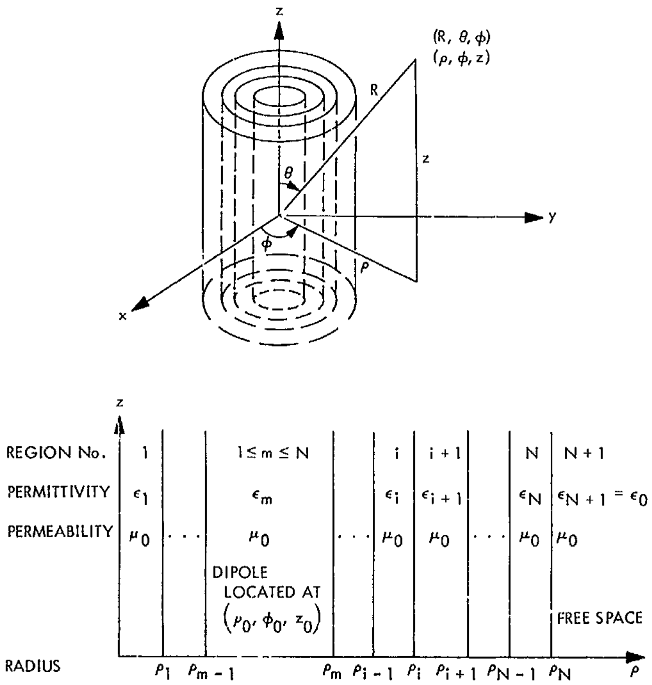

Fig. 3. Geometry of the problem

where

$$\lambda_i^2 = k_i^2 - h^2$$

The superscript i in the coefficients a_n, b_n, c_n, and d_n refers to the fields in region i. Since the fields are finite at $\rho = 0$, $c_n^{(1)} = d_n^{(1)} = 0$. Also, since outgoing waves are in the free-space region $i = N + 1$, $a_n^{(N+1)} = b_n^{(N+1)} = 0$.

The cylindrical components of **E** and **H** for region i can be obtained using Eqs. (3) and (4).

$$E_{zi} = \left(\frac{\partial^2}{\partial z^2} + k_i^2\right)\pi_{zi} \tag{11}$$

$$E_{\phi i} = \frac{1}{\rho}\,\frac{\partial^2 \pi_{zi}}{\partial\phi\,\partial z} + j\omega\mu_0\,\frac{\partial\pi_{zi}^*}{\partial\rho} \tag{12}$$

$$E_{\rho i} = \frac{\partial^2 \pi_{zi}}{\partial\rho\,\partial z} - \frac{j\omega\mu_0}{\rho}\,\frac{\partial\pi_{zi}^*}{\partial\phi} \tag{13}$$

$$H_{zi} = \left(\frac{\partial^2}{\partial z^2} + k_i^2\right)\pi_{zi}^* \tag{14}$$

$$H_{\phi i} = \frac{1}{\rho}\,\frac{\partial^2 \pi_{zi}^*}{\partial\phi\,\partial z} - j\omega\epsilon_i\,\frac{\partial\pi_{zi}}{\partial\rho} \tag{15}$$

$$H_{\rho i} = \frac{\partial^2 \pi_{zi}^*}{\partial\rho\,\partial z} + \frac{j\omega\epsilon_i}{\rho}\,\frac{\partial\pi_{zi}}{\partial\phi} \tag{16}$$

The following are additional components in region m due to the primary field:

$$E_{zm} = \frac{\partial^2 \pi_{xm}}{\partial z\, \partial \rho} \cos \phi - \frac{1}{\rho} \frac{\partial^2 \pi_{xm}}{\partial z\, \partial \phi} \sin \phi \tag{17}$$

$$E_{\phi m} = \left(\frac{\partial^2 \pi_{xm}}{\partial z^2} + \frac{\partial^2 \pi_{xm}}{\partial \rho^2} \right) \sin \phi + \frac{\partial}{\partial \rho} \left(\frac{1}{\rho} \frac{\partial \pi_{xm}}{\partial \phi} \right) \cos \phi \tag{18}$$

$$\begin{aligned} E_{\rho m} = &\left(\frac{1}{\rho^2} \frac{\partial \pi_{xm}}{\partial \phi} - \frac{1}{\rho} \frac{\partial^2 \pi_{xm}}{\partial \phi\, \partial \rho} \right) \sin \phi \\ &- \left(\frac{1}{\rho} \frac{\partial \pi_{xm}}{\partial \rho} + \frac{1}{\rho^2} \frac{\partial^2 \pi_{xm}}{\partial \phi^2} + \frac{\partial^2 \pi_{xm}}{\partial z^2} \right) \cos \phi \end{aligned} \tag{19}$$

$$H_{zm} = -j\omega\epsilon_m \frac{\partial \pi_{xm}}{\partial \rho} \sin \phi - j\omega\epsilon_m \frac{1}{\rho} \left(\frac{\partial \pi_{xm}}{\partial \phi} \right) \cos \phi \tag{20}$$

$$H_{\phi m} = j\omega\epsilon_m \frac{\partial \pi_{xm}}{\partial z} \cos \phi \tag{21}$$

$$H_{\rho m} = j\omega\epsilon_m \frac{\partial \pi_{xm}}{\partial z} \sin \phi \tag{22}$$

The boundary conditions at ρ_i require that the tangential **E** and **H** fields be continuous. Imposing these boundary conditions at each boundary ρ_i yields the following results in matrix form:

$$\begin{bmatrix} 0 \\ 0 \\ c_n^{(N+1)} \\ d_n^{(N+1)} \end{bmatrix} = M_n^{(N)} M_n^{(N-1)} \cdots M_n^{(1)} \begin{bmatrix} a_n^{(1)} \\ b_n^{(1)} \\ 0 \\ 0 \end{bmatrix} - M_n^{(N)} M_n^{(N-1)} \cdots M_n^{(m+1)} \left\{ [B_n^{(m)}]^{-1} \begin{bmatrix} \gamma_n^{(m)} \\ \eta_n^{(m)} \\ \alpha_n^{(m)} \\ \beta_n^{(m)} \end{bmatrix} - M_n^{(m)} [B_n^{(m-1)}]^{-1} \begin{bmatrix} \gamma_n^{(m-1)} \\ \eta_n^{(m-1)} \\ \alpha_n^{(m-1)} \\ \beta_n^{(m-1)} \end{bmatrix} \right\} \tag{23}$$

where

$$M_n^{(i)} = [B_n^{(i)}]^{-1} A_n^{(i)}$$

$$A_n^{(i)} = \begin{bmatrix} \lambda_i^2 J_n(\lambda_i \rho_i) & 0 & \lambda_i^2 H_n^{(2)}(\lambda_i \rho_i) & 0 \\ 0 & \lambda_i^2 J_n(\lambda_i \rho_i) & 0 & \lambda_i^2 H_n^{(2)}(\lambda_i \rho_i) \\ \dfrac{-nh}{\rho_i} J_n(\lambda_i \rho_i) & j\omega\mu_0 \lambda_i J_n'(\lambda_i \rho_i) & \dfrac{-nh}{\rho_i} H_n^{(2)}(\lambda_i \rho_i) & j\omega\mu_0 \lambda_i H_n^{(2)\prime}(\lambda_i \rho_i) \\ -j\omega\epsilon_i \lambda_i J_n'(\lambda_i \rho_i) & \dfrac{-nh}{\rho_i} J_n(\lambda_i \rho_i) & -j\omega\epsilon_i \lambda_i H_n^{(2)\prime}(\lambda_i \rho_i) & \dfrac{-nh}{\rho_i} J_n(\lambda_i \rho_i) \end{bmatrix}$$

$B_n^{(i)}$ is similar to $A_n^{(i)}$ except that λ_i and ϵ_i are replaced by λ_{i+1} and ϵ_{i+1}, respectively; and $[B_n^{(0)}]^{-1} = 0$.

$$\gamma_n^{(m)} = -\frac{Il}{4\pi} \omega\mu_0 \frac{jh\lambda_m}{4k_m^2} [e^{j(n+1)\phi_0} J_{n+1}(\lambda_m \rho_0) - e^{j(n-1)\phi_0} J_{n-1}(\lambda_m \rho_0)] H_n^{(2)}(\lambda_m \rho_m)$$

$$\eta_n^{(m)} = -\frac{Il}{4\pi} \omega\mu_0 \frac{\lambda_m}{4\omega\mu_0} [e^{j(n+1)\phi_0} J_{n+1}(\lambda_m \rho_0) + e^{j(n-1)\phi_0} J_{n-1}(\lambda_m \rho_0)] H_n^{(2)}(\lambda_m \rho_m)$$

$$\begin{aligned} \alpha_n^{(m)} = \frac{Il}{4\pi} \omega\mu_0 \frac{j}{8k_m^2} \{ &[(k_m^2 + h^2) e^{j(n+1)\phi_0} J_{n+1}(\lambda_m \rho_0) + \lambda_m^2 e^{j(n-1)\phi_0} J_{n-1}(\lambda_m \rho_0)]\, H_{n+1}^{(2)}(\lambda_m \rho_m) \\ &- [(k_m^2 + h^2) e^{j(n+1)\phi_0} J_{n-1}(\lambda_m \rho_0) + \lambda_m^2 e^{j(n+1)\phi_0} J_{n+1}(\lambda_m \rho_0)] H_{n-1}^{(2)}(\lambda_m \rho_m) \} \end{aligned}$$

$$\beta_n^{(m)} = \frac{Il}{4\pi} \omega\mu_0 \frac{h}{4\omega\mu_0} [e^{j(n+1)\phi_0} J_{n+1}(\lambda_m \rho_0) H_{n+1}^{(2)}(\lambda_m \rho_m) + e^{j(n-1)\phi_0} J_{n-1}(\lambda_m \rho_0) H_{n-1}^{(2)}(\lambda_m \rho_m)]$$

The quantities $\gamma_n^{(m-1)}$, $\eta_n^{(m-1)}$, $\alpha_n^{(m-1)}$ and $\beta_n^{(m-1)}$ are obtained from $\gamma_n^{(m)}$, $\eta_n^{(m)}$, $\alpha_n^{(m)}$ and $\beta_n^{(m)}$, respectively, by changing ρ_0 to ρ_{m-1} and ρ_m to ρ_0. Equality (23) consists of four equations and four unknown coefficients and can be readily solved. The remaining coefficients are obtained through the following recursion relationship:

$$\begin{bmatrix} a_n^{(i+1)} \\ b_n^{(i+1)} \\ c_n^{(i+1)} \\ d_n^{(i+1)} \end{bmatrix} = M_n^{(i)} \begin{bmatrix} a_n^{(i)} \\ b_n^{(i)} \\ c_n^{(i)} \\ d_n^{(i)} \end{bmatrix} - [B_n^{(m)}]^{-1} \begin{bmatrix} \gamma_n^{(m)} \\ \eta_n^{(m)} \\ \alpha_n^{(m)} \\ \beta_n^{(m)} \end{bmatrix} \delta(i-m) + [B_n^{(m-1)}]^{-1} \begin{bmatrix} \gamma_n^{(m-1)} \\ \eta_n^{(m-1)} \\ \alpha_n^{(m-1)} \\ \beta_n^{(m-1)} \end{bmatrix} \delta(i-m+1) \tag{24}$$

3. Radiation Patterns for Horizontal Dipole

The radiation fields are obtained by using the method of saddle-point integration (Ref. 3) to evaluate the integral expressions of the fields in free space. The resulting spherical components of the radiation fields are

$$\left.\begin{aligned} E_\theta &= -2k^2 \sin\theta \, e^{jkz_0 \cos\theta} \frac{e^{-jkR}}{R} \\ &\quad \times \sum_{n=-\infty}^{\infty} c_n^{(N+1)} \, e^{-jn\phi + j(n+1)\pi/2} \\ H_\phi &= \left(\frac{\epsilon_0}{\mu_0}\right)^{1/2} E_\theta \end{aligned}\right\} \tag{25}$$

$$\left.\begin{aligned} E_\phi &= 2\omega\mu_0 k \sin\theta \, e^{jkz_0 \cos\theta} \frac{e^{-jkR}}{R} \\ &\quad \times \sum_{n=-\infty}^{\infty} d_n^{(N+1)} \, e^{-jn\phi + j(n+1)\pi/2} \\ H_\theta &= -\left(\frac{\epsilon_0}{\mu_0}\right)^{1/2} E_\phi \end{aligned}\right\} \tag{26}$$

where k is the free-space wave number, $c_n^{(N+1)}$ and $d_n^{(N+1)}$ are given in Eq. (23), and

$$\lambda_1^2 = k_1^2 - k^2 \cos^2\theta$$

$$h = k \cos\theta$$

It should be noted that the corresponding modified Bessel functions must be used when $\lambda_1^2 < 0$.

References

1. Wait, J. R., *Electromagnetics and Plasmas*. Holt, Rinehart and Winston, New York, 1968.
2. Wait, J. R., *Electromagnetic Radiation from Cylindrical Structures*. Pergamon Press, New York, 1959.
3. Collin, R. E., *Field Theory of Guided Waves*. McGraw-Hill Book Co., Inc., New York, 1960.

XXII. Spacecraft Telemetry and Command

TELECOMMUNICATIONS DIVISION

A. Approximate Analysis of Channel Imbalance Effects in Non-Coherent FSK Receivers With Large BT Products, *C. Carl*

1. Introduction

Binary non-coherent frequency-shift-keyed (FSK) systems with large IF bandwidth-to-bit-rate ratios, or *BT*, are being considered for applications where simplicity and reliability of operation are worth the cost of decreased efficiency compared with, for example, phase-shift-keyed (PSK) modulation techniques. Such an application is the planetary capsule–spacecraft relay link. The typical receiver is shown in Fig. 1. Either frequency f_1 or f_2 is sent, corresponding to a data 1 or 0, square law detected, integrated over the bit interval *T*, and detected as a data 1 or 0 (bit synchronization at the data detector is assumed). For receiver design purposes, the effect on performance must be determined when the two channels (at f_1 and f_2) are unbalanced with respect to bandwidth, carrier attenuation, etc., so that the appropriate hardware tolerances may be specified. The effect of ac-coupling the data detector must also be considered.

2. Analysis

The analysis involves a straightforward expansion of Glenn's (Ref. 1) work on the balanced receiver. As in Ref. 1, the central-limit theorem is invoked as an approximation for $N = BT \geq 10$; i.e., the statistics at the output of the integrator approach gaussian for large values of N.[1]

The receiver model to be analyzed is shown in Fig. 2, where B_i, α_i, and A_i are the channel bandwidths, carrier attenuation, and channel attenuations, respectively; i.e.,

$$B_i = \frac{\int_{-\infty}^{\infty} | H_i(f) |^2 \, df}{| H_{i_{\max}} |^2}$$

$$\alpha_i = \frac{| H_i(f_i) |^2}{| H_{i_{\max}} |^2}$$

A "balancing amplifier" has been added to channel 2 to ascertain whether the imbalance may be minimized by adjustment of the gain. Let the integrator–detector be dc-coupled for the present. The error probability will be evaluated by calculating the conditional error probabilities, given that a *one* (hypothesis H_1) or a *zero* (H_2) is sent, and averaging them with respect to H_i.

---

[1] Subsequent work has shown this assumption to be pessimistic in performance by a few tenths of a decibel (to be published).

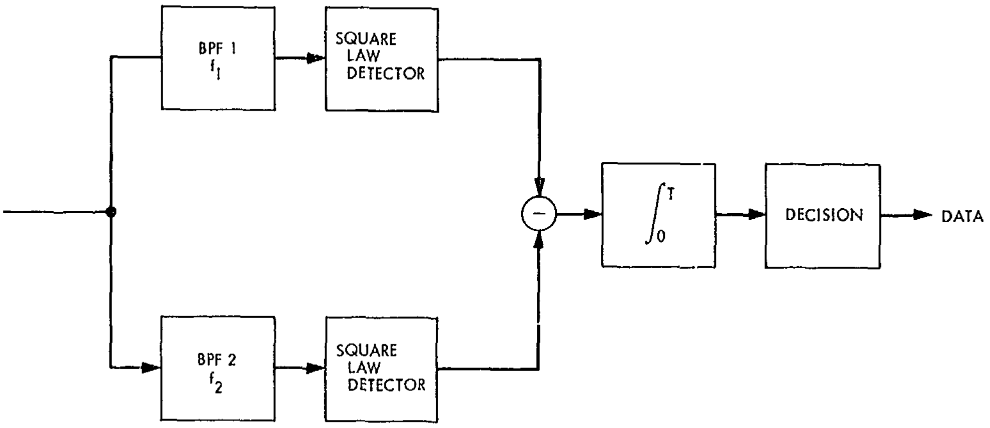

Fig. 1. Typical non-coherent FSK receiver

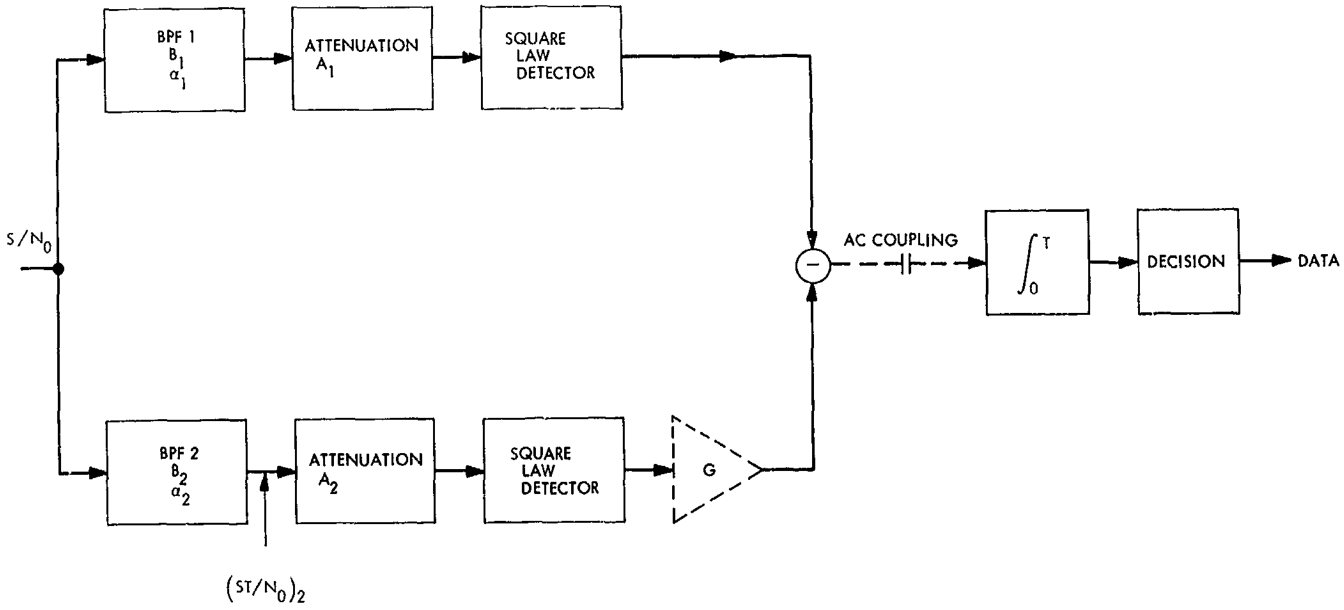

Fig. 2. FSK receiver model

Marcum (Ref. 2) has shown that the probability density of a sum of N samples (i.e., integral) of the output of a square law detector, when the input is signal-plus-noise and noise only, is

$$\left.\begin{aligned} p_{s+n}(y) &= \left(\frac{y}{Na}\right)^{N-1/2} e^{-(y+Na)}\, I_{N-1}\left[2(Nay)^{1/2}\right], \\ p_n(y) &= \frac{y^{N-1}e^{-y}}{(N-1)!}, \end{aligned}\right\} y > 0$$

and the required moments are

$$\mu_{s+n} = N(1+a)$$

$$\sigma^2_{s+n} = N(1+2a)$$

$$\mu_n = N$$

$$\sigma^2_n = N$$

where y is normalized to $2BN_0$ and $a = S/(N_0B)$; S/N_0 is the signal-to-noise density ratio at the receiver input.

Removing the normalization (since B is not the same for both channels) and assuming $H = H_1$, the moments at the integrator output due to each channel separately, neglecting the subtractor, are

$$\mu_1 = 2B_1^2 T N_0 A_1 \left(1 + \frac{\alpha_1 S}{N_0 B_1}\right)$$

$$\sigma_1^2 = 4B_1^3 T N_0^2 A_1^2 \left(1 + \frac{2\alpha_1 S}{N_0 B_1}\right)$$

$$\mu_2 = 2B_2^2 T N_0 A_2 G$$

$$\sigma_2^2 = 4B_2^3 T A_2^2 N_0^2 G^2$$

where G is the amplifier gain. Combining the channels through the subtractor, the probability of error, with the gaussian assumption, is

$$P(e \mid H_1) = \frac{1}{2}\left\{1 - \mathrm{erf}\left[\frac{1}{2}\,\frac{(\mu_1 - \mu_2)^2}{\sigma_1^2 + \sigma_2^2}\right]^{1/2}\right\}$$

where

$$\mathrm{erf}\,(x) = \frac{2}{\pi^{1/2}}\int_0^x e^{-t^2}\,dt$$

After some algebra,

$$P(e \mid H_1) =$$

$$\frac{1}{2}\left(1 - \mathrm{erf}\left\{\frac{1}{2}\,\frac{\left[N_1^2 A_1 - N_2^2 A_2 G + A_1 N_1\left(\frac{\alpha_1 ST}{N_0}\right)\right]^2}{N_1^3 A_1^2 + N_2^3 A_2^2 G^2 + A_1^2 N_1^2\left(\frac{2\alpha_1 ST}{N_0}\right)}\right\}^{1/2}\right) \qquad \text{(1a)}$$

where $N_i = B_i T$. Similarly for $H = H_2$, the probability of error may be evaluated to obtain

$$P(e \mid H_2) = \frac{1}{2}\left(1 - \mathrm{erf}\left\{\frac{1}{2}\,\frac{\left[N_2^2 A_2 G - N_1^2 A_1 + N_2 A_2 G\left(\frac{\alpha_2 ST}{N_0}\right)\right]^2}{N_1^3 A_1^2 + N_2^3 A_2^2 G^2 + G^2 A_2^2 N_2^2\left(\frac{2\alpha_2 ST}{N_0}\right)}\right\}^{1/2}\right) \qquad \text{(1b)}$$

Since $P(H_1) = P(H_2) = \frac{1}{2}$, the average probability of error is

$$P(e) = \frac{1}{2}\,P(e \mid H_1) + \frac{1}{2}\,P(e \mid H_2) \qquad \text{(2)}$$

3. Choice of Amplifier Gain

This amplification may be thought of as an operation that is compensating for *some* of the receiver imbalance by improving the detector efficiency (i.e., approaching a maximum likelihood decision rule). One might speculate on "optimum" values of G that minimize $P(e)$, which in general would be functions of ST/N_0 and therefore be difficult to mechanize in hardware. As a practical matter then, G will be selected by some simple method to determine what improvements in performance (if any) that may be achieved.

First, for $G = 1$ (the unbalanced receiver), the probability of error from Eq. (2) becomes

$$P(e) = \frac{1}{4}\left(2 - \mathrm{erf}\left\{\frac{1}{2}\,\frac{\left[N_1^2 R - N_2^2 + R N_2 \Gamma\left(\frac{ST}{N_0}\right)_2\right]^2}{N_1^3 R^2 + N_2^3 + 2\Gamma R^2 N_1^2\left(\frac{ST}{N_0}\right)_2}\right\}^{1/2} - \mathrm{erf}\left\{\frac{1}{2}\,\frac{\left[N_2^2 - N_1^2 R + N_2\left(\frac{ST}{N_0}\right)_2\right]^2}{R^2 N_1^3 + N_2^3 + 2N_2^2\left(\frac{ST}{N_0}\right)_2}\right\}^{1/2}\right) \qquad \text{(3)}$$

where $(ST/N_0)_2$ is that ratio in channel 2 bandpass; i.e.,

$$\left(\frac{ST}{N_0}\right)_2 = \frac{\alpha_2\,ST}{N_0}$$

and

$$\Gamma = \frac{\alpha_1}{\alpha_2}$$

$$R = \frac{A_1}{A_2}$$

As the second case, let G be chosen such that the signal-only output from each channel are equal or

$$\mu_1 \big|_{H_1} = \mu_2 \big|_{H_2}, \qquad N_0 \to 0$$

Hence,

$$2B_1^2 T N_0 A_1 \left(1 + \frac{\alpha_1 S}{N_0 B_1}\right) \underset{N_0 \to 0}{=} 2B_2^2 T N_0 A_2 G \left(1 + \frac{\alpha_2 S}{B_2 N_0}\right)$$

As $N_0 \to 0$,

$$G = \frac{B_1 \alpha_1 A_1}{B_2 \alpha_2 A_2} = \frac{N_1}{N_2} R\Gamma$$

Substituting this into Eq. (2),

$$P(e) = \frac{1}{4}\left(2 - \operatorname{erf}\left\{\frac{1}{2}\frac{\left[N_1 - N_2\Gamma + \Gamma\left(\frac{ST}{N_0}\right)_2\right]^2}{N_1 + N_2\Gamma^2 + 2\Gamma\left(\frac{ST}{N_0}\right)_2}\right\}^{1/2} - \operatorname{erf}\left\{\frac{1}{2}\frac{\left[N_2\Gamma - N_1 + \Gamma\left(\frac{ST}{N_0}\right)_2\right]^2}{N_1 + N_2\Gamma^2 + 2\Gamma^2\left(\frac{ST}{N_0}\right)_2}\right\}^{1/2}\right) \tag{4}$$

Finally, let G be chosen such that the variance of the two conditional detection densities be equal; i.e.,

$$\sigma_1^2 + \sigma_2^2\big|_{H_1} = \sigma_1^2 + \sigma_2^2\big|_{H_2}$$

Solving, $G = (N_1/N_2)\, R\Gamma^{1/2}$, independent of both ST/N_0, and

$$P(e) = \frac{1}{4}\left(2 - \operatorname{erf}\left\{\frac{1}{2}\frac{\left[N_1 - N_2\Gamma^{1/2} + \Gamma\left(\frac{ST}{N_0}\right)_2\right]^2}{N_1 + N_2\Gamma + 2\Gamma\left(\frac{ST}{N_0}\right)_2}\right\}^{1/2} - \operatorname{erf}\left\{\frac{1}{2}\frac{\left[N_2\Gamma^{1/2} - N_1 + \Gamma^{1/2}\left(\frac{ST}{N_0}\right)_2\right]^2}{N_1 + N_2\Gamma + 2\Gamma\left(\frac{ST}{N_0}\right)_2}\right\}^{1/2}\right) \tag{5}$$

Note that dependence on A_i in Eqs. (4) and (5) has been removed. In addition, if $R = \Gamma = 1$, and $N_1 = N_2 = N$, from Eqs. (3–5) the balanced case

$$P(e) = \frac{1}{2}\left(1 - \operatorname{erf}\left\{\frac{\left(\frac{ST}{N_0}\right)_2^2}{4\left[N + \left(\frac{ST}{N_0}\right)_2\right]}\right\}^{1/2}\right) \tag{6}$$

is obtained, which checks with Ref. 1.

4. AC-Coupling

If the integrator is now ac-coupled, with the given gain settings established above, different performance is achieved. Ac-coupling removes the mean (dc) component, which is $(\mu_{H_1} + \mu_{H_2})/2$, and the means become

$$(\mu_{H_1})_{ac} = \mu_{H_1} - \frac{\mu_{H_1} + \mu_{H_2}}{2} = \frac{\mu_{H_1} - \mu_{H_2}}{2}$$

$$(\mu_{H_2})_{ac} = \mu_{H_2} - \frac{\mu_{H_1} + \mu_{H_2}}{2} = -\frac{\mu_{H_1} - \mu_{H_2}}{2}$$

The variances are unaffected. Making the necessary changes in Eqs. (3–5), the probability of error, for $C = 1$ (imbalance) becomes

$$P(e) = \frac{1}{4}\left\{2 - \operatorname{erf}\left[\frac{1}{2}\frac{\left(\frac{RN_1\Gamma + N_2}{2}\right)^2\left(\frac{ST}{N_0}\right)_2^2}{N_1^3R^2 + N_2^3 + 2\Gamma R^2 N_1^2\left(\frac{ST}{N_0}\right)_2}\right]^{1/2} - \operatorname{erf}\left[\frac{1}{2}\frac{\left(\frac{RN_1\Gamma + N_2}{2}\right)^2\left(\frac{ST}{N_0}\right)_2^2}{N_1^3R^2 + N_2^3 + 2N_2^2\left(\frac{ST}{N_0}\right)_2}\right]^{1/2}\right\} \tag{7}$$

For $G = (N_1/N_2)R\Gamma$ (signal balance),

$$P(e) = \frac{1}{4}\left\{2 - \operatorname{erf}\left[\frac{1}{2}\frac{\Gamma^2\left(\frac{ST}{N_0}\right)_2^2}{N_1 + N_2\Gamma^2 + 2\Gamma\left(\frac{ST}{N_0}\right)_2}\right]^{1/2} - \operatorname{erf}\left[\frac{1}{2}\frac{\Gamma^2\left(\frac{ST}{N_0}\right)_2^2}{N_1 + N_2\Gamma^2 + 2\Gamma^2\left(\frac{ST}{N_0}\right)_2}\right]^{1/2}\right\} \tag{8}$$

For $G = (N_1/N_2)R\Gamma^{1/2}$ (variance balance),

$$P(e) = \frac{1}{2}\left\{1 - \operatorname{erf}\left[\frac{1}{2}\frac{\left(\frac{\Gamma + \Gamma^{1/2}}{2}\right)^2\left(\frac{ST}{N_0}\right)^2_2}{N_1 + N_2\Gamma + 2\Gamma\left(\frac{ST}{N_0}\right)_2}\right]^{1/2}\right\} \tag{9}$$

Some typical results are shown in Figs. 3 and 4. Because $N = BT$, N is expressed in decibels (10 log [ ]) to be compatible with conventional noise bandwidth notation; Γ and R are also expressed in 10 log [ ] form. Given $P_{\text{unbal}}(e) = f_{\text{unbal}}(ST/N_0)$ and $P_{\text{bal}}(e) = f_{\text{bal}}(ST/N_0)$ for the unbalanced and balanced ($N = N_2$) receivers, respectively, degradation (in dB) is defined by

$$\text{Degradation}\left(\frac{ST}{N_0}\right) = \frac{ST}{N_0} - f^{-1}_{\text{bal}}\left[P_{\text{unbal}}(e)\right]$$

Decaying curves with ST/N_0 mean that $P_{\text{unbal}}(e) \rightarrow P_{\text{bal}}(e)$ at high ST/N_0, etc. One may observe from these plots that a balance amplifier can measurably improve performance in some cases, but not in others. Comparing Figs. 3a and 3b, it appears that if the ratio $\log(N_1/N_2)$ is of opposite sign to $\log R$, a "compensation" is effected, improving the unbalanced receiver's performance.

Ac-coupling appears to offer consistent improvement in performance. This is particularly significant in a case as shown in Fig. 5 where the usual $P(e)$ is plotted (degradation plots lose significance when the two curves are substantially different). The reason for such catastrophic dc performance is that the mean term implicit in $P(e \mid H_2)$ in Eq. (3) has become positive and with a "decide-on-zero" detector $P(e \mid H_2) \rightarrow 0.5$. However, it is less positive than the mean term in $P(e \mid H_1)$ so that ac-coupling provides usable performance. Balance amplifiers are not of much use in this case. Particularly alarming is that this case could conceivably be built using crystal filters with ±0.5-dB tolerance in insertion loss R, passband ripple Γ, and noise bandwidth N_1N_2. Clearly, care must be taken when specifying filters for this application.

5. Experimental Work[2]

Using the FSK link described previously (SPS 37-51, Vol. III, pp. 311–313), verification of the theory (signal balance case) by varying the attenuation term R was attempted. The link was as shown in Fig. 2 with the channel attenuations replaced with

$$A_1 = A'_1 \cdot C_1$$

$$A_2 = A'_2 \cdot C_2$$

where the A'_i were accounted for in a signal balance amplifier and the C_i added to test performance after balancing. For $G = (B_1\alpha_1A'_1)/(B_2\alpha_2A'_2)$ and modifying Eq. (4),

$$P(e) = \frac{1}{4}\left\{2 - \operatorname{erf}\left[\frac{1}{2}\frac{\left(N_1C_1 - N_2C_2\Gamma + C_1\Gamma\left(\frac{ST}{N_0}\right)_2\right)^2}{N_2C_2^2\Gamma^2 + N_1C_1^2 + 2\Gamma C_1^2\left(\frac{ST}{N_0}\right)_2}\right]^{1/2} - \operatorname{erf}\left[\frac{1}{2}\frac{\left(N_2\Gamma C_2 - N_1C_1 + \Gamma C_2\left(\frac{ST}{N_0}\right)_2\right)^2}{N_1C_1^2 + N_2C_2^2\Gamma^2 + 2\Gamma^2C_2^2\left(\frac{ST}{N_0}\right)_2}\right]^{1/2}\right\} \tag{10}$$

is obtained for dc-coupling; modifying Eq. (8),

$$P(e) = \frac{1}{4}\left\{2 - \operatorname{erf}\left[\frac{1}{2}\frac{\left(\frac{C_1 + C_2}{2}\right)^2\Gamma^2\left(\frac{ST}{N_0}\right)^2_2}{N_1C_1^2 + N_2C_2^2\Gamma^2 + 2C_1^2\Gamma\left(\frac{ST}{N_0}\right)_2}\right]^{1/2} - \operatorname{erf}\left[\frac{1}{2}\frac{\left(\frac{C_1 + C_2}{2}\right)^2\Gamma^2\left(\frac{ST}{N_0}\right)^2_2}{N_1C_1^2 + N_2C_2^2\Gamma^2 + 2C_2^2\Gamma^2\left(\frac{ST}{N_0}\right)_2}\right]^{1/2}\right\} \tag{11}$$

is obtained for ac-coupling. Figures 6 and 7 show the theoretical results compared with the experimental results. Here degradation is referenced to the case $C_1 = C_2 = 1$ (instead of the balanced receiver as above). The laboratory results correspond well with the theory, the differences are attributed to measurement tolerances.

References

1. Glenn, A. B., "Analysis of Non-Coherent FSK Systems with Large Ratios of Frequency Uncertainties to Information Rates," *RCA Review*, Vol. 27, pp. 272–314, June 1966.
2. Marcum, J. I., "A Statistical Theory of Target Detection by Pulsed Radar," Rand Research Memo RM-754, reprinted in *IRE Transactions on Information Theory*, Vol. IT-6, pp. 161–164, Apr. 1960.

---

[2] Experimental results used in this study were obtained by J. T. Sumida, JPL Spacecraft Telemetry and Command Section.

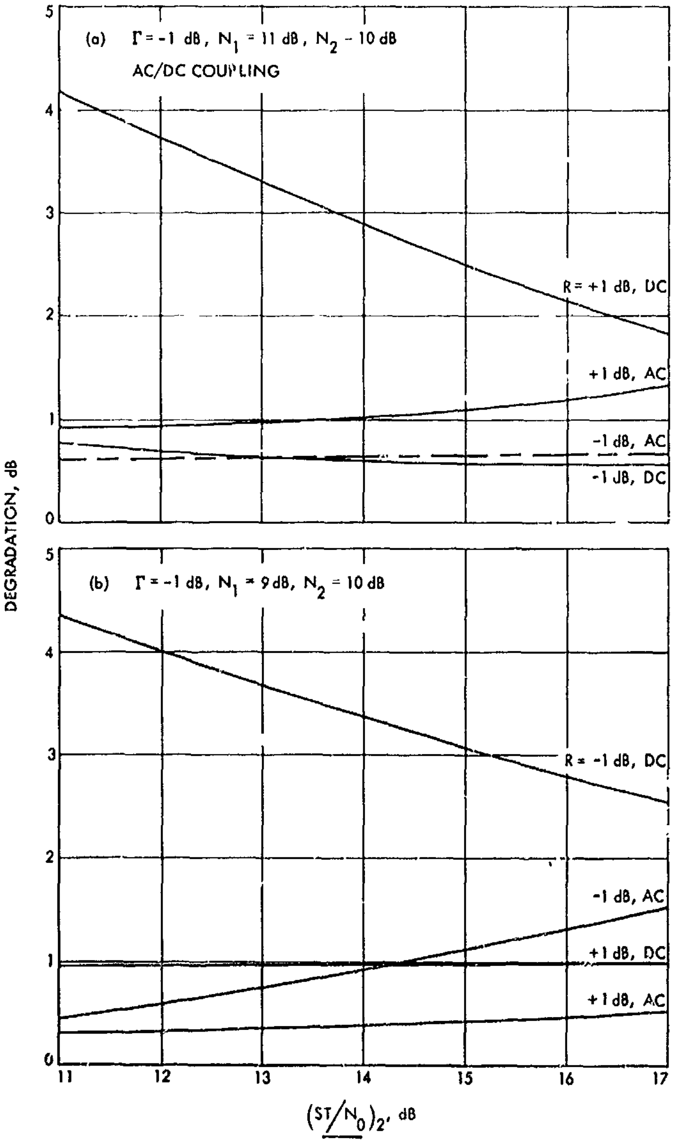

Fig. 3. Degradation of unbalanced receiver

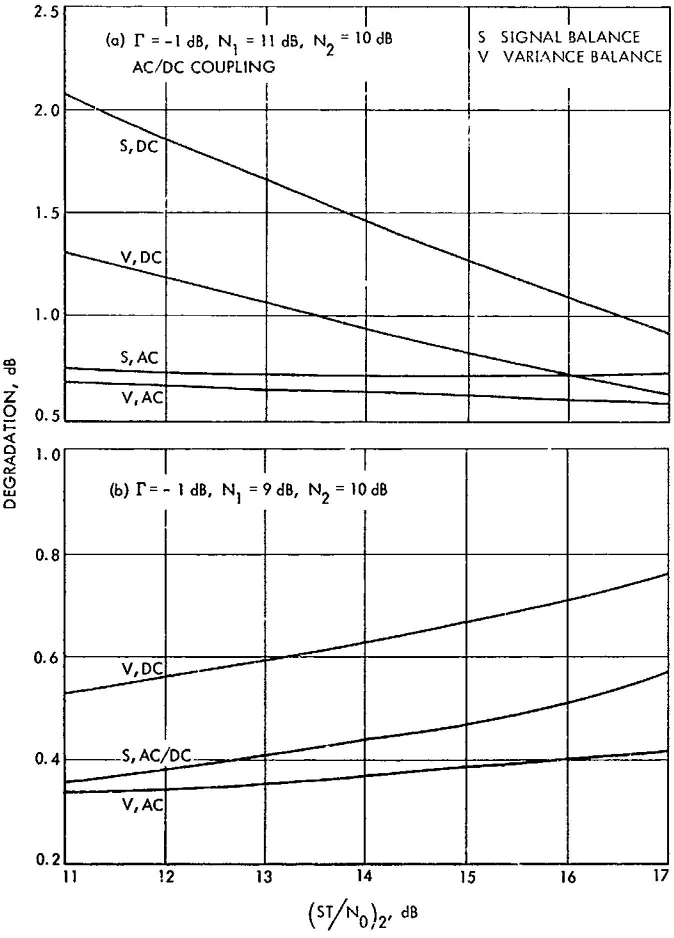

Fig. 4. Degradation of "corrected" receiver

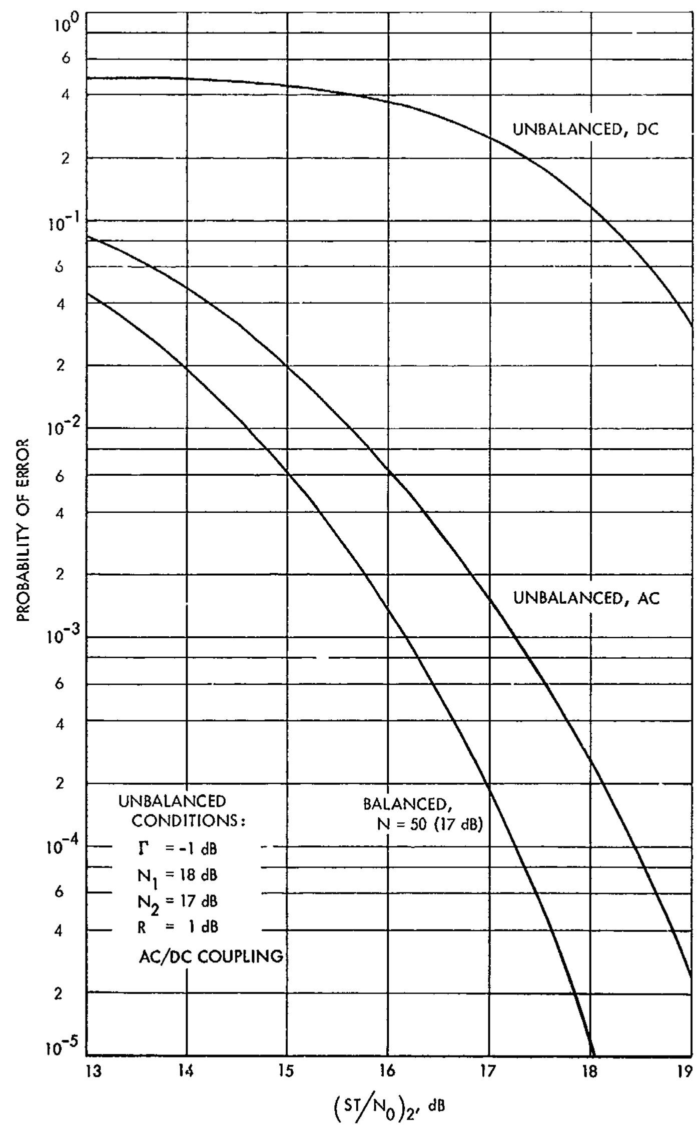

Fig. 5. Comparison of balanced and unbalanced receiver performance

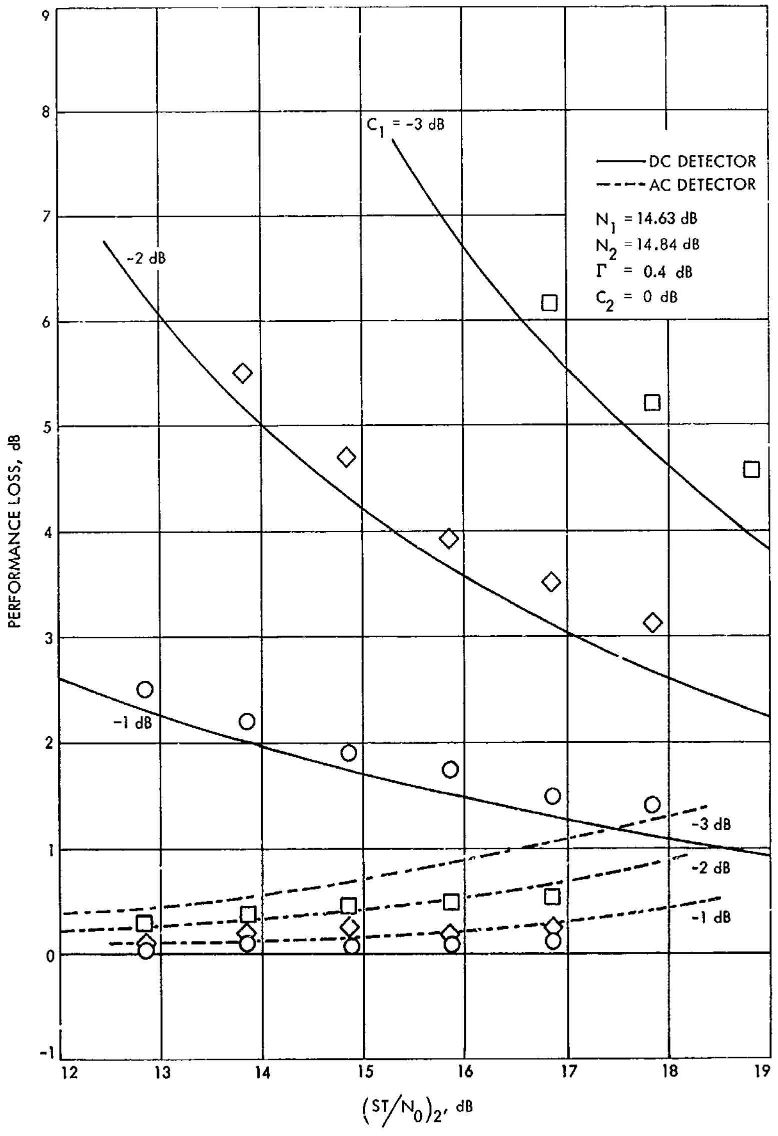

Fig. 6. Comparison of theory and experiment for channel 1 imbalance

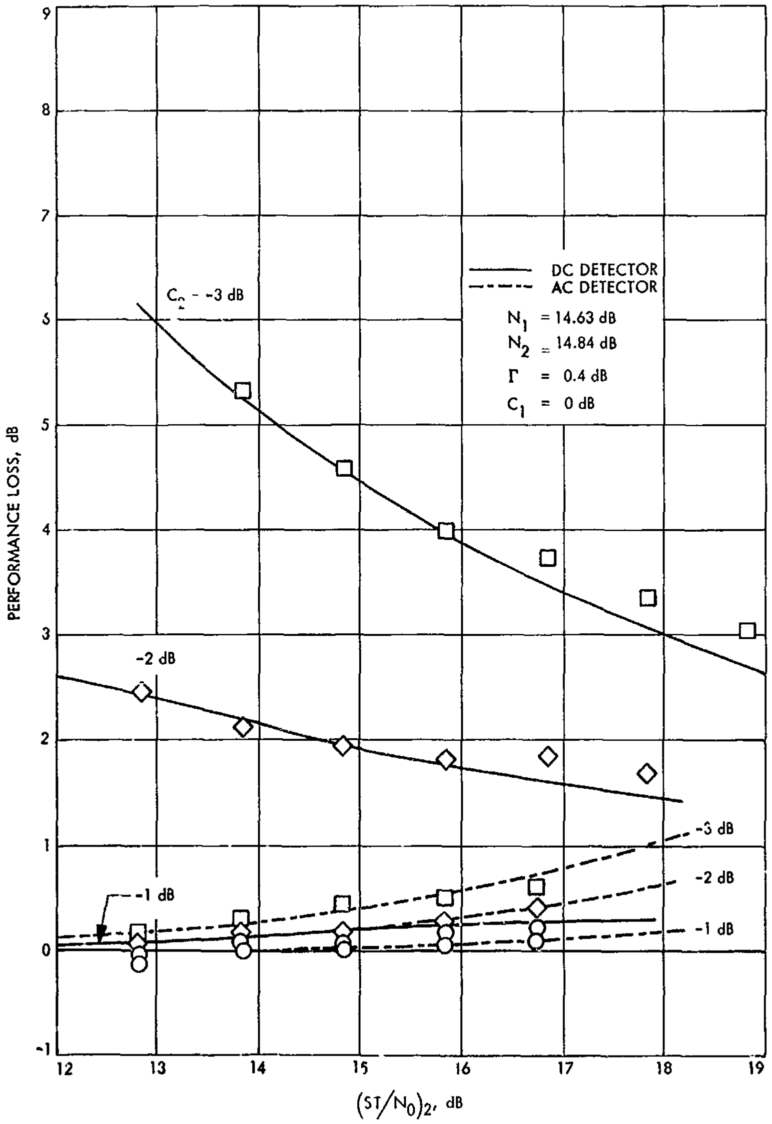

Fig. 7. Comparison of theory and experiment for channel 2 imbalance

XXIII. Spacecraft Radio

TELECOMMUNICATIONS DIVISION

A. Low-Data-Rate Telemetry RF Systems Development, *R. Postal*

1. Introduction

A solid-state multiple frequency shift-keyed (MFSK) 2295-MHz transmitter has been developed as a subassembly for a *m*-ary noncoherent telecommunication system capable of surviving a high impact on a planetary surface. An overall description of the transmitter was given in SPS 37-52, Vol. III, pp. 249–250. Of prime importance is the oscillator frequency stability necessary to achieve the desired communication system efficiency. Although definite stability requirements have not been established, it is desired to have a word separation of only 10 Hz at S-band with a word time of 5 s. In the future, a word time of greater than 20 s may be desired. Until definite requirements can be established, it is an objective of this task to determine the practical limitations of the stability of crystal-controlled oscillators. The discussion in this article pertains to the MFSK oscillator portion of the S-band transmitter.

2. Oscillator Development

In attempting to provide a highly stable MFSK crystal-controlled oscillator, several oscillator design guidelines were found to be necessary. These guidelines are as follows:

(1) Use low noise transistors (2N918 or better).

(2) Maximize isolation of transistor reactances from frequency determining circuitry.

(3) Use low leakage varactor in the control circuit.

(4) Minimize coupling to provide at least 20 dB isolation between the oscillator and the following stage.

(5) Use a low noise, third overtone crystal as a series resonant element in the range of 20–32 MHz.

(6) Set crystal drive level in the range of 50–300 μW.

(7) Minimize variations in crystal drive level.

One oscillator configuration that reflects these guidelines is a modified Colpitts circuit. A description of this circuit was included in SPS 37-40, Vol. III, pp. 198–201.

The additional requirement of high impact resistance resulted in a contract with the Valpey–Fisher Corporation to develop a stable, ruggedized crystal assembly. The necessary manufacturing processes, however, were found to be very stringent and resulted in low yields at a very high cost per unit. A recently available ruggedized

TO-5 crystal assembly was also considered as a possible candidate for the MFSK oscillator. Units manufactured by Monitor Products Company and McCoy Crystal Incorporated are shown in Fig. 1. Both crystals used a third overtone 31.875 MHz AT cut resonator mounted on a four-post TO-5 header. Preliminary tests indicate the TO-5 units would meet the MFSK oscillator requirements. The development contract with Valpey–Fisher has been terminated in view of the readily available, lower cost TO-5 units.

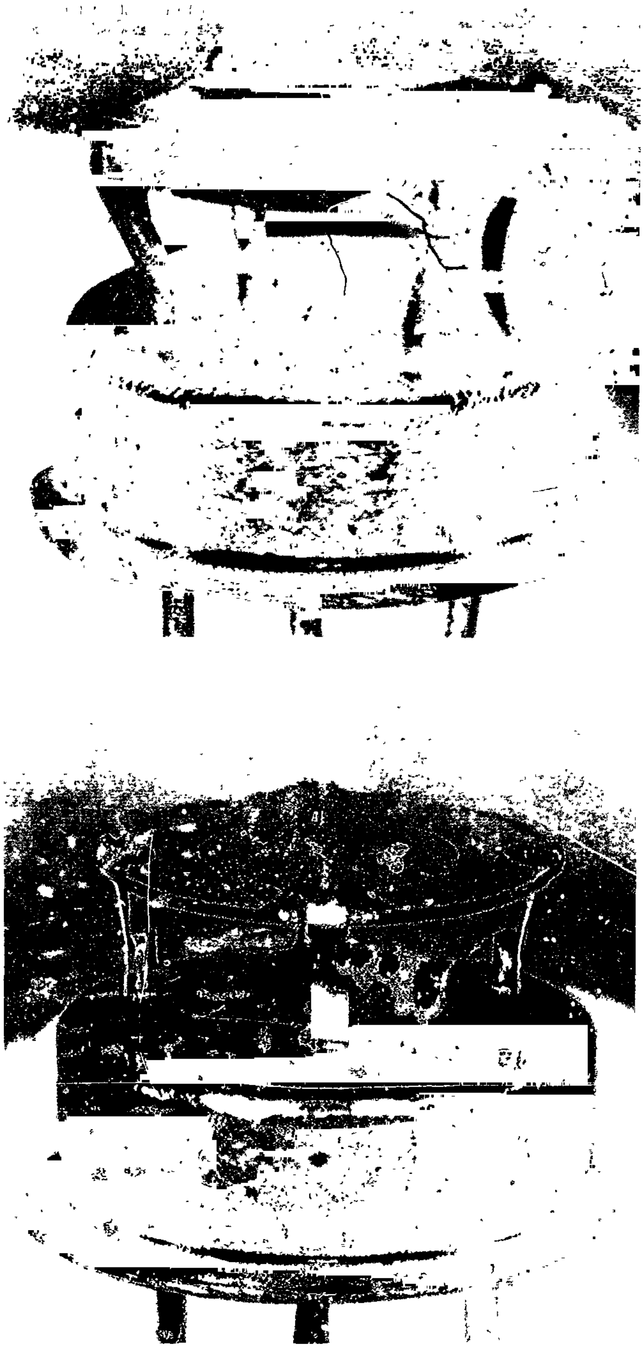

Fig. 1. TO-5 crystal units

3. Test Results

Evaluation of the TO-5 crystal assemblies included high impact tests and measurement of frequency versus temperature, phase noise, and spectral purity. Samples of 12 units each from Monitor Products and McCoy Inc. were used for these tests. Shock tests were performed in three planes at levels ranging from 2000–10,000 g. All units survived 2000 g; however, five McCoy units failed at 5600 g and one Monitor unit failed during the last plane at 10,000 g. Shock caused a $\Delta f/f$ ranging between 1×10^{-7} and 5×10^{-6} per shock. It is believed the ruggedness of the Monitor unit is due to the four-post direct resonator support as opposed to the McCoy ribbon support.

Phase noise and frequency versus temperature data of several TO-5 units are given in Table 1. Phase noise is given as measured phase tracking error at S-band in a phase-locked loop receiver with a noise bandwidth of 20 Hz. Crystal temperature performance is listed as maximum slope of $\Delta f/f$ per °C as measured between 15 and 40°C. Monitor sample 10 and McCoy sample 34 crystals were then selected for spectral purity measurements.

The MFSK crystal-controlled oscillator module was placed in an inoperative oven to minimize frequency drift due to temperature variations. To provide measurements at S-band, the oscillator output frequency was multiplied to 2295 MHz and then translated to 60 KHz for processing in a computer-programmed spectrum analyzer. Spectral analysis is accomplished by sampling the signal with

Table 1. Phase noise and temperature data

Crystal	Phase noise, deg peak	Maximum slope, ppm/°C
Monitor		
10	3.0	0.270
14	3.0	—
15	9.0	0.125
20	9.0	0.188
McCoy		
31	1.5	0.038
34	1.0	0.038
38	2.5	0.132
40	3.5	0.110

an analog-to-digital converter. After N groups of $20T$ samples are collected (where T is equal to sample time and N is greater than 1000), each group is auto-correlated and Fourier transformed to find its spectral peak frequency and value. The program then computes the average value of the amplitude of each peak and computes a loss factor in terms of spectral degradation from an ideal oscillator. Spectral degradation data for the two crystals are:

T, s	Average degradation, dB	
	Monitor 10	McCoy 34
20	5.4	1.38
10	2.3	–
5	0.4	–

Since the McCoy sample 34 showed an improvement of 4 dB over the Monitor sample 10 for the $T = 20$-s case, there was no interest in testing the McCoy unit at smaller sample times.

4. Conclusions

The MFSK oscillator will meet the sterilization and high-impact requirements.

The stability performance indicates that crystal-controlled oscillators have the potential for achieving good MFSK communication system efficiency for word time to at least 20 s. The ultimate performance depends on how well the drift rate of such oscillators can be controlled within the specific mission constraints. Information on this subject will be presented in future articles.

XXIV. *Mariner* Telecommunications

TELECOMMUNICATIONS DIVISION

A. Photon-Actuated Solid-State Switch Development, *D. Bergens*

1. Introduction

The development of a photon-actuated solid-state switch for signal transmission with electrical isolation was introduced in SPS 37-44, Vol. IV, pp. 320–325. The switch's electrical and environmental requirements and general configuration were given. Results were discussed for phase I, which consisted of the design, fabrication, and testing of gallium-arsenide diode–phototransistor combinations, and the electrical design of the gate and driver circuit. The results of phase II, in which the gate–driver was fabricated as an integrated circuit, and complete switches were assembled and tested, are summarized in this article. The photon-switch development was performed by Texas Instruments, Inc. (TI), under a NASA–JPL subcontract.

2. Driver

a. Design. Figure 1 is the schematic diagram of the complete photon switch. The gallium-arsenide diode is D2 and the silicon phototransistor is Q3. The remainder of the circuit is the gate and driver. The circuit is straightforward and needs no explanation, except for R5, which was added to provide a greater off-margin when the switch input is at 1 V, by shunting current around D2. The shunting effect of R5 is not serious at high currents when the driver is on because of the logarithmic characteristic of the diode. The supply voltage requirement was 4 ±½ V.

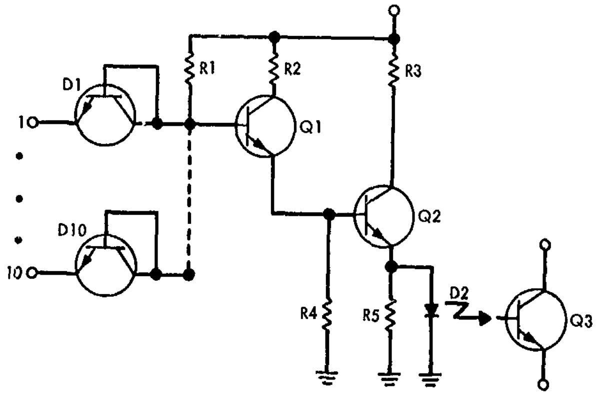

Fig. 1. Photon-switch schematic diagram

The gate–driver design was worst-case-designed with parameters of integrated-circuit transistors and resistors. This required the establishment of margins on the semiconductor processing (resistivity ranges, diffusion depths, etc.). A transistor configuration with which TI had previous experience and data was used for all transistors. Its emitter-base junction was used for the input diodes. The base diffusion was used for all the resistors because it has the lowest temperature coefficient. The resistivity range-of-routine base diffusion was wider than needed for the worst-case design. This problem was resolved in the resistor layout by tapping the resistors and providing a choice of interconnect metalizations to pick up the appropriate taps.

The layout of the gate-driver integrated circuit is shown in Fig. 2. This is also a composite drawing of the mask for the integrated circuit. Several features of the layout require an explanation. Four of the standard transistors were used in parallel for Q2, because its emitter current can be as high as 44 mA and the optimum emitter current of the standard transistor is only 10 mA. For future expansion and yield considerations, 14 input diodes were designed in and around the perimeter of the chip. The resistors were tapped to provide the different lengths needed to account for the resistivity range. A choice of two metalizations was sufficient to match the expected resistivity range to the required resistor ratios. The most critical resistor, R3, is actually two resistors of different dimensions in parallel to provide a finer resolution adjustment. Additional taps were also included for experimental reasons.

b. Processing. Routine triple diffusion processing for integrated circuits was used for the gate–driver circuit. Seven photographic masks were required—3 for diffusions and 4 for contact windows and metalizations. A number of evaluations was made during the processing of the prototype runs. Transistor gains were measured. The resistors were probed on the slice before the final interconnect metalization to establish the resistivity range and the choice between the two metalizations. The base resistivity was within the expected range for the prototype runs.

3. Photon-Switch Assembly

The complete photon switch consists of 7 parts: the gate–driver chip, phototransistor, GaAs diode, 2 ceramic insulators, the 14-lead to TO-84 package, and the package lid. Other materials used in assembling the switch are the SeSAs-glass, epoxy, gold-wire, and gold-solder preforms. The major assembly steps are shown in Fig. 3. The assembly procedure is:

(1) Solder the phototransistor and gate–driver chips to the ceramic insulators.

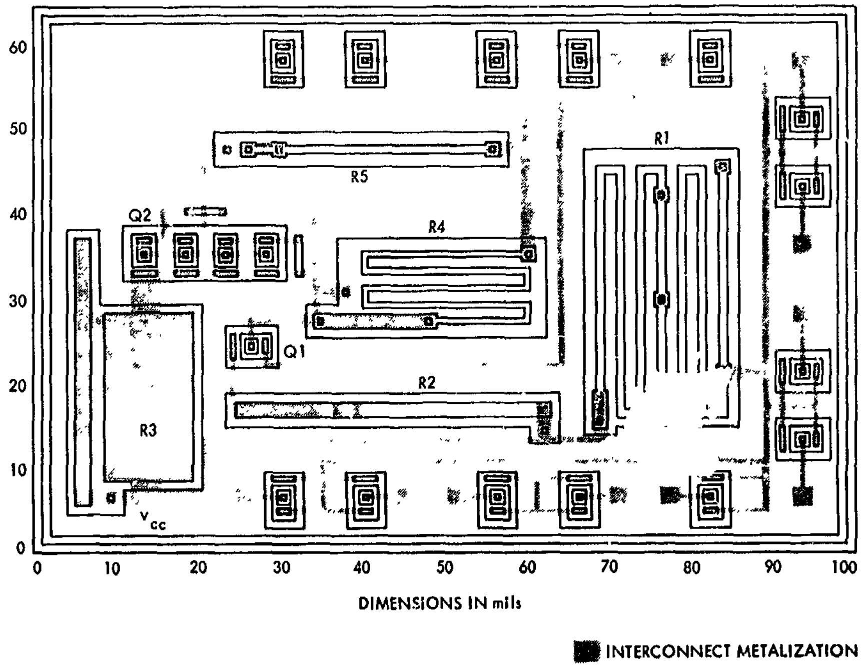

Fig. 2. Gate–driver circuit component layout

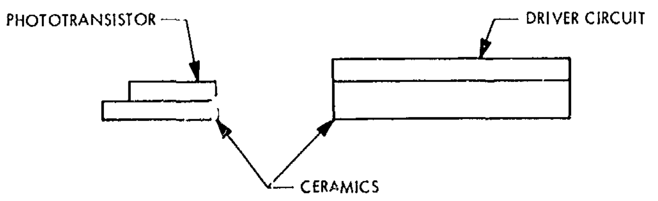

1. MOUNT SI WAFERS ON CERAMICS

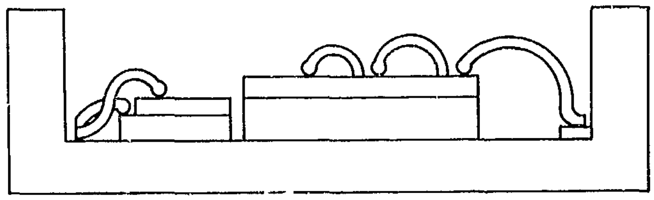

2. MOUNT CERAMICS IN HEADER AND BOND LEADS

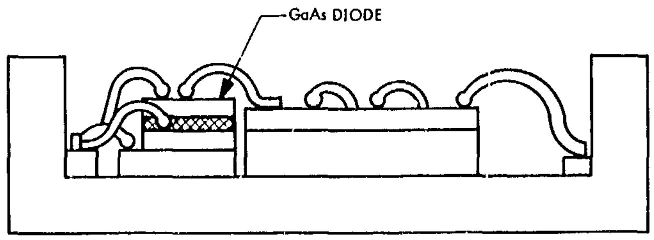

3. MOUNT GaAs DIODE AND BOND LEADS

Fig. 3. Major assembly steps for photon switch

(2) Solder the ceramic subassemblies into the flat package.

(3) Bond leads between pads on the phototransistor and gate-driver chips, and the header pads.

(4) Bond leads to the unmounted GaAs diode.

(5) Mount the diode to the photon-sensitive region of the phototransistor with the SeSAs glass.

(6) Bond the diode leads to the header and gate-driver pads.

(7) Cover the periphery of the diode with epoxy for added support at high temperature.

(8) Clean and hermetically seal the package.

Figure 4 is a sketch of the completed assembly before sealing. The relative size of an unsealed switch is shown in Fig. 5.

4. Tests

a. Environmental. Sample lots of photon switches were subjected to variable frequency vibration, physical shock, centrifuge, and temperature cycling to determine if there were any problems that would preclude their use in spacecraft equipment. There were no failures.

b. Electrical. Thirty photon switches fabricated with prototype drivers were delivered to JPL at the end of phase II. The electrical characteristics of these switches are summarized in Table 1. The parameter I_c is a more sensitive measure of the output than V_{cex}, because I_c is taken at $V_{ce} = 0.6$, which is at the edge of transistor saturation. An explanation of the noise transmissibility parameter was given in SPS 37-44, Vol. IV. Table 1 shows that all the switches met design specifications.

The primary requirement, however, is that the switches meet these specifications after 10,000 h of operation. For this reason, TI established guard bands on I_c and I_{ceo} of 5 mA and 10 μA, respectively, to allow for aging. These two parameters are the ones most likely to change with time. A gradual decrease in I_c is expected due to a very slow degradation of photon output from the diode. This degradation, which is thought to occur only when the photon-emitting diode is on, determines the ultimate life of the switch. Some drift in transistor I_{ceo} with time is not unusual, but it should not change more than 2–1 in good transistors over 10,000 h of operation. The guard band on initial parameters allows for these changes.

c. Life. Twenty-nine of the 30 photon switches were placed on life test in a daisy chain configuration, with the output of one connected to the input of the next, etc. When power is applied, the configuration oscillates because there is an odd number of stages. Each switch is turned on and off at a 1.75-kHz rate. The duty cycle is about 50%. The primary parameter of interest in life testing is I_c because it is the most sensitive indicator of change. In 3,500 h of operation, the degradation of I_c has been minor.

Twelve of the phase I diode–phototransistor pairs were operated with a constant diode current of 30 mA for 14,000 h to determine the aging rate. During this time, the average decrease in I_c was 3 mA, and the maximum decrease was 7½ mA. In 7 of the 12 switches, the decrease

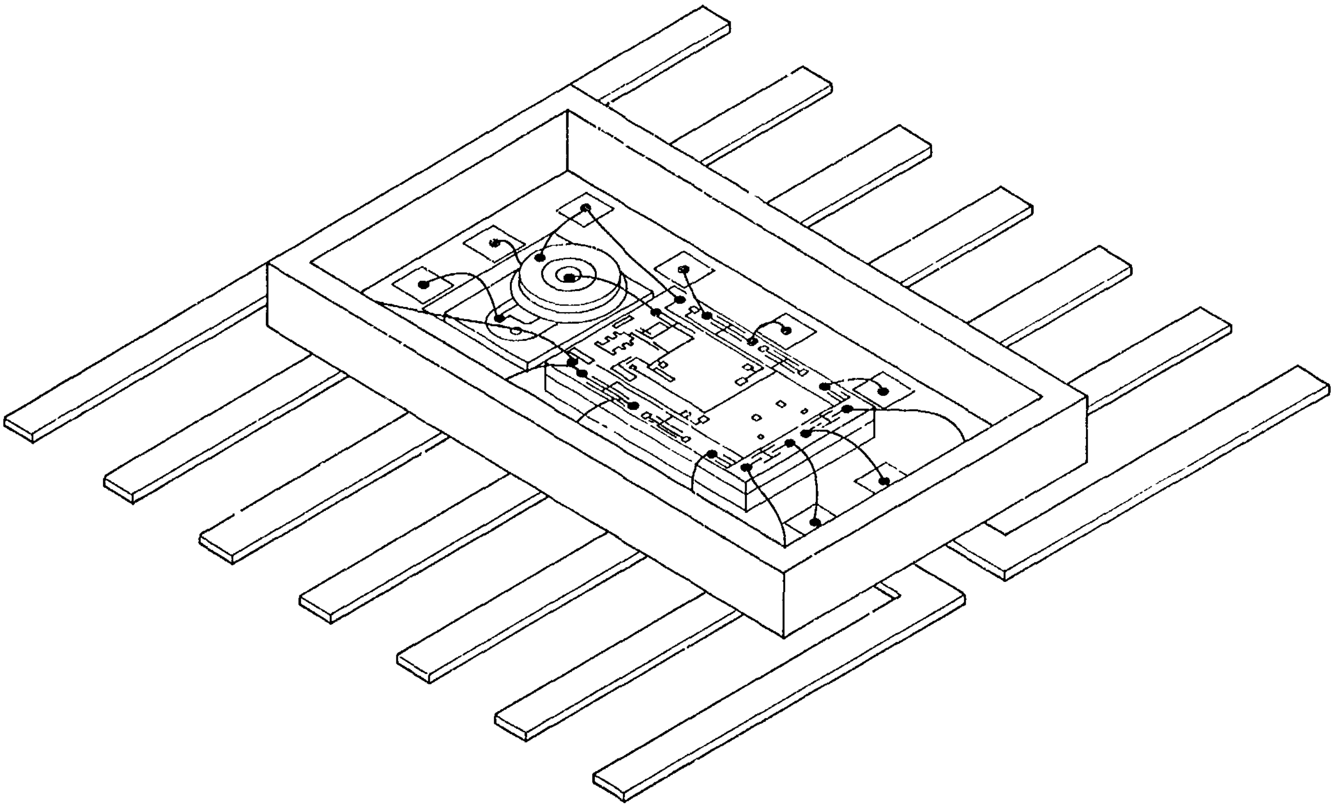

Fig. 4. Completed photo-switch assembly before sealing

Fig. 5. Relative size of photon switch

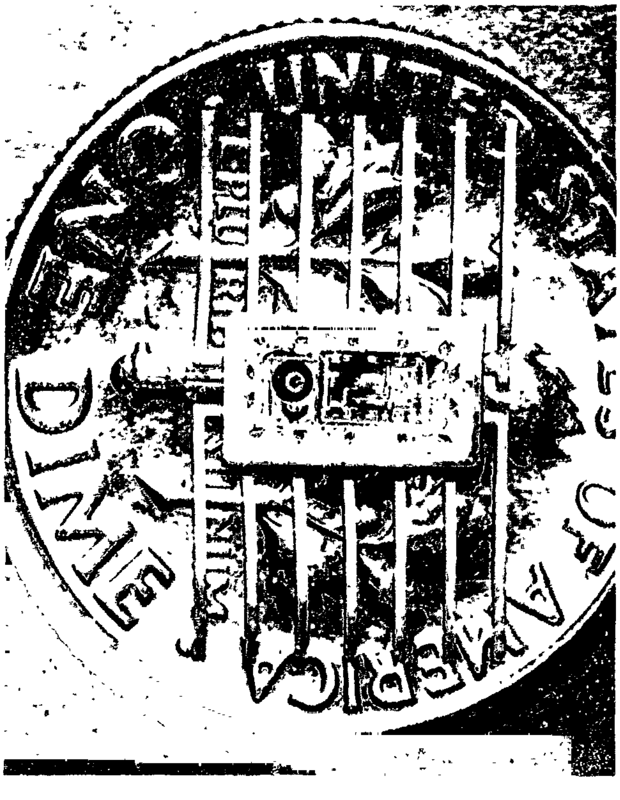

Table 1. Electrical characteristics of 30 photon-actuated isolation switches

Parameter	Test conditions[a,b]	Measured value			Specified value	
		Min	Av	Max	Min	Max
Output on-voltage V_{ces}, V	$I_c = 10$ mA, $V_{cc} = 3.5$ V, $V_{in} = 3.0$ V					
	Temperature = −20°C	—	—	0.115	—	0.6
	+25°C	-	—	0.150	—	0.6
	+100°C	—	—	0.240	—	0.6
Output on-current I_c, mA	$V_{ce} = 0.6$ V, $V_{cc} = 3.5$ V, $V_{in} = 3.0$ V					
	Temperature = −20°C	28	43	57	10	—
	+25°C	26	33	43	10	—
	+100°C	15	19	26	10	—
Output breakdown voltage BV_{ceo}, V	$I_c = 100$ μA	60	68	—	35	—
Output leakage current I_{ceo}, μA	$V_{in} = 1.0$ V, $V_{ce} = 20$ V, $V_{cc} = 4.5$ V					
	Temperature = +25°C	—	0.0013	0.0043	—	0.1
	+100°C	—	2.7	9.9	—	20
Isolation capacitance C_{iso}, pF	Frequency = 1 kHz	—	2.0	2.5	—	10
Input breakdown voltage BV_{DS}, V	$I_{in} = 10$ μA	7.2	8.0	—	6.5	—
Input off-current I_{in}, mA	$V_{in} = 0$, $V_{cc} = 4.5$ V	—	0.19	0.21	—	1
Input on-current, nA	$V_{in} = 6.0$ V, $V_{cc} = 4.5$ V	—	<1	2.2	—	5 × 10^4
Power dissipation-on P_{on}, mW	$V_{in} = 6.0$ V, $V_{cc} = 4.5$ V					
	Temperature = −20°C	155	164	180	—	200
	+25°C	148	158	172	—	200
	+100°C	136	142	153	—	200
Power dissipation-off P_{off}, mW	$V_{in} = 0$, $V_{cc} = 4.5$ V					
	Temperature = −20°C	—	—	0.97	—	1
	+25°C	—	0.89	0.96	—	1
	+100°C	—	—	0.89	—	1
Switching time-on t_1, μs	$I_c = 10$ mA, $V_{cc} = 4.5$ V, $V_{ce(off)} = 20$ V	2.8	4.0	5.8	—	10
Switching time-off t_2, μs	$I_c = 10$ mA, $V_{cc} = 4.5$ V, $V_{ce(off)} = 20$ V	43	71	98	—	100
Noise transmissibility (emitter to collector) V_n, V	$I_c = 2$ mA, $V_{in} = 0$	—	1.8	2.0	—	2

[a] Free air temperature: +25°C unless specified otherwise.

[b] V_{cc} = supply voltage, V_{in} = input voltage, V_{ce} = collector-to-emitter voltage.

was 2 mA or less. The lowest I_c of the 12 switches was 15 mA, after 14,000 h. The rate of change of I_c during the test was approximately linear with time. Eight other diode–transistor pairs that were not operated during the 14,000 h show no change in I_c. The TI engineers believe the aging rate can be directly extrapolated upward in time for switch duty cycles less than 100%. For example, if the duty cycle were 10%, it would take ten times as long for I_c to decrease the same amount.

The saturation voltage of the 12 switches increased an average of 11 mV. The maximum increase was 25 mV. Seven of the 12 increased less than 8 mV. These changes are relatively minor.

One hundred photon switches have been ordered from TI for space flight qualification testing at JPL. When the qualification tests have been successfully completed, the photon switch will be ready for use as interface circuits in the command, central computer and sequencer, and other spacecraft subsystems. They can also be used to interface the ground support equipment with the spacecraft, thus eliminating many of the noise problems encountered during checkout.

TI is marketing the phase I diode–transistor pair in a TO-5 can under the designation TIXL 103. It is called an optically coupled isolator.

A patent application has been filed on the photon switch by JPL. The innovation claimed is "a digital logic gate whose output is electrically isolated from the inputs."

XXV. Future Projects Office

ADVANCED STUDIES

A. Lunar Mission Planning, *R. G. Brereton*

The intent of lunar mission planning is to define an optimum plan for lunar studies. Generally, the rationale for such planning proceeds from a set of scientific goals or objectives that define the "what" and "why" of the plan through a set of scientific experiments, utilization techniques, and time-phased spacecraft missions that define the "how," "where," and "when" of the plan. Considered in this way, lunar mission planning should be a relatively straightforward logic process.

Table 1 discusses the "what" and "why" for lunar exploration in terms of major features or processes that have been studied in the earth—our terrestrial analog. The first column describes the particular feature or process for the earth, the second column describes it for the Moon in terms of total knowledge to date and our terrestrial analog, and the third column presents some information to relate Table 1 to the actual mission planning given in Table 2.

Table 2 is an extension of Table 1, and it may be thought of as presenting the "how" for lunar mission planning and, insofar as is possible at this stage in the planning process, some information about the "where" and "when." A particular scientific objective (1 through 12) for lunar missions is defined in terms of the features or processes defined in Table 1. The first column gives the types of missions that may be useful (i.e., fixed stations, rovers, orbiters, manned, lunar base), the second column gives the principal scientific experiments for the task, the third column gives those experiments or missions that relate to the one under consideration and can be expected to provide correlative information, and the fourth column gives the "where" and "when" of the mission.

Tables 1 and 2 are vertically sequenced in terms of increasing mission complexity, thus investigations of the nature and dimensions of the lunar core are much simpler than the manned missions to study and define lunar structural geology or stratigraphy.

The two tables clearly indicate what types of missions and experiments are necessary to provide meaningful data towards the solution of specific scientific problems; and further, these are related to a real model for which we have much knowledge—the earth. From the tables, it seems that a few specific experiments can be expected to provide much new data on lunar body properties and solve major problems on the internal structure of the moon. These experiments are required to operate over a time span of months, if not years, so they are best automated.

The real significance of the man in the lunar program is in surface exploration, where his knowledge, training, and versatility make him a better data collector than even complex machines.

Table 1. "What" and "why" of lunar mission planning

Earth	Moon	Remarks
1. Core		
The diameter of the core is approximately 6946 km. The seismic velocity discontinuity, marking the mantle–core interface, is at a depth of 2898 km. The core appears to have negligible rigidity in that it will not transmit the shear energy of transverse "S" waves, and it is therefore probably fluid. Seismic data indicate there may be a solid inner core within the outer liquid core. Suggested composition is iron with some nickel, but phase change of mantle material to a more dense form may be the cause of the observed phenomenon.	The mass diameter of the moon does not seem to allow enough density for anything but a very small earth-type core, and most probably there is none. There is certainly no data at the present time that are conclusive either one way or the other as to a core in the moon. Temperature curves for the lunar interior suggest that melting could occur at relatively shallow depth, say 300 km, to produce a large liquid core.	Seismic techniques offer the most direct attack on this problem. A gravimeter at the center of the lunar disk or on the limb, which reads variation in the tidal forces between perigee and apogee, would be useful. Magnetic data as to the existence of a secular lunar magnetic field would be most interesting. The minimum flight program must allow the emplacement of geophysical stations at several geographic positions. Simultaneous operation of stations is required. Seismic source may be required.
2. Mantle		
The mantle of the earth extends downward from the Mohorovicic discontinuity to the core. It appears to be relatively homogeneous; however, it does contain two second-order discontinuities, at depths of 413 km (the so-called 20-deg discontinuity) and 984 km, as evidenced by inflections in the velocity–depth curve. The best guess for the material of the mantle appears to be a magnesium–iron silicate comprising the rock types of peridotite or dunite, and with eclogite present in the upper mantle. Except for local pockets of magma, the mantle appears to be solid.	The best guess appears to be that the whole moon, except for the churned-up surface, is mantle-like in structure. But at the present time, there is not enough data to construct a model of the lunar mantle, its composition, radial structure, state, or dimensions. Both melting and differentiation seem to have occurred, but whether or not this was universal enough to have separated the whole moon, as with the earth, into core, mantle, and crust is not known.	Seismic techniques offer the most direct attack on this problem, with both gravity and heat flow observations providing useful information. Chemical information suggesting the degree of differentiation would be informative. The minimum flight program to study the lunar mantle would be very similar to one designed to study the core—fixed geophysical stations located at several lunar geographic positions and capable of simultaneous operation. A rover may be required to provide gravity and chemical data.
3. Crust		
The terrestrial crust is made up of two major units: (1) a basal unit extending upward from the Mohorovicic discontinuity that is approximately 5 km thick, bowed down under continents and up under oceans, and is basaltic in composition; and (2) the continental blocks. The continental blocks are approximately 28 km thick with local thickening to perhaps 40 km in mountain areas. The continental blocks are generally in isostatic adjustment with the mantle. Approximately 95% of the surface areas of the earth are covered by a few kilometers of sediment.	The lunar terra and maria seem to differ in composition and appearance, thus indicating some differentiation may have occurred on the moon to generate a lunar crust; however, the thickness, horizontal extent, and composition of this crust, if it does indeed exist as a discreet lunar body structure, cannot be predicted from present scientific data.	Seismic techniques to observe the dispersion, or variation of phase and group velocity of surface waves as a function of period, can provide important information here. Perhaps gravity surveys to determine a depth-of-compensation, as well as heat flow and active seismic studies, could be necessary. The minimum flight program requires several fixed geophysical stations. Active seismic and gravity studies can be accomplished best with a rover.

Table 1 (contd)

Earth	Moon	Remarks
4. Gravity field		
The gravitational field of the earth is a function of its size, shape, and mass distribution. In general, it varies from about 982.3 gals at the poles to 978 gals at the equator due to the oblate spheroid shape of the earth and centrifugal acceleration. Large young structural features on the earth, such as mountains and island arcs and trenches, may have Bouguer anomalies of several hundred milligals. Usually, the isostatic anomalies associated with these features are quite small, thus indicating some type of compensating mechanism. Isostatic anomalies to perhaps 50 mg are known, however.	The gravity field of the moon is about 157 gal. The centrifugal effect is very small, but frozen tidal effects may have affected the gross field. A 1-km bulge would represent 190 mg. The tidal effect for an unyielding moon as it goes from perigee to apogee is about 1 mg, but for a yielding fluid moon tides to 16 m could produce gravity variations of about 4 mg. The one-sixth gravity of the moon as compared to the earth may allow for larger masses of material to be piled on the lunar crust, thus producing large Bouguer anomalies. This effect will be a measure of lunar isostasy.	An absolute gravity instrument located at the center of the lunar disk or at the limb through at least one lunar period would provide data on the yielding of the moon to tidal forces. Mobile gravity surveys are necessary to define the anomalous components of the lunar gravity field.
5. Magnetic field		
Both axial rotation and a liquid core seem to be required for the generation of a planetary magnetic field. The geomagnetic field is made up of three parts: (1) a large secular part approximating a dipole situated in the core but missing the center of the earth by 1200 km (the magnitude of this field over the surface of the earth varies from about 60,000 to 70,000 gammas near the poles to 30,000 gammas at the magnetic equator); (2) an external field resulting from interactions of solar particles and field with the geomagnetic field; and (3) an anomalous part produced in crustal rocks by virtue of their magnetic properties.	It is unlikely that the secular component of the lunar magnetic field is greater than 100 gammas; however, large magnetic anomalies resulting from susceptibility contrasts and polarization by flowage, relic fields, or solar fields are possible, as are anomalies resulting from concentrations of ferromagnetic material such as in nickel–iron meteorites.	It is desirable to measure any effects of external fields from both the earth and the sun on the moon. It is desirable to measure the magnetic properties of oriented lunar rock samples. Seismic, gravity, and temperature-gradient data and chemical studies will all provide useful information. Collection of these data will require a roving vehicle.
6. Density		
The density of the crust is 2.8 g/cm^3, but the mean density of the whole terrestrial sphere is 5.5 g/cm^3, suggesting that denser material must be concentrated towards the center. Further, the moment of inertia of the earth is 0.334, as determined from the precession of the equinoxes, but for a uniform sphere of the same dimensions it should be 0.4, which again suggests that denser material must be concentrated towards the center. Numbers depicting the density distribution within the earth are bounded by the total mass of the earth, its moment of inertia and seismic data. Calculations of this type suggest a density of 3.3 g/cm^3 at Mohorovicic, and this increases more or less uniformly to a value of 5.7 g/cm^3 at the base of the mantle. At the top of the core, the value jumps to 9.5 g/cm^3, and this increases to a value of about 17 at the center of the earth.	The average density of the moon as determined from its mass and radius is 3.34 g/cm^3. The pressure at the center of the moon is only 46,500 bars, or as occurs at a depth of 150 km in the earth, and this doesn't seem to be sufficient to have generated the same type of internal structure as the earth. Chemical discontinuities, where the density increases substantially with depth, seem to be limited by the low average density and moment of inertia for the moon. There seems to be evidence for density concentrations in the lunar crust (mascons); also, the moment-of-inertia data suggests a density inversion may occur ($C/MR^2 = 0.60$, i.e., hollow moon). Melting in the moon could have separated the body into a core mantle and crust without violating the mean density.	Seismic techniques to determine the "P" wave velocity–depth function are required. Information on melting in the moon, as may be determined from "S" wave studies and heat flow studies may be required. The minimum flight program here calls for several fixed geophysical stations as required for core and mantle studies. Density contrasts in crustal material, i.e., mascons, can be studied in detail with a rover.

Table 1 (contd)

Earth	Moon	Remarks
7. Temperature		
The temperature gradient as measured within the crust averages about 30°C/km. This figure, along with measured thermal conductivity, gives an average mean heat flow of 1.2×1.0 cal/cm^2—s for both continents and oceans. It seems certain that this temperature gradient does not continue to great depth, and in fact most estimates place the temperature at a depth of 200 km between 1400 and 1750°C, with the temperature depth curve becoming almost flat below a depth of about 400 km. Calculations of the temperature at the center of the earth range from a high of about 5000°C to 2000°C, depending on the thermal model assumed. Calculations seem to indicate that only about 20% of the present-observed heat flow comes from original heat, i.e., say a molten earth; the rest appears to be due to radioactivity of rocks.	The temperature gradient and thermal conductivity for the moon have not been measured. Temperature curves for the lunar interior, considering a range of compositions and ages for models, have been calculated. In general, the hottest models allow for large-scale melting at relatively shallow depth, say about 300 km, while the coldest models allow for interior temperatures of only about 1000°C and perhaps localized surface melting. It seems likely that the heating of the moon by radioactive elements is still continuing. The flux of radiogenic heat away from the moon is probably of the order of only a few ergs/cm^2-s, and a measurement of this will be difficult.	*In situ* measurements in bore holes of the temperature gradient and thermal conductivity are required. Because of the length of time required to make measurements and the depth of measurement, fixed geophysical stations are required. These data from the fixed sites should be supplemented by heat flow data derived in roving vehicle traverses.
8. Radioactivity		
Radioactive elements within the earth possibly provide some of the fuel for endogenic processes, and they also provide the means for absolute age-dating of surface rock units. The distribution of the principal radioactive elements U^{235}, U^{238}, Th^{232}, and K^{40}, as well as some of the shorter life elements in the earth, cannot be directly measured; however, it is apparent that through the process of differentiation these elements have been concentrated in crustal rocks, especially the Sial rocks of the continents.	At the present time, there is no information about the amount or species of radioactive material in the mass of the moon. *Luna 10* did not indicate a gamma-ray count any higher than for normal basaltic rocks, so the lunar terra do not appear to be as radioactive as the earth's Sialic continents. A chondritic moon would have a radioactive content of 1.1×10^{-8} g/g uranium, 4.4×10^{-8} g/g thorium, and 8.0×10^{-4} g/g of potassium, and it should show far more endogenic activity than it does. If the moon is of chondritic composition, then heating has been gradual and is still continuing, and will reach its maximum some 2 or 3 billion yr in the future.	A gamma-ray experiment in an orbiter would provide some useful data on the concentration of radioactive elements in the surface of the moon. Geophysical studies at fixed sites to determine the heat flow and velocity-depth function of "P" waves and the transmissibility of "S" waves will provide interesting data. The degree of melting in the moon is of primary concern for understanding its past and present content and distribution of radioactive elements.

Table 1 (contd)

Earth	Moon	Remarks
9. Chemistry		
The average composition of the accessible portion of the earth's crust is approximately 50% oxygen, 26% silicon, 8% aluminum, 5% iron, 3% each for calcium, sodium, potassium, and magnesium, and 0.63% titanium. It should be observed that the atmosphere, the hydrosphere, the biosphere, and the crust contribute only about 1% of the total mass of the earth. Thus, the bulk composition of the earth is essentially that of the mantle and core. Meteorite data and certain geophysical observations suggest the earth has a periodtite mantle ana a nickel–iron core, with a bulk composition of approximately 28% oxygen, 13% silicon, 35% iron, 17% magnesium, 2.7% sulfur, and 2.7% nickel. Any phase-change hypothesis would of course alter these percentages closer to the composition of mantle material or even solar composition.	The composition of the material on the lunar surface, from *Surveyor* results, is basaltic, and, in general, it is similar to the average composition of the terrestrial surface. The average density of the moon suggests that it does not have the iron content of the earth, or the lunar mass must contain an anomalously high percentage of low-density materials that have not as yet been degassed. The possibility also exists that the apparent high density of the earth's core results from a phase change of magnesium–iron silicates and not a concentration of nickel–iron.	The average composition and mineralogy of the lunar surface must be determined. This will require sampling at a variety of lunar surface features and outcrops in the various geomorphic provinces of the moon. Obviously, this task will require a roving vehicle. These data in conjunction with fixed site geophysical data will permit calculations of the bulk composition of the moon.
10. Geomorphic processes		
Endogenetic processes, sometimes collectively referred to as diastrophism, operate within the earth to produce "constructional land forms," while exogenetic processes through weathering and erosion operate to sculpture and ultimately destroy the original constructional form. In the terrestrial environment of an atmosphere and abundant water, surface rocks are changed by chemical and mechanical processes called weathering. Weathered material may form a residual deposit, but usually agents of erosion—streams, glaciers, waves, wind, and gravity—accomplish loosening and transport of the accumulating material to an area of deposition. The erosional, residual, and depositional features produced on the surface of the earth by the forces of weathering and erosion are very diverse.	Endogenetic processes do not appear to have been as active on the moon as they have been on the earth. Very possibly the energy for the major constructional processes on the moon has come from large meteorite impact, and is therefore exogenetic in origin and in sharp contrast to the earth. Certainly there has been volcanism, and *Surveyor* results suggest considerable differentiation so endogenetic processes must have operated, but "constructional land forms" on the moon do not have a high correlation with terrestrial features. The key to exogenetic processes on the earth is the atmosphere and abundant water. These are absent on the moon, so the processes of weathering and agents of erosion there are not the same as for the earth. It would appear that the major processes operating to shape the surface of the moon are meteorite bombardment, solar radiation, gravity, seismic shock, and thermal shock. Considerable progress has been made in classifying lunar physiographic provinces.	The techniques of field geology offer the most practical approach for studying geomorphic processes. Field investigations will require an "on site" study of the various geomorphic provinces of the moon. The minimum flight program calls for both roving-vehicle and orbiter photographic data. Remote sensor data may be useful for mapping terrain units. Because of the number of sites that must be visited on the lunar surface, roving vehicles will play a very important part in the study of geomorphic processes.

Table 1 (contd)

Earth	Moon	Remarks
11. Structures		
Diastrophism has compressed and folded great wedges of sedimentary rock, formed linear igneous mountain belts, uplifted and lowered great tracts of the crust thousands of feet, and has apparently moved continental blocks thousands of miles. The processes of ocean-basin spreading and continental migration are being seriously studied. The crust of the earth has apparently been very mobile throughout geological time, and it is now broken into structural units that portray its origin and evolution. The study of terrestrial structural units and features has always represented the best effort from earth scientists in the sense that several different geological disciplines may be used to understand a particular problem; also, the field observations can only be made by a highly trained and experienced specialist.	The linear and arcuate structures that characterize the earth are generally replaced on the moon by circular structures. No chains of folded or batholithic mountains are evidenced, nor is there evidence of large horizontal and vertical faulting. Linear scars that radiate from some of the circular basins have been mapped, also rift zones marked by volcanism, such as the area from the Marius Hills on the south to Rumker on the north, which appears as an incipient "Mid-Atlantic Ridge." Although diastrophism has not been as dynamic on the moon as it has been on the earth, the lunar "crust" is very complex and formed of discrete structural units, and the study of the origin and evolution of these may prove important towards understanding geological processes on the earth.	The major structural units, faults, contacts, and lineaments on the moon will have to be mapped and studied by field geology techniques. Orbiters, rovers, and a variety of manned missions will be required. The investigation of lunar structures will involve a rather thorough program of surface exploration with roving vehicles.
12. Stratigraphy		
The sedimentary layers of the crust of the earth were deposited by the geological agents of running water, wind, glaciers, marine action, and gravity. Stratification of this material has usually resulted from changes in the rate, type or nature of the depositing agent, changes in source material, or changes at the site of accumulation. Consolidation of deposited material is accompanied by cementation, metasomatism, and other forms of diagenesis and metamorphism. The law of "faunal succession" based on biological change is used for determining the chronology of the earth's sedimentary record, and this has been selectively related to absolute age dating by radiological methods.	The time and rock stratigraphic units presently defined for the lunar surface were derived from telescopic observations of surface morphology and albedo. At the present time, the major stratigraphic units are, from oldest to youngest, the Imbrian System, which has now been broadened to include the Procellarum Group, the Eratosthenian System, and the Copernican System. Several rock stratigraphic units have been defined within this broad time stratigraphic framework. Stratification is not as pronounced as on the earth, and no color-banded formations and obvious albedo differences signifying layering are observed in vertical exposures. Witness the thousands of feet of vertical exposure in the rim of the crater Copernicus and other craters.	Field mapping will have to include vertical sampling by drilling as required. The investigation of lunar stratigraphy will interrelate and be carried on contemporaneously with studies of lunar structures, geomorphic processes, rocks, minerals, etc. The flight program will need to include orbiters, rovers, and a variety of manned missions. Certainly surface exploration with roving vehicles is required.

Table 2. "How," "where," and "when" of lunar mission planning

Mission type	Principal scientific experiments	Secondary scientific experiments	Remarks
1. Nature and dimensions of lunar core			
Fixed geophysical stations.	Three-axis seismometer. Tidal gravimeter (absolute).	Heat flow studies at fixed geophysical stations.	A minimum of four seismometers on the front face of the moon should be adequate. One of these should be on terra in the southern region, one on the western limb in Oceanus Procellarum, one in Mare Serenitatis, and one in Sinus Medii. These locations are adequate for the gravity experiment. If the moon is aseismic, an artificial source in the northern hemisphere will be required. Simultaneous operation is required.
2. Nature and dimensions of lunar mantle			
Same as above.	Same as above.	Same as above.	Same as above.
3. Nature and dimensions of lunar crust			
Same as above.	Same as above.	Same as above. A rover carrying several seismic sources to work out from fixed geophysical station. Rover gravity studies.	Same as above with emphasis on the observation of surface seismic waves.
4. Shape and magnitude of lunar gravity field (shape of the moon)			
Rover.	Gravimeter. Ranging.	These data will be useful for defining the lunar ephemeris and motions, and may be related to objectives 1, 2, and 3.	Will investigate gravity anomalies in the crust and provide data for isostatic computations and locating frozen tides.
Orbiter.	Radar altimeter. Ranging and orbit parameters.		Will define the shape of the moon and locate large gravity anomalies
Fixed geophysical stations.	Tidal gravimeter (absolute).		Will provide a base for absolute gravity and its variation.
5. Shape and magnitude of lunar magnetic field			
Rover.	Magnetometer (vector).	Observation of electric fields.	Will define anomalies in the lunar magnetic field and locate their source.
Fixed geophysical stations.	Magnetometer. Various fields and particles detectors.		Will define the magnitude and fluctuation of any lunar field.
6. Vertical and horizontal density distribution			
Fixed geophysical stations.	Same as for objectives 1, 2, and 3.	Relates to objective 4.	Same as for objectives 1, 2, and 3.
Rover.	Gravimeter.		Will locate horizontal density contrasts.
7. Vertical and horizontal temperature distribution			
Fixed geophysical stations.	Drill. Thermal probe.	An orbiter infrared radiometer experiment may provide interesting data. A thermal probe on a rover may be useful.	The drill hole should be at least 3 m deep. A greater depth, say 10 m, is desirable. Observations should continue through at least a lunation. The previously-mentioned seismic sites would be suitable for this measurement.

Table 2 (contd)

Mission type	Principal scientific experiments	Secondary scientific experiments	Remarks
8. Distribution of radioactive elements and age dating of lunar rocks			
Sample return.	Sample acquisition and storage.	The techniques of lunar field geology will be important to this objective since they will define the stratigraphic relationship of layered rocks. A rover may be used to acquire samples for sample return mission.	This probably implies manned mission since the sample needs to be rationally selected.
Orbiter.	Gamma-ray spectrometer.		This will give the distribution of radioactive material over the lunar surface to a depth of perhaps a few centimeters.
Rover.	Gamma-ray spectrometer. Drill or surface samples.		To investigate the radioactivity of specific sites.
Manned.	Age dating and stratigraphy by field geology techniques. Manned rover.		The sample will probably have to be returned to earth for analysis. Sample selection and ascertaining its stratigraphic relationship requires a trained geologist.
9. Composition and distribution of lunar material			
Sample return.	Sample acquisition and storage.	The techniques of lunar field geology will define the interrelationship of rock units. The composition of the interior of the moon will have to be extrapolated from geophysical data and surface chemistry. A rover may be used to acquire samples for sample return mission.	This probably implies manned mission since the sample needs to be rationally selected.
Rover.	Drill and sample preparation. X-ray spectrometer. X-ray diffractometer.		Provides the capability to sample large areas of the moon. Acquired samples can be delivered to a pick-up point for earth return.
Manned.	Sample acquisition. Field geology. Manned rover.		Provides the capability for detailed sampling of limited areas of the moon.
10. Endogenetic and exogenetic processes and features of the moon			
Orbiter.	High-resolution stereo and color photography.	The techniques of lunar field geology are important to this objective. This objective is tied in with objectives 9, 11, and 12. A lunar base from which detailed studies could be carried out will eventually be required.	It is desirable to cover as much area as possible at 1-m resolution.
Manned.	Field geology. Manned rover.		Manned exploration of the various physiographic provinces is required.
Rover.	High-resolution camera.		Supplement manned observation in rough or difficult-to-reach areas.
Fixed geophysical station.	Camera. Micrometeoroid detector. Fields and particles detectors.		Observe those phenomena on the lunar surface that operate slowly and so may not be apparent to short stay-time missions.
11. Structural units of the lunar crust			
Orbiter.	High-resolution stereo and color photography.	The techniques of field geology are paramount for this objective. This objective is a rather fundamental one to earth sciences and so it is related to many of the other objectives.	It is desirable to cover as much area as possible at 1-m resolution.
Manned.	Field geology. Manned rover.		Manned investigation of the various structural units and field mapping.
Rover.	High-resolution camera. Drill and sample preparation. X-ray spectrometer. X-ray diffractometer. Petrographic microscope.		Supplement manned observations in rough or difficult-to-reach areas.
Rover (geophysics).	High-resolution camera. Magnetometer. Gravimeter. Active seismometer.		Provide profile data over extended areas or geophysical data in conjunction with manned missions.
Lunar base.	Field geology. Manned rover. Deep drill.		The very detailed study of an interesting lunar site. Considerable maturity in lunar geology is required for site selection.

Table 2 (contd)

Mission type	Principal scientific experiments	Secondary scientific experiments	Remarks
12. Stratigraphic sequence for lunar rocks			
Orbiter.	High-resolution stereo and color photography. High-resolution oblique photography.	The techniques of field geology are paramount for this objective. This objective relates strongly to objective 8.	It is desirable to cover as much area as possible at 1-m resolution.
Manned.	Field geology. Manned rover.		Investigation and mapping of lunar outcrops.
Rover.	Same as above		Supplement manned observations in rough or difficult-to-reach areas. Provide geophysical support.
Lunar base.	Field geology. Manned rover. Deep drill.		The very detailed study of a significant lunar site.

N 69-19436

XXVI. Technical Facilities

FACILITIES OFFICE

A. Variable Optical Techniques Applied to Solar Simulators, *M. N. Wilson and R. R. Beal*

1. Introduction

The extensive modifications to the 25-ft space chamber at JPL, performed during 1966 and 1967, resulted in the creation of a solar simulation scheme that was capable of producing a uniform (±5%), well-collimated (±1 deg) beam of radiant energy on a 15-ft-diam circle within the 25-ft test volume of the space simulator. This system drew upon the experience gained from the earlier JPL 10-ft simulator optical system and used as a source the brightest xenon compact arc lamps (20 kW) that were then available.

In view of past optimism and general experimental unknowns regarding bulb performance, a very conservative design approach was adopted that resulted in the system actually being capable of producing 290 W/ft^2 (with no reserve) or an operational level of about 175–190 W/ft^2 over a 15.5-ft-diam by 25-ft-high test volume.

2. Design and Characteristics

The 37 20-kW xenon compact arc lamp energy sources (Fig. 1) are arranged in a hexagonal pattern in the lamp basement and project, via 27-in. hyperbolic reflectors, the resultant radiant energy onto the front face of the optical mixer elements in a typical gaussian distribution. The front face of the mixer consists of 19 circular lenses and is followed by a second plane of 19 hexagonal lenses. Both are closely packed and together provide 19 parallel but separate light paths through the optical mixer.

Each path is at a slightly different skew angle with respect to the optical axis of the system so a slight amount of power is required at the penetration window to cause the 19 systems to superimpose in the test volume, thus minimizing skirt effects and contributing to the system efficiency. The optical mixer, or integrator, is the essential component that causes the images to superimpose, thereby averaging the various energy contributions of each of the 19 paths so as to produce a single uniform beam. A

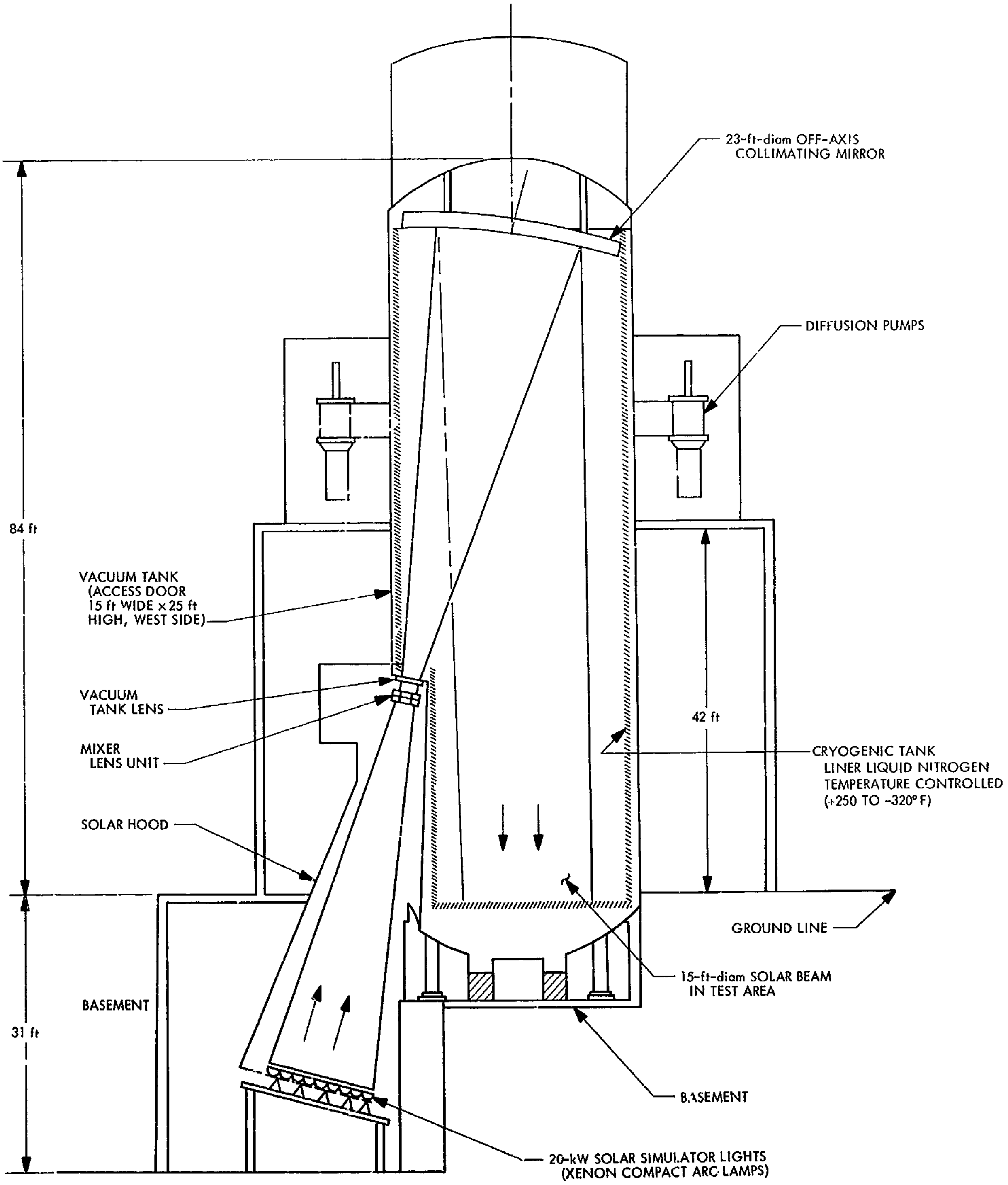

CROSS SECTION (LOOKING EAST)
NOT TO SCALE

Fig. 1. Existing 15-ft-diam earth-intensity sun of 25-ft space simulator

detailed explanation of the optical mixer principle is given in Ref. 1.

The 23-ft temperature-controlled mirror in the top of the vessel serves to reverse the direction of the projected light beam and produces parallel (±1 deg) rays since the mixer, or source of the incident light, is located approximately at the focal point of the mirror. The 23-ft size was selected to handle a future 20-ft beam if it were ever installed in the simulator. Room was also provided in the basement for 24 additional lights should the increased energy for a larger beam be required.

The present 37 20-kW xenon compact arc lamps, when in a "new" condition, will produce 290 W/ft^2 maximum over a 15.5-ft-diam circle. Since the images of all 37 lamps are superimposed at the mixer face, it is clearly possible to reduce beam intensity by either turning off individual bulbs or reducing power levels until the desired intensity is reached. It should be noted, however, that these actions do not change the uniformity, collimation, size, or any other geometric characteristic of the beam. Only the intensity is affected. Thus, the existing system could, potentially, simulate solar radiation rather accurately from near Venus intensity to essentially zero intensity.

The system is rather sensitive to the spacing between the mixer lens elements. The image of the lamp bank is (nominally) contained within the second lens. If these lenses are separated further, this image overfills the second lens and energy is lost; i.e., a portion of the energy of the source is projected as a smaller beam of the same intensity. If these lenses are brought nearer to each other, the image-forming rays of the lamps remain within the second lens but the projected beam size is rapidly increased with resulting loss in maximum intensity. Second order effects, resulting from lens adjustment, are also important as regard changes in uniformity and skirt losses. Thus, for all practical purposes, the system is essentially one of fixed geometrical characteristics. Only major physical changes to the simulator can produce beam sizes other than that of the basic design size.

The capacity of the JPL 25-ft space simulator is such that it can physically and thermally accommodate a 20-ft spacecraft, should it be required. Also, several potential missions have been considered in which the *Titan* is used as a launch vehicle, utilizing its 10-ft-diam shroud. The optimum optical system, then, was one that could cover, without change, this 10- to 20-ft range, with up to Mercury intensity (900 W/ft^2) on the smaller size. Simple area-intensity calculations suggest that sufficient power is available but techniques to produce the desired results had not been developed.

The operational usefulness of the simulator could be increased many fold if extensive modifications were not required for each different test requirement but, instead, a simple remote optical adjustment could be accomplished.

3. Studies

A study[1] was made to investigate the limitations and possible changes to the mixer–projection system to see if a favorable solution was feasible.

It was determined early in the work that systems of 3- or 4-lens mixers offered no advantage over a 2-lens system, that all were essentially fixed geometry systems, and that within reasonable bounds of performance the mixer could not be increased in physical size. The conclusion, as related to the present optical system, is that it cannot be made to reduce the diameter of the projected beam of light while increasing its intensity proportionally.

Later work incorporated additional lenses in the optical path just behind a relocated mixer–integrator so as to take advantage of the 40-in.-diam penetration of the simulator vessel. The ratio of 2:1 (between the 40-in. penetration lens and the 20-in. mixer output) produced the change in the angular subtense of the lens necessary to achieve the increased intensity over the smaller diameter that was anticipated and desired (Fig. 2).

Detailed investigation and analysis of the new system, using computer-plotted ray-tracing techniques, has finally evolved a two-part system: a mixer assembly as the optical integrator and a variable section composed of four separate lenses. Each element of this second section is shaped to optimize uniformity of the projected, variable diameter beam. The center two elements are movable (remotely or manually) to vary the beam diameter by a factor of 2 with the resultant intensity increase desired (Fig. 3).

Any reasonable 2:1 diameter ratio (i.e., 20/10, 16/8, 12/6, etc.) can be produced by simple changes of the mixer elements only, utilizing the same variable optical elements for the 2:1 diameter ratio control. The system further provides a real secondary image where aperture controls may be installed should it be desirable to shape the beam for any special test requirement.

---

[1] Under contract with Optical Research Associates, Pasadena, Calif.

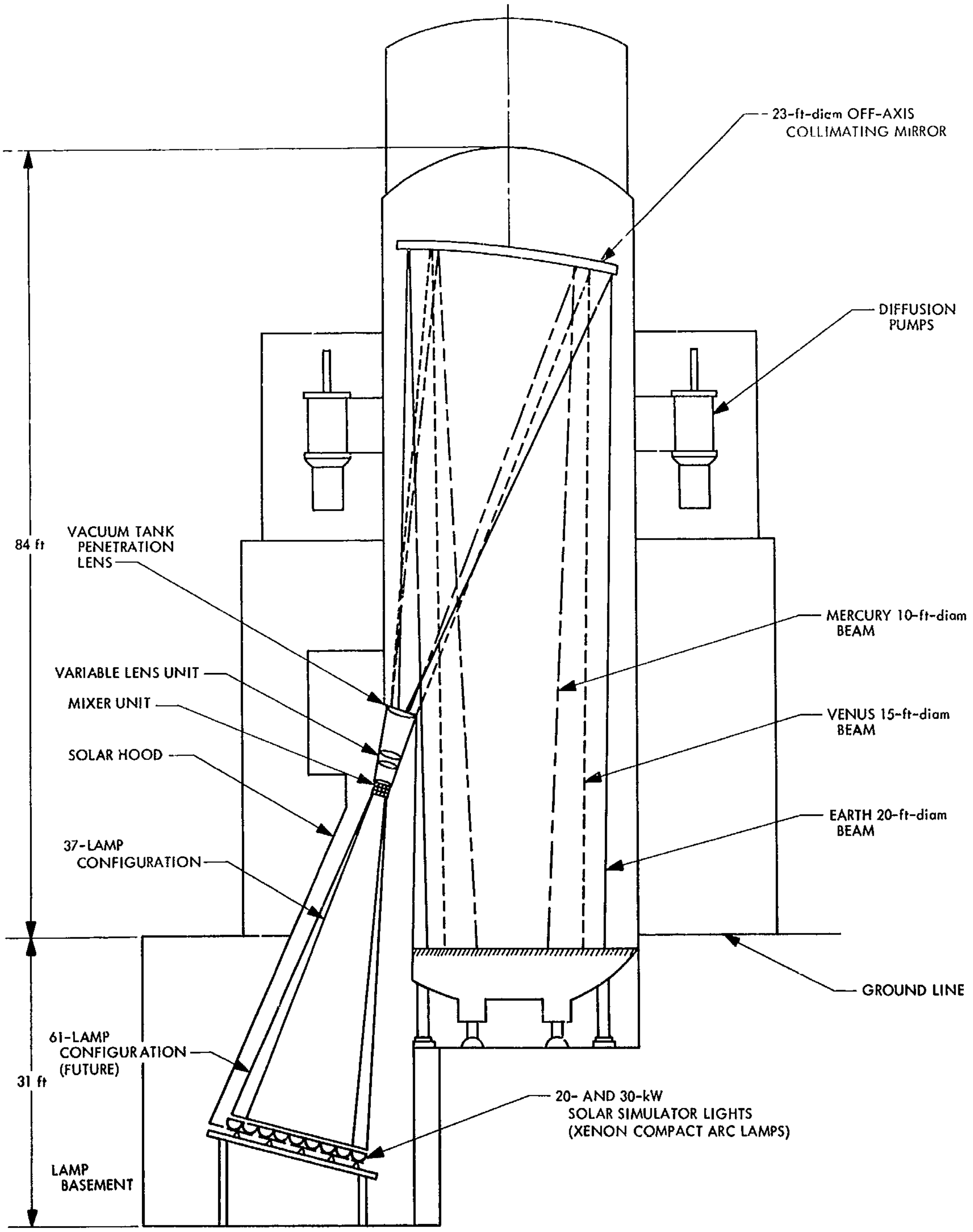

Fig. 2. Simulation capability of 25-ft space simulator with variable optics

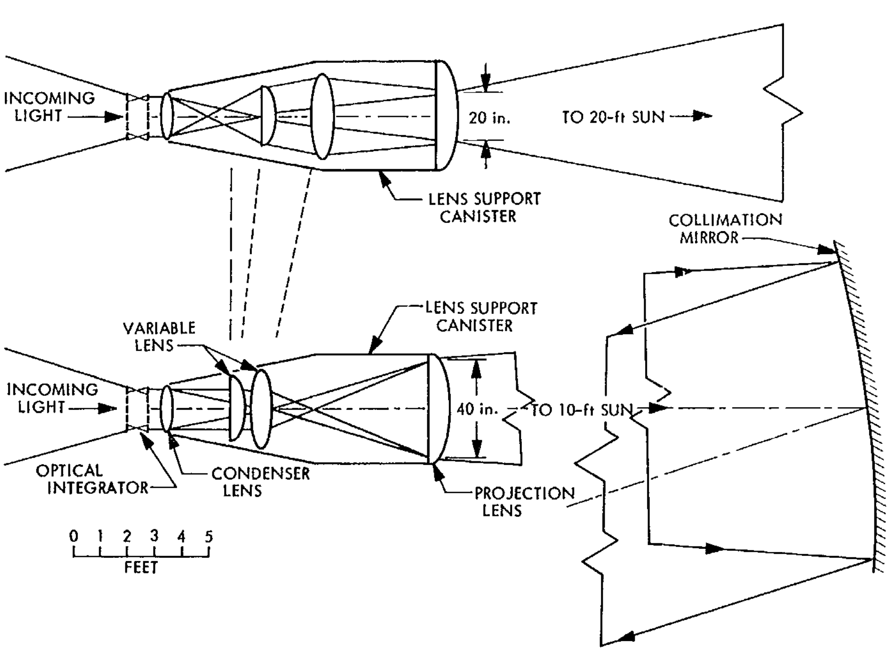

Fig. 3. Variable optics for solar simulator

4. Performance

The optical systems described are capable of the following performance:

Number of Lamps	Mercury intensity 900 W/ft^2		Venus intensity 270 W/ft^2		Uniformity, %
	Diameter, ft	Collimation, deg	Diameter, ft	Collimation, deg	
61	10.0	±1.9	20.0	±1	±3 or less
37	7.8	±1.9	15.6	±1	±3 or less
19	5.6	±1.9	11.2	±1	±3 or less

The 19- and 37-lamp systems are within the present lamp/electrical power limit for the facility, and would not entail any mechanical changes to the basic facility. The 61-lamp system requires the addition of 24 new 30-kW lamps and reflectors as well as the optical modifications. It is clear, from the design of the system, that any intensity level from maximum to zero, is available at any diameter by simply turning off bulbs or reducing their power level. Any intermediate diameter is also available if desired.

The efficiency of the present system very closely approaches 50% (ratio of beam energy to energy projected onto mixer face). Spectral calculations of absorptance, utilization of single layer lens coatings, and considerations of the spectral output of the xenon lamps all combine to project about a 20% loss of energy in the beam over that originally transmitted due to the additional lenses. This represents about 10% of the input energy to the system and can be more than offset by operation of new style bulbs at 25 kW. The selective infrared absorptance of the several lenses reduces the operating temperature of the penetration lens over the present system, thus permitting more optimum sealing. The lens shape (plano-convex) also contributes to the strength of the penetration lens over the current essentially plane window, even though the diameter is doubled.

Reference

1. Bartera, R. E., and Barnett, R. M., *Development of the Jet Propulsion Laboratory Solar Simulator, Type A,* Technical Report 32-638. Jet Propulsion Laboratory, Pasadena, Calif., July 15, 1964.